UNIVERSITÀ
DEGLI STUDI
FIRENZE

DOTTORATO DI RICERCA IN SCIENZE DELLA TERRA

CICLO XXXI

COORDINATORE Prof. Lorella Francalanci

Modellazione 3D di pareti rocciose
finalizzata alla valutazione della pericolosità da caduta massi

Settore Scientifico Disciplinare GEO/05

Dottorando
Dott. Marini Federico

Tutore
Prof. Gigli Giovanni

Coordinatore
Prof. Francalanci Lorella

Anni 2015/2018

Table of contents

List of symbols

α :	dip direction (°)
β :	dip (°)
σ_α :	standard deviation of dip direction
σ_β :	standard deviation of dip
α_{slope} :	dip direction of the slope (°)
β_{slope} :	dip of the slope (°)
α_{disc} :	dip direction of the discontinuity (°)
β_{disc} :	dip of the discontinuity (°)
α_{inters} :	dip direction of the intersection (°)
β_{inters} :	dip of the intersection (°)
φ :	friction angle (°)
c :	cohesion (Pa)
K :	camera intrinsic parameter
c_x :	x optical centre coordinate (pixel)
c_y :	y optical centre coordinate (pixel)
F :	focal length (mm)
f_x :	focal length along x-axis (pixel)
f_y :	focal length along y-axis (pixel)
p_x :	length of the pixel along x-axis (mm)
p_y :	length of the pixel along y-axis (mm)
s :	skew coefficient
k_1, k_2, k_3 :	radial distortion coefficients of the lens
p_1, p_2 :	tangential distortion coefficients of the lens
L :	persistence (m)
σ_L :	standard deviation of persistence
E_L :	mean persistence (m)
λ :	frequency (nr of discontinuities/m)
σ_λ :	standard deviation of frequency
δ :	intersection angle, i.e. the angle between the observation plane or bore hole and the individual joint for Terzaghi weighting
A :	area (m^2)

L : length of the measured section along the core or scanline (m)

wJd : weighted joint density (nr of joints / m or nr of joints / m^2)

ϕ_{peak} : peak friction angle (°)

ϕ_r : residual friction angle (°)

ϕ_b : basal friction angle (°)

JCS : Joint Compressive Strength (MPa)

JRC : Joint Roughness Coefficient

A : wave amplitude

D : distance device-target (m)

n : phase ambiguity; nr of phases of em radiation

N_{pf} : number of poles satisfying plane failure conditions

I_{wf} : number of intersections satisfying wedge failure conditions

N_{bt} : number of poles satisfying block toppling conditions

I_{bt} : number of intersections satisfying block toppling conditions

N_{ft} : number of poles satisfying flexural toppling conditions

N : total number of poles

I : total number of intersections

W : weight (N)

σ : normal stress (Pa)

τ : shear stress (Pa)

σ' : effective normal stress (Pa)

τ' : effective shear stress (Pa)

ψ_p : inclination of the sliding plane (°)

$\hat{v}_1$: unit vector normal to joint plane directed towards the block

$\hat{s}$: sliding direction vector

$N_{\perp}$: normal component of the reaction forces (N)

JP : Joint Pyramid, block which faces are represented by joints

EP : Excavation Pyramid, the half-space constituted by rock

BP : Block Pyramid

γ_w : unit weight of water (9.81 KN/m^3)

h_w : vertical height of water (m)

r : Schmidt rebounds on wet weathered joint surfaces

R :	Schmidt rebounds on dry unweathered joint surfaces
C :	empirical fitting parameter C
θ^* :	inclination of the individual line segments forming the profiles of a joint (°)
θ^*_{max} :	maximum apparent asperity inclination (°)
L_0 :	total length of the profile (m)
L_{θ^*} :	length of the profile steeper than θ^* divided by the total length of the profile (m)
C :	dimensionless fitting parameter, calculated via a non-linear least-squares regression
A_0 :	total surface of the area of the discontinuity (m^2)
A_{θ^*} :	area of the discontinuity steeper than θ^* divided by the total area (m^2)

1. Introduction

Rock slope instabilities represent a major hazard for human activities often causing economic losses, property damages and maintenance costs, as well as injuries or fatalities. Rock slope stability represents so one of the most important issues in mountain areas and mines. Hoek (2000) reported, in fact, that, while rockfalls along highways and railways in mountainous terrains do not pose the same level of economic risk as large-scale failures (which can cause the closure of major transportation routes for several days), the number of people killed by rockfalls tends to be of the same order as people killed by all other forms of rock slope instability. Rockfalls are a great threat for railways and motorways and so the risk zonation along infrastructures has been largely studied (Pfeiffer & Bowen, 1989; Giani, 1992; Agliardi & Crosta, 2003; Dorren, 2003). Indeed, for this reason many classification systems of the risk along transportation routes have been produced (RHRS Rockfall Hazard Rating System FHWA; Pierson et al., 1990; Franklin et al., 1997; Youssef et al., 2003; Budetta, 2004; Santi et al., 2009), in order to give a tool for decision makers of the local transportation offices. The approach for the rockfall hazard classification system is useful also to describe the rockfall hazard along other linear infrastructure, such as pipeline (Porter et al., 2002). The assessment of rockfall risk along roads and pipelines requires the evaluation of the rockfall hazard, besides the vulnerability and the value of the infrastructure.

Rock slope issues represent one of the greatest risks in open pit mines (Hoek & Bray, 1977; Girard & Hugh, 2000; Miller et al., 2000; Whyatt et al., 2004; Dhillon, 2008; Vaziri, 2010; Wyllie & Mah, 2014; Duncan, 2015); for this reason, mining companies have a great concern on safety, in order to avoid economical losses and human lives casualties. According to NIOSH (US National Institute for Occupational Safety and Health), slope failure accidents were responsible for about 12% of U.S. surface mine fatalities from 1995 to 2001 (Girard, 2001) (Figure 1) and 13% in 2011-2015 period (Figure 2). Slope instabilities mostly correspond to rock slope instabilities because of the higher velocity of the movement in rock slope than in soil slope. Cake diagram of letter b in Figure 1 split the number of casualties by extracted commodities. Stone, metals and coal can be roughly associated to rock slope pit, while gravel and sand to soil slope. Although extracted raw material are different by geological setting, the raw material extracted in open pit mines and quarries in the whole USA can be considered globally representative of the risk affecting mining activities. Higher velocity means higher vulnerability, beyond increasing kinetic energy. Nowadays, the high level of automation in mining makes the majority of the fatalities related to issues related to the plants (powered haulage and machinery accidents are responsible for the 27% and 26% respectively, according to Girard, 2001); the second place is then occupied by fall or slip from heights (15%). Slope instabilities represent the third most common cause of fatalities, exceeding also the number of fatalities due to explosions because although blasting is a very risky activity, it involves a small number of workers and has a planned timing, while the fall of material from rock slope can be unexpected.

Mining activities have represented one of the main industrial activities in Australia since the goldrush in 1850s and it is a significant primary industry and contributor to the Australian economy and for the economy of New South Wales too. As regarding the only New South Wales, MacNail (2008) reports the statistics of casualties in open pit mines. On 595 casualties occurred in 1957-2007 period, 40 (7%, see Figure 3) are represented by falls of objects from the top, mostly constituted by falls of blocks, exceeding the number of casualties due to explosions. On the whole Australia (MacNeil, 2008) the fall of blocks is responsible for 16 of the 139 casualties (12%) occurred in 1998-2007 period. As for USA statistics, the number of casualties appears also more relevant if casualties related to machineries and facilities are not considered. Rock slope stability issues in open pit mines can be reduced by 1) a safe geotechnical design of the berms; 2) a secondary support or rockfall catchment systems; 3) a monitoring system for advance warning of impending failures.

Large Open Pit Mine Project (LOP; Read & Stacey, 2014), in fact, underlined the role of geotechnical, geostructural and hydrogeological characterisation for the correct design of open pit (Figure 4). Rock mass

characterisation is so a big issue for open pit mines and quarries management, as for transport infrastructure too.

The development of digital photogrammetric (Chandler, 1999) and laser scanning (Lichti, 2000; Cowan et al, 2002; Slob & Hack, 2004) methods have allowed since late 90s the reconstruction of 3D models of the slope by mesh and point clouds (Wolf & Dewitt, 2000; Sturzenegger & Stead, 2009b). Several authors have recognized the potential of these techniques for rockslope characterisation (Feng & Röshoff, 2004; Monte, 2004; Haneberg et al., 2006; Trinks et al., 2006; Redfern et al., 2007; Tonon & Kottenstette, 2007; Jaboyedoff et al., 2008; Lato et al., 2009). These remote sensing methods have the following strengths:

- accessing parts of the rock walls inaccessible to operators;

- surveying a larger part of the rock wall, providing so more representative statistical samples;

- reducing the risk of the operators because the survey can be carried out in a remote safe location protected from rockfalls;

- creating a 3D model of the slope;

- allowing discontinuity orientation measurements when conventional compass clinometer readings are not reliable because of magnetic orebodies (especially in ore minerals mines this is not a rare occurrence).

While in the past the geostructural survey of the rock mass was uniquely carried out by the traditional methods with the compass clinometer, accessing directly to the rock wall (ISRM, 1978), nowadays two main different levels of automation can be conceived, to extract the most relevant rock mass geomechanical characteristics, hidden in the point cloud. Discontinuity extraction can be performed, in fact, by manual and semiautomatic methods.

Manual discontinuity extraction consists in the drawing of traces and planes of the discontinuities by an operator. The accuracy and the detail of this approach depends on the quality of the digital data and on the skill of the surveyor. Indeed, an optical support is required.

The creation of the 3D model of the rock slope has led in recent years the creation of many codes that permit the semiautomatic extraction of discontinuities (Jointmetrix3D; Surpac; 3DM Analyst; Split-FX; 3DGeomec; Coltop3D (Jaboyedoff et al., 2007); DiAna (Gigli & Casagli, 2011); DSE (Riquelme et al., 2016a; Riquelme et al., 2016b); Facets (Dewez et al., 2016); I-Site Studio (Olsen et al., 2009)). These codes present the advantages of reducing the data from user-related bias and are less time-consuming than traditional geostructural survey, especially facing with large open pit mines or large natural slope too.

The knowledge of the dip and dip direction of the discontinuity and of slope allows to predict the failure modes of the slope by the kinematic analysis, using stereographic projections (Markland, 1972; Goodman, 1976; Hocking, 1976; Hoek & Bray, 1981; Matheson, 1983; Hudson & Harrison, 1997). Because kinematic analysis is related to the local orientation of the slope, point clouds carried out by laser scanner or photogrammetric survey can be processed in order to obtain a susceptibility map for each failure mode, automatically calculating the intersection of the discontinuities with the local orientation of the slope by a code developed for 3D kinematic analysis, DiAna-K (Gigli et al., 2012).

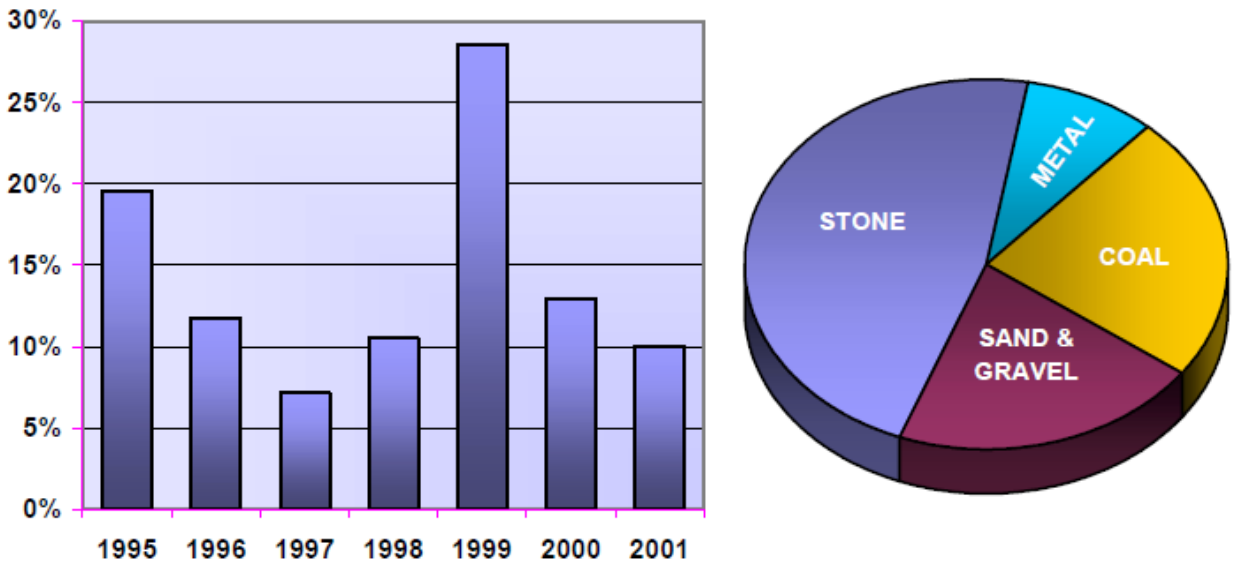

Figure 1 - a) Slope instability incidence on fatalities in open pit mines in USA in 1995-2001 period; b) percentage of fatalities for type of commodities in USA in 1995-2001 period. From Girard (2001)

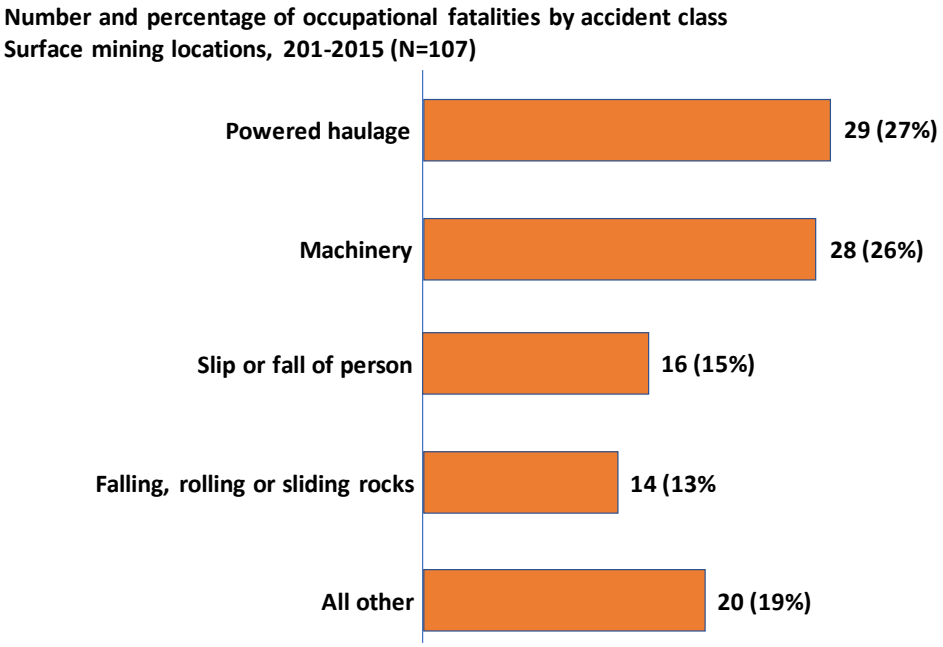

Figure 2 - Incidence of falling of material on the number (107) of fatalities in open pit mines in USA in 2011-2015 period, clustered by type of accident

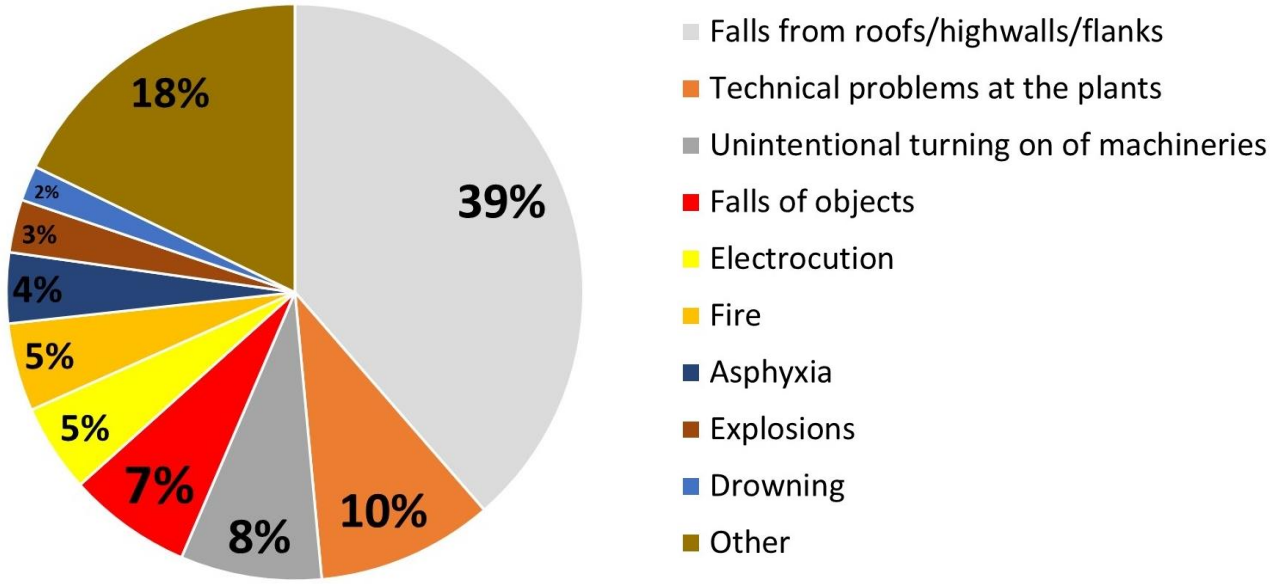

Figure 3 - Overview of the causes of workplace deaths in open-pit mines for New South Wales in 1957-2007 period. From MacNail (2008)

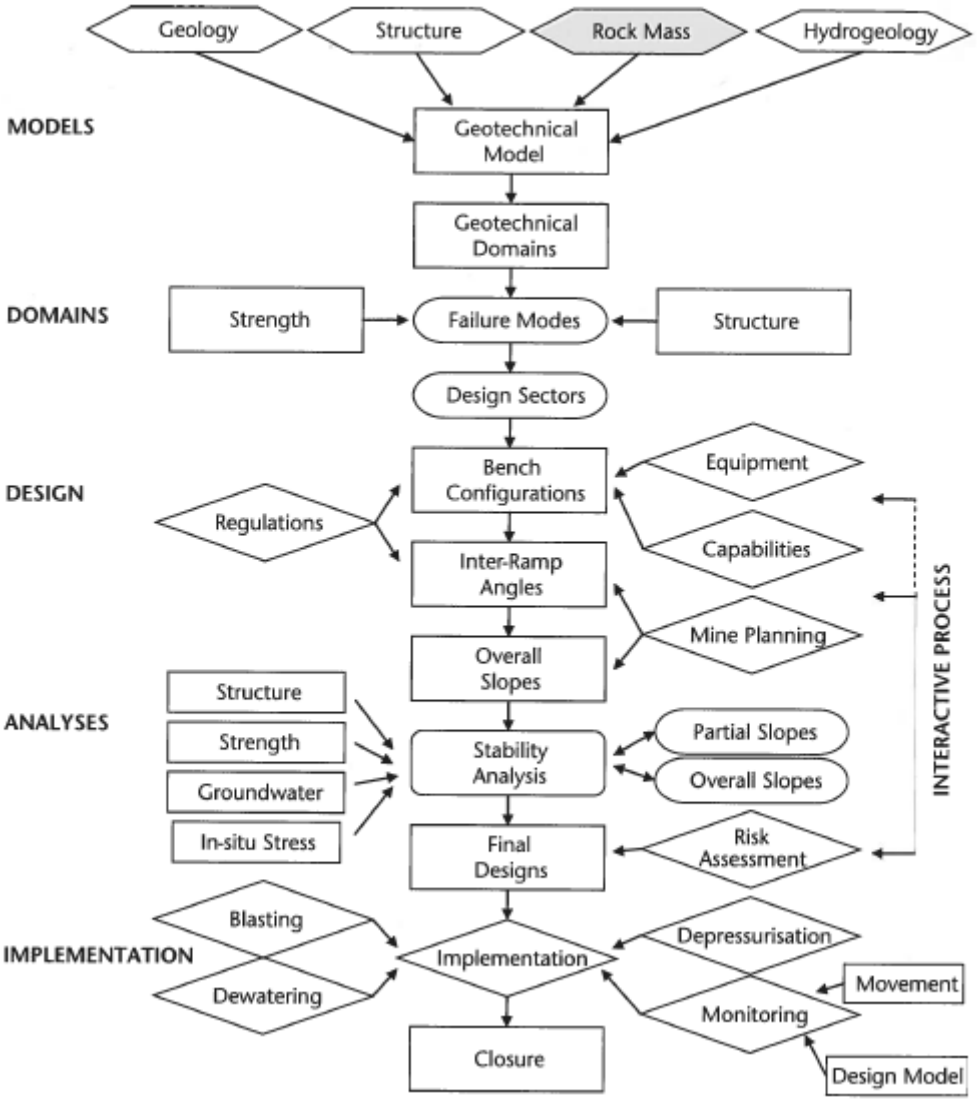

Figure 4 - Rock mass characterisation within the slope design process. From Read & Stacey (2014)

The code SiroModel for polyhedral modelling of rock mass structure developed by Jing (2002), Lu (2002) and Elmouttie et al. (2010) allows to compute the vertices, edges and therefore the faces resulting from the intersections of all *finite persistence* polygons defined in the model. With this information, the polyhedra (rock blocks) that form from the faces can be computed, evaluating the shape and the volume of the removable blocks.

The present research has been carried out in cooperation with the Department of Civil Engineering, University of Newcastle - ARC CGSE (Australian Research Council Centre of Excellence for Geotechnical Science and Engineering), NSW, Australia, where the Ph.D. Candidate was host for a 6 months period during the course of study, under the Supervisor of Associate Professor Anna Giacomini, Co-Supervisor of the thesis. Department of Civil Engineering of the University of Newcastle - ARC CGSE has been working for a number of coal mines. This research has made use of manual and semiautomatic discontinuity extraction methods in two case study coal mines, located within Newcastle Coal Measures, New South Wales, Australia and then evaluated the rock slope stability by kinematic analysis and polyhedral modelling. The goals of this research are so the following:

- increasing the knowledge about rockfall hazard assessment at the base of a sub-vertical rock surfaces in surface mine by remote geostructural survey data;
- comparing recent advanced numerical tools for the detection of the structures in the rock mass in order to evaluate pros and cons of manual and semiautomatic discontinuities extraction methods and understanding their reliability;
- analysing the output of DiAna-K for the 3D kinematic analysis and SiroModel for polyhedral modelling of rock mass in in order to provide parameters necessary for the rockfall analysis (susceptibility of the rock mass for each failure mode, volume and position of the instable blocks). Volume and position of the unstable blocks within the slope are fundamental information for any further eventual modelling of the rockfall simulation, not addressed in this research.

Two open pit coal mines constitute the case studies for this research. The photogrammetric survey and the geomechanical characterisation of overall three highwalls overlying service roads and affected by rockfall have been carried out; the studied rockslope is of case study 1 mine is constituted by two perpendicular highwalls, while the rockslope of case study 2 mine by one highwall. For each highwall, the first step has been to carry out the photogrammetric survey of the slope and a camera Canon mod. EOS 7D with lens with focal length of 50 mm has been used for this purpose. The stereopairs has been then processed to get 3D images of the slope using SiroVision Datamine (CSIRO) software. Then, the 3D models of different stereopairs of the same highwall have been then merged into a single mosaic. Overall three mosaic of the 3D model of the highwal have so been obtained since 12 and 8 photographs for the two highwalls of case study 1 mine and 8 photographs for the highwall of case study 2 mine. In each case, the point cloud of the slope has been extracted.

The geostructural surveys have been carried out using software for manual and semiautomatic methods for discontinuities extraction. SiroJoint code has been used for the manual extraction of the discontinuities and has allow to survey the discontinuities outcropping as planes and as traces. The point clouds have then allowed to extract the discontinuities outcropping as planes thanks to the code for the semiautomatic extraction. Three codes for the semiautomatic extraction of the discontinuities have been used: Maptek I-Site Studio, DiAna (Gigli & Casagli, 2011), and Facets plug-in of CloudCompare (Dewez et al., 2016). These codes require different data input. I-Site Studio allows to identify the planes since the drawing of a planes on the surface and the indication of minimum number of point and the value of the difference of the angles. DiAna requires the selection of a sub-set of the point cloud by the selection of a searching cube and a standard deviation treeshold for the identification of the groups of points constituting a plane and the maximum co-planarity angle. Facets is a plugin allow to extract the planes since the maximum co-planarity angle, the maximum distance of the points from the regression plane, the minimum number of points per facet and the maximum edge length.

Discontinuities datasets have been plotted into polar stereoplots and have provided the values of kinematic indices for each failure mode (plane failure, wedge failure, block toppling, flexural toppling) performing 2D and 3D kinematic analysis. 2D kinematic analysis has been performed on the stereoplots of the discontinuities extracted by SiroJoint, I-Site Studio, DiAna, and Facets, given an average slope orientation, described for the two case studies in Chapter 6 and in Chapter 7. The comparison of the values of the kinematic indices for plane failure, wedge failure, block toppling, and flexural toppling has shown that the values for failure mechanisms involving planes only (plane failure and flexural toppling) are higher in case of semiautomatic methods of discontinuities extraction than in case of manual methods. These differences are related to the traces detection, which pole is not included into the critical areas for plane failure or for flexural toppling. Generally traces are more responsible than planes for failure mechanism related to critical intersection, such as wedge failure and block toppling. The values of the kinematic indices for wedge failure and block toppling are, in fact, higher for the dataset of discontinuities extracted using manual methods. The comparison of the values of the kinematic indices for discontinuities extracted with manual and semiautomatic methods has confirmed the adoption of the surveying of slopes with different orientation. Carrying out the geostructural survey on a slope with the same orientation with semiautomatic methods could, in fact, make the kinematic indices for wedge failure and block toppling underrated, and to the kinematic indices for plane failure and flexural toppling overrated.

Indeed, a code for the 3D kinematic analysis (DiAna-K; Gigli et al., 2012) has allowed to calculate the values of kinematic indices and provided the rock fall susceptibility for each triangle of the mesh of the bench surface. This analysis has allowed to detect the most prone to failure area and estimate the volume of unstable blocks.

The discontinuities distribution has been used as input data for the stochastic modelling of the fractures within the rock mass thanks to a Discrete Fracture Network generator. The Factor of Stability of each block has been calculated with the Limit equilibrium Method proposed by Hoek & Bray and the distribution of the volumes has been carried out for stable and unstable blocks using the Block Analysis of Goodman & Shi. The distribution of the volume of unstable blocks obtained with the Discrete Fracture Network generator has been validated with the volume measurement of the fallen blocks at the base of the bench, while the susceptibility map obtained with the 3D kinematic analysis has been validated with the visual comparison of unstable blocks and of niches detachment of previous fall events.

The stereoplots of the discontinuities extracted with semiautomatic methods show that the variability of the aspect of the slope influences the reliability; for this reason, the research has pointed out that the use of semiautomatic methods is recommended especially in case of natural slope or artificial slope with different slope orientation; for example, it is recommended, in case of artificial slope, the carrying out of the survey on two perpendicular slopes to avoid the bias of the detectability of sets of discontinuity outcropping as traces only on a slope.

The present research has shown that the suitability of manual or semiautomatic methods for the extraction of the discontinuities is related to the complexity of the framework of the discontinuities and to the geometry of the rock slope. In particular, manual methods were found to be useful tools for the geostructural characterisation in case of weathered lithologies, in which the surface is not related to the inner structure of the rock mass. On the other hand, semiautomatic methods are less time-consuming and so their use is convenient especially in case of survey on large surfaces.

The results of the thesis provide useful points to choose semiautomatic or manual methods for discontinuities extraction for the geostructural characterisation of the rock mass; the integration of the 3D kinematic analysis and polyhedral modelling of the discontinuities permit a more reliable description of the paths, of the height and of the kinetic energy of the blocks, increasing the mine safety conditions.

The research is structured in 4 parts.

The first part (Chapter 1-4) provides a general overview of the work and describes the state of art about geostructural characterisation of rock mass (Chapter 2), the use of remote sensing methods for rock mass characterisation (Chapter 3), with a particular focus on the description of manual and semiautomatic codes

for the discontinuity extraction, and the kinematic and stability analysis (Chapter 4) and codes used to perform the kinematic analysis and the polyhedral modelling of rock mass.

The second part (Chapter 5) outlines the geological setting of the sites and the description of the outcrops from a lithological rock mass point of view.

The third part describes the results of the extraction of the discontinuities with manual and semiautomatic methods, the 2D kinematic analysis, the 3D kinematic analysis performed by DiAna and the polyhedral modelling performed by SiroModel for case study 1 mine (Chapter 6) and for case study 2 mine (Chapter 7).

The forth part finally discusses the results of the analysis preformed for the 2 cases study (Chapter 8) and draw the conclusion about pros, cons, and feasibility of the performed methods and describes the failure modes, block size and location of instable areas comparing the results of 3D kinematic analysis and the polyhedral modelling (Chapter 9).

2. Geostructural characterization of rock mass

Geostructural characterisation of the rock mass consists in the quantitative description of the discontinuities (joints, faults, bedding, cleavage) and of the wall strength of the rock. The description of the discontinuities includes orientation (dip/strike, dip direction/plunge), persistence, spacing, filling, roughness, aperture and number of the sets of discontinuities (Priest, 1993).

Rock mass characterisation can be carried out by different ways: 1) outcrop description; 2) drill core/drill hole description; 3) photogrammetric or laser scanning survey.

Traditional geostructural survey on outcrop or on drill core/drill hole is performed with a clinometric compass. Geostructural survey performed with clinometric compass carried out on outcrop can experience various technical issues, from excessive time-consuming operations, to danger for the operators, inaccessibility of part of the outcrop and presence of magnetic ore bodies.

Traditionally, surveys are performed with a clinometric compass, measuring dip and dip direction directly on the discontinuity. Nowadays, it's possible performing the geostructural characterisation by lidar and photogrammetric techniques. Remote sensing has the following pros:

- within the same domain a larger sample of discontinuities can be described within a reasonable time interval. Surveying a larger part of the rock wall, providing so more representative statistical samples allows a more detailed geostructural characterisation to avoid ignoring the sets of discontinuities with lower frequency;
- the safety of the operator. Surveyed walls are also often dangerous walls. We report that also little fragment of rock can provoke serious illness, also in presence of the work helmet. Remote sensing increases the safety of the worker because the survey can be carried out in a remote safe location protected from rockfalls;
- the creation of a detailed 3D model of the slope lays the foundations for the automatic and quantitative analysis of the outcropping planes. The point cloud comparison is, indeed, a useful information for the evaluation of the volume and position of collapsed blocks, providing a tool for the calibration of the stability analysis. The data outcoming from a lidar or photogrammetric survey can be stored, and the analysis can be repeated, without accessing again the wall;
- in case of mines of ore minerals, the rock mass can have a residual magnetization, impeding the traditional compass measurement or anyway affecting the accuracy of the measurement;
- geostructural survey carried out by remote sensing is less time consuming than traditional geostructural survey. Wheter the geostructural survey is performed tracing planes and traces with manual methods on a 3D model with an optical support, or it is performed by semiautomatic extraction methods, there is a large gain of the total time spent by the operator on field. The gap of spent time is larger if considered the time spent on field in the mine, reducing residual risk related to the presence of the operator and allowing working continuity.

Anyway, the availability of remote sensing tools, should not overshadow a careful and critical on-field observation of the jointing of the rock mass, that allows an additional capability of predicting failure modes. For example, the presence of the water flow into the rock mass can increase the mineral alteration along the discontinuities. A detailed description of some of the filling material and spacing of the discontinuities can be realized only by the direct observation of the rock mass. Indeed, also the local alteration of the rock is an important information to predict the stability of the slope. For example, the presence of clay or shale beds under thick and massive beds (i.e.: arenite, limestone) can provoke failure of the uppermost rock cliff, although little jointed. The good analyser of the slope stability is, first of all, a good and perceptive observer. The on field critical observation is useful to achieve representative measurements. I.e., the down-dip base length should exceed the wave length of surface undulations observed on the rock slope because the local dip and

dip direction of non-planar features, so the orientation of a discontinuity should be evaluated based on the wavelength undulation of the surface.

The orientation of a discontinuity is described by 2 angles: the *dip*, that is the inclination of the steepest declination of a surface measured from horizontal, and the *dip direction*, or *strike*, measured clockwise from the north. If the surveyed element is not a plane, but a line, the orientation is given by the *plunge* and the *trend*. The geometrical description of dip, dip direction, trend and plunge are given in Figure 5.

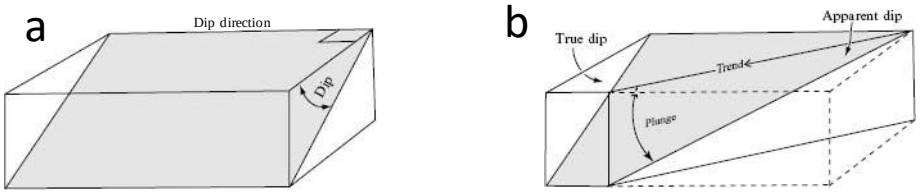

Figure 5 - Orientation angles of a surface. a) graphical definition of dip and dip direction; b) graphical definition of plunge and trend. Modified from Rowland et al. (2013)

Orientation of discontinuities relative to the slope largely controls the possibility of unstable conditions or excessive deformations (Giani, 1992) developing 5 possible failure modes: plane failure (Hoek &Bray, 1981), wedge failure (Hoek & Bray, 1981), block toppling (Goodman & Bray 1976; Matheson 1983; Brideau & Stead, 2010), flexural toppling (Goodman & Bray 1976; Hudson & Harrison, 1997), free fall. The other factors that increase the rock slope stability are spacing and persistence of the discontinuities and the friction angle (ϕ) of the surfaces (Hoek et al., 2002; Cai et al., 2004). The mutual orientation of discontinuities will determine the shape of the individual blocks, beds or mosaics comprising the rock mass and the presence of removable blocks (Goodman, 1995).

The minimum number of measurements for a significative description of a set of discontinuities range, opinion by opinion, from about 80 to 300 (ISRM, 1978), depending on the standard deviation of orientation angles. On the contrary, if the dataset of dip and dip direction is consistent, a smaller number of measurements will be necessary. Higher the standard deviation of the orientation angles, higher the number of measures to statistically characterise the stereoplot of the discontinuities to identify each sets of discontinuities. Of course, the number of measurements is a compromise between accuracy of the survey and accessibility of the crop. Anyway, the suggested minimum number of discontinuities clearly makes evident that in case of a structurally complex rock mass, with 5, 6, 7 or more sets of discontinuities, the survey of thousands of discontinuities is required. This is a time-consuming operation also for a smart technician.

The tool for the description of the orientation of the discontinuities is the compass clinometer (Figure 6). Nowadays, orientation measurements can be taken also with smartphone (Android, iPhone®) or iPad®. Specific apps allow, in fact, to use the accelerometers present inside these devices. The accuracy of the measurements taken with these tools is lower than the accuracy of compass clinometer, but comparable (Lee et al., 2018).

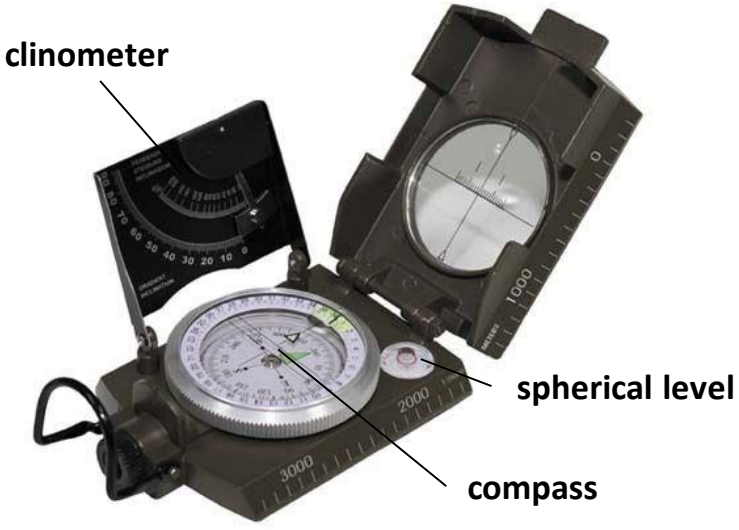

Figure 6 - Compass clinometer mod. Wilkie meridian Pro

The accuracy of the measurements will depend on several factors among which the most important are the accessibility of the plane of interest, the areal extent of the exposed plane, the degree of planarity and smoothness, occasional magnetic anomalies, human errors. Generally speaking, the accuracy of the measurement is 5° about and in case of sub-horizontal discontinuity, with a value of dip >+-5°, the value of dip direction can range ±180°.

Clinometer compass and other devices above listed are not the only methods for discontinuities orientation measurement. In case of solid rock mass, the mean orientation of major discontinuities can be obtained by the coordinates of 3 points lying in the plane of the discontinuity. In the case of surface outcrops, coordinates may be determined by accurate topographic location, by a GPS or by topographic triangulation. The orientation of a discontinuities within the bedrock, instead, can be obtained by 3 boreholes that intersect the plane. Of course. Polarized drilling allows to reduce the number of drill holes to one to solve the issue of the indeterminateness of dip direction. Drilling can be oriented using geological information about bedrock (i.e.: the orientation of bedding, if known) or using artificial orientation devices (Beach & McLeod, 2007). Alternatively, the orientation of minor discontinuities can be estimated by down-hole viewing techniques such as borehole television cameras, photographic cameras and borehole periscopes. Automatic digital image analyser software allows to quickly extract the orientation of the discontinuities from the images carried out by these survey methods. Besides orientation, these methods also provide invaluable information concerning spacing, thickness of the filling of the discontinuities and the level of seepage paths and, of course, about Rock Quality Designation (RQD; Deere, 1964). A special core recovery method known as the integrated sampling method is recommended for obtaining orientation data in heavily fragmented rock masses. The method essentially consists of recovering a core sample which has previously been reinforced with o grouted bar whose azimuth is known from positioning rods.

The orientation of the discontinuities can be described and grouped on rosettes diagrams or on stereoplots. Rosettes diagrams indicate the relative frequency of dip direction split by a radial spacing (usually 10°, for a total number of 36 spindles; stereoplots indicate the projection of the intersection between a hemisphere (upper or lower) and the vector described with the dip and dip direction angles.

Rosette diagram, of course, does not consider the dip. The standard deviation of dip direction, that depends on many above-mentioned reasons, influences the best range for the classes. Dip direction value can greatly range in case of sub horizontal discontinuity, especially if dip direction is minor than the compass accuracy, as previously described (+-5°). The use of rosettes diagram in this case is so unreliable.

Stereoplots are largely used to describe orientation of the surfaces in geology and engineering, both for tectonics as for slope stability purpose. Several projection methods are used to represent the orientation of geological planes. Stereoplot representation can change by:

- Hemisphere (upper or lower);
- Kind of deformation (equal angle or equal area);
- Presence of Terzaghi weighting;
- Contouring.

The projection on a plane of the 3D hemisphere can follow different logics and comply with the adhesion to the angle or to the area ratio. Equal angle representation deforms the areal extension of the contouring, while equal area representation deforms the angles between poles. As result, similarly to the conform and equivalent projections in cartography respectively, equal angle distribution provides a more homogeneous distribution of the poles in case of step dip values, while equal area distribution shift poles towards the edge.

The orientation of a joint compared to an observation surface or a bore hole influences the number of joints observed in a spatial square or linear range (Terzaghi, 1965; Franklin et al., 1971; Palmström, 1996). The geostructural analysis carried out on an acritical representation of poles without considering this bias could so underrate the rock mass fracturing. In particular, in case of geostructural survey carried out on a slope, discontinuity spacing of discontinuities with an orientation similar to the slope could be underrated; this could lead to underrate the risk of failure (Gordon et al., 2008). Joints perpendicular to the surface plane or the bore hole will be more frequently intersected than other joints. This effect frequently biases the observations. For

this reason, Hudson & Priest (1983) recommend, where drillings are applied, to perform three bore holes in different directions for obtaining information on the 3-dimensional jointing in a rock mass. Such solutions are, however, costly and time-consuming.

A cheaper solution is applying different weights to the discontinuities on base of their underrating. Fewer the angle between the discontinuity and the normal of the slope or the scanline, higher the weight to give for a corrected geostructural characterization of the whole bedrock.

Terzaghi weighting (Terzaghi, 1965) applies a correction in order to reduce these biases related to the relative direction of the wall or of the borehole. Palmström (1995) provided so 2 equations (Equation 1 and 2) to calculate the weighted joint density wJd for surfaces and for boreholes, or scanlines.

Equation 1

$$wJd = (1/\sqrt{A}) \sum (1/\sin\delta) = (1/\sqrt{A}) \sum f_i$$

Equation 2

$$wJd = (1/\sqrt{A}) \sum (1/\sin\delta) = (1/\sqrt{A}) \sum f_i$$

Figure 7 provides the graphical meaning of δ angle in case of scanline/borehole (letter a) and in case of surface (letter b).

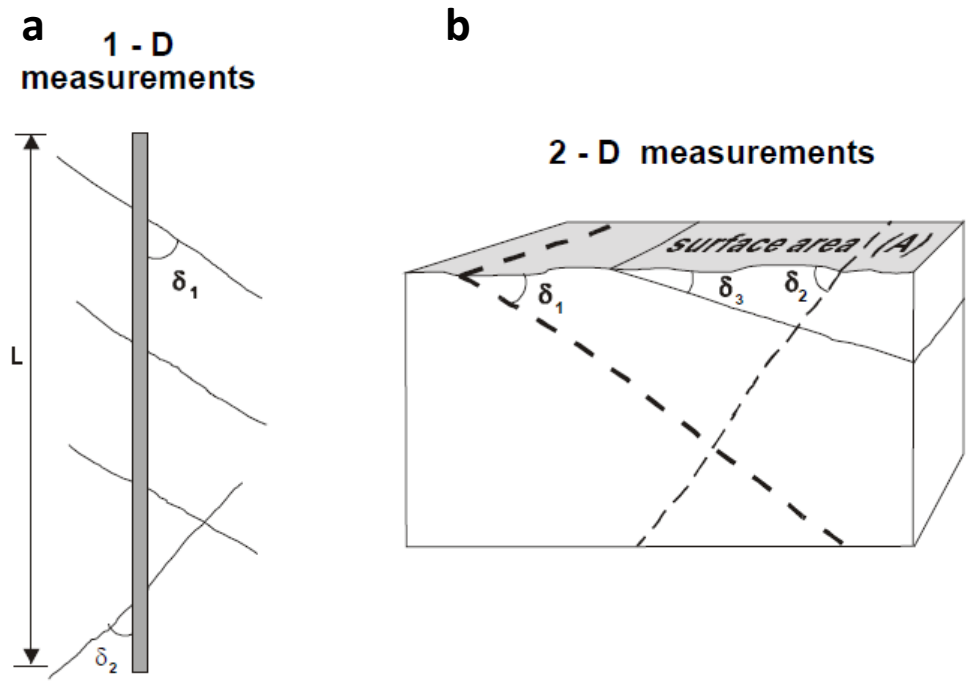

Figure 7 - Graphical representation of the angle between each joint and the surface or the bore hole (Palmström, 1995)

Terzaghi argued that low values of δ could greatly afflict the data likelihood. For this reason, *"no correction whatsoever can be applied if δ is zero"*. For this reason, the weighting method would fail to correctly indicate the frequency of discontinuities the δ of which is close to 0°. A single discontinuity subparallel to a scanline/borehole or surface could affect the survey, disturbing the geostructural characterisation. Usually, in fact, no data correction is applied for δ < 20°.

Contouring in geomechanics allows to interpolate isolines of the poles concentration. Two interpolation methods of contouring are used: Schmidt distribution and Fisher distribution (Fisher, 1953). Fisher method gives a weight to the poles concentration that is related to the distance of the pole for the point, within a sphere with a defined radium. The weight ranges from 0 (behind the sphere surface) to 1 (close to the point, that is the centre of the sphere), with a bell-shape normal distribution. Every pole counts for 1. The sum of the product of the value of all the poles (1) for the weight of all the poles (from 0 to 1) gives the local value of contouring using Fisher method.

The Schmidt distribution is the classical method, in which each pole is assigned a constant influence value of 1. Convention dictates the use of a counting circle with an area equivalent to 1% of the lower hemisphere surface. For each pole plotted, any grid point falling within a circle of arbitrary constant radius centred on this pole is incremented by the value of the pole. After the influence of all plotted poles is thus distributed, the density plotted at each grid point is calculated by dividing the pole count at that grid point by the total pole influence.

For great amounts of poles, no noteworthy differences are shown in case of one method rather the other one; the situation is different if the number of poles is lower than some hundreds because the Schmidt distribution produces crude contour lines and often inaccurate results, since each measurement is assumed to be 100 percent accurate and any existing errors are exaggerated due to lack of data. Fisher distribution (Fisher, 1953), instead, tends to ignore the presence of single random pole and provides a more robust statistical distribution because a greater number of poles concurs to the discretisation of the pole distribution. Fisher computation is more time-consuming than Schmidt one; anyway, nowadays calculation power of computers makes time difference neglectable and for this reason using Fisher distribution is preferable.

The relations between sets of discontinuities and failure modes will be deeply discussed in Chapter 4.1; anyway, Figure 8 is a cornerstone and provides clear examples to understand the geometrical connections between discontinuity in the rock mass and location of poles and cyclographic lines in the stereoplot.

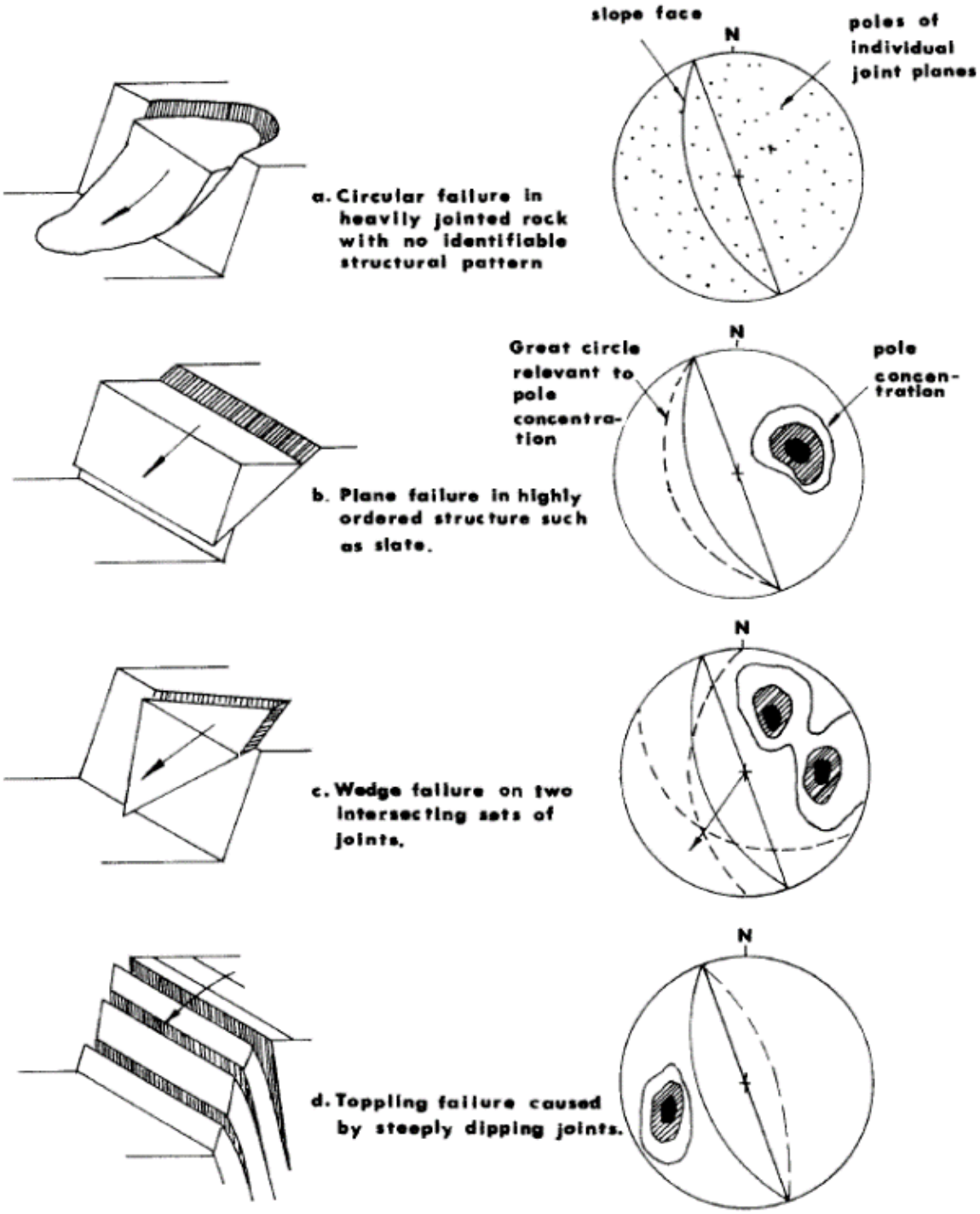

Figure 8 - Representation of structural data concerning the four possible failure modes, plotted on equatorial equal area nets as poles and great circles (from Hoek & Bray, 1974)

The perpendicular spacing between discontinuities of the same sets is the most important parameter for the block size. A little spacing is, indeed, fundamental in case of heavily foliated rock mass for flexural toppling.

Indeed the volume of potentially unstable blocks is a key parameter for reliable rockfall hazard analysis. The volumes extracted through the stability analysis tool can be validated with block volumes estimated from the geostructural characteristics of the rock mass and with an inventory of fallen blocks.

Block volumes can be estimated through the relation proposed by Palmström (2001) (Equation 3):

Equation 3

$$V_b = \beta \times {J_v}^{-3} \times \frac{1}{\sin\gamma_1 \times \sin\gamma_2 \times \sin\gamma_3}$$

where V_b is block volume (in m^3), J_v is the Volumetric Joint Count (Palmström, 1995), and γ_1, γ_2, γ_3 are the intersecting angles of the three sets of joints forming the block. J_v is defined as the number of joints intersecting a volume of 1 m^3, and corresponds so to the sum of the inverse of the spacing of all sets of joints (Equation 4):

Equation 4

$$J_v = 1/S1 + 1/S2 + 1/S3$$

β is the block shape factor (Palmström, 1995; Equation 5) and S_1, S_2, and S_3 are the average spacings for the three joint sets with S1 ≥ S2 ≥ S3. The volume of the block is so given by a factor related to the joint density, $J_v \times \beta$, and to a factor related to the joint orientation, $\frac{1}{\sin\gamma_1 \times \sin\gamma_2 \times \sin\gamma_3}$.

Equation 5

$$\beta = \frac{\left(\frac{S_2}{S_1} + \frac{S_2}{S_1} \times \frac{S_3}{S_1} + \frac{S_3}{S_1}\right)^3}{\left(\frac{S_2}{S_1} \times \frac{S_3}{S_1}\right)}$$

Equation 3 can be used if joint orientation is not irregular. Anyway, many times the blocks formed by the joints are irregular, especially for not layered rocks, and so splitting joint is difficult, as providing significant spacing values. In these cases the volume can be stimated Palmström (2001) by the direct measurement, by the rock slope geostructural survey or by a drill core where the fragments are small enough to be measured in the core. In case spacing is large enough to make the spacing measurement not possible, suggests the use of the following relations (Equation 6 and 7):

Equation 6

$$V_b = S1^3 \times 25$$

with 1 set of joints

Equation 7

$$V_b = S1^2 \times S2 \times 5$$

with 2 sets of joints

The block shape, described in Equation 5, depends on the ratios between the values of the spacings of the sets of joints S_1, S_2, S_3. Equation 5 is referred to a block formed by 3 sets of joints; for blocks formed by more than 3 sets, Palmström (2001) has proposed a simplified expression (Equation 8):

Equation 8

$$\beta = 20 + 7 \times \frac{a_3}{a_1}$$

where a_3 is the longest and a_1 is the shortest dimension of the block.

Persistence is the length or areal extension of a discontinuity within the rock mass and is one of the most important rock mass parameters because affects the fragmentation of the rock mass and so the number of removable blocks on a rock slope. This value is often referred to the whole set of discontinuity; so usually geostructural analysis assigns an only value of persistence to the whole set of discontinuities. Fragmentation

and weathering of a rock mass increase the difficult of a proper evaluation of the persistence of a discontinuity or - of a whole set of discontinuity: more a rock mass is fragmented and weathered, more difficult is the evaluation of the persistence. For these reasons, a proper evaluation of a representative value of persistence cannot be separated from a careful on field expert judgement of the whole rock mass (Sturzenegger et al., 2009).

Because of the difficulty of evaluating how much a discontinuity keeps on within the rock mass, this is one of the most difficult parameters to quantify in crude terms (ISRM, 1978). As regarding the evaluation of the persistence, extraction methods, that will be largely described in Chapter 3, influence the evaluation of the persistence and its feasibility.

Riquelme et al. (2018) distinguish 3 types of persistence when investigating rock masses: visible persistence, real persistence, and estimated persistence.

Visible persistence is the persistence extracted from visible data on rocky outcrops, such as visible traces and planes.

Real persistence is the length of the discontinuity within the rock mass, that can be estimated integrating on field survey data with boreholes data, or thanks to geophysics.

Estimated persistence is derived from surface information of the rock slope. Riquelme et al. (2018) calculate estimated persistence considering that some superficial characteristics (i.e., orientation, spacing, persistence and roughness) are also present inside the rock mass.

Persistence of discontinuities extracted with manual methods, that have an optical support, is of course different from the persistence of planes extracted by semiautomatic methods. Discontinuities extracted by manual methods, in fact, represent the visible persistence, while the persistence of the planes extracted by semiautomatic methods could be associated to intermittent discontinuity planes because of the presence of blocks that locally cover the discontinuity or to the lack of rock, that apparently splits the surface into 2 parts (Riquelme et al., 2018).

ISRM (1978) defines the persistence description on the basis of the length of the discontinuity and on the basis of on the geometrical relationship with the other sets of discontinuity. On particular 5 classes of persistence have been defined based on the length of the discontinuity:

Very low persistence			L	<	1 m
Low persistence	1 m	<	L	<	3 m
Medium persistence	3 m	<	L	<	10 m
High persistence	10 m	<	L	<	20 m
Very high persistence			L	>	20 m

Persistence of the discontinuities is among the parameters most significantly affecting rock mass strength (Cai, 1992). Persistence, in fact, affects the block volume distribution. Equation 3 indicates the volume of the blocks considering an infinite persistence. Cai & Horii (2004), have so modified Equation 3 and carried out the following equation (Equation 9) for the calculation of the block volume in case of not persistent joints.

Equation 9

$$V_b = \beta \times {J_v}^{-3} \times \frac{1}{\sin\gamma_1 \times \sin\gamma_2 \times \sin\gamma_3 \times \left(\sqrt[3]{L_1 \times L_2 \times L_3}\right)}$$

While relatively small bridges of intact rock between otherwise continuous joints subatsantially increase strength, the mapping of

ISRM (1978) provides, indeed, a distinction among discontinuities on base on the geometrical relation of the terminations (Figure 9). On particular, ISRM (1978) resumes the description of Muller (1963) and of Price (1966) and defines the discontinuities as persistent or not persistent differencing the discontinuity, the termination of which ends in rock or against another discontinuity (letter g in Figure 9); indeed, a general scheme of the discontinuity pattern is given (letters a-f in Figure 9).

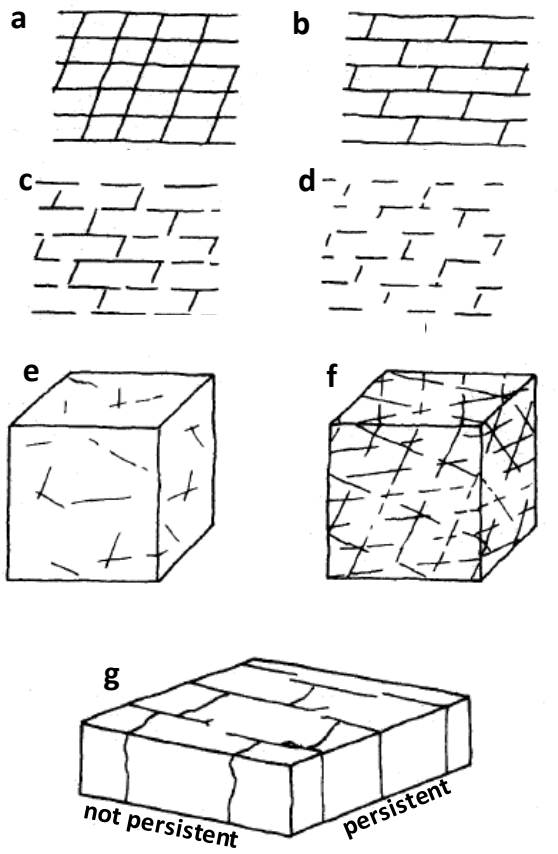

Figure 9 - Letters a-f: examples of discontinuities pattern; f: graphical representation of persistent and not persistent discontinuities. From ISRM (1978), adapted from Muller (1963) and Price (1966)

Aperture, filling and roughness of a discontinuity are three important features for slope stability because largely responsible for the ϕ value along the discontinuity surface.

Discontinuity aperture is the perpendicular distance separating two rock sides bordering a discontinuity. It has a strong influence on slope stability because ϕ value is related to the thickness of the aperture: wider is the aperture, fever is the ϕ of the discontinuity. Wider apertures are responsible for slope stability for two reasons:

- Wider apertures increase the water flow within the rock mass. Water content increases water overpressure, that decreases ϕ' value. Indeed, water flow within rock mass locally alters the mineralogical composition, decreasing its mechanical properties;
- Wider apertures can make the two rock walls of the discontinuity free to move. For this reason, if aperture exceeds the roughness of the discontinuity surface, ϕ of the discontinuity greatly decreases because the movement of the 2 blocks will not require the reach of the peak strength of the intact

rock (Hoek & Brown failure criterion; Hoek & Brown, 1980; Hoek & Brown, 1997), but of the filling (Mohr-Coulomb-Terzaghi failure criterion; Terzaghi, 1951).

Discontinuity are defined *open*, *gapped* or *closed* depending on the thickness of the opening (Table 1).

Table 1 - Discontinuity aperture classification. From ISRM (1978)

Aperture	Description	
<0.1 mm	Very tight	*Closed* features
0.1 - 0.25 mm	Tight	
0.25 - 0.5 mm	Partly open	
0.5 - 2.5 mm	Open	*Gapped* features
2.5 - 10 mm	Moderately wide	
>10 mm	Wide	
1 - 10 cm	Very wide	*Open* features
10 - 100 cm	Extremely wide	
> 1m	Cavernous	

Φ in closed and gapped discontinuity is mainly related to the roughness of the surface and to the rock wall strength, while in open discontinuities ϕ is corresponds to the ϕ of the filling. Roughness of the discontinuities, rock wall strength and filling concur so to the rock mass characterisation. In particular, roughness plays a very important role in the mechanical behaviour of closed and gapped discontinuities, while filling affects ϕ and c in case of open discontinuities (Table 1).

Roughness represents an index of the waviness affecting a surface. Barton (1973) performed direct shear tests (Figure 13) on model tension fractures and have provided a very realistic picture of the behaviour of unfilled joints, predicting with acceptable accuracy ϕ_{peak} of rough-undulating joints since the knowledge of the effective Joint wall Compressive Strength (JCS; Deere & Miller, 1966) and of the Joint Roughness Coefficient (JRC; Barton, 1977) values. Joint wall Compressive Strength can be evaluated measuring the Schmidt hardness of the rock and using Equation 10.

Equation 10

$$\log_{10}(JCS) = 0.00088 \times \gamma \times R_{(\downarrow)} + 1.01$$

JRC value is so fundamental to evaluate ϕ_w. JRC values can be carried out by visual comparison (as originally suggested by Barton & Choubey, 1978), or sampling a number of orientation samples on the surface (ISRM, 1978), or on the surface surface lengths along profiles (Maerz et al., 1990), root mean square characterisation of local slopes (Tse & Cruden, 1979), surface topography (Grasselli et al., 2002), fractal dimensions (Baker et al., 2008) and quantitative analysis of point clouds extracted by laser scanning or photogrammetric surveys (Rahman et al., 2006; Gigli & Casagli, 2011; Gigli et al., 2014; Iakovlev et al., 2016).

The most practical method for estimating the roughness of a discontinuity is the visual confrontation of the profile of the surface, surveyed with a profile gauge (Figure 10), with standard profiles published by Barton & Choubey (1978) (Figure 11). ISRM (1978) suggests splitting the surfaces profile into overall 9 classes, by 3 classes of roughness (rough, smooth, slickensided) and by 3 classes of planarity of the surface (stepped, undulating, planar). Figure 12 provides a general rank of the roughness value for 1 to 10 m persistent discontinuities. According to ISRM (1978) classification of the roughness of the surface, roughness increases from planar to undulating and to stepped surfaces. Visual confrontation of the surface with the Barton & Choubey have limitations: pocket profile gauges can produce the survey only on 10 cm - 15 cm long profiles and the interpretation of the roughness values is user-dependant. Alternatively, survey on the whole surfaces can give more representative values of the roughness. ISRM (1978) suggests two methods for the roughness assessment. One method consists into the measurement of a minimum number of 250 values of the local

orientation using different diameters. On particular, a minimum number of 25 measures with a 40 cm plate, 50 with a 20 cm plate, 75 with a 10 cm plate and 100 with a 5 cm plate are required. This procedure is so time-consuming and potentially dangerous for the operator because the direct presence close to the rock slope is necessary to take the measurement. The second method suggested by ISRM is, instead, based on analogical photogrammetry. Nowadays, digital photogrammetry and terrestrial laser scanning are suitable techniques for numerical rock mass characterization at the outcrop scale (Slob et al. 2004; Haneberg 2005; Sagy et al. 2005; Kemeny et al., 2006; Renard et al. 2006; Hanenberg, 2007; Poropat, 2009). Both techniques, as widely described in Chapter 3, can produce a dense aggregate of coordinates, named point cloud, defining the 3D surface of the slope, on which numerical modelling allow to extract the roughness value (Rahman et al., 2006; Gigli & Casagli, 2011; Gigli et al., 2014; Iakovlev et al., 2016). These methods will be widely showed in Chapter 3 and have the cons of allowing roughness evaluation without a direct and dangerous access to the slope. Roughness evaluation is so a less time-consuming, dangerous and user-dependant assessment thanks to remote sensing techniques. JRC can be, indeed, calculated by a laboratory tilt test. The tilt test allows to measure the α angle of the sliding slab; Equation 11 allows then to calculate JRC from α of the sliding slab, ϕ_r, σ_{n0} of the test and JCS.

Figure 10 - Profile gauge mod. Vitrex - 6 inch

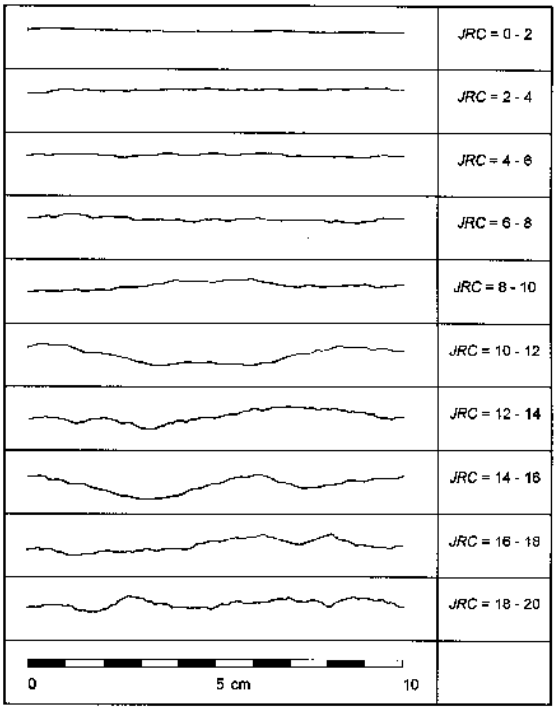

Figure 11 - Relation between roughness profile and JRC index. From Barton & Choubey (1978)

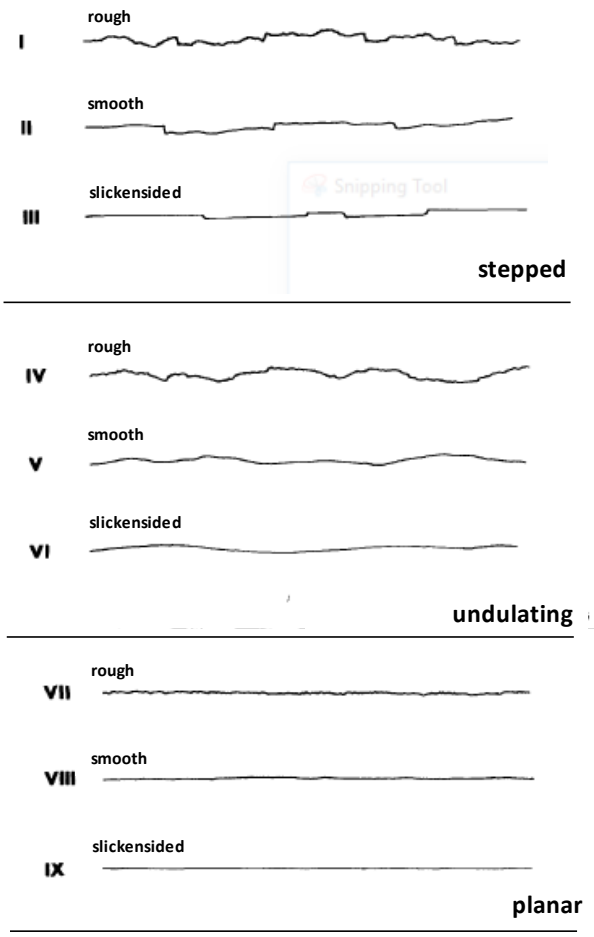

Figure 12 - Classes of roughness according ISRM (1978)

Equation 11

$$JRC = \frac{\alpha - \varphi_r}{\log_{10}\left(\frac{JCS}{\sigma_{n0}}\right)}$$

Barton (1973) relates the JRC to the JCS, ϕ_{peak}, and ϕ_b (Equation 12). The direct relation between ϕ_{peak}, and JRC and JCS is due to the greater amount of energy to break and overcome the asperities.

Equation 12

$$\varphi_{peak} = JRC \times \log_{10}\left(\frac{JCS}{\sigma_n}\right) + \varphi_b$$

Equation 12 clearly describes the factors concurring to ϕ_{peak}:

- $JRC \times \log_{10}\left(\frac{JCS}{\sigma_n}\right)$: is a geometrical factor. The roughness (JRC) of the discontinuity increases the friction along the discontinuity. Higher value of JCS, indeed, make the break of the indentation less probable, preventing the reduction of the friction along the discontinuity;
- φ_b : is a friction factor and depends on the material only.

The equation has been further updated (Barton & Bandis, 1990; Barton, 2013) to describe the shear strength for weathered rocks (ϕ_w) substituting ϕ_b with ϕ_r (Equation 13). The relation between ϕ_b and ϕ_r of a weathered rock, measuring the value of Schmidt rebound on dry unweathered and on wet weathered rock, is described in Equation 14 (Barton & Choubey, 1977).

Equation 13

$$\varphi_w = JRC \times \log_{10}\left(\frac{JCS}{\sigma_n}\right) + \varphi_r$$

Equation 14

$$\varphi_r = \varphi_b - 20° + 20° \times \frac{r}{R}$$

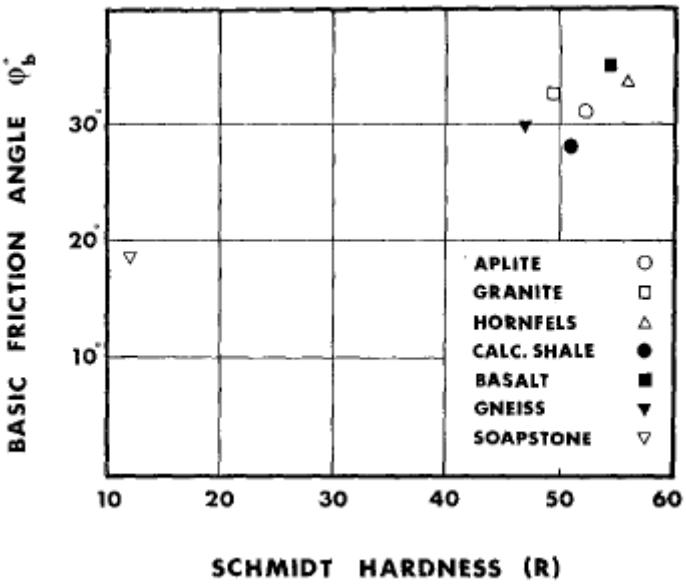

Figure 13 – Mean results of residual tilt tests to determinate φ_b for unweathered rocks. both the tilt tests and the Schmidt rebound tests were performed on dry joint surfaces. From Barton & Choubey (1973)

A number of studies has been carried out about the relation between JRC and JCS and the size of the sliding surface. The scale dependency of joint shear behaviour shows conflicting results. Some of these studies showed that as the joint length increased, the peak shear strength decreased (negative scale effect) while others showed an increase in the peak shear strength with increase of the joint length (positive scale effect) or no scale effect (Barton & Choubey, 1977; Pratt et al., 1974; Swan & Zongqi, 1985; Maerz & Franklin, 1990; Fardin et al., 2001, 2008; Tatone & Grasselli, 2010). Hence, the effect of scale on the mechanical behaviour of rock joints is still unknown and remains as an ongoing debate.
The most comprehensive laboratory investigation about scale effect on the shear behaviour of rock joints was carried out by Bandis et al. (1981) and by Barton & Bandis (1982). Their experiments were carried out on joint replicas of eleven natural joints of different lithologies (sandstone, siltstone, limestone, and metamorphosed fine grained sandstone), using sample sizes of 36 to 40 cm as well as subdivided samples. Results of their direct shear tests showed that the increase of joint length resulted in (Figure 14 and 15):

- a decrease in the JRC and JCS (letter a and b in Figure 15) (negative scale effect);
- a decrease in the magnitude of scale effects with a decrease in the joint roughness;
- a gradual increase in the peak shear displacement;
- a decrease in the peak dilation angle.

They noted that this negative scale effect was attributed partly to the change in the intact asperity strength and partly to the change in effective roughness with scale. Therefore, they related this effect to the parameters of JRC and JCS in the Barton empirical model (Barton, 1973; Barton & Choubey, 1977).

Wide joints require so a lower shear streght to move. The lower ϕ_w for the displacement of large discontinuities is well known in structural geological rock studies and is responsible for different scale phenomena, from the displacement of metric discontinuities, to the faults and suture zones reactivation.

Barton et al. (1981) and Barton & Bandis (1982) have so described the scale effect of the ϕ_w for rock stability by tilt test (Figure 14) and examined the relation between length of the joint and ϕ_w. Because laboratory test scale observation is lower than on field discontinuities length, a scale factor has been calculated since the tests. ϕ_r is a not scale-dependant parameter, while JCS nd JRC decrease with the length of the joint and derived the Equation 15 and 16. Equation 15 and 16 are valid considering L_0 of the joint within the range 10^{-2}-1 m. These empirical relations can be physically explained Equation 15. Later, Barton & Bandis (1990) found that the predicted values of JRC and JCS using these equations lead to unreasonably low shear strength value for discontinuities larger than 5 m and they recommended that the largest value of L_n should be limited to the average block size of the rock mass which is typically less than 5 m.

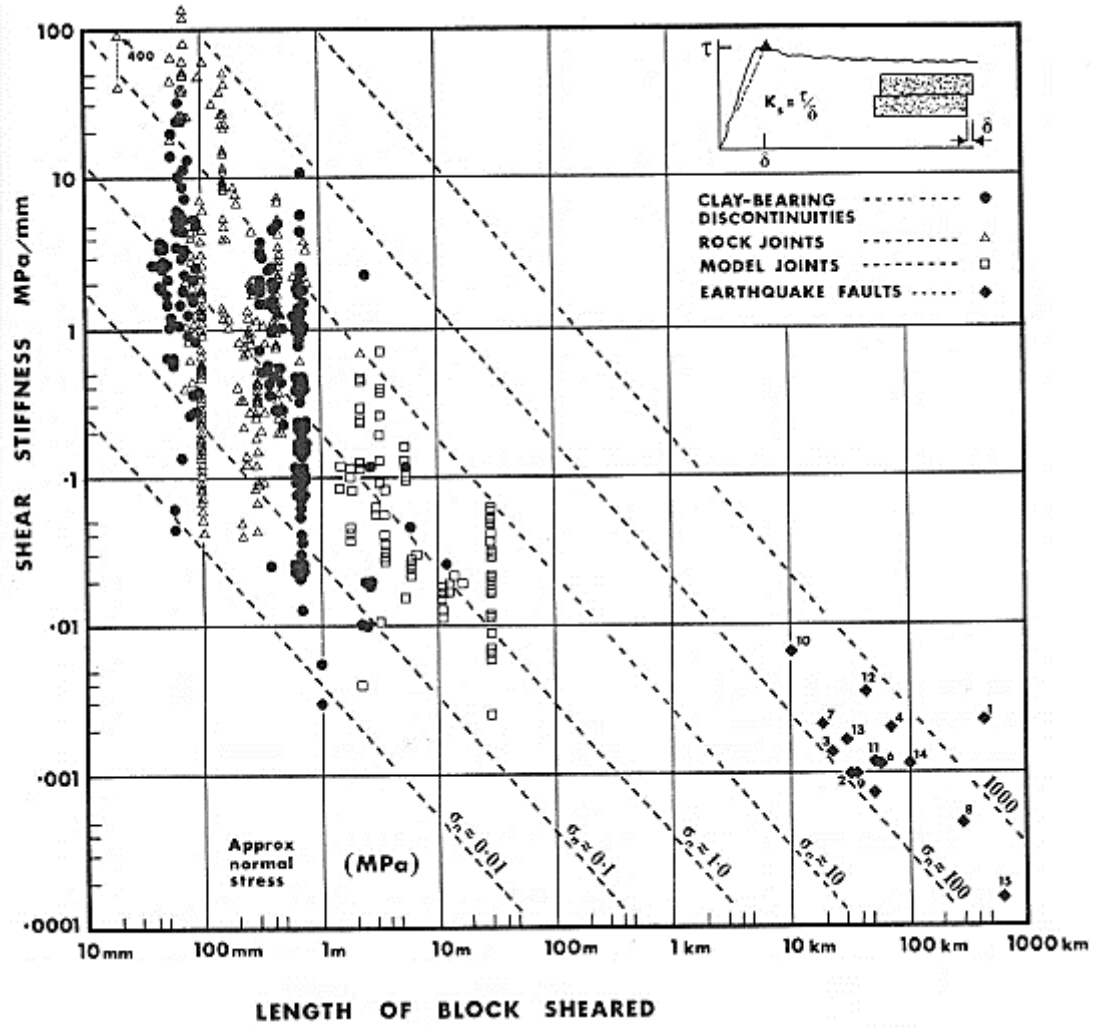

Figure 14 – Relation between the length of the block sheared and the φ_w. From 1cm- scale up to 10^{-3} km-scale, longer the discontinuity, lower φ_w. From Barton & Bandis (1982)

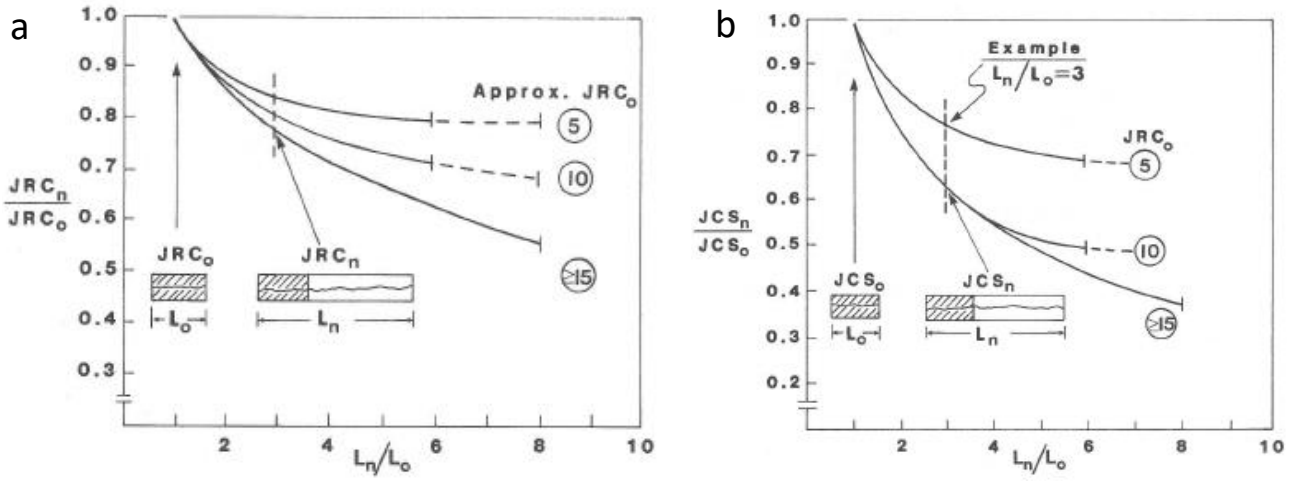

Figure 15 – Description of the role of the size (L_n/L_0) for the decrease of the value of JRC and JCS, considering a sample with JRC equal to 5, 10, and 15. a) the decrease of the JRC_n/JRC_0 ratio increasing the length of the sample; b) the decrease of the JCS_n/JCS_0 ratio increasing the length of the sample. From Bandis et al. (1981)

Equation 15

$$JRC_n = JRC_0 \left(\frac{L_n}{L_0}\right)^{-0.002 \times JRC_0}$$

Equation 16

$$JCS_n = JCS_0 \left(\frac{L_n}{L_0}\right)^{-0.003 \times JCS_0}$$

The visual comparison proposed by Barton & Choubey (1977) and the laboratory tests are affected by limitations. In particular, the visual comparison is a strongly user-related judgement (Hsiung et al., 1993; Beer et al., 2002; Grasselli & Egger, 2003; Du et al., 2009); laboratory tests are affected by scale factor both as regarding the length of the discontinuity samples as regarding the low normal stress in which it is performed and are for this reason strongly criticised (Harrison 2008; Hencher, 2012). Many authors have so proposed alghorythms for the automated calculation of JRC from digitez profiles comparison (Tse & Cruden, 1979; Maerz et al. 1990; Tatone & Grasselli, 2009, 2010).

Tse & Cruden (1979) derived the empirical relation between Z_2 (Myers, 1962) and JRC (Equation 17), with Z_2 corresponding to the second derivative of the profile (Equation 18). Tse & Cruden digitalised 10 standard profiles enlarged 2.5 times and compared for each profile the relation between Z_2 and JRC, evaluated by tilt test, and found a linear relation between these parameters (Figure 16).

Equation 17

$$JRC = 32.2 + 32.47 \times \log Z_2$$

Equation 18

$$Z_2 = \frac{1}{L_0} \times \int_{x-0}^{x=L_0} \left(\frac{dy}{dx}\right)^2$$

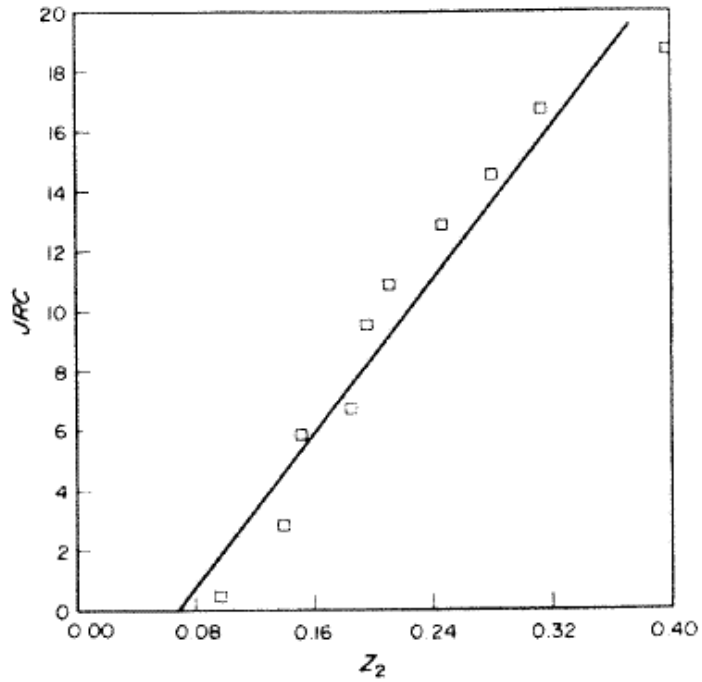

Figure 16 – Empirical relation between JRC, evaluated with test results, and Z_2. From Tse & Cruden (1979)

Maertz et al. (1990) defined the Roughness Profile index (R_p) parameter, as the ration of the true length of a fracture surface trace to its projected length in the fracture (El-Soudani, 1978). The minimum value of Rp is, of course 1 (flat surface), while experimental surveys show maximum values of 1.25 (very rough surface). 124 profiles of schist of Hemlo Mine obtained by profile gouge were used to carry out Rp and compare it with the JRC values with the roughness profile of Barton & Choubey (1976); indeed, direct shear and tilt test were carried out to calculate JRC with Equation 13. The comparison between JRC obtained with the two methods (profile gouge and laboratory tests) are illustrated in (Figure 17). The linear relation between Rp and JRC carried out by Barton & Choubey (1976) profiles and between Rp and JRC obtained by laboratory tests are described in Equation 19 and 20.

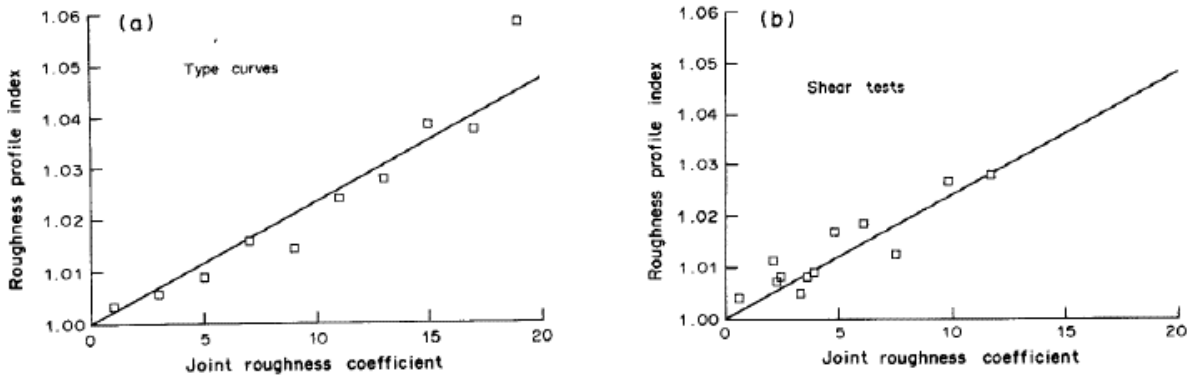

Figure 17 – Correlation between Rp and JRC: a) obtained by photoanalysis of the type-profiles of Barton & Choubey (1976); b) determined from laboratory tilt and direct shear tests on schist rock sample. From Maertz et al. (1990)

Equation 19

$$JRC = 411 \times (R_p - 1)$$

Equation 20

$$JRC = 401 \times (R_p - 1)$$

Tatone & Grasselli derived a roughness index (C index) from 3D (Tatone & Grasselli, 2009) and 2D (Tatone & Grasselli, 2010) surface survey and empirical equations that relate C factor to JRC. The sliding along the supposed direction can be, in fact, described using a 2D roughness profile; indeed, the analysis of 2D profiles formed the conventional approach to roughness estimation in rock engineering for many years, it is valuable to understand how 2D parameters compare to 3D parameters. The method proposed consists in 4 steps, both for 3D and 2D profiles: acquisition of the profiles; alignment of the profiles; analysis of the aligned profiles; evaluation of the roughness metric for each profile.

For 3D profiles (Tatone & Grasselli, 2009) the first step consists in analyzing the 3D roughness from a point cloud converted into a triangulated irregular network (TIN) obtained with photogrammetry or laser scanning. Alignment phase consists in the establishing of the best-fit plane through the surface to be analysed and in the transformation of the coordinates of the TIN since the xy plane equation. The analysis of a 2D profile consists in the calculation of the inclination θ* of each triangle of the TIN. For this porpoise, a specific analysis direction must be selected, and then the orientation must be indicated. Then, a threshold value of inclination is chosen and the fractional value A_θ* between the triangles with an inclination greater than θ*, and the overall length of the profile, A_t, is calculated. For each value of θ*, Equation 21 allows to calculate the value of A_θ*, that is the area normalized to A_0.; A_θ* represent so the area of the surface with an apparent θ* greater than a selected threshold value normalized with respect to the total area of the surface, A_t. The knowledge of A_0, θ*, and θ^*_{max} allows then to evaluate the dimensionless parameter C by performing a least square linear regression on the logarithmic form of Equation 21.

Equation 21

$$A_{\vartheta *} = A_0 \left(\frac{\vartheta *_{max} - \vartheta *}{\vartheta *_{max}} \right)^C$$

Tatone & Grasselli (Tatone & Grasselli, 2010) have, indeed, applied the same procedure with the 2D approach. The sliding along the supposed direction can be, in fact, described using a 2D roughness profile; indeed, the analysis of 2D profiles formed the conventional approach to roughness estimation in rock engineering for many years, it is valuable to understand 2D parameters compared to 3D parameters. Similar to the 3D methodology, the first step in analyzing the 2D roughness involves measuring the discontinuity surface. Two-dimensional profiles can either be extracted from a TIN or measured directly with a gouge scale. The procedure for the roughness evaluation is analogous in comparison with the 3D approach, but the C coefficient is calculated by the knowledge of the inclination of each sampling interval of the 2D sections (Equation 22). The equation, of course, takes in to account the length of the profile and not the area of the surface and so A_θ* and A_0 are replaced by L_θ* and L_0 respectively.

Equation 22

$$L_{\vartheta *} = L_0 \left(\frac{\vartheta *_{max} - \vartheta *}{\vartheta *_{max}} \right)^C$$

Tatone & Grasselli (2010) have then developed two empirical relations to calculate JRC from 2D section, using a 0.5 mm (Equation 23) and 1.0 mm (Equation 24) sampling interval grid respectively.

Equation 23

$$JRC = 3.95 \times \left[\frac{\theta^*_{max}}{(C+1)_{2D}} \right]^{0.7} - 7.98$$

Equation 24

$$JRC = 2.40 \times \left[\frac{\theta^*_{max}}{(C+1)_{2D}} \right]^{0.85} - 4.42$$

3. Photogrammetry and lidar methods for rock mass characterisation

Remote sensing of rock mass surfaces makes use a mess of techniques; among these we can cite laser scanning (Rosser et al., 2005), photogrammetry (Wickens & Barton, 1971; ISRM, 1978; Hanenberg, 2008), visible-near, shortwave, mid and thermal infrared (Hunt, 1977, Salisbury et al., 1989, Cooper et al., 2002), synthetic aperture radar interferometry (Li et al., 1990; Wu et al., 2000; Tarchi et al. 2003; Antonello et al., 2004; Tofani et al., 2013), muons (Morishima et al., 2017).

Remote sensing techniques are traditionally split in active and passive. Figure 18 gives a general overview of the subdivision of remote sensing methods. Active remote sensing methods analyse the effect given by an artificial pulse on the rock mass; this is the case, for example, of active infrared thermography, where the prospected material is artificially heated before survey or laser scanning. Photogrammetry in underground condition could be considered an active system. Passive systems, instead, measure the physical properties of the surface without giving any artificial energy input, using natural source, as, for example, passive thermography or photogrammetry without the use of artificial illumination. Other subdivisions of sensing devices and methods include the kind of restitution (a spectral data or an image-raster data), or the way of construction of the output dataset (a framing or a scanning system).

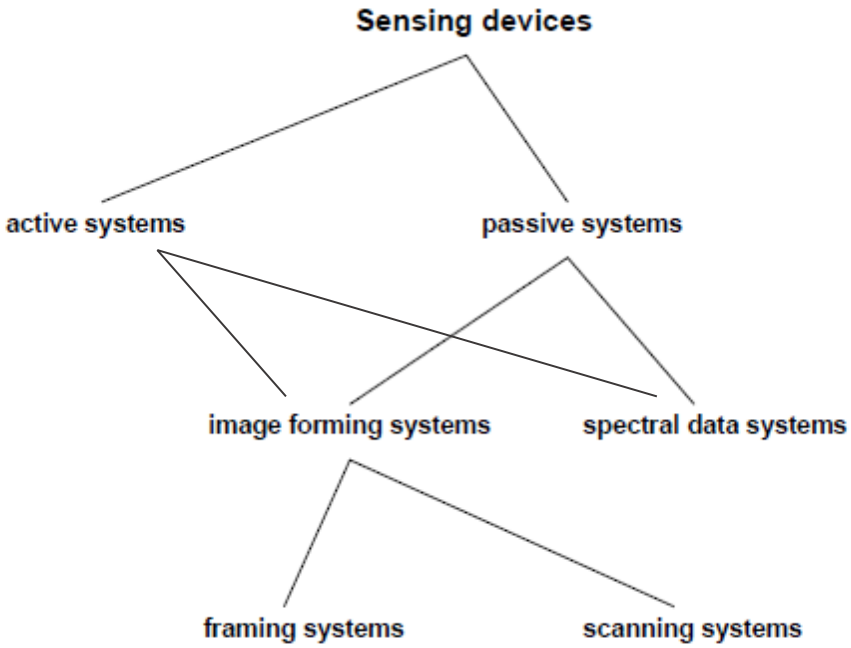

Figure 18 - General overview of remote sensing technics classification. Modified from Schenk (2005)

Image forming systems include the systems the input of which is represented by a raster describing a physical dimension referred to the cell; this is the case of thermography, the physical measured parameter of which is the infrared spectral radiancy of the superficial material, or of photogrammetry. Synthetic aperture radar also provides a grid, that represents as physical parameter the phase difference of a radar beam. Laser scanning devices can be included into this class too. Of course, image should not be understood only as optical image, but in a wider sense. Spectral data system, instead, include the techniques the input of which is constituted by a spectrum of the investigated object, such as a spectrometer.

Image forming systems can be, indeed, split by the construction of the dataset. Framing systems provide the data in the whole frame at the same time (this is the case of photogrammetry, because we can consider the arrive of the light on the image sensor as a synchronous event), while scanning systems provide flipping

through data by raw and column such as a plow (laser scanning, the duration of which ranges by the extent of the surveyed surface).

3.1. Photogrammetric method

Photogrammetry is the elaboration of two coupled images, named stereopairs, in order to obtain a 3D model of the object exploiting artificial stereoscopic vision, that reproduces the binocular human vision. 3D in human sight is permitted thanks to the acquisition of two images from different points of view. The photogrammetric process reproduces the images processing of human sight, substituting the eyes with two stereocameras, and elaborating a way, the *stereoscopy*, to create or enhancing the illusion of depth, obtaining a 3D model since two images. Photogrammetry has been the first remote sensing method to obtain a real 3D representation, dating since the invention of photography. Until the invention of digital photography, photogrammetry had consisted into the visual elaboration of the images of a stereopair, printed on two films. The visual comparison of the two images of a stereopair was carried out by a visual comparator, the *stereoscope*. Digital photography is the image acquisition on a light-sensitive electronic device. Digital photography adoption has been a revolution for photogrammetry and has allowed the conversion of a physical dimension, the amount of electromagnetic radiation of the light wavelength, into an electronic pulse, that can be easily stored into mass memory devices. Digital photography, besides largely increasing the definition and quality of images and data transfer, has revolutionised images post-processing and photogrammetric restitution. Since the adoption of digital photography, the stereoscope has been so substituted by photogrammetric software, the algorithms of which convert the grids made of pixels, in which the electromagnetic radiation of the visible wavelength has been converted into an electric pulse, into a mesh, or clouds of georeferenced points, named *point cloud*. The bulk of the operating sketch of photogrammetric method is anyway similar and theoretical model can be described by the sketch of binocular vision in Figure 19. The measure of ϕ_1 and ϕ_2 angle allows to calculate the distances d_A and d_B of A and B targets respectively. The knowledge of:

- x y z coordinates of left camera L;
- x y z coordinated of right camera R;
- bearing angle of LOS of L;
- tilting angles of LOS of L;
- bearing angle of LOS of R;
- tilting angles of LOS of R.

allows so to calculate x y z coordinates of a point on the surface.

Photogrammetry distance ranges from metric to kilometric and is suitable for a large number of technical, industrial and scientific purposes; surveyed surfaces range from portions of the earth's surface to small object, such as industrial parts, historical buildings or human bodies to astronomical objects.

Traditionally, a long-range photogrammetry, commonly named LRP, from a close-range photogrammetry, commonly named CRP is distinguished. Usually, LRP is referred to any photogrammetric survey aimed to represent objects (commonly airborne survey of terrestrial surface) located at least 300 m far. While LRP is often focused on the airborne survey of terrestrial surface, CRP is often used with ground-based devices. The use of compact and high performing cameras mounted on UAV has in the last decade spread the use of CRP on airborne surveys. The use of cameras on UAV has made aerophotogrammetry feasible also for rock slope characterisation, both of natural slope (Puppala et al., 2018) and of mine (Thoeni et al., 2016), while in the past aerophotogrammetry had operational limits related to the distance of the target on to the line of sight for subvertical object.

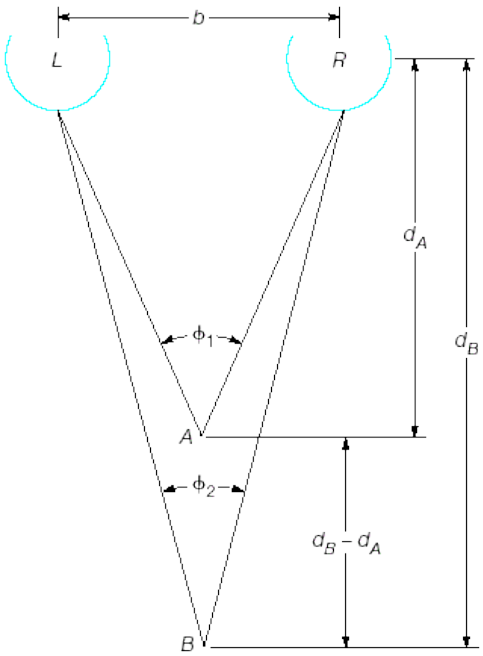

Figure 19 - Sketch of the binocular vision. From Wolf & Dewitt (2000)

Precision of the surface model is, of course, related to the distance of the stereopair from the object, at the same focal conditions; CRP is so largely used for rock mass survey for its greater precision and for the different line of sight, that is more suitable to describe step or subvertical surfaces.

The generic name for data acquisition devices is sensor, consisting of an optical and detector system. The most typical sensors are cameras where photographic material serves as detectors. The sensor can be mounted on a platform, such as an airplane, or a drone.

The photogrammetric products fall into three categories, that reflect three steps: photographic products, computational results, and maps.

The first product of photogrammetry is the orthophotographic image of the surface. This can be product from a single stereopairs or from a mosaic of multiple stereo pairs (orthophotomosaic).

During the time of exposure, a latent image is formed and is developed to a negative on the film of the camera. Stereoimages product with photogrammetry can be affected by a distortion related to the orientation of the camera with the surface; the image needs so a correction, named *rectification*, that allows to the new image to be parallel to the ground. If the ground has a relief, then the rectified photograph still has an error; an example of this error is given by Google Earth images, that are not orthorectified and that are affected by a deformation related to the 3-dimensionality of Google Earth images. Once an image is orthorectified, a map, or generally speaking a 3D model of the surface, can be derived. Orthophotos can be then merged into larger orthophotomosaic.

Computational results include the models that represent the surface of the object (mesh, point cloud, digital elevation models). These models require the presence of ground control points with known coordinates and/or the knowledge of other geographic information such as the coordinates of the cameras and tilting and bearing angles of the cameras.

Finally, the model of the surface is the input data for the production of the map of the surface, that includes graphic information such as contour line of the elevation plus eventual additional thematic items (toponomastic, hydrography, ways, morphological features, etc).

Photogrammetric computational results have been carried out by specific software for 3D topographic modelling since last 3 decades; one of this software, used in this research, is SiroVision, developed by CSIRO.

Software have significantly increased the feasibility of digital photogrammetry, making the triangulation of digital images, named soft-copy (Chandler, 1999; Lane et al., 2000) e feasible tool for large areas. Nowadays, in fact, soft-copy triangulation allows the triangulation by overlapping areas of a large number of images, taken by ground-based system, or airborne (Westoby et al., 2012). UAV diffusion nowadays makes photogrammetry a quick tool for the remote sensing of meso-scale areas (up to some square kilometres), included mines thanks to the availability of image large dataset. Increased computation power makes processing of larger number of images possible, allowing the use of close-range photogrammetry for wide areas. *Structure-from-Motion photogrammetry*, developed by Westoby et al., (2012) has been developed to process large dataset of images and operates under the same basic tenets as stereoscopic photogrammetry, although differs fundamentally from conventional photogrammetry, in that the geometry of the scene, camera positions and orientation. The construction of the 3D model is solved automatically without the need to specify a priori, a network of targets with known 3-D positions, the georeferencing operation of which is a time-consuming operation and that could be not possible in remote or step areas. *Structure-from-Motion photogrammetry* is so an useful tools for surface characterisation, such as monitoring of fluvial morphology, as regarding river bed (Lane, 2000; Chandler et al., 2002; Brasington & Smart, 2003; Bird et al., 2010), as regarding erosion process (Barker et al., 1997; Pyle et al.,1997; Betts & DeRose, 1999), and for soil loss evaluation (Stojic et al., 1998; Hancock & Willgoose, 2001; Rieke-Zapp & Nearing, 2005; Heng et al., 2010). *Structure-from-Motion photogrammetry* has been successfully applied to discontinuity characterisation (Krosley et al., 2006; Sturznegger & Stead, 2009b; Thoeni et al., 2014; Vasuki et al., 2014), and rock slope stability analysis (Haneberg, 2008) also in open pit mines (Thoeni et al., 2012; Thoeni et al., 2014; Santise et al., 2018).

3.2. Lidar method

Lidar (Laser Imaging Detection and Ranging) is a surveying method that measures distance by illuminating the target with a laser beam and measuring the reflected pulses with a sensor. Differences in laser return-time and wavelengths can then be used to produce digital 3-D representations of the surface.

The use of a monochromatic and coherent beam of electromagnetic (em) radiation with high intensity (light amplification by stimulated emission of radiation - L.A.S.E.R. beam) had its first applications for precision operations for industry. Laser beam has 3 main characteristics:

- Unidirectionality;
- Homogeneity of the frequency of the beam;
- Temporal and spatial coherence of frequency and wavelength. Waves with the same frequency and phase get amplified producing a wave train with high intensity.

An em beam allows to calculate the distance of a target from a laser device in 2 possible ways:

- Measuring Δt between the time of emitting of em radiation and the arrival time (pulsed laser);
- Measuring the phase difference Δy (Figure 20; Equation 25 - 29) between emitted em beam and received em beam (continuous-wave laser).

Equation 25

$$\Phi = \frac{2\pi}{\Lambda} \times x \times n$$

Equation 26

$$y = \sin(\Phi) \times A = \frac{2\pi}{\Lambda} \times A \times x \times n$$

$$x = 2D$$

Equation 27

$$y_1 = \frac{2\pi \times A}{\Lambda} \times 2D \times n_1$$

Equation 28

$$y_2 = \frac{2\pi \times A}{\Lambda} \times 2D \times n_2$$

Equation 29

$$\Delta y = \frac{2\pi \times A}{\Lambda} \times 2D \times n$$

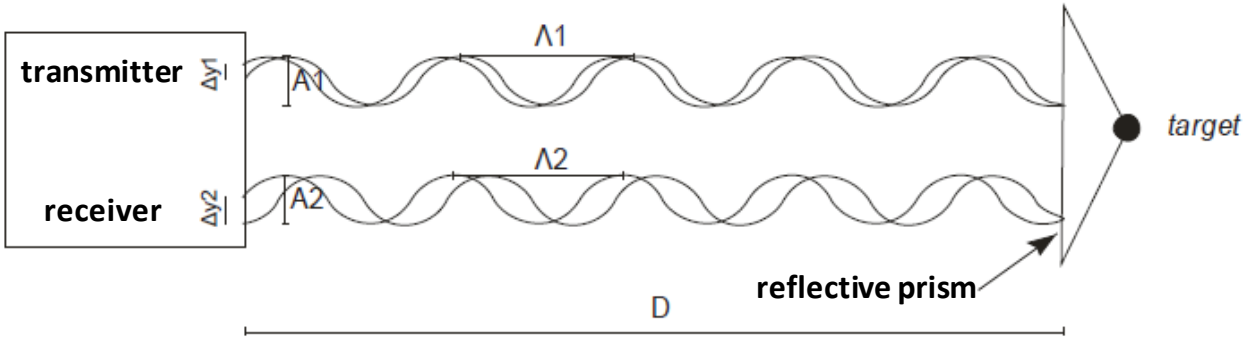

Figure 20 - sketch of a laser system. D: distance between the laser device

The calculation of the number of phases n is then required. The most commonly used method consists in the increase of the wavelength of the beam 10 times. A first measurement of the phase of the waves is taken using a very long wavelength, more than the double of the laser device- target distance: $\Lambda_1 > 2D$. For this first measure the number of phases is 0 $n_1 = 0$

A first approximated value of the distance laser device-target D is so obtained with Equation 30 - 32.

Equation 30

$$D = \frac{n \times \Lambda_1}{2} + L_1 = \frac{n \times \Lambda_2}{2} + L_2$$

Equation 31

$$L_1 = \frac{\Delta_{\Phi_1} \times \Lambda_1}{4}$$

Equation 32

$$L_2 = \frac{\Delta_{\Phi_2} \times \Lambda_2}{4}$$

The method use then shorter wavelength until the required precision is reached.

Laser technology has been applied in remote sensing environment since the end of the 1990s. Since then its application in rock slope stability has been largely increased, both from ground-based (*Terrestrial Laser Scanning*), as from airborne-based platforms (*Aerial Laser Scanning*). Aerial Laser Scanning applications range from landslide mapping (Van Den Eeckhaut et al., 2007; Corsini et al., 2009; Borkowski et al., 2011; Đomlija et al., 2014) to monitoring of wide scale processes (Thoma et al., 2005; Corsini et al., 2009). Rather, Terrestrial Laser Scanning has been widely applied to characterization of rock masses (Slob and Hack, 2002; Rahman et al., 2006; Jaboyedoff et al., 2007; Slob, 2008; Lato et al., 2009; Sturzenegger & Stead, 2009a; Gigli et al., 2013, 2014) and monitoring, especially rockfalls (Rosser et al., 2005; Abellán et al., 2009; Abellán et al., 2011), rockslides (Oppikofer et al., 2009) and other landslide types (Teza et al., 2007; Monserrat & Crosetto, 2008; Jaboyedoff et al., 2009; Prokop & Panholzer, 2009).

3.3. Building a surface 3D model from a photogrammetric survey: Siro3D code

The software package SiroVision (http://www.SiroVision.com/) has been used for the data acquisition and analysis. The software includes two codes: a code for the building of a georeferenced 3D model (Siro3D) and a module for the discontinuities extraction (SiroJoint).

SiroVision is a commercial software specifically developed to mapping geologic features and that allows to import and to elaborate stereo pairs to produce a mesh of the rock wall surface on the insert planes of which and joints in order to obtain a geostructural model of the rock wall. It uses a scanning light and a pair of Charge-Coupled Device (CCD) cameras to determinate the 3D geometry of rock mass (Cheung et al., 1996). SiroVision is a geology / geotechnical mapping and analysis system that indeed generates accurate, scaled 3D images of rock faces,both in open pit and in underground environments. Although SirioVision development has been focused on mining environment, geomechanical data extraction is obviously suitable to assess the rock mass stability and the failure mechanism affecting rock mass, both in natural slopes and in anthropic cuts.

It is constituted by Siro3D module, that allows to import stereo pairs image and elaborate a mesh of the surface, and SiroJoint, that allows to insert the geomechanical relief on the 3D model made with Siro3D.

Purchased from the Commonwealth Scientific Industrial and Research Organization (CSIRO) in Australia, it is commercially distributed by Datamine ltd, world leading provider of mining software technology and services that are required to plan, manage and optimize mining operations. SiroVision first version was developed in 1991 (Ord & Cheung, 1991; Ord et al., 1991) and was based on SiroJoint and SiroFrag aspects.

Siro3D input data include:

- Type of sensor (camera or stereo-camera). The following stereo camera model are suitable for input data images: CSIRO Stereo Camera, CAE Mining Stereo Camera Mark I, Datamine Stereo Camera Mark II;
- In case optical sensor is constituted by a camera, a camera calibration file and the model and serial number of the camera and of the lens are needed. Camera calibration file can be a .iwp or .txt file. This file indicates pixel width, pixel height, image width, image height camera model, focal length in mm (C), principal point x and y coordinates (X_P; Y_P), radial distortion of the lens (K_1; K_2; K_3), tangential distortion of the lens (P_1; P_2), affinity (B_1) and skew (B_2) parameters. SiroVision contains libraries of camera calibration file files produced with model of camera/focal length of lens. In case the survey has

been carried out with a coupling model of camera/focal length of lens present in the list, the .ccf file will be imported by selecting the coupling used; otherwise, the user can create a custom camera calibration file indicating model of camera, focal length of lens, principal point x and y coordinates (X_P; Y_P), radial distortion of the lens (K_1; K_2; K_3), tangential distortion of the lens (P_1; P_2), affinity (B_1) and skew (B_2) parameters. For case study 1 of this project, a camera calibration file has been imported by the selection of a model of camera/focal length of lens coupling present in the library, while for case study 2 has been used a coupling model of camera/focal length of lens not present within the list and so a camera calibration file has been on porpoise created;

- Survey_file (.txt, .csv or .nmea file formats): indicates the spatial coordinates xyz of camera position and/or of reference points. This file is imported during georeferencing phase.

Stereo pairs processing requires to indicate if a Generic Calibration File, previously set, or a Custom Calibration File will be used, and if a new image data will be created or an existing image data will be uploaded. In case of existing image data, a Task_Setup_Data.txt file with the coordinates of the task points of the two images to merge into a stereo couple, and a Matching_Data_File.dat (Figure 21) must be uploaded. In case of new image data, a Task_Setup_Data.txt and Matching_Data_File.dat file can be produced in a second moment by the command "Build 3D image", after the selection of the two images of the stereo pair. It is possible to reduce the image size and the number of colours of the chromatic scale in order to reduce memory and time consume. The last step of the stereo pair processing is creating the 3D image of the surface by the "Build 3D image" command of the Project Explorer tool.

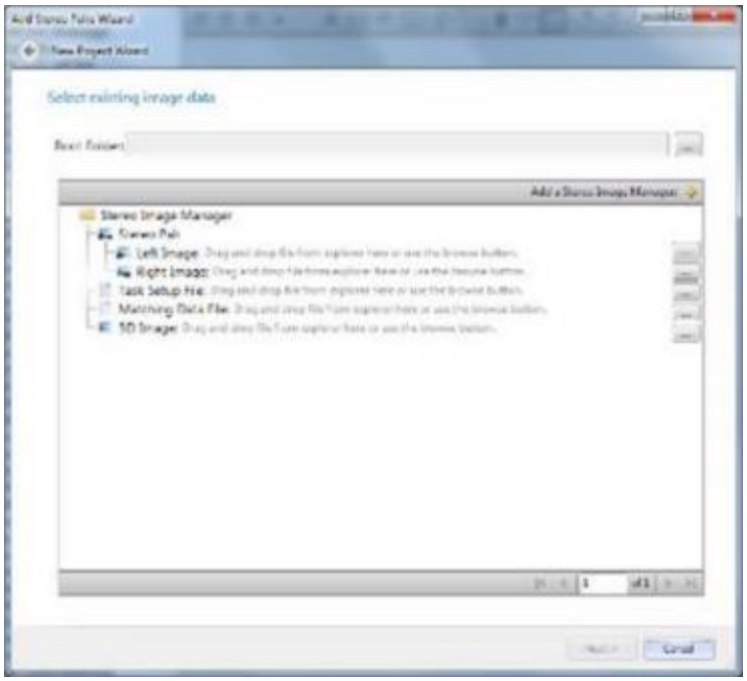

Figure 21 - selection of the stereo pairs, task setup file and matching data file to build a stereo couple from an existing image data

Siro3D allows to view the point cloud and the 3D wireframe, as well as 2D images and 3D images projected of the wireframe. 3D images can be exported by the Export Wizard command of the Tools menu as .tiff, .pdf3D, .dxf, .ply or .obj file.

3.4. Use of photogrammetry and lidar methods for the rock mass characterisation

3.4.1. SiroJoint

SiroJoint allows to import both 2D images (.tif or .cr2) and 3D images (.tiff), that can be produced by Siro3D. Planes and traces can be manually added on the images by the commands 'Add plane' and 'Add tracing' of the Image View Workspace. The command Add Plane Assisted of the Image View Workspace indeed adds a plane in a semiauthomatical way by clicking on a plane of the image. Stereoplot and rose plot of the discontinuity are visible in Stereoplot and Rose Plot workspaces and enable to recognize which discontinuities could be grouped into a set. Within 'Property view' tab is possible selecting and deselecting which elements (i.e.: traces, planes, scanlines, survey lines, etc.) made visible on the 3D image window and on the stereoplot window. Because λ and spacing of the sets of discontinuities can differ lithology by lithology, SiroVision V.6 allows to suggest a subdivision of the rock mass on base of the chromatic differences of the outcropping lithologies. A specific tool allows also to split the rock mass into different structural domains.

As for the 3D images, also planes, traces, scanlines, survey lines and mineral classification can be exported in .csv and .dxf format. Discontinuities can be exported also in .datamine, .bs, .surpac or .minesight format and can be analysed with other software for the geostructural rock mass characterization (i.e. Bs, Minescape, RokDoc GeoMechanics, StereoNet, StereoStat).

SiroJoint code is the second part of SiroVision package and with Siro3D forms a single tool for the description of the slope. This tool allows to draw traces and planes with a low time consume (an experienced user can draw hundreds of traces and/or planes an hour, depending on the freshness of the discontinuities, the distance of the wall from the camera position and on the definition of the images). The possibility to extract the discontinuities identified and the build 3D surface with .dxf format allow to carry out also the block stability analysis with specific software for slope stability and block removability analysis (i.e. SiroModel, used in this research). The code allows to export a number of parameters of traces and planes, such as: β (or plunge), α (or trend), λ, Terzaghi weighting, displacement (σ of the points that form the plane from its centroid), reliability (Figure 22 and 23). The program has both spherical (equal angle or equal area) and rose diagrams, that can be automatically updated as each discontinuity is measured and represents a useful tool to have a first general idea about the number of sets.

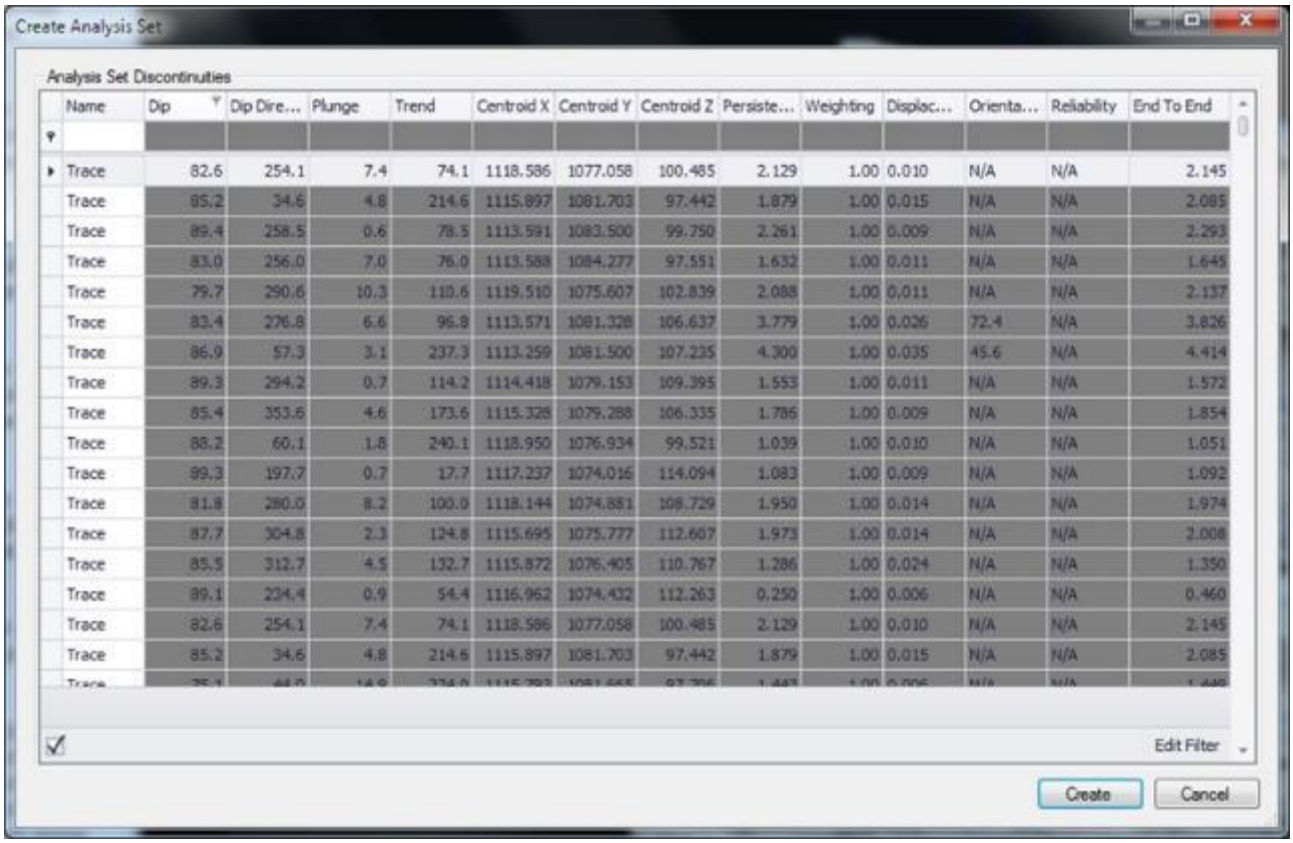

Name	Dip	Dip Dire...	Plunge	Trend	Centroid X	Centroid Y	Centroid Z	Persiste...	Weighting	Displac...	Orienta...	Reliability	End To End
Trace	82.6	254.1	7.4	74.1	1118.586	1077.058	100.485	2.129	1.00	0.010	N/A	N/A	2.145
Trace	85.2	34.6	4.8	214.6	1115.897	1081.703	97.442	1.879	1.00	0.015	N/A	N/A	2.085
Trace	89.4	258.5	0.6	78.5	1113.591	1083.500	99.750	2.261	1.00	0.009	N/A	N/A	2.293
Trace	83.0	256.0	7.0	76.0	1113.588	1084.277	97.551	1.632	1.00	0.011	N/A	N/A	1.645
Trace	79.7	290.6	10.3	110.6	1119.510	1075.607	102.839	2.088	1.00	0.011	N/A	N/A	2.137
Trace	83.4	276.8	6.6	96.8	1113.571	1081.328	106.637	3.779	1.00	0.026	72.4	N/A	3.826
Trace	86.9	57.3	3.1	237.3	1113.259	1081.500	107.235	4.300	1.00	0.035	45.6	N/A	4.414
Trace	89.3	294.2	0.7	114.2	1114.418	1079.153	109.395	1.553	1.00	0.011	N/A	N/A	1.572
Trace	85.4	353.6	4.6	173.6	1115.328	1079.288	106.335	1.786	1.00	0.009	N/A	N/A	1.854
Trace	88.2	60.1	1.8	240.1	1118.950	1076.934	99.521	1.039	1.00	0.010	N/A	N/A	1.051
Trace	99.3	197.7	0.7	17.7	1117.237	1074.016	114.094	1.083	1.00	0.009	N/A	N/A	1.092
Trace	81.8	280.0	8.2	100.0	1118.144	1074.881	108.729	1.950	1.00	0.014	N/A	N/A	1.974
Trace	87.7	304.8	2.3	124.8	1115.695	1075.777	112.607	1.973	1.00	0.014	N/A	N/A	2.008
Trace	85.5	312.7	4.5	132.7	1115.872	1076.405	110.767	1.286	1.00	0.024	N/A	N/A	1.350
Trace	89.1	234.4	0.9	54.4	1116.962	1074.432	112.263	0.250	1.00	0.006	N/A	N/A	0.460
Trace	82.6	254.1	7.4	74.1	1118.586	1077.058	100.485	2.129	1.00	0.010	N/A	N/A	2.145
Trace	85.2	34.6	4.8	214.6	1115.897	1081.703	97.442	1.879	1.00	0.015	N/A	N/A	2.085

Figure 22 - Fields of the table of SiroJoint that describes traces and planes

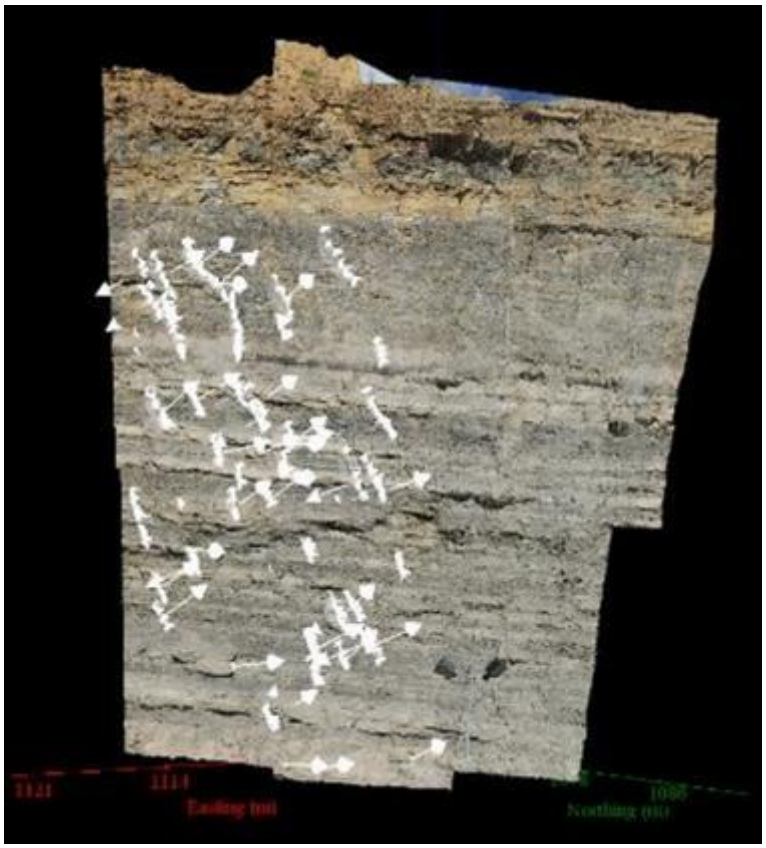

Figure 23 - Location of the discontinuities extracted in Figure 24

Figure 24- Selection of filter parameter to extract the sets of discontinuities by SiroJoint

3.4.2. I-Site Studio

I-Site Studio is a wide commercial package developed by Maptek for mining, civil, geological and other surveying applications and helps to integrate mine processes, allowing efficient and accurate delivery of spatial information to support slope design and slope risk assessment. It runs on Windows operative system (64 bit) and is a semiquantitative tool for the extraction of the discontinuities. Despite the other semiquantitative tools used, it needs, besides a point cloud, an optical information too. The software contains a specialised geotechnical module that allow to identify the planes since the drawing of a planes on the surface and the indication of minimum number of point and the value of the difference of the angles. For this reason, it is an intuitive tool for discontinuities extraction. It is a low time-consuming tool and its reliability makes it widely used in mining industry. It allows to import the surface (x y z RGB) with .3Di, 3Dp, 3Dr, .asc, e57, .fls, .ixf, .las, .mpc, .ptg, .ptx, .toc, .txt, .zfs format or, alternatively, with a customized file format.

This code has been chosen within the present study because it differs from other semiautomatic discontinuity extraction codes and it represents a hybrid tool between manual and automatic discontinuities extraction tools. It is a manual tool as regarding the selection of β, α and minimum number of points parameters of the planes, but it then automatically extracts the planes that satisfy the selected conditions.

3.4.3. DiAna

DiAna code (Gigli & Casagli, 2011) allows the semiautomatic extraction of discontinuities and is based on 3 main steps: 1) identifying of the planes; 2) bounding the planes; 3) clustering into sets. The approach is based on the selection of a sub-set of the point cloud (red points in Figure 25) contained within a searching cube (red cube in Figure 25).

Planes are identified by the definition of the minimum number of points to consider building the best fitting plane and of the σ range value of the plane within the searching cube (Figure 25). The minimum number of points must be chosen in order to avoid the extraction of small and not representative sets. Then the best fitting plane (blue grid in Figure 25) according to the least squares method is found for the cubic selection.

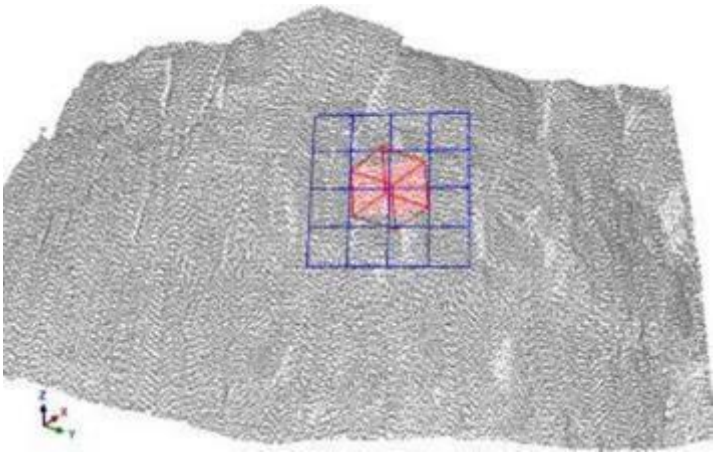

Figure 25 - Space partitioning and extraction of planes within the reference cube. From Gigli & Casagli (2011)

Another parameter that allow to detect planes is the σ. Maximum σ threshold is chosen by the operator to extract planes. This parameter must be chosen on base of the large-scale roughness characteristics of the rock slope: fewer roughness of the rock slope implies a greater maximum σ threshold. Planes are defined by indicating the size of the research window, the minimum number of points and the maximum co-planarity angle. Once a valid cluster has been identified, the associated plane orientation is found. The next step is grouping all the adjoining planes of the same discontinuity plane. This is done by comparing the orientation of all neighbouring planes: if their orientation is less than the maximum coplanarity angle, previously set, they are supposed to belong to the same discontinuity surface. By counting the number of discontinuities belonging to the same set intersected by the cylinder (hatched polygons, Figure 26) and measuring the maximum distance between them (Figure 26) it is possible to assess the mean, minimum and maximum joint spacing, and the associated frequency of each set. If a set is defined to be infinitely persistent (i.e. bedding planes), its spacing is calculated by considering all the discontinuities belonging to that set, independently from their position.

With DiAna code 6 of the 10 parameters suggested by ISRM (1978) (Chapter 2) for the quantitative description of discontinuities (orientation, spacing, persistence, roughness, number of sets and block size) can be semi-automatically calculated. These 6 parameters represent all the parameters suggested by ISRM (1978) for the rock mass description because the remaining four parameters (aperture, seepage, wall strength and filling) cannot be assessed from conventional high-resolution point clouds, as their estimation requires direct access to the rock slope.

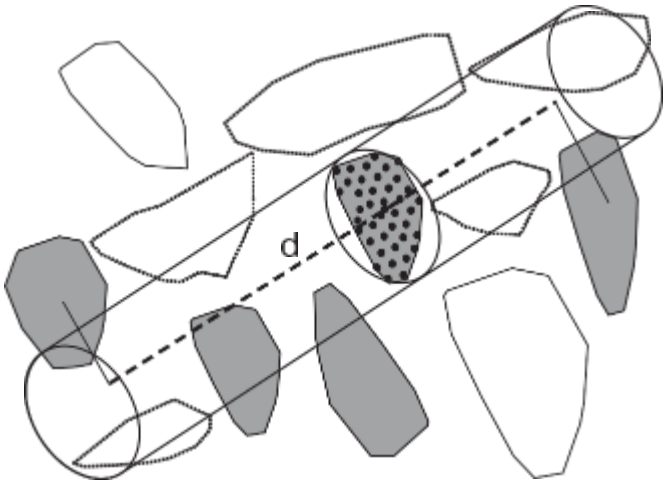

Figure 26 - Calculation of the true spacing and frequency of discontinuity sets with DiAna. From Gigli & Casagli (2011)

3.4.4. Facets

Facet is a plugin (http://www.cloudcompare.org/doc/wiki/index.php?title=Facets_(plugin); Dewez et al., 2016) of the Cloud Compare package. Cloud Compare has been developed by Girardeau-Montaut for 3D point cloud (and triangular mesh) editing and processing. Originally developed to compare dense 3D point clouds, now is a wide package that allows to work on points clouds and meshes and has been implemented with many processing algorithms (registration, resampling, colour/normal vectors/scalar fields management, statistics computation, sensor management, interactive or automatic segmentation, etc.) and tools (custom colour ramps, colour & normal vectors handling, calibrated pictures handling, OpenGL shaders, plugins, etc.). Many plugins have been added (qAnimation, mesh boolean animation, qVirtualBroom, qHoughNormals, qHPR, qPCL, qPCV, qPoissonRecon, qRansacSD, qSRA, qM3C2, qCork, qAnimation, Facets, Compass), some of which for geological and geotechnical porpoise (Facets, Compass). In particular, Facets has been developed with the financial support of BRGM. Both CloudCompare and Facets are license-free and available for Windows (XP, Vista, Windows7, Windows8, Windows10) 64 bits and 64 bits stereo, MAC OS 64bits and Linux 64 bits, with ATI or successive graphic cards. It represents so a useful and free tool that could have a widespread diffusion. It has been already used for the characterization of rockfall hazard and fracture systems in natural outcrops (Inama, 2016; Massiot et al., 2017; Thiele et al., 2017), in underground workings (Blanch et al., 2017; Vazaios et al., 2017) and cavities (Dewez et al., 2017), but also in open pit mines (Sampaleanu et al., 2017), man-made cuts (Riquelme et al., 2017), and historical sites (Hatzopoulos et al. 2017), with points clouds collected both with Lidar (Hatzoupoulous et al. 2017; Thiele et al., 2017; Vazaios et al., 2017;), and with photogrammetry (Blanch et al., 2017; Riquelme et al., 2017; Thiele et al., 2017). Although its recent development (2016) it has been used in many studies also because it is free. Its possible wide use represents the reason because this tool has been included in this research.

It allows two methods to describe the sets of discontinuities of a rock wall:

- *Kd trees method*: this method recursively divides the cloud in small planar patches. These planar patches are then regrouped in bigger 'facets'. As for DiAna, the maximum co-planarity angle must be provided (Figure 27).
- *Fast Marching method*: this method divides the surface into surface with similar area values. Therefore, all the patches will have almost the same size, but some may be very flat while others not (depending on the resolution). The fusion process is based on a (Fast Marching) front propagation (Figure 27).

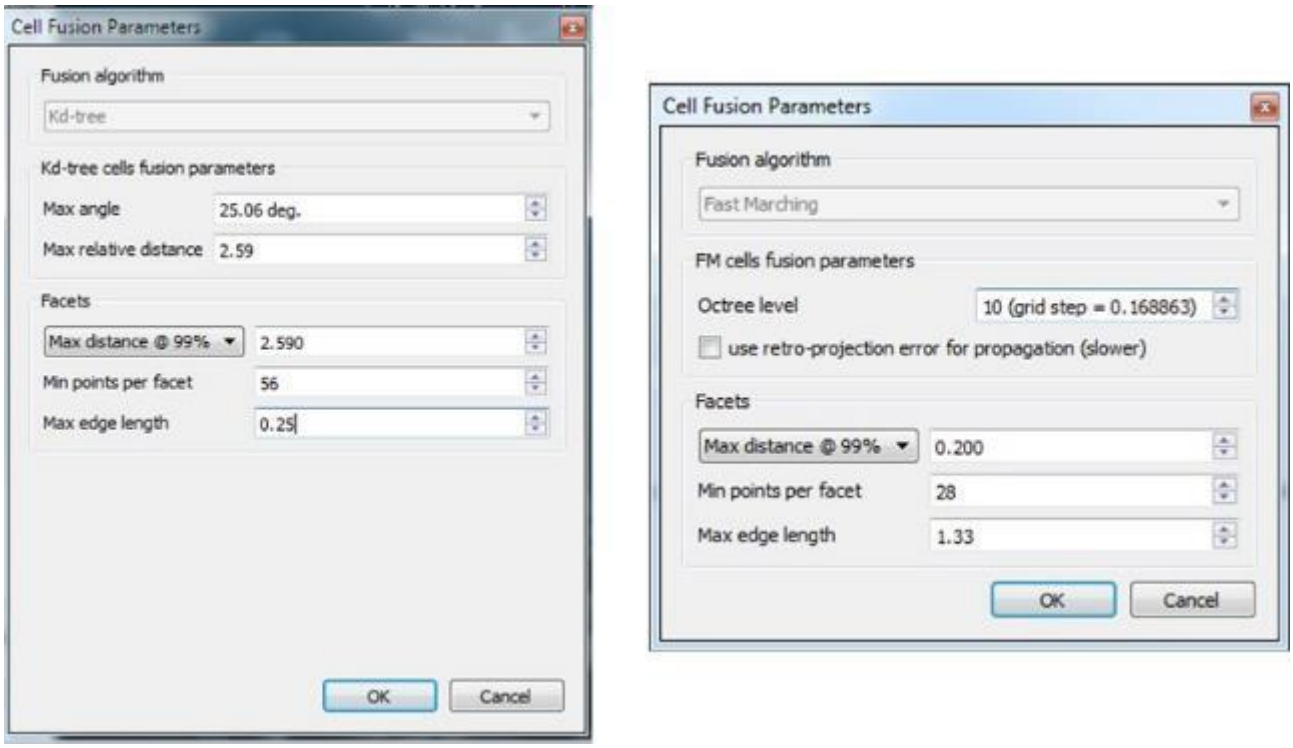

Figure 27 - Input parameters for Facet plugin of Cloud Compare. Left: with a kd-tree; right: with a Fast Marching

The difference between the two methods is the algorithm for the identification of the planes. Both Kd trees method as Fast Marching method requires (Facet frame) 3 criteria to evaluate if considerate as valid the detected plane. These criteria are the distance of the points from the regression plane, the minimum number of points per facet and the maximum edge length (Figure 27).

To summarize, Facet plugin requires the following parameters:

- Kd-tree cells fusion parameters:
  - Max angle: maximum angle between neighbour patches to merge them together;
  - Max relative distance: maximum distance between the merged patches and the current facet centre.
- For the Fast Marching process two parameters can be set by the user:
  - the grid resolution (expressed as the subdivision level of the cloud octree as we use the octree for a faster initialization);
  - whether to re-compute the facet retro-projection error each time a patch is merged (slower but more accurate)
- Facets frame:
  - Distance criterion: indicates the maximum distance between the regression plane and the points. It's possible to indicate the maximum distance of 68%, 95%, 99% or 100% of the points as criterion to establish co-planarity of the points. For instance, 'Max distance @ 95%' means that 95% of points have to be closer to the value specified in the field on the right;
  - Min points per facet: facets smaller than this value will be discarded. This parameter must be set on the size of the faces and on the resolution of the point cloud. More the rock mass is heavily fractured, minor the number of points to define a plane, more the point cloud is dense, more the minimum number of points to distinguish a plane;

- Max edge length: parameter used to extract the facet (concave) contour (the smaller the closer to the points the contour should be);

Outputs of the code are the the facets (.shp, .txt, .csv, .xyz, .bin, .neu, .pts, .las, .laz, .e57, .dp, pdc, .pov, .pv, .pn, .vtk, .ply), the stereoplot of the poles of the discontinuities (Figure 28) and the subsetting of the discontinuities. To summarize, Facet plugin allows to:

- automatically extract planar facets (e.g. fracture planes) from point clouds;
- export the facets to SHP files;
- classify the facets based on their orientation and their (orthogonal) distance;
- display the orientations on a stereogram/Stereoplot;
- filter the facets (or the points if they have normal) based on their orientation.

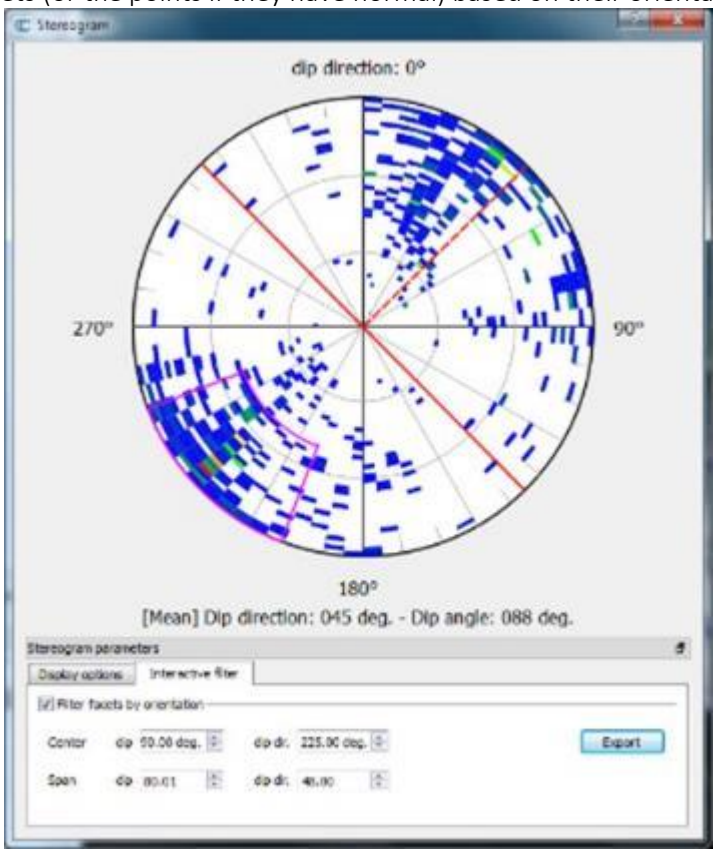

Figure 28 - Facet plugin outputs: the stereoplot

4. Quantitative assessment methods for rock slope stability

The best design of a man-cut rock slope is strictly related to its safety and so to its stability. The stability of a slope can be studied by different approaches and methods describing the rock slope stability can be mainly subdivide into the following categories:

- Kinematic analysis methods: describe the failure modes of the blocks (plane failure, wedge failure, block toppling, flexural toppling). Formulas related to kinematic analysis calculate the relative probability for each single failure mode, that corresponds to the percentage of poles (i.e.: plane failure and flexural failure), or of discontinuity intersections (i.e: wedge failure or block toppling) into critical areas of the stereoplot;
- Block Theory: describes which block is removable from the surface of the slope;
- Limit Equilibrium Methods: describe the Factor of Safety (FOS) of a slope, or of a single block, that is the ratio of the shear strength to the shear stress required for equilibrium;

In this Chapter the kinematic analysis, the Block Theory and the Limit Equilibrium Method will be exposed. These issues constitute the bulk architecture of the codes used for the study of the rock slope stability performed by Dips (2D kinematic analysis), DiAna-K (3D kinematic analysis) and SiroModel (Block Theory and Limit Equilibrium Method).

Kinematic analysis is a quantitative study that allows to choose the best cost-benefits solution for road tracks and bench orientation, comparing different results changing the β and α of the planned man-made cut. Kinematic analysis allows to calculate the kinematic stability thanks to the formulas prosed by Goodman & Bray (1976), Hoek & Bray (1981), Matheson (1983), and Hudson & Harrison (1997). For this reason, formulas have been derived for different failure modes and allow to evaluate the best design solution, both for open pit mines, and for road cuts. Because a homogenous rock mass can be described with the β and α of its discontinuities, the stereoplot allows to use simple geometrical relations between the orientation of the discontinuities to evaluate the stability of the outcropping blocks. Kinematic analysis is so a useful tool to choose the best design of the slope, by comparing the index calculated with these formulas. Kinematic analysis has 2 assumptions: each discontinuity is infinitely persistent and with c = 0. Each discontinuity is so equally weighted despite its persistence.

Block Theory (Goodman & Shi, 1985) provides a classification of the blocks inside rock mass dividing by removability and stability condition. Some blocks are not able to move into the free space of the excavation, by virtue of their shape, size, or orientation and because they are prevented from moving by other blocks. Other blocks are, instead, immediately in a position to move, as described in Figure 29. The main aim of Block Theory is so individuating the critical blocks, named *keyblocks*, (Figure 29), that prevent the movement of the other blocks. This analysis is carried out by the 3D analysis the system of discontinuities. The intersections of numerous discontinuities create blocks of irregular polyhedral shape in the rock mass; then, when the excavation is made, many new blocks get removable with the new free surfaces. Block Theory considers the discontinuity infinitely persistent and set cohesion to 0.

Another approach to slope stability, is given by the Limit Equilibrium Method. The Limit Equilibrium Method (Fellenius, 1936; Janbu, 1954; Bishop, 1955; Spencer, 1967; Sarma, 1979; Hoek & Bray, 1981) is based on the definition of the FOS, that is the ratio of the shear strength (or, alternatively, an equivalent measure of shear resistance or capacity) to the shear stress (or other equivalent measure) required for equilibrium. So, if FOS<1, the slope or the block will collapse, otherwise it is stable. Limit Equilibrium Method considers a known or assumed potential slip surface affecting the slope, both soil slope, and rock slope, and are based on the comparison of forces, moments, or stresses resisting movement of the mass. In case of rock slope, methods describe the block failure along distinct discontinuities and have as output of the FOS of the block. If the value of FOS is less than 1, the block is unstable, otherwise is stable.

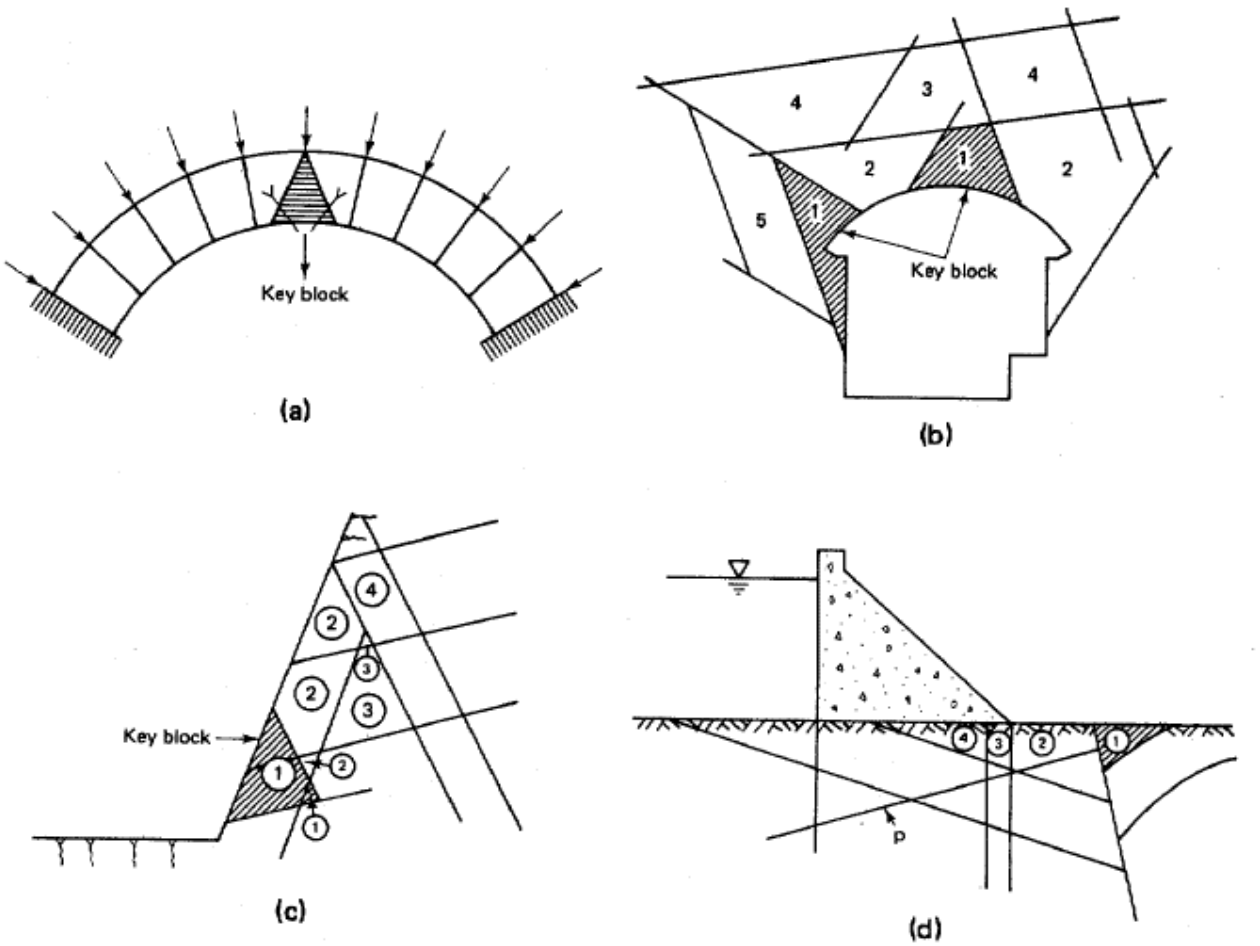

Figure 29 - The detection of removable blocks for Block Theory (Goodman & Shi, 1985) in different cases. The numbers indicate the removal order of the blocks. Streaked blocks indicate the key blocks. (a) an arch; (b) the roof inside a tunnel; (c) a berm, or rock slope; (d) the foundation of a dam. From Goodman & Shi (1985)

4.1. Kinematic analysis

When discontinuities or discontinuities intersection are unfavourably oriented, 4 failure modes could involve a block: plane failure, wedge failure, block toppling, flexural toppling (Figure 30). Kinematic mechanisms can be subdivided in failure (see rock-slide in Varnes landslides classification in Figure 31) and toppling. Failure has one or two basal planes (sliding planes) that are stepper than ϕ. Toppling (rock topple in Varnes landslides classification, Figure 31) has instead one (flexural toppling) or two (block toppling) discontinuity planes that detach the block from the rock mass, along a hanging-wall; a basal plane less step than the ϕ can be present (block toppling) or not (flexural toppling); anyway intermediate case are possible (block-flexure toppling in letter c of Figure 32).

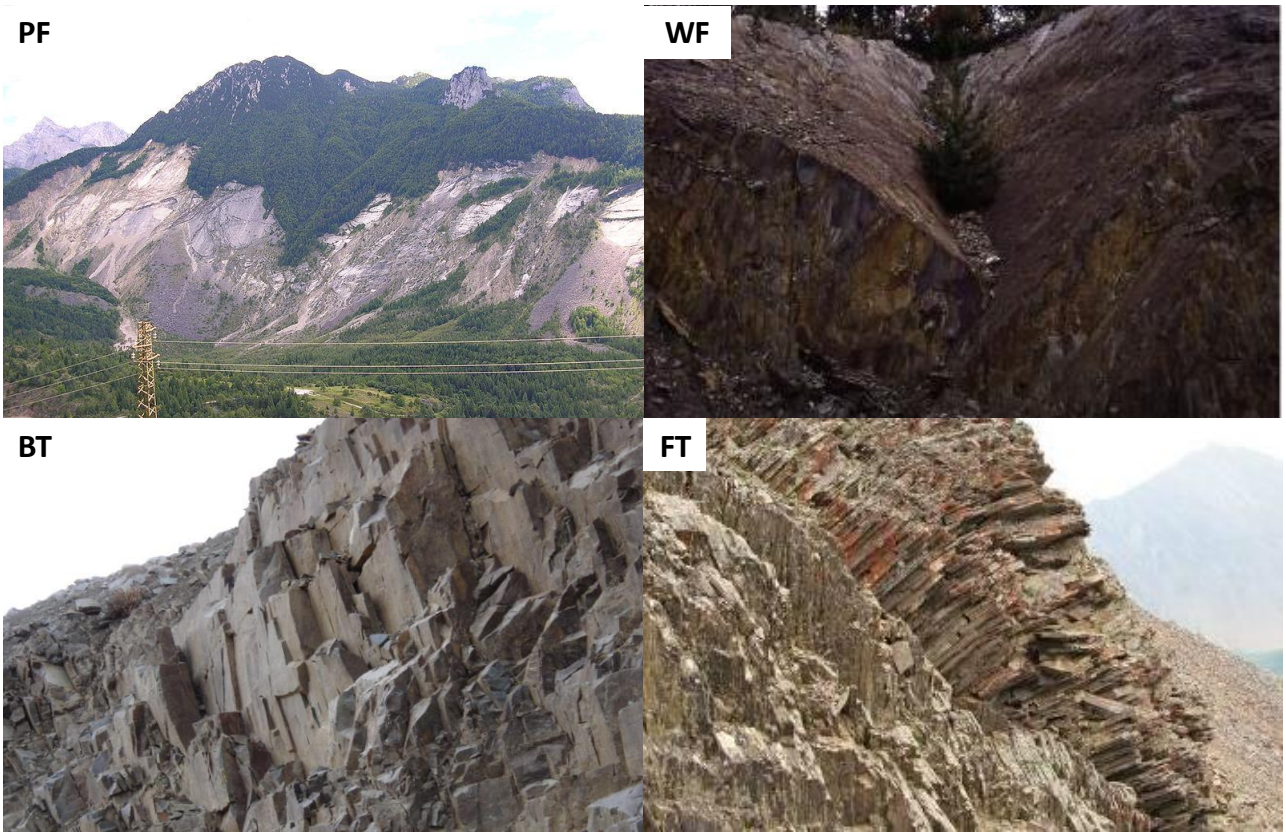

Figure 30 - Example of landslides affecting rock slopes; PF) plane failure, Vajont landslide, Northern Italy; WF) wedge failure. From Stead et al. (2011); BT) block toppling; FT) flexural toppling, Highwood Pass, Alberta, Canada. From Cruden & Hu (1994)

Type of movement	Type of material		
		Engineering soils	
	Bedrock	Predominantly coarse	Predominantly fine
Falls	Rockfall	Debris fall	Earth fall
Topples	Rock topple	rocktopple	Earth topple
Slides: rotational			
A few units	Rock slump	Debris slump	Earth slump
Slides: translationals			
A few unites	Rock block slide	Debris block slide	Earth block slide
Many units	Rock slide	Debris slide	Earth slide
Lateral spread	Rock spread	Debris spread	Earth spread
Flows	Rock flow (deep creep)	Debris flow (soil creep)	Earth flow (soil creep)
Complex	Combination of two or more principal types of movements		

Figure 31 - The movements classification proposed by Varnes (1978)

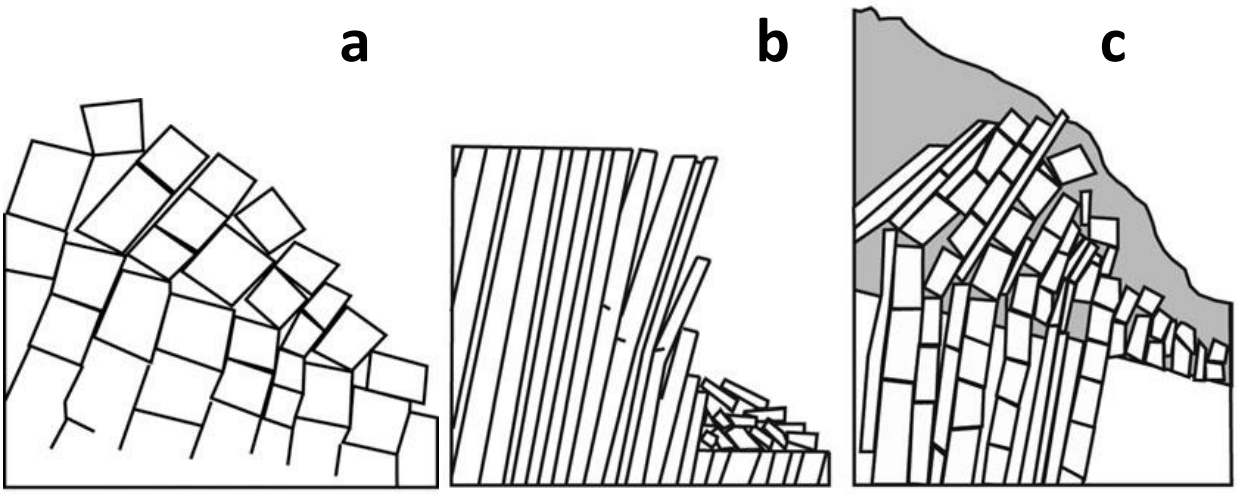

Figure 32 - Sketch of toppling failure modes: a) block toppling; b) flexural toppling; c) block-flexure toppling. From Hoek & Bray (1976)

The sketches and of these failure modes and related stereoplots are illustrated in Figure 8 in Chapter 2.

Failure conditions have been exposed by Hoek & Bray (1976) for plane failure and wedge failure, by Goodman & Bray (1976) and by Matheson (1983) for block toppling, and by Goodman & Bray (1976) and by Hudson & Harrison (1997) for flexural toppling. Casagli & Pini (1993) introduced an index, ranging 0 (no hazard) to 100, the Kinematic Hazard Index, for each failure mechanism. The values of Kinematic Hazard Index are calculated by counting the poles or the discontinuities intersections falling in critical areas within the stereographic projection.

- Plane failure conditions (Hoek & Bray, 1981):

Plane failure is the sliding of a block the contact of which with the rock mass is constituted by an only contact plane (letter a in Figure 33). In this case, 3 conditions must be satisfied for the movement of the block. These geometrical conditions are related to the orientation of the discontinuity, to the orientation of the slope, and to the ϕ (Equation 33). In particular, as regarding the β_{disc}, it must be greater than ϕ. In this case, the block will slide (law of the inclined plane) because the component of the gravity tangential to the basal plane is greater to the friction force. Another condition necessary for plane failure is that the angle between α_{slope} and α_{disc} is less than 20°, as suggested by Hoek & Bray (1981). Finally, the third condition is that the angular distance between the slope and the discontinuity orientations is less than $\beta_{slope}/2$; this condition makes that all the discontinuity with β_{disc} greater than β_{slope} are stable (dip slope stepper than escarpment case). The critical area for plane failure on the stereoplot is exposed in letter b in Figure 33.

Equation 33

$$\begin{cases} \alpha_{slope} - 20° \leq \alpha_{disc} \leq \alpha_{slope} + 20° \\ \beta_{disc} > \phi \\ \sqrt{(\alpha_{slope} - \alpha_{disc})^2 + (\beta_{slope} - \beta_{disc})^2} \leq \beta_{slope}/2 \end{cases}$$

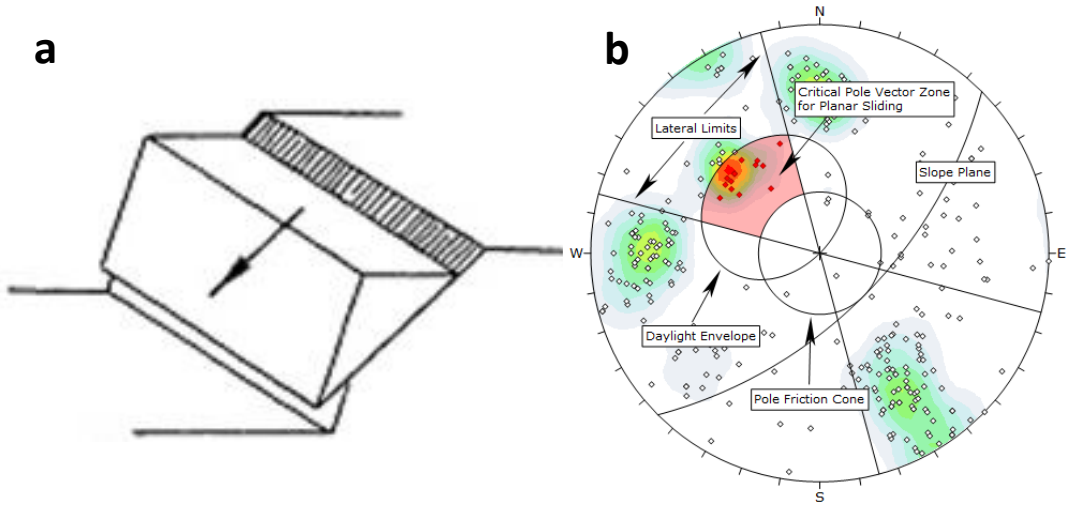

Figure 33 - Description of plane failure. a) Schematic representation of plane failure on the slope (Hoek & Bray, 1981); b) critical area for plane failure on the stereoplot (https://www.rocscience.com)

For plane failure, Kinematic Hazard Index is the percentage of poles critical to plane failure in comparison to the total amount of poles of the rock mass (Equation 34).

Equation 34

$$C_{pf} = 100 \times (N_{pf}/N)$$

- Wedge failure conditions (Hoek & Bray, 1981):

Wedge failure is the sliding of a block on 2 basal planes (letter a in Figure 34). Failure condition are graphically exposed by the Markland's test (letter b in Figure 34). An only ϕ value for both basal planes is assumed. For wedge failure, a primary and a secondary critical zone can be distinguished.

Primary critical zone includes planes intersections that satisfy frictional and kinematic conditions for sliding. It is represented by a crescent shaped made by the intersection of the friction cone with the spindle of the slope plane. According to Markland's test (Markland, 1972), wedge failure condition is related to the orientation of the intersection line between the 2 basal planes. In this case β_{inters} is between 90°- ϕ and β_{slope} because if β_{inters} < 90° - ϕ the wedge does not slide because of friction and because if $\beta_{inters} > \beta_{slope}$ the wedge does not slide because the directrix of the movement of the wedge points towards the rock mass. In a few words, primary critical zone for wedge failure is the crescent shaped area inside the plane friction cone and outside the slope plane (pink area of letter b in Figure 34). Depending on the wedge geometry, a wedge may slide along the line of intersection (so on two discontinuities) or on an only discontinuity. Sliding on an only discontinuity occurs if one of the basal planes has a more favourable orientation for sliding than discontinuities intersection. In case the intersection is included into primary critical zone, the block can slide both on a single and on two planes.

Secondary critical zone for wedge failure is included between the primary critical zone and a plane inclined at the ϕ (yellow area of letter b in Figure 34). In this region, the intersections are inclined at less than the ϕ, and so sliding can take place on a single discontinuity stepper than ϕ. In case of secondary critical zone for wedge failure, sliding will occur on a single plane. The sketch of the kinematic mechanism on the slope is exposed in Figure 34.

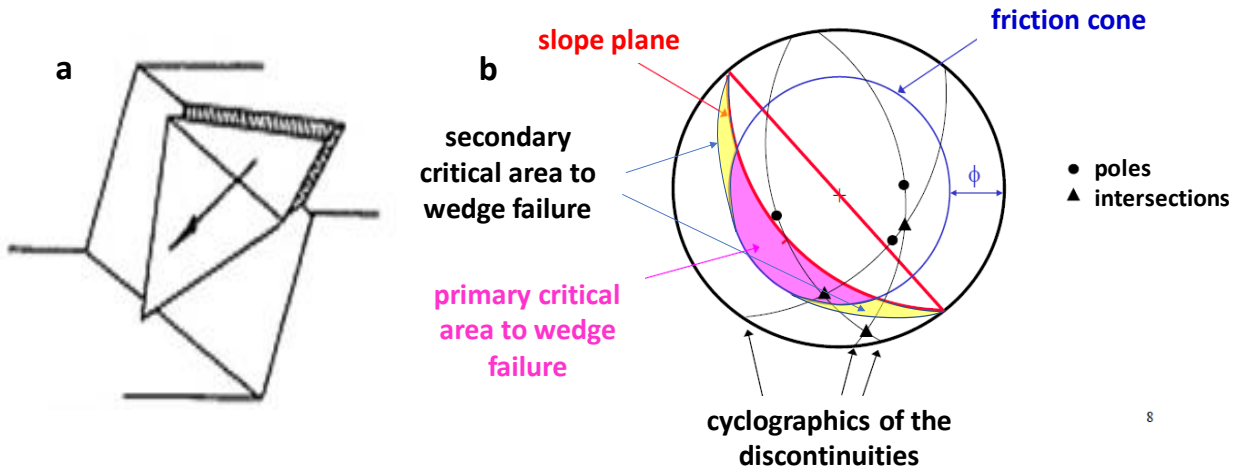

Figure 34 - Description of wedge failure. a) Schematic representation of wedge failure on the slope (Hoek & Bray, 1981); b) critical area for wedge failure on the stereoplot (Markland's test)

Kinematic Hazard Index (Casagli & Pini, 1993) of wedge failure is the percentage of intersections critical to wedge failure in comparison to the total amount of intersections of the discontinuities of the rock mass (Equation 35).

Equation 35

$$C_{wf} = 100 \times (I_{wf}/I)$$

- Block toppling conditions (Goodman & Bray, 1976; Matheson, 1983):

Block toppling is the detachment (letter a in Figure 35) of a blocks thanks to 3 discontinuities: an intersection of step two discontinuities bordering the block from the rock mass and a basal plane less steeply inclined than the ϕ. Goodman (1989) defined failure conditions for block toppling. According to Goodman:

"If layers have an angle of friction ϕ_j, slip will occur only if the direction of the applied compression makes an angle greater than the ϕ with the normal to the layers. Thus, a pre-condition for interlayer slip is that the normals be inclined less steeply than a line inclined ϕ_j above the plane of the slope. If the β of the layers is σ, then toppling failure with a slope inclined α degrees with the horizontal can occur if (90 - σ) + ϕ_j < α".

As for wedge failure, a primary critical zone and a secondary critical zone are (letter b in Figure 35).

Primary critical zone includes the sector critical for the basal plane, while secondary critical zone includes the area critical for the discontinuities intersection. As result, primary critical zone includes the poles of the discontinuities with values of βs less than 90°- ϕ and values of α included in α_{slope} ± 20°.

Secondary critical zone includes instead the intersection of discontinuities with β less than ϕ. The intersection included within secondary critical zone and with α α_{slope} ± 20° (so included also in primary critical zone) resent the most prone to block toppling; intersections that with β less than ϕ but outside primary critical zone are instead less prone to block toppling and are referred to as oblique toppling intersections (yellow areas of letter b in Figure 35). The sketch of the kinematic mechanism on the slope is exposed in Figure 35.

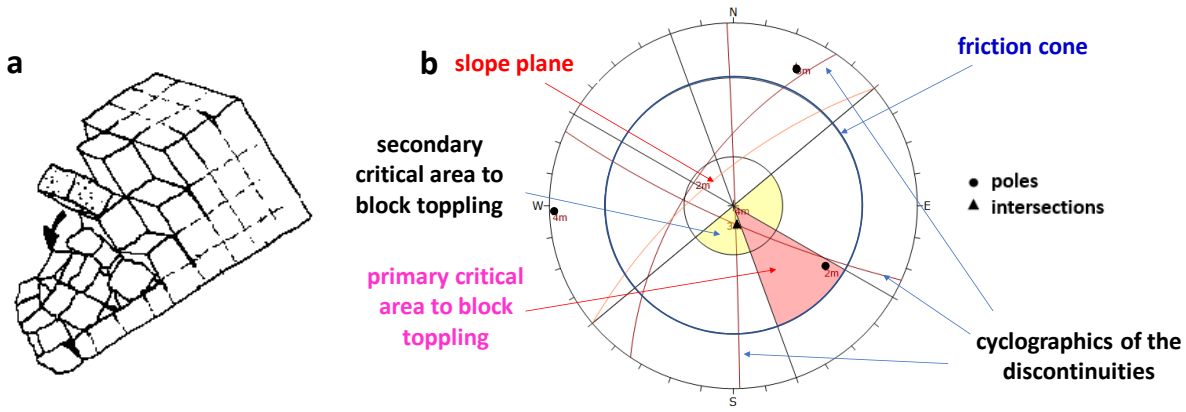

Figure 35 - Description of block toppling. a) Schematic representation of block toppling on the slope; b) critical area for block toppling on the stereoplot

Kinematic Hazard Index of block toppling for Casagli & Pini (1993) is given by the products of the ratio of intersections prone to block toppling (intersections within secondary critical areas) and of the ratio of plane suitable as basal plane (poles within primary critical areas) (Equation 36).

Equation 36

$$C_{bt} = 100 \times (N_{bt}/N) \times (I_{bt}/I)$$

- Flexural toppling conditions (Goodman & Bray, 1976; Hudson & Harrison, 1997):

Flexural toppling (Figure 36) requires two conditions. The first condition is the failure of slab-like blocks due to the detachment thanks to a subvertical and β slope discontinuity between the block and the rock mass. Discontinuities prone to flexural toppling are so stepper than complementary angle of β_{slope}, plus ϕ. The second condition for flexural toppling is that αdisc ranges between α_{slope} +160° and α_{slope} +200°. For this latter reason, flexural slope is possible only in case $\alpha_{slope} > \phi$. Failure conditions for flexural toppling are summarized in Equation 37.

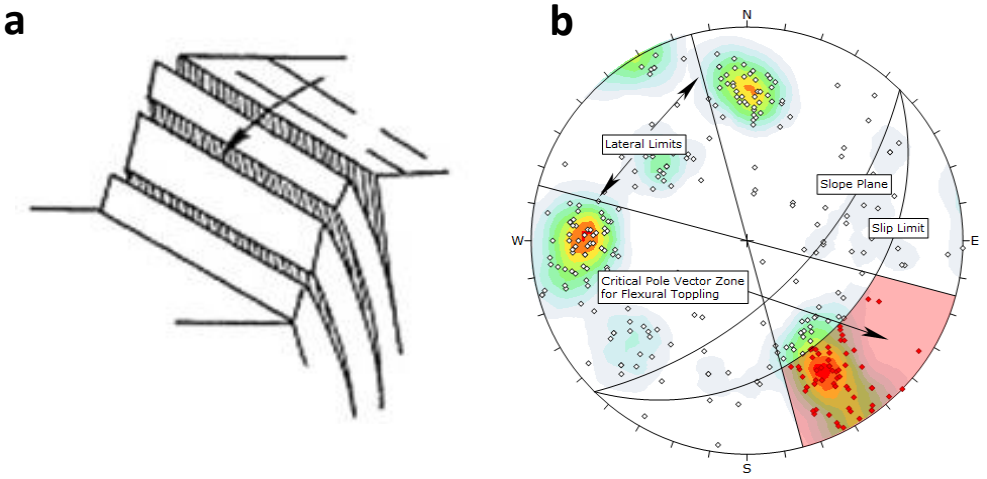

Figure 36 - Description of flexural toppling. a) Schematic representation of flexural toppling on the slope (Hoek & Bray, 1981); b) critical area for flexural toppling on the stereoplot (https://www.rocscience.com)

Equation 37

$$\begin{cases} \beta_{\text{disc}} > 90° - \beta_{\text{slope}} + \phi \\ \alpha_{\text{slope}} + 160° \leq \alpha_{\text{disc}} \leq \alpha_{\text{slope}} + 200° \end{cases}$$

Kinematic Hazard Index for flexural toppling is the percentage of poles critical to flexural toppling in comparison to the total amount of poles of the rock mass (Equation 38) (Casagli & Pini, 1993).

Equation 38

$$C_{ft} = 100 \times (N_{ft}/N)$$

4.2. Block theory and Goodman & Shi blocks classification criterion

Block Theory (Goodman & Shi, 1985) classifies blocks into overall 6 types (Figure 37): I) finite and removable unstable blocks (*keyblocks*); II) finite and removable blocks stable with sufficient friction (*potential keyblocks*); III) finite and removable blocks stable even without friction; IV) non removable finite blocks; V) infinite blocks; VI) blocks inside the rock mass.

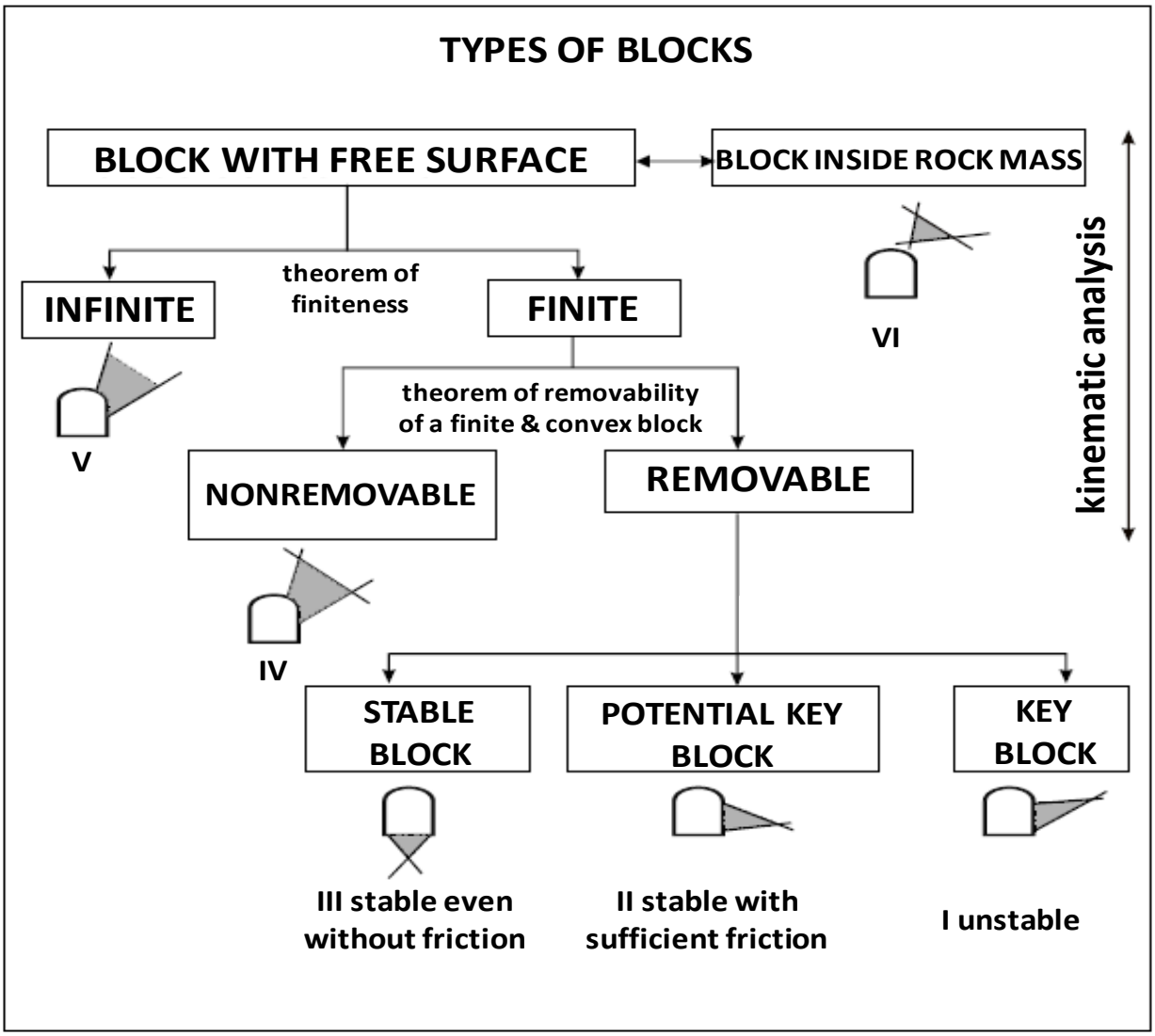

Figure 37 - Scheme of blocks classification for Blocks Theory and 2D representation of the types of blocks. From Goodman & Shi (1985)

Type I, II, III, and IV are finite. A first partition of outcropping convex blocks is, in fact, between infinite and finite blocks. The theory exposes the finiteness theorem:

"A convex block is finite if its block pyramid is empty. Conversely, a convex block is infinite if its block pyramid is not empty."

Goodman & Shi (1985) define so the edges and the discontinuity planes and the planes of the block pyramids (BP) (Figure 38 and 39). The edge of the block pyramids are "lines passing through the origin [i.e., x_o : (X_o,Yo,Z_r): (0,0,0)]". Block pyramid (BP) is the intersection of all the half-spaces bunded by the planes of the block translated to origin. Therefore, the equations of the edges (Equation 39 and 40) are:

Equation 39

$$x = tX_1$$

Equation 40

$$X = tX_1$$
$$Y = tY_1$$
$$Z = tZ_1$$

Block pyramids with a free surface are described by Equation 41:

Equation 41

$$BP = JP \cap EP = \emptyset$$

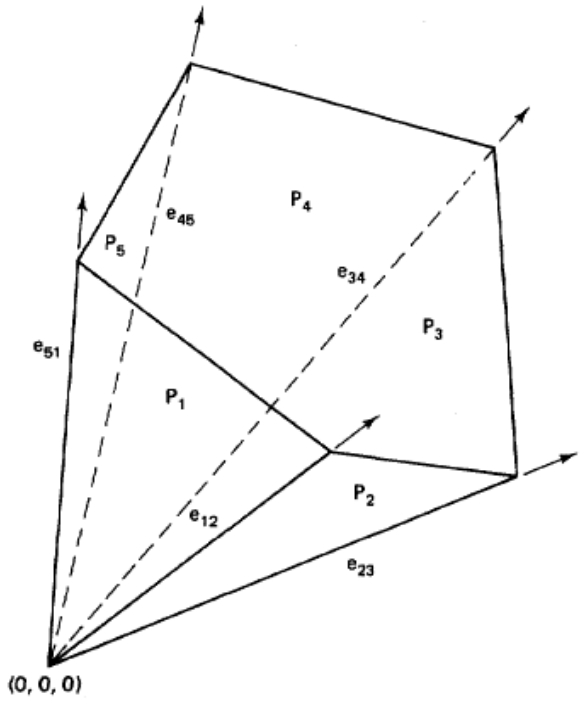

Figure 38 - Example of block pyramid. From Goodman & Shi (1985)

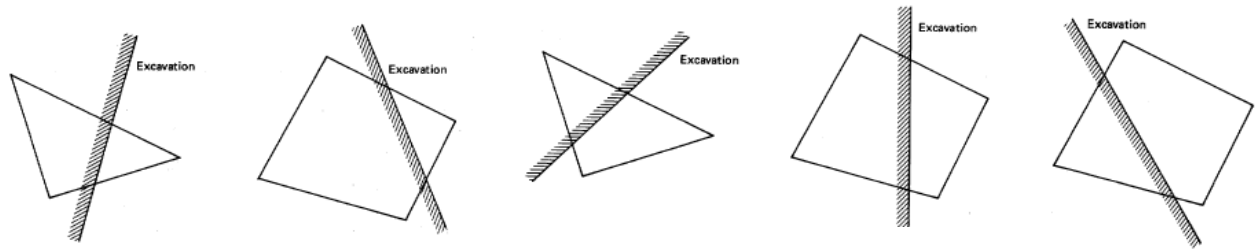

Figure 39 - Examples of in 2D of pyramids outcropping of the excavated slope. Modified from Goodman & Shi (1985)

Therefore, the X Y Z coordinates of the edges, obtained from are described in Equation 39 and in 40:

Indeed, any plane (i) of the block pyramid includes the origin [0;0;0]. Given Equation 42 and 43,

Equation 42

$$D = x \times \hat{n}_p$$

Equation 43

$$D = AX + BY + CZ$$

the equation of the discontinuity plane is so given by Equation 44.

Equation 44

$$D = A_i X + B_i Y + C_i Z$$

For Block Theory, if $JP \subset \mathrm{SP}$, a convex block is infinite; for $JP \not\subset \mathrm{SP}$, a convex block is, instead, finite.

Once defined if a block is finite or not, Block Theory then defines the removability of finite convex blocks. For Blocks Theory:

“A convex block is removable if its block pyramid is empty and its joint pyramid is not empty. A convex block is not removable (tapered) if its block pyramid is empty and its joint pyramid is also empty”.

Joint pyramid is the set of the points that are included into the half-spaces bunded by the space of the pyramid on the surface of the block. The coordinates of these points are recalculated by centring each surface on the origin [0,0,0] and so can be plotted on a stereonet, showing the lines of longitude and latitude of the entire sphere. Supposing that there are n nonparallel sets of joints (i.e. 4 as in Figure 40), each determined in orientation by a plane passing through the origin [0, 0, 0], the system of planes cuts the whole sphere into a number of pyramids all having their apex at [0, 0, 0], that is included into the barred area in Figure 40, that is the intersection of the cyclographics of the planes of the faces of the pyramid. If the joint pyramid, represented in the stereographic projection with the barred area, is empty, its apex is located into the excavated part of the slope and so the block is embedded by other blocks and not removable; if, instead, the joint pyramid is not empty, its apex is located within the rock mass and so the block is removable (Figure 41).

Because a non-convex block can be the combination of more simple convex blocks, the two statements about finiteness and removability of the blocks can be rewritten (Goodman & Shi, 1985) for non-convex blocks as it follows:

“A non-convex block is a united block which consists of some convex blocks. If all of its convex sub-blocks are finite, the non-convex block is finite. If there exists one convex sub-block infinite, the non-convex block is also infinite”.

"A finite non-convex block is a united block which consists of some finite convex blocks. If all of its convex sub-blocks are removable, the non-convex block is removable. If there exists one convex sub-block unremovable, the non-convex block is also unremovable".

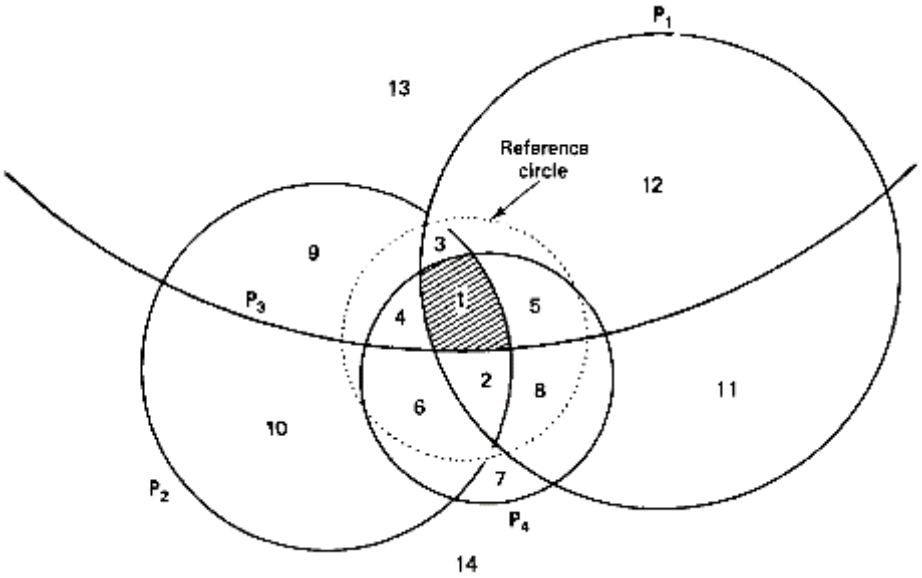

Figure 40 - Example of stereographic projection of joint pyramid. From Goodman & Shi (1985)

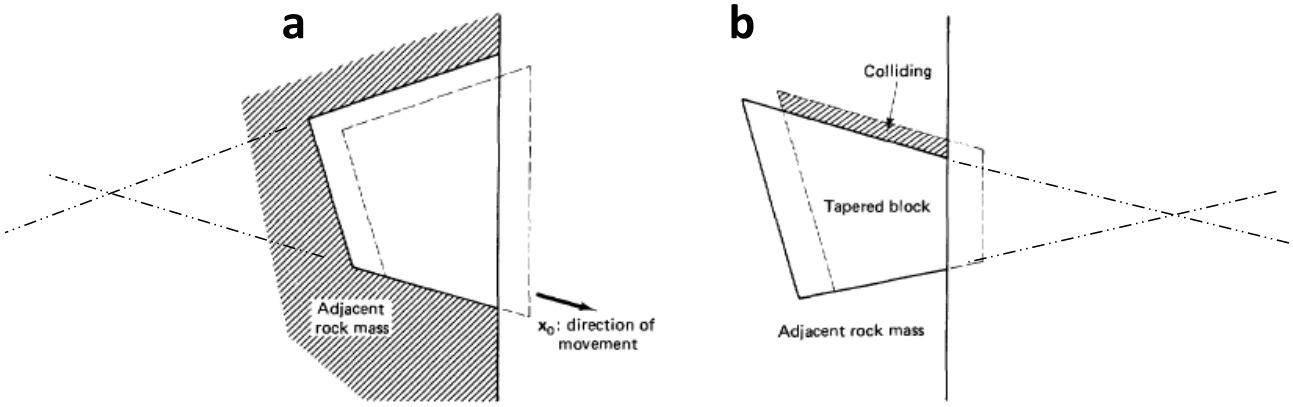

Figure 41 - Example of pyramids. a) pyramids of removable block; b) pyramid of nor removable block. Modified from Goodman & Shi (1985)

Stability analysis makes on removable blocks only, because infinite and not removable blocks are by sure stable without the removal of keyblocks. Blocks behind the slope surface (type VI blocks) free and not-removable blocks (type IV blocks), in fact, have no space to move around if no keyblock vacates its position. Infinite blocks (type V blocks), of course could move only in case they become finite blocks thanks to fracturing.

Block Theory subdivides removable blocks into 3 types by 2 kinds of analysis. First, a mode analysis is performed to evaluate the direction of the vector of the gravity towards the slope. Mode analysis allows to distinguish stable blocks (Type III) from potential or real keyblocks (Type II and Type I).

A block can move in 3 modes: lifting, sliding on a single face, sliding on 2 faces. First, the resultant of the normal components of the reaction forces $N_{\perp}$ is defined (Equation 45).

Equation 45

$$\mathrm{N}_{\perp} = \sum_i N_i \, \hat{v}_I$$

The resultant T of the tangential frictional forces is so given by Equation 46:

Equation 46

$$T_I = -N_I \times \tan \varphi_I \hat{s}$$

The resultant of this and the fictitious force is given by Equation 47, that is simplified in Equation 48:

Equation 47

$$-T\hat{s} = \sum_i N_i \times \tan \varphi_I \hat{s} - F\hat{s}$$

Equation 48

$$T = \sum_i N_i \times \tan \varphi_I - F$$

Obviously, to detect Type 1 blocks from Type II or Type III blocks, we can use $\varphi_I = 0$. If, in fact, $\varphi_I = 0$, a differential mode will involve the block: given $\varphi_I = 0$, if the block is stable even without friction, the block does not move, if instead the block is a real or potential keyblock, it moves.

Finally, the stability analysis of a given block on the sliding surface is performed by the Limit Equilibrium Method. The orientation of the sliding surfaces and the value of the friction angle and c allows to detect block stable even without friction from potential keyblocks or real keyblocks.

4.3. Limit Equilibrium Method (Hoek & Bray, 1981) for the analysis of rock slope stability

Limit Equilibrium Method allows to carry on the analysis to calculate the FOS of a slope or of a block, with a given sliding surface. FOS is the ratio between the forces that prevent the movement and the forces that drive it (Equation 49). Values higher than 1 indicate that the slope or the block is stable, less than 1 that is prone to failure. Different FOS values have been recommended for slope designed in different contexts; the design FOS value can vary upon the importance of the slope and the consequences of failure, for economic, strategic and human losses. For example, Canadian Geotechnical Society recommends reaching FOS values equal or greater than 1.3 for slopes the failure of which could involves heavily travelled roads, taking into account the worst condition as regarding saturation, load and geostructural and lithological setting (Canadian Geotechnical Society, 1992; Wyllie & Mah, 2004).

Equation 49

$$FOS = \frac{resisting\ forces}{driving\ forces}$$

The stability is so related to the shear strength along the sliding plane. The relation between shear strength and stress is exposed in Equation 50 (Mohr-Coulomb criterion):

Equation 50

$$\tau = c + \sigma' \tan \varphi$$

Equation 50 describes so a linear relation between τ and σ', the angular coefficient of which is related to the value of the friction angle (letter a in Figure 42). Normal stress is normal to the plane; in a natural discontinuity (letter b in Figure 42), the normal stress is the component of the weight normal to the surface. Σ is so described by Equation 51 and τ by Equation 52.

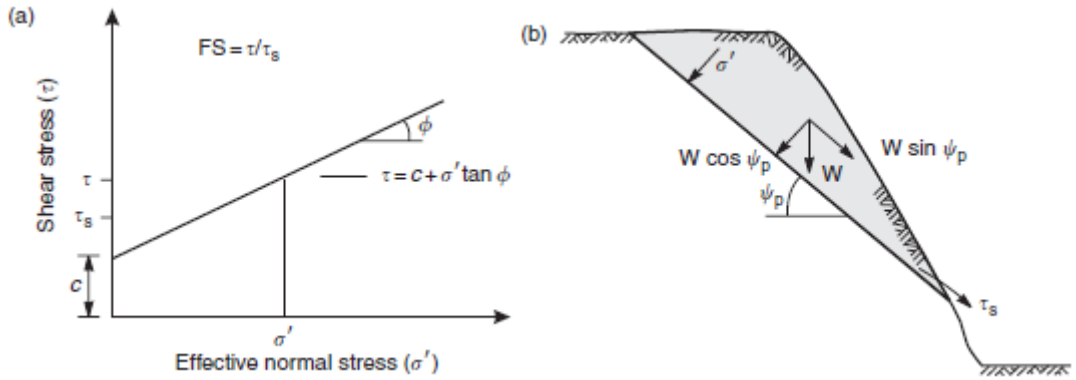

Figure 42 - σ and τ for a sliding block: a) the function of Mohr-Coulomb criterion plotted into Mohr diagram (b) resolution of force W due to weight of block into components; b) representation of τ, σ and W along a discontinuity in a natural slope. From Hoek & Bray (2014)

Equation 51

$$\sigma = \frac{W \cos \psi_p}{A}$$

Equation 52

$$\tau_s = \frac{W \cos \psi_p}{A}$$

Substituting σ and τ and expressing them in function of ψ_p and W as in Equation 51 and in Equation 52, Equation 50 can be so re-written as it follows (Equation 53):

Equation 53

$$\tau = c + \frac{W \cos \psi_p \tan \varphi}{A}$$

Equation 52 and Equation 53 are so re-written (Equation 54 and 55):

Equation 54

$$\tau_s A = W \sin \psi_p$$

Equation 55

$$\tau A = c + W \cos \psi_p \tan \varphi$$

τA and $\tau_s A$ represent the product of a pressure (N/m^2) for an area (m^2), and so are two forces. In particular, τA is the resultant force acting down the sliding plane, so the driving force, while $\tau_s A$ is the shear strength forces acting up the plane, so the resisting force. The ratio between τA (Equation 54) and $\tau_s A$ (Equation 55) describes so the FOS (Equation 56) of the sliding block.

Equation 56

$$\mathrm{FOS} = \frac{c + W \cos \psi_p \tan \varphi}{W \sin \psi_p}$$

Hoek & Bray (1981) method for the calculation of FOS require so the knowledge of the weight of the block, of the cohesion and of the friction angle of the discontinuity and of the dip of the sliding surface. In case no filling is present on the sliding discontinuity, c = 0 and FOS is equal to the product of $\cot(\psi_p)$ and $\tan(\phi)$ (Equation 57). For $\psi_p = \phi$, FOS =1.

Equation 57

$$\mathrm{FOS} = \cot \psi_p \tan \varphi$$

Limit Equilibrium Method can also consider the water forces acting on a sliding surface partially or totally filled by water. Water pressure of the water can be written as it follows (Equation 58):

Equation 58

$$\mathrm{p_w} = \gamma_w h_w$$

Basing on the sliding block in Figure 43 (letter a), the forces acting on the tension crack filled by water U, and on the sliding surface U can be written (Equation 59 and Equation 60):

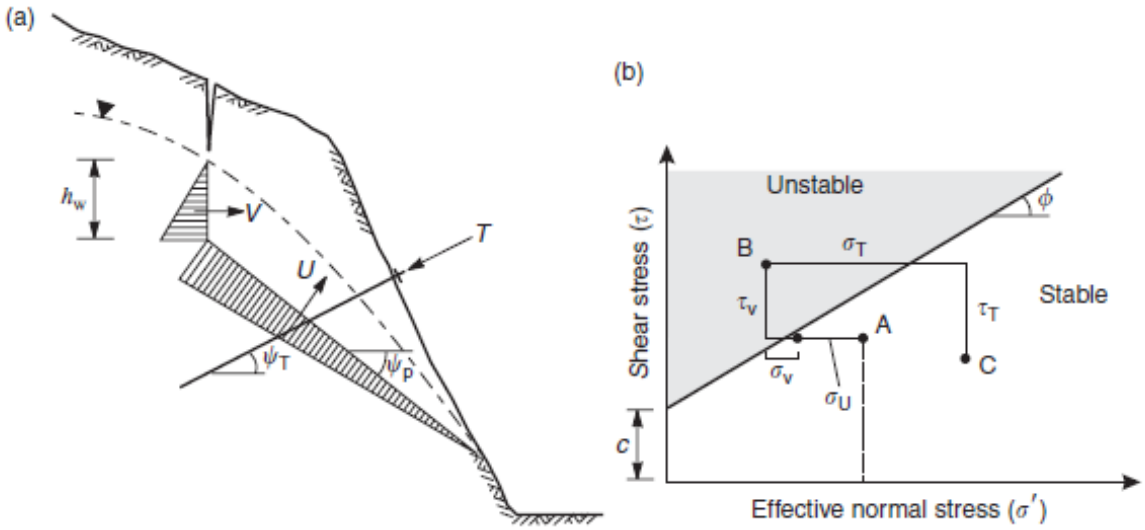

Figure 43 - FOS and the effect of water filling of discontinuities and bolt forces of the rock mass. a) representation of U, V and T acting on a slope; b) stable and unstable stability conditions described by Mohr diagram. From Hoek & Bray (2014)

Equation 59

$$V = \frac{1}{2}\gamma_w {h_w}^2$$

Equation 60

$$U = \frac{1}{2}\gamma_w h_w A$$

V and U represent a sliding force and a resisting force respectively, so they can be added to the FOS ratio in Equation 56. Equation 61 so describes the FOS for a sliding block in a slope with water filtration:

Equation 61

$$\mathrm{FOS} = \frac{c + (W\cos\psi_p - U - V\sin\psi_p)\tan\varphi}{W\sin\psi_p + V\cos\psi_p}$$

The application of a bolting system increases the FOS of the block. The projection of the tension of the bolt on the sliding surface (normal force) and on the vertical of the sliding surface (shear force) (letter b in Figure 43) contributes to the FOS of the block. The two components of the tension T of the bolt can be easily calculated (Equation 62 and Equation 63):

Equation 62

$$\mathrm{N_T} = T\sin(\psi_\mathrm{T} + \psi_p)$$

Equation 63

$$\mathrm{S_T} = T\cos(\psi_\mathrm{T} + \psi_p)$$

N_T and S_T represent so two terms that contribute to the stability to the slope and must be added to the numerator and to the denominator of the FOS ratio. Although S_T is enumerated within the sliding forces, its direction is contrary to the slope failure direction, so it is < 0 and decreases the sum of the sliding forces. Equation 64 is the equation for the calculation of the Limit Equilibrium (Hoek & Bray, 1981) and describes the FOS of a sliding block, considering the effects of water filtration and of bolting systems.

Equation 64

$$\mathrm{FOS} = \frac{c + (W\cos\psi_p - U - V\sin\psi_p + T\sin(\psi_T + \psi_p))\tan\varphi}{W\sin\psi_p + V\cos\psi_p - T\cos(\psi_T + \psi_p)}$$

4.4. Used methods for quantitative assessment of rock slope stability

4.4.1. DiAna-K

DiAna-K performs the kinematic analyses considering the sets of discontinuities extracted with DiAna (Chapter 3.4.3) and the point cloud of the rock slope, obtained with Lidar or photogrammetric survey. Once obtained a mesh of the slope surface, an orientation value is given for each triangle of the mesh. Each triangle of the mesh is so a local slope, the orientation of which makes proper kinematic conditions and kinematic indices. Then, a true 3D kinematic analysis is performed.

Different results can be obtained for different triangle of the mesh with distinctive values of slope and aspect. DiAna-K allows to obtain:

- 5 susceptibility maps, one for each failure mechanism (plane failure, wedge failure, block toppling, and flexural toppling, and free fall). The colour range of the indices can be scaled on the value range for each kinematic mechanism or on the value range for the most probable kinematic mechanism only;
- A general map of rockfall susceptibility with the highest kinematic index for each triangle of the mesh among the 5 kinematic indices of the failure mechanism (General Kinematic Index, GKI).

Since the percentage of poles (as regarding plane failure, block toppling and flexural toppling) (Figure 33, 35, and 36) or intersections (as regarding wedge failure and block toppling) (Figure 34 and 36) within the critical area,, the calculation of the kinematic index for plane failure (Equation 34), wedge failure (Equation 35), block toppling (Equation 36), and flexural toppling (Equation 38) for each triangle of the mesh allows to:

- build a susceptibility map of the rockfall hazard. If the kinematic indices are calculated assuming a simplified slope instead of a mesh, kinematic indices provide a general value of susceptibility referred to whole rock slope;
- identify the most prone to failure blocks and use this information for safety work or for rockfall analysis;
- furnish a realistic and comprehensive assessment of the slope stability, considering local variation to the general orientation of the slope.

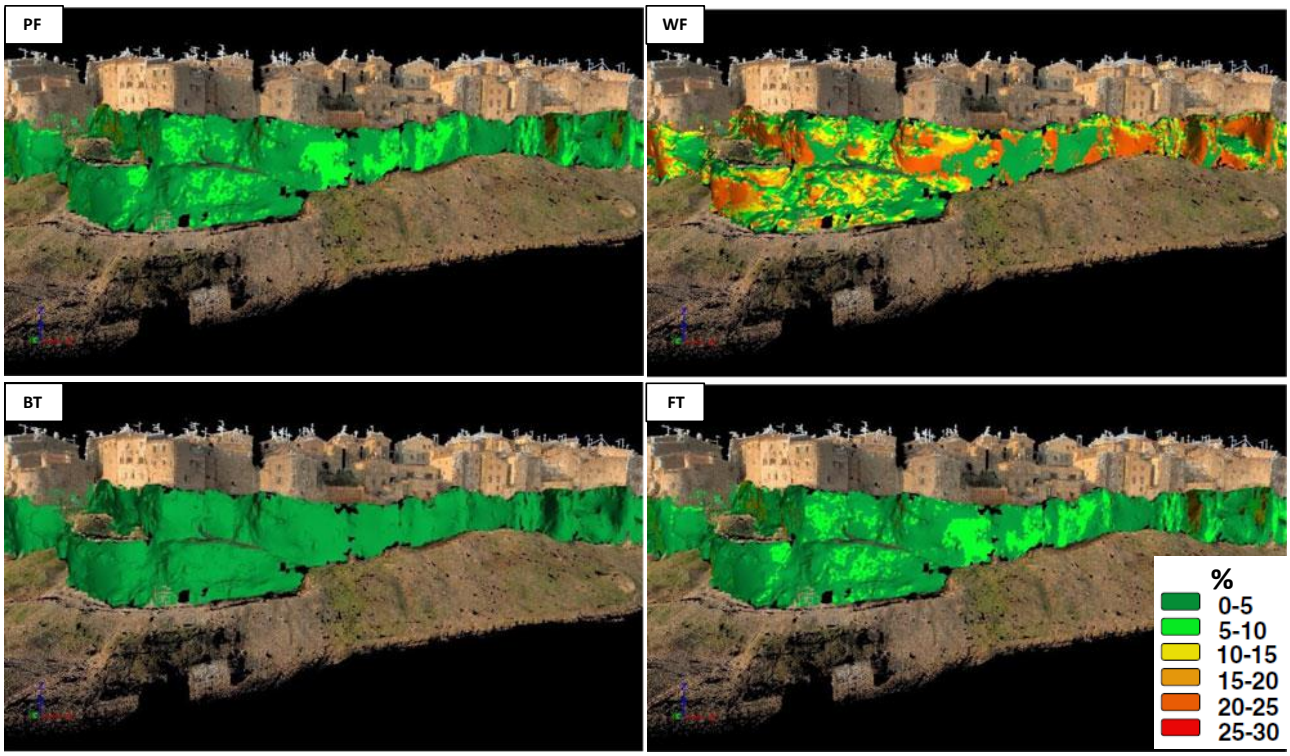

Figure 44 - Kinematic analysis of the cliff around Pitigliano citadel (Central Italy) performed by DiAna-K. PF) plane failure; WF) wedge failure; BT) block toppling; FT) flexural toppling. From Fanti et al. (2013)

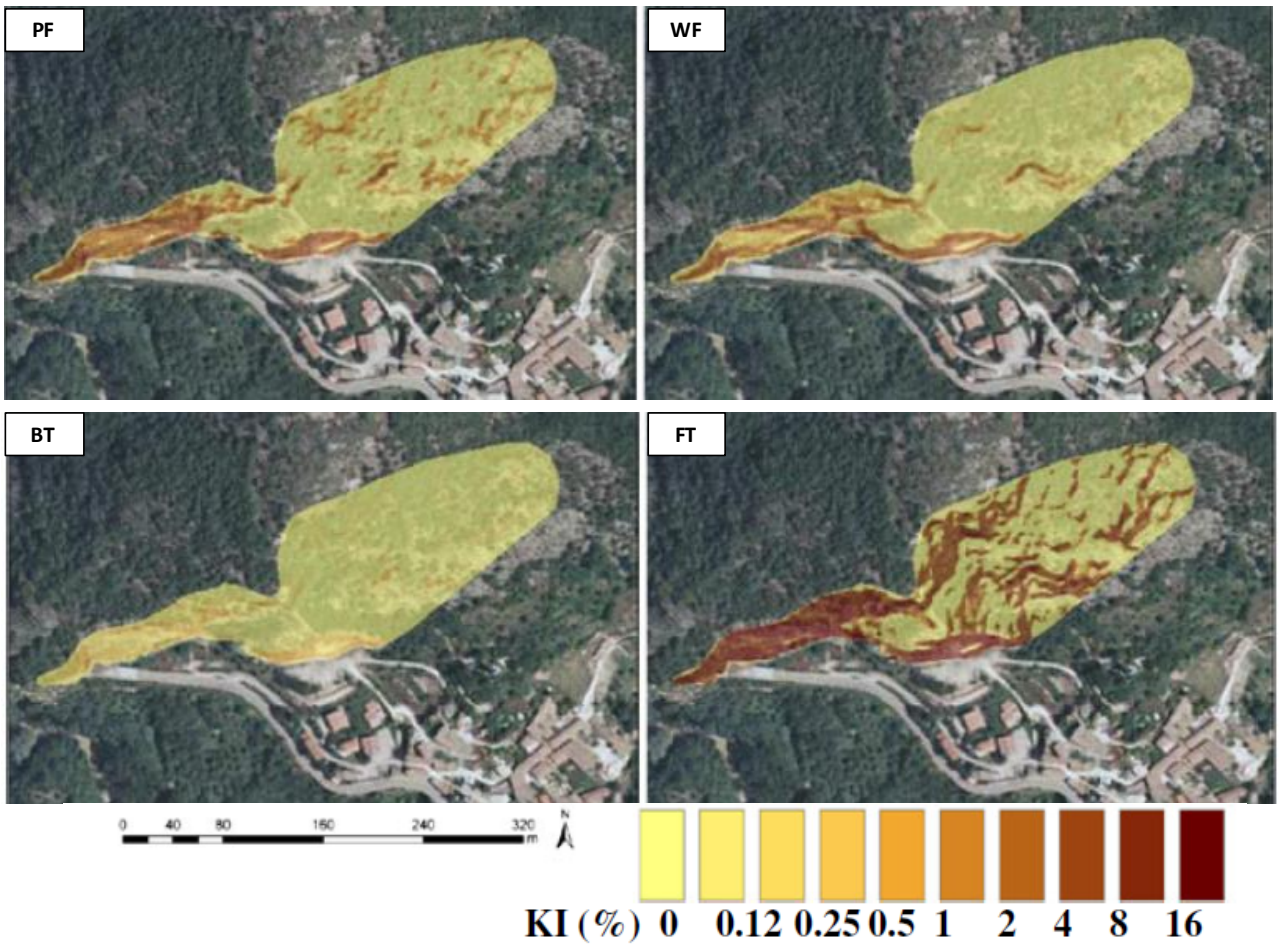

Figure 45 - Kinematic analysis performed by DiAna-K for the rock slope on a motorway (Central Italy) performed by DiAna-K. PF) plane failure; WF) wedge failure; BT) block toppling; FT) flexural toppling. From Gigli et al. (2014)

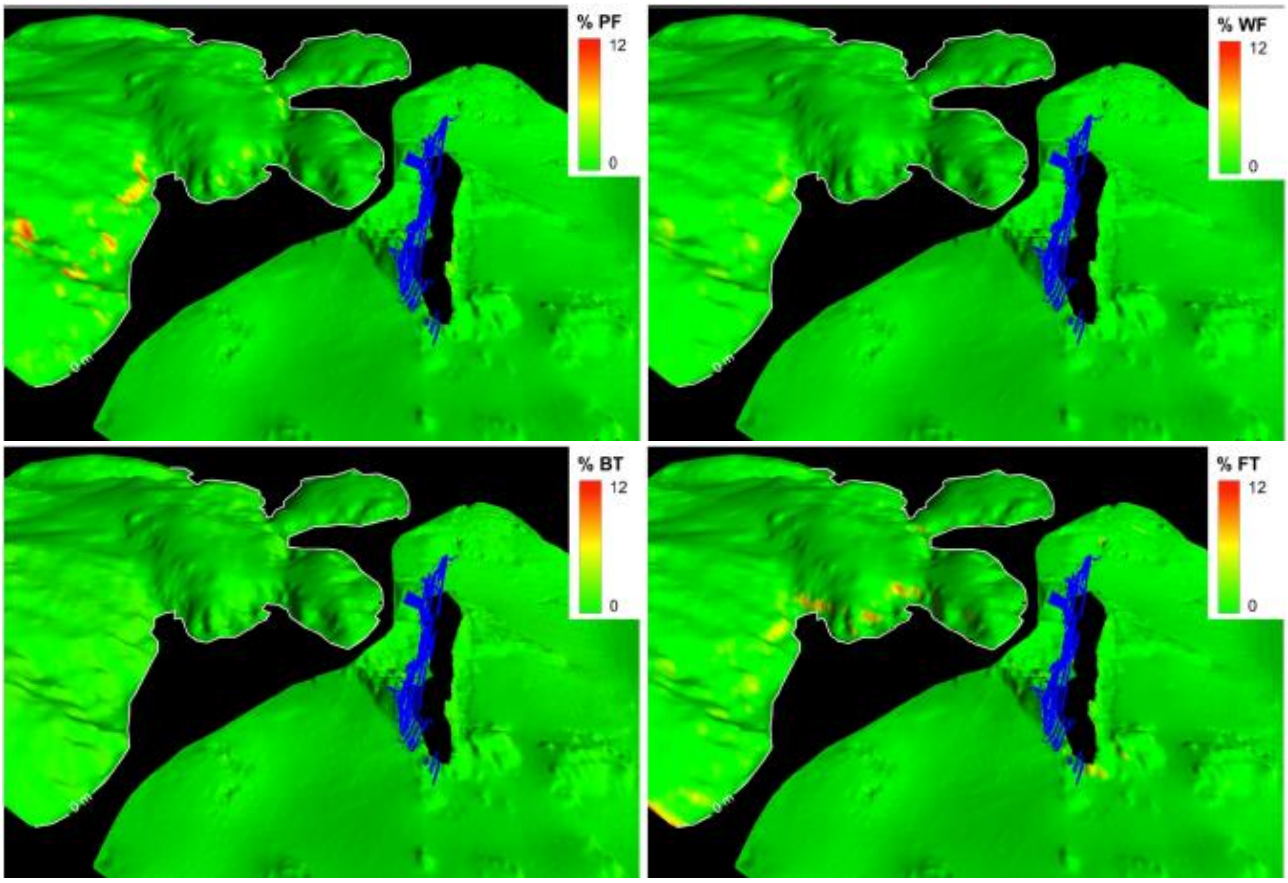

Figure 46 - Kinematic analysis of the cliff around Costa Concordia shipwreck, on Giglio Island (Central Italy) performed by DiAna-K. PF) plane failure; WF) wedge failure; BT) block toppling; FT) flexural toppling. From Dotta et al. (2017)

4.4.2. SiroModel

SiroModel is a software developed by CSIRO within the Large Open Pit Mine Slope Stability Project for the evaluation of the pit slope stability. It allows to generate a 3D profile of the pit slope, adding the discontinuities to build a geostructural model of the slope, generate a 3D fracture network to identify the blocks of the slope and, thanks to the Block Theory (Goodman & Shi, 1985) identify removable blocks (Types I, II, and III of Goodman & Shi, 1985). Then, Types I, II, and III blocks are recognised with the Limit Equilibrium Method, that attributes a FOS to each block. Finally, the block model analysis allows a number of analysis of the blocks of a single or multiple project, filtering them by volume, removability, FOS, bench number, bounding to non-release surfaces. The outputs include for each block the number of faces and vertices, FOS, volume, area, coordinates, removal vector, exposed face area, Topple, Number of fractures and fracture area within the block. SiroModel is so a flexible tool that provides a large number of output data and has a large number of functions and data retrieval queries in order to describe the complex geostructural and geological issues (water table, pore pressure, faults, beds, lithological domains) both for open pit slope and underground excavations.

The building of the 3D model of the slope with SiroModel is strongly related to the slope design of open pit mines. Profile can by defined or by uploading a .dxf file with the slope profile (Figure 47) or describing the proper geometry of the pit slope (Figure 48), defining dip direction of the slope, dip, height and number of the

bench, dip and width of the berm and indicating the presence of a linear or circular slope. SiroModel has been developed for large open pit mines, the slope of which can be properly represented by a simplified slope model. Although it has been developed for the slope modelling in open pit mines, the input model can be so also un underground excavation. The use of the proper geometry of the slope greatly increases the time-consume of the elaboration, so a maximum number of 500 vertices is recommended (CSIRO, 2017).

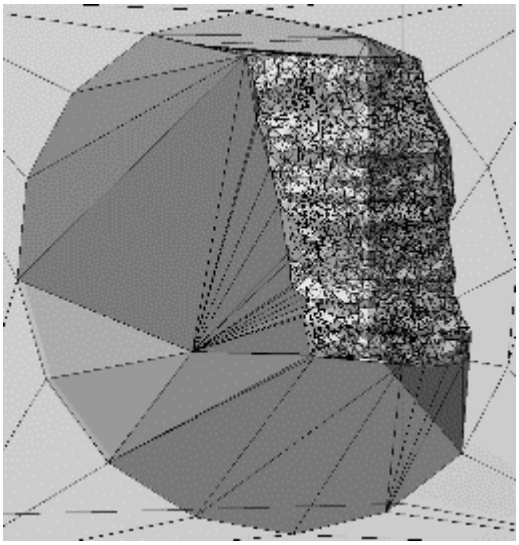

Figure 47 - Model of the slope build by SiroModel uploading a .dxf surface

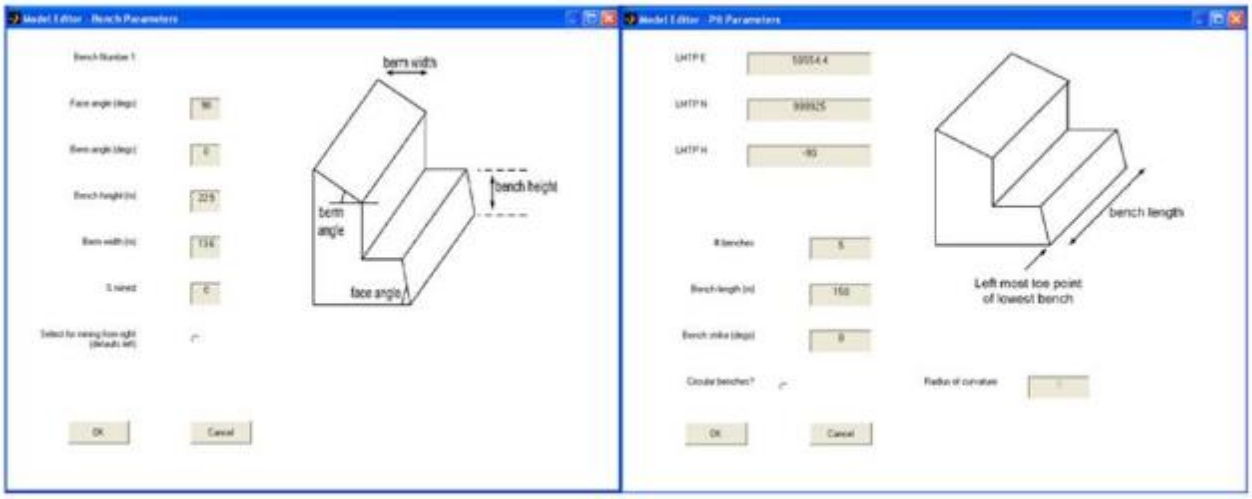

Figure 48 - Input for the model building of the slope with SiroModel. From https://www.csiro.au/

Once the slope is set, is possible to upload a deterministic or stochastic geostructural description of the rock mass. Deterministic geostructural description of the rock mass includes the single surveyed discontinuities expressed in .ascii, Dips .ascii or .dxf file format; stochastic geostructural description requires the indication of σ_α, σ_β, α_{disc}, β_{disc}, L, σ_L, ϕ, λ (areal, linear or volumetric) and c for each set of discontinuities.

Defined the model of the slope and described the discontinuity joints, the fracture network is generated. In case one or more sets of discontinuities has been stochastically defined, the multi-function Discrete Fracture Network generator runs out the geostructural model. The joint set generator currently only supports the *Baecher Model* (Baecher et al., 1977) and slight variants thereof. Baecher Model makes the following assumptions:

- joints are discs;
- joints are uniformly distributed throughout the simulation volume in a geological domain;

- the distribution of persistence, dip and dip direction of the discontinuities of a set adheres to the Poisson process (i.e. a binomial distribution tailored for large numbers of low probability events); the distribution of joints is so log-normal.

Indeed, the joint set generator utilises expressions relating the expected moments of the radial distribution to their trace length counterparts for the assumed radial distribution (Chan & Goodman, 1983; Lyman, 2003) assuming areal or line sampling methods are used (Warburton, 1980) in order to prevent bias for the persistence measurement related to the sampling method. σ_L and EL are related by Equation 65 for areal sampling and by Equation 66 for linear sampling. In case of σ_L value greater than 0 but less than the values calculated with Equation 65 for areal sampling and by Equation 66 for linear sampling, σ_L is adjusted if too small to be consistent with the previously referred equations (Warburton, 1980).

Equation 65

$$\sigma_L > 0.28 \times E_L$$

Equation 66

$$\sigma_L > 0.20 \times E_L$$

Obtained the geostructural deterministic model, Block Theory analysis is performed for each block and removable blocks (Type I, Type II and Type III blocks of Goodman & Shi, 1985) are extracted applying to the removability theorem (Chapter 4.2). Finally, on removable blocks only Limit Equilibrium Method analysis is performed using for c and friction angle the values previously added. As described in Chapter 4.3, blocks are subdivide into Type I (FOS= ∞), Type II (∞>FOS ≥1), and Type III (FOS<1) (Figure 49 and 50) using the formula developed by Hoek & Bray (1981) (Equation 64).

A number of further analysis can be carried out on removable blocks; of course, carrying out a relevant number of simulations is recommended to obtain statistically significative and reliable results. Single simulations can be indeed merged into a unique dataset. Blocks can be then analysed and filtered by:

- selected projects. Excludes blocks related to a project;
- volumes. Excludes out from a minimum-maximum range. This function is very useful to exclude very small blocks the volume of which is too small and that are not relevant for the further rock slope stability. For example, in case scree is present at the base of the bench, small blocks will not continue their run-out;
- FOS. Excludes blocks out a range of FOS. This discriminant allows further separate analysis for Type I, Type II, and Type III blocks;
- bench number. Excludes blocks located into a bench;
- non-release surfaces. Excludes blocks that are bound to non-release surfaces (i.e. back, base and sides of a user defined model);
- Filter removable blocks. Excludes removable blocks from the analysis.

Once a cogitated filtering of the block has been carried out, the dataset can be analysed by a number of tools. SiroModel allows, in fact, to draw the histogram of the block by number of the project, by volume, by position, by shape, by FOS, and by failure modes. Histogram of the blocks by volume (Figure 51) and by failure modes are the most relevant to assess the rockfall hazard and the slope stability. The maximum volume and the distribution of the volume of Type I and Type II blocks provides, in fact, a fundamental information for the modelling of the run-out. The histogram of the block distribution by failure mode subdivides the blocks by number of contact planes. Because if the blocks slides on 1 contact plane only it is prone to plane failure and if it slides on 2 or more contact planes it is prone to wedge failure (CSIRO, 2017), this kind of analysis for Type

I and Type II blocks indicates which sliding is more probable for a given rock slope and provide an estimation of the number of poised blocks.

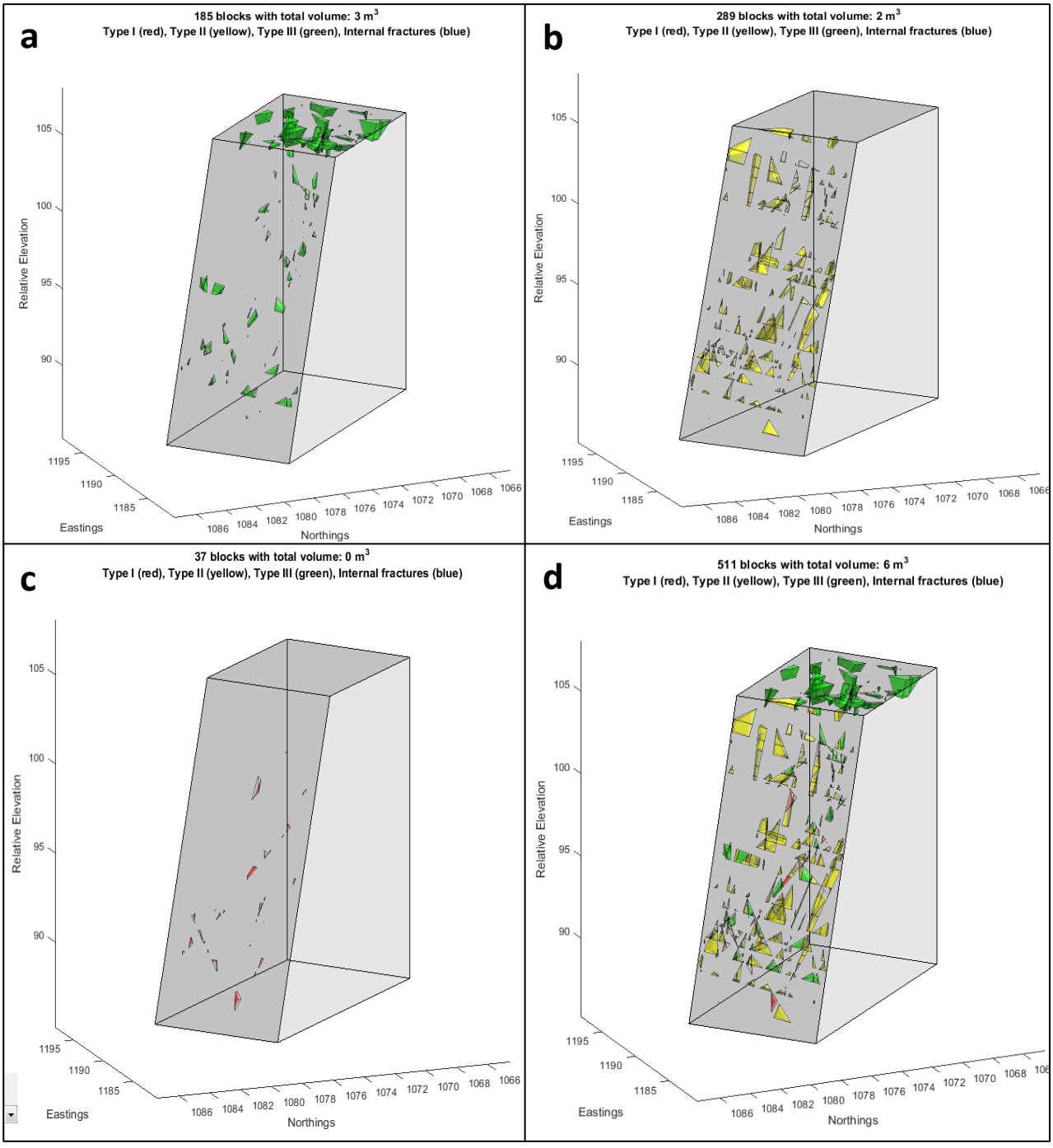

Figure 49 - Stability analysis performed by SiroModel. a) Type I blocks; b) Type II blocks; c) Type III blocks; d) overview of removable blocks

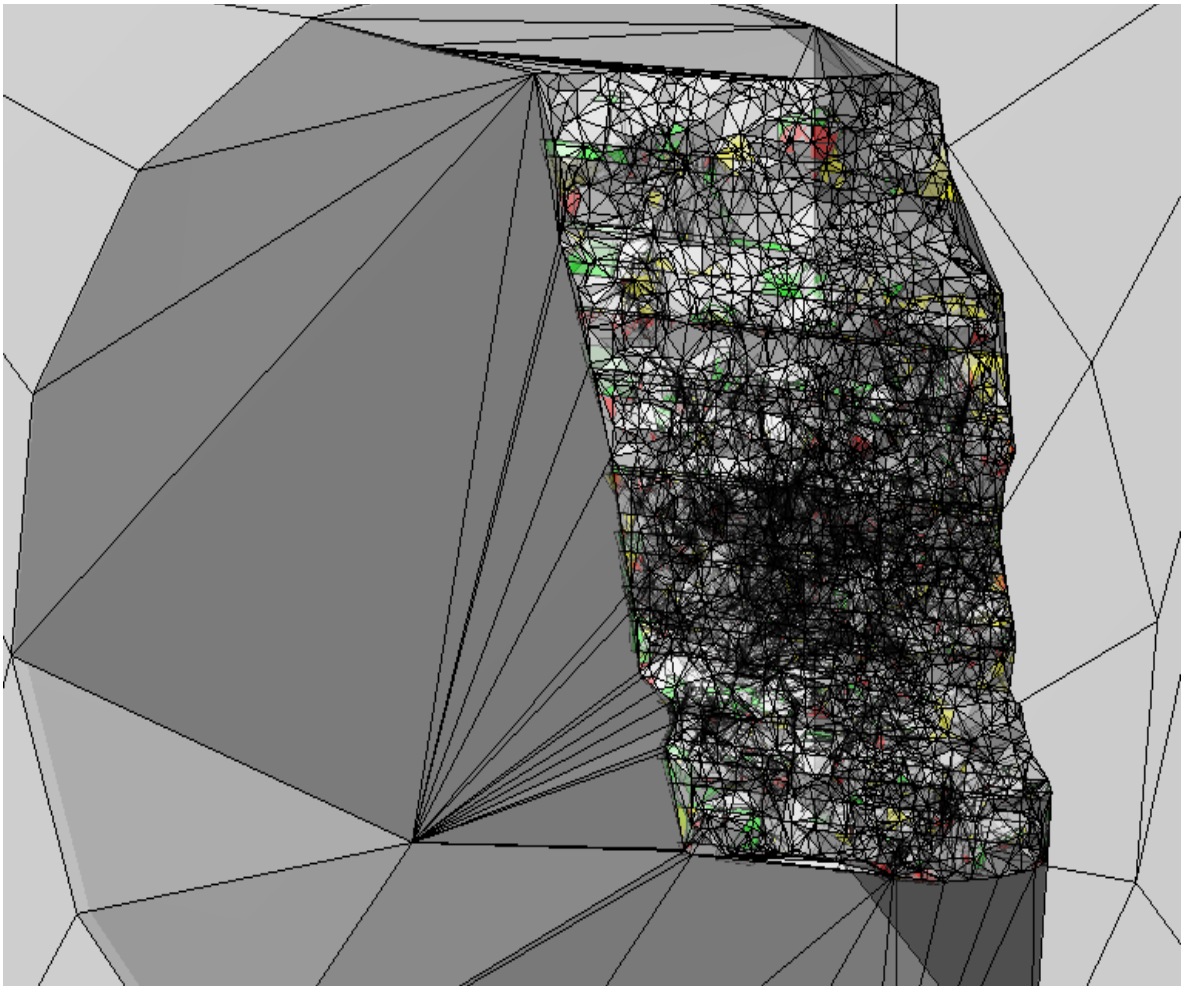

Figure 50 - Type I (red color), Type II (yellow color) and Type III (green color) on a model of the slope build by SiroModel uploading a .dxf surface

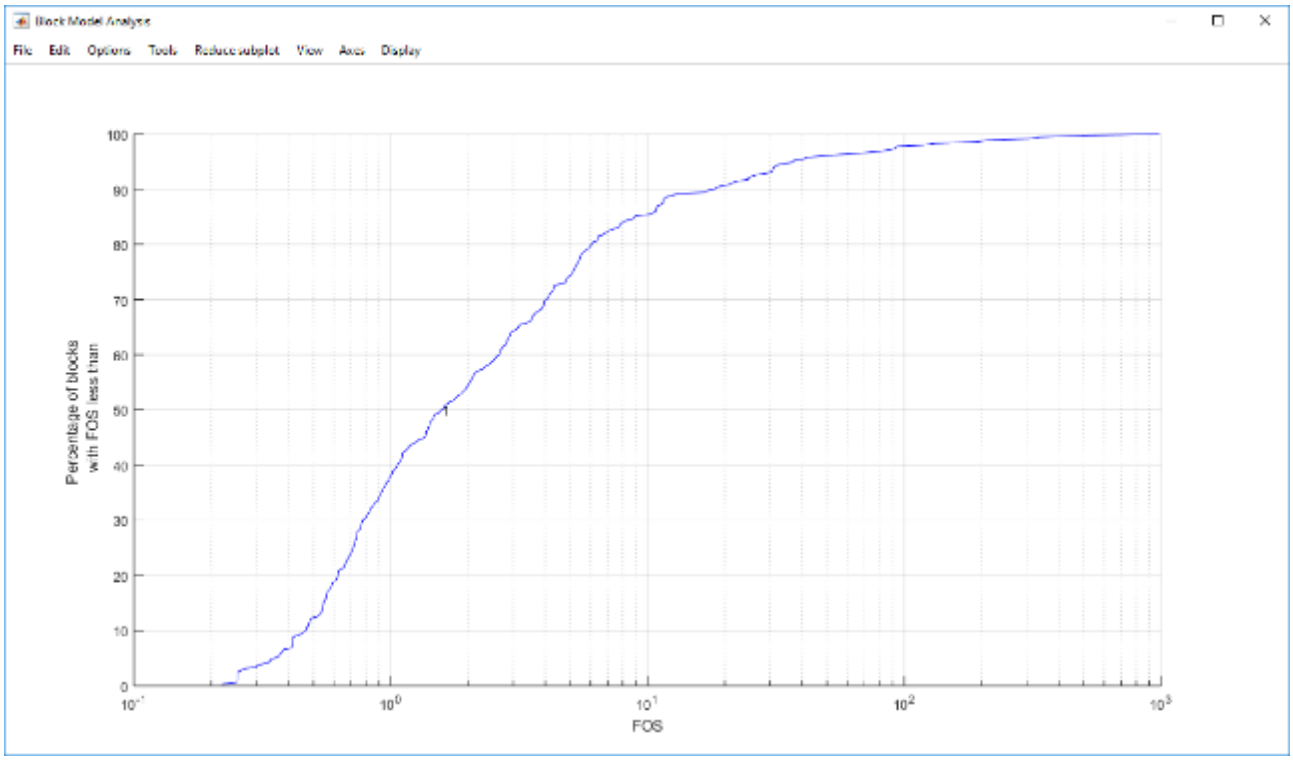

Figure 51 - Example of cumulative frequency plot of FOS for 100 simulations ((CSIRO, http://www.sirovision.com/)

5. Specificity of the sites

5.1. Geological setting

Australian Plate is one of the widest plates of the southern hemisphere. It spreads far beyond the coastline of Australia; Australian Plate includes, in fact, also Tasmania, as well portions of New Guinea, New Zealand, and parts of the Indian Ocean and Tasman Sea basins. The plate boundaries surrounding Australian Plate represent a number of geodynamical conditions. They include different kinds of plate boundary; locally, the plate boundary is convergent, divergent, or transcurrent. On the western part, the oceanic ridge divides Australian Plate from Antarctic Plate, Indian Plate and Somalian Plate; before the oceanic crust spreading these plates (Mesozoic), together New Zealand Plate, African Plate, Arabian Plate and South American Plate, formed an only landmass, the Gondwana Supercontinent. The plate boundary between Australian Plate and Sunda Plate, as well as the boundary with the Pacific Plate, is convergent. A long orogenic arc, forming the Indonesia archipelago, extends along the northern border of the plate. Along this arc, the oceanic crust of the Australian Plate subducts underneath the continental crust of Sunda Plate. The convergent boundary between Australian Plate and Pacific Plate is partly different from the boundary between Australian Plate sand Sunda Plate because here the oceanic crust of Australian Plate subducts under other oceanic crust. On the eastern side, Australian Plate borders with the Pacific Plate and the New Zealand Plate. The boundary with New Zealand Plate, that includes the North Island, the Howe Rise and the Challenge Plateau, is represented by the aborted ridge of the Tasman Sea (Luyendyk, 1995). The area between the North Island and South Island is a geologically complex area, where the Australian Plate subducts underneath the continental crust of the South Island of New Zealand, that Is part of the Pacific Plate. The direction of the subduction plane is westward for the North Island and eastward for the South Island, with a weakness dextral shear zone (Alpine Fault) splitting these two parts.

Australia is one of the oldest continents. Its bedrock is mostly constituted by old cratonic rocks and has a very long geological history. Oldest dated geological samples of Australia, the detrital zircons within metamorphosed sandstone conglomerate in the Jack Hills of the Narryer Gneiss Terrane of Western Australia (Nebel-Jacobsen et al., 2010), are also the oldest materials of terrestrial origin all over the world and have been dated back to 4.404±0.008 Ga by radiometric datation (Wilde et al., 2001).

Basing on the geodynamic evolution, Australia geological history can be split, from elder to younger, into 5 major events:

- First cratonic core formation and growth (3800-2100 My)
- Nuna Supercontinent (2100-1300 My)
- Rodinia Supercontinent (1300-600 My)
- Pangea Supercontinent (600-160 My)
- Australia Continent (160 My-Actual)

The geological history of the Australia Continent as is nowadays sketched, involves the last 160 My only, but most of the Australian rocks and the sedimentary covers are older and related to the landmasses of supercontinents, the last one, the Pangea Supercontinent ended about 160 My ago, thanks to the break-up of the continental crust, the splitting of the Australia-India-Antarctic plate from Africa plate and the spreading of the Indian Ocean ridge. Although most of the outcropping rocks in Australia are related to Nuna or Rodinia Supercontinents, the Great Dividing Range, that is the most important chain, is mostly related to the orogens of Pangea Supercontinent and of Australia Continent. Australia can be, in fact, split into 3 parts, from West to East with Archean rocks mostly on the West side, Proterozoic rocks in the centre, and Phanerozoic rocks on

the East side. 4 main geological domains summarise the simplified geological sketch and history of the continent. These domains are, from westerner to easterner and from older to younger:

- Yilgarn Craton (West Australia) Archaean age
- Pilbara Craton (North Western Australia) Archaean - Proterozoic
- Gawler Craton (Southern Australia) and Willyama Block (Southern-Central Australia), Archaean - Proterozoic
- Great Dividing Range and Hunter-Bower Orogen (Eastern Australia) Phanerozoic

Minor Proterozoic orogenic belts and sedimentary basins are indeed present, notably the:

- Musgrave Block of granulite gneiss and igneous rocks;
- Arunta Block of amphibolite grade metamorphic rocks and granites;
- Gascoyne Complex, Glengarry Basin, and Bangemall Basin sandwiched between the Yilgarn and Arunta Blocks.

New South Wales has been divided into various geological domains (Packham, 1969; Glen, 2005) (Figure 52 and 53). These domains are, from oldest to youngest one:

- Delamerian Orogen;
- Lachlan Orogen;
- New England Orogen;
- Sydney Basin;
- Gunnedah Basin
- Clarence-Moreton Basin;
- Bowen Basin;
- Surat Basin;
- Murray-Darling Basin.

Obviously, oldest rocks outcrop along orogens, because in basins the bedrock is covered by more recent sediments. Orogens are fold belts are constituted by rocks aged from early Palaeozoic to early Mesozoic and are heavily tectonized.

The oldest structure of the land is the Delamerian orogen, which is located along the western border, close to the confine with South Australia, within the so called “Adelaide geosyncline” (Glaessner & Daily, 1959). It is made by marine sedimentary sequences, aged from Middle Neoproterozoic to the Upper Cambrian. These old deposits contain a well-known and important Neoproterozoic fossil record, such as the Ediacara fossil Lagerstätten. The sedimentation end because of the tectonic uplift related to the Delamerian Orogeny, that according to Foden et al. (2006) lasted from ~ 514 Ma to 500 Ma (Figure 54).

Lachlan Orogen is an old accretionary wedge (Glen, 1992) made by rocks aged from pre-Cambrian to Lower Palaeozoic (Figure 55). These outcrops are divided by sediments Palaeozoic in age, that involve Central and Southern Fold Belt (Branagan & Packham, 1967).

New England fold belt is made by rocks aged from Lower to Upper Palaeozoic, mainly Devonian and Permian. These rocks are intra-oceanic and represent a supra-subduction zone assemblage that formed in island arc, backarc and possibly forearc setting, related to a westward subduction plane. An earlier Cambrian ophiolitic complex has been recognized in New South Wales, involved in an accretionary wedge, related to a classic convergent continental margin including a western volcanic arc, central forearc basin, and eastern accretionary wedge. Westward subduction had been persisting almost until the end of the Carboniferous and established the basic structural pattern. The Permian rollback of the slab put end to the subduction, while on the western side of the range back-arc basins developed.

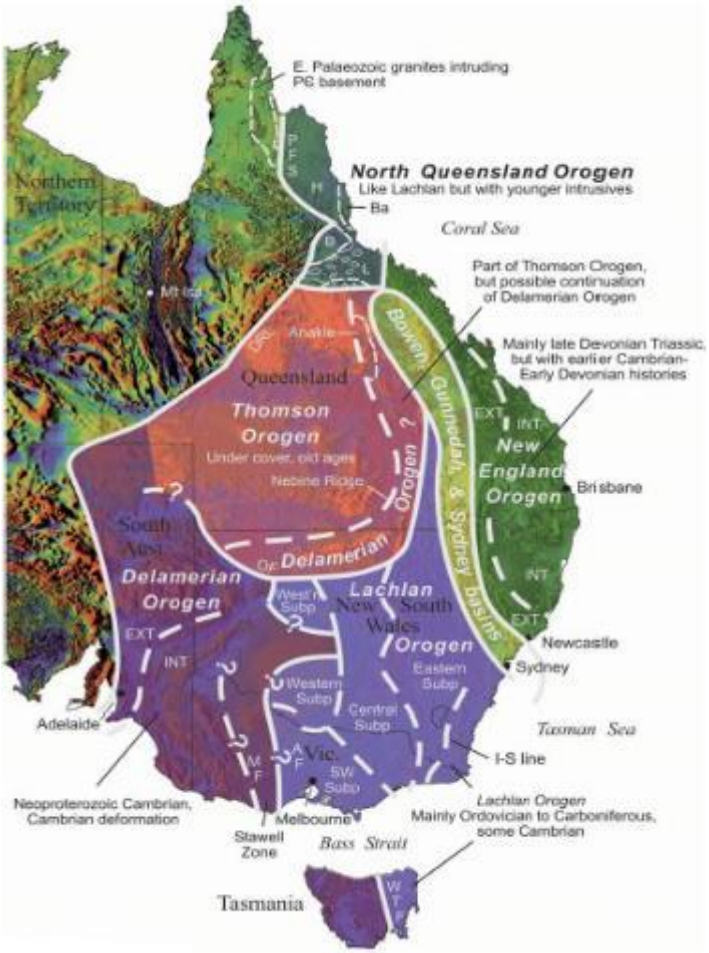

Figure 52 - Tectonic sketch of the main structures of Eastern Australia. From Glen (2006)

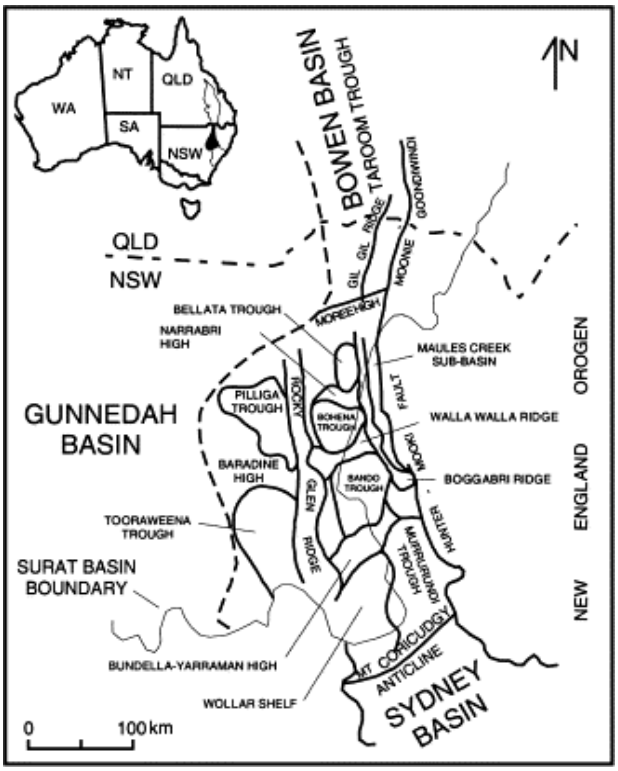

Figure 53 - Relations between Bowen Basin, Sydney Basin, Gunnedah Basin and Surat Basin (Tadros, 1995; modified by Othman & Ward, 2002)

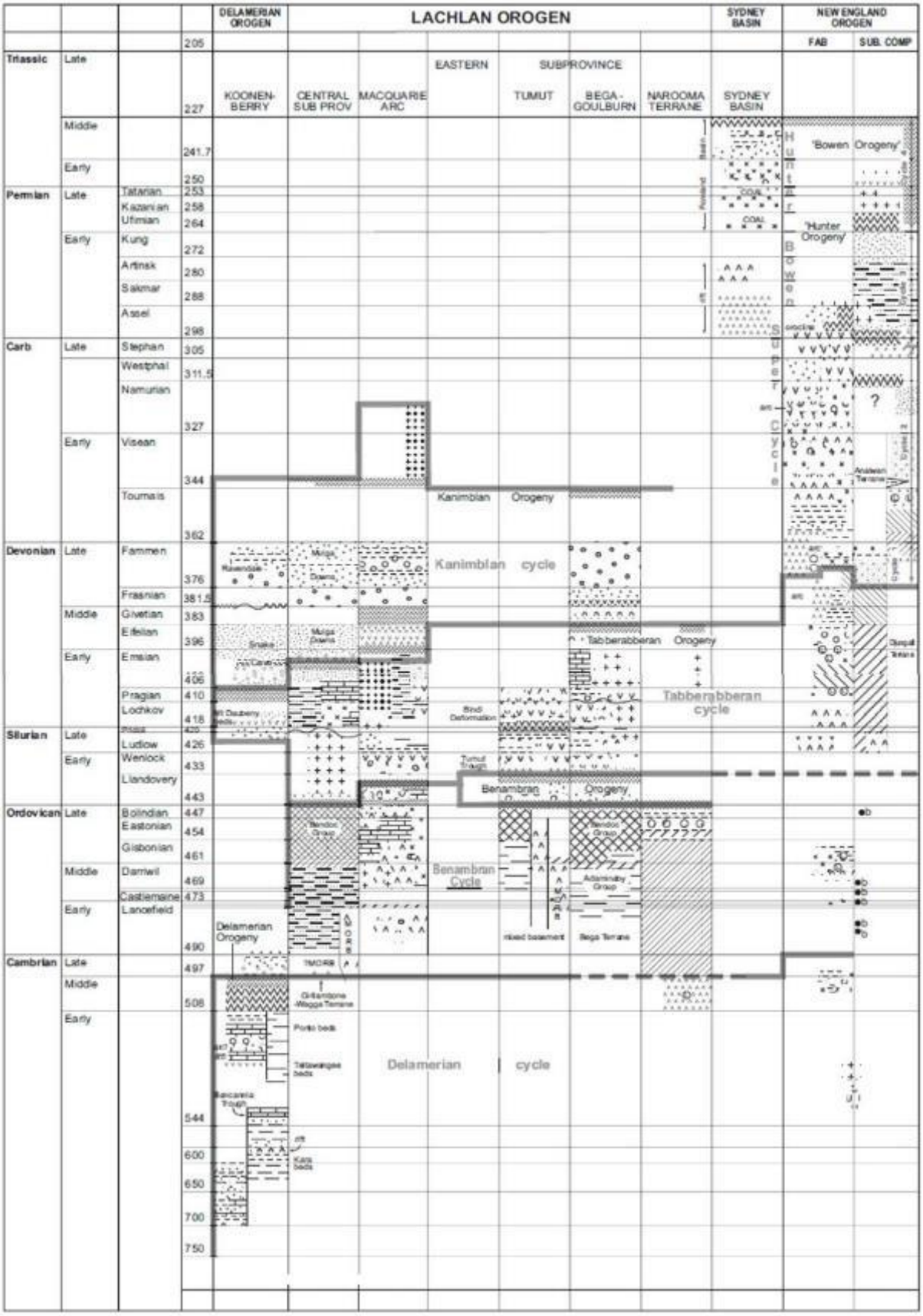

Figure 54 - Chronological comparison sketch of the main lithological units of Delamerian Orogens in Koonenberry zone, of the Delamerian Orogen in Central Sub-province, Maquarie Arc, Tumut, Begagoulburn zone, and Naroma Terrane, of the Sydney Basin and of the New England Orogen. Data collected mainly by Aitchison (1992), Roberts & Geeve (1999), Mills (2002; 2003), Thomas et al. (2002), Colquhuon et al. (2004), Glen et al. (2004), Percival & Glen (2006), and Meffre & Glen (2007). From Glen (2016)

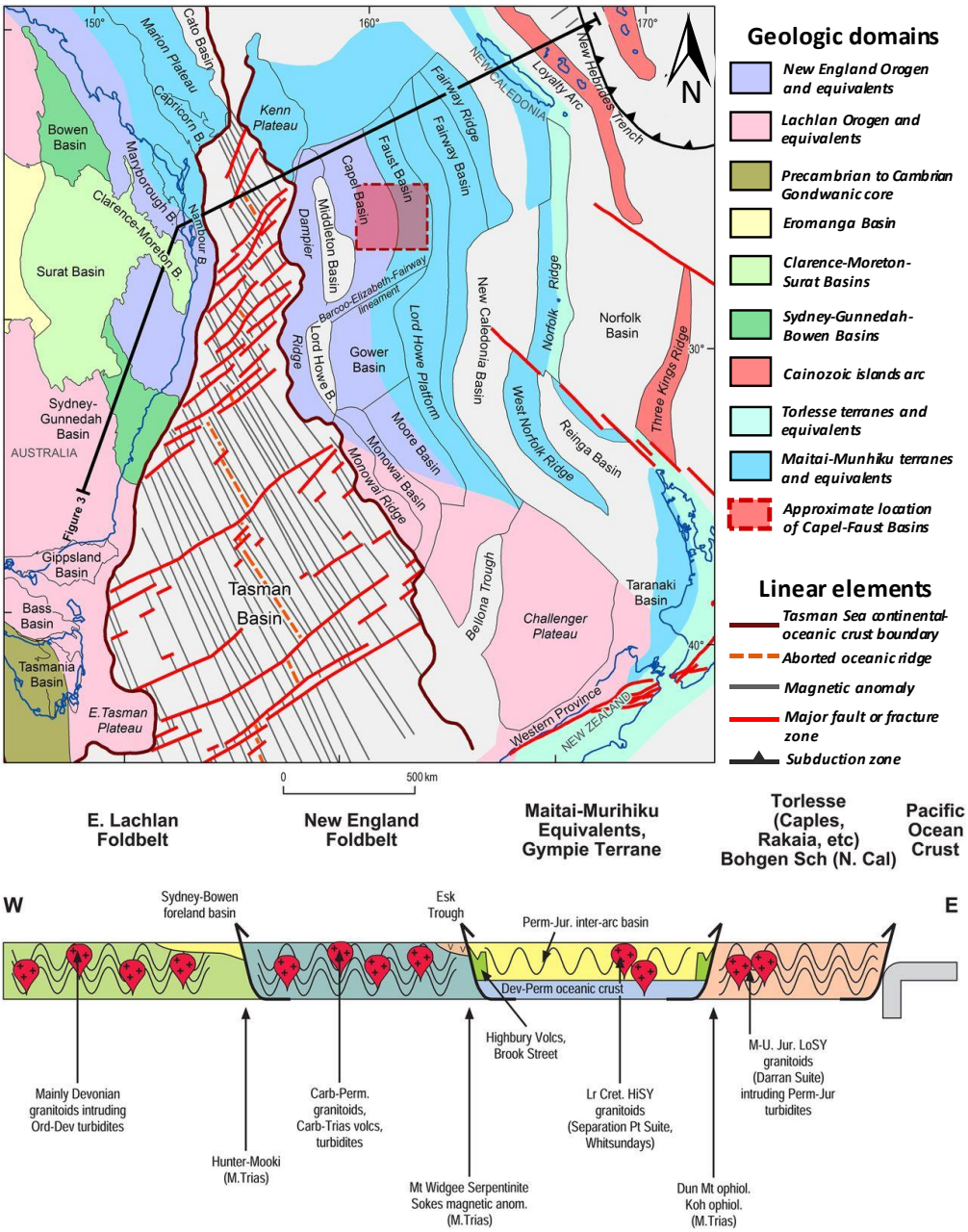

Figure 55 - Above: Inferred distribution of tectonostratigraphic terranes in the Tasman Borderland region (after Norvick et al. 2008). Below: Schematic east-west cross-section of major pre-rift terranes in the Tasman Borderland region (after Norvick et al. *2008); locations are shown in Figure 53*

Bowen, Gunnedah and Sydney basins are related to extensional or transtensional rifts due to the break-up of Gondwana (from 300 to 280 Ma) and to the following (from 280 to 268 Ma) N-S compression and dextral transtension (O'Neil & Danis, 2013). These basins constitute low structural areas, Carboniferous to Triassic in age, for an extension about 1600 km long (Glen, 2005), that extends from the south coast of New South Wales, near Ulladulla, almost to Bowen on the coast of northern Queensland and covers an area of over 260,000 km^2 (Cadman & Pain 1998). The whole Bowen, Gunnedah and Sydney has up to 10 km of sediments, within the most relevant coal deposits of Australia is present.

Sydney basin divides New England Orogen and Central Fold Belt from Southern Fold Belt. Its sediments are Carboniferous, Permian and Triassic in age (Figure 54) and, as the Great artesian Basin ones, contain the main coalfields of the continent. Hunter Valley is included in Sydney Basin and represents the area with the maximum sediment thickness. The thickness of the sediments decreases towards north-west, where Sydney basin borders on Gunnedah Basin (Figure 53 and 56), and towards south-west, where the pre-orogenic basement of the Lachlan Orogen outcrops. The general sedimentary architecture is, in fact, strongly

asymmetrical and the maximum sediment thickness is reached close to the north-eastern edge of the basin, near the Hunter Mooki thrust zone, that allowed the fast tectonic-driven sedimentation of relevant thickness of sediments from the New England uplifting range.

Gunnedah Basin divides Sydney Basin, on the southern side, and Bowen Basin, on the northern side (Figure 53, 56, and 57). Marine and non-marine sequences from the Permian and Triassic are present; Permian coal deposits too are present (Tadros, 1993). The Permian sequences are unconformably overlaid by the Triassic clastic coarse deposits. These deposits remark the uplift of the close New England Orogen. The remnants of this basin are spread across the structural high that separates Bowen Basin and Sydney Basin (main elements are, i.e., Baradine High, Rocky Glen Ridge, Boggabri Ridge, Walla Walla Ridge in Figure 53). Anyway, these three basins are the consequence of a mega-fold and can be referred as an only basin (Sydney-Gunnedah-Bowen basin). Within this structural high, there is Gunnedah Basin, Permo-triassic in age. A regional unconformity separates the Gunnedah basin from the overlying Surat Basin, of Jurassic age (Tadros, 1993).

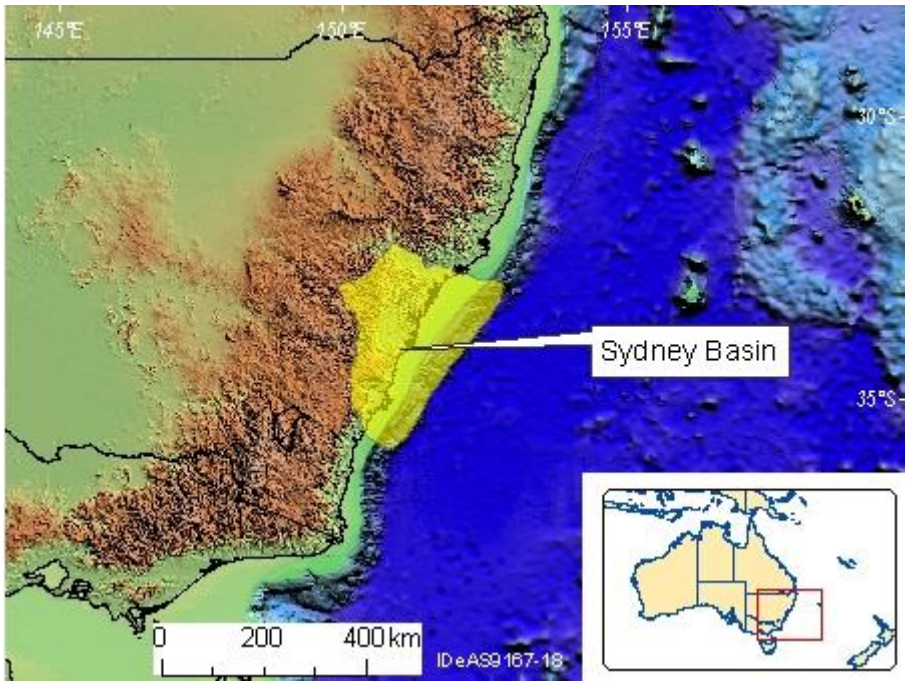

*Figure 56 - Location of Sydney basin (**http://www.ga.gov.au/home**)*

Although the first studies on the region date back to the coal beam discovery in 1877 (Dunne, 1950), there has been a great debate among scientists about the relation between Bowen, Gunnedah and Sydney basins. Surat Basin, Jurassic-Cretaceous in age, extends across these 3 Permo-triassic basins (Figure 53). Surat Basin is partly covered by Bowen Basin and Gunnedah Basin, separated by a regional scale unconformity (de Caritat & Brown, 1992).

Surat Basin (Figure 58) has a sedimentation the age of which ranges from Jurassic to Cretaceous. The Jurassic sediments are continental, fluviatile and consist of fining-upward megacycles, each more than 100 m thick, while the Cretaceous ones are marine and demonstrate the marine transgression of the Early Cretaceous. Both during Jurassic age, and during Cretaceous one, volcanic episodes have been recorded. The basin has been affected by relevant folding episodes and the sequence is almost flat-lying. Only a few drapes placement and synsedimentary faulting has affected the gentle basin-ward dip. While deposition during the Jurassic and Lower Cretaceous was dominantly, it gave way to erosion during the Late Cretaceous and Early Tertiary. Last geodynamic process affecting the Surat Basin was the Oligocene and Miocene volcanism, that was accompanied by epeirogenic basinward tilting.

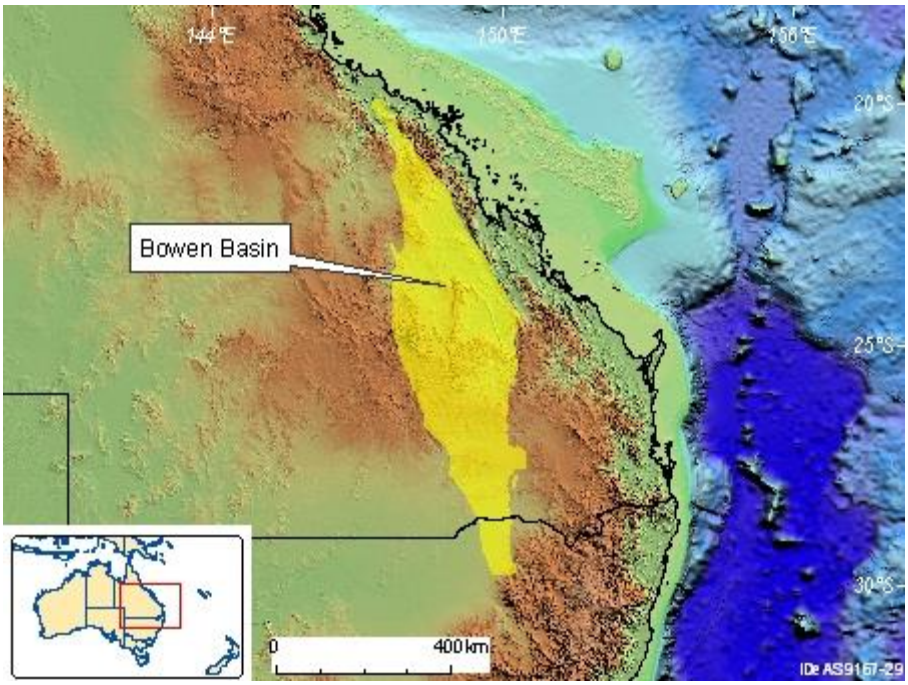

*Figure 57 - Location of Bowen basin (**http://www.ga.gov.au/home**)*

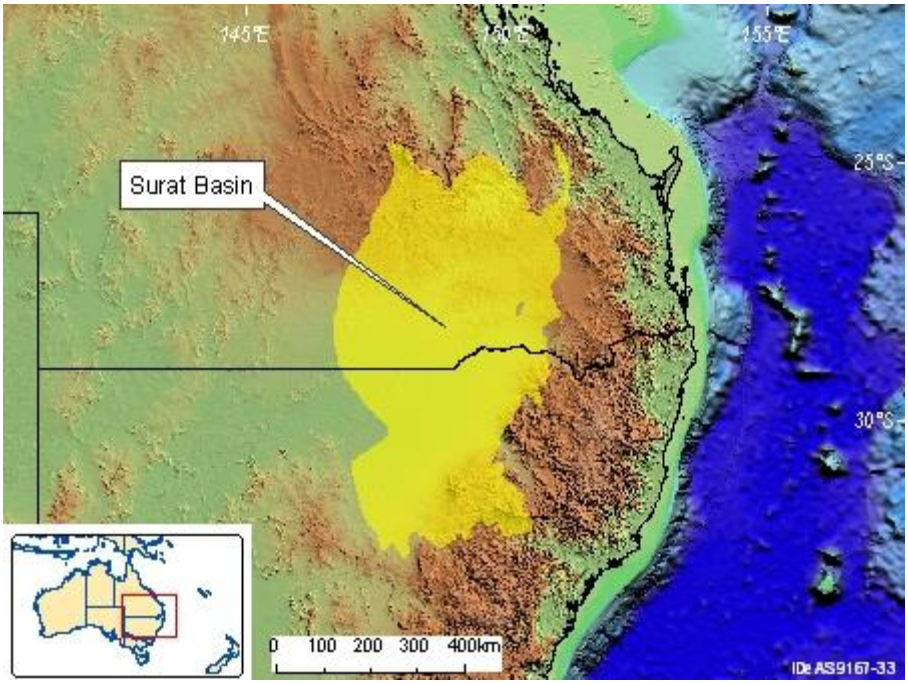

*Figure 58 - Location of Surat basin (**http://www.ga.gov.au/home**)*

- Geology of the Sydney Basin

Case study 2 mine is located mine is in Singleton area, within Sydney Basin. As previously described, Sydney Basin is bounded by two Pre-Cambrian to Palaeozoic Orogens, the Lachlan Orogen westward and the New England Orogen eastward; it is indeed bordered by the Permo-triassic Gunnedah Basin northward and by the continental shelf/slope edge of the Australian Plate towards the Tasman Sea (Figure 55). The contact between these different domains has different origin and is related to different geological structures (Figure 59). The border with the Gunnedah Basin is the Mount Coricudgy Anticline (Bembrick et al., 1980; Danis et al., 2011). Anyway, despite this structural high, some connection between these two basins remained because units of the northern Sydney Basin are present north of the anticline (Rasmus et al., 1969; Engel et al., 1991a, 1991b; Roberts et al., 1991a, 1991b). This structure is responsible of the minor thickness of the basin sediments near

Mount Coricudgy; anyway, the thickness of the sediments, although minor than other areas of Sydney Basin (O'Neill & Danis, 2013), reaches however 1.5 km over the Mount Coricudgy Anticline (Danis et al., 2011).

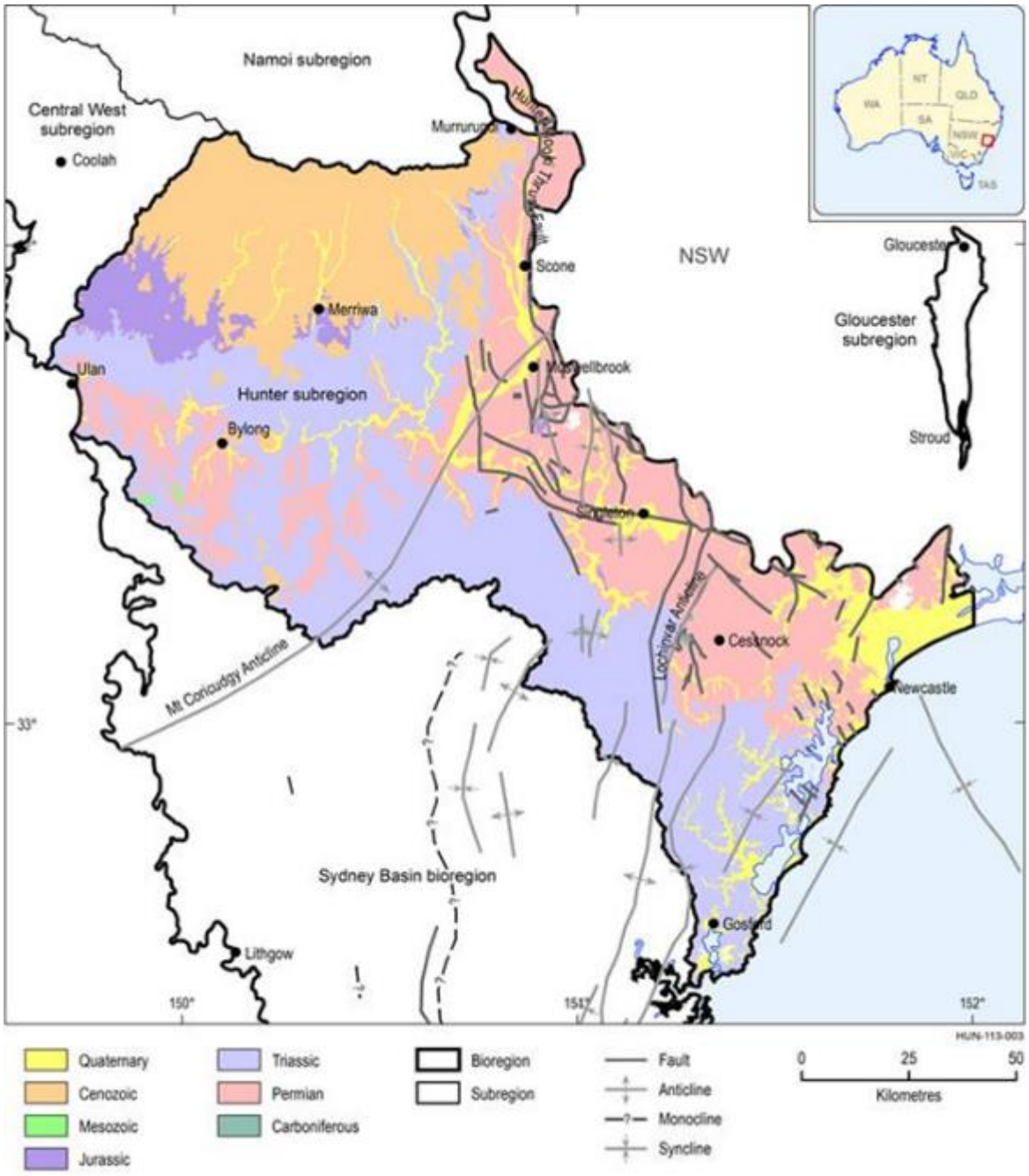

*Figure 59 - Geochronological subdivision of the rocks outcropping in Sydney Basin (**http://www.ga.gov.au/home**)*

Sydney basin can be split into 4 main coalfields (Figure 60 and 61):

- Newcastle Coalfield;
- Hunter Coalfield;
- Western Coalfield;
- Southern Coalfield.

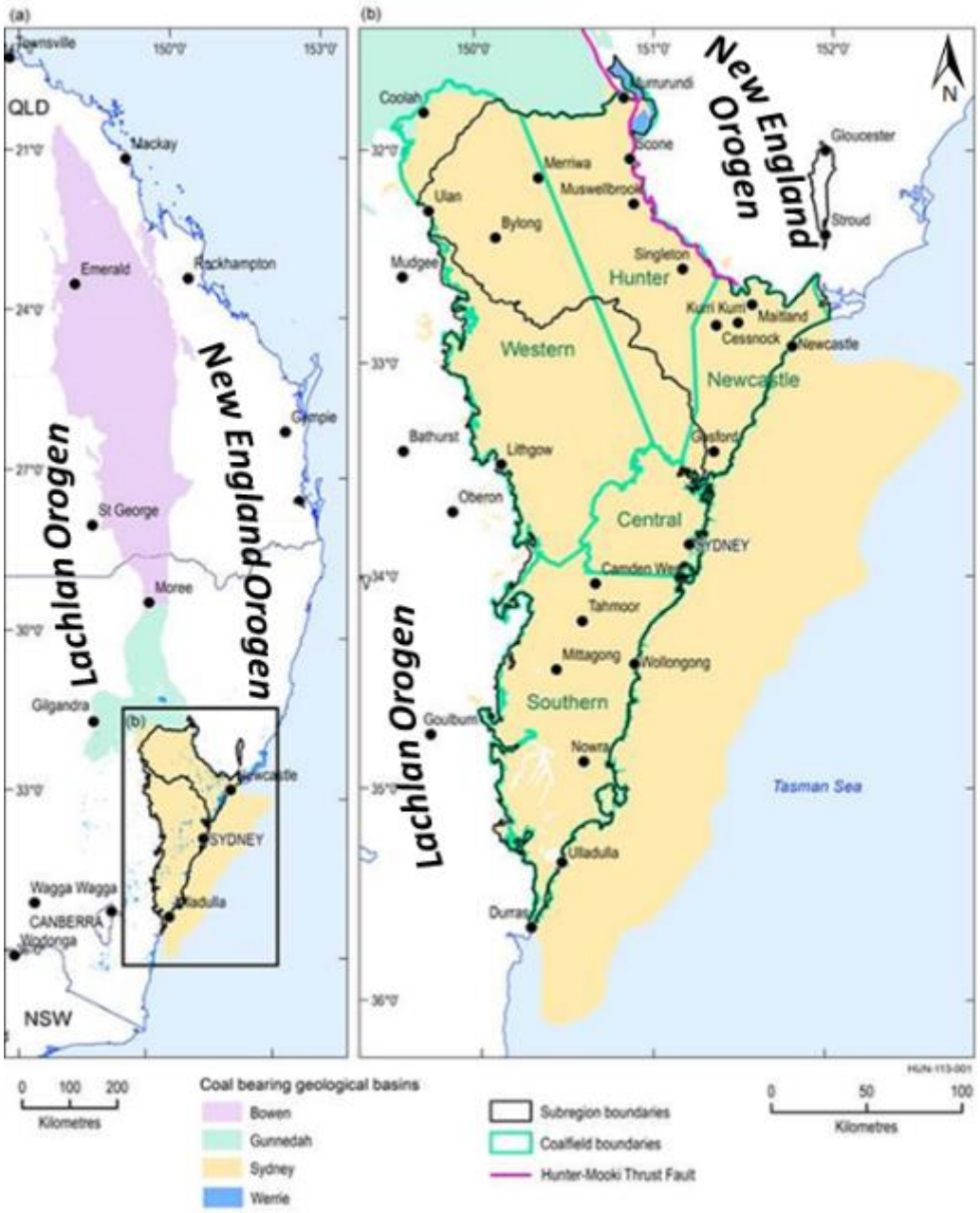

Figure 60 - Location of the Sydney Basin (a) and the 4 main coalfields within it (b). (http://www.ga.gov.au/home)

The lithostratigraphic columns of these 4 coalfields shows some similarities (Figure 61). In particular, Hunter Coalfield succession can be related to Newcastle Coalfield succession and Western Coalfield succession can be related to Southern Coalfield Succession. Hunter Coalfield and Newcastle Coalfield successions are very similar and differ only for the presence of marine Terrigal Formation instead of the continental Gosford Group at the top of the red beds of Clifton Subgroup, due to local subsidence, that caused limited transgression and an upward transition to fluvio-deltaic deposits of the upper Narrabeen Group (O'Neill & Danis, 2013). Tomago Coal Measures, instead of Newcastle Coalfield, is indeed equivalent to Wittingham Coal Measures within the second coal cycle (Stephenson & Burch, 2004).

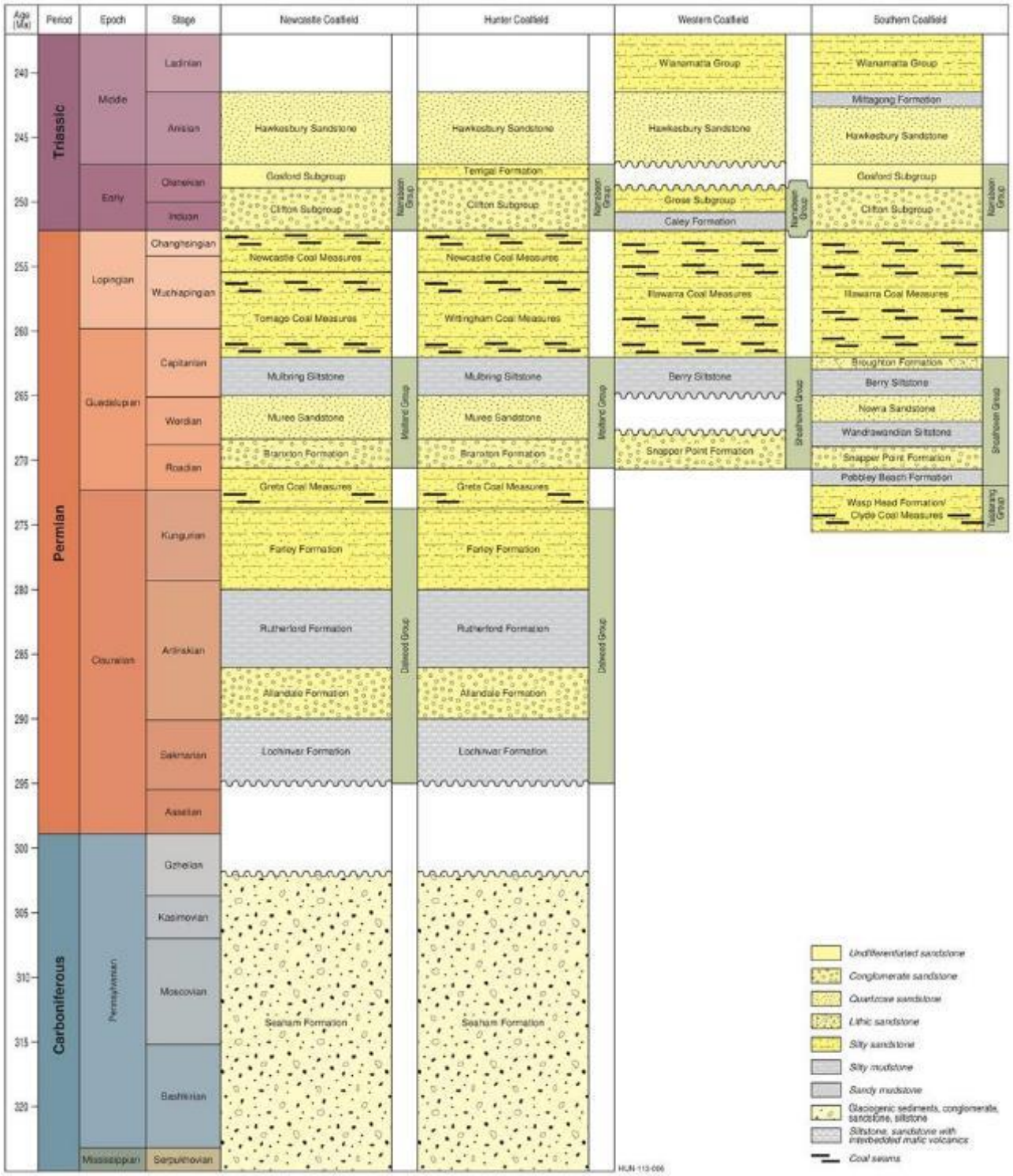

Figure 61 - Lithostratigraphy of the main coalfields of Sydney Basin. ***http://www.ga.gov.au/scientific-topics/energy/province-sedimentary-basin-geology/petroleum/offshore-eastern-australia/sydney***

Western Coalfield succession is instead similar to Southern Coalfield one; the begin of the sedimentation of these two successions is more recent than the beginning of Newcastle and Hunter ones (Middle Permian instead of Mississippian in age) and is related to the regional scale tectonic subsidence and marine transgression related to the deposition of Greta Coal Measures in Hunter and Newcastle Coalfield and of Clyde Coal Measures in Southern Coalfield. Western Coalfield differs from Southern Coalfield for the presence of two main erosive events and for the different stratigraphic units within the Triassic basins filling sedimentation, at the base and at the top of Hawkesbury Sandstone. The first erosive event dates to middle Permian and has been related to the westward sea movement, on the Lachlan Orogen, that eroded considerable quantities of

boulders and pebbles from coastal cliffs, while the second erosional event within Western Coalfield succession has been related to the uplift of the Lachlan Fold Belt, that caused the sea regression (O'Neill & Danis, 2013). The top of these last two succession ends in Ladinian, with the sedimentation of Wianamatta Group (not present in Newcastle and Hunter Coalfields succession), that testifies the last phase of sedimentation directly related to the tectonic development of the whole Sydney Basin. This last unit shows an upward environment transition from subaqueous, to shoreline and ultimately to alluvial during a single major regression (Herbert & Helby, 1980).

- Lithostratigraphy of Hunter Coalfield

Hunter Coalfield succession, as the related Newcastle Coalfield succession too, covers a time interval of 80 Ma about, from Mississippian to Middle Triassic epochs (Figure 61). Sedimentation of these two coalfields begins in the Upper Mississippian with the Seaham Formation (David, 1896; Whetten, 1965; Fielding et al., 2005) and ends during Middle Triassic with Hawkesbury Sandstone (Rust & Jones, 1987; Liu et al., 1996; Miall & Jones, 2003).

Since the discovery of the coal deposits, the stratigraphic mapping and describing of the outcropping formations has gotten a great interest for mining. Anyway, the lack of a regional-scale overview has allowed the proliferation of a great amount of lithostratigraphic units, especially for old geological studies. Nowadays, Hunter Coalfield succession has been split into the following lithostratigraphic Units, from lowest to uppermost (Figure 61):

- Seaham Formation (Mississippian-Pennysilvanian) (Roberts, 1965);
- Daelwood Group (Cisuralian) (Voisey, 1958);
    - Lochinvar Formation (Voisey, 1958);
    - Allandale Formation (Fairbridge, 1953);
    - Rutherford Formation (Voisey, 1958);
    - Fairley Formation (Voisey, 1958);
- Greta Coal Measures (Cisuralian-Guadalupian) (Whitehouse, 1926);
- Maitland Group (Guadalupian) (Joplin et al., 1956);
    - Branxton Formation (Nashar, 1964);
    - Muree Sandstone (Fairbridge, 1953);
    - Mulbring Siltstone (Nashar, 1964);
- Wittingham Coal Measures (Guadalupian-Lopingian) (Britten, 1972);
- Newcastle Coal Measures (Lopingian) (Fairbridge, 1953);
- Narrabeen Group (early Triassic) (Joplin et al., 1952);
    - Clifton Subgroup (McElroy, 1957);
    - Terrigale Formation (Herbert, 1970);
- Hawkesbury Sandstone (Middle Triassic) (Smith, 1891).

Seaham Formation (Mississippian-Pennsylvanian; Roberts et al., 2006)

During Late Carboniferous, the subduction of Panthalassan Ocean underneath the active gondwanic margin caused the opening of Bowen-Gunnedah-Sydney Basin, the anatectical volcanism along the rift (Kuttung Volcanics) and a strong energy of the relief, with stood elevated at more than 600 m (Herbert 1972). This fact, together with the low latitude of this part of Gondwana landmass (Figure 62), provoked the deposition of glacial deposits made by coarse and unsorted conglomerates (tillites) (David, 1896) and lacustrine glacial shale deposits (varves) (Süssmilch & David, 1919). The maximum thickness of the formation is 600 m (Roberts et al., 2006). At the top of Seaham Formation an erosional surface and a stratigraphic lack separate the Seaham Formation from the Permian Daelwood Group.

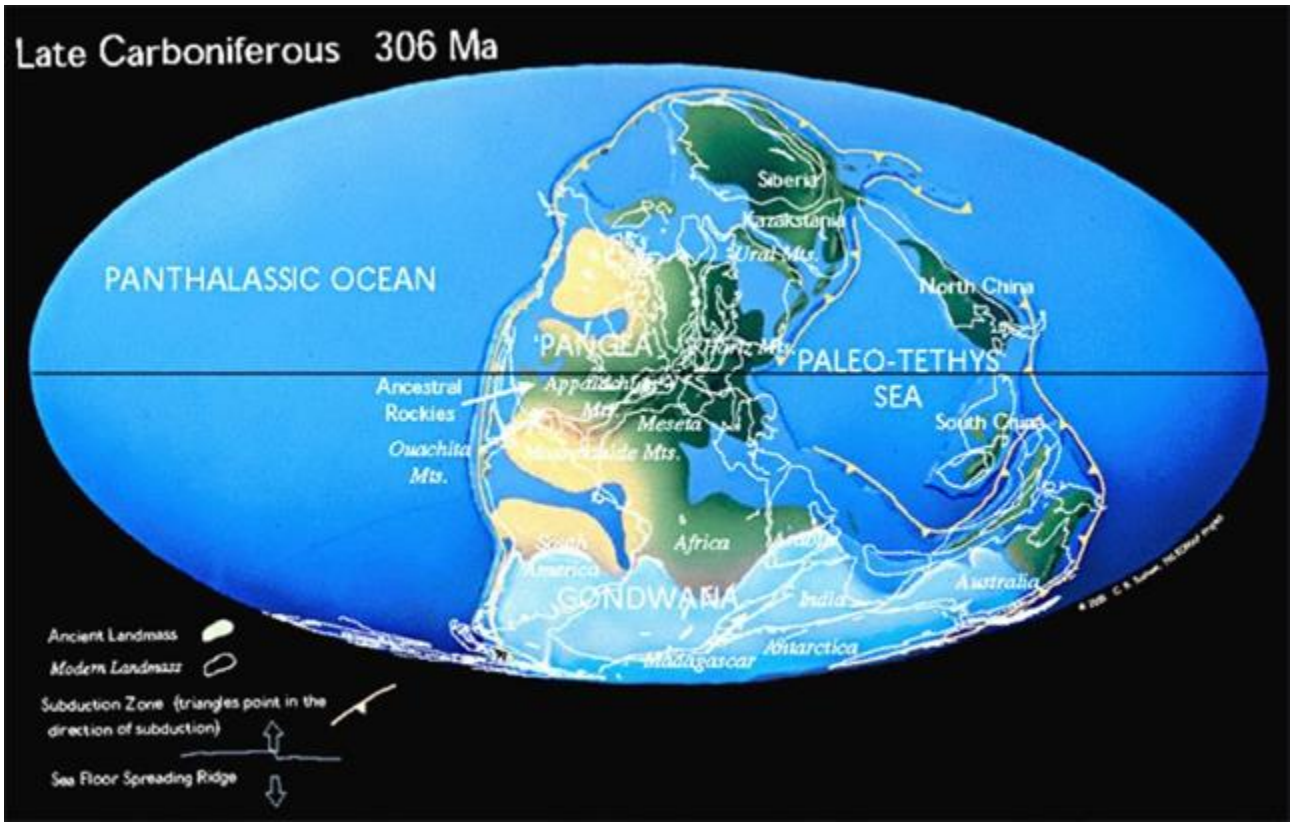

Figure 62 - Landmass distribution during Late Carboniferous and spreading of the glacial cover. The land mass disposal permitted the spreading of the glacial cover until the current Australia. On the eastern margin of Australia is present the subduction zone of Pantahlassic Ocean underneath the Gondwana. From PaleoMap Project ***http://www.scotese.com/***

Daelwood Group (Cisuralian)

Daelwood Group testifies a regional-scale marine transgression related to the tectonic of the rifting of Gondwana. This succession begins with an erosional surface and the Lochinvar Formation, that is made by thick basaltic and rhyolitic sequences and shows the volcanic activity connected to the crustal thinning of the on-going rifting. Daelwood Group is entirely constituted by marine units (Percival et al., 2012).

Lochinvar Formation

Lochinvar Formation is a coarsening-upward sequence (Evans & Migliucci 1991) of mudstone and sandstone of marine to sublittoral environment (Voisey, 1958), with interbedded basalt flows (McClung, 1980). It is poorly exposed and has generally very limited fossil content.

Allandale Formation

Allandale Formation is made by interbedded lithic sandstone and conglomerate, and commonly contains abundant invertebrate marine fossils (McClung, 1980) of shelf and infralittoral environment (Percival et al., 2012).

Rutherford Formation

Rutherford Formation consists dominantly of micaceous sandy siltstone, mudstone, shale, silty sandstone and sandstone, with some thin limestone and marl horizons and poorly sorted conglomeratic, lithic sandstone at the base. Limestone, marl and sandy limestone locally occur. It is interpreted to have been deposited below wave base (Evans & Migliucci, 1991).

Fairley Formation

Fairley Formation is a poorly sorted, fine- to medium-grained silty sandstone. The unit is coarsening and coarsening upward, with a probable northern source area. Bedding is generally massive, and bioturbation is evident in laminations. It is approximately 300 m thick (Percival et al., 2012) and contains abundant and disarticulated fossils (brachiopods, Conularia and gastropods; Heeswijck, 2001) within a coarsening-upward sequence of silty sandstone (McClung, 1980), probably deposited above wave base (Evans & Migliucci, 1991). At the top of the formation, Reinhold (1963) reported an unconformable boundary with Greta Coal Measures.

Greta Coal Measures (Cisuralian-Guadalupian)

The Greta Coal Measures represent the oldest non-marine unit of the Permian succession. It consists of conglomerates and sandstones with a thin siltstone and mudstone layers (McClung, 1980) deposited in deltaic and fluvial environment, with local crevasse-splay, marsh or lacustrine, and coal swamp deposits (Sniffin & Beckett, 1995). The deposits have been, in fact, related to lowstand regression events (Mayne et al. 1974) in an alluvial fan delta (Evans & Migliucci, 1991). Greta Coal Measures were deposited with the fluvial and deltaic sediment systems progradation into the basin and are exposed in the northern part of the coalfield near Muswellbrook, and in the southern part along the western limb of the Lochinvar Anticline. The sequence occurs to depths greater than 600 m in the Hunter Coalfield and are exposed mainly in areas close to high structural features, such as Muswellbrook and Lochinvar anticlines. Its thickness spaces in the Hunter Valley from 60-75 m in the Lochinvar area up to 200 m in the Muswellbrook area (Basden, 1969). The conglomerates are often coarsening and thickening upwards, with coal levels with a maximum thickness is 11 m (McClung, 1980). Several coal seams have been described (Figure 63) within these Measures; these seams differ from Musswellbrook anticline and Lochinvar anticline outcrops.

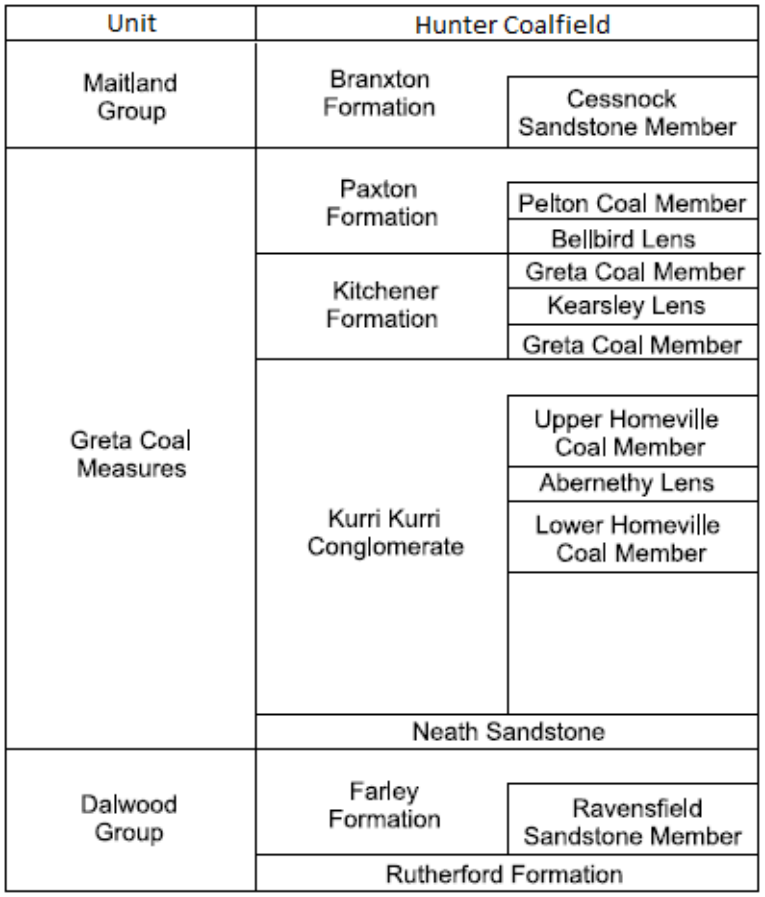

Figure 63 - Lithostratigraphy of the Greta Coal Measures and bounding formations. Data from Slee (1968) and Hawley & Brunton (1995); from Heeswijck (2001), with modifications

6 seams are identified in Muswellbrook area, although these cannot be consistently correlated between the northern and southern parts of the anticline (Beckett, 1988). Seams detected in this anticline are 1 m (Idemitsu Kosan, 2010) to 10 m about thick. The coal seam levels at Lochinvar anticline are less thick than the level detected at Muswellbrook anticline. In this area the Greta Coal Measures includes the Lower and Upper Homeville coal members, which are low ash-yielding coals. The informally named Greta Coal Seam is up to 11 m thick and split by the Kearsley Lens, with a maximum thickness of 5 m about.

The unit is made, from the lowest to the uppermost, by the Neath Sandstone, Kurri Kurri conglomerate, Kitchener Formation and Paxton Formation. The massive, fine-grained, well-sorted Neath Sandstone rests on the Dalwood Group formations and is overlain by the poorly sorted, jasperoid Kurri Kurri conglomerate, which hosts the Lower and Upper Homeville Coal Members. Kitchener Formation and Paxton Formation overlies Kurri Kurri Conglomerate, that are both coal-bearing and host Greta Coal members (Lower and Upper), and Pelton coal member respectively.

The tectonic activity coeval and successive to the sedimentation is testified by the presence of igneous intrusions, that locally occur (Basden, 1969; Beckett, 1988) and thermally affect the coal seams, and by the presence of widespread faulting that displaces the bedding. The top of the Greta Coal Measures has been dated at 271 My using U-Pb CA-IDTIMS single zircon technique (Metcalfe et al., 2015).

- Maitland Group (Guadalupian)

Maitland Group testifies two transgressive events between the Carboniferous coal seams episodes.

Branxton Formation

The Branxton Formation is an upward-fining, quartz-lithic marine sandstone to siltstone unit. It has a massive structure and exhibits strongly developed bioturbations. The marine depositional environment testifies transgressive marine conditions. Branxton Formation is constituted by fluvio-deltaic sediment derived from erodingthe erosion of Late Devonian quartzite headlands. This erosional event within the Lachlan Orogen is related to the sea westwards movement over the chain.

Muree Sandstone

Muree Sandstone represents a brief regressive episode prior to resumption of transgression between Branxton Formation and Mulbring Formation transgressive events (McClung, 1980) and is constituted by fan delta sediments (conglomerate and interbedded sandstone and siltstone)

Mulbring Formation

At the top of Muree Sandstone, a new marine transgression has been documented (Sniffin & Beckett, 1995). This formation is constituted by relatively uniform sandy claystone, shale and cherty shale (Booker, 1957) and is up to 330 m thick at the type section (McClung, 1980).

Whittingham Coal Measures (Guadalupian-Lopingian)

In the Late Permian a new stage of the Hunter - Bowen Orogeny causes the faulting and the folding on the north side of the basin. This relief rejuvenation provokes the massif arrival of sediments and the regression of the coastline. The marine environment of Mulbring Formation is so substituted by deltaic, river and marshy environments, where the anoxic conditions allows the deposits of coal seams. This tectonic episode causes so the deposition of the Tomago Coal Measures in Newcastle Coalfield and of Whittingham Coal Measures in Hunter Coalfield.

Whittingham Coal Measures is constituted by the following lithostratigraphic units, from lowest to the uppermost: Saltwater Creek Formation, Vane Subgroup (Foybrook Formation and Bulga Formation), Jerrys Plain Subgroup (Althorpe Formation, Burnamwood Formation, Fairford Formation, Malabar Formation, Milbrodale Formation, Mount Leonard Formation, and Mount Ogilvie Formation), Denman Formation, and Archerfield Sandstone (Geoscience Australia and Australian Stratigraphy Commission, 2015).

Vane Subgroup and Jerrys Plain Subgroup stratigraphy are here described in detail because the two case study mines are included within these units. Vane Subgroup is constituted by Foybrook Formation and Bulga Formation. Foybrook Formation outcrops in the case study 2 mine. It is constituted by many coal member (Arties Coal Member, Barrett Coal Member, Bengalla Coal Member, Clanricard Coal Member, Edderton Coal Member, Edinglassie Coal Member, Hebden Gully Coal Member, Lemington Coal Member, Liddell Coal Member, Pikes Gully Coal Member, Ramrod Creek Coal Member, Wynn Coal Member), that testify the facies change from lower to upper delta plain deposits (Sniffin & Beckett, 1995). The thickness of the coal member is quite homogeneous, and the thickness of the whole formation changes from the maximum value of 300 m in the middle of the basin until 60-75 m around the high structural of the Lochinvar Anticline.

The thickness of the coal member is fundamental to evaluate mining cost-effectiveness: thin members mining is, in fact, less profitable; most of the seams are characterised by multiple splitting, thus, individual coal seams tend to be thin and of less mining interest (Sniffin & Beckett, 1995).

The stratigraphic succession of case study 2 mine shows that Foybrook Formation here comprises a sequence of coal seams, mudstone, siltstone, sandstone and conglomerate; this succession is 300-350 m thick (Glencore, 2014). As for the rest of the Foybrook Formation, here too a transition from lower to upper delta plain deposits is present. In particular, the lower seams (Hebden, Barrett, Lower Liddell and Middle Liddell) are thought to have developed in a lower delta plain environment. The higher seams (Upper Liddell, Arties and Pikes Gully) shows a lateral condition that testifies, from lower to the upper part and from the inner to the outer basin

part of the succession, the transition towards an upper delta plain environment (Glencore, 2014). As shown in the lithostratigraphic column in Figure 83, the Foybrook Formation, in the case study 2 mine area represents a coarsening upward cycle: the thickest coal levels are at the base of the formation, while the coarsest levels, made by conglomerates and pebbly sandstone, typical of upper delta fan environment, are moreover present at the top. The coal level of uppermost member of Foybrook Formation, the Lemington Coal Member, has a maximum total seam thickness of 107.8 m and a maximum net coal thickness of 16.1 m. The coal seams in the case study 2 mine area are situated between two regional thrust faults, the Hunter Thrust and Hebden Thrust, each limiting the lateral extent of the coal deposits (Glencore, 2014). The Foybrook Formation is here overlaid by the Bulga Formation, a relatively thin (15m) bioturbated laminite, and then by the Jerrys Plain Subgroup.

Jerrys Plain Subgroup in Whittingham Coal Measures represents an upper delta fan environment, with a coal distribution more variable compared to that of the Vane Subgroup. Although most of the upper delta plain seams are laterally extensive (Sniffin & Beckett, 1995), large variations occur in some of its coal members (Pinetown, 2012). The thickness of the seams of the subgroup changes area by area: in the eastern part it is primarily absent because of the erosion due to the tectonic uplift, while in the central part of the coalfield, seam thickness is less variable than in the south. Seams of the Jerrys Plains Subgroup in the north of the coalfield generally have similar splitting behaviour and distribution patterns to those in the central and southern regions. Maximum thickness of the subgroup is 800 m.

Whittingham Coal Measures end with a new marine incursion, that puts end to the deposition of the Jerrys Plain Subgroup. This event is documented by the presence of the marine Denman Formation and the Archerfield Sandstone. The maximum thickness of Denman Formation is 30 m; in the southern part of the basin, Denman Formation is absent (Sniffin & Beckett, 1995) and Archerfield Sandstone lays directly on Jerrys Plain Subgroup. Whittingham Coal Measures in Hunter Coalfield can be referred to Tomago Coal Measures in Newcastle Coalfield from a lithostratigraphic point of view. Both Whittingham Coal Measures and Tomago Coal Measures represent continental succession overlaid by a marine episode.

Newcastle Coal Measures

Newcastle Coal Measures represent a marine regression episode occurring before the Permian-Triassic limit, both in Newcastle Coalfield, and in Hunter Coalfield. This episode is separated from the previous coal measures, the Tomago Coal Measures in Newcastle Coalfield and the Whittingham Coal Measures in Hunter Coalfield (Figure 61) by a sea transgression episode. The coal seams of the Newcastle Coal Measures are present only towards the West and show distribution patterns that indicate fluvial depositional conditions with rapid channel migration depositing thinner coal seams, with seams of the Abbey Green Coal split and varying between 0.8 and 97.4 m thick (Pinetown, 2012). The upper coal seams south to the Hunter River Cross Fault are generally thin, indicating fluvial conditions with rapid channel migration, seam splitting and erosion towards the end of coal measure deposition (Sniffin & Beckett, 1995). Tuff locally interbed the sedimentary rocks (Branagan, 1967; Ives et al., 1999; Grevenitz et al., 2003; Creech & Rigby, 2006; Umwelt Pty Limited, 2011).

Narrabeen Group (Early Triassic)

Narrabeen Group is made by Early Triassic detritical rocks (conglomerate, quartz-lithic sandstone, quartzose sandstone siltstone and sandstone; Stroud et al., 1985; Clark & Jones, 1991; Yoo et al., 2001). The surface between the Narrabeen Group and the Late Permian coal Measures in Sydney basin is a disconformity except in the Lochinvar Anticline where it is a low-angle unconformity; uplift and erosion are, in fact, confined to the Lochinvar Anticline (Herbert, 1993) and succession moderately thins westwards (Yoo et al., 2001). Overall, the quartz-lithic sandstones of the Narrabeen Group form near-continuous and mesa-like plateaux. These geomorphological features are characteristic of the Narrabeen Group outcrops in the Western Coalfield; i.e. the “Three Sisters” are part of this mesa-like plateau. Narrabeen Group in Hunter Coalfield includes the Clifton Subgroup and the Terrigale Formation.

Clifton Subgroup

Clifton Subgroup is constituted mostly by quartz-lithic sandstone and reddish to greenish shale. The prevalent lithology at the base of the succession is constituted by fine to medium-grained lithic sandstone and at the top by reddish-brownish shale (*redbeds*) (Stroud et al., 1985; Clark & Jones, 1991).

Terrigale Formation

Terrigale Formation lithologies consist in interbedded laminate shale and quartz to quartz-lithic sandstone with local clay pellet (Herbert & West, 1983).

Hawkesbury Sandstone (Anisian)

Hawkesbury Sandstone represents an important Anisian cover deposit in Sydney basin. Hawkesbury Sandstone is known as commodity as "Sydney Sandstone" and constitutes one of the most important and widespread building stone in the area. Its durability and its golden chromatism make it, in fact, very suitable as stone building. It has been deposited in a fluviatile delta. Hawkesbury Sandstone is a quartz-sandstone with minor amount of siderite laminae, that give the brownish coloured veins.

5.2. Description of the sites

The sites of the two case studies are located in the Hunter Coalfield (Hunter Valley, New South Wales, Australia). The Hunter Coalfield is located in the inland (Figure 64 and 65) of Newcastle, that is at the Hunter river mouth. With three terminals appositely dedicated to coal cargo, the Carrington coal terminal, the Kooragang Coal Terminal, and the NCIG Coal Export Terminal, for a combined annual capacity of 211 million tons, the Port of Newcastle is the world's leading hub for coal export. Dated back since the second half of the 19th century, when large coal deposits of the upper and lower Hunter Valley where discovered, in 2014 has been sold to a 50/50 joint venture between Chinese and Australian companies' interests. Coal exports represent more than 90% of total tonnage, mostly destined for Chinese and Japanese market, for which is the most important coal supply.

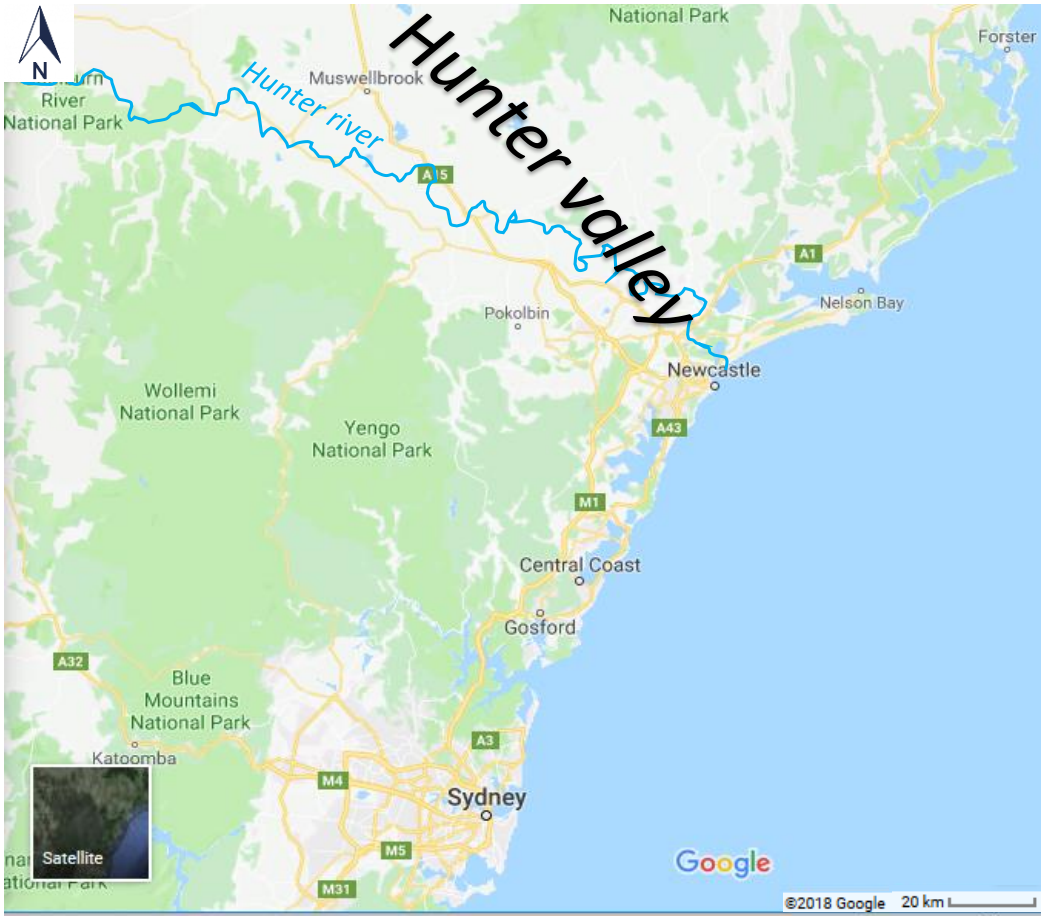

Figure 64 - Location of the Hunter Valley

These sites were chosen due to their weathered lithology, high fracturing and strong manmade character, in order to test the effectiveness and reliability of the presented methods to reconstruct and analyse geostructurally unfavorable rock masses.

As regards discontinuity shear resistance (input parameter for the kinematic analyses described in the following section), Lindsay et al. (2001) evaluated the value of the ϕ in case of dry condition for Waikato Coal Measures in open pits in the Waikato coal region, for siltstone with organic matter, shale, and coal beds. Using the rock mass classifications proposed by Laubscher (1991), Romana (1991), Hoek et al. (1997), and Hack (1998), Lindsay et al. (2001) evaluated the values of ϕ ranging from 25.7° to 41°. Fuenkajorn (2005) carried on a series shear tests in an attempt at assessing the predictive capability of Barton's joint shear strength criterion derived from field-identified parameters and for arenites ϕ values range between 29-34 degrees. Suchowerska Iwanec (2014) has indeed evaluate a ϕ=30° as input representative parameter value for Hunter Valley coalfield. 30° has been so considered a representative and precautionary ϕ value.

For these reasons a unique value of c and ϕ of the discontinuities equal to 0 kPa and 30°, respectively have been chosen for the kinematic analyses presented in the following sections.

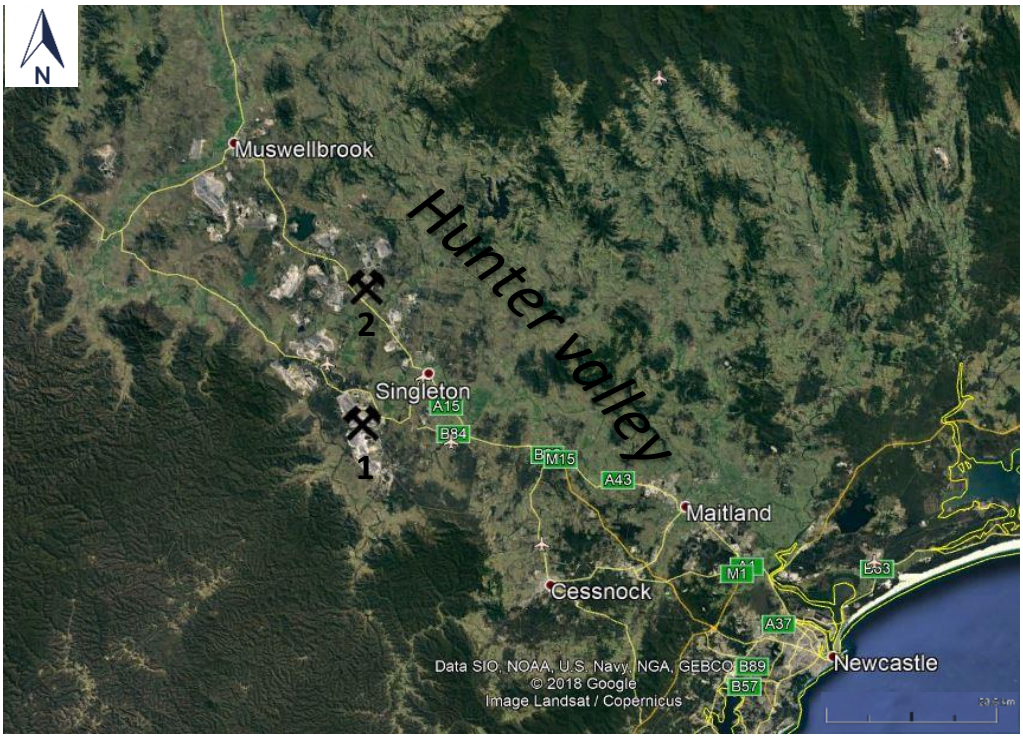

Figure 65 - Location of the two case study mines within the Hunter Valley

5.2.1. Case study 1

Case study 1 mine is located southwest to Singleton, within the Wittingham Coal Measures (Figure 66). The outcrop is located within the upper part of the Wittingham Coal Measures, between the Jerry Plains Subgroup and the Denman Formation. Ten coal levels have been described into the mine (Figure 67): Hedben, Barrett, Lower Liddell, Middle Lindell B, Middle Lindell A, Upper Liddell, Arties, Pikes Gully B, Pikes Gully A, and Lemington A.

As regarding the outcrop stratigraphy, at the base of the berm, a 1 m meter thick coal layer is present. The studied section includes, both for highwall 1 and for highwall 2 (Figure 68):

- 6.5 m of greyish thinly layered pelite and shale, with coal-rich layers
- 2.5 m of yellowish massive arenite
- 10 m of a fining upward alternance made by pelite, arenite and shale
- 2 m of carbon-rich shale

These beds can be referred to the top of the Jerrys Plain Subgroup.

At the top of the stratigraphic section included into the studied part of the highwall, the stratigraphy of the berm includes:

- 1 m of greyish arenite and pelite alternance
- a decimetric layer of coal
- 3 m of yellowish arenite with layers of decametric thickness

The greyish arenite and the coal level can be referred still to the Jerrys Plain Subgroup; the yellowish arenite have been, instead, referred to the Denman Formation (Figure 68), of marine environment (Standing Committee Coalfield Geol. NSW, 1986).

The geostructural characterization and the kinematic and stability analysis have been carried out on two perpendicular highwalls; the position of the highwalls is described in Figure 69 and 70.

The β_{slope} of the highwalls is 70° (Lambert et al., 2012). The whole height of the mosaics of highwall 1 and highwall 2 is 31.73 m and 31.92 m, respectively, while the distance between the highwall and the mean cameras position, located low ground at the base of the berm, is 43.55 m and 40.23 m. The images of the uppermost part of the berm has so a lower definition and have not been used for the analysis of the highwalls. Indeed, also the right part of highwall 1 has not been used because covered by a drapery system. Geostructural survey has been so carried out on a 14 m long and 21 m high section for highwall 1 and on a 22 m long and 21 m high section for highwall 2. The areas of the studied sectors of highwall 1 (Figure 71) and of highwall 2 (Figure 72) are 313 m^2 and 492 m^2, respectively. The bedding orientation (Lambert et al., 2011) is α = 281.6° β = 8.6°. The geostructural survey carried out by SiroJoint has confirmed the values of dip and dip direction reported by Lambert et al. (2011); λ and σ_λ have been evaluated by a scanline. The description of the set of discontinuity of the bedding, for both highwall, is described in Table 2.

Table 2 - Description of the set of discontinuities related to bedding for case study 1 mine

Set	α (°)	σ_α	β (°)	σ_β	L (m)	σ_L	Nr discontinuities
bedding	261.6	0	8.6	0	∞	2	0.83

Many studies have been carried out on the slope stability and rockfall hazard on the highwalls of case study 1.

Thoeni et al. (2011a) described the highwall 1 producing a geostructural characterisation of the rock mass and performed the rockfall analysis of the slope. Geostructural description of the rock mass was performed using SiroJoint on a 3D model built with SiroVision since a photogrammetric survey. Then the polyhedral model of the rock mass structure was made using SiroModel. Once the geostructural model was built and the stability analysis was performed with SiroModel, rockfall analysis was performed with CRSP (Colorado Rockfall Simulation Program) code (CRSP, 1979), using the profiles of the model built with SiroVision and spherical blocks with a radium of 0.3 m, 0.6 m, and 1.0 m. The rockfall simulation showed maximum velocity values ranging from 26.34 m/s to 27.12 m/s at the base of the bench.

Giacomini et al. (2011) reproduced the fall of the blocks sampled at the base of the bench, recording the fall using high speed cameras. The blocks real trajectories were so compared with the modelled one for the rockfall hazard management. Further studies were performed on this case study about the modelling of the drapery system (Thoeni et al., 2011b), and the development of rapid and accurate 3D reconstruction of highwalls by photogrammetric survey (Thoeni et al., 2012).
Casagrande in its MSc thesis (Casagrande, 2012) made the geostructural description of the rock mass of highwall 1, calculating the compressive normal strength and Young modulus of the shale and of the arenite, sampling the rock size distribution of the blocks at the base of the slope and performed the rockfall analysis of the slope. Geostructural description of the rock mass was performed using SiroJoint on a 3D model 1 built with SiroVision since a photogrammetric survey. Sampling of the fallen blocks at the base of the bench was performed by or the visual analysis of the photographs in order to reduce as more as possible the time spent under the "no-go zone", or by the direct access of an operator for the biggest blocks. Casagrande noticed that the volume of the biggest fallen block was 1.5 m^3. Uniaxial compressive strength and Young modulus were evaluated with the uniaxial compressive strength test and with the Point Load Test. Uniaxial compressive strength values ranged from 13.7 MPa to 115.9 MPa with an average of 58.9 MPa for arenite and from 3.3 MPa to 8.1 MPa with an average of 5.8 MPa for the shale. The values of Young modulus ranged from 0.44 to

15.41 (average 7.2) for the arenite and from 0.002 to 0.27 (average 0.1) for the shale. 2D rockfall analysis were performed by CRSP and the dimension of the block sampled at the base of the bench. The velocities at the base of the bench ranged from 3.5 m/s to 27 m/s and were calculated performing 16 simulations for block different for lithology (arenite or shale) using blocks 183 kg weight for shale and 139 kg weight for arenite.

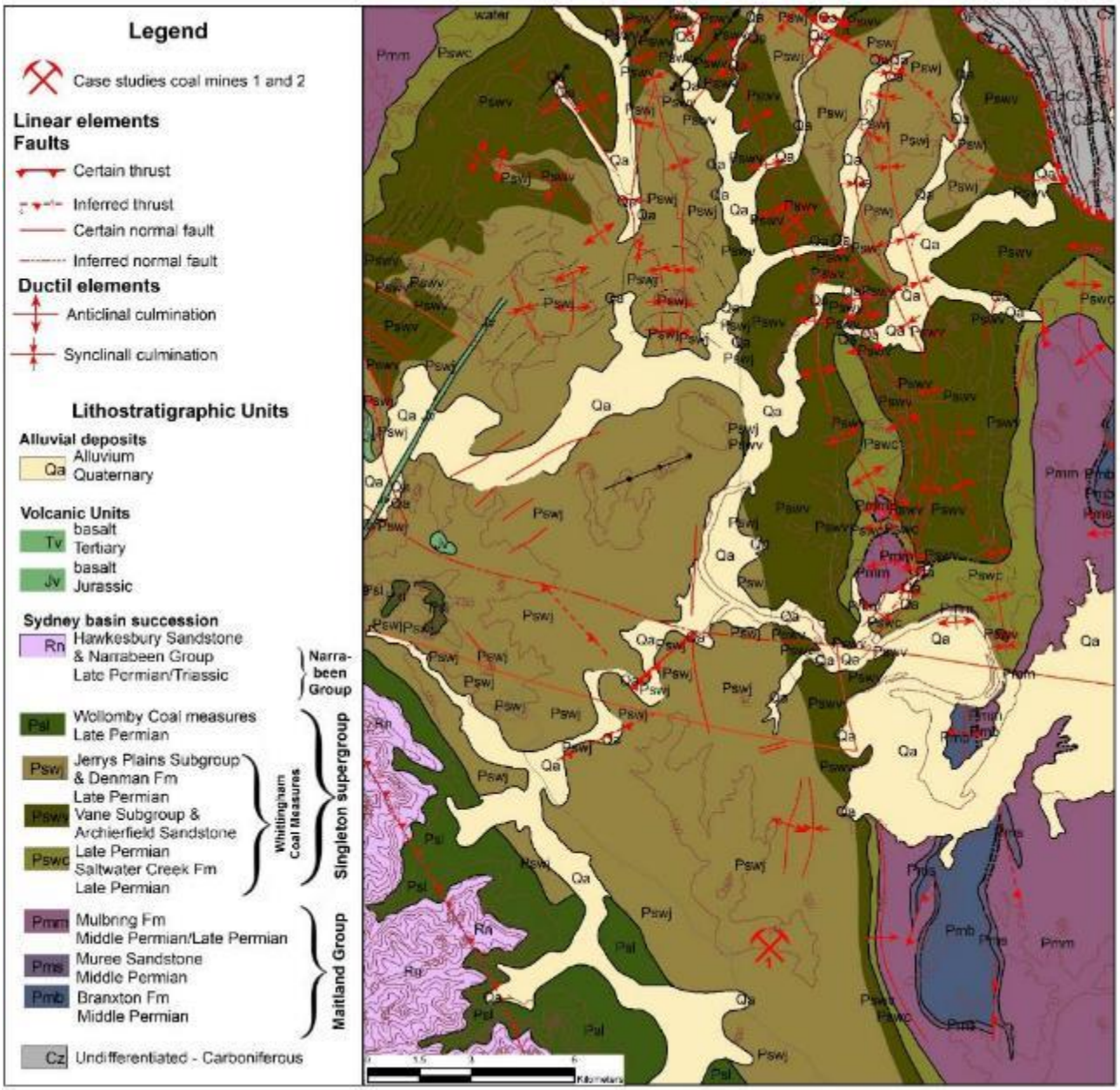

Figure 66 - Geological map of the area of Singleton. Modified from Rasmus et al. (1969)

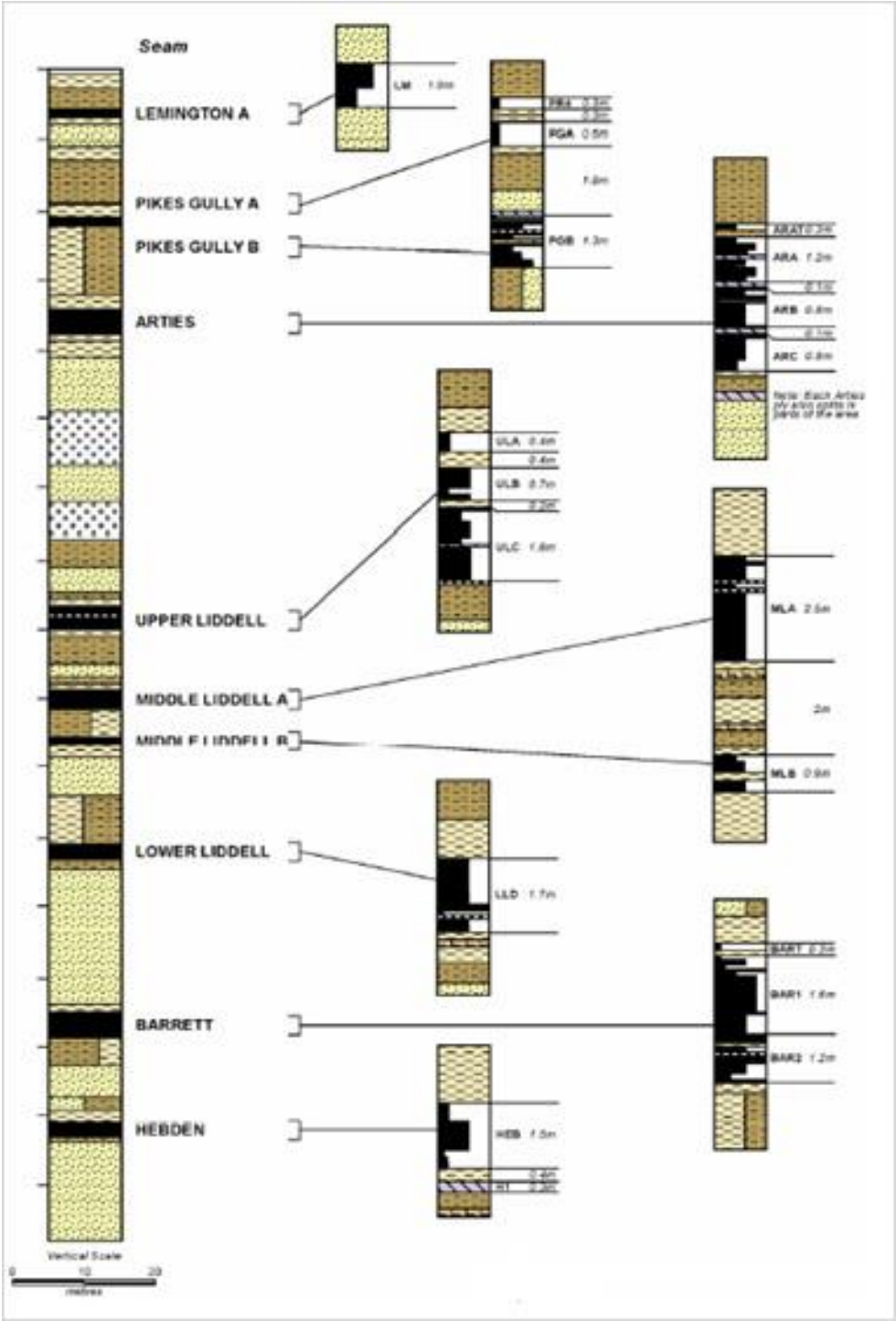

Figure 67 - Lithostratigraphic column of the case study 1 mine

Lambert et al. (2012) performed the accurate fracture fabric representation with non-persistent Discontinuities to model with SiroModel the block size distribution of the rock mass from which size related failure frequencies were obtained. The distribution of the volume of unstable blocks (Type I) were so obtained. Using a typical profile of the slope, 2D rockfall analysis with CRSP was performed. Using a database of the rockfall events, the probability of reach and the energy frequencies for each block size were calculated and combined for the rockfall hazard zoning. Lambert et al. (2012) observed that large blocks or large energies do not represent the highest hazard at the toe of the highwall.

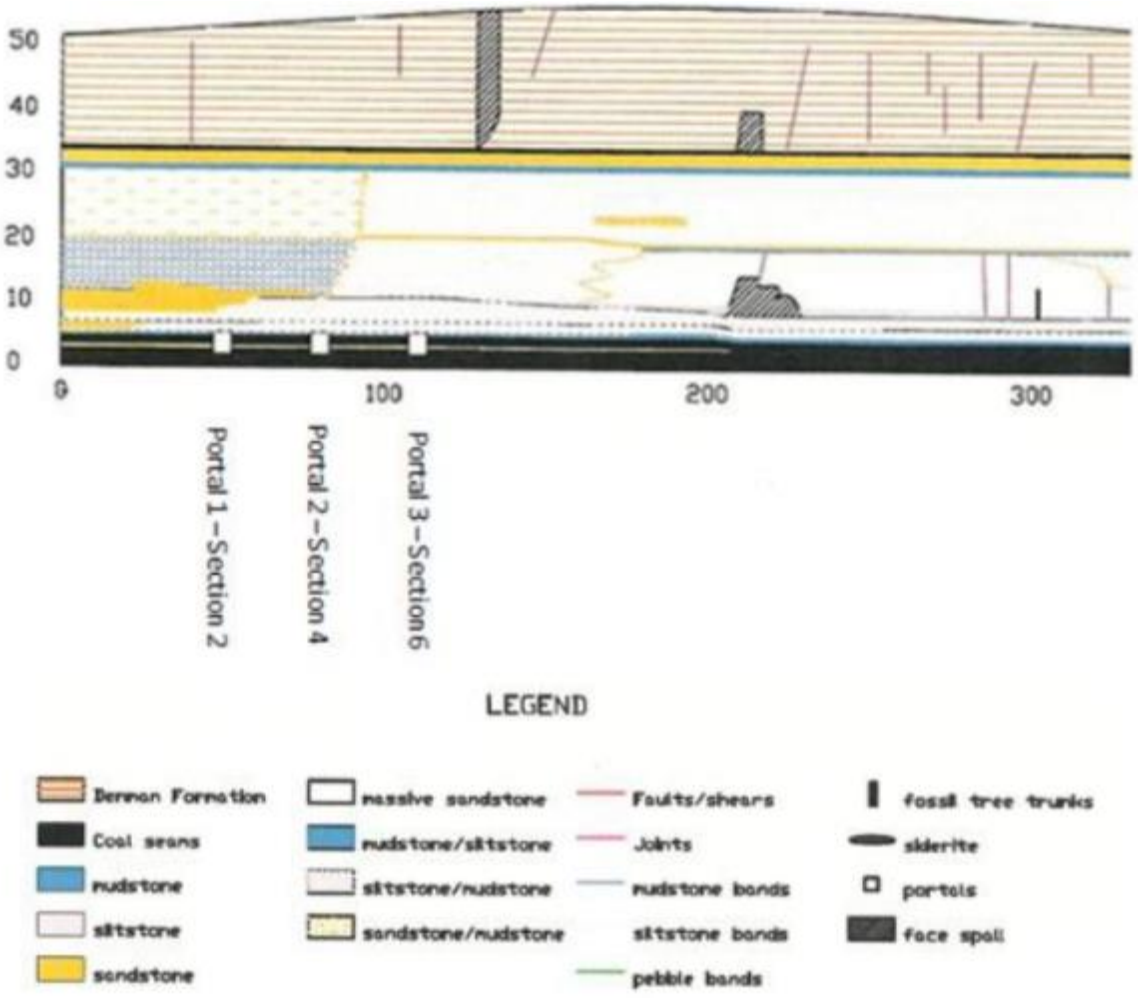

Figure 68 - Sketch of the lithological composition of the studied highwalls. From Casagrande (2012)

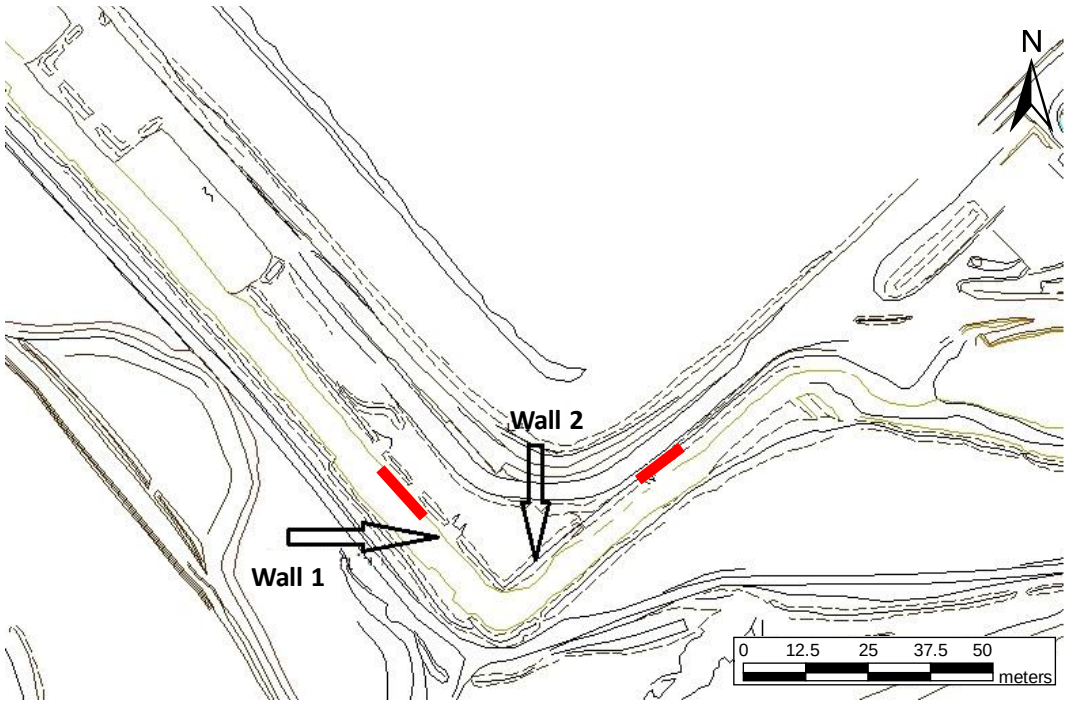

Figure 69 - Position of the two highwalls of case study 1 mine. The red stripes indicate the described sectors (Casagrande, 2012)

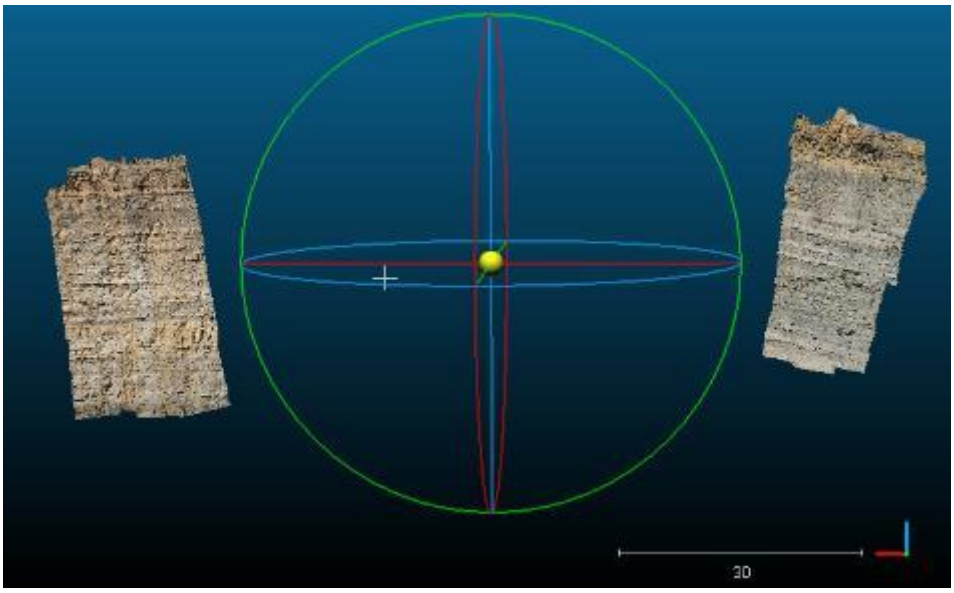

Figure 70 - Overview of the two highwalls of case study 1 mine

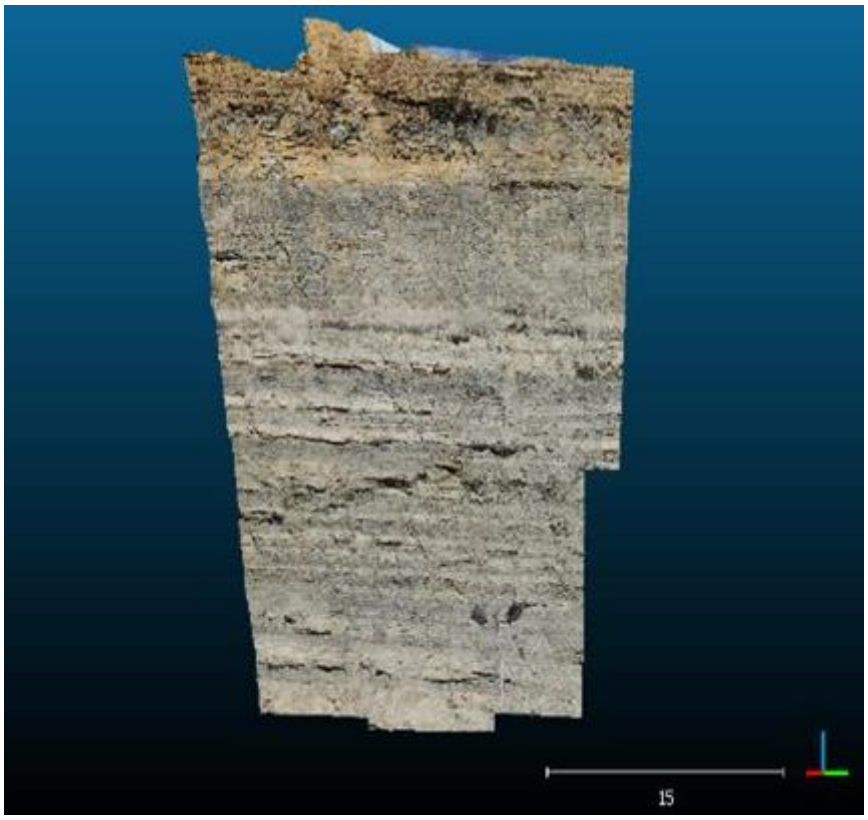

Figure 71 - 3D model carried out with the stereo pairs of the highwall nr 1

Figure 72 - 3D model carried out with the stereo pairs of the highwall nr 2

The photogrammetric survey of the highwalls of case study 1 mine has been carried out on 5 sections, 3 sections for highwall 1 and 2 sections for highwall 2. Each section is contiguous to the other sections of the highwall and so two 3D models, one for each slope, have been built. Each section is made by 2 stereo pairs, one for the top and one at the base; each section is so overall formed by 4 images. Highwall 1 survey is made by 3 sections, 6 stereo pairs and 12 stereo pairs (Figure 73, 74, 75, and 76), while highwall 2 survey is instead made by 2 sections, 4 stereo pairs and 8 stereo pairs (Figure 77, 78, and 79). The position of the tiles within the mosaic is described in Figure 80 for highwall 1 and in Figure 81 for highwall 2. Overall 10 stereo pairs (6 for highwall 1 and 4 for highwall 2) have been so used. Each stereo pair has been shot using a Canon mod. EOS 7D with lens with focal length of 50 mm. The parts of slope covered by the net, or by the scree, have been discarded because the surface of the 3D model is not representative of the surface of the rock mass.

These slopes are strongly affected by rockfall and a rockfall protection drapery system, clearly visible in Figure 73, 75, 76, and 80, has been installed (Giacomini et al., 2011; Thoeni et al., 2011b). The diameter scree at the base of the bench ranges from the order of the decimetre up to the order of the metre (Casagrande, 2012).

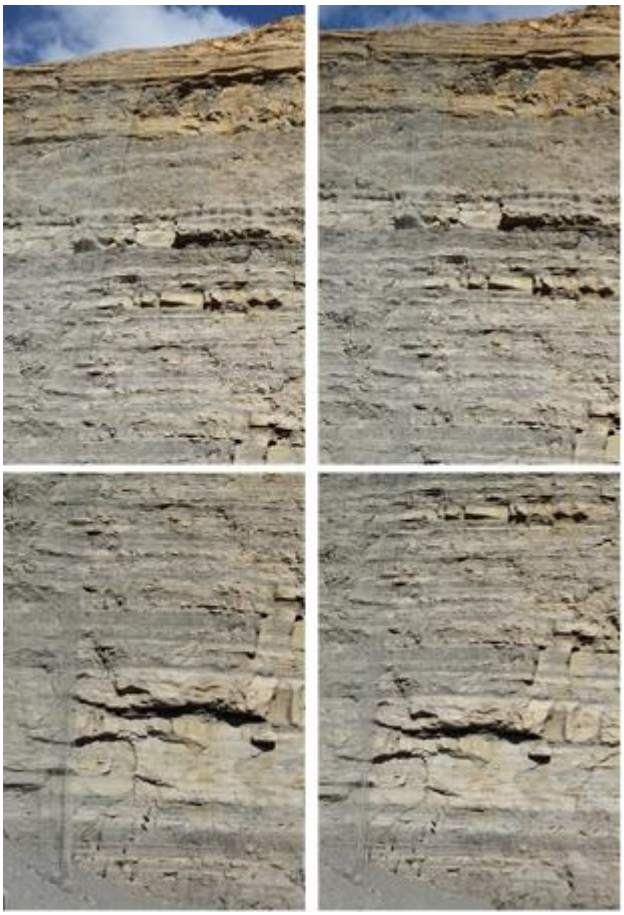

Figure 73 - Stereo pairs of section 1 of highwall 1

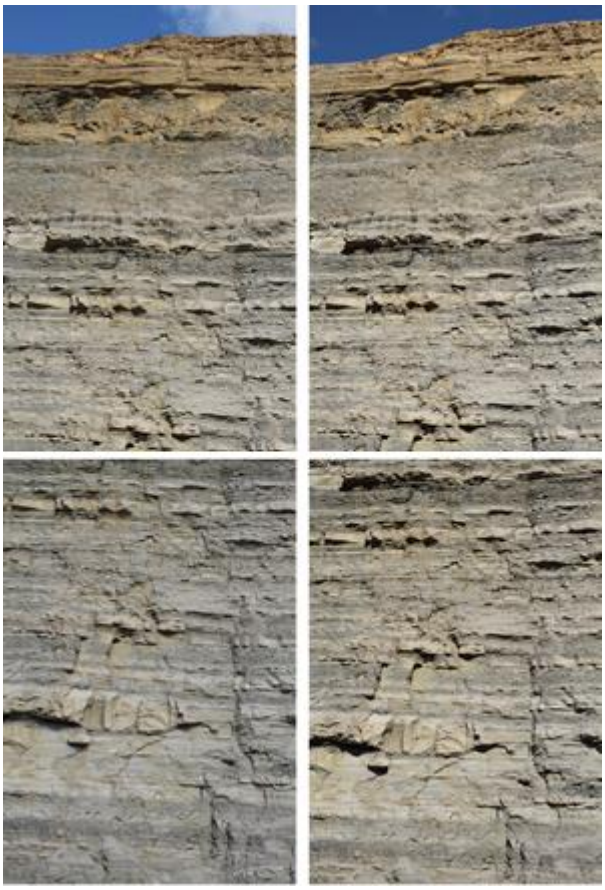

Figure 74 - Stereo pairs of section 2 of highwall 1

Figure 75 - Stereo pairs of section 3 of highwall 1

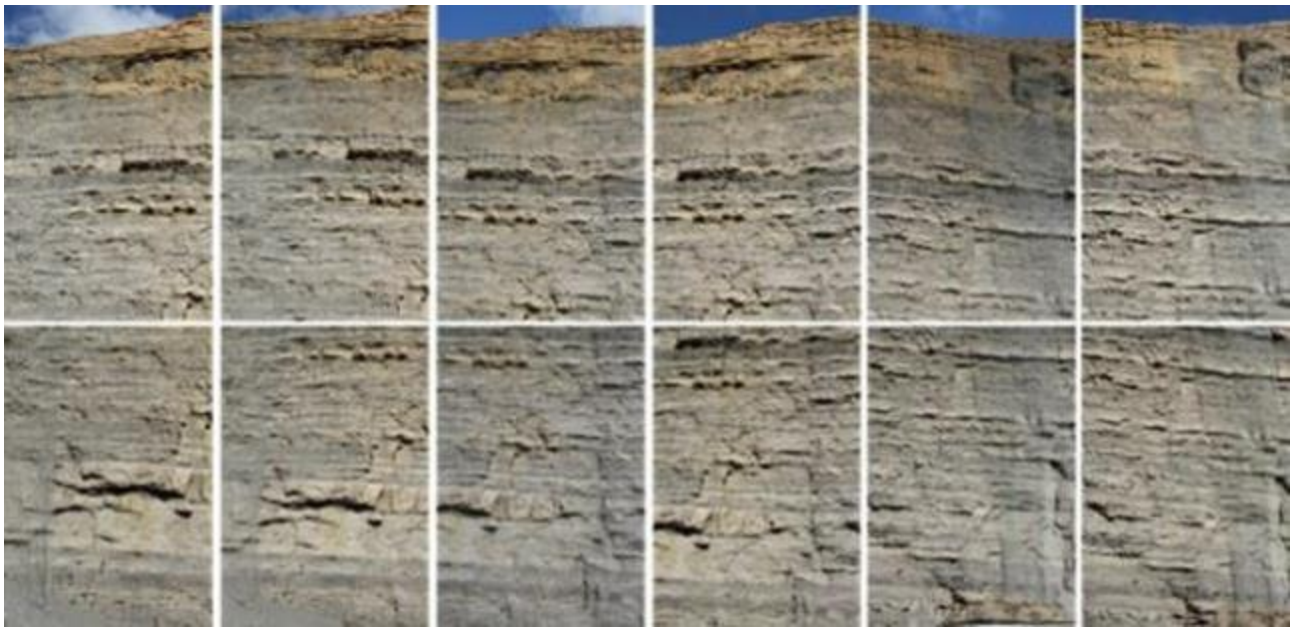

Figure 76 - Overview of the stereo pairs of highwall 1. At the base of the section are present greyish coal-rich shale layers, referred to Jerrys Plains Subgroup, while at the top outcrop the yellowish arenitic layers, referred to Denman Formation (Figure 67 and 68)

Figure 77 - Stereo pairs of section 1 of highwall 2

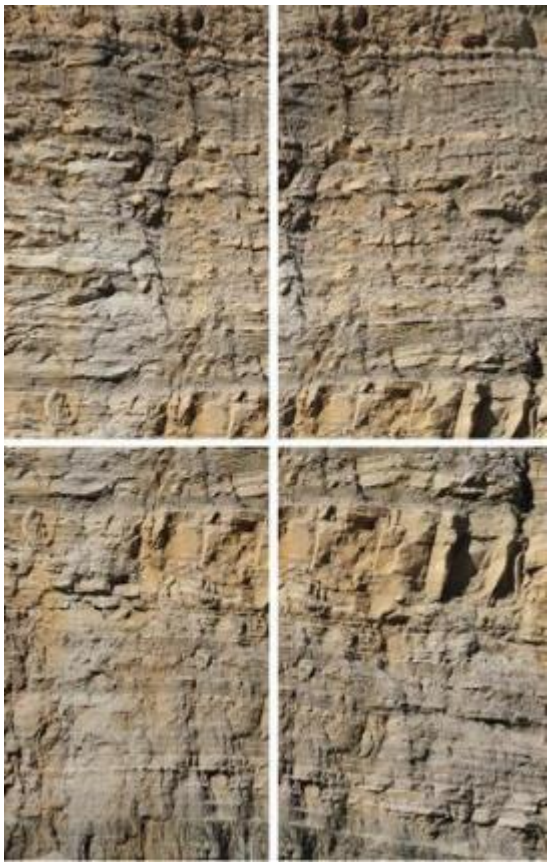

Figure 78 - Stereo pairs of section 2 of highwall 2

Figure 79 - Overview of stereo pairs of highwall 2

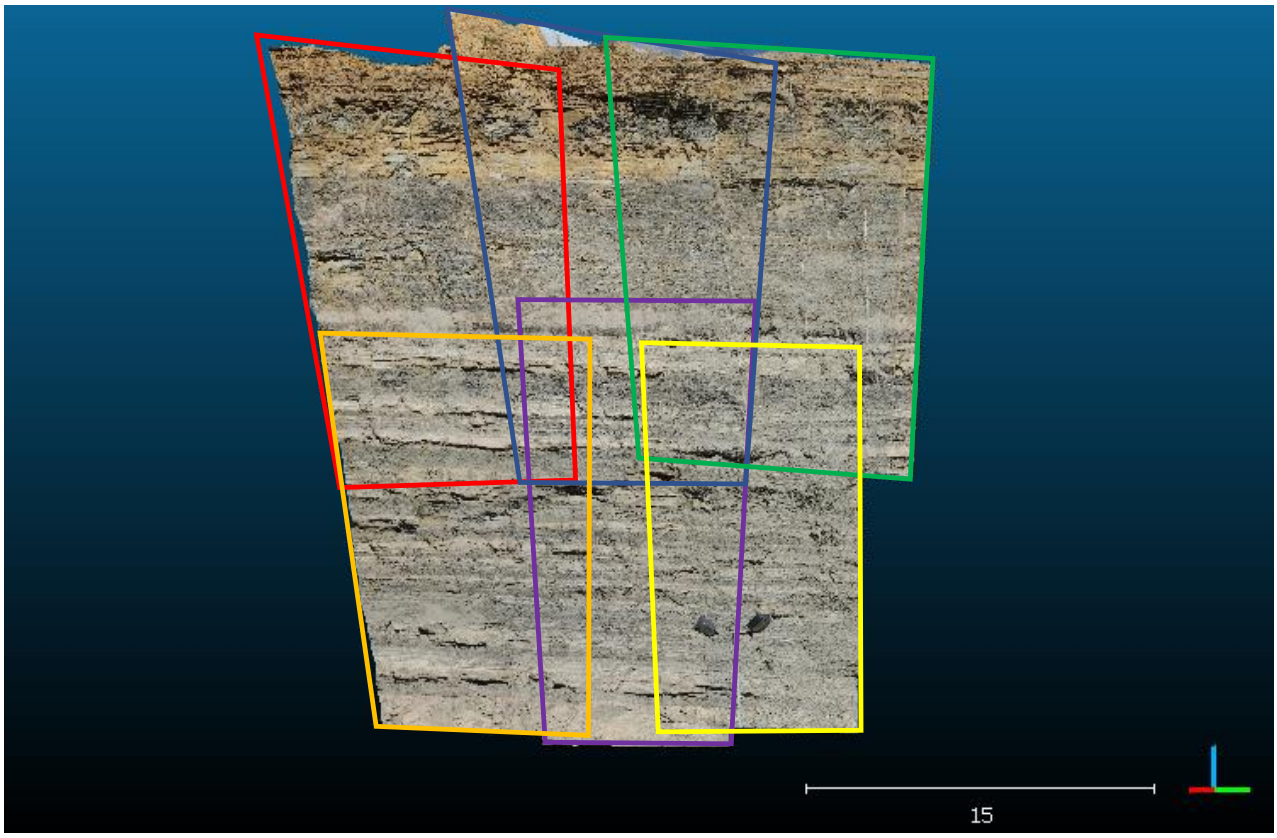

Figure 80 - Stereo pairs of highwall 1 of the case study 1 mine

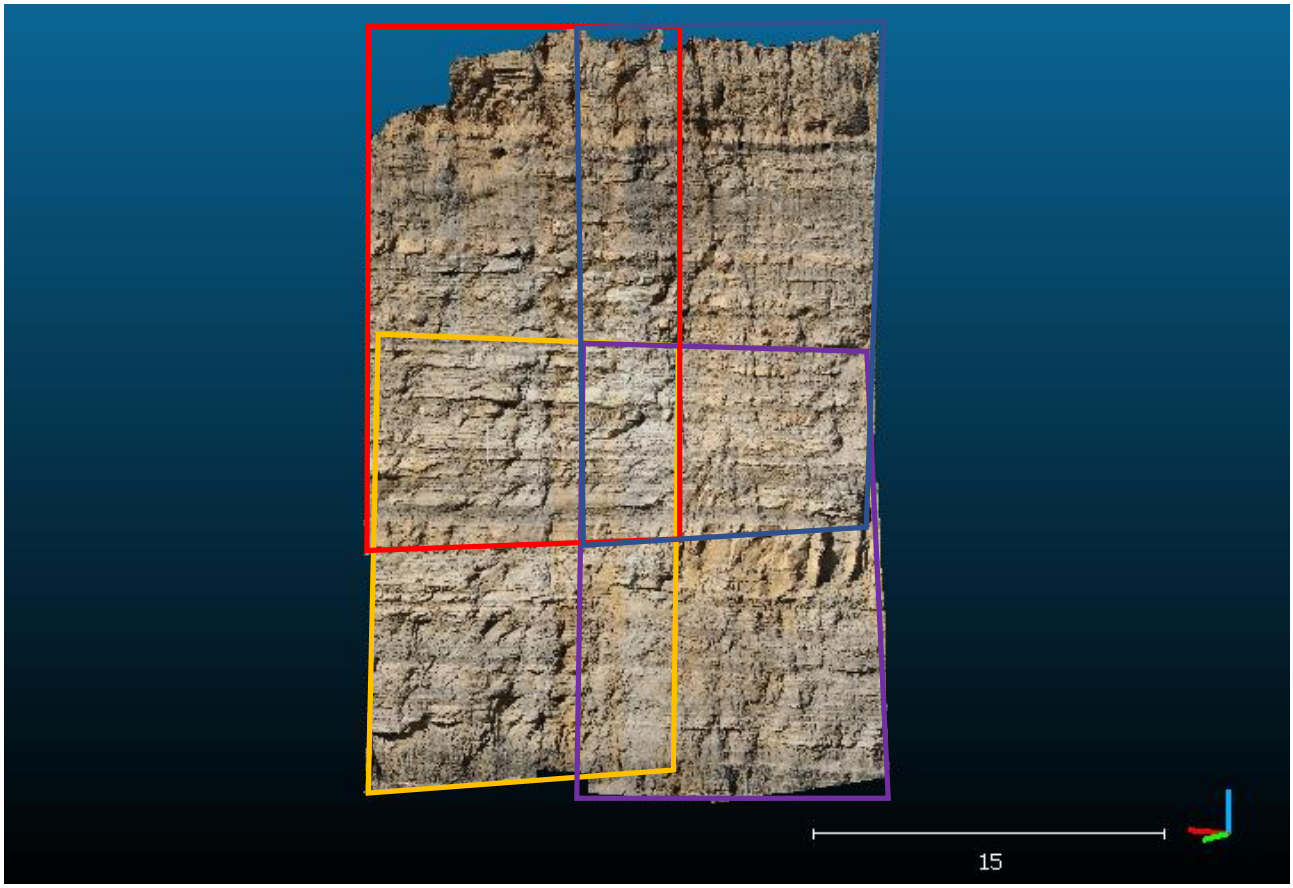

Figure 81 - Stereo pairs of highwall 2 of the case study 1 mine

5.2.2. Case study 2

Case study 2 mine is located north-western to Singleton (Figure 65) and is located within the Wittingham Coal Measures, in the Vane Subgroup (Figure 82), within an anticline. Along the culmination of the anticline the Vane Subgroup outcrops, while on the flank the Denman Formation and Jerrys Plains Subgroup, more recent in age (Figure 82). The anticline is a ramp-anticline and is bordered on the eastern side by an inferred thrust fault with an East-West direction, the hanging wall of which is the block on the western side. The Permian beds are locally covered by Quaternary deposits. The mine is located into the Foybrook Formation, the stratigraphic column of which is shown in Figure 83.

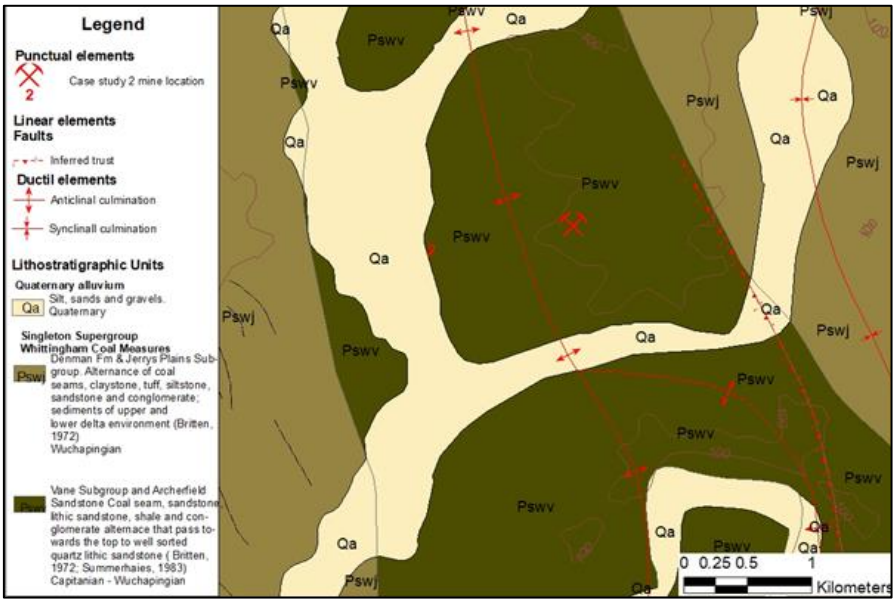

Figure 82 - Geological map of the area of case study 2 mine. Modified from Rasmus et al. (1969)

The studied slope is a section of highwall 73 m long, 26 m high (Figure 84), with on average α_{slope} = 74° and β_{inters} = 134°. Within the wall, a metric coal level is present. From the bottom to the top, the following units have been observed:

- 7.5 m of greyish thinly layered pelite and arenite;
- 8 m of greyish thinning-layered shale, with thin level rich in organic material;
- 2 m of a a continuous coal level;
- 4.5 m of greyish pelite;
- 3.5 m of massive arenite.

Differently from the 1st site, no previous analyses were available for case study 2. It was selected in order to highlights the key information related to rockfall hazard from remotely acquired data only.

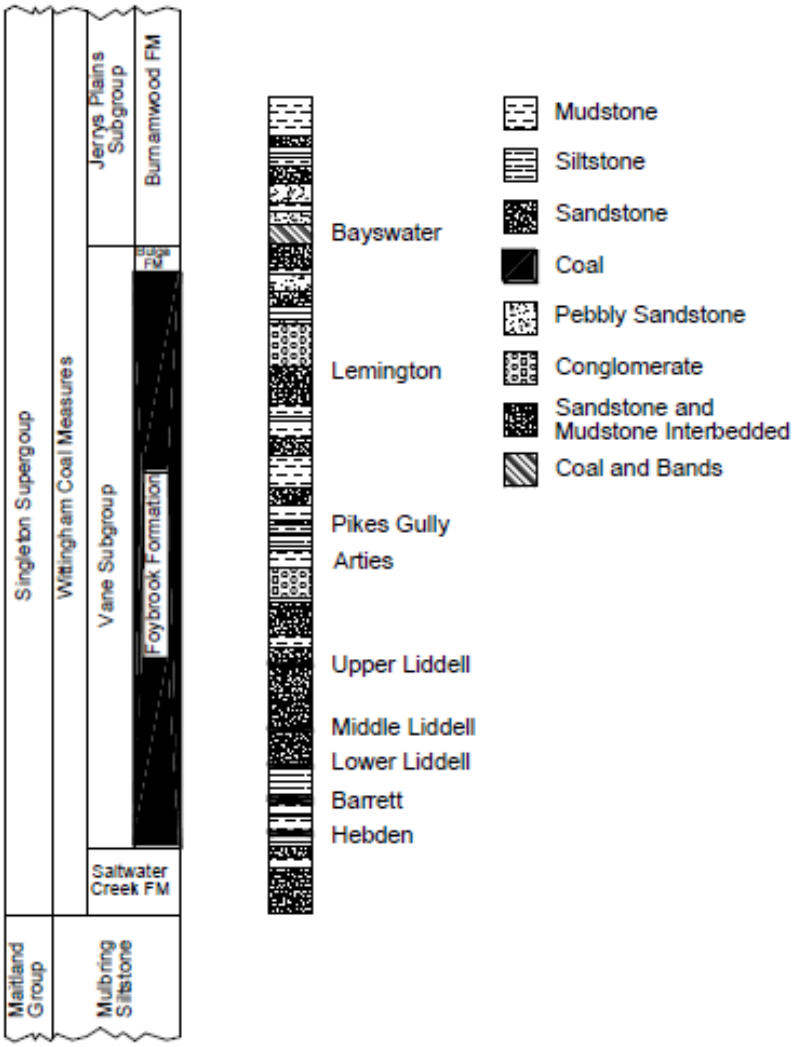

Figure 83 - Lithostratigraphic column of case study 2 mine

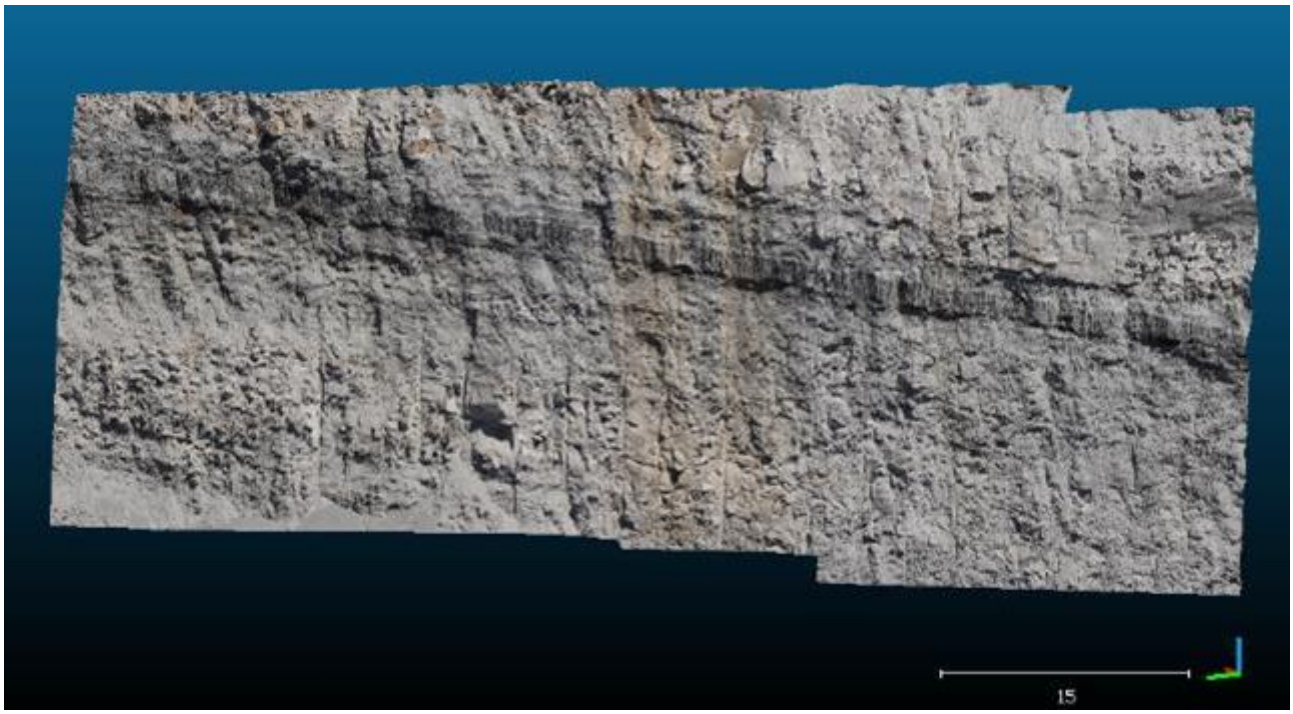

Figure 84 - The studied highwall of case study 2 mine

The 3D model of case study 2 highwall has been elaborated from 4 stereo pairs, the position of which is described in Figure 85, and georeferenced thanks to the knowledge of the coordinates of 4 camera positions and of 10 reference points (Figure 86). From each stereo pair a 3D model of the slope describing a section of the bench (Figure 87) has been built; a Canon camera model EOS 7D with lens with focal length of 28 mm has been used. Stereo pair nr 1 has been then discarded because the stereomodel showed local distortions on the left side, while the right side was already covered by the stereo pair nr 2, the image definition of which is higher. Finally, the areas covered by the scree have been retailed. The scree and the size of the blocks size at the base of the bench indicate that this slope is affected by rockfall.

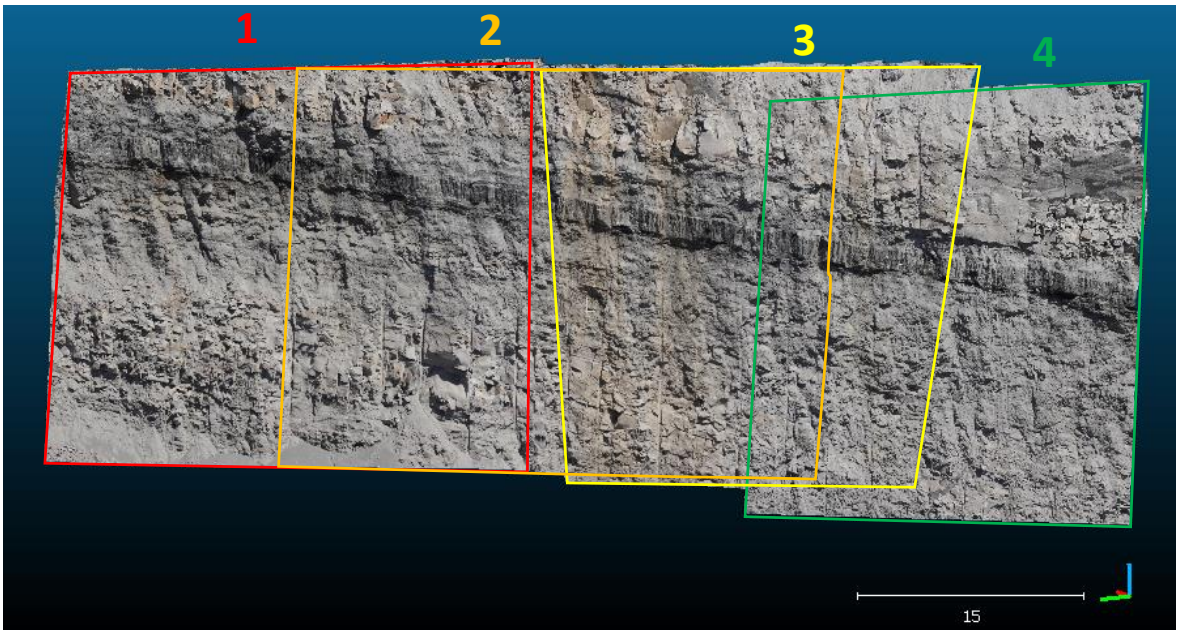

Figure 85 - Stereo pairs of the case study 2 mine highwall

Figure 86 - Position of the 10 reference points used to orient the stereomodel

Figure 87 - Images of case study 2 highwall. The numbers indicate the order of the stereo pairs of Figure 86, from left to right

6. Case study 1 results

6.1. Geostructural analysis

A total number of 3 sets have been recognized on case study 1 mine. The sets of discontinuity have been recognized using the automatic sets extraction tool of Dips and representing the poles with stereoplots with equal area projection, because more suitable than equal angle projection to recognise the sets of discontinuities (Rocscience, 2018). 2 sets (1m and 2m) are the most populated and have been clearly identified with every code, while 3m set is less evident. Indeed, the concentration of the poles of the discontinuities show locally higher values outside the areas of the sets of discontinuities; these concentrations have been observed on the stereoplots of the discontinuities extracted with SiroJoint and with DiAna; in particular, an area with concentrated poles has been observed on the stereoplot of the discontinuities extracted with SiroJoint close to the 3m set, while a number of sub horizontal discontinuities has been extracted with DiAna. The stereoplots of the discontinuities extracted with SiroJoint, I-Site Studio, DiAna, and Facets are shown in

Figure 88, 89, 90, and 91. To make the comparison clearer, the set limits are the same for each stereoplot. In the following sections orientation data are summarized in a specific table for each set whenever a relevant number of poles fall within the set limits, regardless of their local concentration.

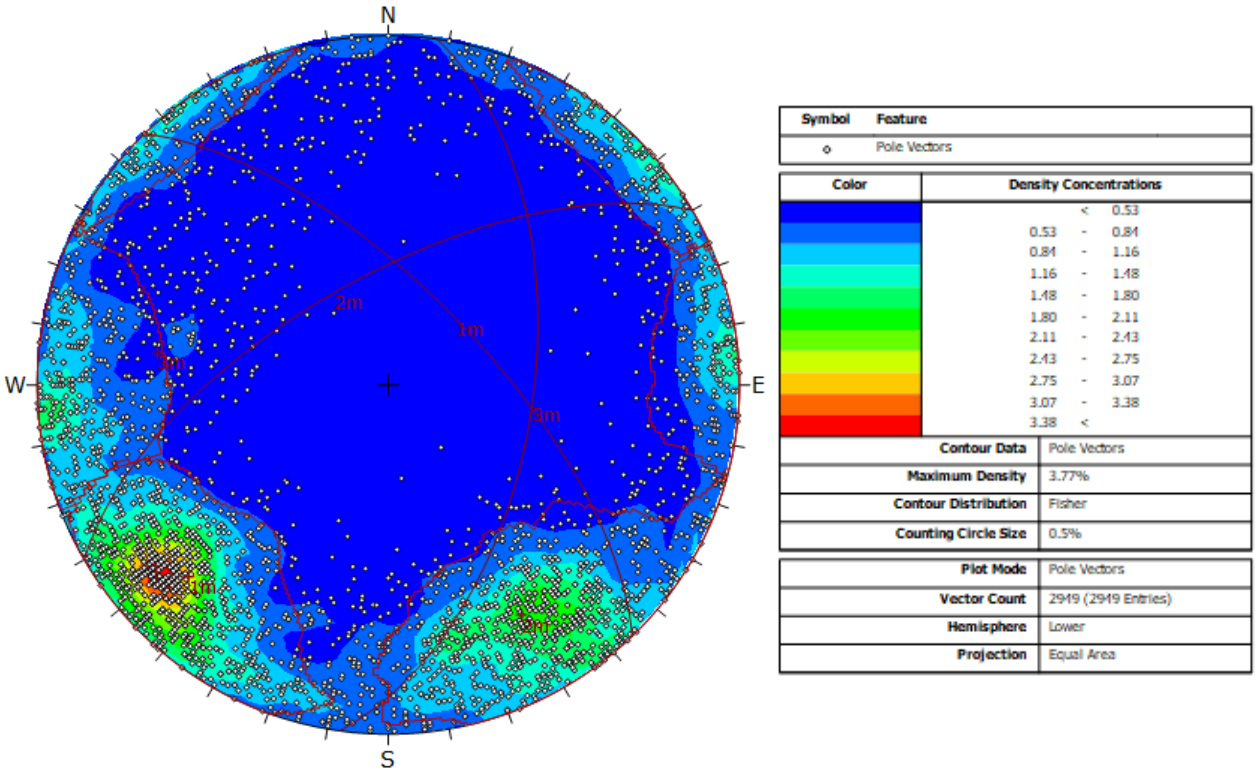

Figure 88 - Stereoplot with equal area of the discontinuities extracted with SiroJoint for highwall 1 of case study 1 mine

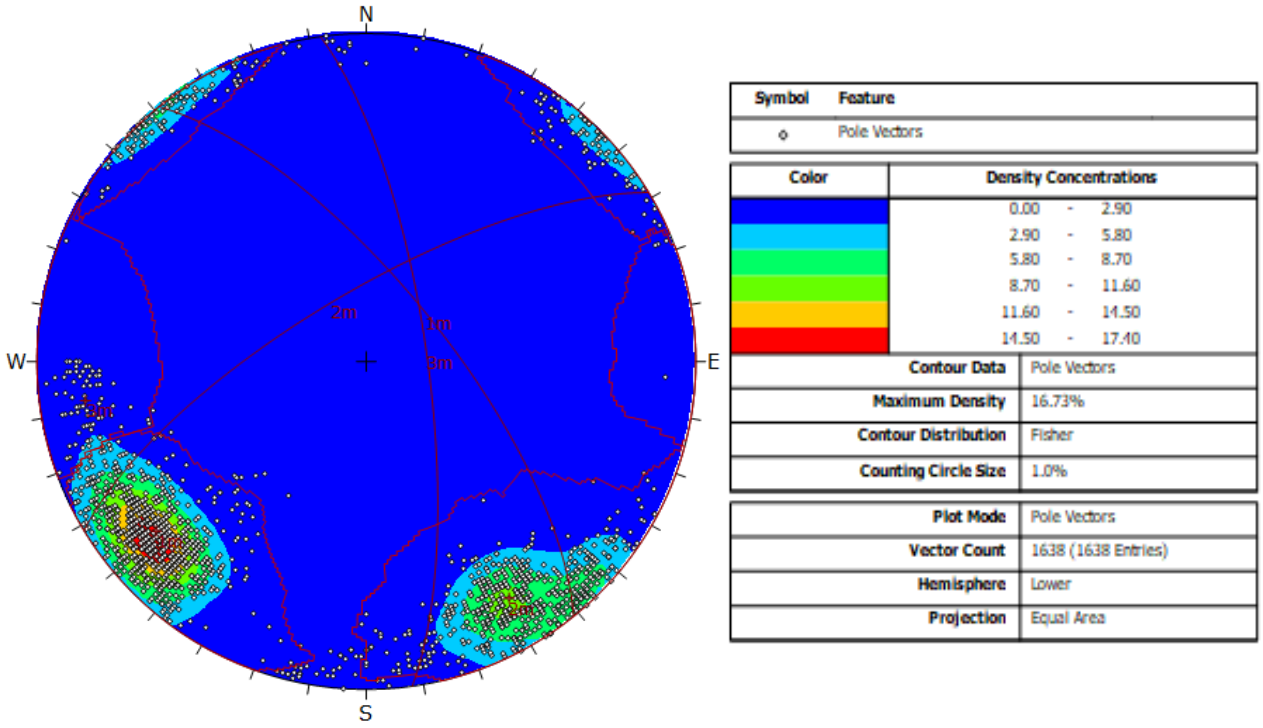

Figure 89 - Stereoplot with equal area of the discontinuities extracted with I-Site Studio for case study 1 mine

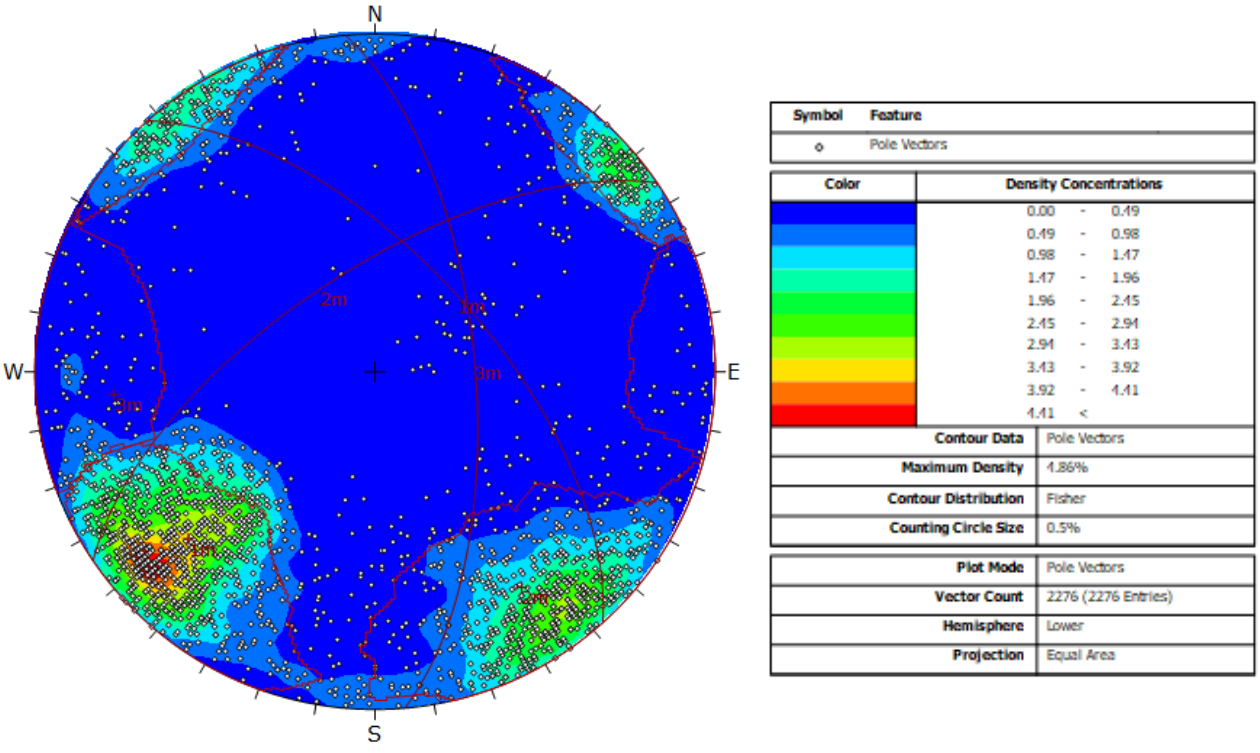

Figure 90 - Stereoplot with equal area of the discontinuities extracted with DiAna for case study 1 mine

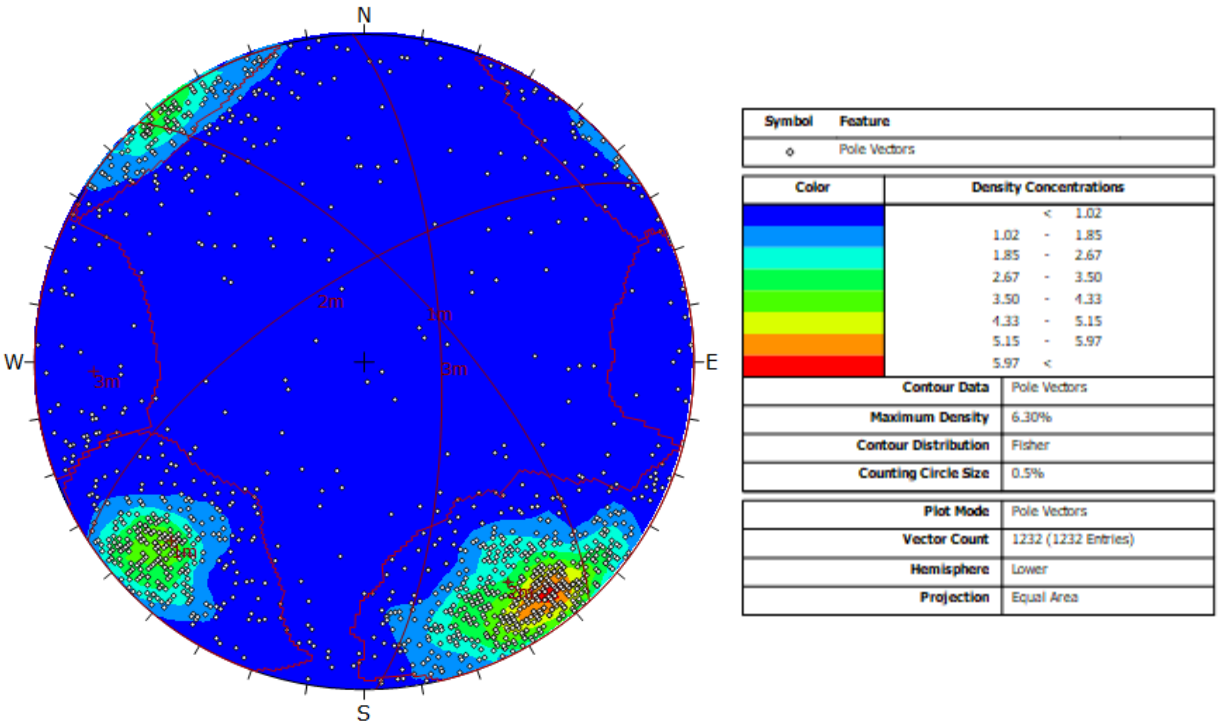

Figure 91 - Stereoplot with equal area of the discontinuities extracted with Facets for case study 1 mine

6.1.1. Geostructural analysis of highwall 1

- SiroJoint

A total of 1382 discontinuities (911 planes and 471 traces) have been detected with SiroJoint (Figure 92 and Table 3). To avoid the blurring of the other sets, the bedding planes were intentionally not drawn in this phase, as its structural setting is very easy to be detected and can be accounted for at a later time.

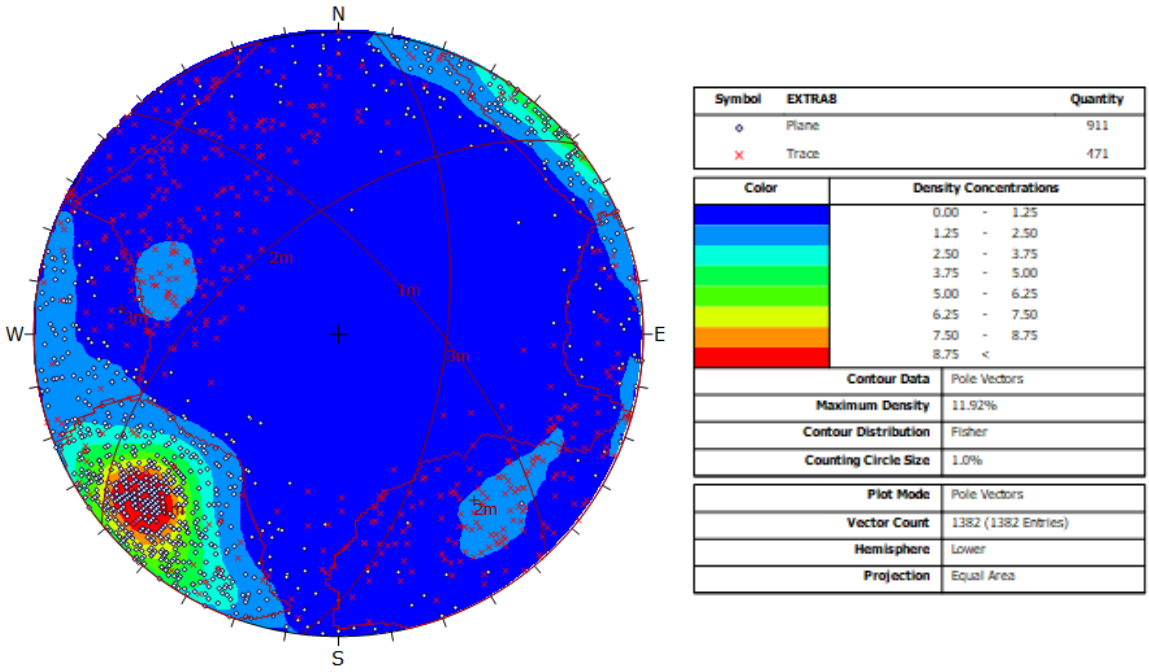

Figure 92 - Stereoplot with equal area of the discontinuities extracted with SiroJoint for highwall 1 of case study 1 mine. 4 sets of planes have been recognised

The most populated set is 1m set, with 693 discontinuities; 2m and 3m sets of discontinuities are well represented too, with 167 and 197 discontinuities respectively. 325 discontinuities have not been assigned to any set; anyway, the value of the concentration of the poles of discontinuities outside the sets of discontinuities locally shows values included into the 1.25-2.50 poles/square degree. The outcropping of planes despite of traces in each set is ruled by the geometrical relation between the orientation of the slope and the orientation of the discontinuities: 1m set of discontinuities, the orientation of which (46°/75°) is subparallel to the slope one (50°/70°), is so mostly represented by planes, while 2m and 3m sets of discontinuities, the orientation of which (289°/71° and 92°/79°) is normal to the slope one, are mostly constituted by traces. The maximum L of the discontinuities ranges from 1.81 m of 3m set to 6.60 of 1m set of discontinuities. Without considering the discontinuities related to the bedding, the maximum value of L is thus related to the set of discontinuities subparallel to the slope orientation (1m).

Table 3 - α, σ_α, β, σ_β, L and σ_L of the sets of discontinuities extracted with SiroJoint for highwall 1 of case study 1 mine

Set	α (°)	σ_α	β (°)	σ_β	L (m)	σ_L	Nr discontinuities
1m	46	11.47	75	10.22	6.60	0.50	693
2m	324	23.90	71	11.75	1.81	2.20	167
3m	92	15.12	79	8.40	1.98	2.27	197

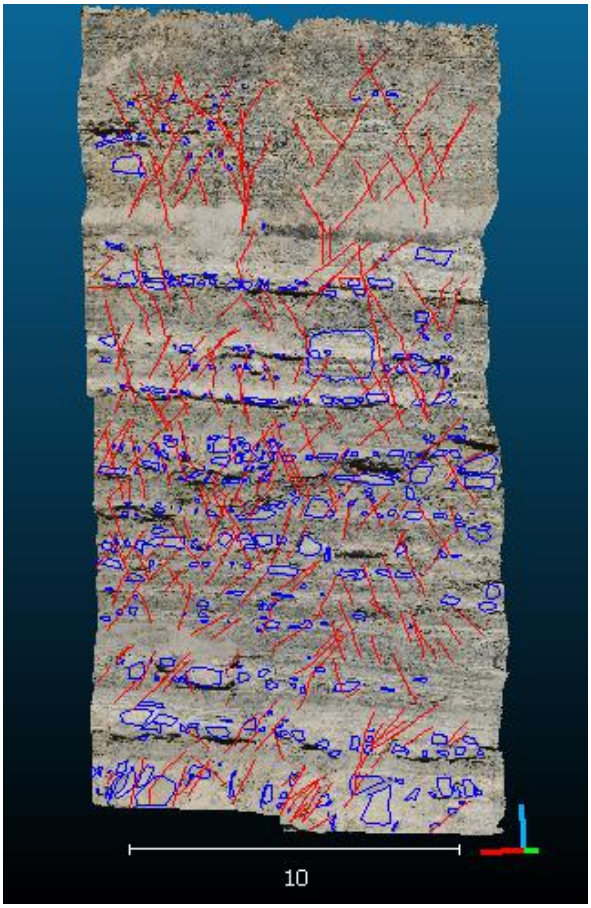

Figure 93 - Location of the planes (blue) and of the traces (red) extracted by SiroJoint on highwall 1. Traces are coloured red, planes blue

- I-Site Studio

Overall 926 planes have been instead extracted by I-Site Studio (Figure 94 and Table 4). These planes are related to 2 sets of discontinuities only; 1m and 3m sets of discontinuities include 789 and 105 planes respectively, while 32 planes have not been assigned to any set. No discontinuity has been recognised in the area of the stereoplot in correspondence of the traces extracted with SiroJoint. 2m set of discontinuities has been recognised with SiroJoint but not by I-Site Studio, although partly constituted by planes; we argue that the difficulties to detect this set could be related to the lower extent of planes because of the orientation normal to the slope. σ_β and σ_α range 7.91 to 16.23 (Table 4); these values are comparable to the values of σ_β and σ_α for 1m and 3m sets of discontinuities extracted by SiroJoint. Nevertheless, the observation that 32/926 planes only have not been assigned to any set of discontinuities, shows that the output measurements are so less scattered than the measurements carried out by SiroJoint. This statement is a consequence of the sampling mode of the code, that implies the indication of the angular range (besides α, β, minimum number of points, and maximum standard deviation of the planes) between the detected plane and other planes extracted by the point cloud. The minor L in comparison to the results of the discontinuities extraction by SiroJoint, depends on the fact planes only, the apparent L of which is clearly minor than the apparent L of the traces. The minor values of L of the discontinuities extracted by I-Site Studio in comparison to the discontinuities extracted by SiroJoint, is related to the absence of traces in the dataset extracted by I-Site Studio.

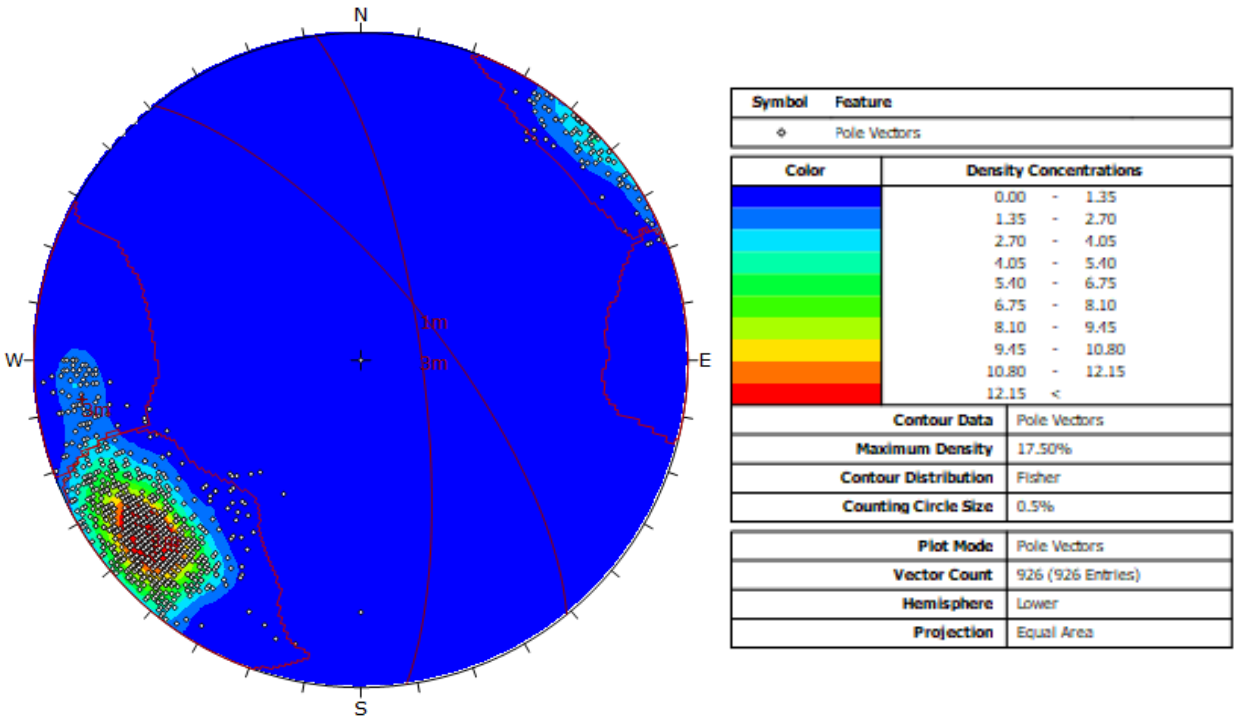

Figure 94 - Stereoplot with equal area of the discontinuities extracted with I-Site Studio for highwall 1 of case study 1 mine. 2 sets of planes have been recognised

Table 4 - α, σ_α, β, σ_β, L and σ_L of the sets of discontinuities extracted with I-Site Studio for highwall 1 of case study 1 mine

Set	α (°)	σ_α	β (°)	σ_β	L (m)	σ_L	Nr discontinuities
1m	51	7.91	75	8.53	4.50	0.55	789
3m	81	12.52	75	16.23	1.33	0.31	105

- DiAna

The overlapping areas between two contiguous stereo pairs have been retailed to avoid the doubling of the mesh and differential vertices density. Although many factors concur to the vertex concentration of a point cloud carried out by photogrammetric survey, the point clouds of highwall 1 of case study 1 mine do not show great difference of vertices average concentration, once removed the overlapping areas, because sunlight condition, that greatly affects the quality of the point cloud carried out by photogrammetric survey, is similar for each stereo pair. The point clouds have been resampled with RiScanPro software in order to obtain an ordered point cloud. A box searching cube box with 7 points long side, with a minimum of 30 points (for areas close to the mesh edge) has been chosen to extract the planes for the ordered point cloud. Standard deviation of the point cloud using the previously described searching cube is a parameter sensitive to the point cloud density; nevertheless, the homogeneity of the density of the 6 point clouds of the stereo pairs has allowed to use a single range of standard deviation as discriminant parameter for discontinuity extraction on the whole mesh (Figure 95). A comparative preliminary analysis of the standard deviation of the point clouds carried out using a searching box with the same parameters and a standard deviation range of 0-0.022 has been carried out on the whole surface.

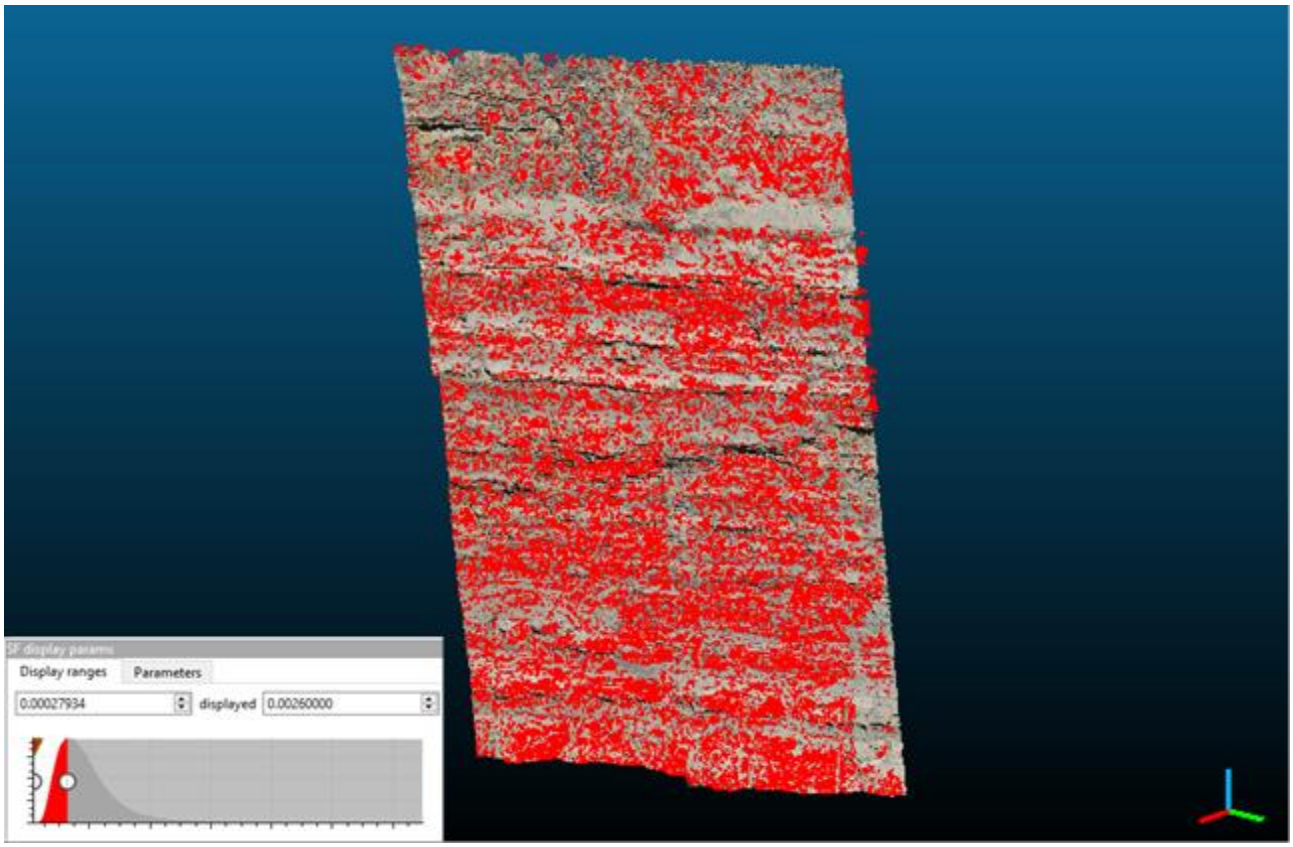

Figure 95 - Overview of highwall 1 of case study 1 mine: the red areas indicate the points with standard deviation of the distance between the subsampled point clouds using a 3 -points range and their regression plane with values <0.022.

This observation has allowed to understand that an only geostructural analysis performed by DiAna has been sufficient to characterise the whole surface in consequence of the similar accuracy of the point clouds of the 6 stereo pairs. Geostructural analysis carried out by DiAna has allowed the extraction of 1316 planes, subdivided into 2 sets of discontinuities (Figure 97 and Table 5). 1m and 3m sets of discontinuities correspond to the same set of discontinuities extracted by SiroJoint. A cluster of sub horizontal discontinuities corresponds instead to the bedding; Figure 96, in fact, clearly shows these discontinuities (red colour), that are located along the layers and that 1m (blue colour) and 3m (green colour) sets are related to two sets of planes present on the slope. Anyway, the poles concentration of this cluster is not sufficiently significative to represent it as a sure set. 1024 and 27 discontinuities are related to 1m and 3m sets of discontinuities σ_α and σ_β of 1m and 3m sets range 4.53-14.91.

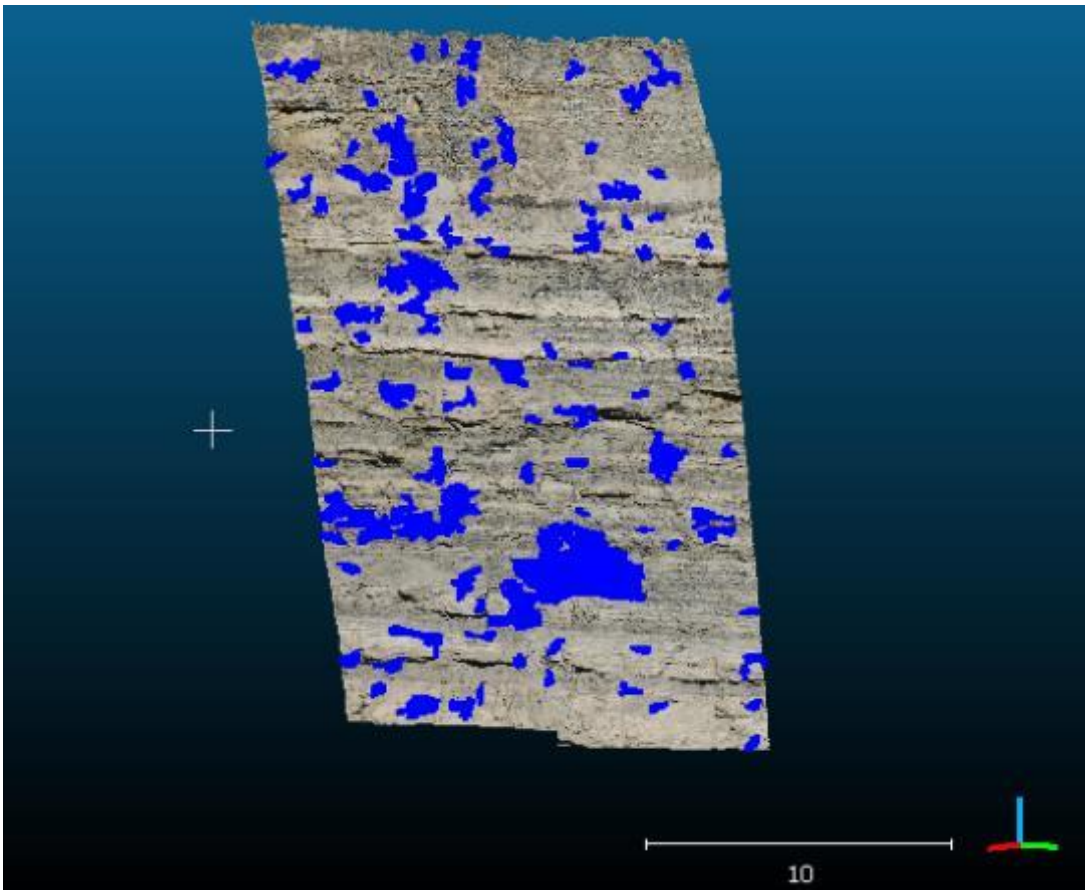

Figure 96 - Positions of the discontinuities extracted by DiAna on highwall 1

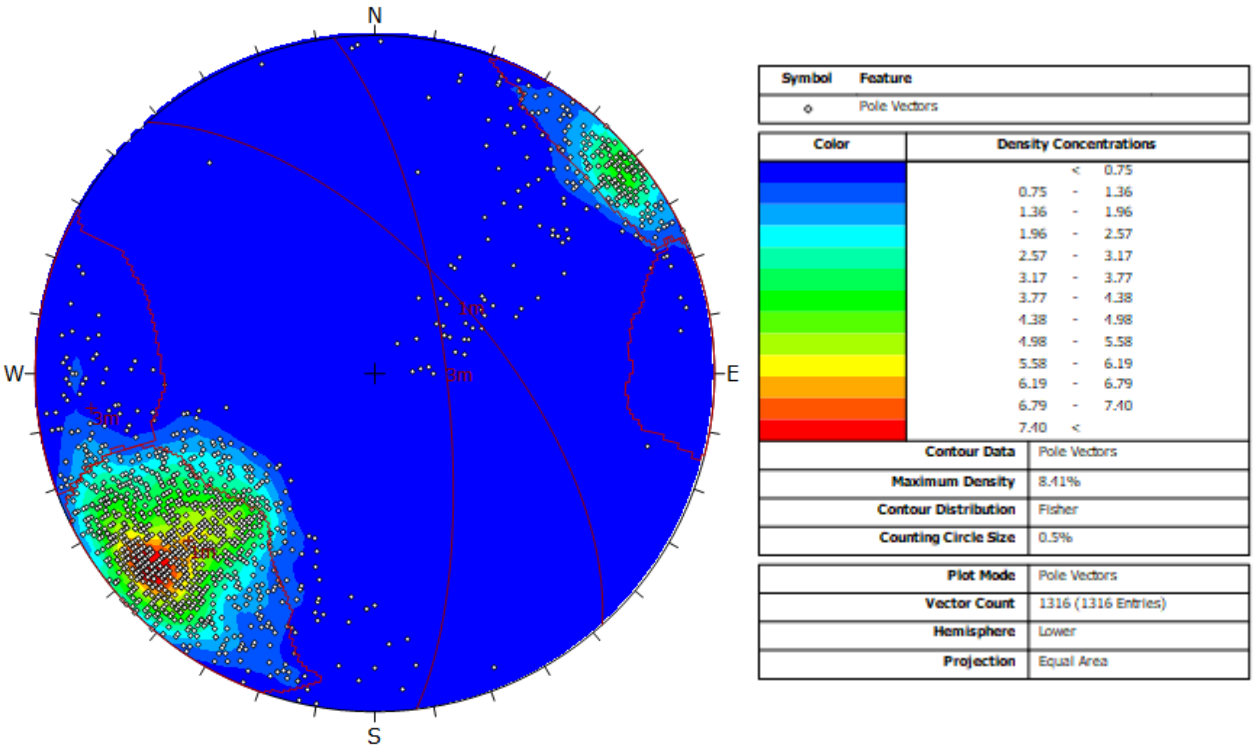

Figure 97 - Stereoplot with equal area of the discontinuities extracted with DiAna for highwall 1 of case study 1 mine. 2 sets of planes have been recognised

Table 5 - α, σ_α, β, σ_β, L and σ_L of the sets of discontinuities extracted with DiAna for highwall 1 of case study 1 mine

Set	α	σ_α	β	σ_β	L	σ_L	Nr discontinuities
1m	49	10.60	69	13.26	6.72	0.52	1024
3m	89	6.53	77	4.53	1.27	0.21	27

- Facets code

Overall 476 planes have been extracted by Facets plugin. Because of the small dimension of the outcropping planes a low number of points (88) has been set as criterium for plane extraction, despite the point cloud concentration is about 8800 points /m^2. The minimum number of points has been chosen by the minimum surface of the planes from the 3D model (0.01 m^2 about). Thus, the observed planes are at least constituted by 88 points about. This number is greater than the number of points chosen to extract discontinuities by DiAna because DiAna requires a resample of the point cloud, that reduces the point cloud concentration. Maximum distance between the points and the regression surface has been set to 0.2 m and maximum edge length to 0.16 m. The planes extraction has been carried out by an octree level = 8. Some of the extracted planes have been judged as not realistic, because too large and approximate, or because too small and have been so filtered (Figure 98). Planes with surface < 0.01 m^2 or > 4 m^2, or with a retro-projection error (RMS) > 0.1 have been so discharged. A total number of 401 planes has been used for the geostructural characterisation of the rock mass (Figure 99 and Table 6).

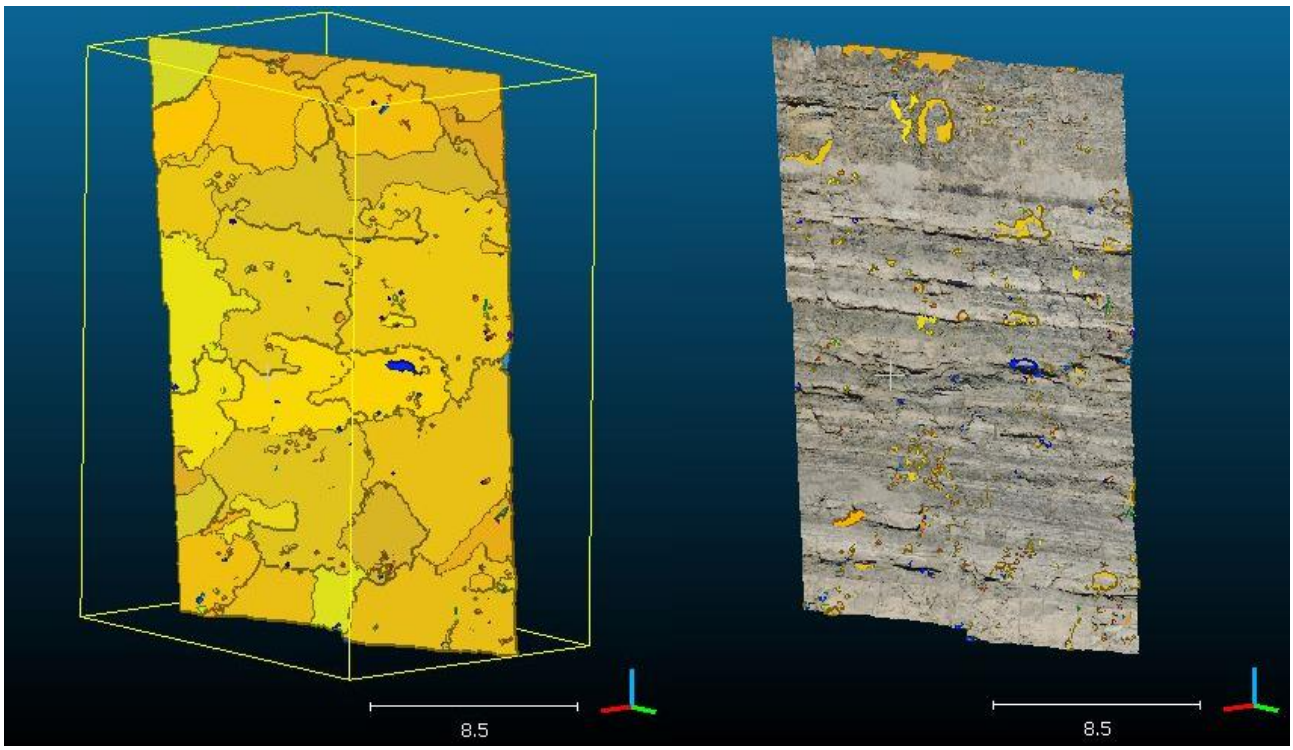

Figure 98 - Planes extracted by Facets plug in of CloudCompare. Left: before filtering by RMS and maximum surface; right: after filtering. Largest planes of not filtered surfaces are not representative of real discontinuities within the rock mass. The colour of the planes depends on the aspect; yellow planes are related to 1m set, blue planes to 3m set

2 sets of discontinuities have been recognised. These sets correspond to 1m and 3m sets of discontinuities extracted by the other used methods. Most of the planes (320/401) can be assigned to 1m set of discontinuities, while 25/401 are related to 3m set of discontinuities; 56/401 have not been assigned to any

set of discontinuities. Although no other evident cluster of poles can be recognised; the sub horizontal extracted discontinuities could be anyway related to the bedding surfaces.

σ_α αnd σ_β range from 0.51 to 8.66 (Table 6). L is not a direct output parameter of Facets, that anyway provides information about the length of the axis of the box including each plane; the diagonal of the box can be considered a good proxy of L; L of the planes is 4.26 and 1.06 for 1m and 3m sets of discontinuities, respectively, while the σ_L is 1.02 and 0.24. This difference can be explained thanks to the best outcropping of 1m planes, that increase L value standard deviation. 3m planes are usually smaller and more homogeneous as regarding the surface extension. All the discarded planes with surface > 4 m^2 are related to 1m set of discontinuities.

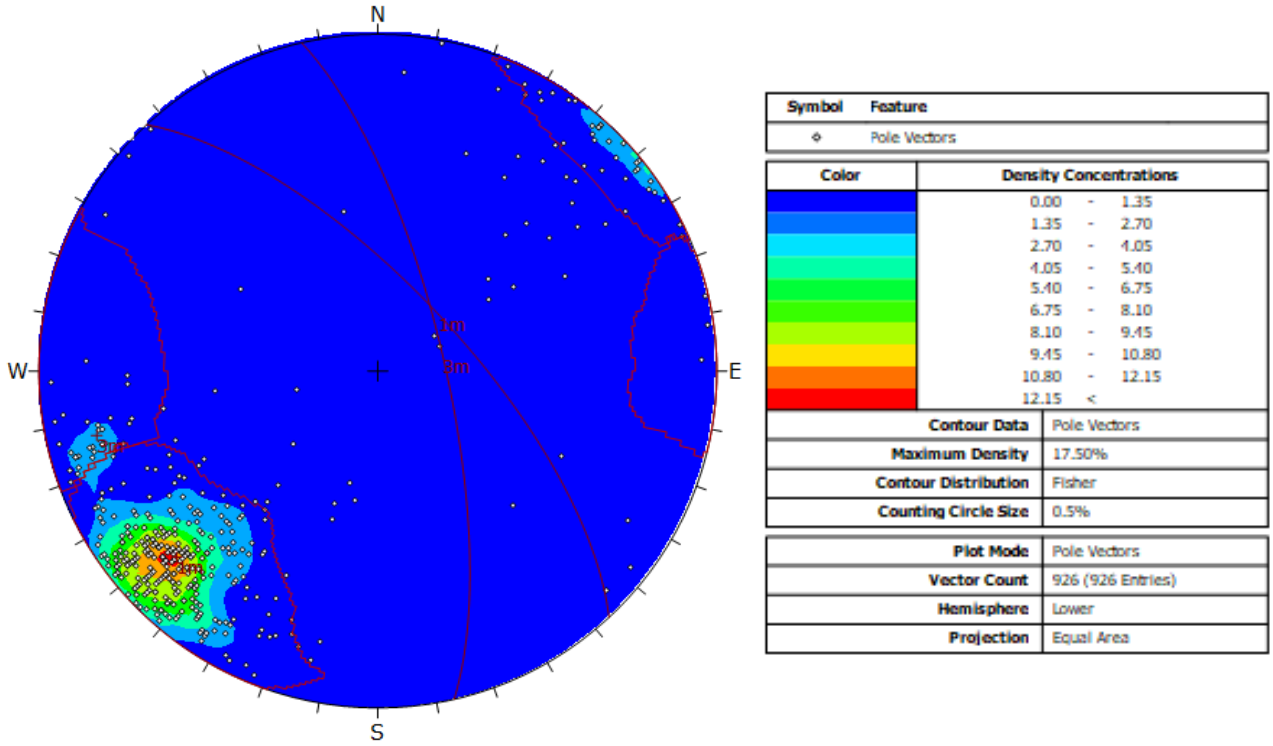

Figure 99 - Stereoplot with equal area of the discontinuities extracted with Facets plug-in of CloudCompare for highwall 1 of case study 1 mine. 2 sets of planes have been recognised

Table 6 - α, σ_α, β, σ_β, L and σ_L of the sets of discontinuities extracted with Facets plug-in of CloudCompare for highwall 1 of case study 1 mine

Set	α (°)	σ_α	β (°)	σ_β	L (m)	σ_L	Nr discontinuities
1m	47	7.54	77	8.66	4.26	0.90	320
3m	71	3.79	75	0.51	1.06	0.13	25

6.1.2. Geostructural analysis of highwall 2

- SiroJoint

1567 discontinuities (1054 planes and 513 traces) have been detected with SiroJoint. The discontinuities of the studied highwall have been split into 3 sets (Figure 100 and Table 7). The most populated set is 2m set (599/1567), the orientation of which is similar to the highwall one (331°/73° vs 320°/70°). 1m and 3m sets of discontinuities are well represented too, with 260/1567 and 268/1567 discontinuities respectively. 438 discontinuities have not been assigned to any set. As for the other highwall, the outcropping of planes despite of traces in each set is ruled by the geometrical relation between the slope orientation and the orientation of the set of discontinuities. Sets that are subparallel to the slope are mostly constituted by planes, while 1m and 3m sets of discontinuities are mostly constituted by traces. 3m set of discontinuities is so mostly represented by planes, while 1m and 3m sets of discontinuities, the orientation of which (53°/83° and 87°/86°) is normal to the slope one, are mostly constituted by traces.

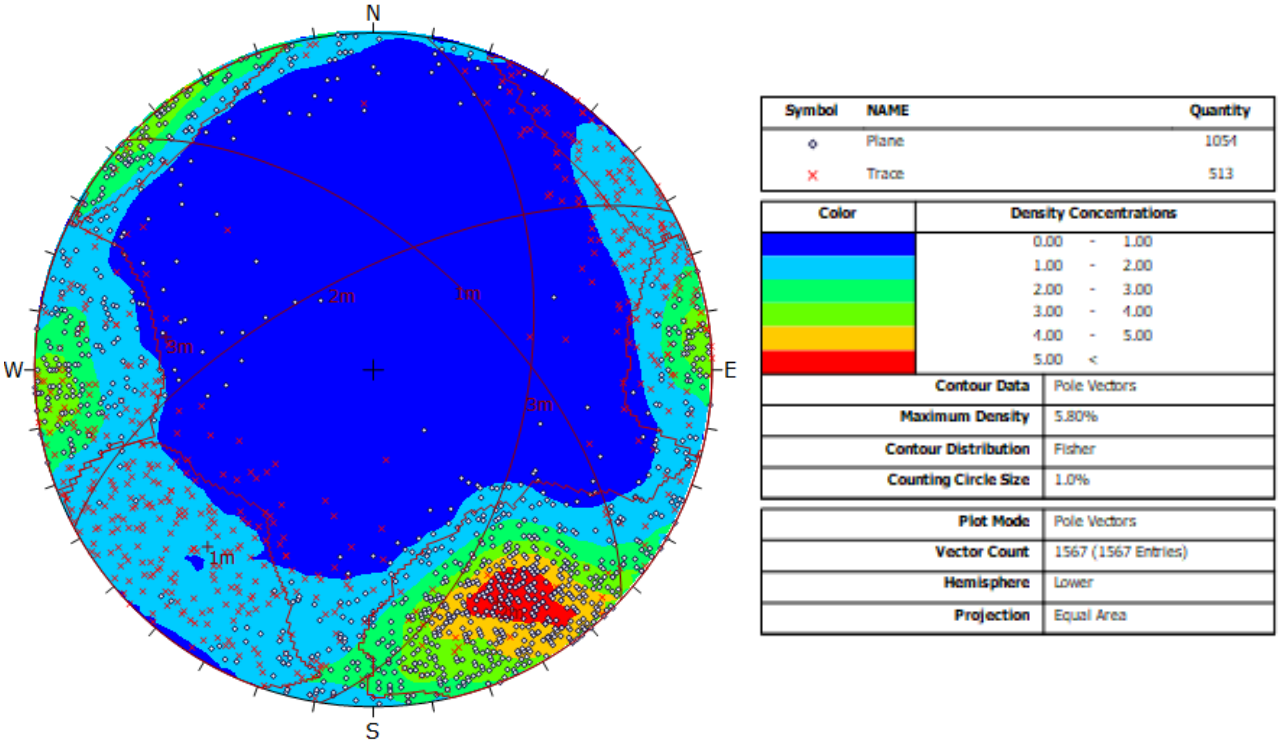

Figure 100 - Stereoplot with equal area of the discontinuities extracted with SiroJoint for highwall 2 of case study 1 mine. 3 sets of planes have been recognised

Table 7 - α, σ_α, β, σ_β, L and σ_L of the sets of discontinuities extracted with SiroJoint for highwall 2 of case study 1 mine

Set	α (°)	σ_α	β (°)	σ_β	L (m)	σ_L	Nr discontinuities
1m	53	12.52	83	11.46	6.45	0.97	260
2m	331	20.88	73	12.01	3.91	0.50	599
3m	87	8.26	86	8.32	5.79	0.99	268

- I-Site Studio

I-Site Studio has allowed to extract 713 planes on highwall 2 (Figure 101 and Table 8). Only one set of discontinuities has been recognised; overall 660/713 discontinuities are related to this set (2m), while the remnant 120 discontinuities have not been assigned to any set (Figure 101 and Table 8). The only recognised set of discontinuities is subparallel to the slope. σ_α αnd σ_β are 9.63 and 8.09, respectively (Table 8); these values are comparable to the values of standard deviation of the planes of highwall 1 extracted by I-Site Studio. Nevertheless, the observation that 53/713 planes only have not been assigned to any set of discontinuities, shows that the output measurements are so less scattered than the measurements carried out by other codes. As indicated for the other highwall, this statement is a consequence of the sampling mode of the code. Also in this case, L of the discontinuities extracted by SiroJoint is greater than L of the discontinuities extracted by I-Site Studio. The minor value of L in comparison to the results of the discontinuities extraction by SiroJoint, depends on the fact that I-Site Studio geostructural characterisation is based on planes only and not on traces, the L of which is greater.

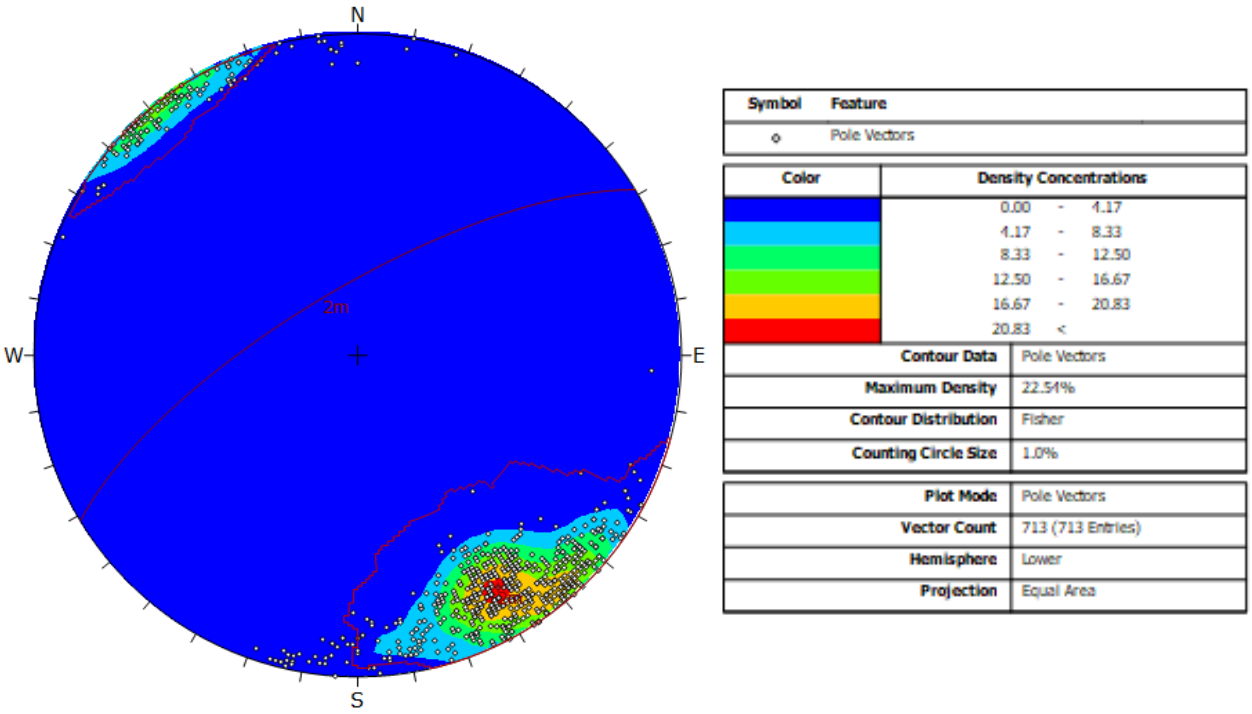

Figure 101 - Stereoplot with equal area of the discontinuities extracted with I-Site Studio for highwall 2 of case study 1 mine. 1 set of planes has been recognised

Table 8 - α, σ_α, β, σ_β, L and σ_L of the sets of discontinuities extracted with I-Site Studio for highwall 1 of case study 1 mine

Set	α (°)	σ_α	β (°)	σ_β	L (m)	σ_L	Nr discontinuities
2m	326	9.63	79	8.09	2.45	0.29	713

- DiAna

The 3D model of highwall 2, built by the mosaic of the models of 4 stereo pairs, has a number of overlapping areas between two contiguous stereo pairs. These areas have been retailed to avoid the doubling of the mesh and differential vertex density. Also in this case, similarly to highwall 1, the point clouds of each stereomodels of the mosaic do not show great differences of vertices concentration thanks to similar sunlight condition. The

point clouds have been resampled with RiScanPro software in order to obtain an ordered point cloud. A box searching cube box with 7 points long side, with a minimum of 30 points (for areas close to the mesh edge) has been chosen to extract the planes for the ordered point cloud. A threshold of 0.007 has been chosen as maximum value of standard deviation of the planes (Figure 102 and 104). The geostructural analysis of the highwall carried out by DiAna has allowed the extraction of 960 planes; 638 of them related to 2m set of discontinuities (Figure 104 and Table 9). Indeed, the spread of the poles shows a cluster in the area related to 3m set of discontinuities; anyway the poles concentration is very low.

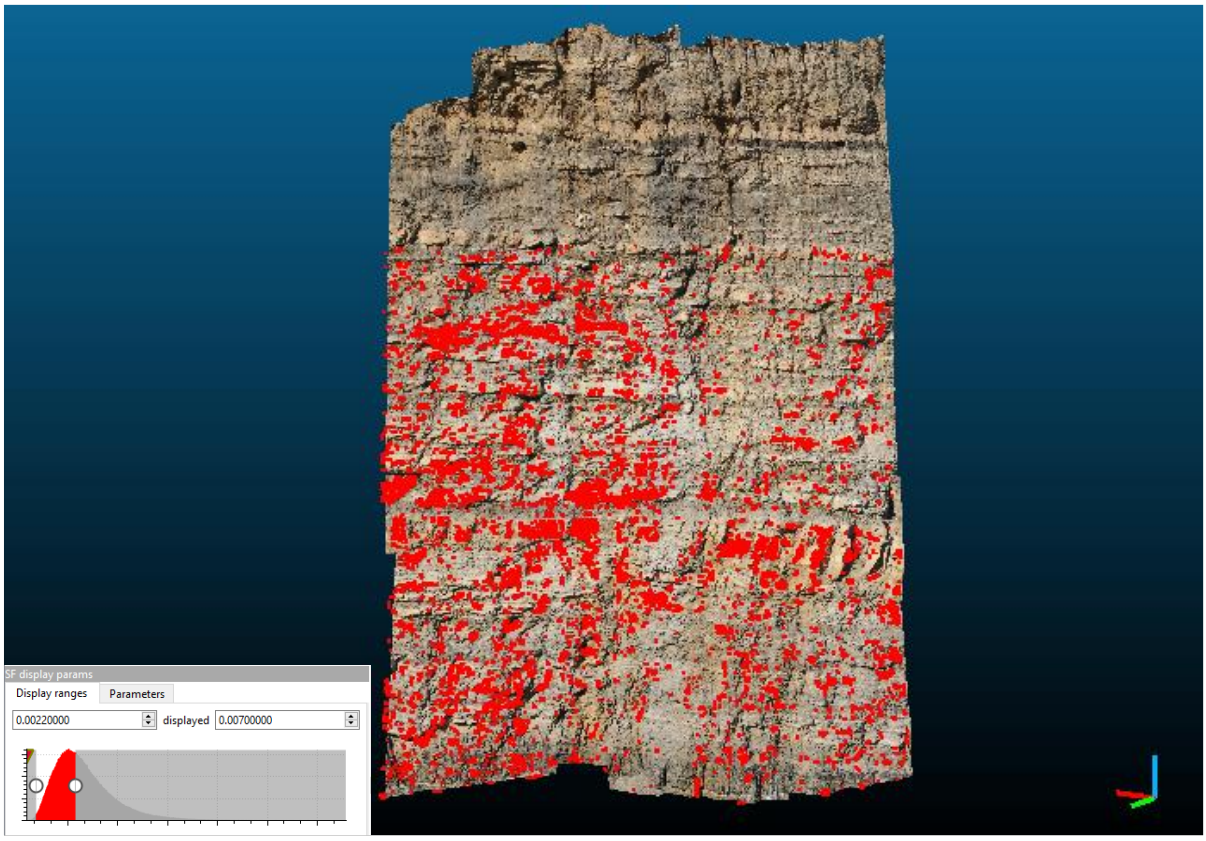

Figure 102 - Overview of highwall 2 of case study 1 mine highwall: the red areas indicate the points with standard deviation of the distance between the subsampled point clouds using a 3 -points range (30 points) and their regression plane with values <0.007. Standard deviation distribution pattern shows that the right part of the point cloud has lower values

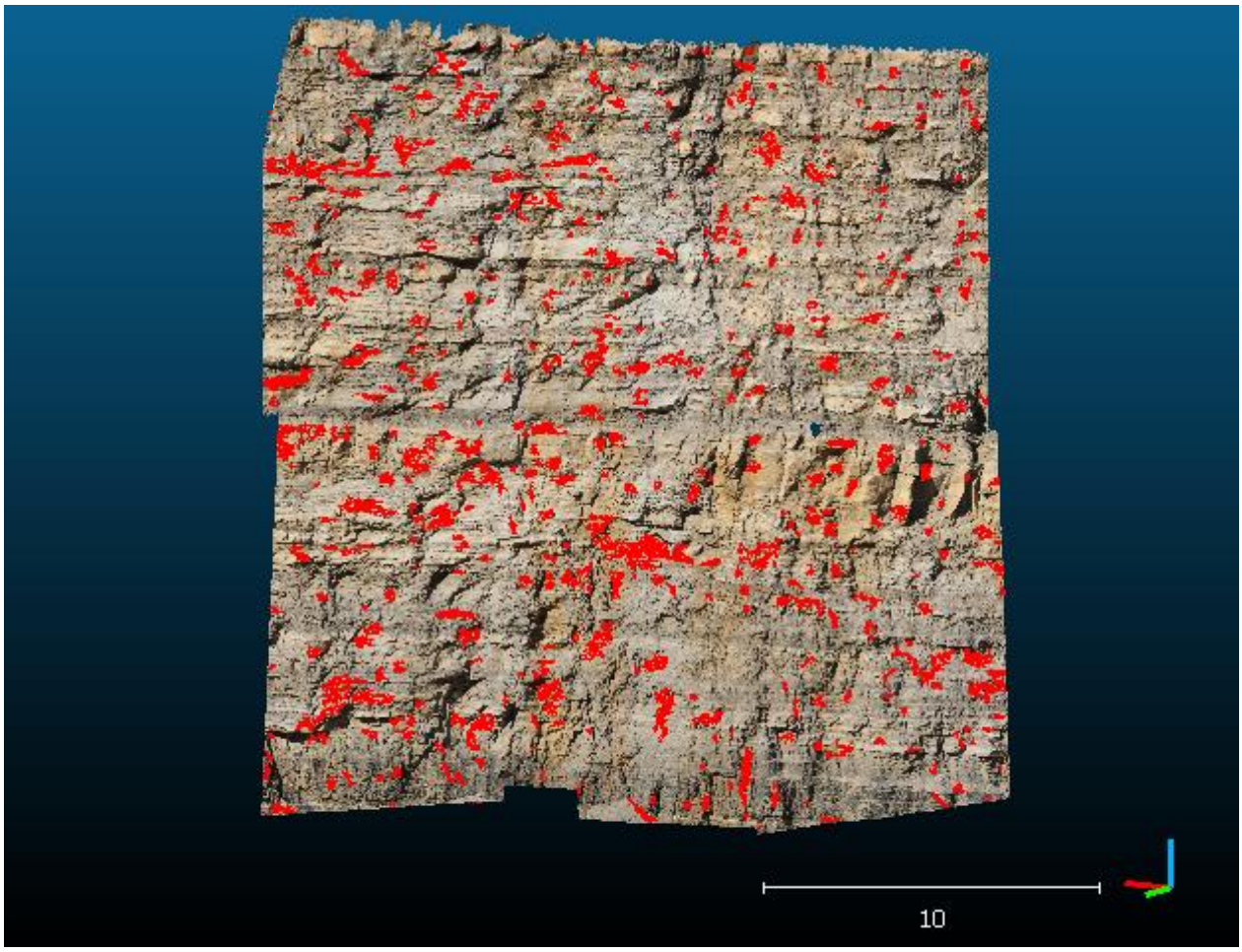

Figure 103 - Position of the sets of discontinuities extracted by DiAna on highwall 2

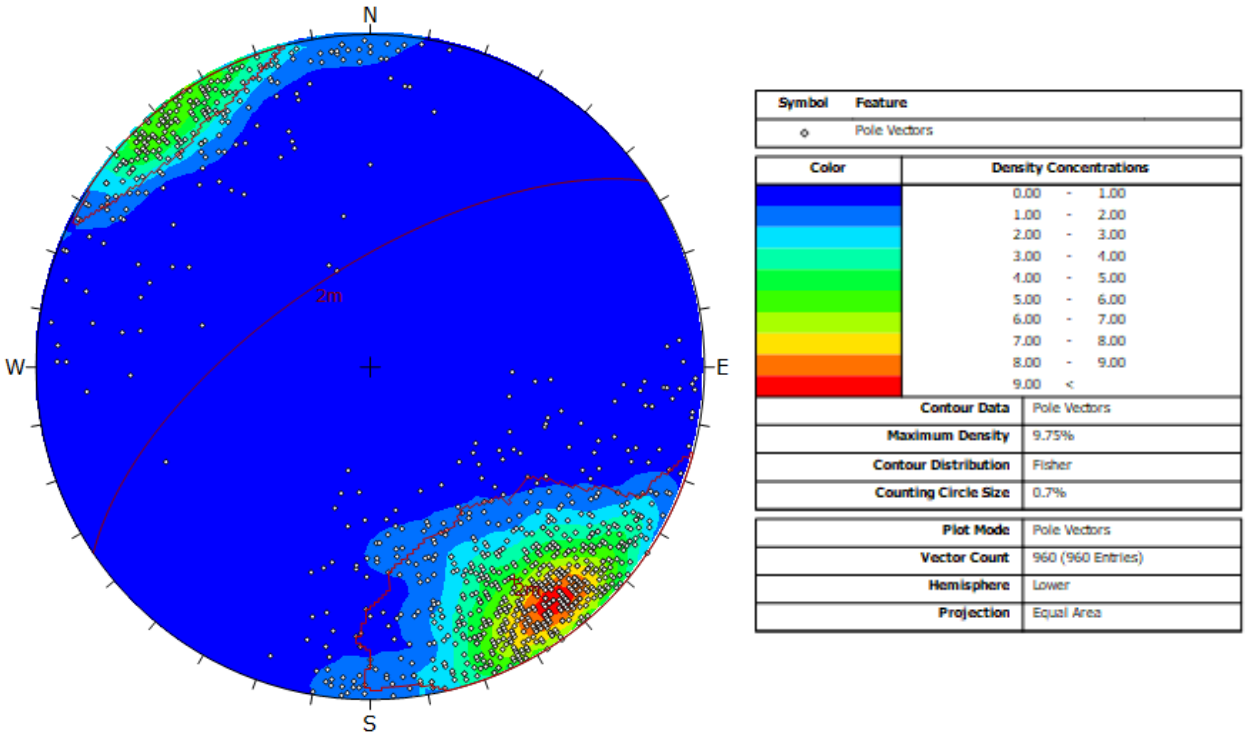

Figure 104 - Stereoplot with equal area of the discontinuities extracted with DiAna for highwall 2 of case study 1 mine. 2 sets of planes have been recognised

Table 9 - α, σ_α, β, σ_β, L and σ_L of the sets of discontinuities extracted with DiAna for highwall 2 of case study 1 mine

Set	α (°)	σ_α	β (°)	σ_β	L (m)	σ_L	Nr discontinuities
2m	323	10.87	80	8.89	1.49	0.12	638

- Facets code

Overall 865 planes have been extracted by Facets plugin (Figure 105 and Table 10). Because of the small dimension of the outcropping planes a low number of points (95) has been set as criterium for plane extraction, despite the point cloud concentration is 9496 points/m^2. As for highwall 1, the minimum number of points has been chosen by the minimum surface of the planes from the 3D model (0.01 m^2 about). Because the point cloud concentration is 9496 points /m^2, observed planes are at east constituted by 95 points about. The same parameters used for the discontinuities extraction of highwall 1 have been used for the discontinuities extraction of highwall 2. Also in this case, some of the extracted planes have been judged as not realistic, because too large and approximate, or because too small. Planes with surface < 0.01 m^2 or > 4 m^2, or with an RMS > 0.1 have been so discharged. A total number of 831 planes has been used for the geostructural characterisation of the rock mass (Figure 105 and Table 10). The only recognised set of discontinuities can be related to 2m set extracted by the other used methods (Table 10). σ_α αnd σ_β are 10.46 and 8.46 respectively (Table 10). The set L is equal to 4.45, with a σ_L value of 0.63.

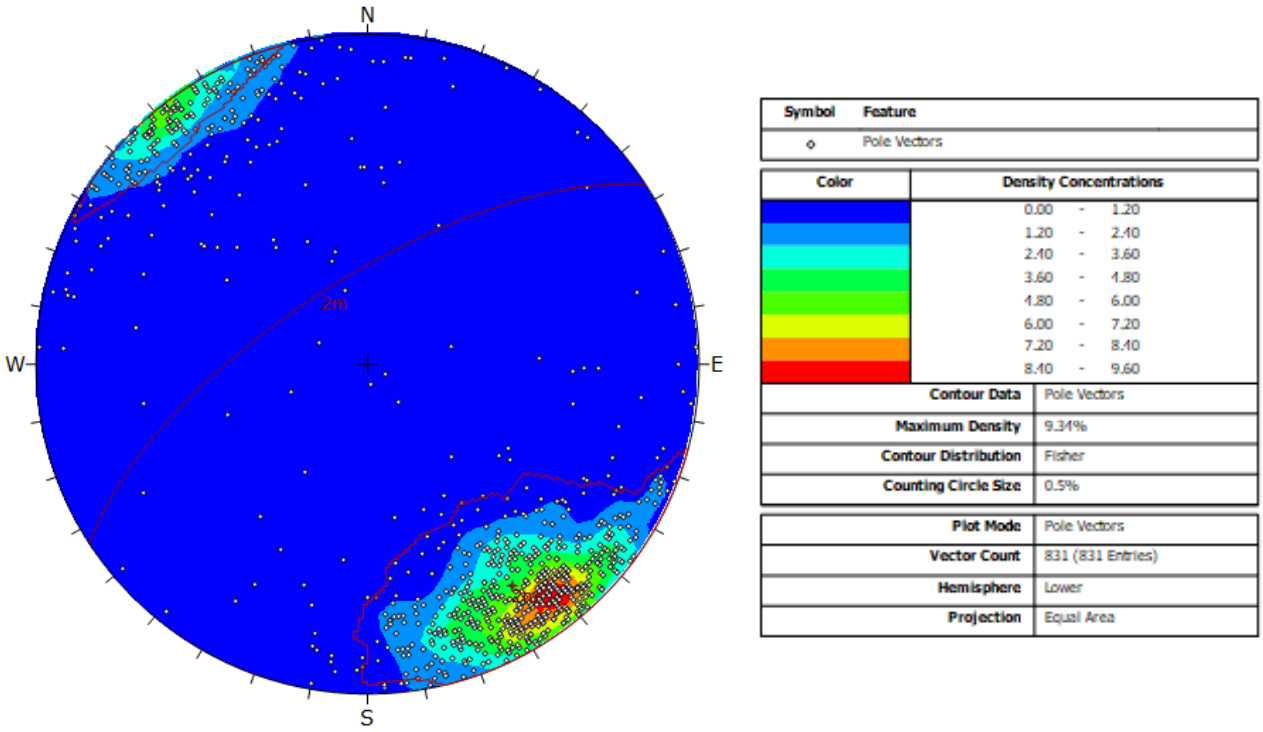

Figure 105 - Stereoplot with equal area of the discontinuities extracted with Facets plug-in of CloudCompare for highwall 2 of case study 1 mine

Table 10 - α, σ_α, β, σ_β, L and σ_L of the sets of discontinuities extracted with Facets plug-in of CloudCompare for highwall 2 of case study 1 mine

Set	α (°)	σ_α	β (°)	σ_β	L (m)	σ_L	Nr discontinuities
2m	325	10.49	79	8.46	4.45	0.63	565

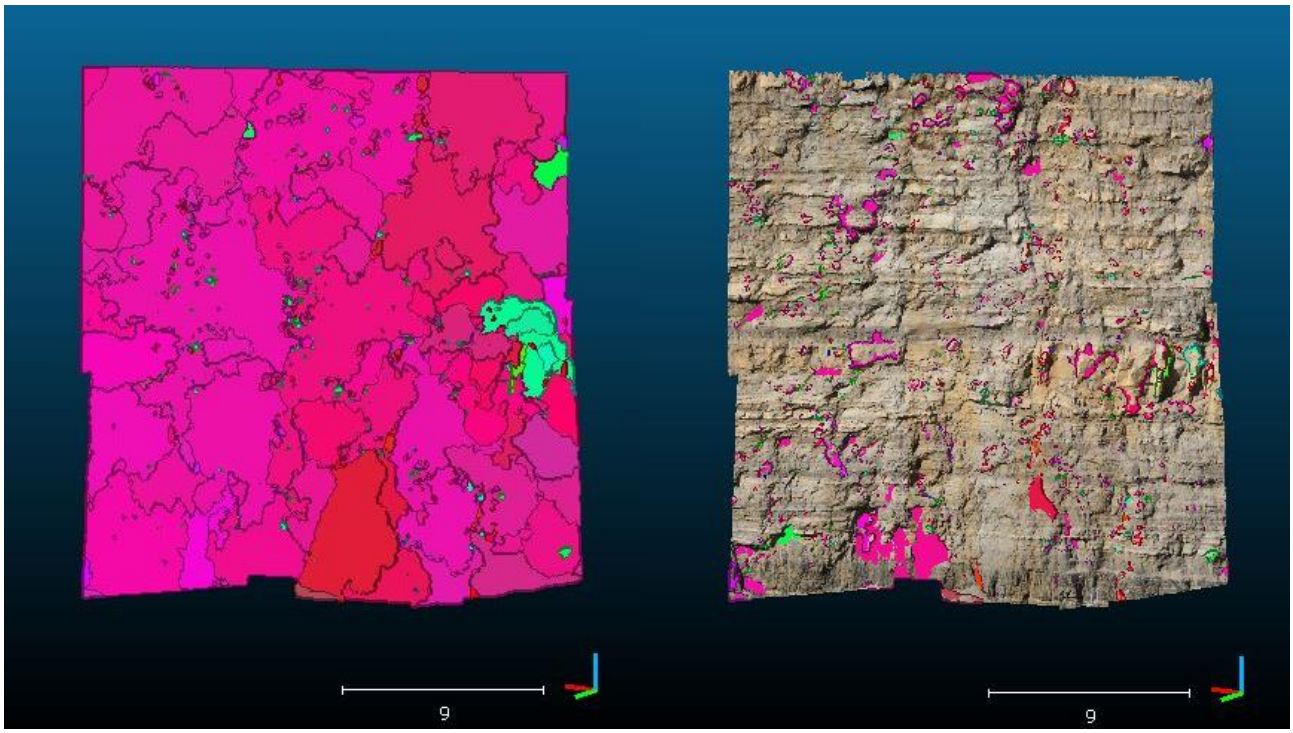

Figure 106 - Planes extracted by Facets plug in of CloudCompare. Left: before filtering by RMS and maximum surface; right: after filtering. Largest planes of not filtered surfaces are not representative of real discontinuities within the rock mass. The colour of the discontinuities depends on the aspect of the plane; pink planes are related to 2m set

6.2. Kinematic analysis

2D and 3D kinematic analysis have been performed on the two highwalls of case study 1 mine. 2D kinematic analysis has been carried using the Kinematic analysis tool of Dips (Rocscience), given a simplified model of the slope (with α_{slope} = 70° and β_{slope} = 140° for highwall 1 and with α_{slope} = 70° and β_{slope} = 140° for highwall 2), while 3D kinematic analysis has been performed using DiAna-K code on the real 3D model built with the photogrammetric survey. As described in Chapter 5.2, ϕ has been put equal to 30° basing on the values reported by Lindsay et al. (2001), Fuenkajorn (2005), and Suchowerska Iwanec (2014).

6.2.1. Kinematic analysis of highwall 1

2D Kinematic analysis carried out on discontinuities extracted by SiroJoint, I-Site Studio, and DiAna has revealed the sets of discontinuities involved for plane failure, wedge failure, block toppling and flexural toppling mechanisms.

2D kinematic analysis shows that plane failure is a suitable failure mechanism for highwall 1. SiroJoint results show that plane failure is strongly related on the presence of 1m set of discontinuities. As regarding the orientation of 1m set, α_{disc} is included within the range $\alpha_{slope} \pm 20°$, β_{disc} is > φ and the direction is within an angular distance of $\beta_{slope}/2$ from the direction [α_{slope}; $\beta_{slope}/2$] (Chapter 3.1.1). 200 discontinuities out of 1382 (14.47 %) satisfy the failure conditions for plane failure (pink area in Figure 107). These discontinuities are moreover related to 1m set of discontinuities (186/200); the remnant ones (14/200) are not related to any other set. Discontinuities are mainly constituted by planes (189/200; Figure 108); kinematic analysis carried out on planes only (Figure 108) does not greatly differs from kinematic analysis carried out both on planes and

traces (Figure 107). Figure 107 shows that the highest concentration (11.08 poles/deg^2) of poles extracted by SiroJoint is located close to the plane failure critical sector.

Kinematic analysis carried out on discontinuities extracted by I-Site Studio has revealed that plane failure involves a percentage of 23.54% discontinuities (218/926) (Figure 109), most of them are related to 1m sets of discontinuities (173/218) also in this case. The remnant planes critical for plane failure are not related to any set of discontinuities. Similarly, the stereo plot of the discontinuities extracted by SiroJoint (Figure 107), the highest discontinuities concentration (17.68 poles/deg^2) is located close to envelop of the discontinuities coming out from the slope. Although an overestimation of the number of discontinuities with an orientation similar to the orientation of the slope (1m) should be considered, the distribution of the poles of the discontinuities suggests that the β_{slope} strongly affects plane failure probability of occurrence.

Kinematic analysis performed on discontinuities extracted by DiAna shows that plane failure involves 463/1316 discontinuities (35.11 %) (Figure 110), almost entirely related to 1m sets of discontinuities (383/463). The remnant ones (80/463) are not related to any set.

The discontinuities extracted by Facets revealed that plane failure involves 96/453 discontinuities (23.94 %) (Figure 111), most of them are related to 1m sets of discontinuities (86/91). Also in this case, the remnant ones (5/96) are not related to any set.

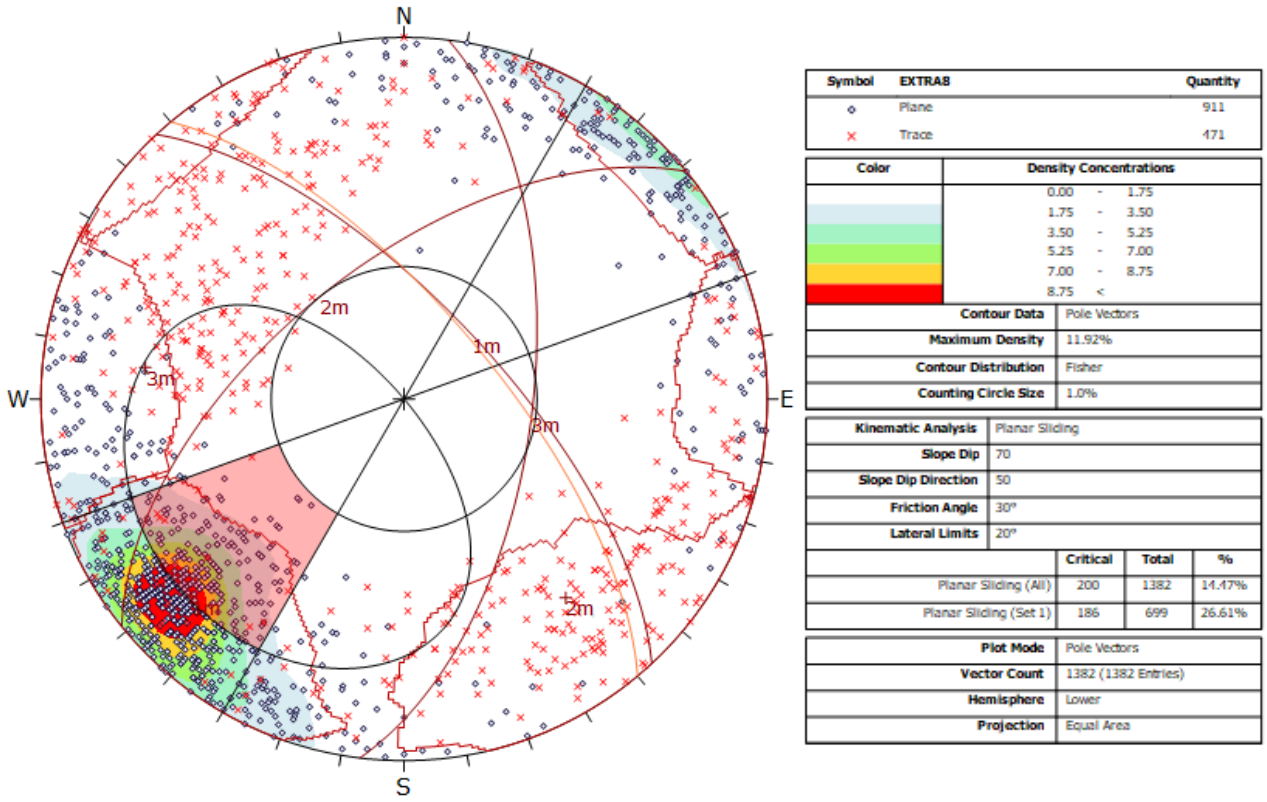

Symbol	EXTRA8	Quantity
◇	Plane	911
×	Trace	471

Color	Density Concentrations
	0.00 - 1.75
	1.75 - 3.50
	3.50 - 5.25
	5.25 - 7.00
	7.00 - 8.75
	8.75 <

Contour Data	Pole Vectors
Maximum Density	11.92%
Contour Distribution	Fisher
Counting Circle Size	1.0%

Kinematic Analysis	Planar Sliding
Slope Dip	70
Slope Dip Direction	50
Friction Angle	30°
Lateral Limits	20°

	Critical	Total	%
Planar Sliding (All)	200	1382	14.47%
Planar Sliding (Set 1)	186	699	26.61%

Plot Mode	Pole Vectors
Vector Count	1382 (1382 Entries)
Hemisphere	Lower
Projection	Equal Area

Figure 107 - Kinematic analysis of planes and traces of highwall 1 of case study 1 mine for plane failure on geostructural data carried out by SiroJoint. Orange cyclographic: slope orientation; pink area: area of the stereo plot with intersection of planes coupling affected by plane failure

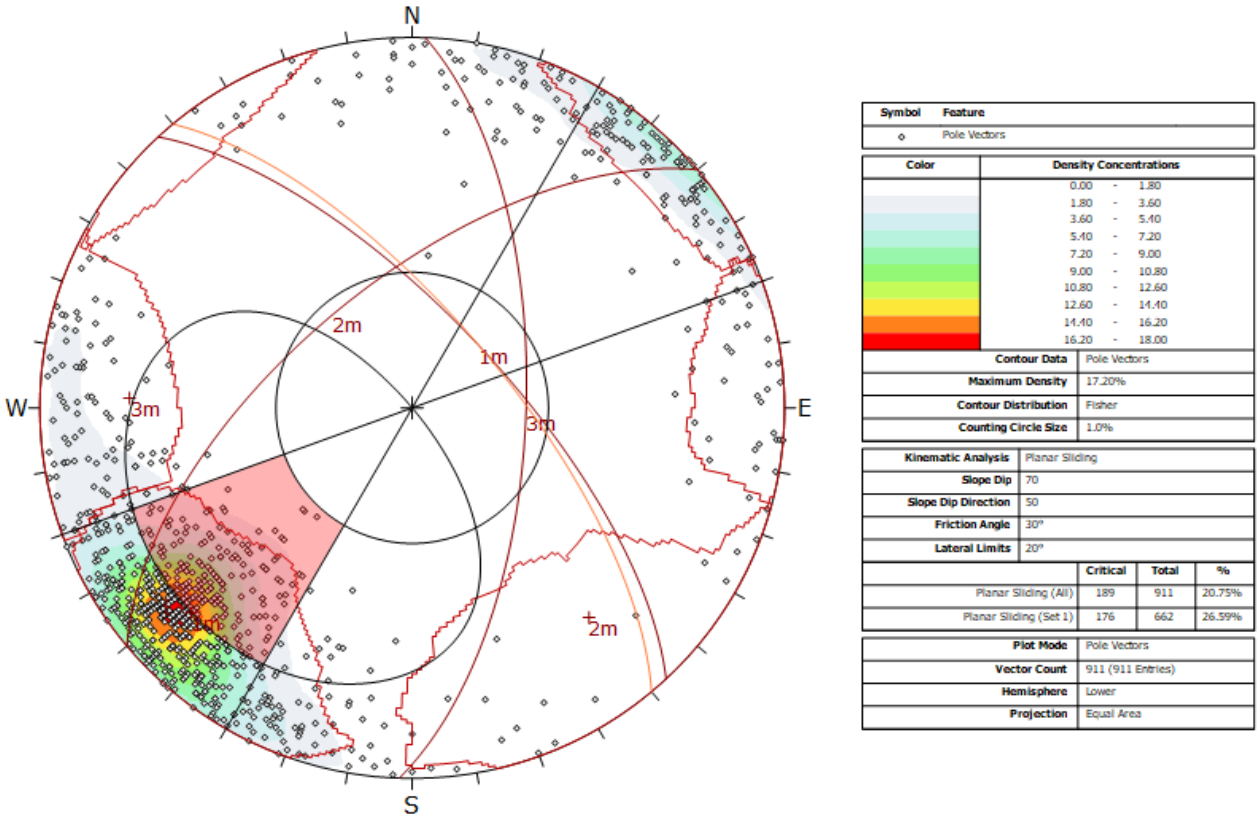

Symbol	Feature
◇	Pole Vectors

Color	Density Concentrations
	0.00 - 1.80
	1.80 - 3.60
	3.60 - 5.40
	5.40 - 7.20
	7.20 - 9.00
	9.00 - 10.80
	10.80 - 12.60
	12.60 - 14.40
	14.40 - 16.20
	16.20 - 18.00

Contour Data	Pole Vectors
Maximum Density	17.20%
Contour Distribution	Fisher
Counting Circle Size	1.0%

Kinematic Analysis	Planar Sliding
Slope Dip	70
Slope Dip Direction	50
Friction Angle	30°
Lateral Limits	20°

	Critical	Total	%
Planar Sliding (All)	189	911	20.75%
Planar Sliding (Set 1)	176	662	26.59%

Plot Mode	Pole Vectors
Vector Count	911 (911 Entries)
Hemisphere	Lower
Projection	Equal Area

Figure 108 - Kinematic analysis of planes only of highwall 1 of case study 1 mine for plane failure on geostructural data carried out by SiroJoint. Orange cyclographic: slope orientation; pink area: area of the stereo plot with intersection of planes coupling affected by plane failure

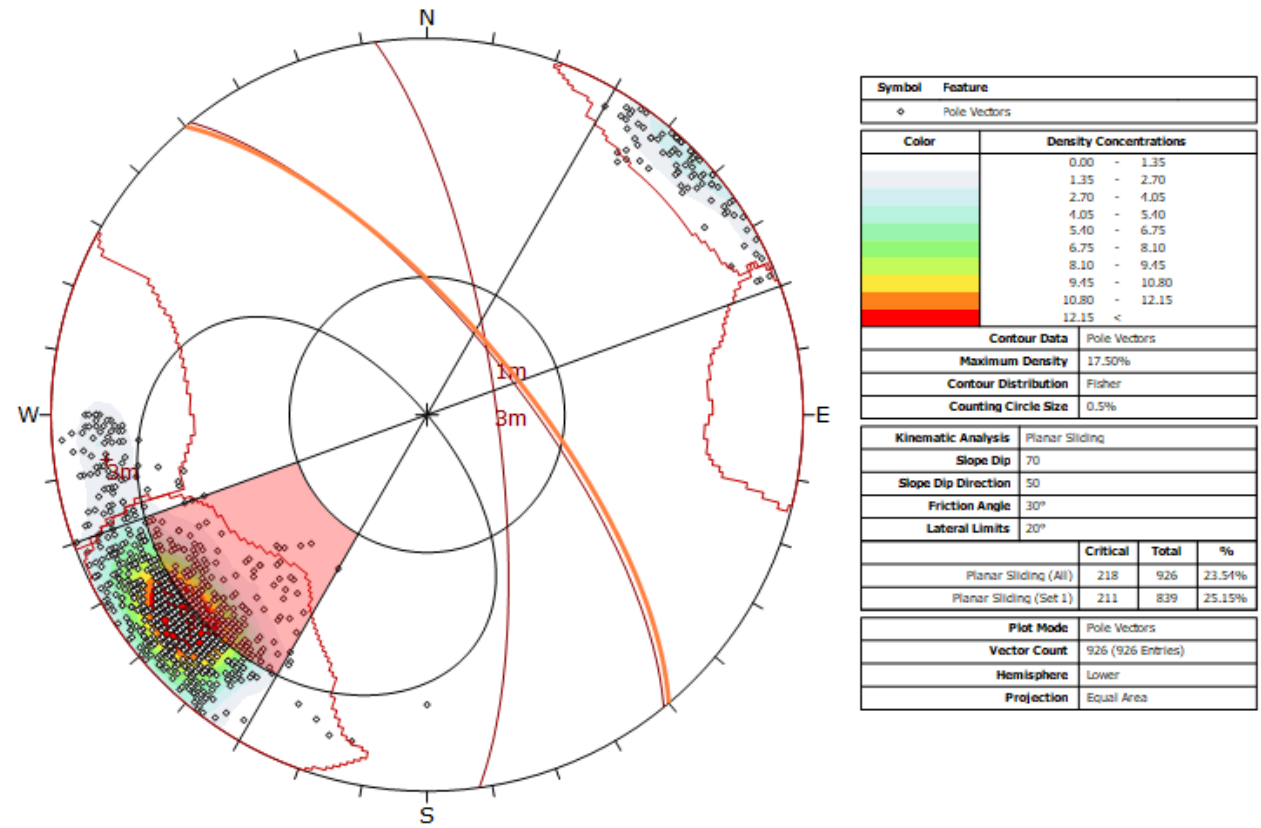

Symbol	Feature
◇	Pole Vectors

Color	Density Concentrations
	0.00 - 1.35
	1.35 - 2.70
	2.70 - 4.05
	4.05 - 5.40
	5.40 - 6.75
	6.75 - 8.10
	8.10 - 9.45
	9.45 - 10.80
	10.80 - 12.15
	12.15 <

Contour Data	Pole Vectors
Maximum Density	17.50%
Contour Distribution	Fisher
Counting Circle Size	0.5%

Kinematic Analysis	Planar Sliding
Slope Dip	70
Slope Dip Direction	50
Friction Angle	30°
Lateral Limits	20°

	Critical	Total	%
Planar Sliding (All)	218	926	23.54%
Planar Sliding (Set 1)	211	839	25.15%

Plot Mode	Pole Vectors
Vector Count	926 (926 Entries)
Hemisphere	Lower
Projection	Equal Area

Figure 109- Kinematic analysis of highwall 1 of case study 1 mine for plane failure on geostructural data carried out by I-Site Studio. Orange cyclographic: slope orientation; pink area: area of the stereo plot with intersection of planes coupling affected by plane failure

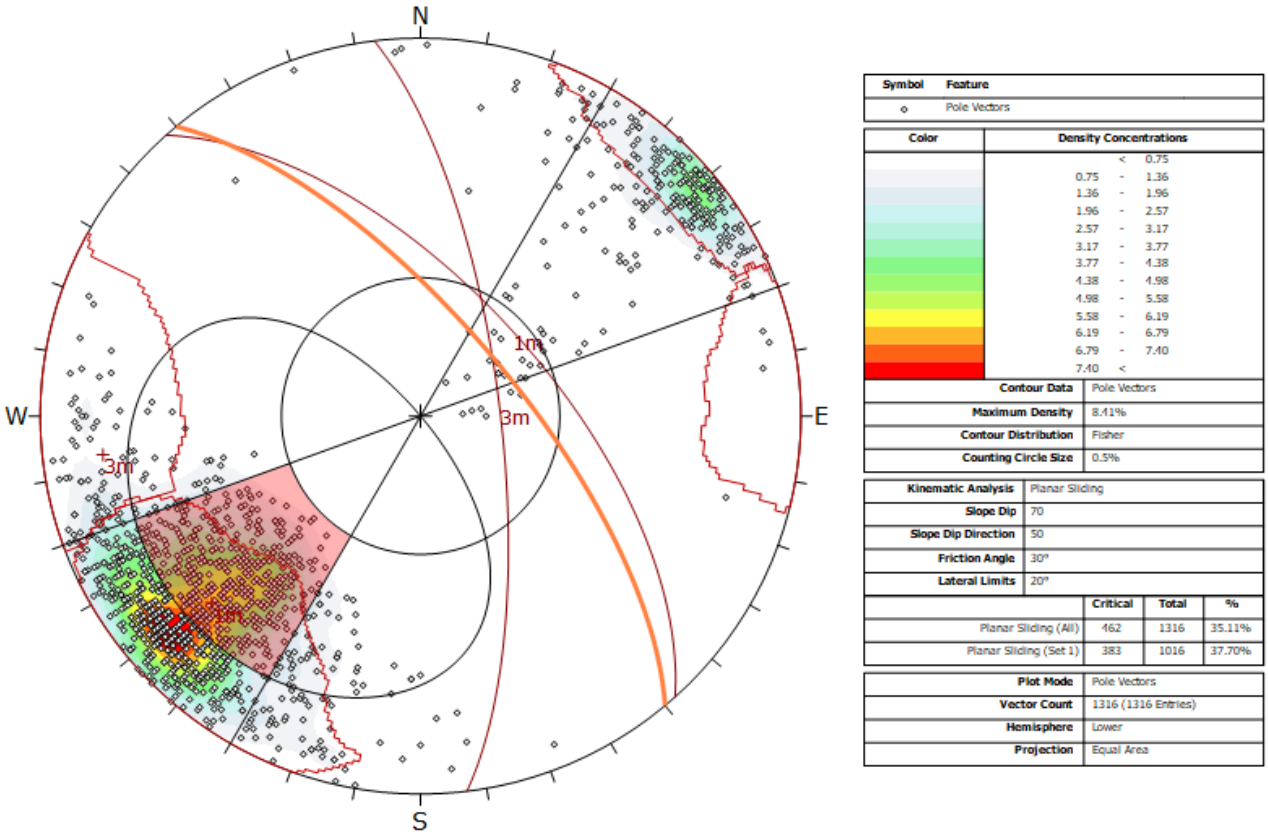

Symbol	Feature
◇	Pole Vectors

Color	Density Concentrations
	< 0.75
	0.75 - 1.36
	1.36 - 1.96
	1.96 - 2.57
	2.57 - 3.17
	3.17 - 3.77
	3.77 - 4.38
	4.38 - 4.98
	4.98 - 5.58
	5.58 - 6.19
	6.19 - 6.79
	6.79 - 7.40
	7.40 <

Contour Data	Pole Vectors
Maximum Density	8.41%
Contour Distribution	Fisher
Counting Circle Size	0.5%

Kinematic Analysis	Planar Sliding
Slope Dip	70
Slope Dip Direction	50
Friction Angle	30°
Lateral Limits	20°

	Critical	Total	%
Planar Sliding (All)	462	1316	35.11%
Planar Sliding (Set 1)	383	1016	37.70%

Plot Mode	Pole Vectors
Vector Count	1316 (1316 Entries)
Hemisphere	Lower
Projection	Equal Area

Figure 110 - Kinematic analysis of highwall 1 of case study 1 mine for plane failure on geostructural data carried out by DiAna. Orange cyclographic: slope orientation; pink area: area of the stereo plot with intersection of planes coupling affected by plane failure

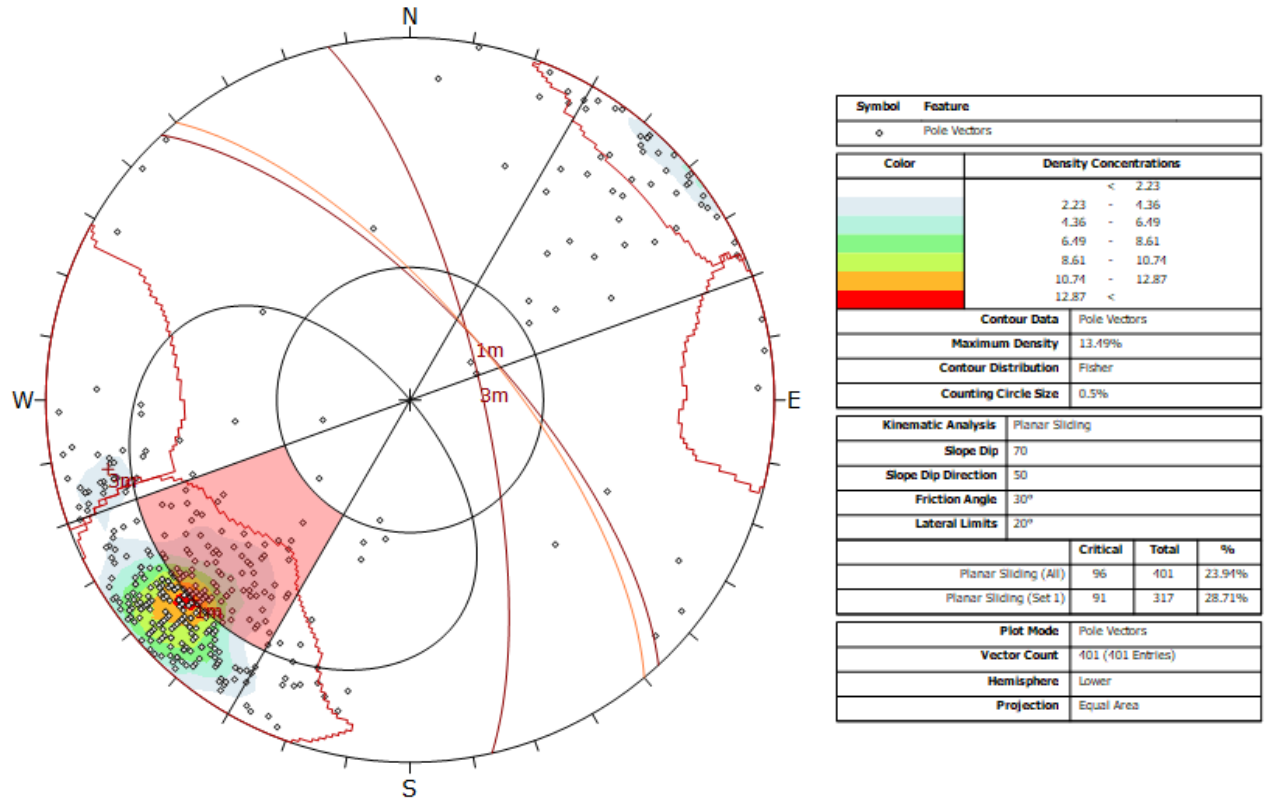

Symbol	Feature
◇	Pole Vectors

Color	Density Concentrations
	< 2.23
	2.23 - 4.36
	4.36 - 6.49
	6.49 - 8.61
	8.61 - 10.74
	10.74 - 12.87
	12.87 <

Contour Data	Pole Vectors
Maximum Density	13.49%
Contour Distribution	Fisher
Counting Circle Size	0.5%

Kinematic Analysis	Planar Sliding
Slope Dip	70
Slope Dip Direction	50
Friction Angle	30°
Lateral Limits	20°

	Critical	Total	%
Planar Sliding (All)	96	401	23.94%
Planar Sliding (Set 1)	91	317	28.71%

Plot Mode	Pole Vectors
Vector Count	401 (401 Entries)
Hemisphere	Lower
Projection	Equal Area

Figure 111 - Kinematic analysis of highwall 1 of case study 1 mine for plane failure on geostructural data carried out by Facets plug-in of CloudCompare. Orange cyclographic: slope orientation; pink area: area of the stereo plot with intersection of planes coupling affected by plane failure

2D kinematic analysis shows that wedge failure is a feasible failure mechanism, whatever the code is used for the discontinuities extraction. As regarding SiroJoint, the average planes intersections show that all the intersection of the three detected sets are critical for wedge failure. Overall, 31.11 % of the intersections (2968009) intersect the wedge failure prone area (Figure 112). Results of the kinematic analysis do not greatly change considering, instead, planes only: also in this case, only 1m-2m and 2m-3m sets of discontinuities intersections are included into stereo-plot wedge failure prone area and the percentage of critical intersection is similar (30.41 % vs 31.11 %) (Figure 113).
The kinematic analyses carried out with I-Site Studio (Figure 114), DiAna (Figure 115), and Facets (Figure 116) show similar results as regarding wedge failure. Whatever code has been used for the extraction of the discontinuities, the intersection 1m-2m is included into the critical area. Overall 24.21 %, 36.61 %, and 19.24 % of the intersections extracted with I-Site Studio, DiAna, and Facets respectively is critical for wedge failure.

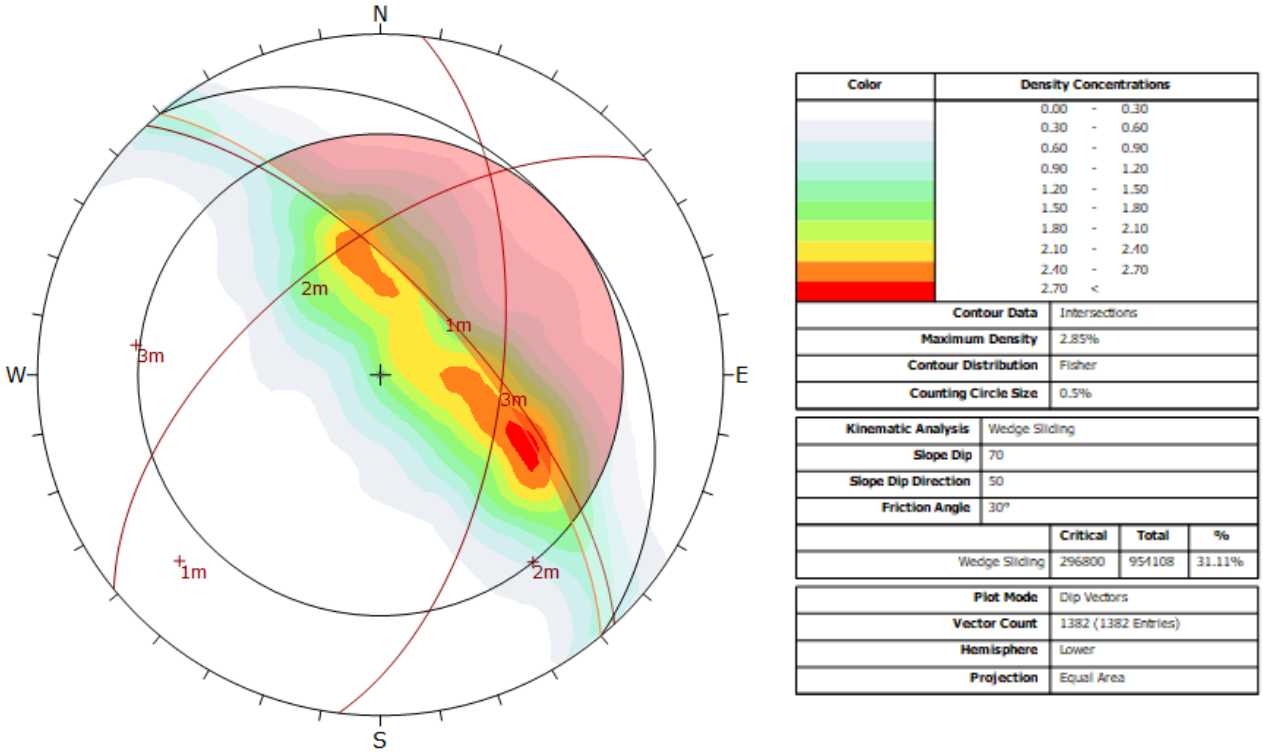

Color	Density Concentrations
	0.00 - 0.30
	0.30 - 0.60
	0.60 - 0.90
	0.90 - 1.20
	1.20 - 1.50
	1.50 - 1.80
	1.80 - 2.10
	2.10 - 2.40
	2.40 - 2.70
	2.70 <

Contour Data	Intersections
Maximum Density	2.85%
Contour Distribution	Fisher
Counting Circle Size	0.5%

Kinematic Analysis	Wedge Sliding		
Slope Dip	70		
Slope Dip Direction	50		
Friction Angle	30°		
	Critical	Total	%
Wedge Sliding	296800	954108	31.11%

Plot Mode	Dip Vectors
Vector Count	1382 (1382 Entries)
Hemisphere	Lower
Projection	Equal Area

Figure 112 - Kinematic analysis of planes and traces of highwall 1 of case study 1 mine for wedge failure on geostructural data carried out by SiroJoint. Orange cyclographic: slope orientation; pink spherical spindle: area of the stereo plot with intersection of planes coupling affected by wedge failure

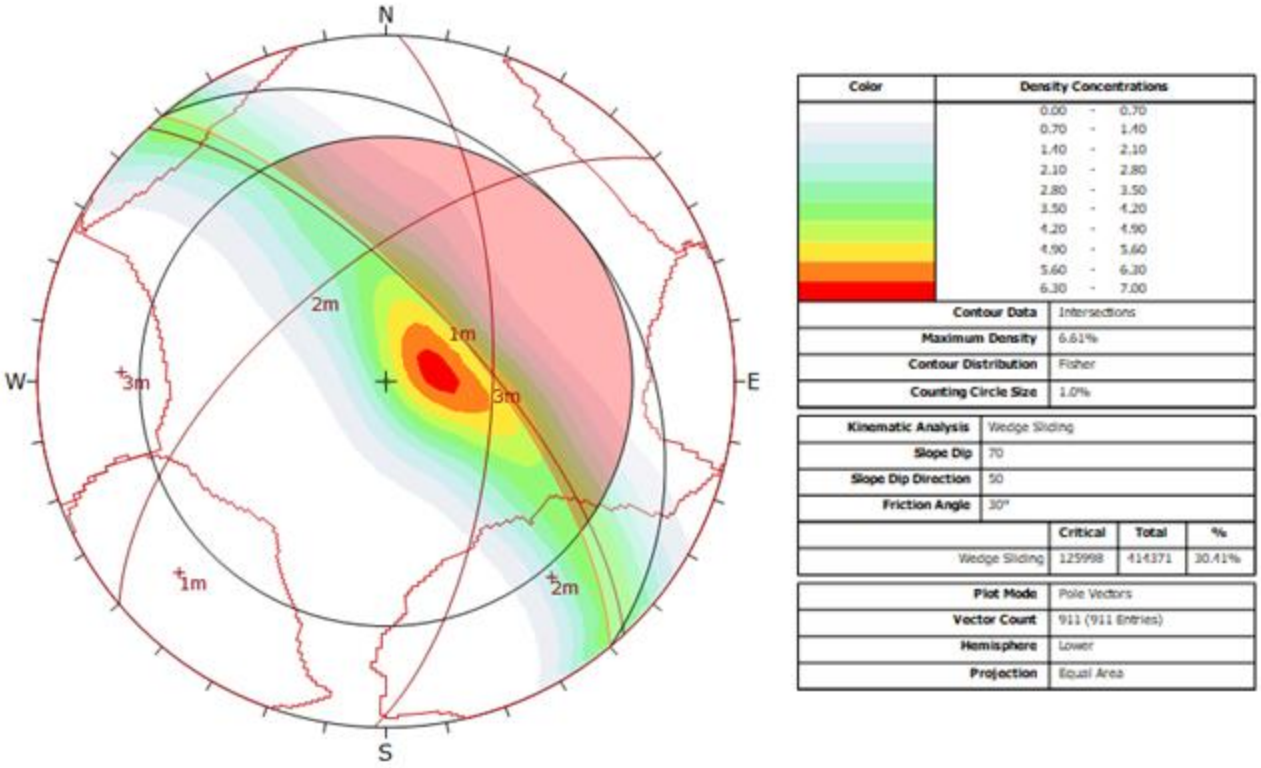

Color	Density Concentrations
	0.00 - 0.70
	0.70 - 1.40
	1.40 - 2.10
	2.10 - 2.80
	2.80 - 3.50
	3.50 - 4.20
	4.20 - 4.90
	4.90 - 5.60
	5.60 - 6.30
	6.30 - 7.00

Contour Data	Intersections
Maximum Density	6.61%
Contour Distribution	Fisher
Counting Circle Size	1.0%

Kinematic Analysis	Wedge Sliding
Slope Dip	70
Slope Dip Direction	50
Friction Angle	30°

	Critical	Total	%
Wedge Sliding	125998	414371	30.41%

Plot Mode	Pole Vectors
Vector Count	911 (911 Entries)
Hemisphere	Lower
Projection	Equal Area

Figure 113 - Kinematic analysis of planes only of highwall 1 of case study 1 mine for wedge failure on geostructural data carried out by SiroJoint. Orange cyclographic: slope orientation; pink spherical spindle: area of the stereo plot with intersection of planes coupling affected by wedge failure

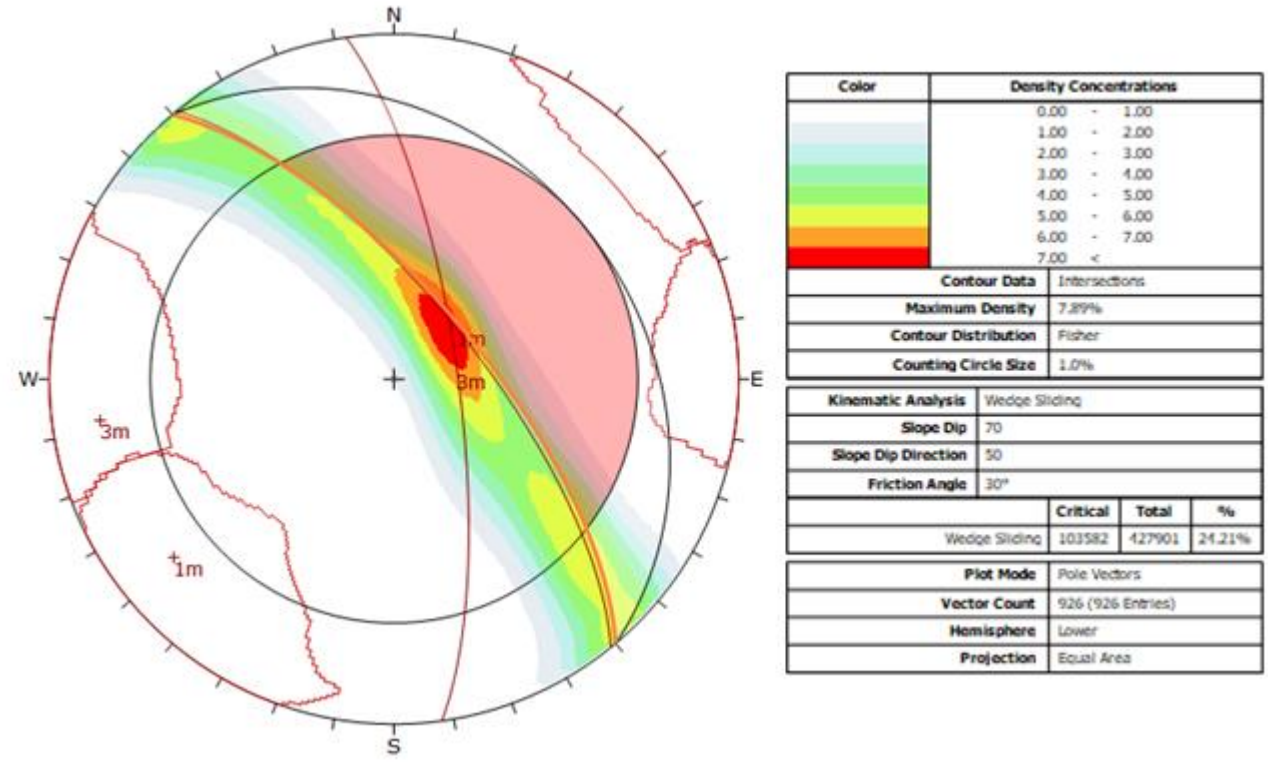

Color	Density Concentrations
	0.00 - 1.00
	1.00 - 2.00
	2.00 - 3.00
	3.00 - 4.00
	4.00 - 5.00
	5.00 - 6.00
	6.00 - 7.00
	7.00 <

Contour Data	Intersections
Maximum Density	7.89%
Contour Distribution	Fisher
Counting Circle Size	1.0%

Kinematic Analysis	Wedge Sliding
Slope Dip	70
Slope Dip Direction	50
Friction Angle	30°

	Critical	Total	%
Wedge Sliding	103582	427901	24.21%

Plot Mode	Pole Vectors
Vector Count	926 (926 Entries)
Hemisphere	Lower
Projection	Equal Area

Figure 114 - Kinematic analysis of highwall 1 of case study 1 mine for wedge failure on geostructural data carried out by I-Site Studio. Orange cyclographic: slope orientation; pink spherical spindle: area of the stereo plot with intersection of planes coupling affected by wedge failure

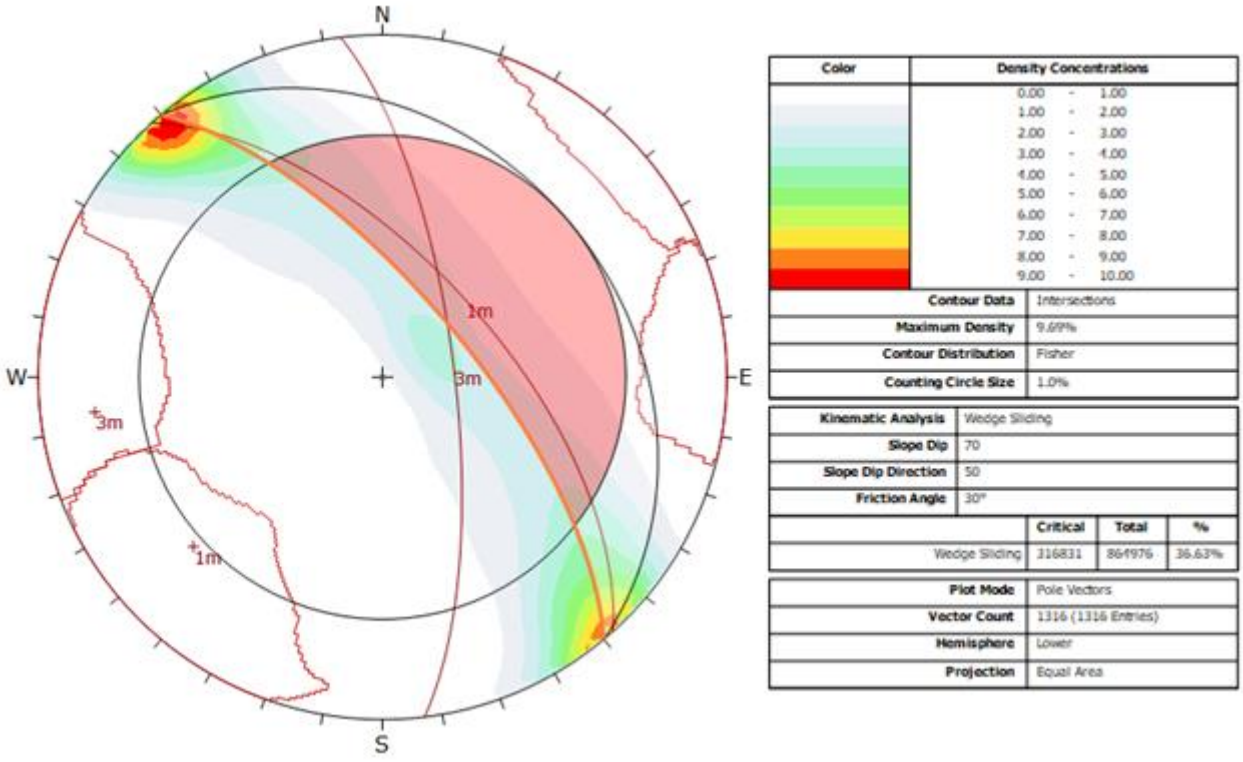

Figure 115 - Kinematic analysis of highwall 1 of case study 1 mine for wedge failure on geostructural data carried out by DiAna. Orange cyclographic: slope orientation; pink spherical spindle: area of the stereo plot with intersection of planes coupling affected by wedge failure

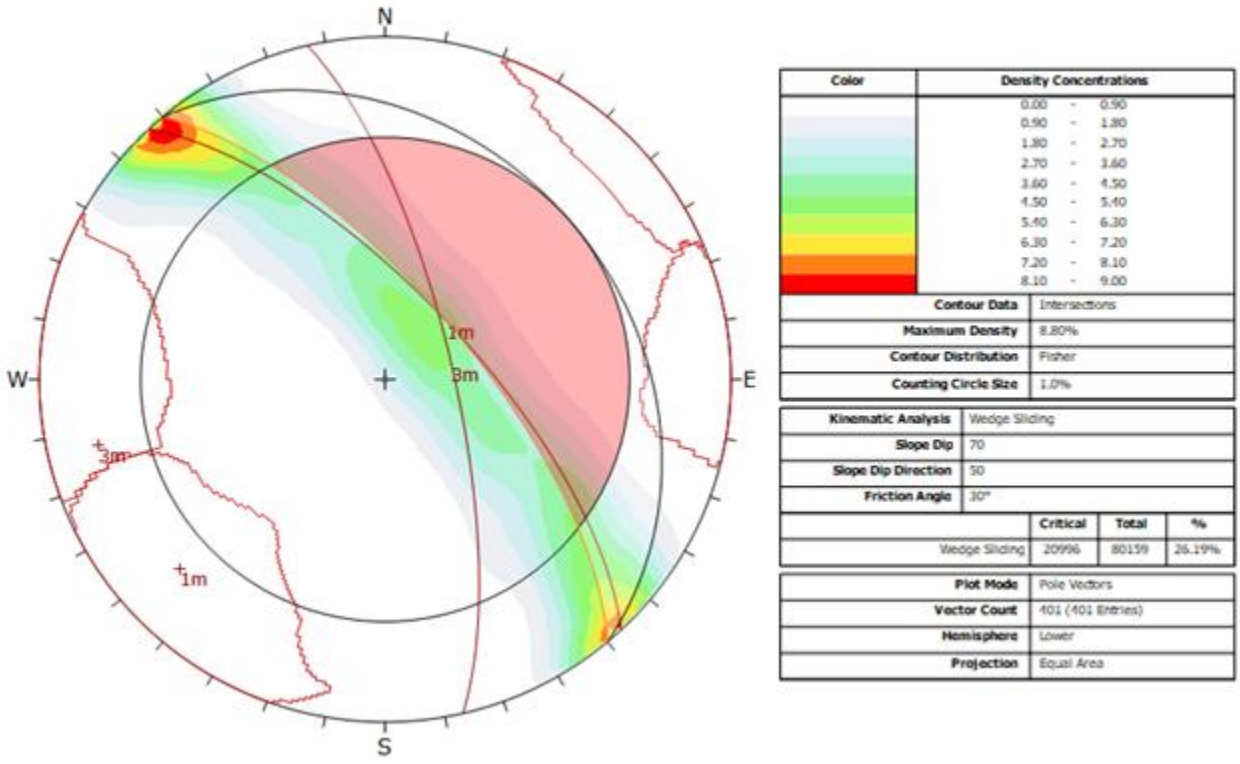

Figure 116 - Kinematic analysis of highwall 1 of case study 1 mine for wedge failure on geostructural data carried out by Facets plug-in of CloudCompare. Orange cyclographic: slope orientation; pink spherical spindle: area of the stereo plot with intersection of planes coupling affected by wedge failure

Generally speaking, block toppling conditions are rarely satisfied; these conditions are not present on highwall 1 and codes used for the extractions of the discontinuities have not produced stereoplots that indicate hazardous conditions.

The geostructural survey carried out with SiroJoint has, in fact, revealed that no hazardous intersection involves the stereoplot and that 20208 only on overall 954108 intersections are critical for block toppling (2.54 %). This assertion is demonstrated by comparison of the stereoplot of all the discontinuities extracted by SiroJoint (Figure 117) with the stereoplot of the only discontinuities related to planes (Figure 118). The kinematic analysis carried out on the 2 stereoplots shows, in fact, that considering both planes and traces 2.54 % of the intersections are critical for block toppling, while considering planes only, the percentage of critical intersections decreases to 0.74 %. This demonstrated that 2m set of discontinuities, the α of which is perpendicular to the α of the slope, is responsible for most of the block detachments. 226/1382 discontinuities are reliable as basal plane (Figure 117). These discontinuities are almost entirely related to 1m set of discontinuities. All the discontinuities suitable as basal planes have β greater than ϕ. This means that block toppling is not a reliable failure mechanism and that the detached block could eventually fall sliding on 1m sliding plane, not toppling. The geostructural conditions are so more critical for plane failure than for block toppling because ϕ < β of 1m set of discontinuities.

The kinematic analysis carried out by the discontinuities extracted by I-Site Studio, DiAna and Facets confirms that it is not a reliable failure mechanism and only 0.09 %, 0.25 %, and 0.28 % of the intersections are, in fact, critical (Figure 119, 120, and 121).

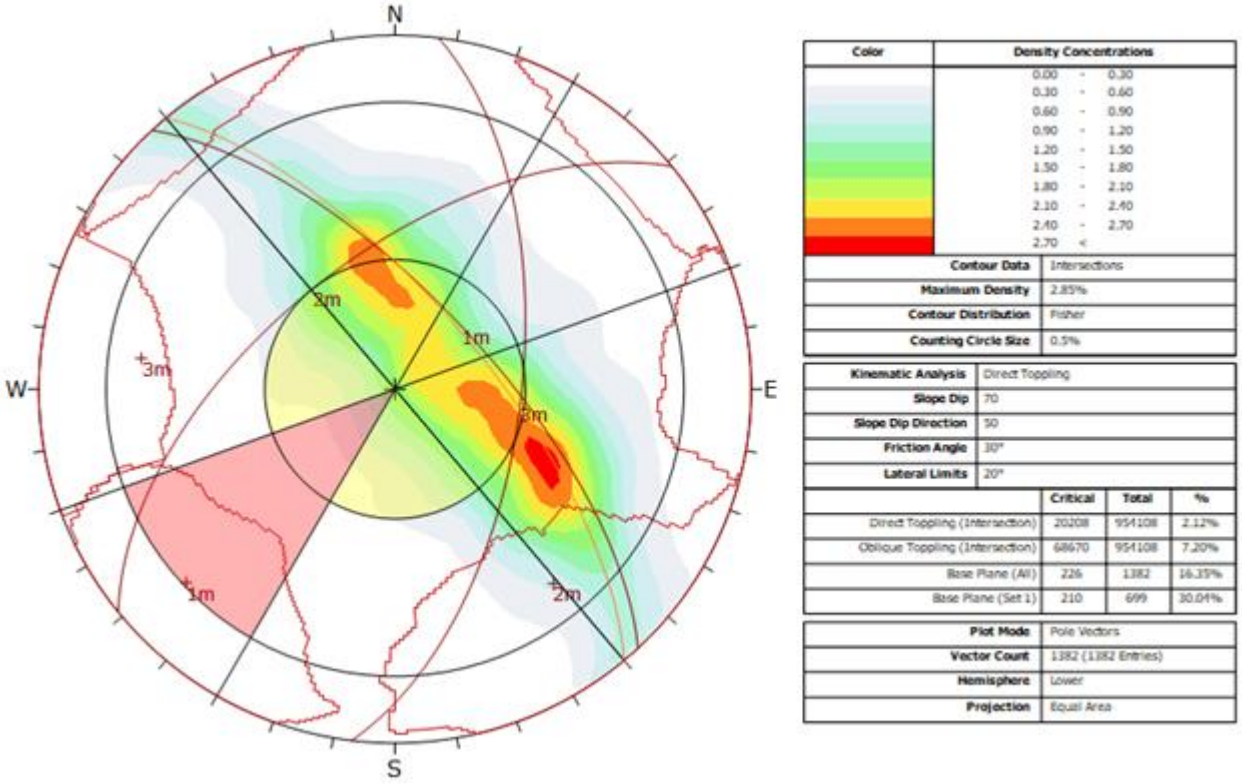

Figure 117 - Kinematic analysis of planes and traces of highwall 1 of case study 1 mine for block toppling on geostructural data carried out by SiroJoint. Orange cyclographic: slope orientation; orange circumference: set of poles of the planes with a β lower than the β_{slope} (74° for this case study); pink section of circumference: area of the stereo plot with intersection of planes coupling affected by block toppling in case of $\beta_{slope} < 90° - \varphi$; yellow sections of circumference: extension of the areas of the stereo plot with intersection of planes coupling affected by block toppling in case of dep slope ($\beta_{slope} > 90° - \varphi$)

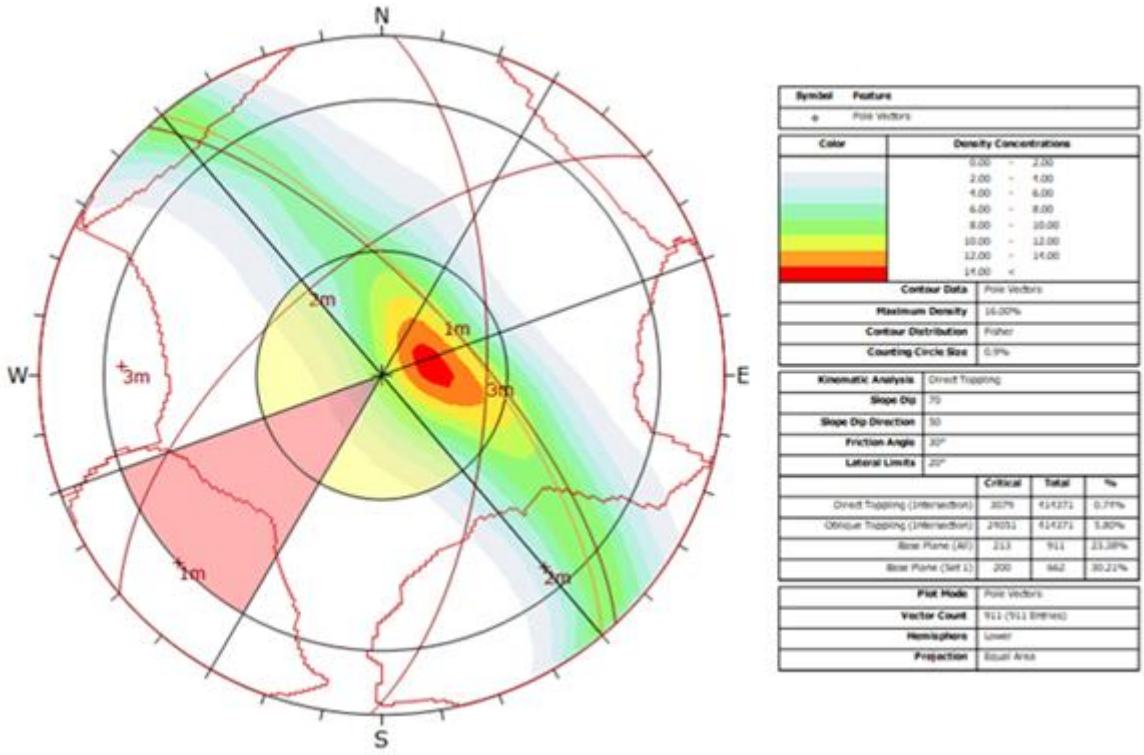

Figure 118 - Kinematic analysis of planes only of highwall 1 of case study 1 mine for block toppling on geostructural data carried out by SiroJoint. Orange cyclographic: slope orientation; orange circumference: set of poles of the planes with a β lower than the β_{slope} (74° for this case study); pink section of circumference: area of the stereo plot with intersection of planes coupling affected by block toppling in case of β_{slope} < 90° - φ; yellow sections of circumference: extension of the areas of the stereo plot with intersection of planes coupling affected by block toppling in case of dep slope (β_{slope} > 90° - φ)

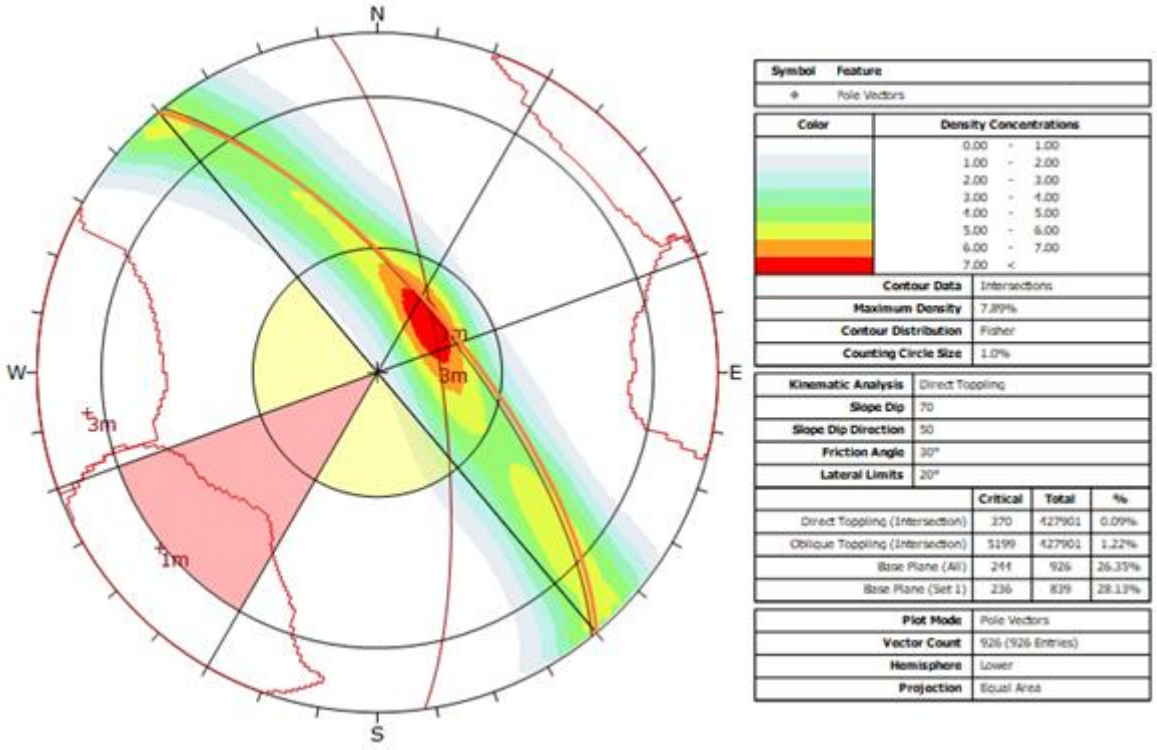

Figure 119 - Kinematic analysis of highwall 1 of case study 1 mine for block toppling on geostructural data carried out by I-Site Studio. Orange cyclographic: slope orientation; orange circumference: set of poles of the planes with a β lower than the β_{slope} (74° for this case study); pink section of circumference: area of the stereo plot with intersection of planes coupling affected by block toppling in case of β_{slope} <90 ° - φ; yellow sections of circumference: extension of the areas of the stereo plot with intersection of planes coupling affected by block toppling in case of dep slope (β_{slope} > 90 ° - φ)

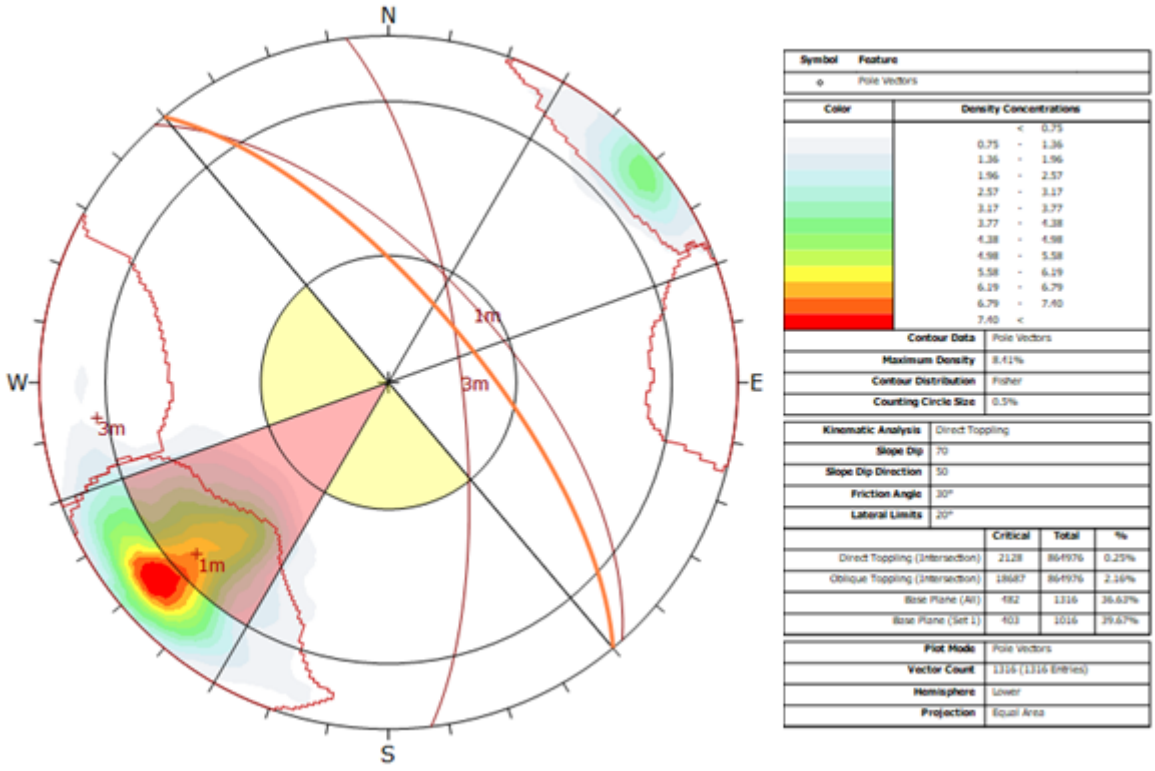

Figure 120 - Kinematic analysis of highwall 1 of case study 1 mine highwall for block toppling on geostructural data carried out by DiAna. Orange cyclographic: slope orientation; orange circumference: set of poles of the planes with a β lower than the β_{slope} (74° for this case study); pink section of circumference: area of the stereo plot with intersection of planes coupling affected by block toppling in case of β_{slope} <90 ° - φ; yellow sections of circumference: extension of the areas of the stereo plot with intersection of planes coupling affected by block toppling in case of dep slope (β_{slope} > 90 ° - φ)

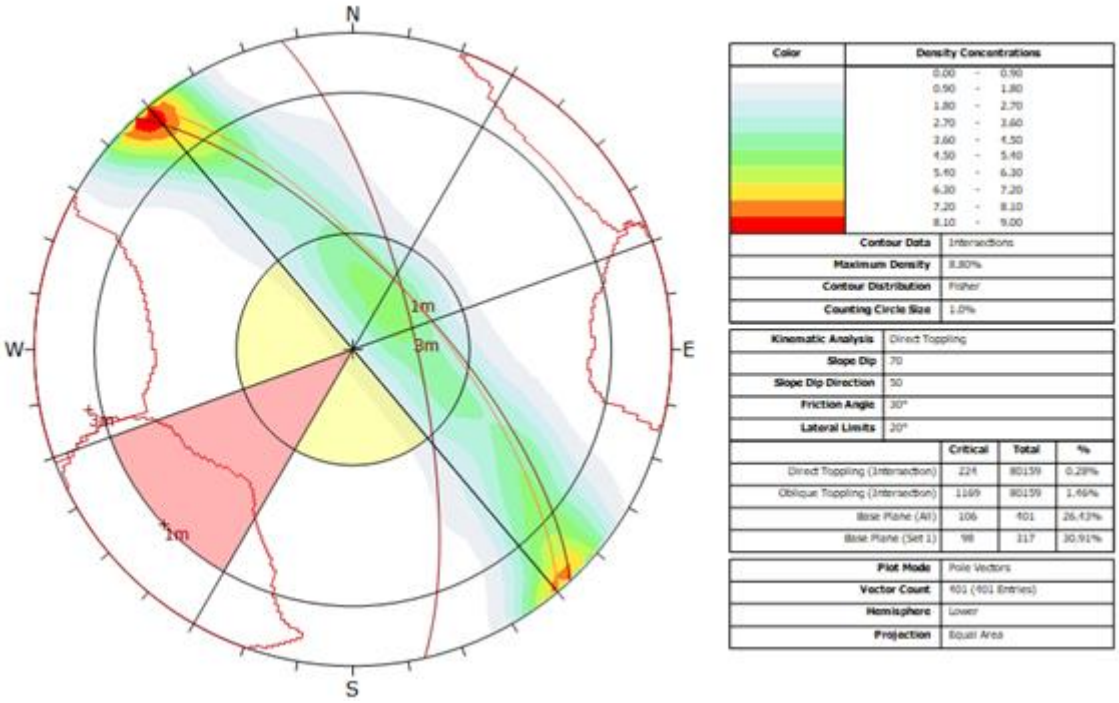

Figure 121 - Kinematic analysis of highwall 1 of case study 1 mine for block toppling on geostructural data carried out by Facets plug-in of CloudCompare. Orange cyclographic: slope orientation; orange circumference: set of poles of the planes with a β lower than the β_{slope} (74° for this case study); pink section of circumference: area of the stereo plot with intersection of planes coupling affected by block toppling in case of β_{slope} <90 ° - φ; yellow sections of circumference: extension of the areas of the stereo plot with intersection of planes coupling affected by block toppling in case of dep slope (β_{slope} > 90 ° - φ)

Kinematic analysis for flexural toppling shows that the percentage of discontinuities suitable for this failure mechanism ranges from 6.80 % to 14.27 %. SiroJoint results show that overall 94 discontinuities (90 planes and 4 traces, overall 6.80 % of the discontinuities) satisfy flexural toppling failure conditions; 54/94 are related to 1m set of discontinuities and the remnant 40/94 have not been assigned to any set of discontinuities (Figure 122 and 123). Discontinuities prone to flexural toppling are entirely constituted by planes (Figure 123).
I-Site Studio results confirm that 1m set of discontinuities is involved by flexural toppling; overall 83 discontinuities on 926 (8.96 %, Figure 124) are prone to flexural toppling; 79/83 and 3/83 have been related to 1m and 3m sets of discontinuities and 10/33 to have not assigned to any set of discontinuities.
188 discontinuities on overall 1316 extracted by DiAna are critical for flexural toppling (14.29 %, Figure 125), 147 most of them are related to 1m set of discontinuities.; 4 discontinuities reliable to flexural toppling are related to 3m set of discontinuities.
Kinematic analysis carried out on the discontinuities extracted by Facets shows that 42/401 (10.47 %) of the discontinuities are prone to flexural toppling; 29 are overhanging discontinuities related to 1m set, 1 to 3m set, while the others are not related to any set of discontinuities (Figure 126).

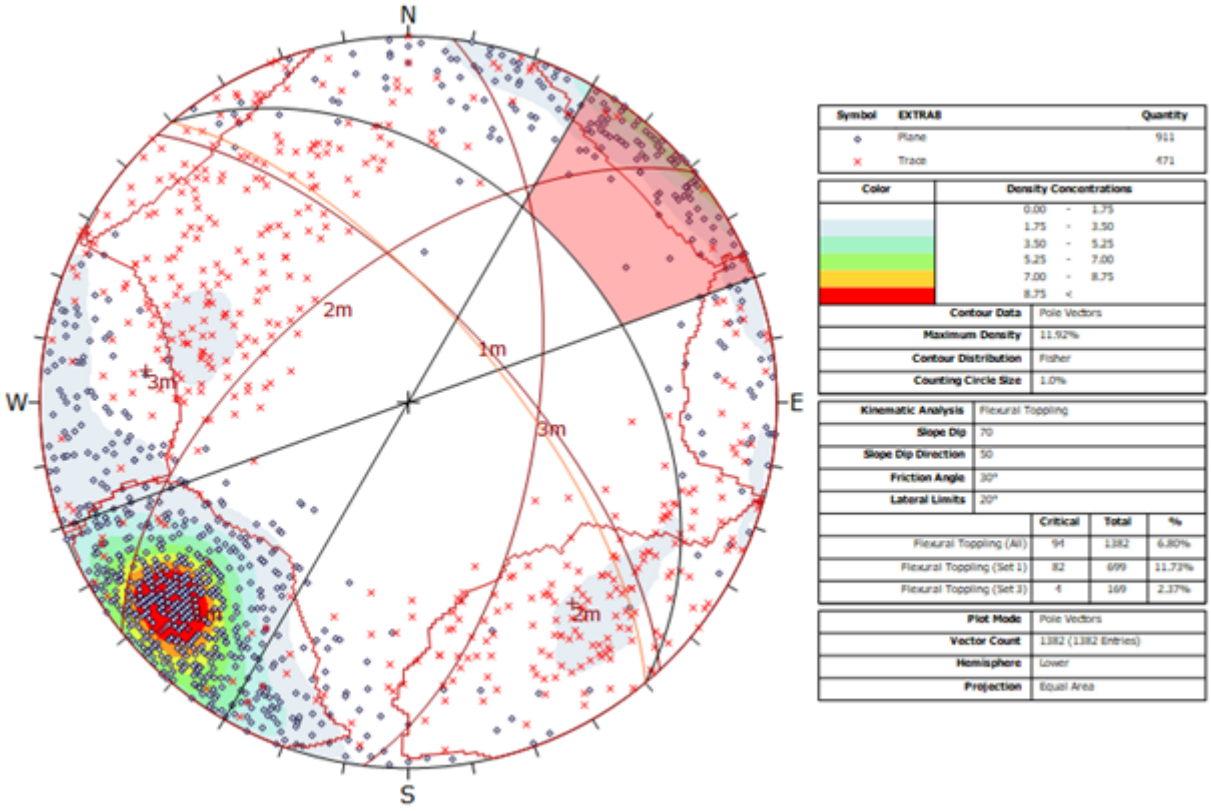

Figure 122 - Kinematic analysis of planes and traces of highwall 1 of case study 1 mine for flexural toppling on geostructural data carried out by SiroJoint. Orange cyclographic: slope orientation; black cyclographic: instability plane for flexural toppling (90 ° -β_{slope} +φ; α_{slope}); pink section of spindle of sphere: area of the stereo plot with the poles of the planes affected by flexural toppling

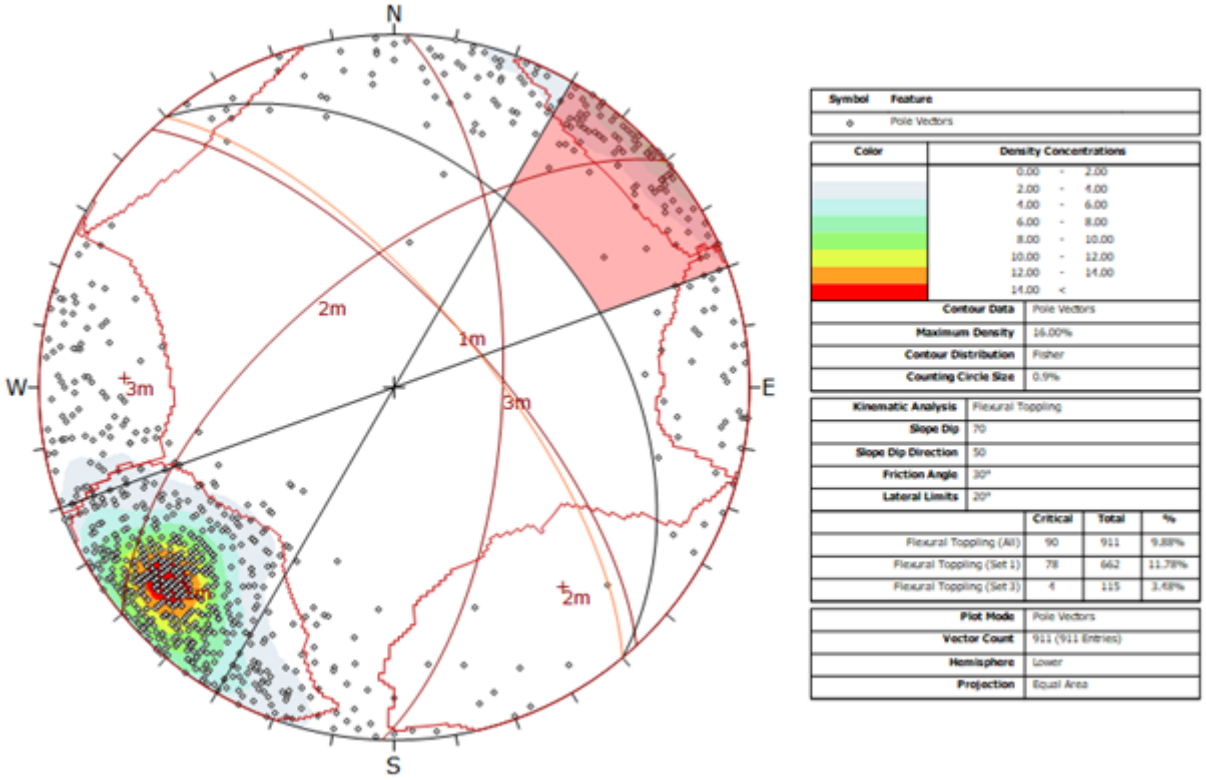

Figure 123 - Kinematic analysis of planes only of highwall 1 of case study 1 mine for flexural toppling on geostructural data carried out by SiroJoint. Orange cyclographic: slope orientation; black cyclographic: instability plane for flexural toppling (90 ° -θ_{slope} +φ; α_{slope}); pink section of spindle of sphere: area of the stereo plot with the poles of the planes affected by flexural toppling

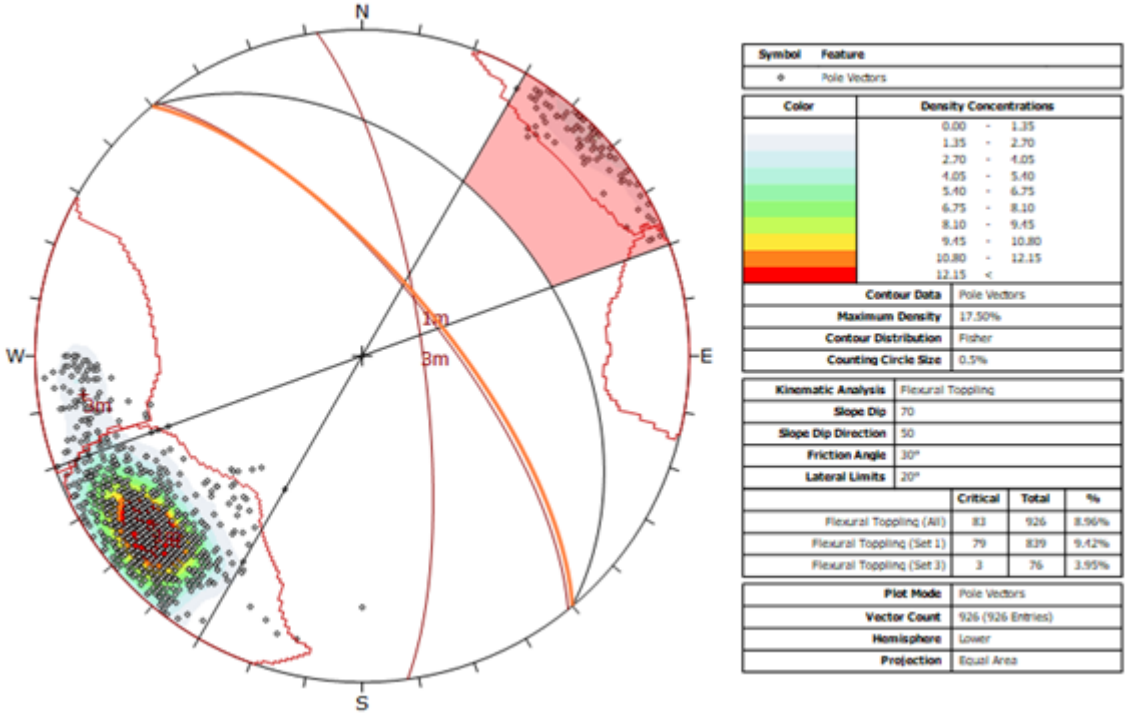

Figure 124 - Kinematic analysis of highwall 1 of case study 1 mine for flexural toppling on geostructural data carried out by I-Site Studio. Orange cyclographic: slope orientation; black cyclographic: instability plane for flexural toppling (90 ° -θ_{slope} +φ; α_{slope}); pink section of spindle of sphere: area of the stereo plot with the poles of the planes affected by flexural toppling

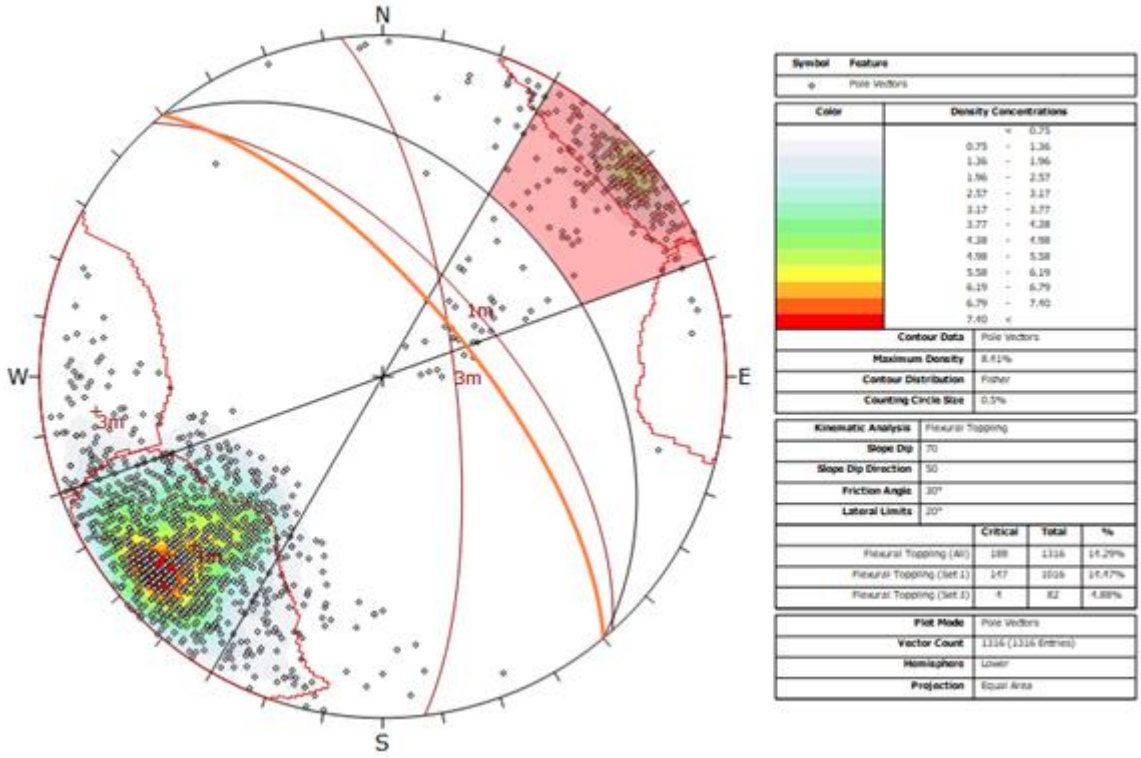

Figure 125 - Kinematic analysis of highwall 1 of case study 1 mine highwall for flexural toppling on geostructural data carried out by DiAna. Orange cyclographic: slope orientation; black cyclographic: instability plane for flexural toppling (90 ° -βslope +φ; αslope); pink section of spindle of sphere: area of the stereo plot with the poles of the planes affected by flexural toppling

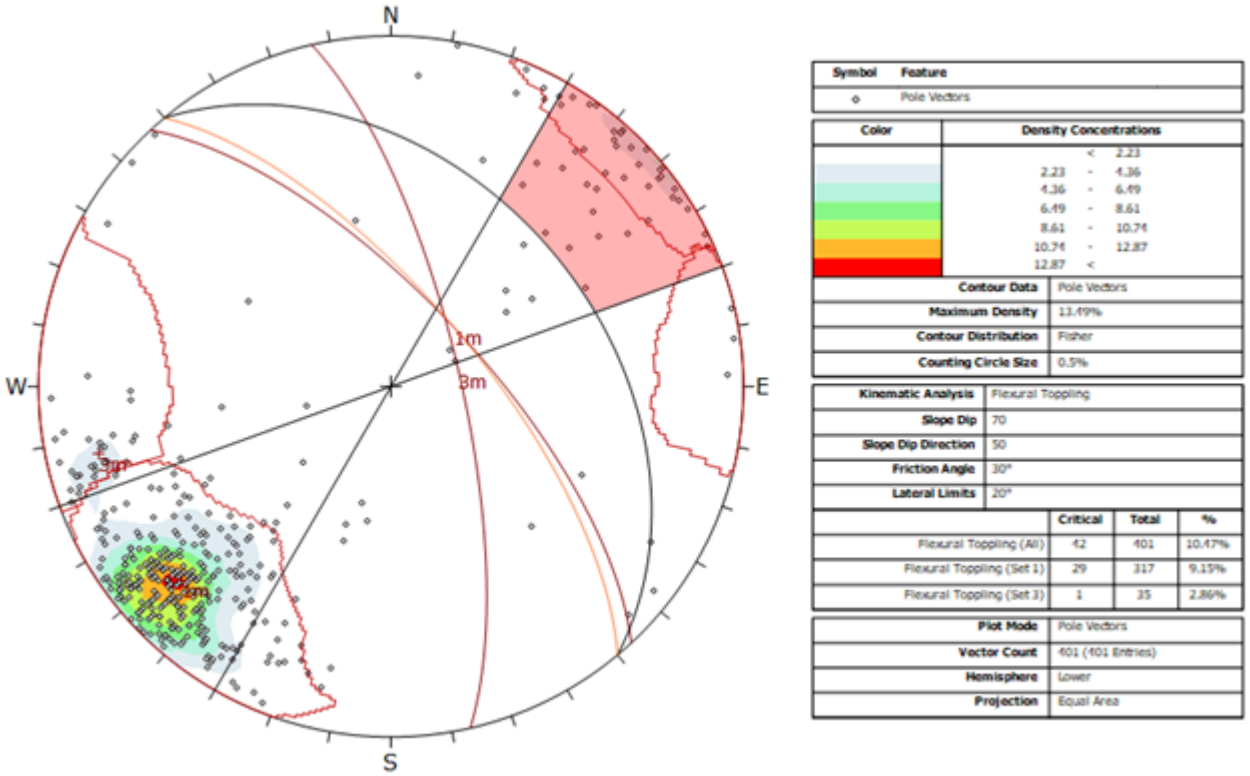

Figure 126 - Kinematic analysis of highwall 1 of case study 1 mine for flexural toppling on geostructural data carried out by DiAna. Orange cyclographic: slope orientation; black cyclographic: instability plane for flexural toppling (90 ° -β_{slope} +φ; α_{slope}); pink section of spindle of sphere: area of the stereo plot with the poles of the planes affected by flexural toppling

Results of 3D kinematic analysis performed by DiAna-K on highwall 1 shows that plane failure is the most relevant failure mechanism. Wedge failure affects most of the surface of the highwall, while block toppling and flexural toppling are extremely umprobable mechanism. Indeed, free fall affects overhanging areas (Figure 127).

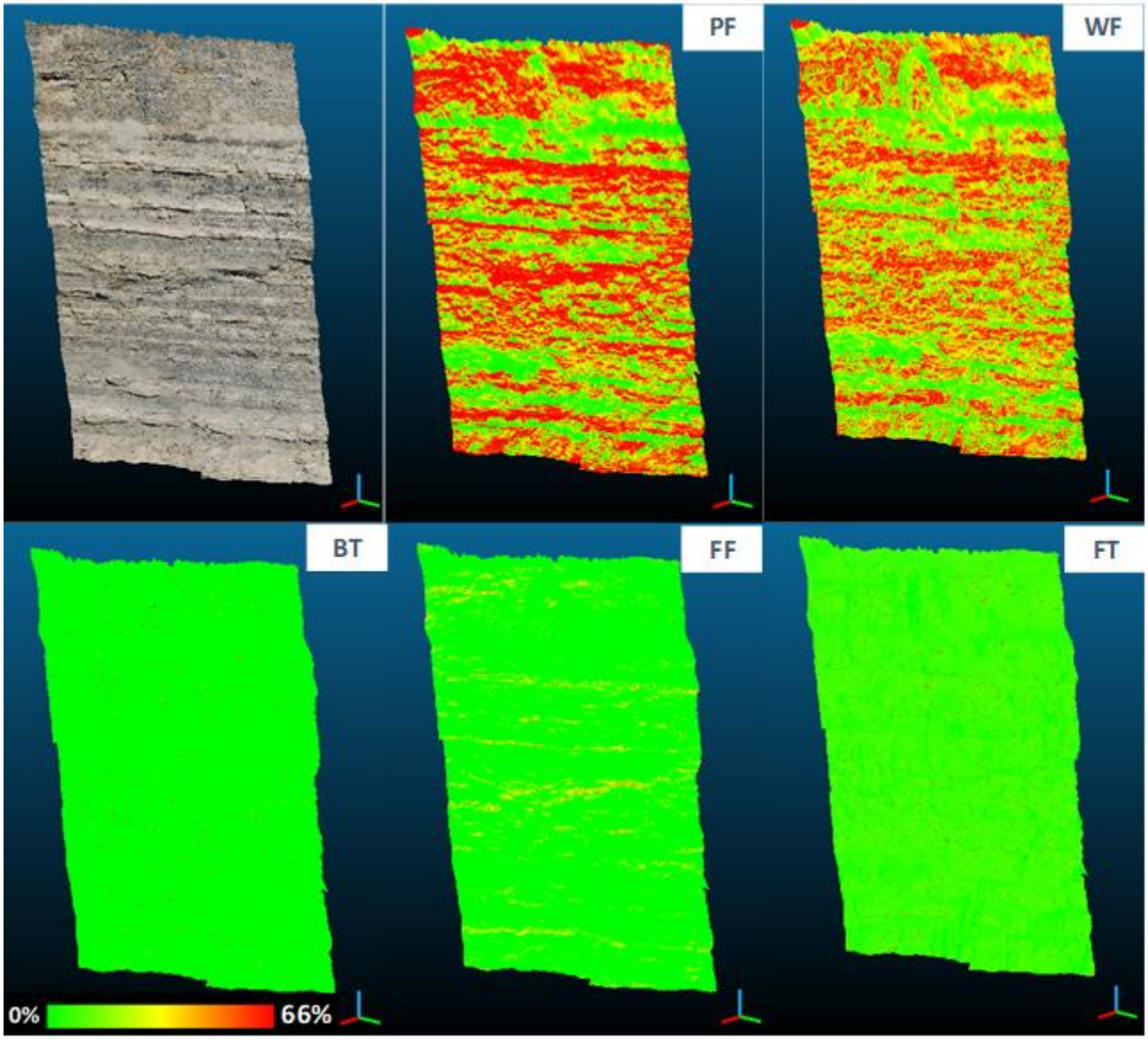

Figure 127 - Susceptibility maps for each failure mechanism, carried out from the kinematic analysis performed by DiAna-K on highwall 2 of case study 1 mine. WF: wedge failure; PF: plane failure; BT block toppling; FF: free fall; FT flexural toppling

Figure 128 shows the most probable failure mechanism. This map integrated the susceptibility maps of Figure 127, giving an overview about the distribution of the failure susceptibility on the highwall for each failure mechanism. Although generally speaking plane failure is the most probable failure mechanism, some areas are more prone to wedge failure; on particular, plane failure is more probable on parts of the slope the α of which is parallel to the α_{slope} (140°), while wedge failure is the more probable mechanism on parts of the slope the α of which is perpendicular to the α_{slope}. Routing of 90° the slope orientation of the stereoplots for kinematic analysis, in fact, no one set of discontinuities extracted by DiAna (Figure 97) is prone to plane failure, while 2m and 3m sets of discontinuities intersection is included in the wedge failure prone sector.

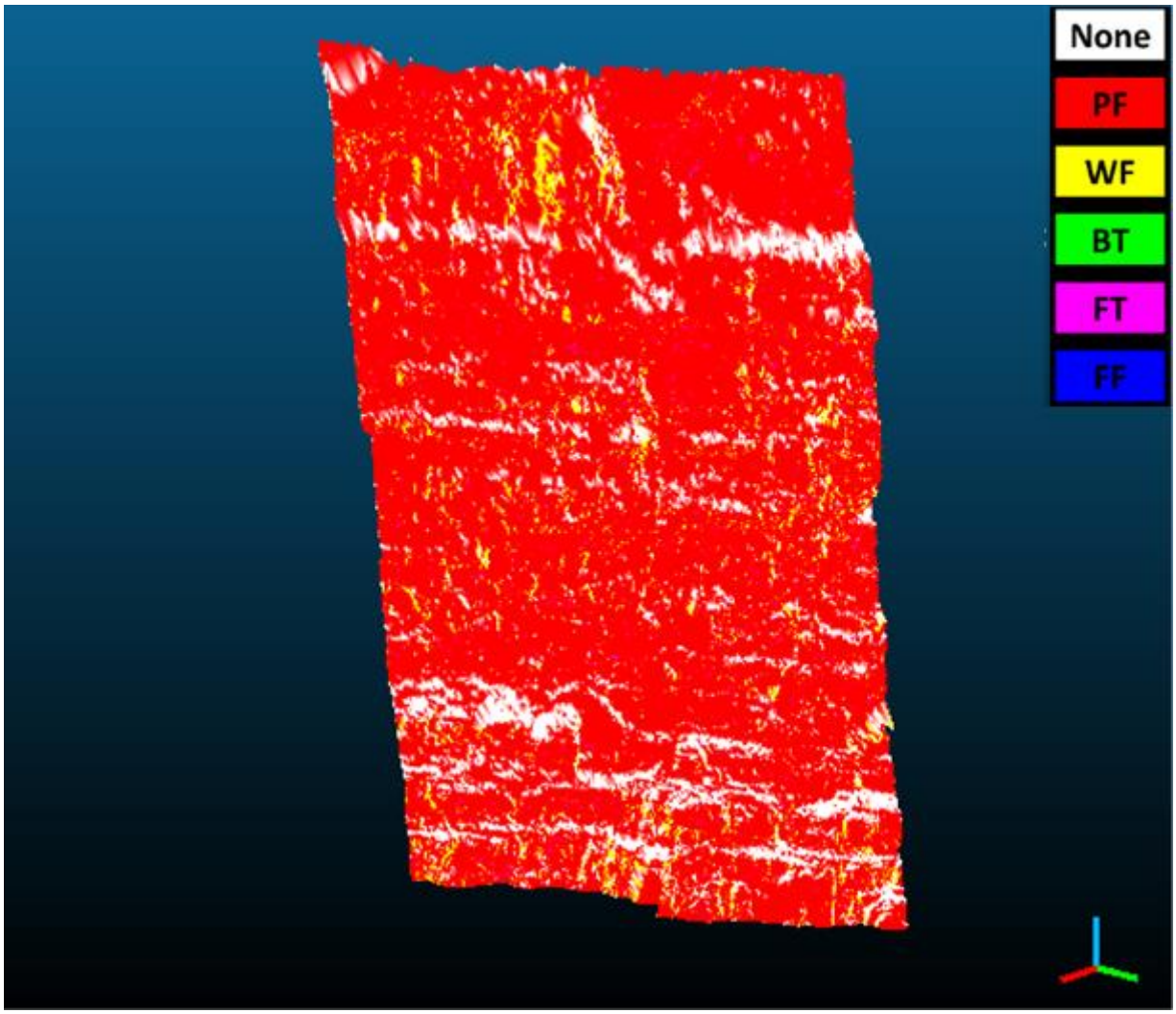

Figure 128 - Most probable failure mechanisms according to DiAna-K on highwall 1 of case study1 mine. PF: Plane Failure; WF: Wedge failure; BT: Block Toppling; FT: Flexural Toppling; FF: Free Fall

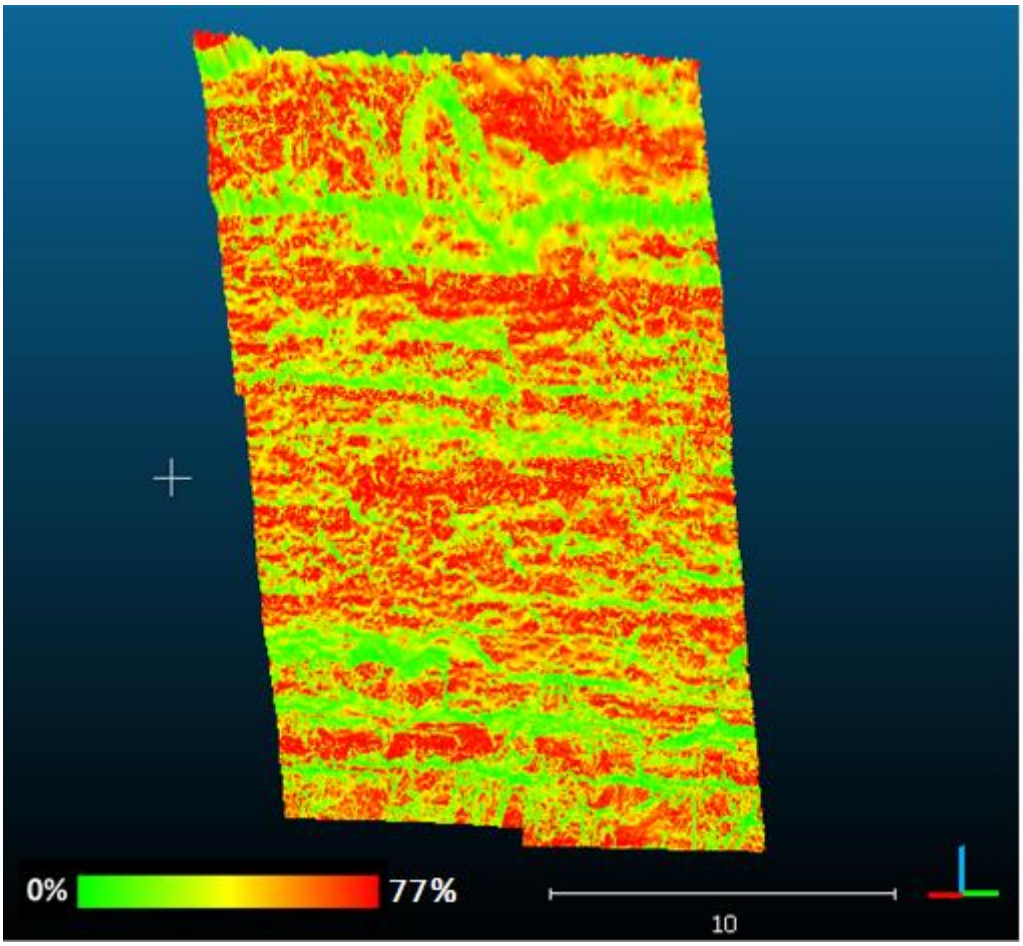

Figure 129 - Susceptibility value map for highwall 1 of case study 1 mine for all failure mechanism

6.2.2. Kinematic analysis of highwall 2

As for highwall 1, on highwall 2 have been carried out the 2D kinematic analysis with on the stereoplots of the discontinuities extracted by SiroJoint, I-Site Studio, DiAna, and facets, and the 3D kinematic analysis with DiAna-K.

Plane failure is a feasible failure mechanism, whatever is the code used for discontinuities extraction. SiroJoint results show that plane failure is strongly related on the presence of 3m set of discontinuities because α_{disc} and β_{disc} are included in the critical area. 3m set of discontinuities so represents a set that satisfies for plane failure. 200 discontinuities on 1567 (12.76 %) are prone to plane failure (pink area in Figure 130). These discontinuities are moreover related to 3m set of discontinuities (188/200); the remnant ones (12/200) are not related to any other set. These discontinuities, related to the sliding plane, are mainly constituted by planes (197/200; Figure 131); kinematic analysis carried out on planes only (Figure 131) shows that considering planes only instead of both planes and traces (Figure 130), the percentage of critical discontinuities is higher (18.69 % vs 12.76 %). Figure 130 shows that the highest concentration (3.25 poles/deg^2) of poles extracted by SiroJoint is located close to critical area for plane failure.

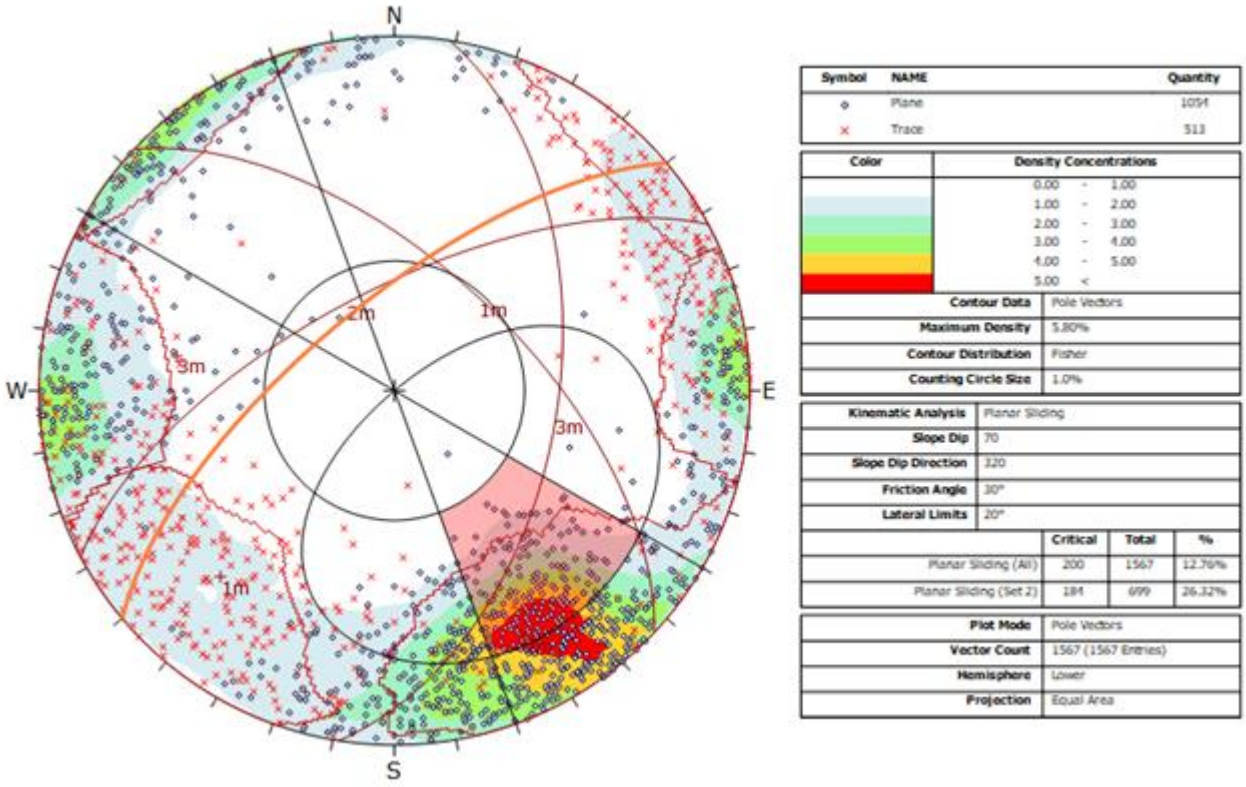

Figure 130 - Kinematic analysis of planes and traces of highwall 2 of case study 1 mine for plane failure on geostructural data carried out by SiroJoint. Orange cyclographic: slope orientation; pink area: area of the stereo plot with intersection of planes coupling affected by plane failure

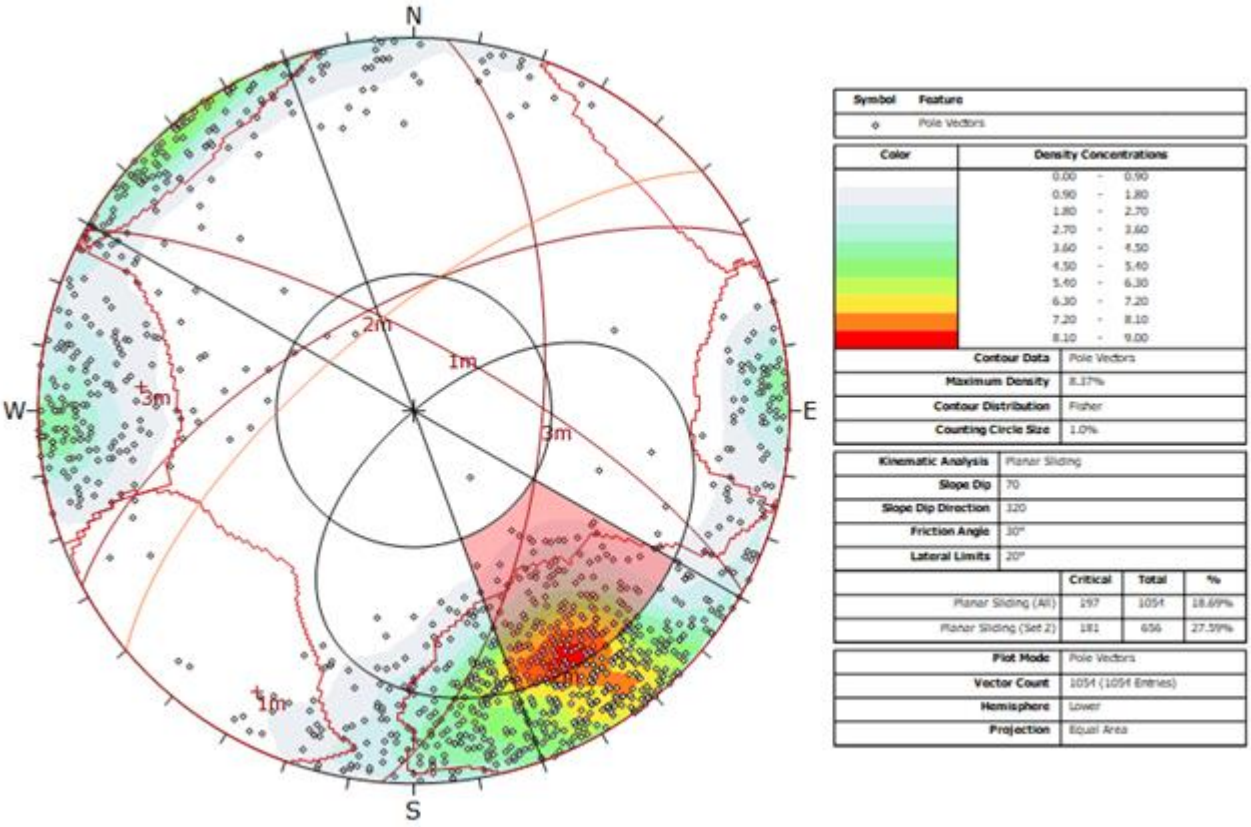

Figure 131 - Kinematic analysis of planes only of highwall 2 of case study 1 mine for wedge failure on geostructural data carried out by SiroJoint. Orange cyclographic: slope orientation; pink area: area of the stereo plot with intersection of planes coupling affected by plane failure

Kinematic analysis carried out on discontinuities extracted by I-Site Studio has revealed that plane failure involves 101/713 discontinuities (Figure 132), all of them are related to 2m sets of discontinuities. Similarly, the stereo plot of the discontinuities extracted by SiroJoint (Figure 130), the highest discontinuities concentration (22.64 poles/deg^2) is located close to envelop of the discontinuities coming out from the slope. Kinematic analysis carried out on discontinuities extracted by DiAna has revealed that plane failure involves 163/960 discontinuities (16.98 %) (Figure 133), most of them (145/163) are related to 2m sets of discontinuities. The remnant 18 are not related to any set.
The stereoplot of the discontinuities extracted by Facets has revealed that 128/831 discontinuities (15.40 %) are prone to plane failure (Figure 134), most of them are related to 2m sets of discontinuities (121/128). The remnant ones (8/129) are not related to any set.
Also wedge failure represents a suitable failure mechanism for highwall 2. The percentage of critical intersections ranges from 17.09 % on the stereoplot of the discontinuities extracted by I-Site Studio, to 30.98 % on the stereoplot of the discontinuities extracted by SiroJoint.
The kinematic analysis carried out with the discontinuities extracted by SiroJoint shows, in fact, that the intersection among 1m and 2m sets of discontinuities is close to the area critical for wedge failure (Figure 135). Results of the kinematic analysis do not greatly change considering planes only: the percentage of critical intersection is similar (30.98 % vs 31.36 %) (Figure 136). This suggests that the sets of discontinuities almost entirely constituted by traces (1m) is responsible of wedge failure as the other sets as a whole.

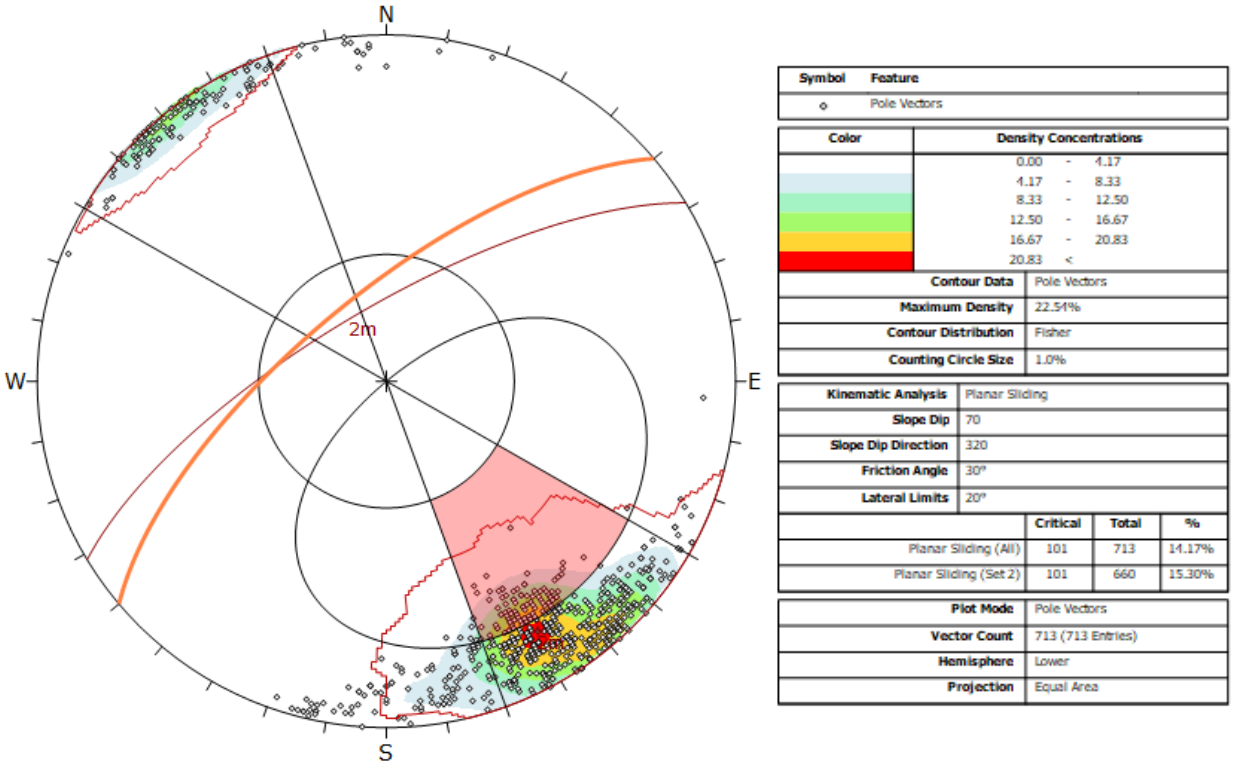

Figure 132 - Kinematic analysis of highwall 2 of case study 1 mine for plane failure on geostructural data carried out by I-Site Studio. Orange cyclographic: slope orientation; pink area: area of the stereo plot with intersection of planes coupling affected by plane failure

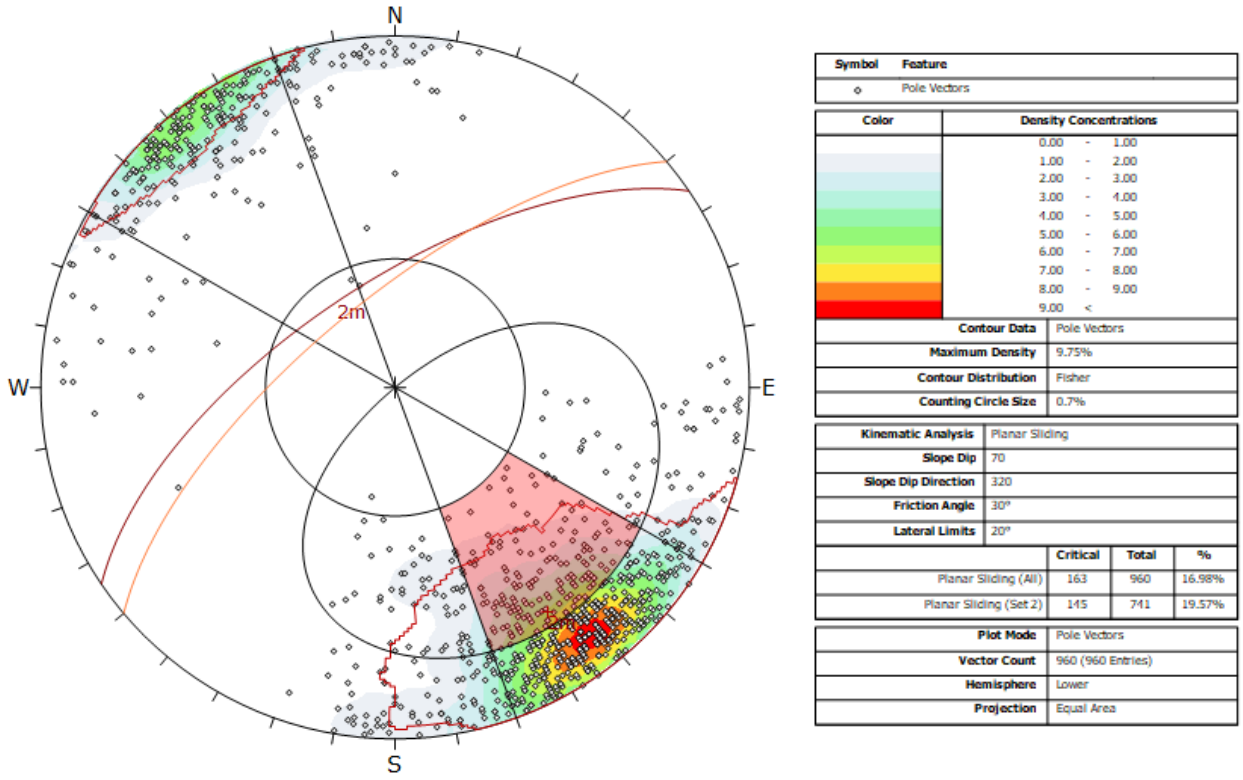

Symbol	Feature
◇	Pole Vectors

Color	Density Concentrations
	0.00 - 1.00
	1.00 - 2.00
	2.00 - 3.00
	3.00 - 4.00
	4.00 - 5.00
	5.00 - 6.00
	6.00 - 7.00
	7.00 - 8.00
	8.00 - 9.00
	9.00 <

Contour Data	Pole Vectors
Maximum Density	9.75%
Contour Distribution	Fisher
Counting Circle Size	0.7%

Kinematic Analysis	Planar Sliding
Slope Dip	70
Slope Dip Direction	320
Friction Angle	30°
Lateral Limits	20°

	Critical	Total	%
Planar Sliding (All)	163	960	16.98%
Planar Sliding (Set 2)	145	741	19.57%

Plot Mode	Pole Vectors
Vector Count	960 (960 Entries)
Hemisphere	Lower
Projection	Equal Area

Figure 133 - Kinematic analysis of highwall 2 of case study 1 mine for plane failure on geostructural data carried out by DiAna. Orange cyclographic: slope orientation; pink area: area of the stereo plot with intersection of planes coupling affected by plane failure

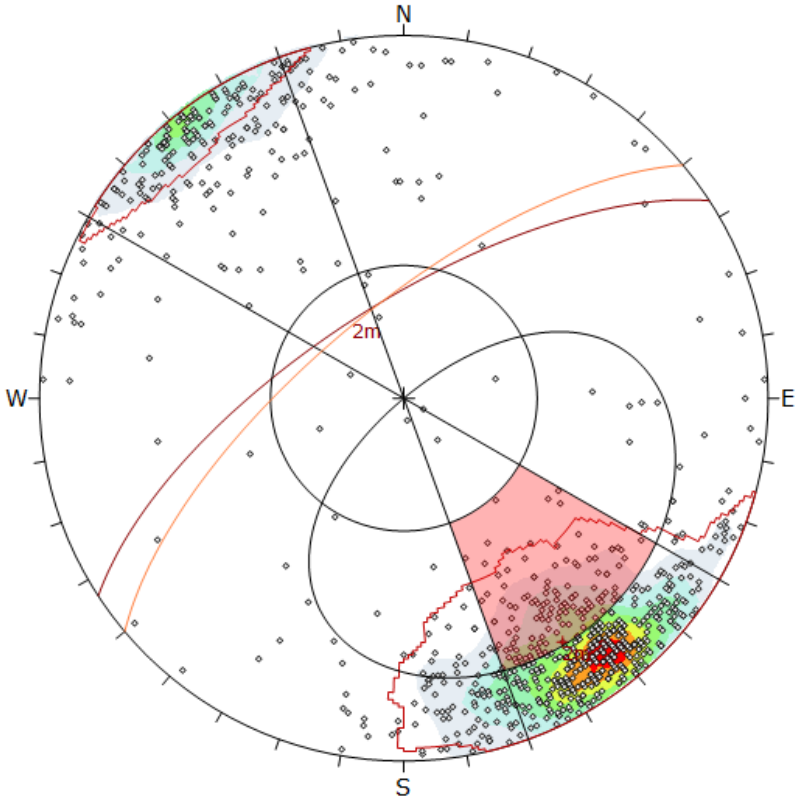

Symbol	Feature
◇	Pole Vectors

Color	Density Concentrations
	0.00 - 1.20
	1.20 - 2.40
	2.40 - 3.60
	3.60 - 4.80
	4.80 - 6.00
	6.00 - 7.20
	7.20 - 8.40
	8.40 - 9.60

Contour Data	Pole Vectors
Maximum Density	9.34%
Contour Distribution	Fisher
Counting Circle Size	0.5%

Kinematic Analysis	Planar Sliding
Slope Dip	70
Slope Dip Direction	320
Friction Angle	30°
Lateral Limits	20°

	Critical	Total	%
Planar Sliding (All)	128	831	15.40%
Planar Sliding (Set 2)	121	659	18.36%

Plot Mode	Pole Vectors
Vector Count	831 (831 Entries)
Hemisphere	Lower
Projection	Equal Area

Figure 134 - Kinematic analysis of highwall 2 of case study 1 mine highwall for plane failure on geostructural data carried out by Facets plug-in of CloudCompare. Orange cyclographic: slope orientation; pink area: area of the stereo plot with intersection of planes coupling affected by plane failure

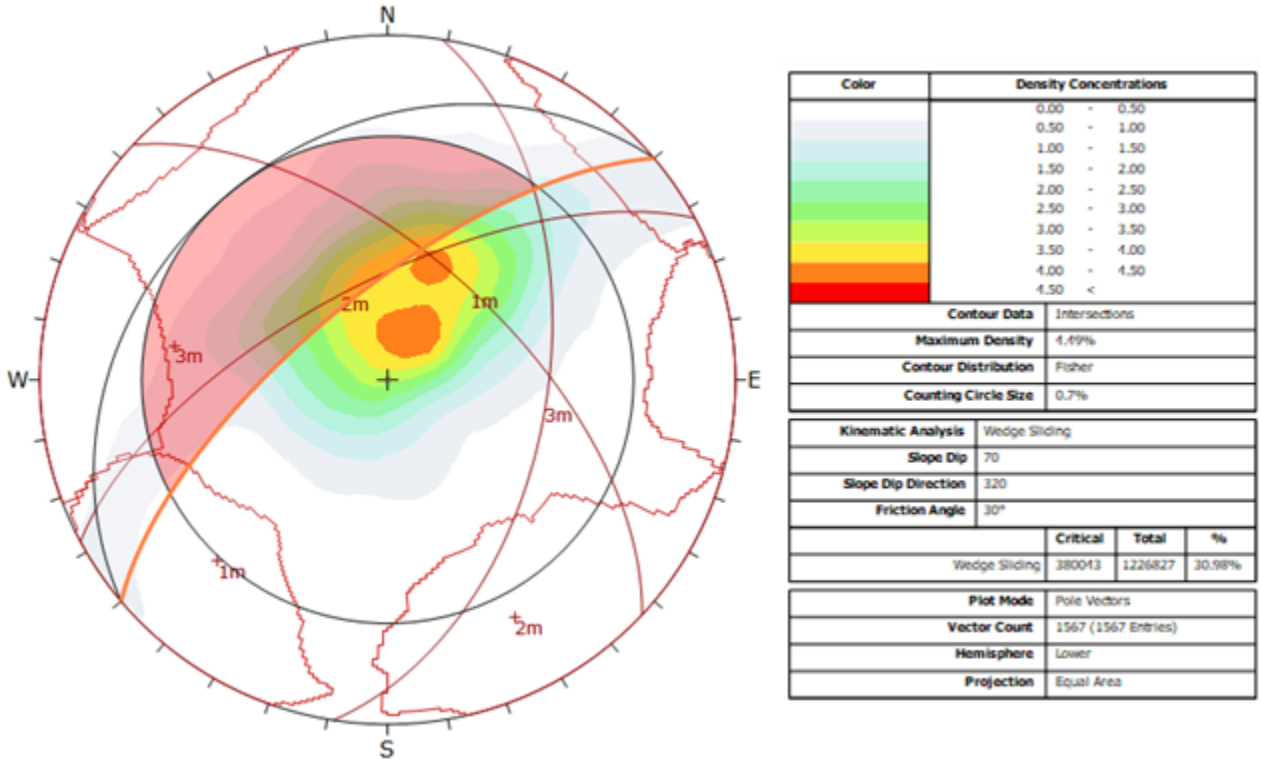

Figure 135 - Kinematic analysis of planes and traces of highwall 2 of case study 1 mine highwall for wedge failure on geostructural data carried out by SiroJoint. Orange cyclographic: slope orientation; pink spherical spindle: area of the stereo plot with intersection of planes coupling affected by wedge failure

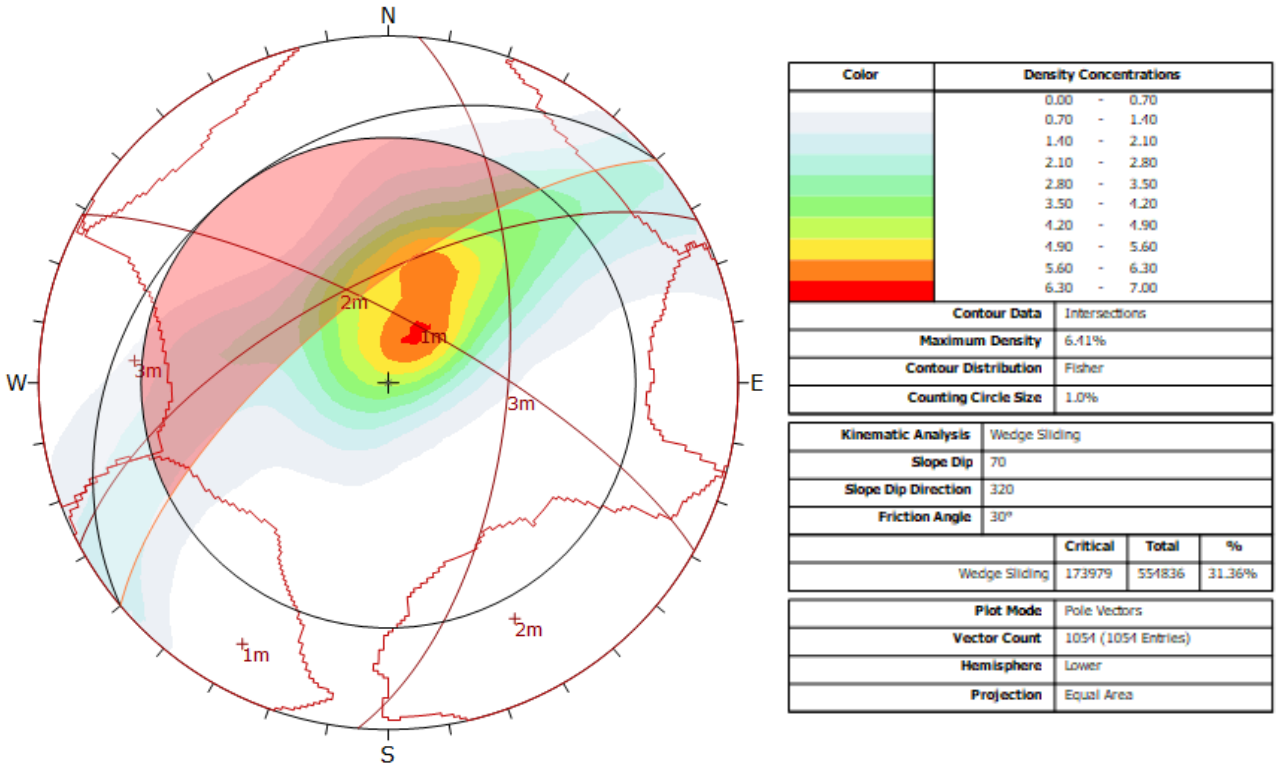

Figure 136 - Kinematic analysis of planes only of highwall 2 of case study 1 mine highwall for wedge failure on geostructural data carried out by SiroJoint. Orange cyclographic: slope orientation; pink spherical spindle: area of the stereo plot with intersection of planes coupling affected by wedge failure

The kinematic analysis carried out with I-Site Studio output data shows that overall 17.09 % of the intersections (43332) intersect the wedge failure prone area. Similar values involve the stereoplot of the discontinuities extracted by DiAna and by Facets; overall, 21.70 % of the intersections extracted by DiAna (99856) is included into the most critical area (Figure 138), while the percentage of the intersections of the discontinuities extracted by Facets prone to wedge failure is equal to 18.34 % (63230) (Figure 139).

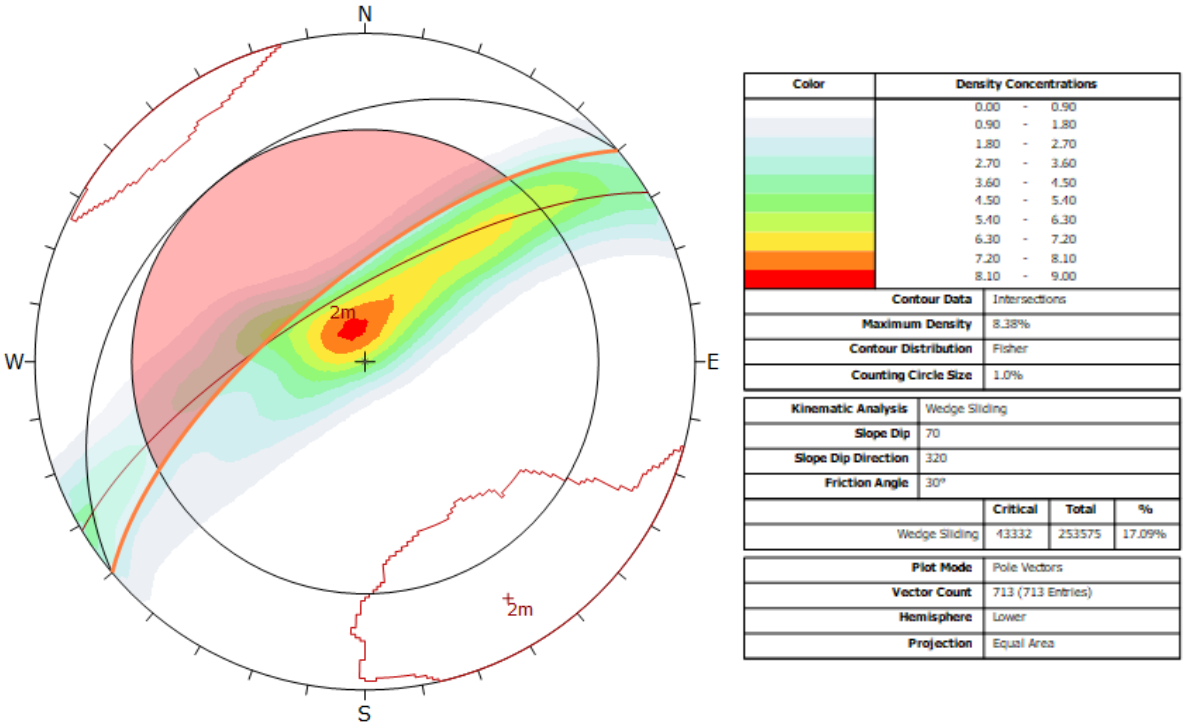

Color	Density Concentrations
	0.00 - 0.90
	0.90 - 1.80
	1.80 - 2.70
	2.70 - 3.60
	3.60 - 4.50
	4.50 - 5.40
	5.40 - 6.30
	6.30 - 7.20
	7.20 - 8.10
	8.10 - 9.00

Contour Data	Intersections
Maximum Density	8.38%
Contour Distribution	Fisher
Counting Circle Size	1.0%

Kinematic Analysis	Wedge Sliding
Slope Dip	70
Slope Dip Direction	320
Friction Angle	30°

	Critical	Total	%
Wedge Sliding	43332	253575	17.09%

Plot Mode	Pole Vectors
Vector Count	713 (713 Entries)
Hemisphere	Lower
Projection	Equal Area

Figure 137 - Kinematic analysis of highwall 2 of case study 1 mine highwall for wedge failure on geostructural data carried out by I-Site Studio. Orange cyclographic: slope orientation; pink spherical spindle: area of the stereo plot with intersection of planes coupling affected by wedge failure

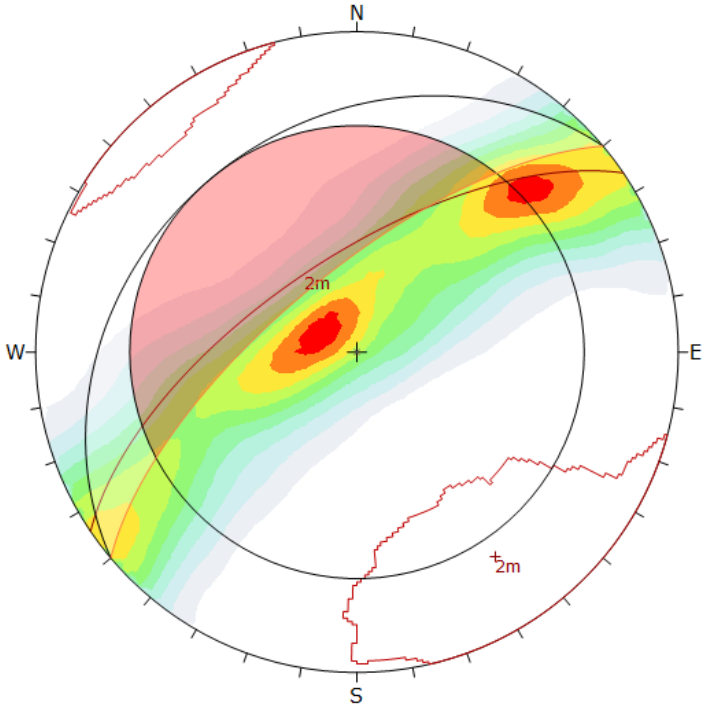

Color	Density Concentrations
	0.00 - 0.50
	0.50 - 1.00
	1.00 - 1.50
	1.50 - 2.00
	2.00 - 2.50
	2.50 - 3.00
	3.00 - 3.50
	3.50 - 4.00
	4.00 - 4.50
	4.50 - 5.00

Contour Data	Intersections
Maximum Density	4.81%
Contour Distribution	Fisher
Counting Circle Size	1.0%

Kinematic Analysis	Wedge Sliding
Slope Dip	70
Slope Dip Direction	320
Friction Angle	30°

	Critical	Total	%
Wedge Sliding	99856	460181	21.70%

Plot Mode	Pole Vectors
Vector Count	960 (960 Entries)
Hemisphere	Lower
Projection	Equal Area

Figure 138 - Kinematic analysis of highwall 2 of case study 1 for wedge failure on geostructural data carried out by DiAna. Orange cyclographic: slope orientation; pink spherical spindle: area of the stereo plot with intersection of planes coupling affected by wedge failure

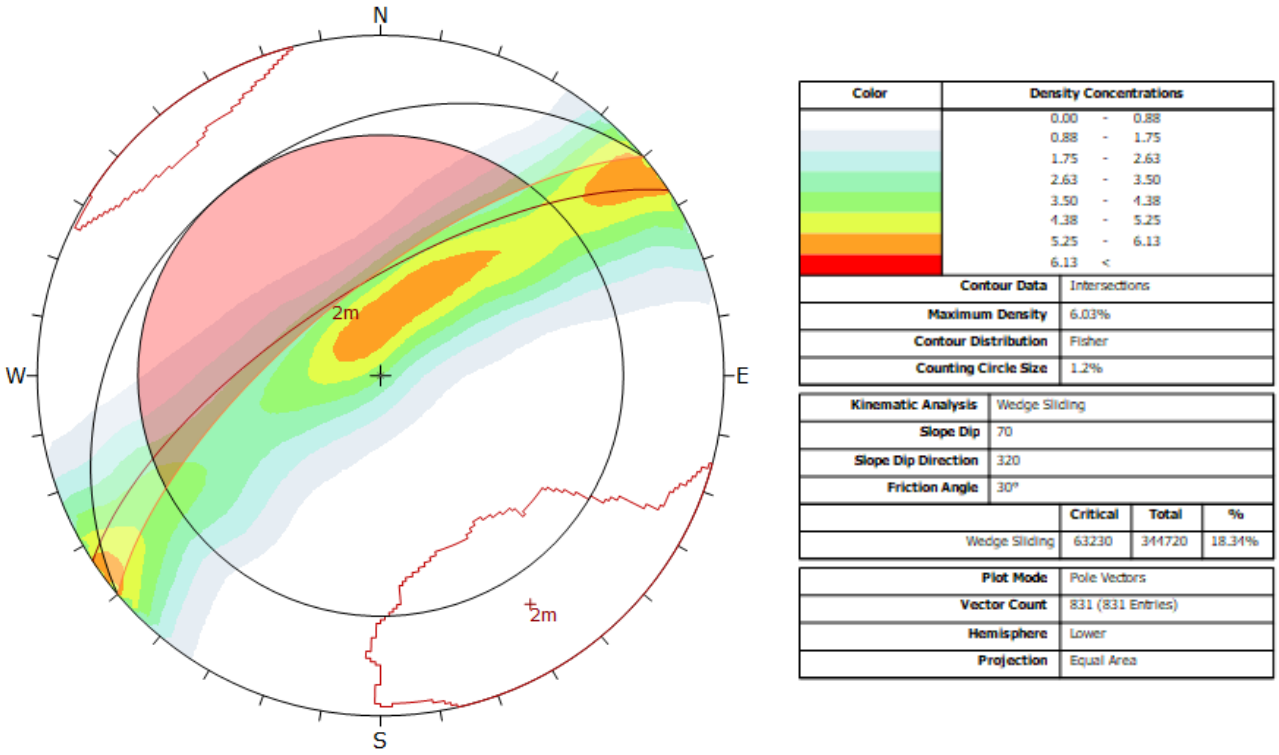

Color	Density Concentrations
	0.00 - 0.88
	0.88 - 1.75
	1.75 - 2.63
	2.63 - 3.50
	3.50 - 4.38
	4.38 - 5.25
	5.25 - 6.13
	6.13 <

Contour Data	Intersections
Maximum Density	6.03%
Contour Distribution	Fisher
Counting Circle Size	1.2%

Kinematic Analysis	Wedge Sliding		
Slope Dip	70		
Slope Dip Direction	320		
Friction Angle	30°		
	Critical	Total	%
Wedge Sliding	63230	344720	18.34%

Plot Mode	Pole Vectors
Vector Count	831 (831 Entries)
Hemisphere	Lower
Projection	Equal Area

Figure 139 - Kinematic analysis of highwall 2 oh case study 1 mine highwall for wedge failure on geostructural data carried out by Facets plug-in of CloudCompare. Orange cyclographic: slope orientation; pink spherical spindle: area of the stereo plot with intersection of planes coupling affected by wedge failure

The kinematic analysis has shown that block toppling is not a probable failure mechanism for highwall 2: the percentage of critical intersections is very low, ranging from 0.34 %, using the discontinuities extracted by I-Site Studio, to 3.40 % using the discontinuities extracted by SiroJoint.
As regarding the discontinuities extracted by SiroJoint, the low percentage of intersections critical for block toppling decreases from 3.40 % to 1.33 % in case kinematical analysis is carried out on planes only (Figure 141); this means that traces, that are mostly related to 1m set of discontinuities and the α of which is mostly perpendicular to α_{slope}, are more critical for block toppling than planes. 217 discontinuities on overall 1567 discontinuities extracted with SiroJoint are suitable as basal plane. 211/217 of these discontinuities are constituted by planes and 199/217 are related to 2m set of discontinuities. 13.85 % of the discontinuities are indeed suitable as basal plane; of course, similarly to the plane failure (Figure 130) these discontinuities are mostly related to 2m set.
Block toppling (Figure 142) involves 0.34 % only of (872/253575) of the intersections extracted by I-Site Studio. 113/713 discontinuities are suitable as basal plane.

Similar considerations can be made on the results carried out on the discontinuities extracted by DiAna. The kinematic analysis of the stereoplot shows that block toppling is an improbable failure mechanism and that 0.73 % of the intersections only are critical for this failure mechanism (Figure 143); as regarding the basal plane, 175/960 discontinuities are suitable as sliding surface.

Facets output data show that 0.76 % of the intersections are critical for this failure mechanism (Figure 144) and that 142/831 planes are suitable as basal plane. In this case too, most of the basal planes are stepper than ϕ value, so block toppling is an improbable mechanism.

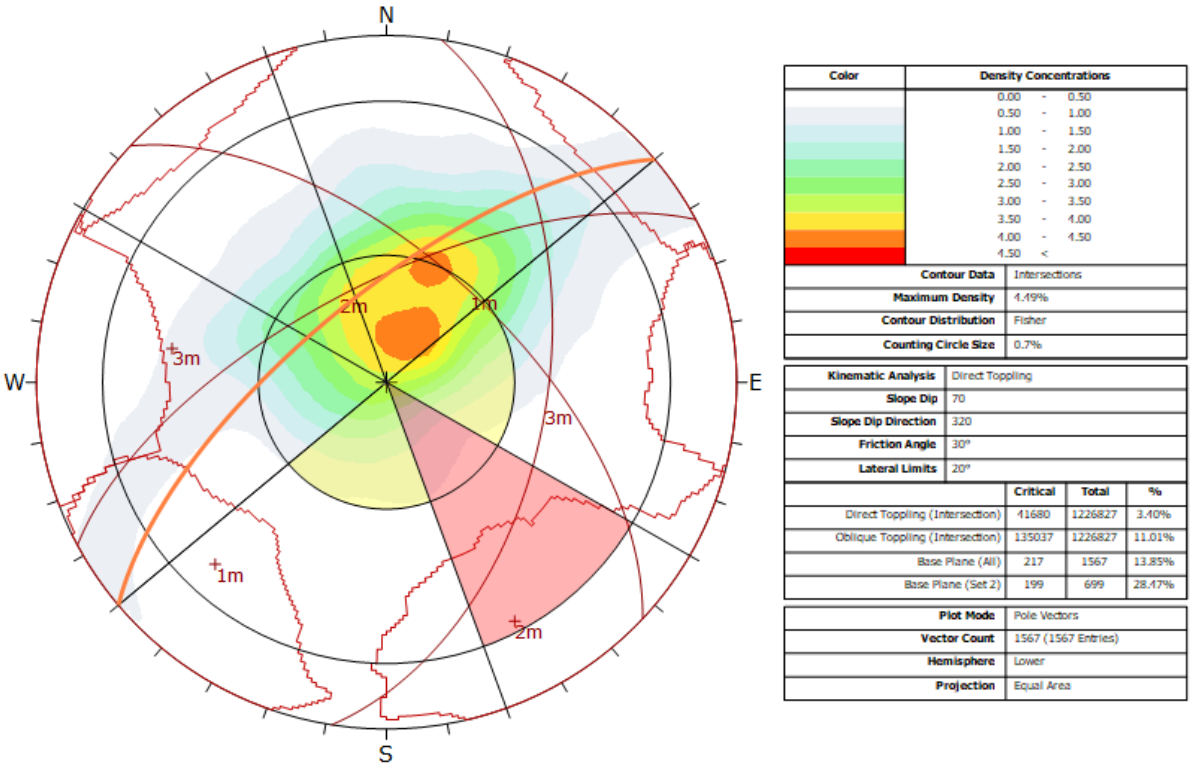

Color	Density Concentrations
	0.00 - 0.50
	0.50 - 1.00
	1.00 - 1.50
	1.50 - 2.00
	2.00 - 2.50
	2.50 - 3.00
	3.00 - 3.50
	3.50 - 4.00
	4.00 - 4.50
	4.50 <

Contour Data	Intersections
Maximum Density	4.49%
Contour Distribution	Fisher
Counting Circle Size	0.7%

Kinematic Analysis	Direct Toppling
Slope Dip	70
Slope Dip Direction	320
Friction Angle	30°
Lateral Limits	20°

	Critical	Total	%
Direct Toppling (Intersection)	41680	1226827	3.40%
Oblique Toppling (Intersection)	135037	1226827	11.01%
Base Plane (All)	217	1567	13.85%
Base Plane (Set 2)	199	699	28.47%

Plot Mode	Pole Vectors
Vector Count	1567 (1567 Entries)
Hemisphere	Lower
Projection	Equal Area

Figure 140 - Kinematic analysis of planes and traces of highwall 2 of case study 1 mine for block toppling on geostructural data carried out by SiroJoint. Orange cyclographic: slope orientation; orange circumference: set of poles of the planes with a β lower than the β_{slope} (74° for this case study); pink section of circumference: area of the stereo plot with intersection of planes coupling affected by block toppling in case of β_{slope} <90 ° - φ; yellow sections of circumference: extension of the areas of the stereo plot with intersection of planes coupling affected by block toppling in case of dep slope (β_{slope} > 90 ° - φ)

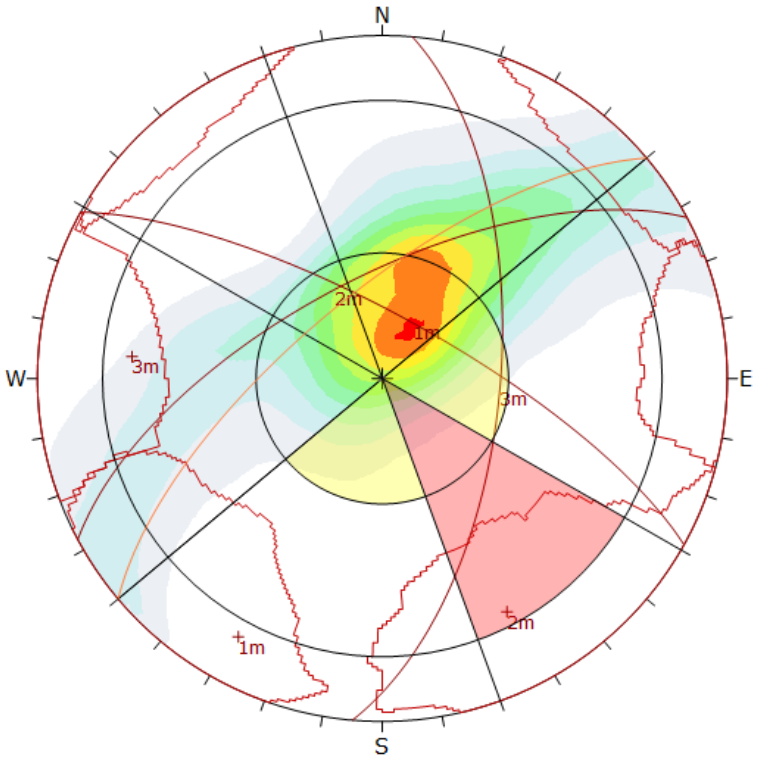

Color	Density Concentrations
	0.00 - 0.70
	0.70 - 1.40
	1.40 - 2.10
	2.10 - 2.80
	2.80 - 3.50
	3.50 - 4.20
	4.20 - 4.90
	4.90 - 5.60
	5.60 - 6.30
	6.30 - 7.00

Contour Data	Intersections
Maximum Density	6.41%
Contour Distribution	Fisher
Counting Circle Size	1.0%

Kinematic Analysis	Direct Toppling
Slope Dip	70
Slope Dip Direction	320
Friction Angle	30°
Lateral Limits	20°

	Critical	Total	%
Direct Toppling (Intersection)	7400	554836	1.33%
Oblique Toppling (Intersection)	52258	554836	9.42%
Base Plane (All)	211	1054	20.02%
Base Plane (Set 2)	194	656	29.57%

Plot Mode	Pole Vectors
Vector Count	1054 (1054 Entries)
Hemisphere	Lower
Projection	Equal Area

Figure 141 - Kinematic analysis of planes only of highwall 2 of case study 1 mine highwall for block toppling on geostructural data carried out by SiroJoint. Orange cyclographic: slope orientation; orange circumference: set of poles of the planes with a β lower than the β_{slope} (74° for this case study); pink section of circumference: area of the stereo plot with intersection of planes coupling affected by block toppling in case of β_{slope} <90 ° - φ; yellow sections of circumference: extension of the areas of the stereo plot with intersection of planes coupling affected by block toppling in case of dep slope (β_{slope} > 90 ° - φ)

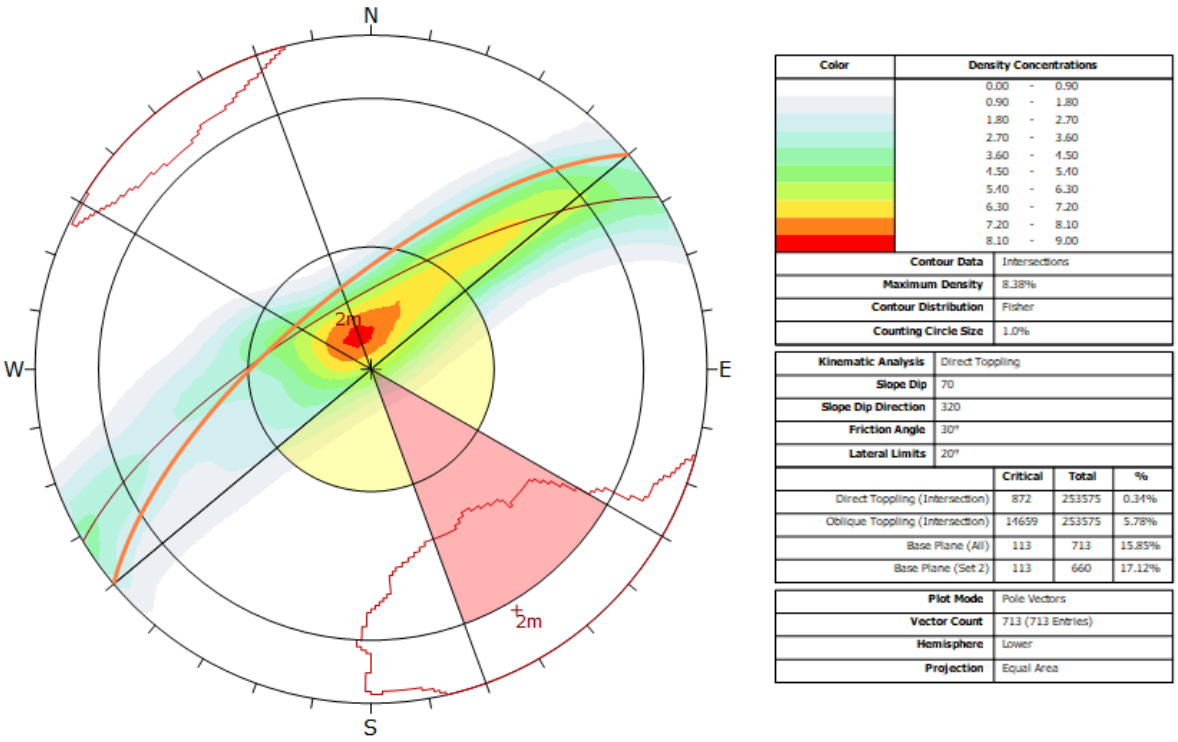

Color	Density Concentrations
	0.00 - 0.90
	0.90 - 1.80
	1.80 - 2.70
	2.70 - 3.60
	3.60 - 4.50
	4.50 - 5.40
	5.40 - 6.30
	6.30 - 7.20
	7.20 - 8.10
	8.10 - 9.00

Contour Data	Intersections
Maximum Density	8.38%
Contour Distribution	Fisher
Counting Circle Size	1.0%

Kinematic Analysis	Direct Toppling
Slope Dip	70
Slope Dip Direction	320
Friction Angle	30°
Lateral Limits	20°

	Critical	Total	%
Direct Toppling (Intersection)	872	253575	0.34%
Oblique Toppling (Intersection)	14659	253575	5.78%
Base Plane (All)	113	713	15.85%
Base Plane (Set 2)	113	660	17.12%

Plot Mode	Pole Vectors
Vector Count	713 (713 Entries)
Hemisphere	Lower
Projection	Equal Area

Figure 142 - Kinematic analysis of highwall 2 of case study 1 mine for block toppling on geostructural data carried out by I-Site Studio. Orange cyclographic: slope orientation; orange circumference: set of poles of the planes with a β lower than the β_{slope} (74° for this case study); pink section of circumference: area of the stereo plot with intersection of planes coupling affected by block toppling in case of β_{slope} <90 ° - φ; yellow sections of circumference: extension of the areas of the stereo plot with intersection of planes coupling affected by block toppling in case of dep slope (β_{slope} > 90 ° - φ)

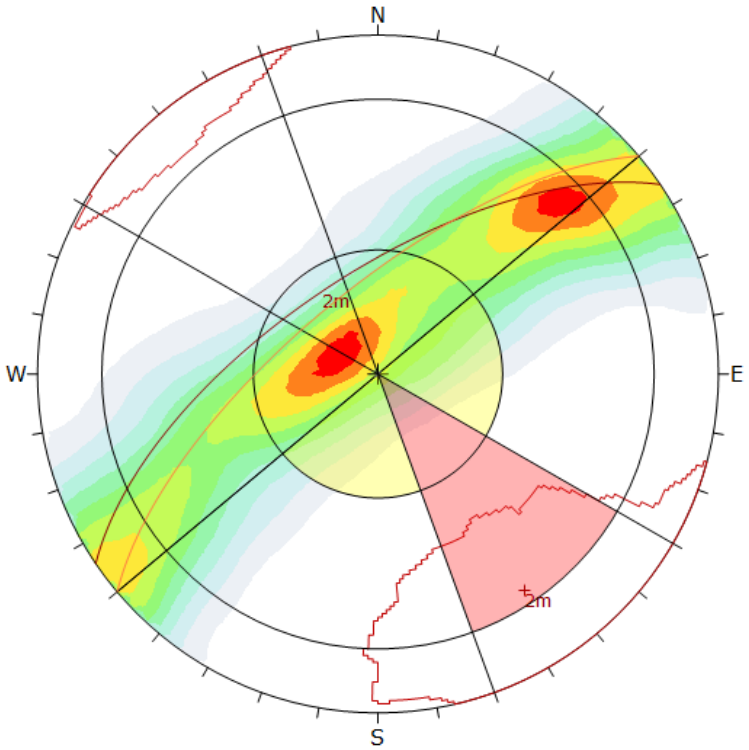

Symbol	Feature
◇	Pole Vectors

Color	Density Concentrations
	0.00 - 0.50
	0.50 - 1.00
	1.00 - 1.50
	1.50 - 2.00
	2.00 - 2.50
	2.50 - 3.00
	3.00 - 3.50
	3.50 - 4.00
	4.00 - 4.50
	4.50 - 5.00

Contour Data	Intersections
Maximum Density	4.81%
Contour Distribution	Fisher
Counting Circle Size	1.0%

Kinematic Analysis	Direct Toppling
Slope Dip	70
Slope Dip Direction	320
Friction Angle	30°
Lateral Limits	20°

	Critical	Total	%
Direct Toppling (Intersection)	3356	460181	0.73%
Oblique Toppling (Intersection)	31036	460181	6.74%
Base Plane (All)	175	960	18.23%
Base Plane (Set 2)	156	741	21.05%

Plot Mode	Pole Vectors
Vector Count	960 (960 Entries)
Hemisphere	Lower
Projection	Equal Area

Figure 143 - Kinematic analysis of highwall 2 of case study 1 mine for block toppling on geostructural data carried out by DiAna. Orange cyclographic: slope orientation; orange circumference: set of poles of the planes with a β lower than the β_{slope} (74° for this case study); pink section of circumference: area of the stereo plot with intersection of planes coupling affected by block toppling in case of β_{slope} <90 ° - φ; yellow sections of circumference: extension of the areas of the stereo plot with intersection of planes coupling affected by block toppling in case of dep slope (β_{slope} > 90 ° - φ)

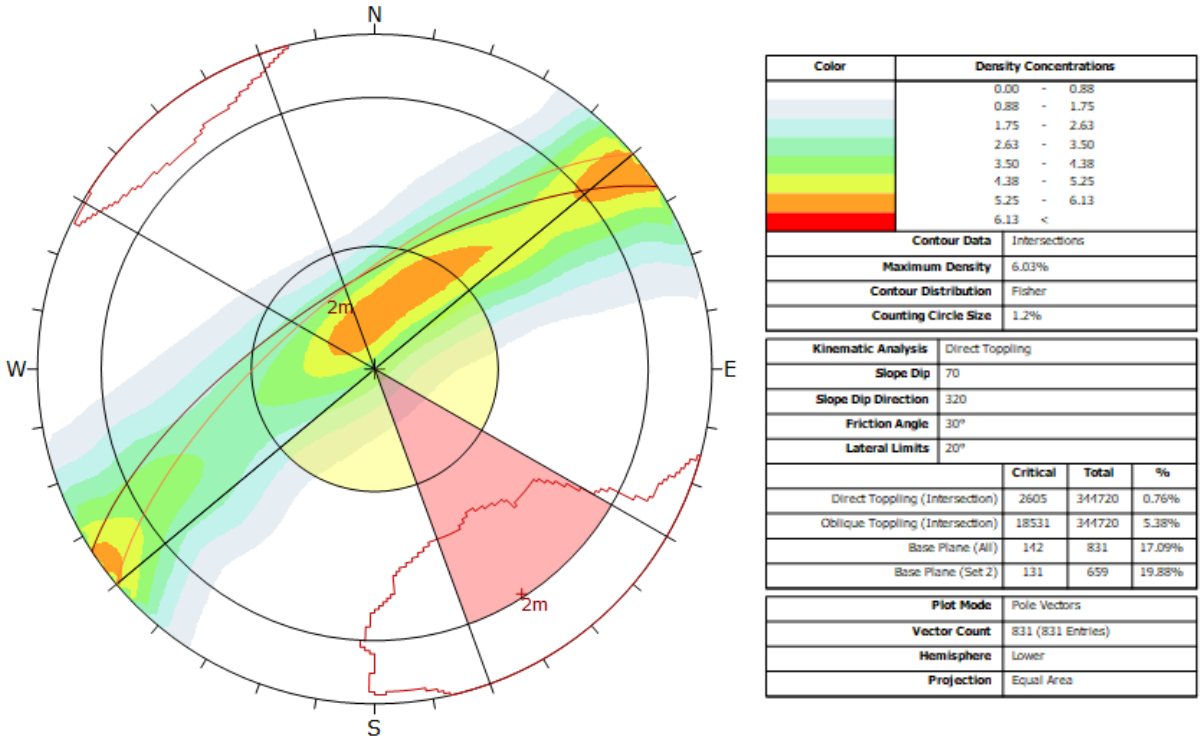

Color	Density Concentrations
	0.00 - 0.88
	0.88 - 1.75
	1.75 - 2.63
	2.63 - 3.50
	3.50 - 4.38
	4.38 - 5.25
	5.25 - 6.13
	6.13 <

Contour Data	Intersections
Maximum Density	6.03%
Contour Distribution	Fisher
Counting Circle Size	1.2%

Kinematic Analysis	Direct Toppling
Slope Dip	70
Slope Dip Direction	320
Friction Angle	30°
Lateral Limits	20°

	Critical	Total	%
Direct Toppling (Intersection)	2605	344720	0.76%
Oblique Toppling (Intersection)	18531	344720	5.38%
Base Plane (All)	142	831	17.09%
Base Plane (Set 2)	131	659	19.88%

Plot Mode	Pole Vectors
Vector Count	831 (831 Entries)
Hemisphere	Lower
Projection	Equal Area

Figure 144 - Kinematic analysis of highwall 2 of case study 1 mine highwall for block toppling on geostructural data carried out by Facets plug-in of CloudCompare. Orange cyclographic: slope orientation; orange circumference: set of poles of the planes with a β lower than the β_{slope} (74° for this case study); pink section of circumference: area of the stereo plot with intersection of planes coupling affected by block toppling in case of β_{slope} <90 ° - φ; yellow sections of circumference: extension of the areas of the stereo plot with intersection of planes coupling affected by block toppling in case of dep slope (β_{slope} > 90 ° - φ)

2D kinematic analysis shows that flexural toppling is a possible failure mechanism for highwall 2 and that the percentage of critical discontinuities ranges from 6.83 % to 18.75 %, most of them are related to 2m set of discontinuities.

SiroJoint results show that overall 107 discontinuities (100 planes and 7 traces, overall 6.83 % of the discontinuities) satisfy flexural toppling failure conditions. 81/107 to 2m set of discontinuities and the remnant 26/107 have not been assigned to any set of discontinuities (Figure 145 and 146).

I-Site Studio results confirm that 2m set of discontinuities is involved by flexural toppling; overall 100 discontinuities on 713 (14.03 %, Figure 147) are prone to flexural toppling; 99 discontinuities on 100 have been related to 2m set of discontinuities and the remnant one has not been assigned to any set of discontinuities.

The percentage of discontinuities extracted by DiAna and by Facets prone to flexural toppling are 18.53 % and 18.75 % respectively: 180 discontinuities on overall 960 extracted by DiAna are critical for flexural toppling (18.75 %, Figure 148), most of them (140/180) are related to 2m set of discontinuities; as regarding Facets, 154 of the 831 discontinuities extracted by are critical for flexural toppling (18.53 %, Figure 149), 106 of them are related to 2m set of discontinuities.

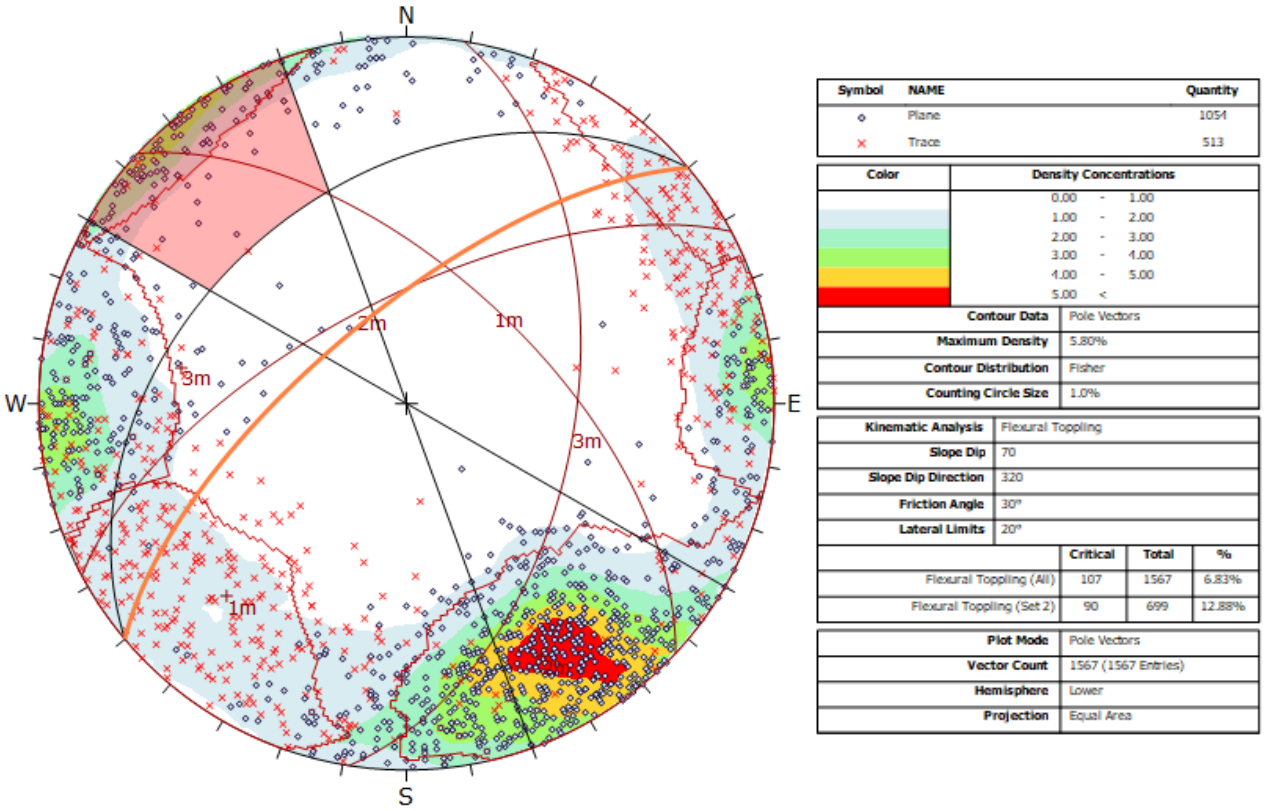

Symbol	NAME	Quantity
◇	Plane	1054
×	Trace	513

Color	Density Concentrations
	0.00 - 1.00
	1.00 - 2.00
	2.00 - 3.00
	3.00 - 4.00
	4.00 - 5.00
	5.00 <

Contour Data	Pole Vectors
Maximum Density	5.80%
Contour Distribution	Fisher
Counting Circle Size	1.0%

Kinematic Analysis	Flexural Toppling
Slope Dip	70
Slope Dip Direction	320
Friction Angle	30°
Lateral Limits	20°

	Critical	Total	%
Flexural Toppling (All)	107	1567	6.83%
Flexural Toppling (Set 2)	90	699	12.88%

Plot Mode	Pole Vectors
Vector Count	1567 (1567 Entries)
Hemisphere	Lower
Projection	Equal Area

Figure 145 - Kinematic analysis of planes and traces of highwall 2 of case study 1 mine highwall for flexural toppling on geostructural data carried out by SiroJoint. Orange cyclographic: slope orientation; black cyclographic: instability plane for flexural toppling (90 ° - β_{slope} +φ; α_{slope}); pink section of spindle of sphere: area of the stereo plot with the poles of the planes affected by flexural toppling

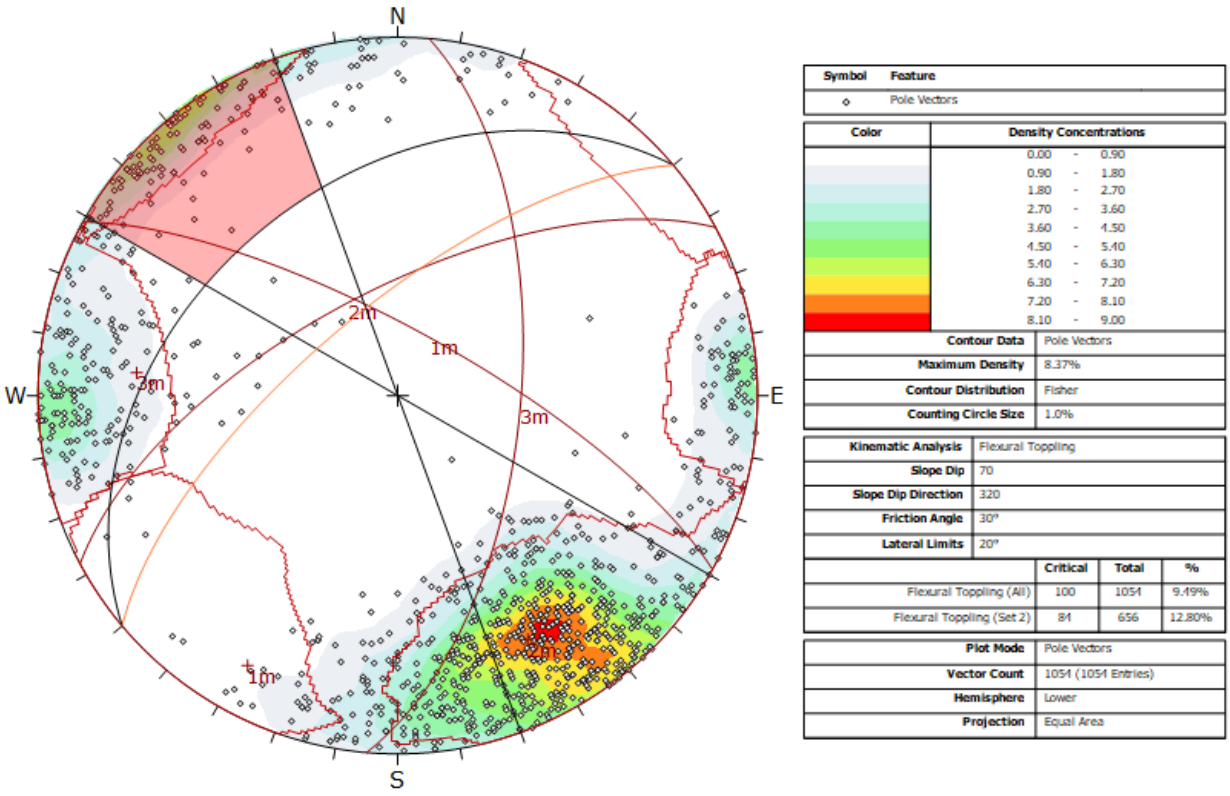

Symbol	Feature
◇	Pole Vectors

Color	Density Concentrations
	0.00 - 0.90
	0.90 - 1.80
	1.80 - 2.70
	2.70 - 3.60
	3.60 - 4.50
	4.50 - 5.40
	5.40 - 6.30
	6.30 - 7.20
	7.20 - 8.10
	8.10 - 9.00

Contour Data	Pole Vectors
Maximum Density	8.37%
Contour Distribution	Fisher
Counting Circle Size	1.0%

Kinematic Analysis	Flexural Toppling
Slope Dip	70
Slope Dip Direction	320
Friction Angle	30°
Lateral Limits	20°

	Critical	Total	%
Flexural Toppling (All)	100	1054	9.49%
Flexural Toppling (Set 2)	84	656	12.80%

Plot Mode	Pole Vectors
Vector Count	1054 (1054 Entries)
Hemisphere	Lower
Projection	Equal Area

Figure 146 - Kinematic analysis of planes only of highwall 2 of case study 1 mine highwall for flexural toppling on geostructural data carried out by SiroJoint. Orange cyclographic: slope orientation; black cyclographic: instability plane for flexural toppling (90 ° -β_{slope} +φ; α_{slope}); pink section of spindle of sphere: area of the stereo plot with the poles of the planes affected by flexural toppling

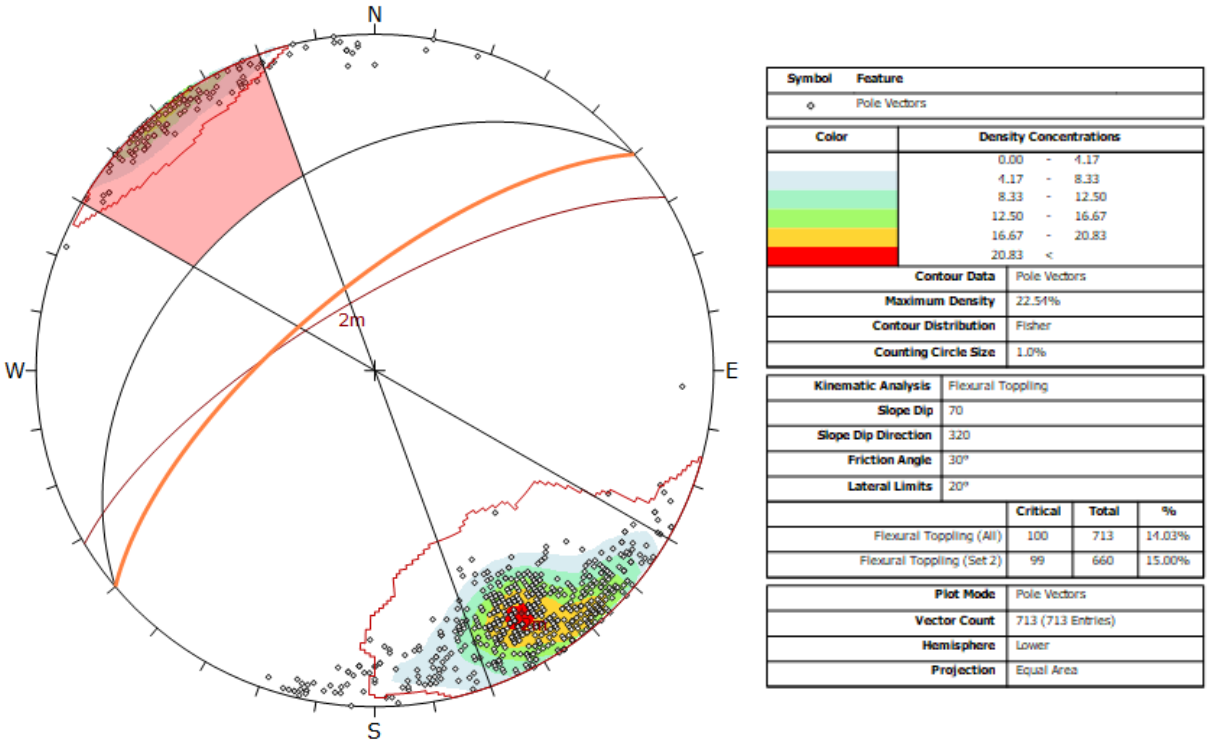

Figure 147 - Kinematic analysis of highwall 2 of case study 1 mine for flexural toppling on geostructural data carried out by I-Site Studio. Orange cyclographic: slope orientation; black cyclographic: instability plane for flexural toppling (90 ° -β_{slope} +φ; α_{slope}); pink section of spindle of sphere: area of the stereo plot with the poles of the planes affected by flexural toppling

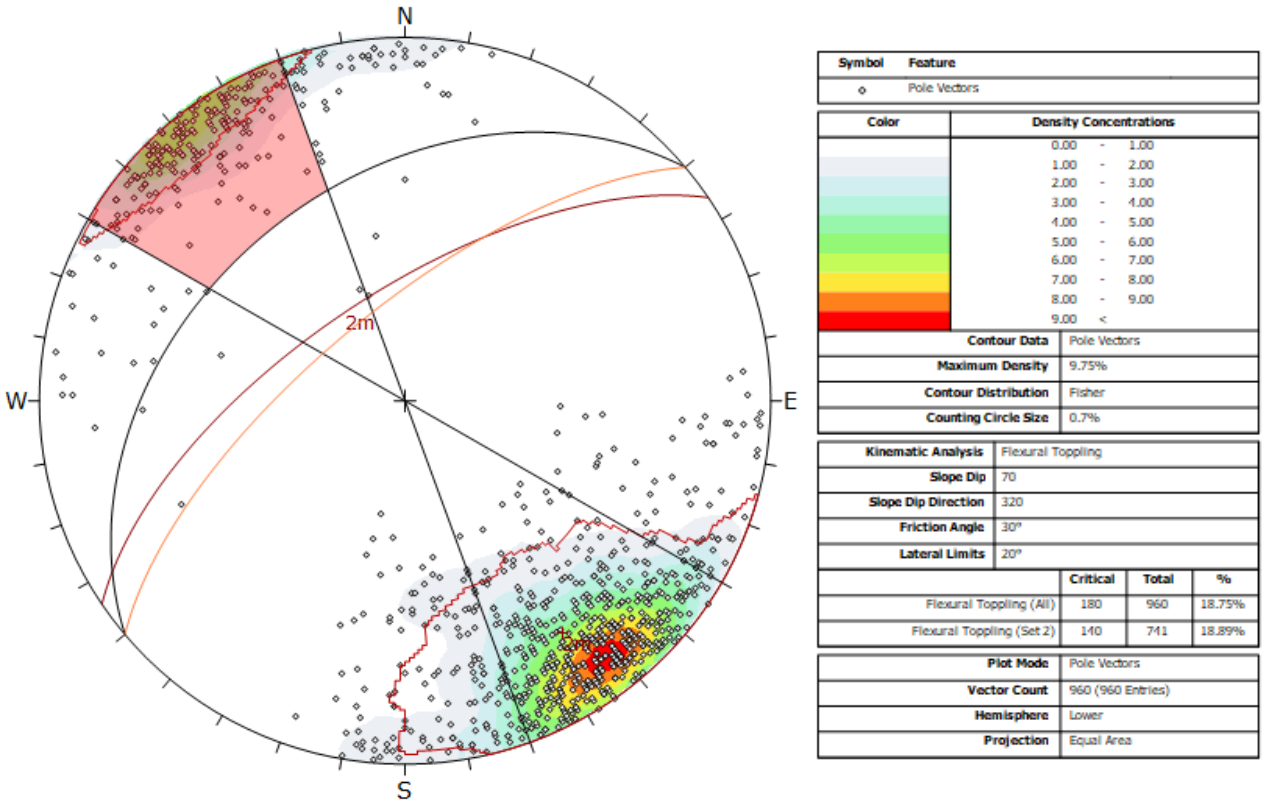

Figure 148 - Kinematic analysis of highwall 2 of case study 1 mine for flexural toppling on geostructural data carried out by DiAna. Orange cyclographic: slope orientation; black cyclographic: instability plane for flexural toppling (90 ° -β_{slope} +φ; α_{slope}); pink section of spindle of sphere: area of the stereo plot with the poles of the planes affected by flexural toppling

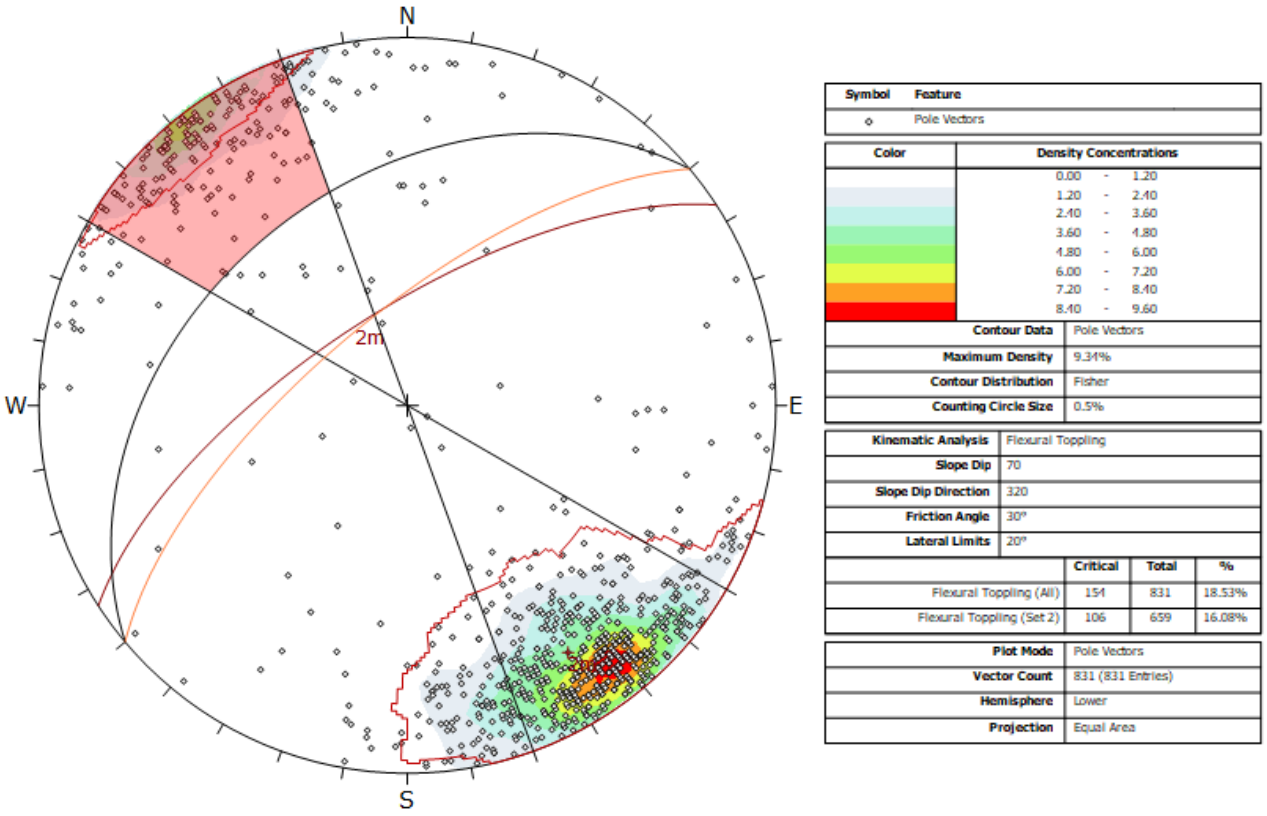

Figure 149 - Kinematic analysis of highwall 2 of case study 1 mine for flexural toppling on geostructural data carried out by Facets plug-in of CloudCompare. Orange cyclographic: slope orientation; black cyclographic: instability plane for flexural toppling (90 ° -β_{slope} +φ; α_{slope}); pink section of spindle of sphere: area of the stereo plot with the poles of the planes affected by flexural toppling

Results of 3D kinematic analysis performed by DiAna-K on highwall 2 are quite similar to the results for highwall 1. Susceptibility maps (Figure 150 and 151) show that plane failure is the most relevant failure mechanism. Wedge failure and flexural topplig too affect many areas of the highwall. Free fall involves steepest areas only, while block toppling is an extremely umprobable mechanism.

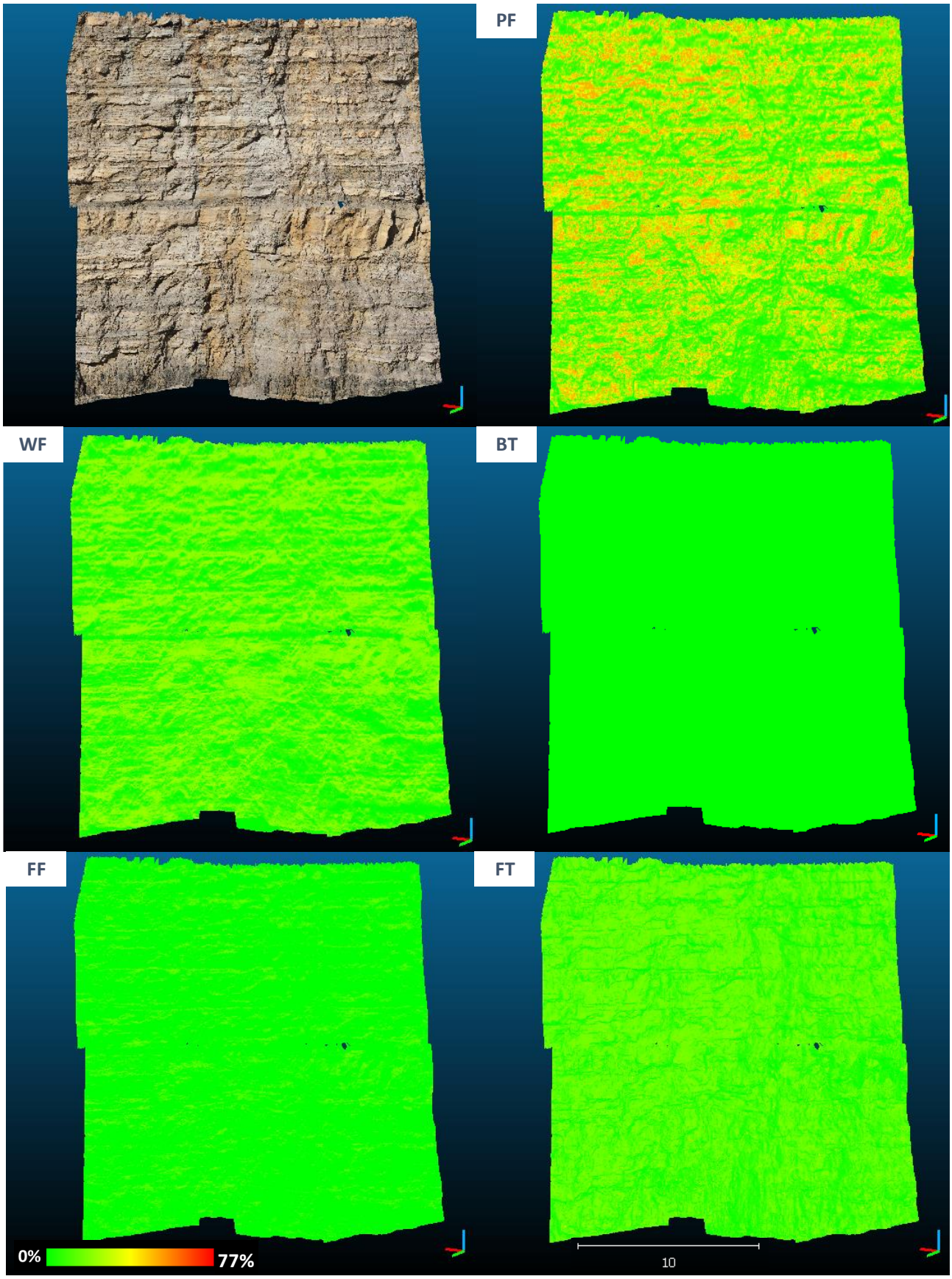

Figure 150 - Susceptibility maps for each failure mechanism, carried out from the kinematic analysis performed by DiAna-K on highwall 1 of case study 1 mine. WF: wedge failure; PF: plane failure; BT block toppling; FF: free fall; FT flexural toppling. All the susceptibility maps are normalized

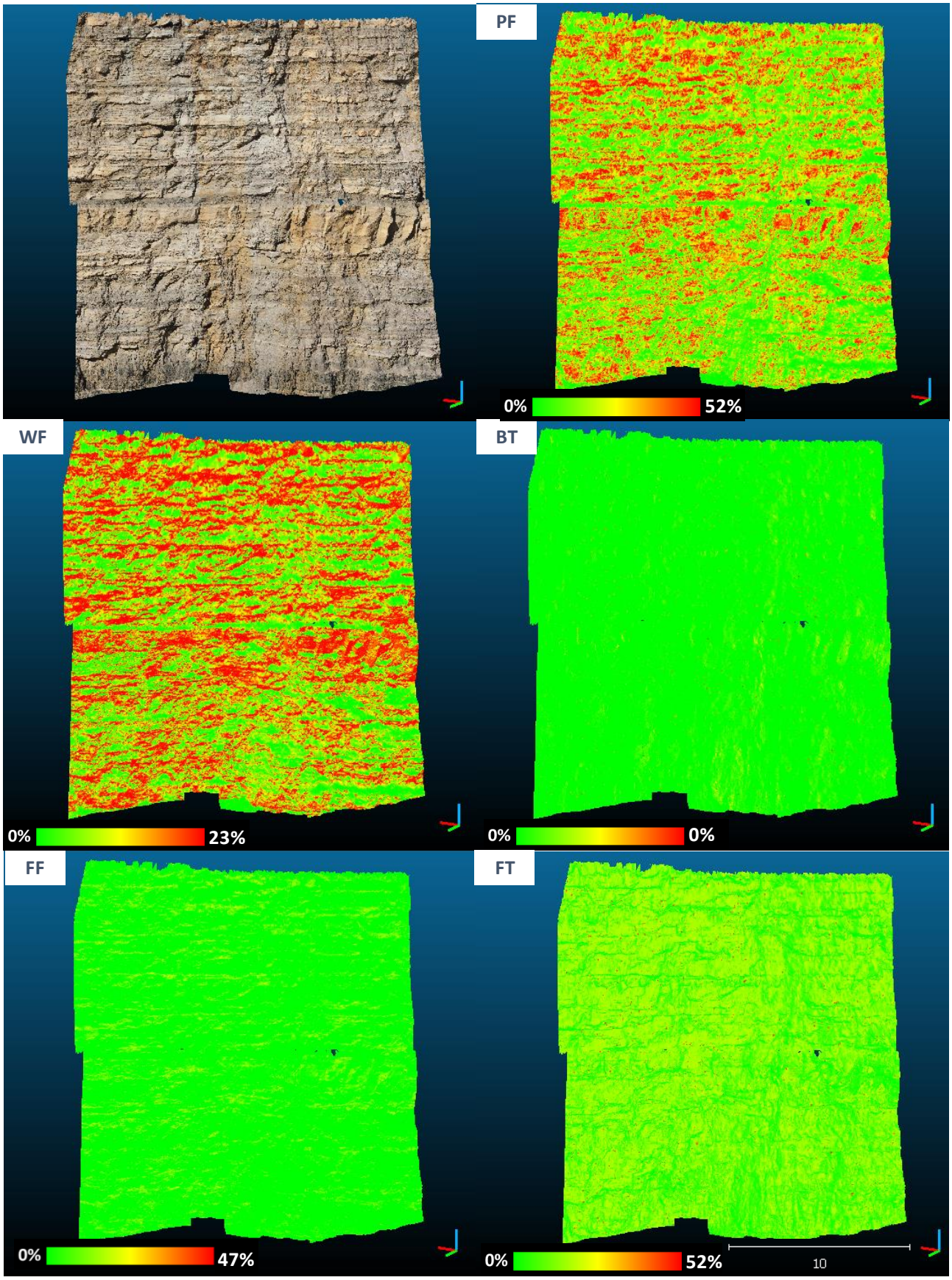

Figure 151 - Susceptibility maps for each failure mechanism, carried out from the kinematic analysis performed by DiAna-K on highwall 1 of case study 1 mine. WF: wedge failure; PF: plane failure; BT block toppling; FF: free fall; FT flexural toppling.

Three failure mechanisms are locally the most probable. As shown in Figure 152, most of the surface is moreover affected by plane failure; this failure mechanism affects mainly areas with dip direction similar to 3m sets of discontinuities. Areas with dip direction perpendicular to α_{slope} are, instead, mainly affected by wedge failure, as for highwall 1. The same consideration exposed for highwall 1 can be made also for this other highwall: routing 90° the stereoplot, main failure mechanism is not plane failure (related to 3m set in this case), but wedge failure. As for plane failure with a slope with the same orientation of highwall 2. Less step areas are not affected by plane failure or wedge failure. These areas are so mostly affected by flexural toppling or are not affected by any noteworthy failure mechanism. Locally, flexural toppling, although not a probable failure mechanism in absolute terms (Figure 153), is the most probable failure mechanism thanks to the presence of anti-dip slope discontinuities within 3m set of discontinuities. Some areas among the less step ones, are not affected by any failure mechanism anyway; this difference between areas affected mainly by flexural toppling and areas not affected by failure mechanisms at all, depends from the local α_{slope} and by the fulfilment of the requirements for flexural toppling: in case the local α_{slope} ranges greatly from the α of the average slope, no discontinuities are located within the critical area for flexural toppling (Figure 148).

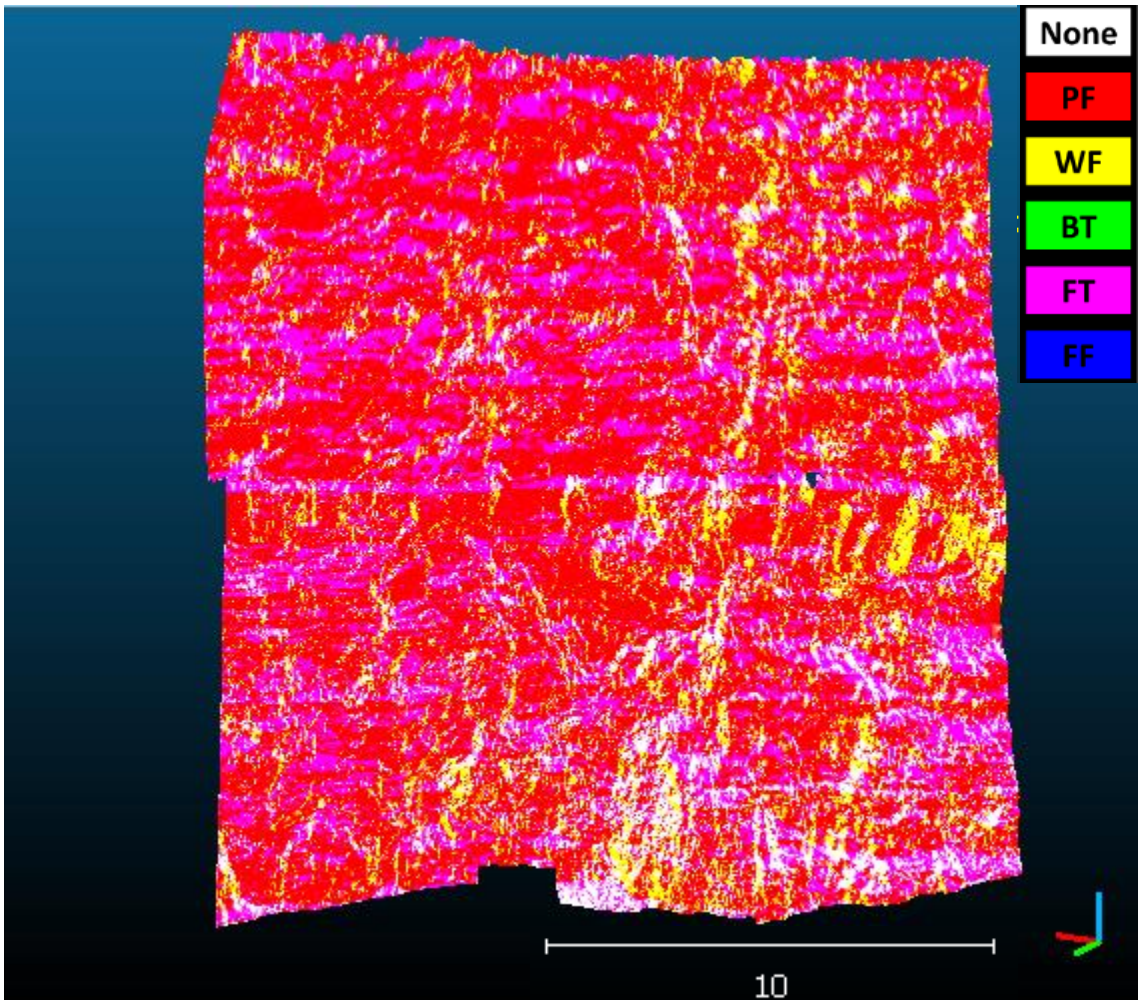

Figure 152 - Most probable failure mechanisms according to DiAna-K on highwall 2 of case study1 mine. PF: Plane Failure; WF: Wedge failure; BT: Block Toppling; FT: Flexural Toppling; FF: Free Fall

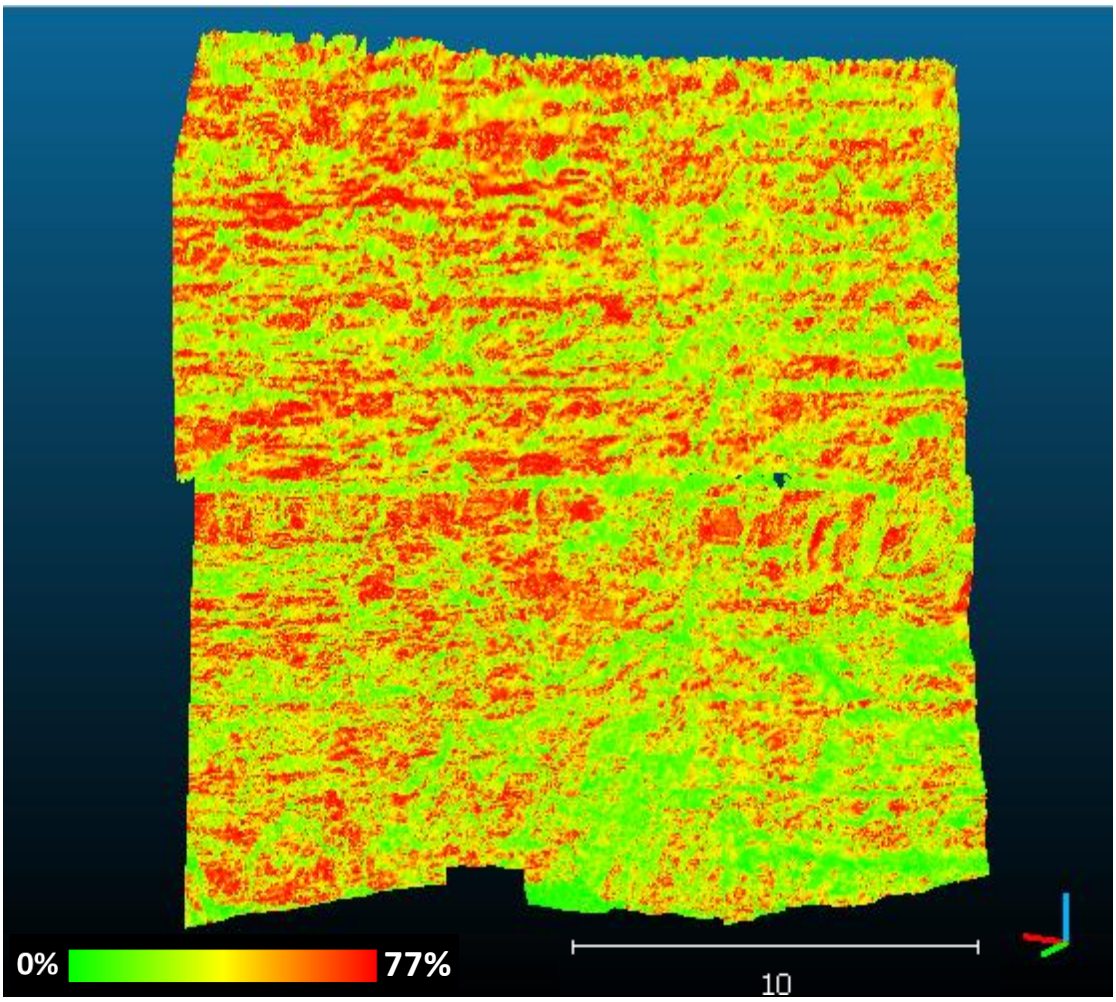

Figure 153 - Susceptibility value map for highwall 2 of case study 1 mine for all failure mechanism

6.3. Stability analysis

6.3.1. Stability analysis of highwall 1

The analysis of the stability of the highwall carried out by SiroModel has allowed to evaluate volume and number of the removable blocks referred to Type I, Type II and Type III (Goodman & Shi, 1985). 20 simulations have been performed, using as input data a simplified shape of the bench (Figure 154) and the stochastical mode data input for the 3 sets of discontinuities (Figure 155 and 156). 10 more simulation have been then carried out in order to evaluate if the number of simulation is sufficient to stochastically defined block size distribution. The number of contact planes of the removable blocks allows to discriminate plane failure (1 contact plane) from wedge failure (2 contact planes) (Figure 155, 156, 157, and 158), as described in Chapter 4.4.2.

The blocks distribution analysis performed on 20 simulations, shows that overall 7720 blocks have been extracted (Figure 155). 2773/7720 have one contact plane and 4947/7720 have two contact planes (letter a in Figure 155). 5375/7720 are removable and stable, 1236/7720 are removable and stable thanks to ϕ, 1109/7720 are removable and unstable. 805/2773 of the blocks with an only contact plane and 304/4947 of

the blocks with two contact planes are unstable (letter b in Figure 155); no block with an only contact plane and 1236/4947 of the blocks with two contact planes are stable (letter c in Figure 155); finally, 1968/2773 of the blocks with an only contact plane and 3407/4947 of the blocks with two contact planes are stable (letter d in Figure 155).

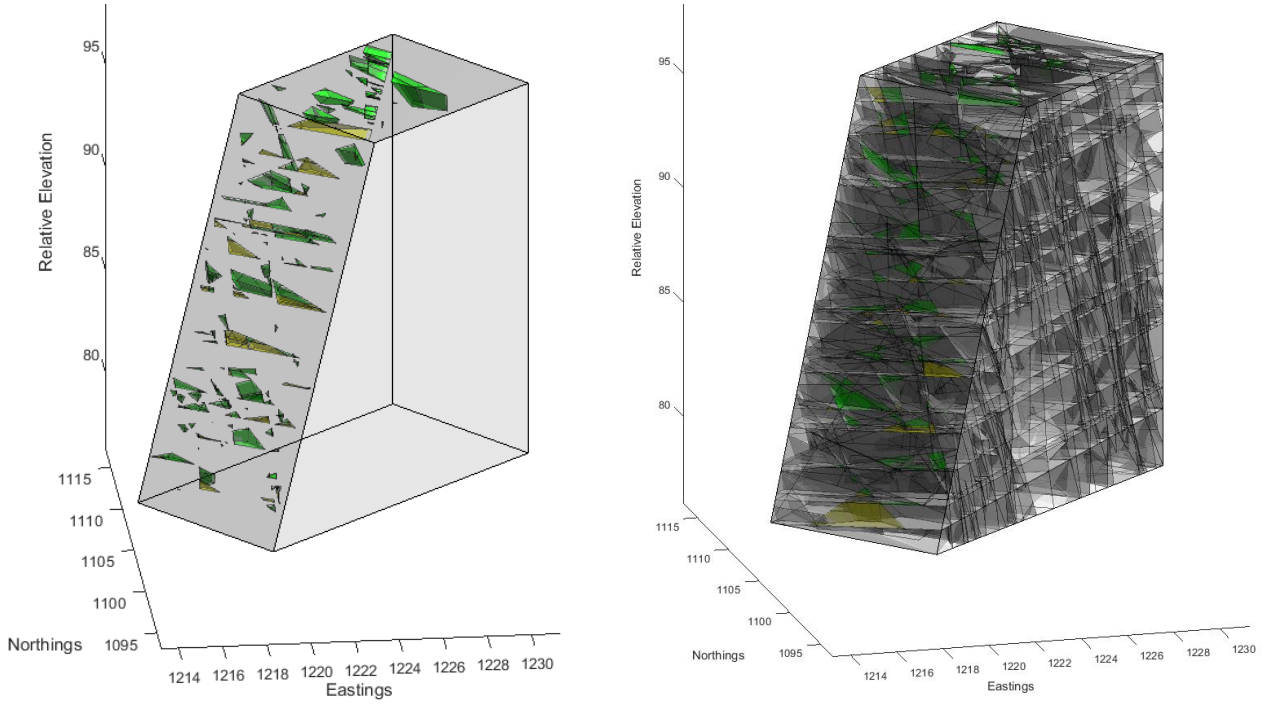

Figure 154 - The model of the slope for highwall 1 of SiroModel. Left: the model and the removable blocks; right: the discontinuities generated for the simulation. Red; Type I blocks; yellow: Type II blocks; green: Type III blocks

Simulations have been repeated selecting blocks with a minimum volume of 10^{-3} m^3 (Figure 156) in order to avoid blocks the volumetry of which is not dangerous for the operative condition at the base of the highwall. In this case, blocks extracted are 3329, 954/3329 of them with an only contact plane and 2375/3329 with two contact planes (letter a in Figure 156). As regarding the stability of the blocks, 2381/3329 are removable and stable, 621/3329 are removable and stable thanks to ϕ, 327/3329 are removable and unstable. As regarding the number of contact planes of the block, 227/954 of the blocks with an only contact plane and 100/2375 of the blocks with two contact planes are unstable (letter b in Figure 156); no block with an only contact plane and 621/2375 of the blocks with two contact planes are stable thanks to ϕ (letter c in Figure 156); 727/954 of the blocks with an only contact plane and 1654/2375 of the blocks with two contact planes are stable (letter d in Figure 156).

Overall, the diagrams of the distribution of all blocks by number of conctact planes and stability conditions is similar to the diagram of the distribution of the blocks with a minimum volume of 10^{-3} m^3; the comparison demonstrates so that the number of simulations carried out is sufficient to achieve a representative block volume distribution.

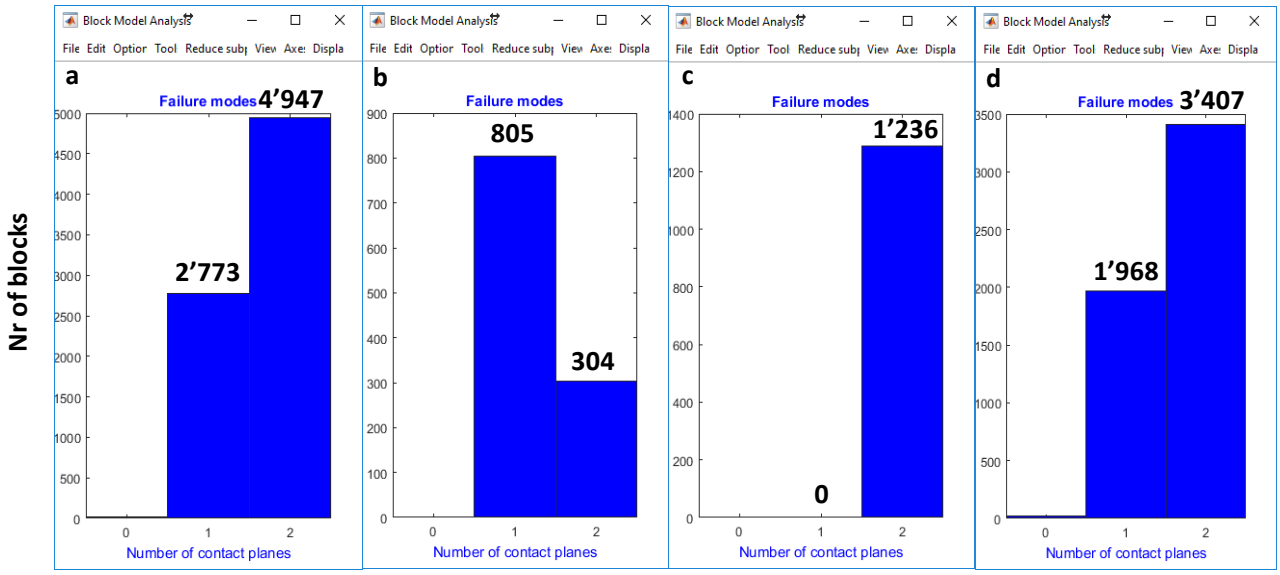

Figure 155 - Failure modes of highwall 1 of mine 1 case study performed on 20 simulations, without minimum block volume selection. a: Type I, Type II and Type III blocks (all removable blocks); b: Type I block (removable unstable blocks); c: Type II blocks (removable and stable with φ); d: Type III blocks (removable and stable)

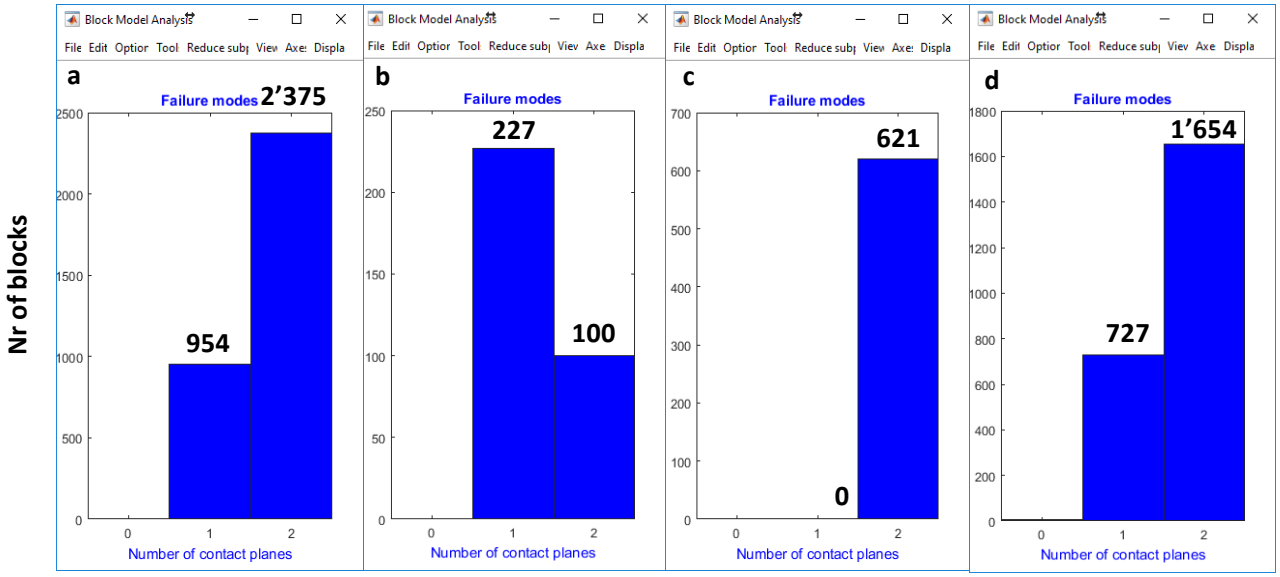

Figure 156 - Failure modes of highwall 1 of mine 1 case study performed on 20 simulations, considering blocks with a minimum 10^{-3} m^3 volume only. a: Type I, Type II and Type III blocks (all removable blocks); b: Type I block (removable unstable blocks); c: Type II blocks (removable and stable with φ); d: Type III blocks (removable and stable)

Performing 30 simulations, 10663 removable blocks (Goodman & Shi, 1985) have been extracted. The cumulative diagram of the blocks distribution performed on 30 simulations, shows that 10663 removable blocks distribution by number of contact plane (Figure 157). On overall 10663 blocks, 3853 have one contact plane and 6810 two contact planes (letter a in Figure 157); 1545 are related to Type I, 1768 are related to Type II, and 7350 to Type III. Among the blocks with an only contact plane, the number of blocks related to Type I, Type II and Type 3 is 1125, 34, and 2694 respectively. Among the blocks with two contact planes, the number of blocks of Type I, Type II and Type III is 420, 1734, and 4656, respectively (letter b, c, and d in Figure 157).

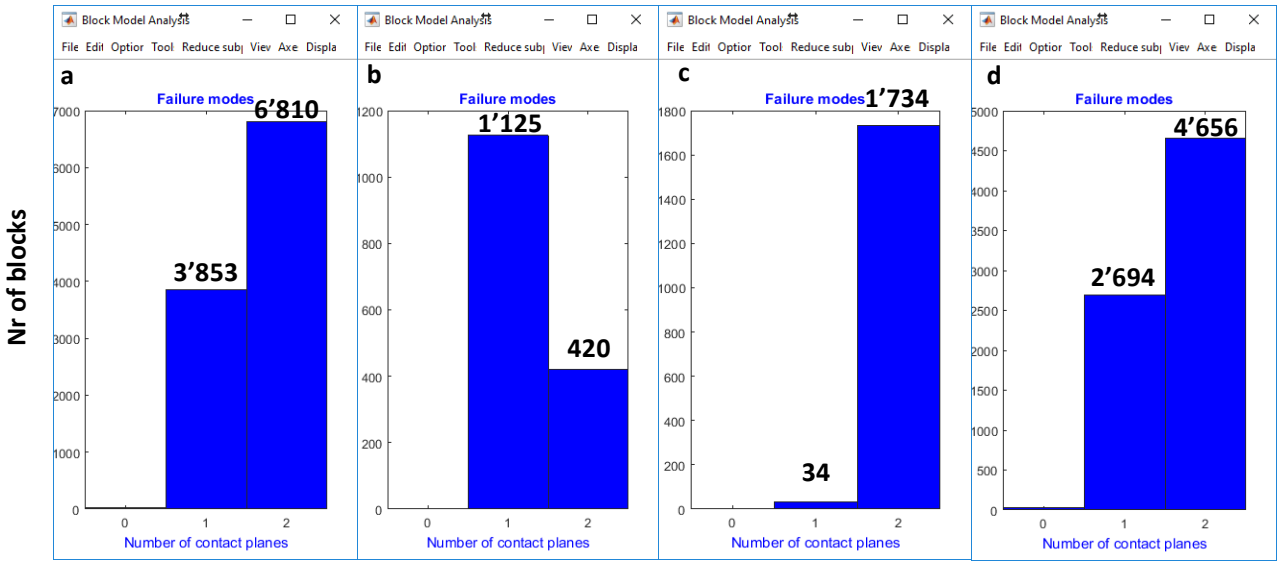

Figure 157 - Failure modes of highwall 1 of mine 1 case study performed on 30 simulations, without minimum block volume selection. a: Type I, Type II and Type III blocks (all removable blocks); b: Type I block (removable unstable blocks); c: Type II blocks (removable and stable with φ); d: Type III blocks (removable and stable)

Also in this case has been carried out the analysis of the block distribution by stability conditions and failure mode on blocks with volume > 10^{-3} m^3. 4939 blocks with volume > 10^{-3} m^3 have been extracted on 30 simulations, 1352/4939 of them with an only contact plane and 3587/4939 with two contact planes (letter a in Figure 158). As regarding the stability of the blocks, 3826/4939 are removable and stable, 859/4939 are removable and stable thanks to ϕ, 447/4939 are removable and unstable. As regarding the number of contact planes of the block, 339/1352 of the blocks with an only contact plane and 108/3587 of the blocks with two contact planes are unstable (letter b in Figure 158); 15/1352 of the blocks with an only contact plane and 844/3587 of the blocks with two contact planes are stable thanks to ϕ (letter c in Figure 158; 1006/1352 of the blocks with an only contact plane and 2820/3587 of the blocks with two contact planes are stable (letter d in Figure 158).

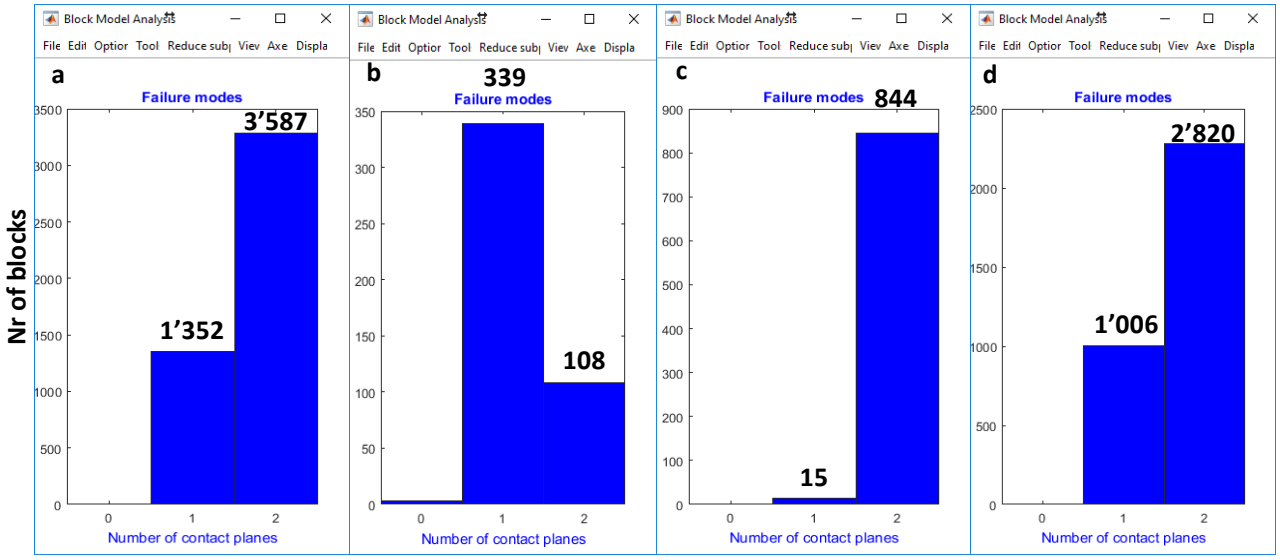

Figure 158 - Failure modes of highwall 1 of mine 1 case study performed on 30 simulations, considering blocks with a minimum 10^{-3} m^3 volume only. a: Type I, Type II and Type III blocks (all removable blocks); b: Type I block (removable unstable blocks); c: Type II blocks (removable and stable with φ); d: Type III blocks (removable and stable)

The distribution of the volume on 20 simulations shows that the range of volume of stable blocks (letter d in Figure 159) is greater than unstable blocks volume (letter b in Figure 159) or blocks stable thanks to ϕ (letter

c Figure 159). Similar considerations can be conducted performing 30 simulations (Figure 160). Anyway, performing 30 simulation instead of 20 doe not increase the value of the maximum volum of Type I (lecter b in Figure 159 and 160) and Type II blocks (lecter c in Figure 159 and 160). Indeed, comparing the number of blocks obtained with 20 and 30 simulations, is evident that the number of blocks for each class, except class with a very low number of blocks (i.e. blocks removable and stable thanks to ϕ, with on only contact plane) is proportional to the number of simulational carried out. For these reasons, 30 simulations are sufficient to describe the blocks distribution of this highwall as regarding the volume and the stability condition, and no futher simulation has been carried out.

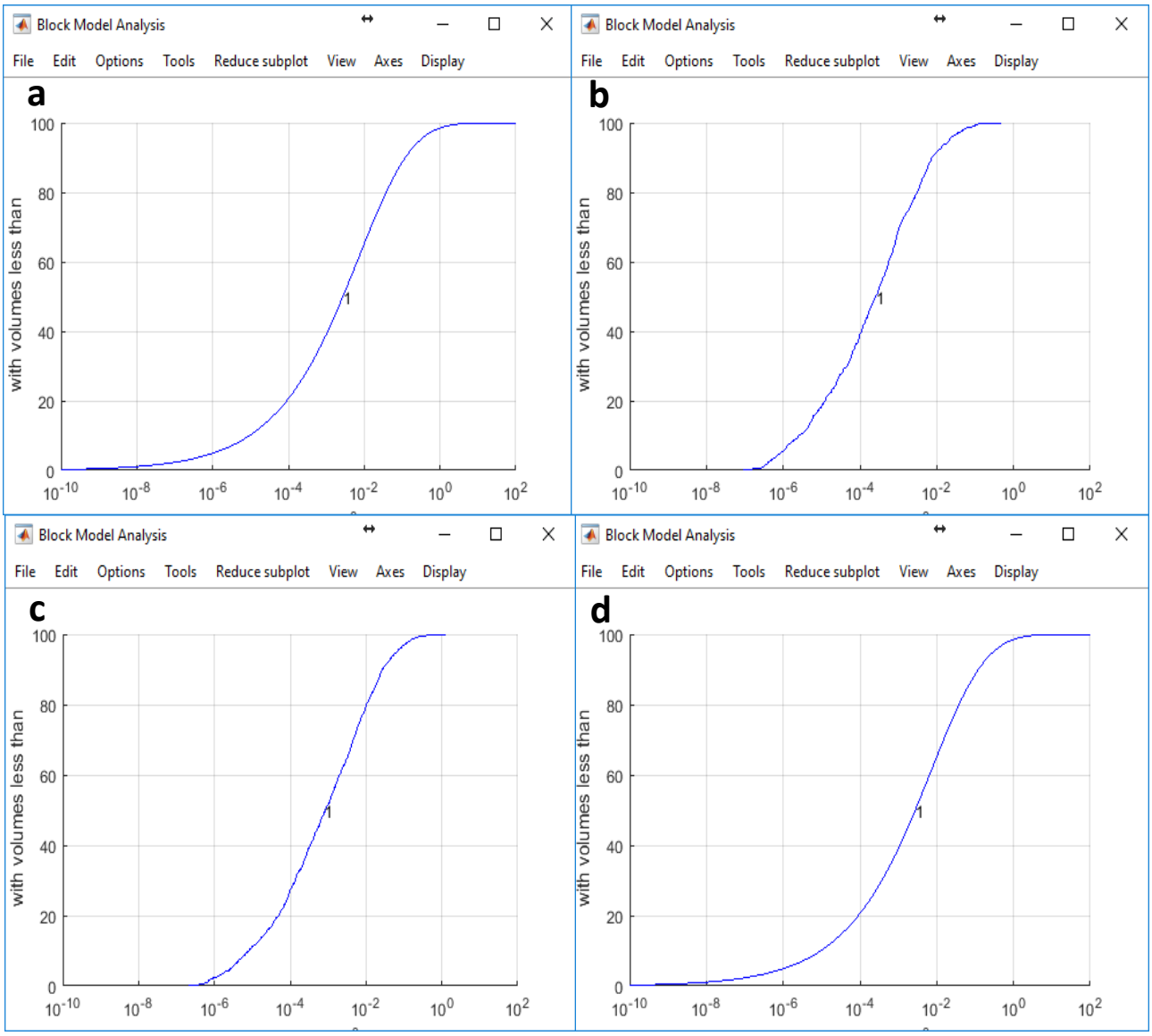

Figure 159 - Volume of removable blocks of highwall 1 of mine 1 case study performed on 20 simulations. a: Type I, Type II and Type III blocks (all removable blocks); b: Type I block (removable unstable blocks); c: Type II blocks (removable and stable with φ); d: Type III blocks (removable and stable)

In Table 11 and 12 are summarized the evaluated number of blocks for 20 and 30 simulations, divided by block Type and by number of contact planes. Table 11 describes the total number of blocks for 20 and 30 simulations, while Table 12 the average number of blocks. The average number of blocks for 20 simulations does not differ greatly from the average number of blocks for 30 simulations simulation, so the average number of blocks of 30 simulations is statistically representative of the rock mass block distributon. The average number of blocks on 30 simulation is 355; 128/355 have one contact plane and 227/355 have two contact planes. 52/355 blocks are related to Type I, 59/355 are related to Type II and 245/355 to Type III. Only 1 block is stable thanks to ϕ

and lays on an only contact plane; this can be explained because 3m set of discontinuities of Figure 117 are stepper than the ϕ angle, so blocks with an only sliding plane are unstable (β_{disc} (2m set) > ϕ). This deduction is in agreement also with the low probability of block toppling estimated with the kinematic analysis carried out with all the codes used and with the kinematic index of DiAna as well, as described in the following paragraph.

As regarding the volumes of the blocks, the median value of the volumes (Figure 159 and 160) is equal to 5×10^{-3} m^3; greatest volume for removable blocks stable thanks to ϕ is 1.20 m^3 (letter c in Figure 160), while the greatest volume for removable and unstable blocks is instead 0.88 m^3 (letter b in Figure 160).

As previously written for the kinematic analysis carried out on discontinuities extracted by SiroJoint, plane failure is mainly related to 1m set of discontinuities, and to a lesser extent, to 2m set of discontinuities; the integrated analysis of the graphs in Figure 155, 156, 157, 158, 159, 160, and of the stereoplot in Figure 92 allows to understand that the geostructural and kinematic analysis carried out with SiroJoint and SiroModel shows that among Type I blocks plane failure is more probable than plane failure (38 blocks vs 14 blocks on average for simulation, Table 12). The comparison shows, indeed, that plane failure is related to 1m and 2m set of discontinuities and that 2m set of discontinuities represents the most prone to failure set of discontinuities. Only a few blocks for simulation are prone to plane failure and related to Type II blocks, while 58 blocks prone to wedge failure are related to Type II blocks (Table 12). This means that in case of heavy weathering of rock mass or increase of water overpressure, wedge failure blocks is much more probable than plane failure. Finally, the performing of 30 simulations on a 8.5 m wide and 26 m heigh section, the maximum volume for Type I blocks is 0.88 m^3 (letter b in Figure 160).

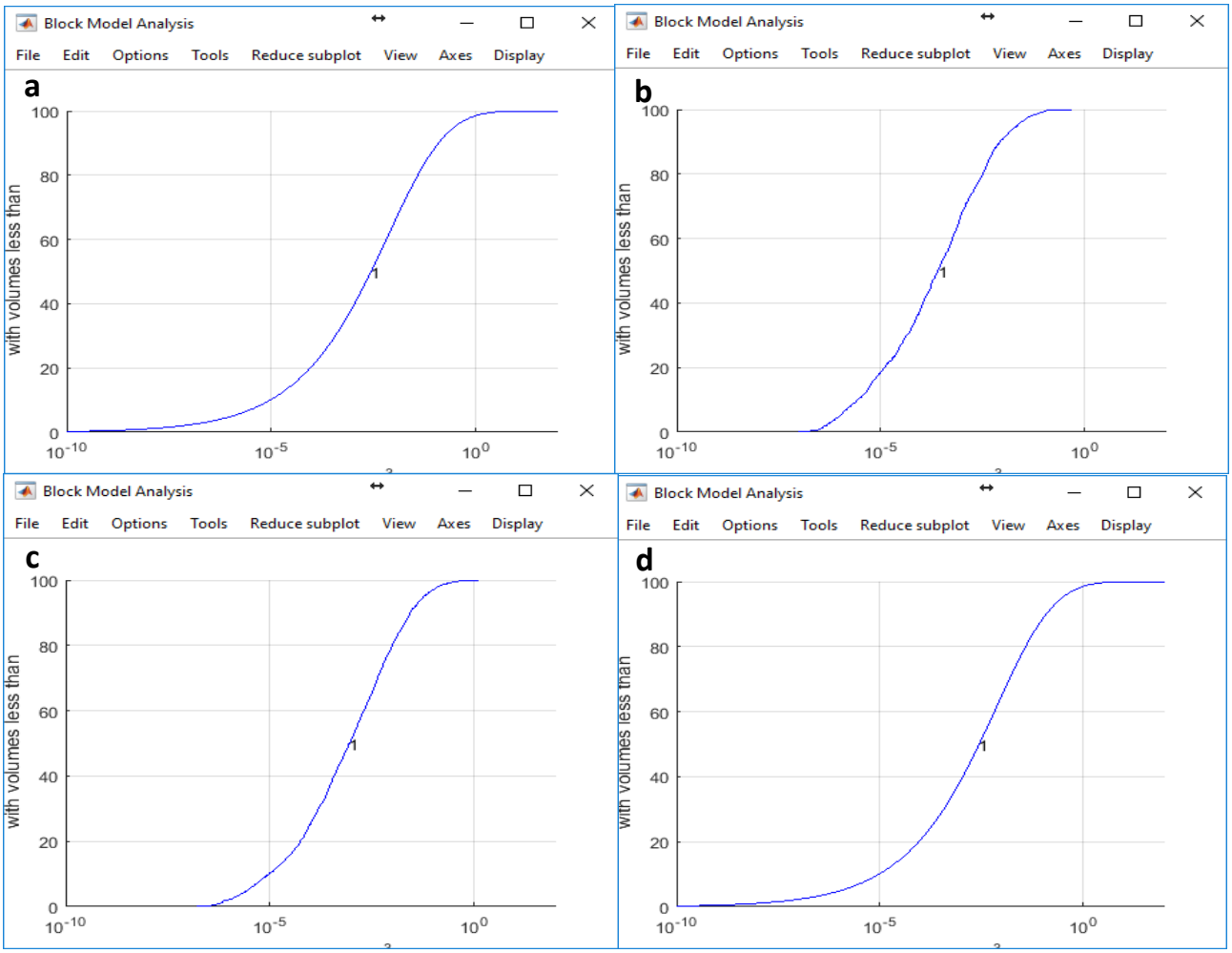

Figure 160 - Volume of removable blocks of highwall 1 of mine 1 case study performed on 30 simulations. a: Type I, Type II and Type III blocks (all removable blocks); b: Type I block (removable unstable blocks); c: Type II blocks (removable and stable with φ); d: Type III blocks (removable and stable)

Table 11 - Nr of blocks sorted by Type of block (Type I: unstable blocks; Type II: blocks stable thanks to φ; Type III : stable blocks) considering 20 and 30 simulations

Nr of simulations	Nr total blocks	All blocks		Type I blocks		Type II blocks		Type III blocks	
		1 contact plane	2 contact planes	1 contact plane	2 contact planes	1 contact plane	2 contact planes	1 contact plane	2 contact planes
20	7720	2773	4947	805	304	0	1236	1968	3407
30	10663	3853	6810	1125	420	34	1734	2694	4656

Table 12 - Average nr of blocks sorted by Type of block (Type I: unstable blocks; Type II: blocks stable thanks to φ; Type III: stable blocks) considering 20 and 30 simulations

Nr of simulations	Nr total blocks	All blocks (average)		Type I blocks (average)		Type II blocks (average)		Type III blocks (average)	
		1 contact plane	2 contact planes	1 contact plane	2 contact planes	1 contact plane	2 contact planes	1 contact plane	2 contact planes
20	386	139	247	40	15	0	62	98	170
30	355	128	227	38	14	1	58	90	155

6.3.2. Stability analysis of highwall 2

The blocks distribution analysis performed on 20 simulations, using as slope model the simplified slope shown in Figure 161, shows that overall 7807 blocks have been modelled (Figure 162). 2485/7807 have one contact plane and 5322/7807 have two contact planes (letter a in Figure 162). 6953/7807 are removable and stable, 967/7807 are removable and stable thanks to ϕ, 897/7807 are removable and unstable. 695/2485 of the blocks with an only contact plane and 192/5322 of the blocks with two contact planes are unstable (letter b in Figure 162); 37/2485 of the blocks with an only contact plane and 930/5322 of the blocks with two contact planes are stable (letter c in Figure 162); 1753/2485 of the blocks with an only contact plane and 4200/5322 of the blocks with two contact planes are stable (letter d in Figure 162).

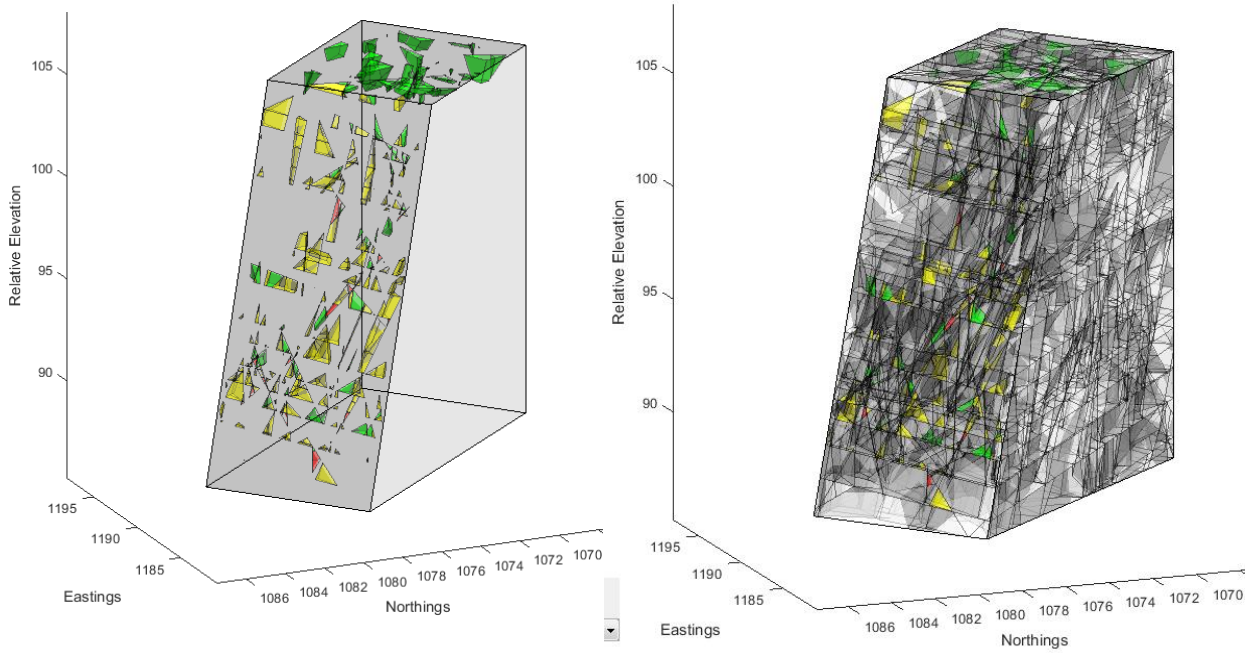

Figure 161 - The model of the slope of highwall 2 of SiroModel. Left: the model and the removable blocks; right: the discontinuities generated for the simulation. Red; Type I blocks; yellow: Type II blocks; green: Type III blocks

3522 blocks of Type I, Type II and Type III have a volume greater than 10^{-3} m^3 (Figure 163); among these blocks, 906/3522 have an only contact plane and 2616/3522 with two contact planes (letter a in Figure 163). As regarding the stability of the blocks, 283/3522 are related to Type I, 2781/3522 to Type II, and 458/3522 to Type III. As regarding the number of contact planes of the block, 216/906 of the blocks with an only contact plane and 67/2616 of the blocks with two contact planes are of Type I (letter b in Figure 163); 14/906 of the blocks with an only contact plane and 444/2616 of the blocks with two contact planes are of Type II (letter c in Figure 163); 676/906 of the blocks with an only contact plane and 2105/2616 of the blocks with two contact planes are of Type III (letter d in Figure 163). Overall, the diagrams of the distribution of the blocks with a minimum volume of 10^{-3} m^3 by number of conctact planes and stability conditions is similar to the diagram of the distribution of all blocks.

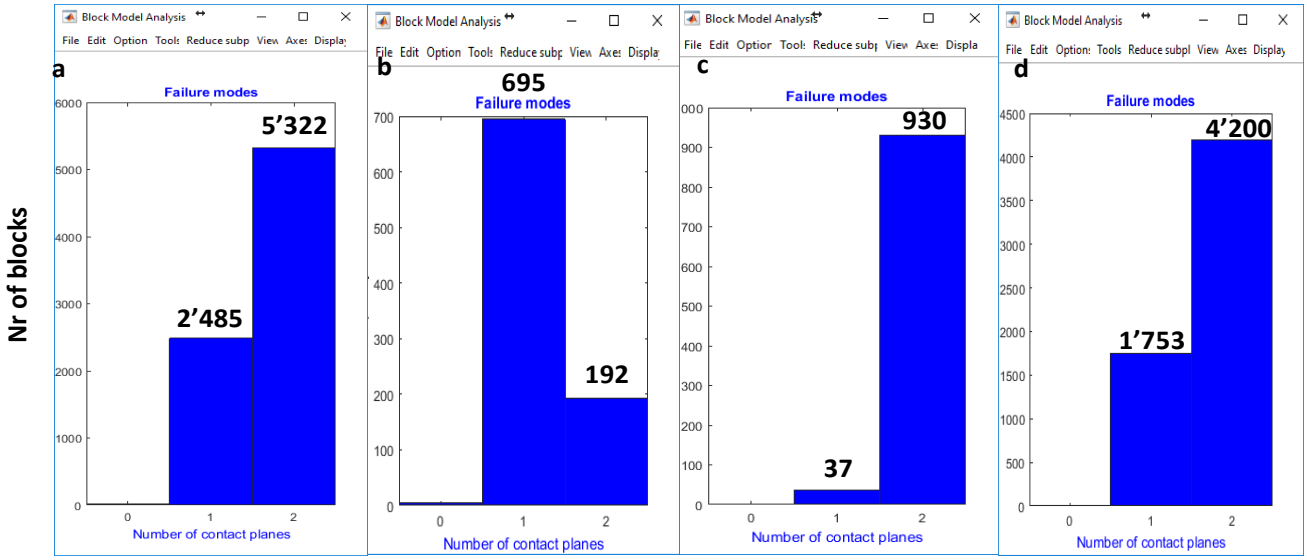

Figure 162 - Failure modes of highwall 2 of mine 1 case study performed on 20 simulations, without minimum block volume selection. a: Type I, Type II and Type III blocks (all removable blocks); b: Type I block (removable unstable blocks); c: Type II blocks (removable and stable with φ); d: Type III blocks (removable and stable)

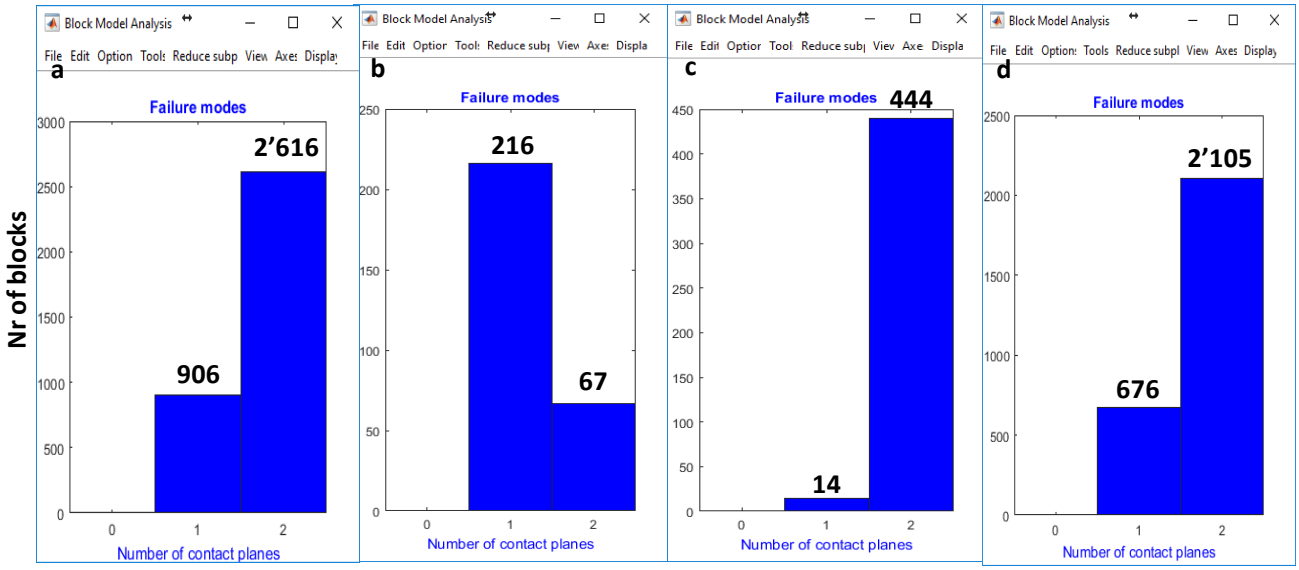

Figure 163 - Failure modes of highwall 2 of mine 1 case study performed on 20 simulations, considering blocks with a minimum 10^{-3} m^3 volume only. a: Type I, Type II and Type III blocks (all removable blocks); b: Type I block (removable unstable blocks); c: Type II blocks (removable and stable with φ); d: Type III blocks (removable and stable)

30 simulations have been performed by SiroModel also for highwall 2. Figure 163 shows the districution of the removable blocks; On overall 11382 blocks, 3689 have one contact plane and 7693 have two contact planes

(letter a in Figure 164); the number of Type I, Type II and Type III blocks is 1395, 1376 and 8611, respectively. 1091/3689 of the blocks with an only contact plane and 304/7693 of the blocks with two contact planes are of Type I (letter b in Figure 164); 37/3689 of the blocks with an only contact plane and 1339/7693 of the blocks with two contact planes are of Type II; 2561/3689 of the blocks with an only contact plane and 6050/7693 of the blocks with two contact planes are instead of Type III (letter d in Figure 164).

Also in this case has been carried out the analysis of the block distribution by stability conditions and failure mode (Figure 165) on blocks with volume > 10^{-3} m^3 to get a better description by FOS nad failure mode of the blocks that could be dangerous because of their size. On over 11382 extracted with 30 simulation, 5106 have a volume greater than 10^{-3}. 1353/5106 of them have one contact plane and 3753/5106 two contact planes (letter a in Figure 165). As regarding the stability of the blocks, the number of blocks related to Type I, Type II and Type II is 447, 651 and 4008 respectively. Finally, 339/1353 of the blocks with an only contact plane and 108/3753 of the blocks with two contact planes are of Type I (letter b in Figure 165); 14/1353 of the blocks with an only contact plane and 637/3753 of the blocks with two contact planes are of Type II (letter c in Figure 165); 1000/1353 of the blocks with an only contact plane and 3008/3753 of the blocks with two contact planes are instead of Type III (letter d in Figure 165).

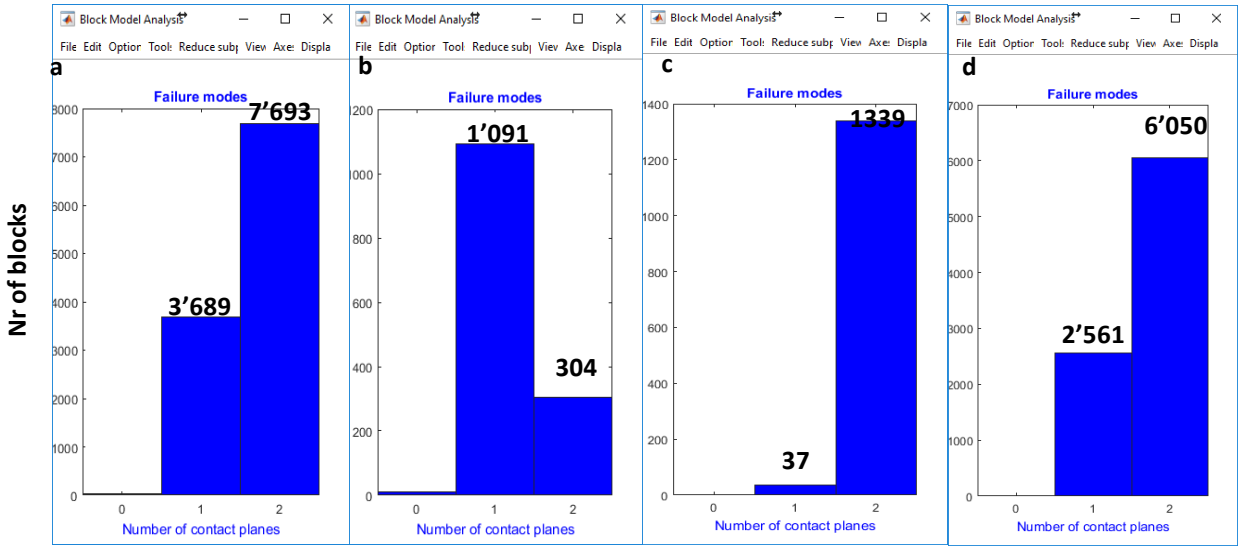

Figure 164 - Failure modes of highwall 2 of mine 1 case study performed on 30 simulations, without minimum block volume selection. a: Type I, Type II and Type III blocks (all removable blocks); b: Type I block (removable unstable blocks); c: Type II blocks (removable and stable with φ); d: Type III blocks (removable and stable)

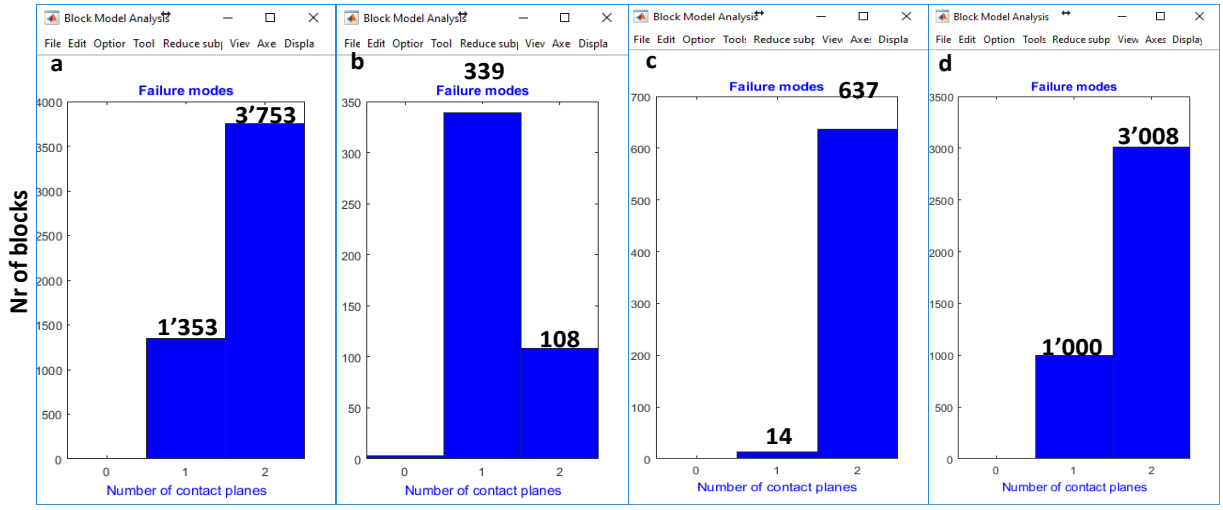

Figure 165 - Failure modes of highwall 2 of mine 1 case study performed on 30 simulations, considering blocks with a minimum 10^{-3} m^3 volume only. a: Type I, Type II and Type III blocks (all removable blocks); b: Type I block (removable unstable blocks); c: Type II blocks (removable and stable with φ); d: Type III blocks (removable and stable)

The distribution of the volumes of the blocks extracted performing 30 simulation is similar to the distribution of the blocks extracted on 20 simulations (Figure 166 vs Figure 167). We remark that, as for highwall 1, the distribution of the volume of Type III blocks (letter d in Figure 166 and 167) is wider than the distribution for Type I and Type II blocks (letter b and c in Figure 166 and 167), both performing 20 simulations, and performing 30. The maximum volume performing 20 or 30 simulation does not varies; in particular, the maximum volume for Type I and for Type II is the same, while the maximum volume for Type II blocks is 0.72 m^3 (letter b in Figure 166 and 167) and 1.18 m^3 (letter c in Figure 166 and 167); the median volume of all the blocks is $5*10^{-3}$ m^3 (letter d in Figure 166 and 167).

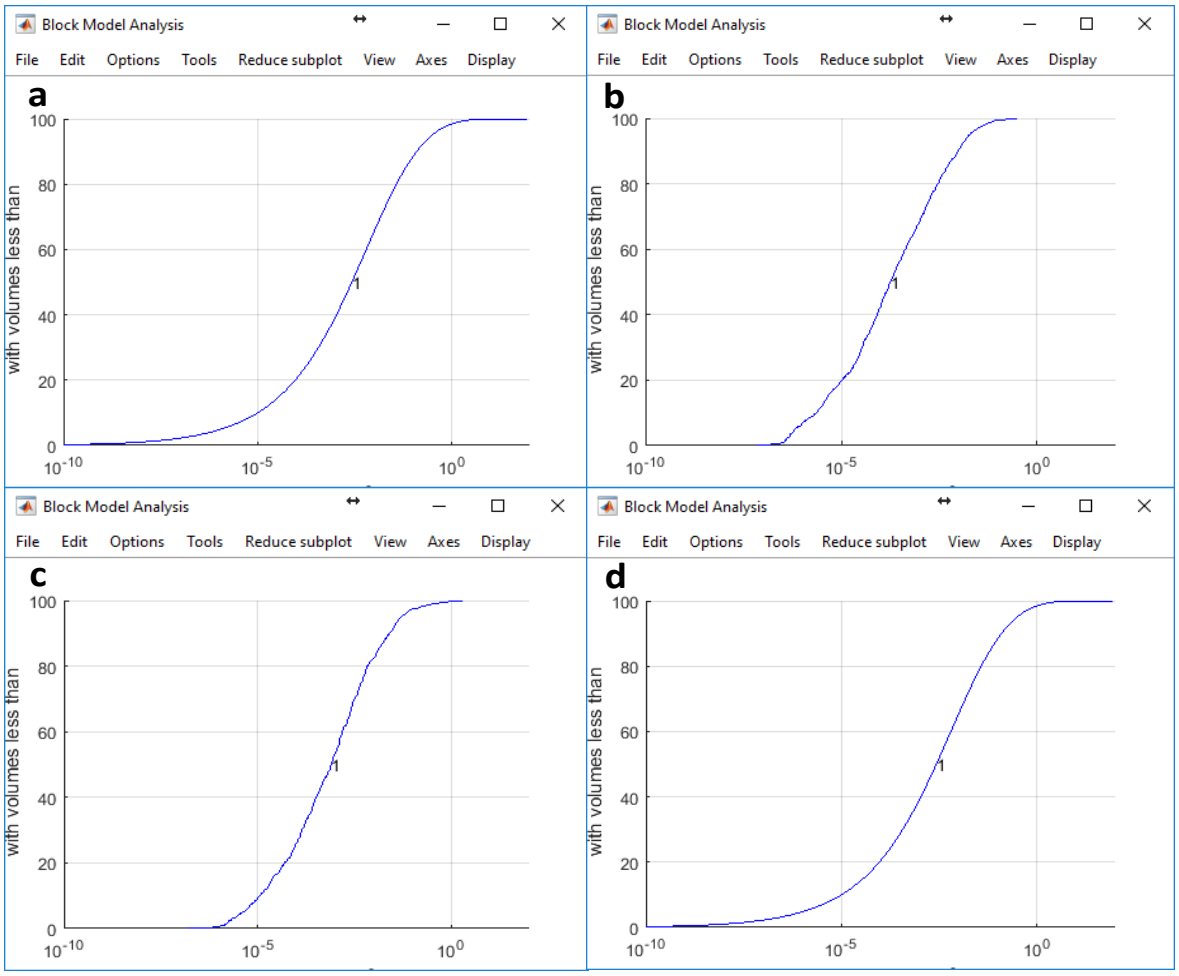

Figure 166 - Volume of removable blocks of highwall 2 of mine 1 case study performed on 20 simulations. a: Type I, Type II and Type III blocks (all removable blocks); b: Type I block; c: Type II blocks; d: Type III blocks

The total number of blocks and the average number of blocks for simulation are reported in Table 13 and 14 respectively. In particular, Table 13 describes the total number of blocks for 20 and 30 simulations, while Table 14 the average number of blocks, splitting the blocks by Type and by the number of contact planes. V shows that no significative changes affect the total amount of blocks performing 30 simulation instead of 20; so, the average number of blocks of 30 simulations is statistically representative of the rock mass block distribution. The average number of removable blocks, considering a 8.5 m wide and 21 m height section, is 379 performing on 30 simulations; 123/379 have one contact plane and 256/379 have two contact planes. 46/379 blocks are related to Type I, 45/379 are related to Type II and 307/379 to Type III. On average, 0.47 blocks only are stable thanks to ϕ and lie on an only contact plane; this can be explained because 3m set of discontinuities of Figure 117 are stepper than the ϕ angle, so blocks with an only sliding plane are unstable (β_{disc} (2m set) > ϕ).
Figure 130 shows that plane failure is mostly related to 3m set of discontinuities on this slope, while wedge failure (Figure 135) is related to the intersection of 1m, 2m and 3m sets of discontinuities; the integrated

analysis of the graphs in Figure 162, 163, 164, 165, 166, and 167, with the stereoplots in Figure 130 and 135 allows a better characterisation of the stability analysis for highwall 2 and enable to understand that plane failure, related to 3m set of discontinuities, is more probable than wedge failure (Table 14), related to the intersection 1m-2m, 1m-3m, and 2m-3m

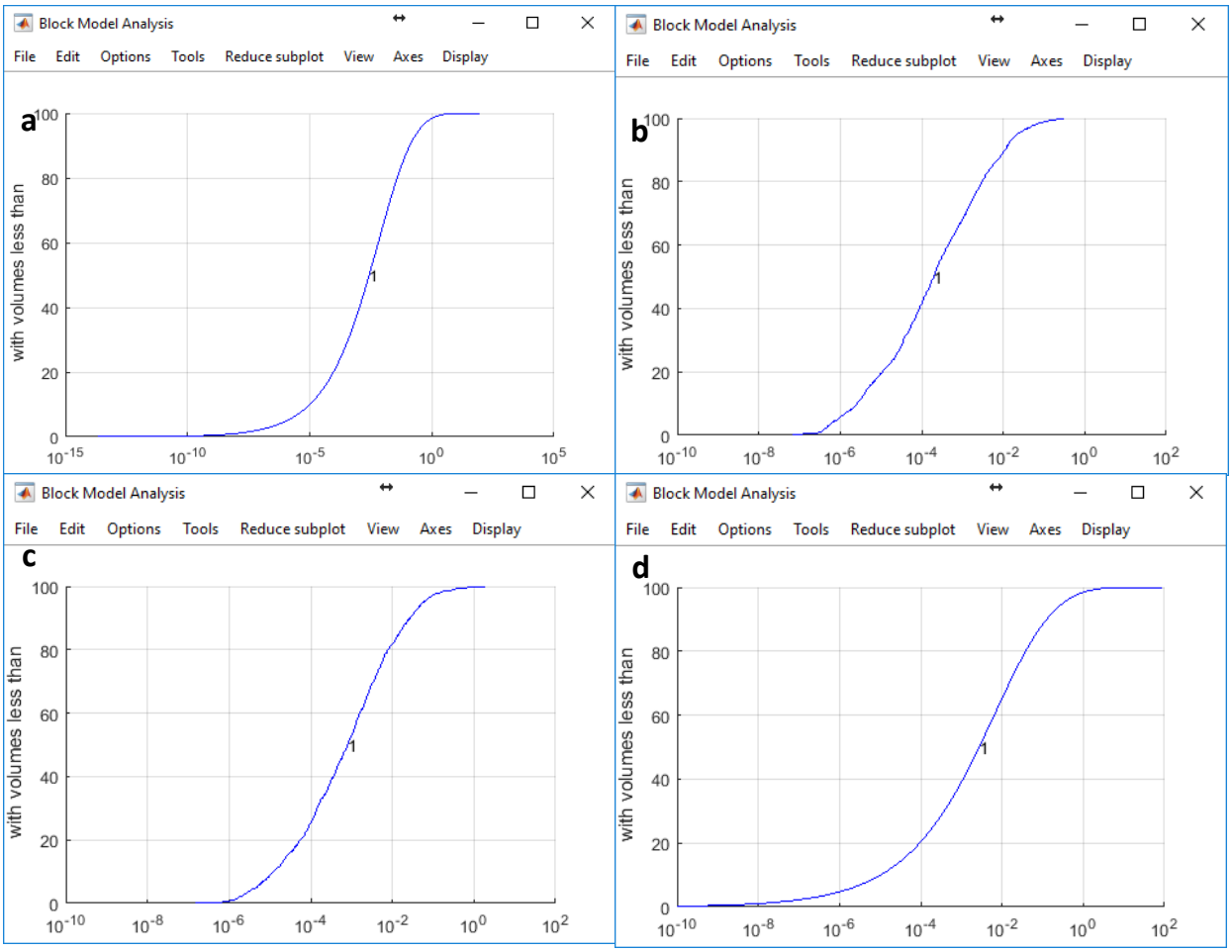

Figure 167 - Volume of removable blocks of highwall 2 of mine 1 case study performed on 30 simulations. a: Type I, Type II and Type III blocks (all removable blocks); b: Type I block (removable unstable blocks); c: Type II blocks (removable and stable with φ); d: Type III blocks (removable and stable)

Table 13 - Nr of blocks sorted by Type of block (Type I: unstable blocks; Type II: blocks stable thanks to φ; Type III: stable blocks) considering 20 and 30 simulations

Nr of simulations	Nr total blocks	All blocks		Type I blocks		Type II blocks		Type III blocks	
		1 contact plane	2 contact planes	1 contact plane	2 contact planes	1 contact plane	2 contact planes	1 contact plane	2 contact planes
20	7807	2485	5322	695	192	14	930	1753	4200
30	10482	3689	7693	1091	304	14	1339	2561	6050

Table 14 - Average nr of blocks sorted by Type of block (Type I: unstable blocks; Type II: blocks stable thanks to φ; Type III: stable blocks) considering 20 and 30 simulations

Nr of simulations	Nr total blocks	All blocks (average)		Type I blocks (average)		Type II blocks (average)		Type III blocks (average)	
		1 contact plane	2 contact planes	1 contact plane	2 contact planes	1 contact plane	2 contact planes	1 contact plane	2 contact planes
20	390	124	266	35	10	1	47	88	210
30	379	123	256	36	10	0.47	45	85	202

7. Case study 2 results

7.1. Geostructural analysis

- SiroJoint

5 sets, including overall 1520 discontinuities (948 planes and 572 traces) (Figure 92 and Table 3), have been described with SiroJoint. The most important, including 626 discontinuities, is the 1m, the orientation of which is similar to the highwall one (70°/340° vs 74°/314°). 1m set is mostly constituted by planes and has an orientation similar to the slope, as 2m as well. The remaining sets (3m, 4m, and 5m) are mostly constituted by traces. 410 discontinuities have not been assigned to any set. We noticed that the orientation of the sets of discontinuities compared to the slope orientation, influences the outcropping of planes or traces; discontinuities the orientation of which is parallel to the slope are mostly represented by planes, while discontinuities the orientation of which is perpendicular to the slope one are mostly represented by traces. Of course, any plane is associated to a trace; during the discontinuities sampling double sampling of the same discontinuity has been avoided to prevent oversampling of sets of discontinuities with orientation similar to the slope. The dips of 1m and 2m sets of discontinuities (289° and 352° respectively) are parallel to the α_{slope} and are, in fact, represented by planes, while the dips of 3m, 4m, and 5m sets of discontinuities (75°, 224°, and 49° respectively) are perpendicular to the α_{slope} and are instead represented by traces.

The maximum L of the discontinuities ranges from the values of 8.18 metres of 4m set of discontinuities to 13.90 of 2m set. Among the sets mainly represented by planes (1m and 2m sets) the set with the orientation most similar to the orientation of the slope (2m set) has the highest value of L (13.90 m), while among the sets mainly represented by traces (5m, 3m, and 4m sets), the highest values of L (13.38 m) is reached by the 3m.

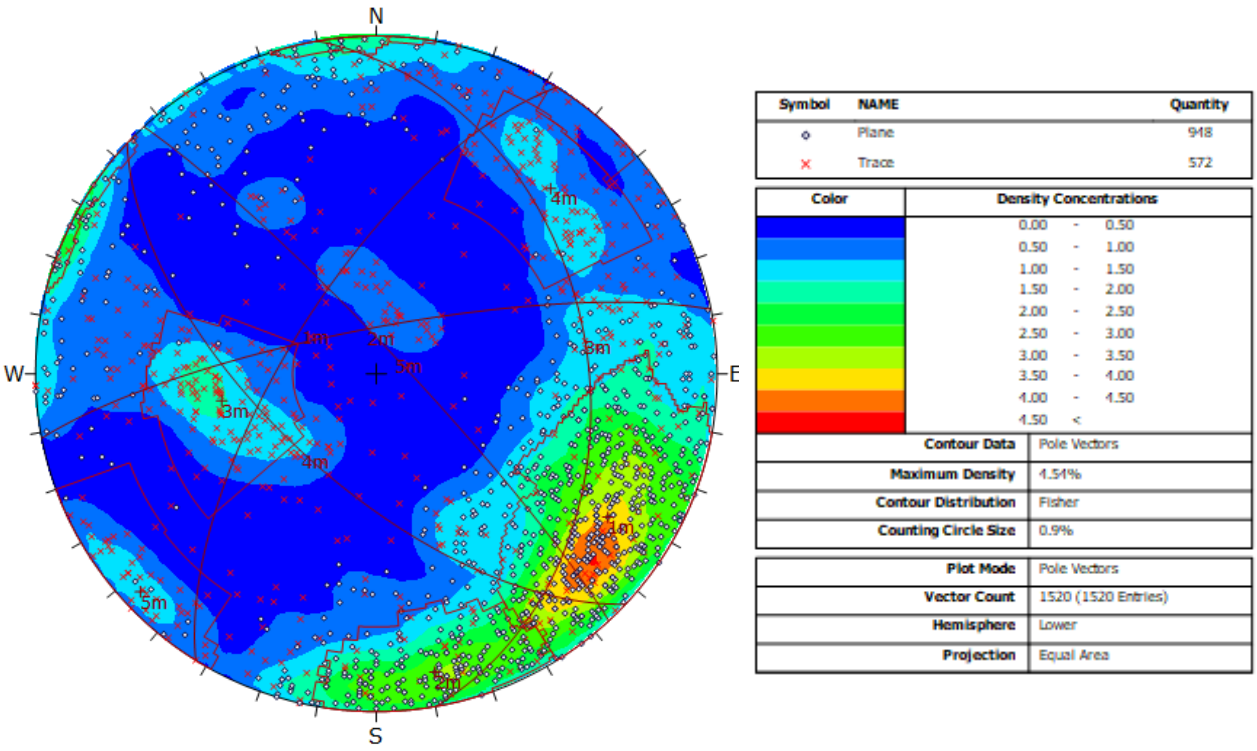

Figure 168 - Stereoplot with equal angle of the discontinuities extracted with SiroJoint for case study 2 mine wall. 5 sets of discontinuities have been recognised

Table 15 - α, σ_α, β, σ_β, L and σ_L of the sets of discontinuities extracted with SiroJoint for case study 2 mine

Set	α (°)	σ_α	β (°)	σ_β	L (m)	σ_L	Nr discontinuities
1m	289	14.67	72	13.05	11.78	2.20	626
2m	352	5.82	80	7.47	13.90	1.53	220
3m	75	18.64	37	9.78	13.38	1.99	133
4m	224	14.54	66	7.57	8.180	1.62	78
5m	49	8.19	84	4.38	8.32	1.57	53

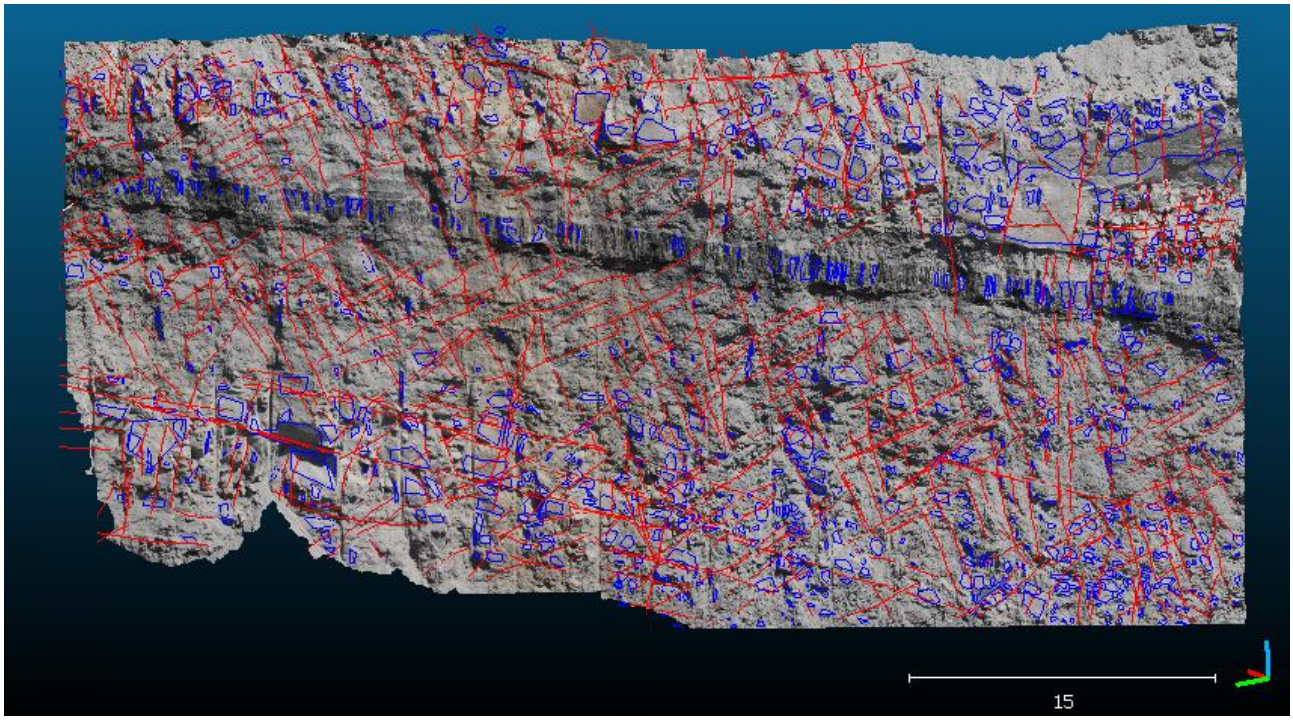

Figure 169 - Location of the planes (blue) and of the traces (red) extracted by SiroJoint on highwall of case study 1. Traces are coloured red, planes blue

- I-Site Studio

I-Site Studio has allowed to extract 1795 planes (Figure 170 and Table 16). An only set of discontinuities, 1m set, has been recognised by I-Site Studio (Figure 170 and Table 16). As for case study 1, the sets extracted by SiroJoint and related to traces (3m, 4m, and 5m sets of discontinuities in Figure 170 and Table 16) have not been detected with I-Site Studio. 1m set includes most of the discontinuities extracted (1635 on overall 1795 discontinuities). The values of σ_α and σ_β are 13.09 and 9.09 respectively (Table 16). The low number of poles outside the limits of the set clearly testifies that the output measurements are so less scattered than the measurements carried out by SiroJoint. This statement is a consequence of the sampling mode of the code, that implies the indication of the angular range between the detected plane and other planes extracted by the point cloud. The minor L in comparison to the results of the discontinuities extraction by SiroJoint, depends on the fact planes only, the apparent L of which is clearly minor than the apparent L of the traces.

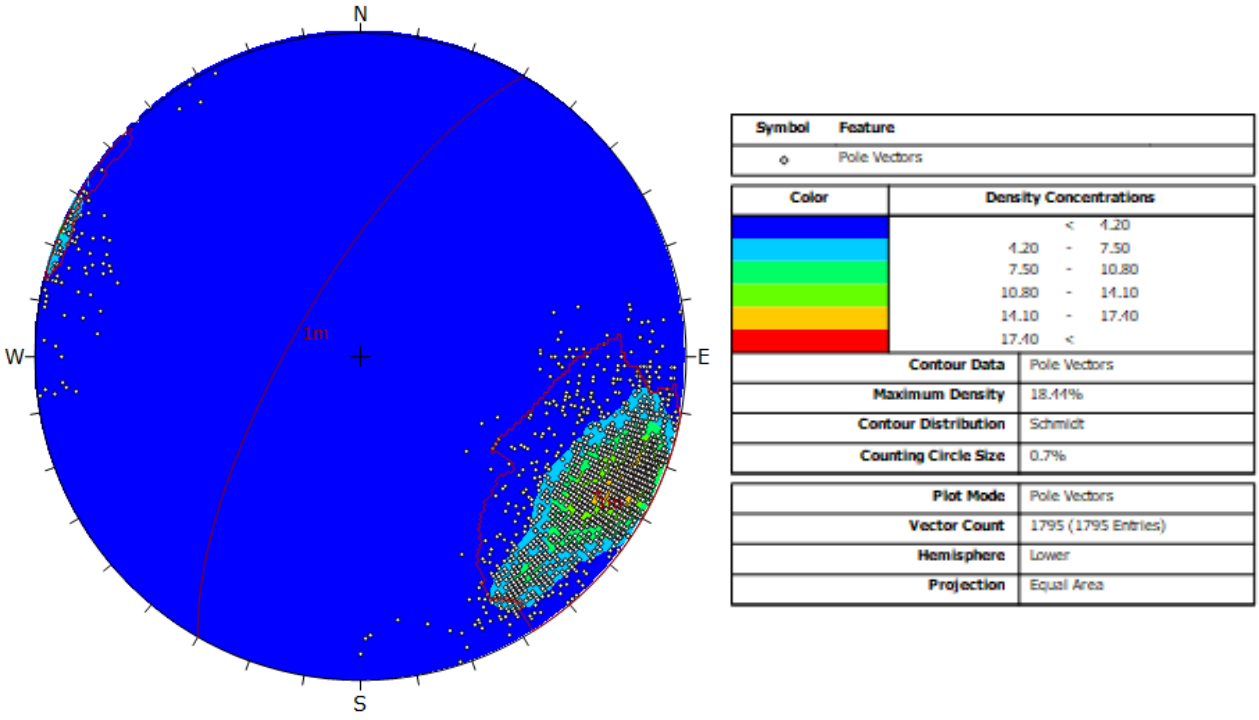

Figure 170 - Stereoplot with equal angle of the discontinuities extracted with I-Site Studio for case study 2 mine wall

Table 16 - α, σ_α, β, σ_β, L and σ_L of the sets of discontinuities extracted with I-Site Studio for case study 2 mine

Set	α (°)	σ_α	β (°)	σ_β	L (m)	σ_L	Nr discontinuities
1m	300	13.09	74	9.09	6.39	0.57	1635

- DiAna

The first step to perform the geostructural characterisation of the rock mass has been the retailment of the overlapping areas in order to avoid the doubling of the 3D model. The stereomodel of the stereo pair nr 3 (Figure 85) has not so been used because entirely overlapped by the stereomodels of the stereopair nr 2 on the left and nr 4 on the right; the overlapping area between the stereomodels of stereo pair nr 2 and nr 4 too has been discarded. Both for the stereo pair nr 2 as for stereo pair nr 4, a searching box with 7 points large, corresponding to 49 points, with a minimum of 30 points (in case of areas close to the mesh edge). The number of triangles, the number of vertices, the area, the vertices average concentration and the triangles average area are summarized in concentration of the stereo pair nr 2 (left stereo pair) is higher than vertices average concentration of the stereo pair nr 4 (right stereo pair) (4,775 vs 2,129 points/m^2), while the triangles average area is lower (9.85×10^{-4} vs 2.591×10^{-3}); the mesh produced with the left stereo pair has so a higher concentration. The point clouds have been resampled with RiScanPro software in order to obtain an ordered point cloud and to reduce the difference of density of the two point clouds.

Table 17 - Nr of vertices, nr of triangles, area, concentration and average triangles area for stereo pairs nr 2 and nr 4. (*) area evaluated by the surface of the mesh

	Nr of vertices	Nr of triangles	Area (m2)	Vertices average concentration (nr vertices/m2)	Triangles average area (m2)
Stereo pair nr 2 (left)	2,124,863	451,840	949	2,239	$2.10 \times 10-3$
Stereo pair nr 4 (right)	1,026,351	186,009	939	1,093	$5.04 \times 10-3$
Resampled stereo pair nr 2 (left)	204,386	- (point cloud)	949	215	- (point cloud)
Resampled stereo pair nr 4 (right)	185,084	- (point cloud)	939	197	- (point cloud)

Table 17 - Nr of vertices, nr of triangles, area, concentration and average triangles area for stereo pairs nr 2 and nr 4. (*) area evaluated by the surface of the mesh

	Nr of vertices	Nr of triangles	Area (m^2)	Vertices average concentration (nr vertices/m^2)	Triangles average area (m^2)
Stereo pair nr 2 (left)	2,124,863	451,840	949	2,239	2.10×10^{-3}
Stereo pair nr 4 (right)	1,026,351	186,009	939	1,093	5.04×10^{-3}
Resampled stereo pair nr 2 (left)	204,386	- (point cloud)	949	215	- (point cloud)
Resampled stereo pair nr 4 (right)	185,084	- (point cloud)	939	197	- (point cloud)

Geostructural analysis performed by DiAna on case study 2 mine has been carried out processing left and right point clouds separately (Figure 171).

A comparative preliminary analysis of the standard deviation of the point clouds carried out using a searching box with the same parameters has, in fact, shown that a unique range of standard deviation values cannot be used to extract the planes for the left stereo pair and the right stereo pair at the same time. Despite, in fact, resampling has allowed to homogenise the difference of the vertices average concentration from 2239/1039 = 2.15 to 215/197 = 1.09 (Table 17), making so comparable densities of the two point-clouds, the analysis of the standard deviation has shown that planes are clearly more detectable in right stereo pair point cloud because the values of the standard deviation where planes outcrop are lower than in left stereo pair point cloud (Figure 172). The apparently lower evidence of the planes in the 3D model carried out with the left stereo pair is due to the higher definition of these two images in comparison to the images of the right stereo pair, that allow the building of a more detailed and real surface model; the 3D model built with the right stereo pair is instead affected by a "discretisation" due to the worst focusing affecting this stereo pair. The triangles built with Siro3D appear so wider and the surface to which they belong sharper.

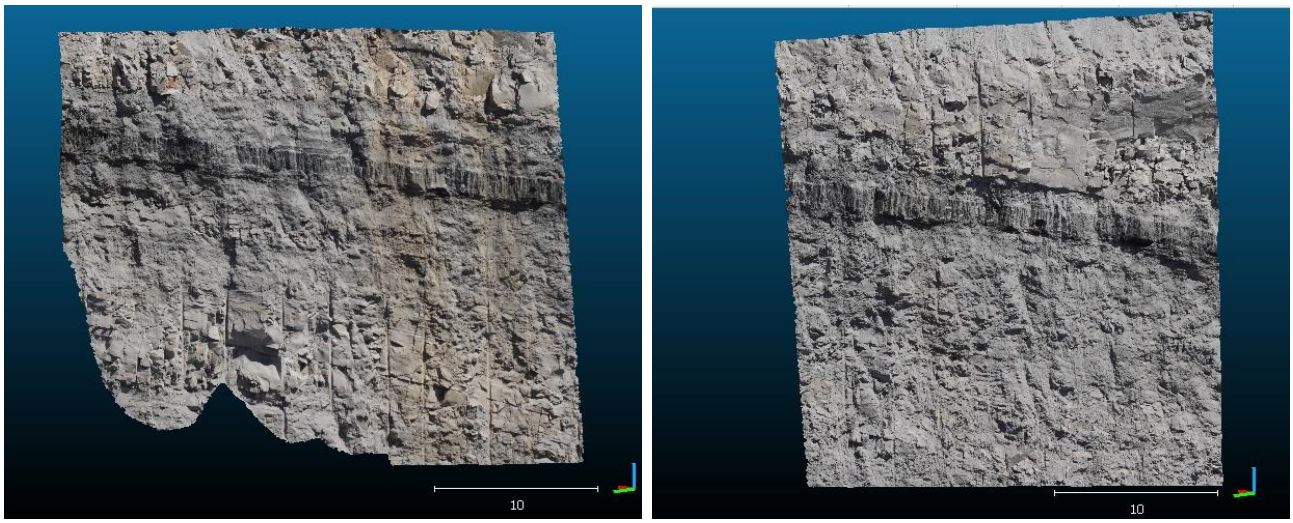

Figure 171 - Left and right stereo pair of the highwall of case study 2 used for the discontinuities extraction with DiAna

This observation has allowed to understand that two distinct geostructural analysis must be carried on for left and right stereo pairs because planes extraction requires different geometrical parameters in consequence of different accuracy of the point cloud of the left and right stereo pair. The different standard deviation values of the two point clouds are related to the different accuracy of the two 3D models of the highwall surface. As described in Chapter 3, many factors concur to the accuracy of a 3D model carried out by photogrammetric survey; in this survey the same devices and geometrical characteristic of the survey planes (cameras interdistance, overlapping, stereo pair-highwall distance, tilting and bearing angle, LOS-surveyed surface angle). On an optical observation a different sunlight affects the two couples of images, although only a few minutes long period divides the acquisition of the two stereo pairs; while, in fact the images of the left stereo pair, the insolation condition are slightly different and, on particular, the right stereo pair images have been taken in a sunnier moment, while the shadows on the left stereo pair images allow a more detailed representation of the 3D surface.

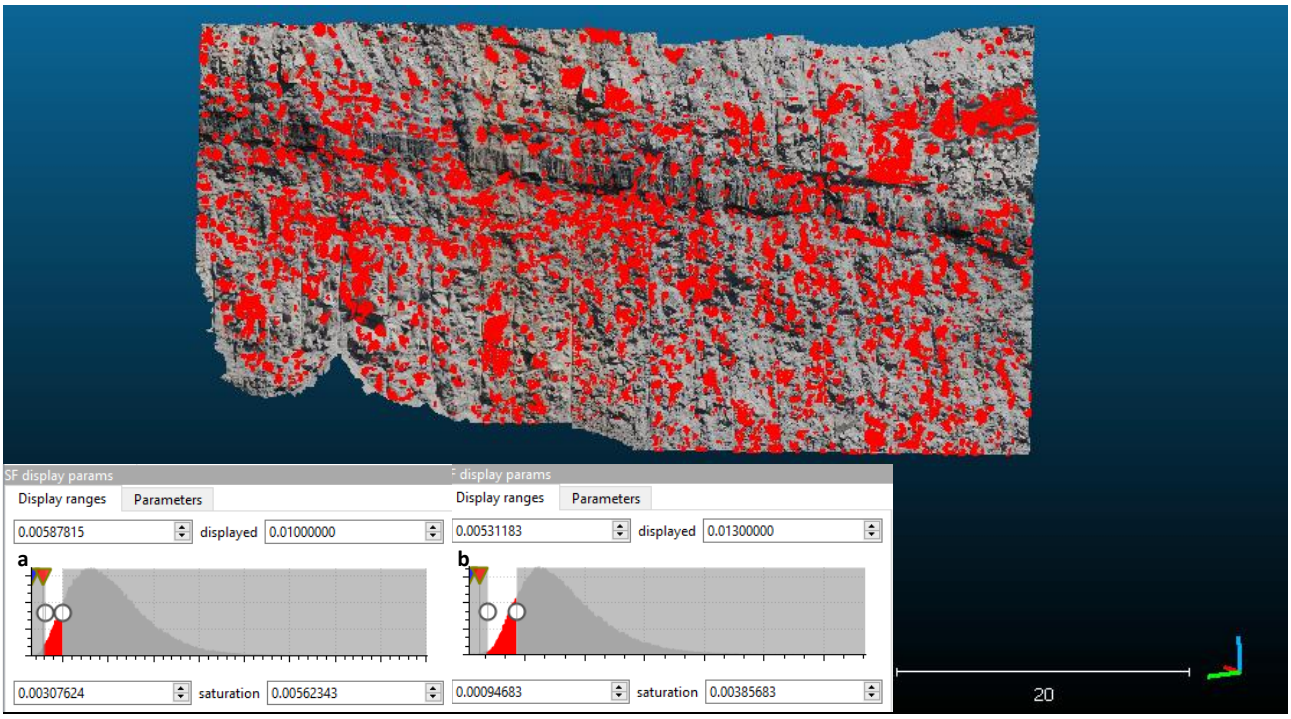

Figure 172 - Overview of the case study 2 mine highwall: the red areas indicate the points with standard deviation of the distance between the subsampled point clouds using a 3-points range. Different range of standard deviation have been used as criterion for planes extraction; a) standard deviation range for left stereo pair; b) standard deviation range for right stereo pair

Two different ranges of standard deviation have been used for planes extraction for the left and for the right point cloud (Figure 172): for the point cloud extracted from the left stereo pair has been set a maximum value of standard deviation equal to 0.01, while for the point cloud extracted with the right stereo pair, the maximum value of standard deviation has been set to 0.013.

Geostructural analysis of the highwall carried out by DiAna has allowed the extraction of 1259 planes (Figure 173). As for I-Site Studio, one set of discontinuities only has been recognised. The recognised set of discontinuities includes 916 discontinuities (Table 18). The values of σ_{α} and σ_{β} correspond to 14.72 and 9.75 respectively. The position of the discontinuities, divided by set, extracted by DiAna is shown in Figure 174.

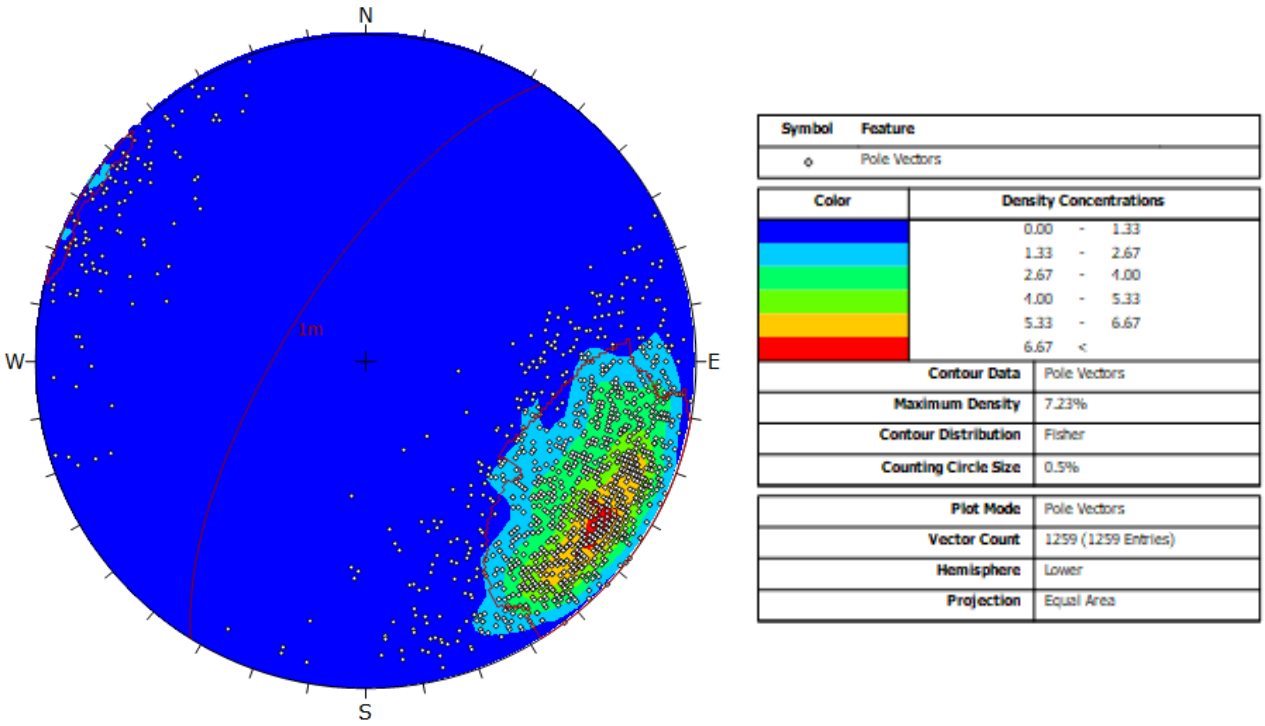

Figure 173 - Stereoplot with equal angle of the discontinuities extracted with DiAna for case study 2 mine wall.

Table 18 - α, σ_α, β, σ_β, L and σ_L of the sets of discontinuities extracted with DiAna for case study 2 mine

Set	α (°)	σ_α	β (°)	σ_β	L (m)	σ_L	Nr discontinuities
1m	302	14.72	71	9.75	5.78	0.74	916

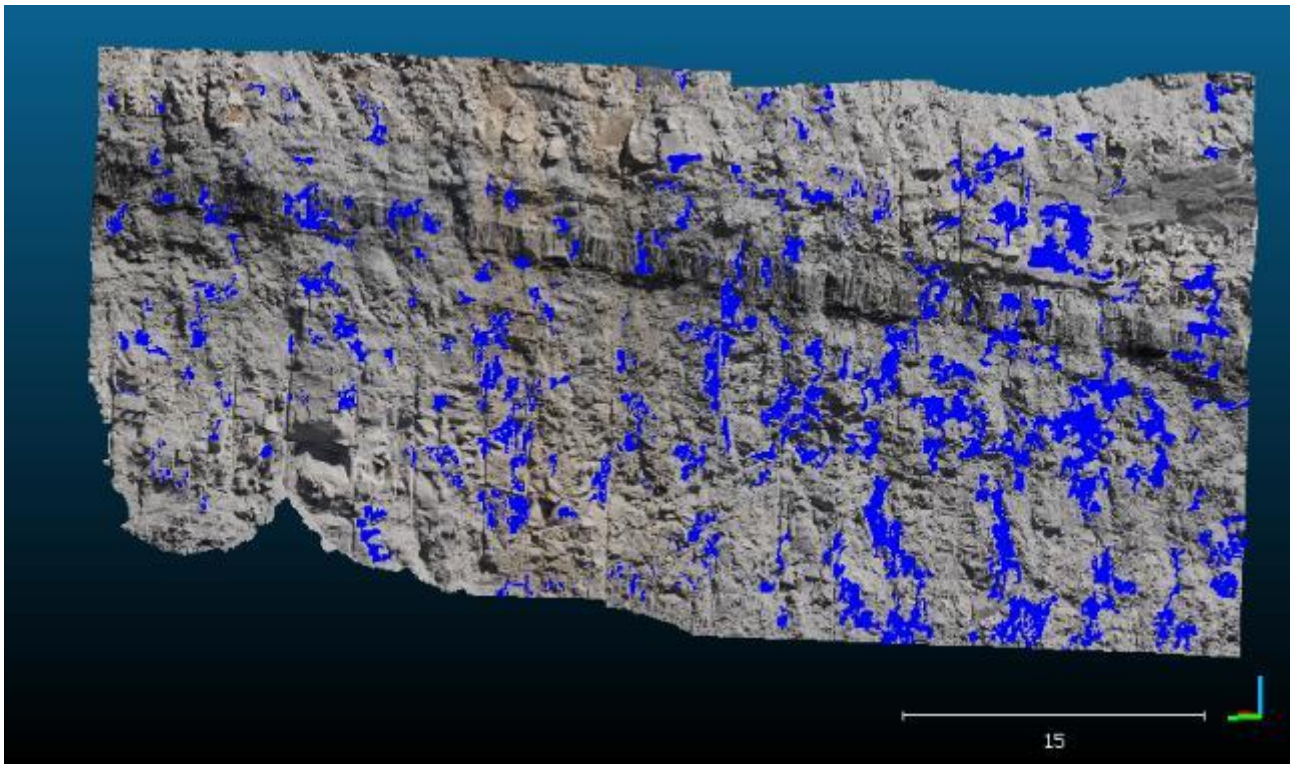

Figure 174 - The position of the discontinuities extracted by DiAna

- Facets

The vertices average concentration of the point cloud of the left stereo pair and of the right stereo pair has suggested a distinct discontinuity extraction for left and right part, using a different extraction parameters minimum of points as criterium for plane extraction, considering the minimum surface of the planes from the 3D model (0.04 m^2 about). Indeed, 0.25 and 0.2 has been chosen for the maximum distance between the points and the regression surface and for the maximum edge length respectively. The planes extraction has been carried out by an octree level = 8. Not realistic planes have been discarded by selecting only planes with a surface included into 0.01 m^2 and 5 m^2 range and with a retro-projection error > 0.1.

Facets code has allowed to extract 741 discontinuities, 548 of which are related to 1m set of discontinuities (Figure 99 and Table 19). As for I-Site Studio and DiAna, no discontinuity related to the sets extracted by SiroJoint and related to traces (3m, 4m, and 5m sets of discontinuities) has been detected.

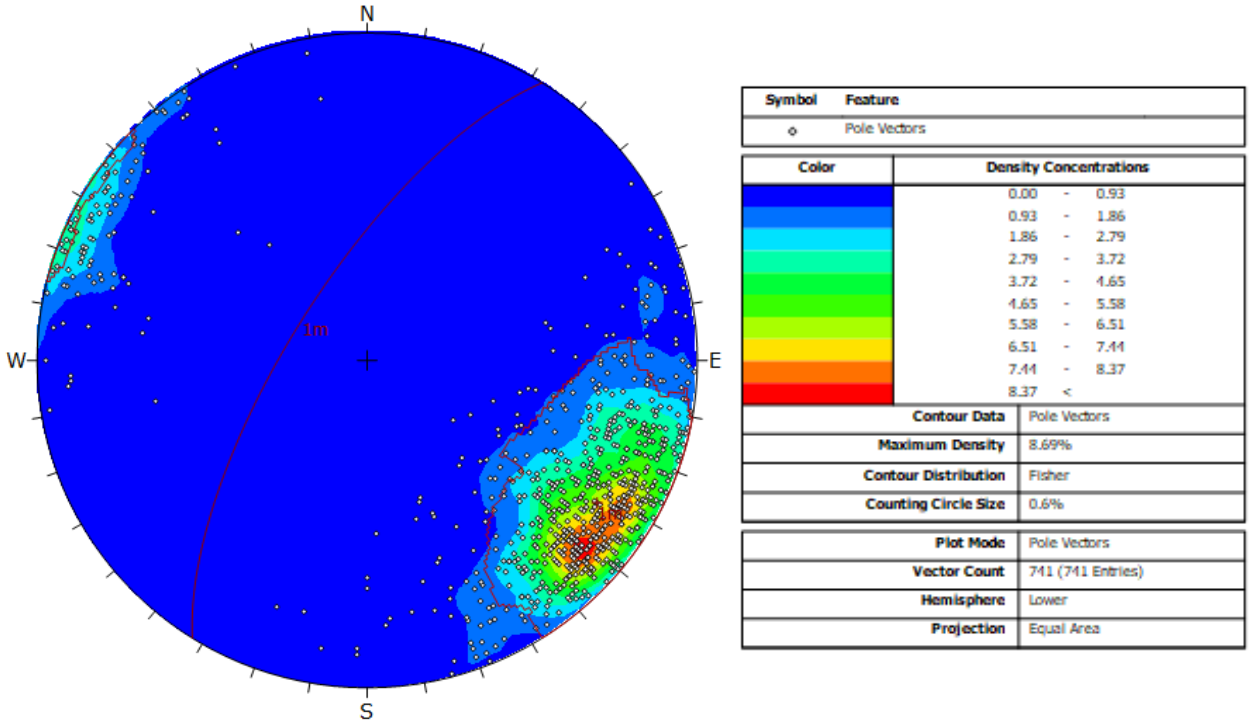

Figure 175 - Stereoplot with equal angle of the discontinuities extracted with Facets plug-in of CloudCompare for case study 2 mine wall

Table 19 - α, σ_α, β, σ_β, L and σ_L of the sets of discontinuities extracted with Facets plug-in of CloudCompare for case study 2 mine

Set	α (°)	σ_α	β (°)	σ_β	L (m)	σ_L	Nr discontinuities
1m	302	13.23	73	10.56	0.90	0.09	548

7.2. Kinematic analysis

2D and 3D kinematic analysis has been carried on for case study 2 slope, as for case study 1. 2D kinematic analysis has been performed using as slope a simplified model of the slope with α_{slope} = 74° and β_{slope} = 134°. 2D Kinematic analysis carried out on discontinuities extracted by SiroJoint, I-Site Studio, and DiAna has revealed the sets of discontinuities involved for plane failure, wedge failure, block toppling and flexural

toppling mechanisms, while 3D kinematic analysis has been performed using DiAna-K code on the real 3D model built with the photogrammetric survey.

7.2.1. Plane Failure

The 2D kinematic analysis performed on the stereoplots obtained with the discontinuities extracted indicates that plane failure is a feasible failure mechanism. In particular, as regarding the discontinuities extracted with SiroModel, 236 discontinuities on 1520 are prone to failure. 191 among these discontinuities are moreover related to 1m set of discontinuities, and 4 only are related to 2m set of discontinuities; the remnant 41 are not related to any other set. These discontinuities are mainly constituted by planes (218/236) and are entirely related to sets with an orientation similar to the slope one. Overall 15.53 % of the discontinuities are prone to plane failure (Figure 176).

The percentage of discontinuities critical for plane failure increases if we consider the stereoplots of the discontinuities represented by planes. For example, the percentage of discontinuities critical to plane failure considering only the planes extracted with SiroJoint (Figure 177) is equal to 23.00%. As regarding I-Site Studio, the percentage is equal to 34.09% (Figure 178), as regarding DiAna 33.20% (Figure 179) and as regarding Facets 31.58% (Figure 180). Discontinuities prone to plane failure are related entirely to 1m or 2m sets of discontinuities; in the stereoplot with the discontinuities extracted with I-Site Studio, 144 are related to 2m set and 459 to 1m set among the discontinuities critical for plane failure, while in the stereoplot with the discontinuities extracted with DiAna 559 are related to 2m set and 60 to 1m set. Among the critical discontinuities in the stereoplot with the discontinuities extracted with Facets, 198 are related to 2m set and none to 1m set.

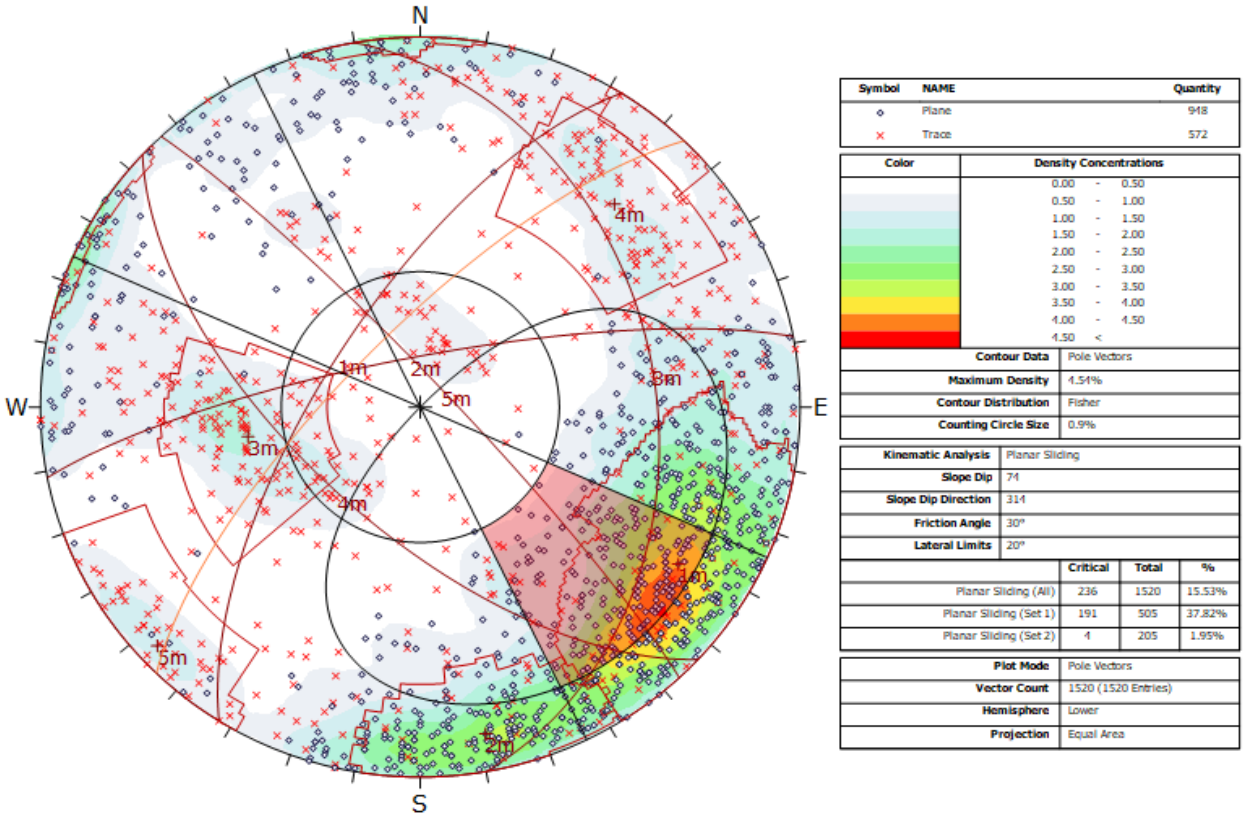

Symbol	NAME	Quantity
◇	Plane	918
×	Trace	572

Color	Density Concentrations
	0.00 - 0.50
	0.50 - 1.00
	1.00 - 1.50
	1.50 - 2.00
	2.00 - 2.50
	2.50 - 3.00
	3.00 - 3.50
	3.50 - 4.00
	4.00 - 4.50
	4.50 <

Contour Data	Pole Vectors
Maximum Density	4.54%
Contour Distribution	Fisher
Counting Circle Size	0.9%

Kinematic Analysis	Planar Sliding
Slope Dip	74
Slope Dip Direction	314
Friction Angle	30°
Lateral Limits	20°

	Critical	Total	%
Planar Sliding (All)	236	1520	15.53%
Planar Sliding (Set 1)	191	505	37.82%
Planar Sliding (Set 2)	4	205	1.95%

Plot Mode	Pole Vectors
Vector Count	1520 (1520 Entries)
Hemisphere	Lower
Projection	Equal Area

Figure 176 - Kinematic analysis of planes and traces of case study 2 mine wall for plane failure on geostructural data carried out by SiroJoint. Orange cyclographic: slope orientation; pink area: area of the stereo plot with intersection of planes coupling affected by plane failure

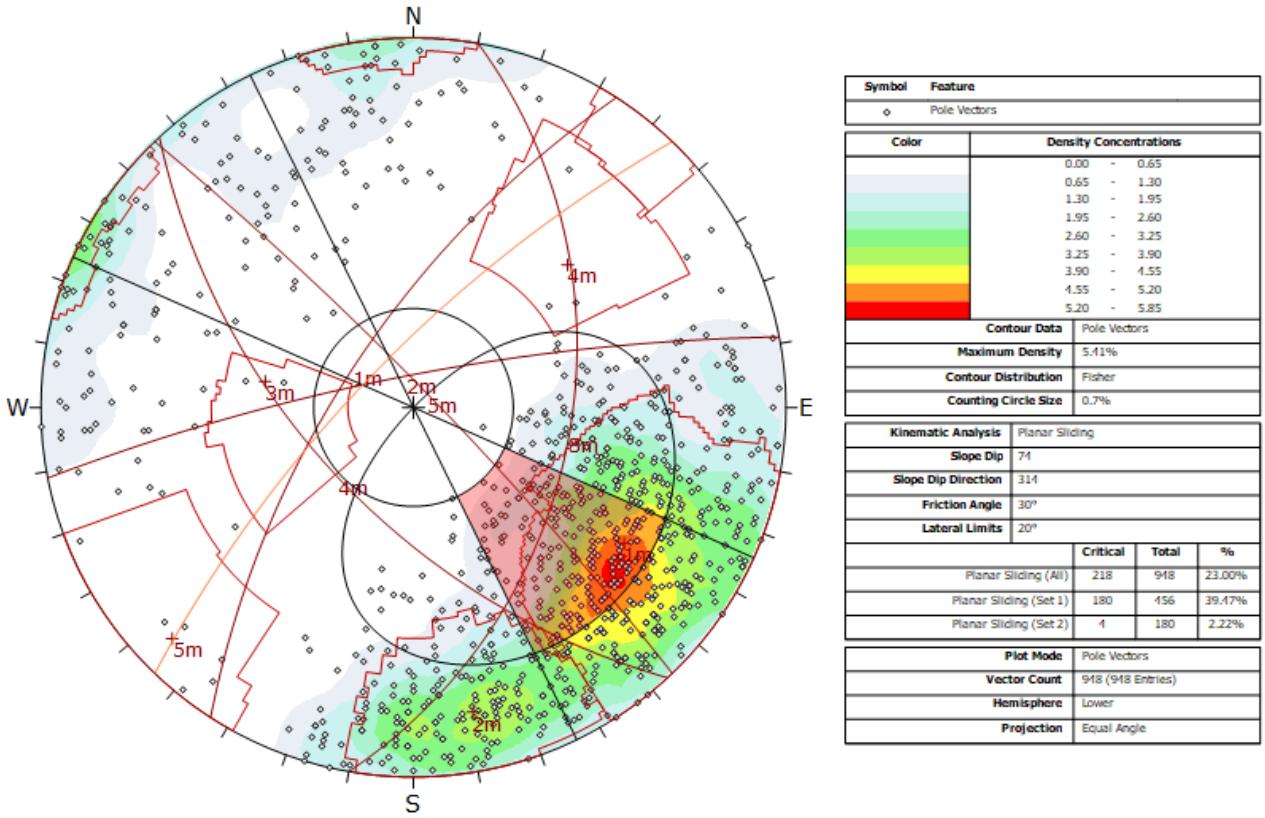

Figure 177 - Kinematic analysis of planes only of case study 2 mine wall for plane failure on geostructural data carried out by SiroJoint. Orange cyclographic: slope orientation; pink area: area of the stereo plot with intersection of planes coupling affected by plane failure

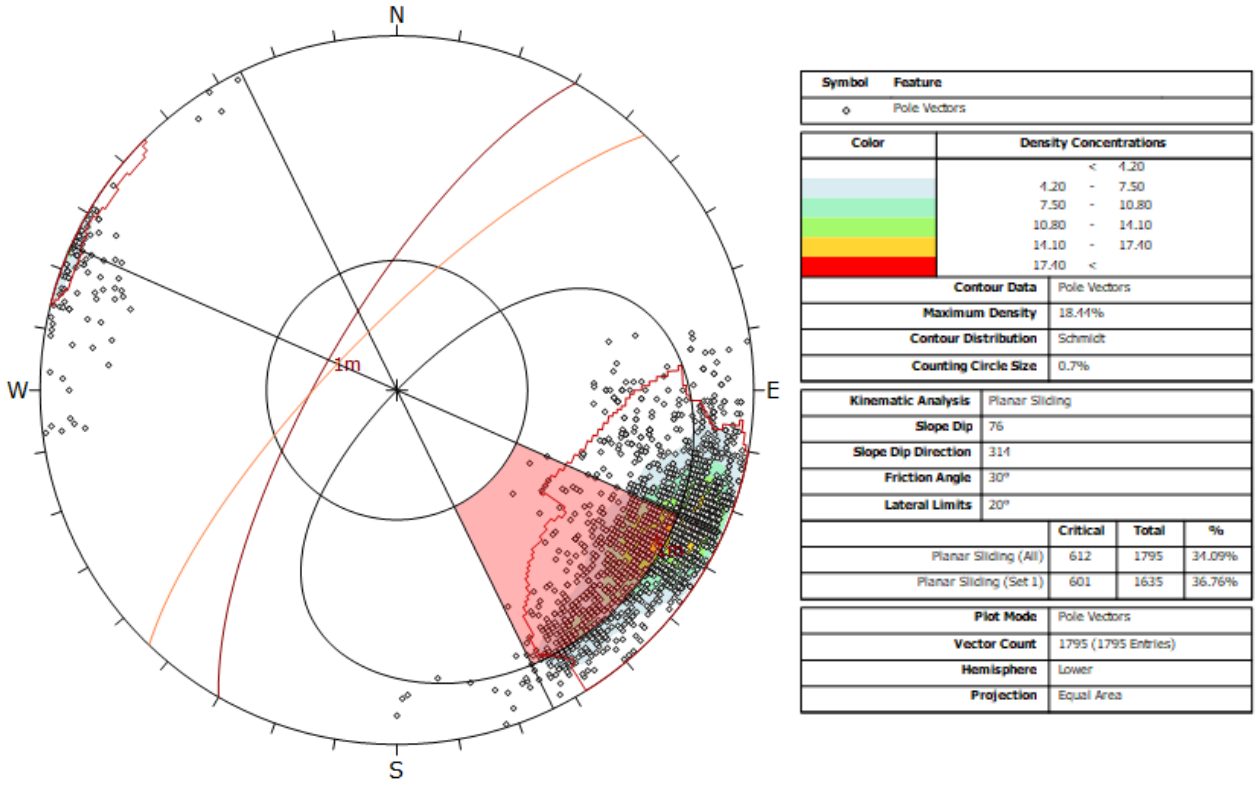

Figure 178 - Kinematic analysis of case study 2 mine wall for plane failure on geostructural data carried out by I-Site Studio. Orange cyclographic: slope orientation; pink area: area of the stereo plot with intersection of planes coupling affected by plane failure

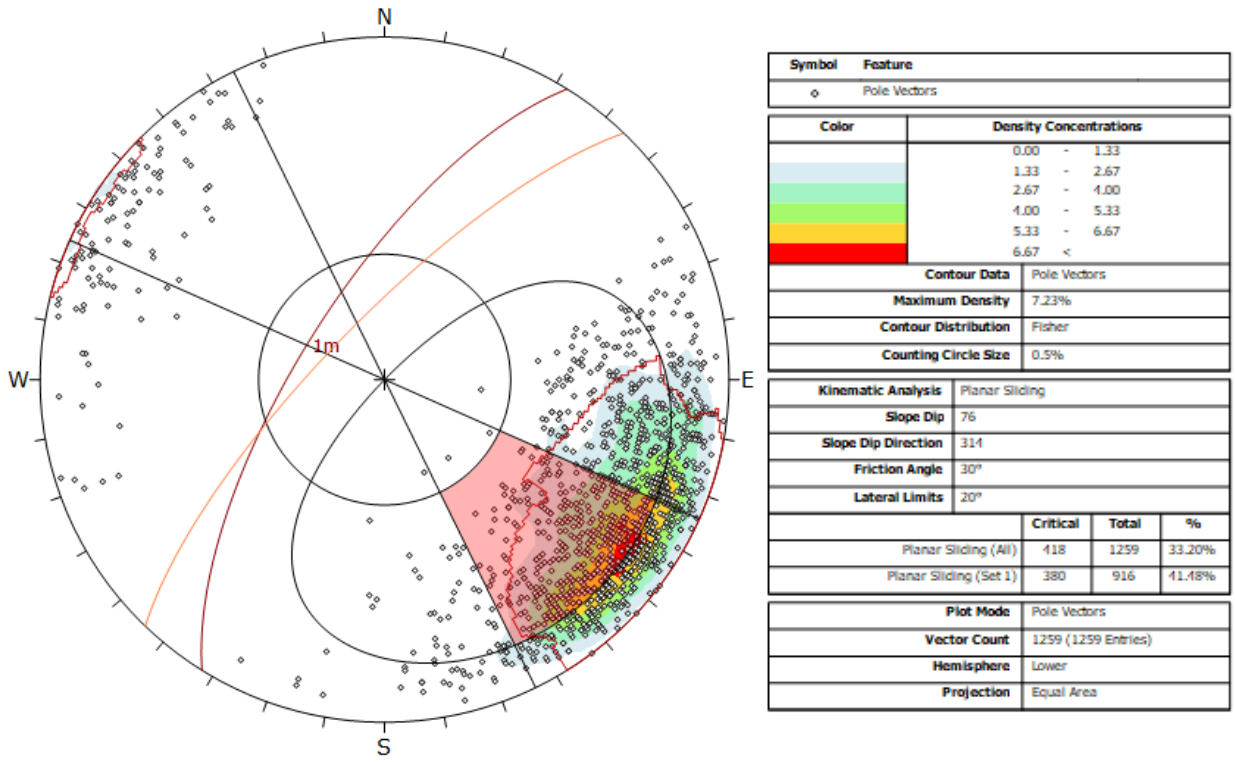

Figure 179 - Kinematic analysis of case study 2 mine wall for plane failure on geostructural data carried out by DiAna. Orange cyclographic: slope orientation; pink area: area of the stereo plot with intersection of planes coupling affected by plane failure

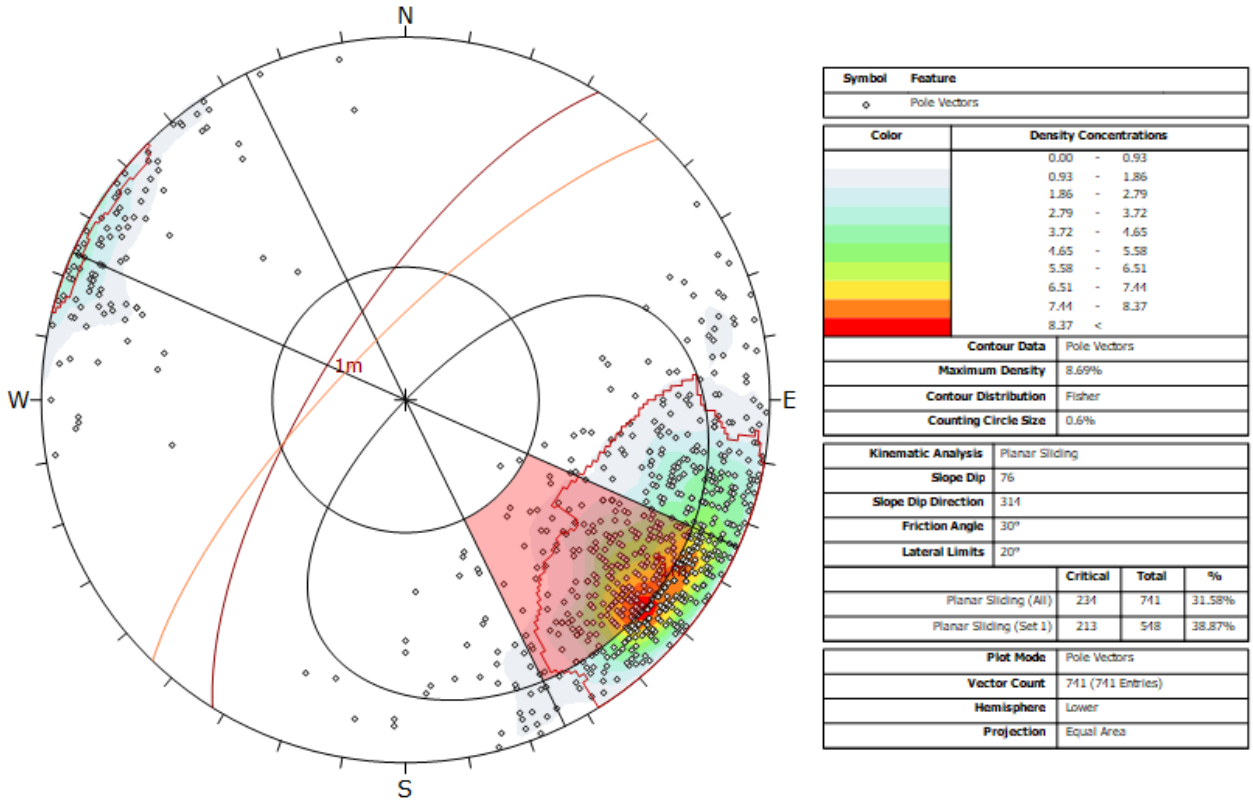

Figure 180 - Kinematic analysis of case study 2 mine wall for plane failure on geostructural data carried out by Facets plug-in of CloudCompare. Orange cyclographic: slope orientation; pink area: area of the stereo plot with intersection of planes coupling affected by plane failure

7.2.2. Wedge Failure

2D kinematic analysis shows that wedge failure is a feasible failure mechanism, whatever the code is used for the discontinuities extraction. As regarding SiroJoint, the average planes intersections show 1m-2m, 1m-4m, 1m-5m, and 2m-4m intersections are critical for wedge failure. A large number of critical intersections are so related to 1m set, also because is the most populated set. Overall, 37.70% of the intersections (2968009) intersect the wedge failure prone area (Figure 181). The kinematic index increases in case planes only are considered (37.70 % vs 46.53 %) (Figure 182): this confirm that the intersections of 1m set are critical for wedge failure.
The kinematic analysis carried out with I-Site Studio (Figure 183), DiAna (Figure 184), and Facets (Figure 185) shows that the intersection within is critical for wedge failure and that a percentage of intersections of 50.59%, 50.88% and 47.57% is included into the critical area respectively.

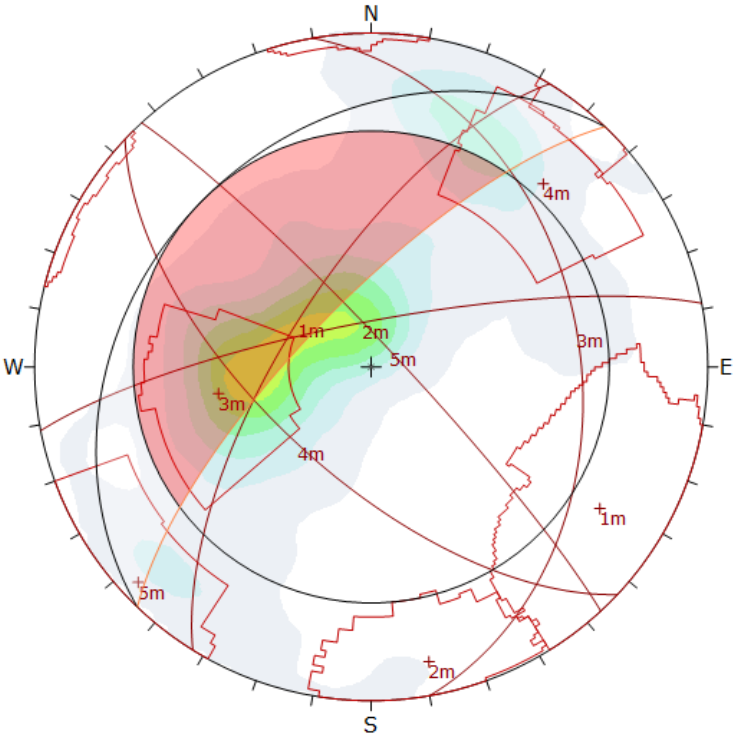

Color	Density Concentrations
	0.00 - 0.50
	0.50 - 1.00
	1.00 - 1.50
	1.50 - 2.00
	2.00 - 2.50
	2.50 - 3.00
	3.00 - 3.50
	3.50 - 4.00
	4.00 - 4.50
	4.50 <

Contour Data	Intersections
Maximum Density	3.49%
Contour Distribution	Fisher
Counting Circle Size	0.7%

Kinematic Analysis	Wedge Sliding
Slope Dip	74
Slope Dip Direction	314
Friction Angle	30°

	Critical	Total	%
Wedge Sliding	435221	1154336	37.70%

Plot Mode	Pole Vectors
Vector Count	1520 (1520 Entries)
Hemisphere	Lower
Projection	Equal Area

Figure 181 - Kinematic analysis of planes and traces of case study 2 mine wall for wedge failure on geostructural data carried out by SiroJoint. Orange cyclographic: slope orientation; pink spherical spindle: area of the stereo plot with intersection of planes coupling affected by wedge failure

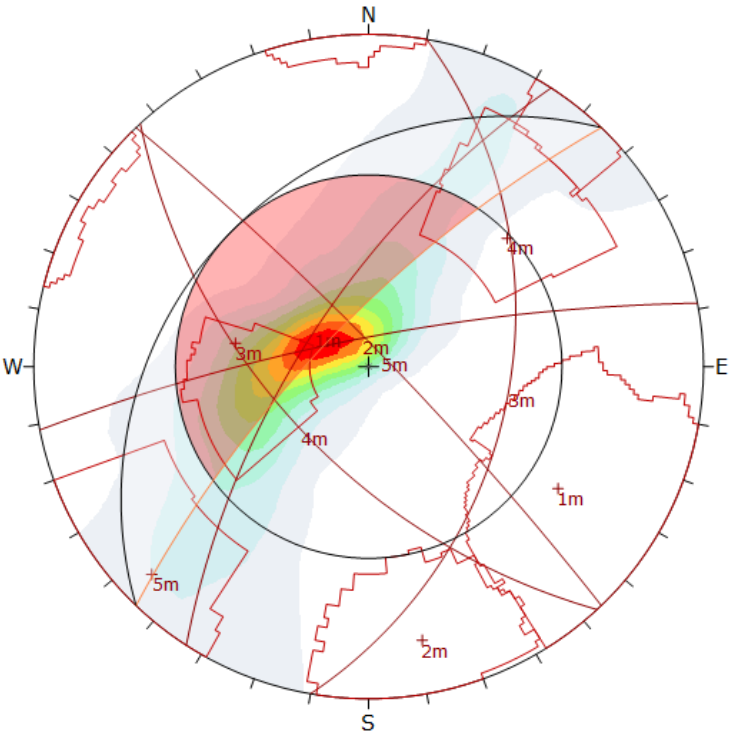

Color	Density Concentrations
	0.00 - 0.70
	0.70 - 1.40
	1.40 - 2.10
	2.10 - 2.80
	2.80 - 3.50
	3.50 - 4.20
	4.20 - 4.90
	4.90 - 5.60
	5.60 - 6.30
	6.30 - 7.00

Contour Data	Intersections
Maximum Density	6.97%
Contour Distribution	Fisher
Counting Circle Size	1.0%

Kinematic Analysis	Wedge Sliding
Slope Dip	74
Slope Dip Direction	314
Friction Angle	30°

	Critical	Total	%
Wedge Sliding	208814	448801	46.53%

Plot Mode	Pole Vectors
Vector Count	948 (948 Entries)
Hemisphere	Lower
Projection	Equal Angle

Figure 182 - Kinematic analysis of planes only of case study 2 mine wall for wedge failure on geostructural data carried out by SiroJoint. Orange cyclographic: slope orientation; pink spherical spindle: area of the stereo plot with intersection of planes coupling affected by wedge failure

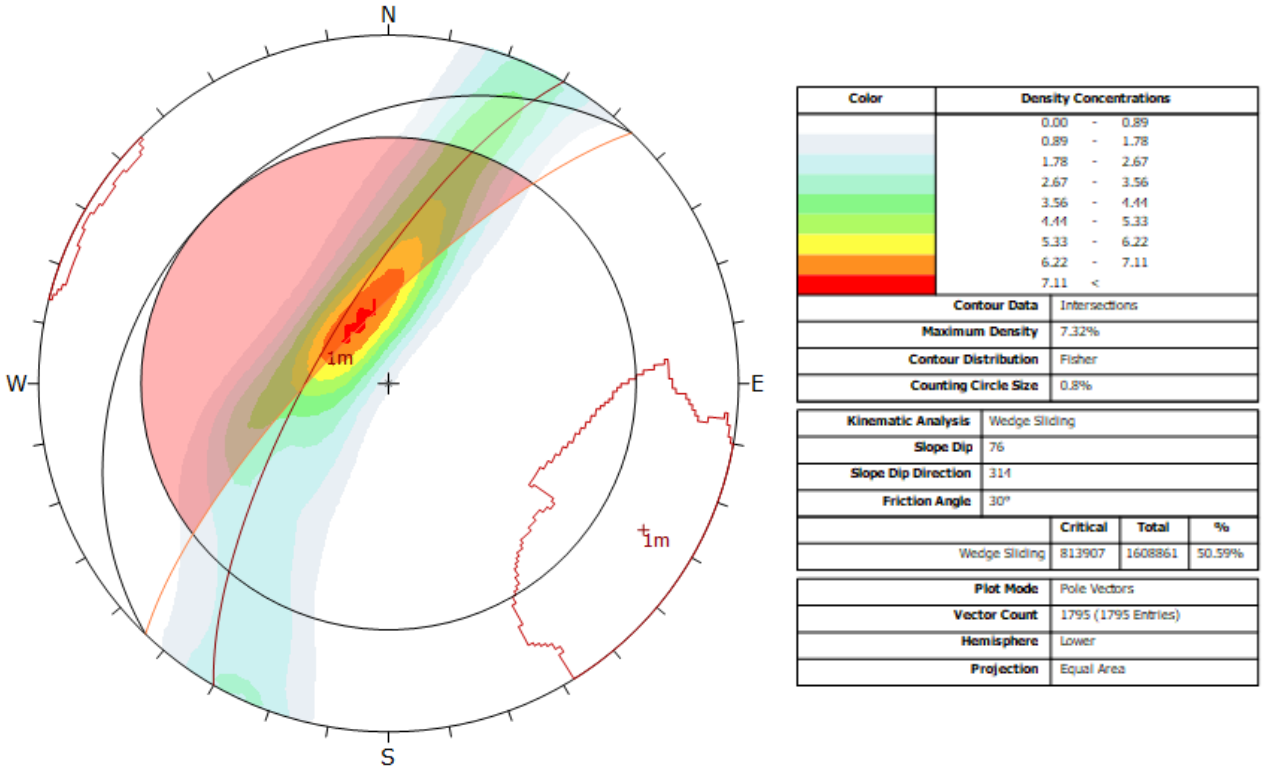

Color	Density Concentrations
	0.00 - 0.89
	0.89 - 1.78
	1.78 - 2.67
	2.67 - 3.56
	3.56 - 4.44
	4.44 - 5.33
	5.33 - 6.22
	6.22 - 7.11
	7.11 <

Contour Data	Intersections
Maximum Density	7.32%
Contour Distribution	Fisher
Counting Circle Size	0.8%

Kinematic Analysis	Wedge Sliding		
Slope Dip	76		
Slope Dip Direction	314		
Friction Angle	30°		
	Critical	Total	%
Wedge Sliding	813907	1608861	50.59%

Plot Mode	Pole Vectors
Vector Count	1795 (1795 Entries)
Hemisphere	Lower
Projection	Equal Area

Figure 183 - Kinematic analysis of case study 2 mine wall for wedge failure on geostructural data carried out by I-Site Studio. Orange cyclographic: slope orientation; pink spherical spindle: area of the stereo plot with intersection of planes coupling affected by wedge failure

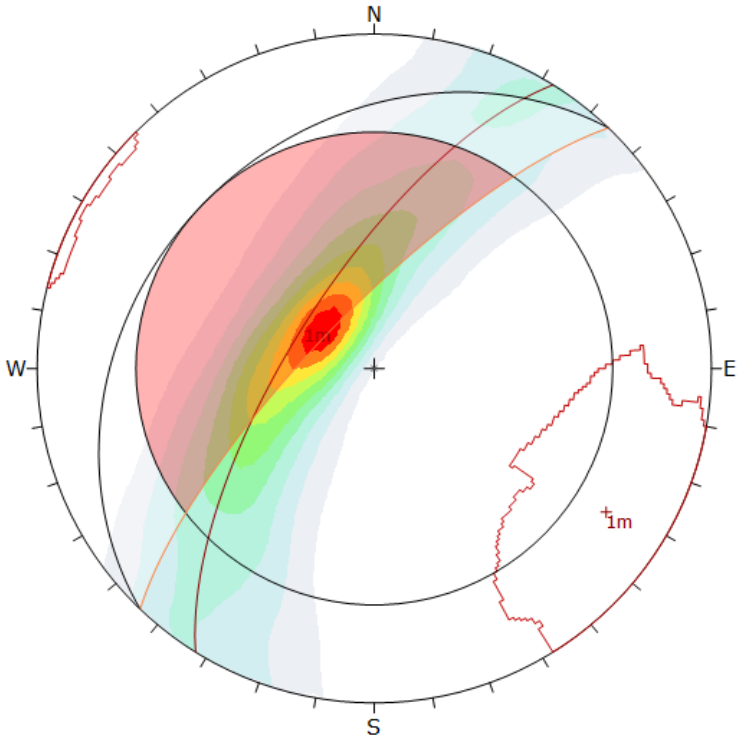

Color	Density Concentrations
	0.00 - 0.80
	0.80 - 1.60
	1.60 - 2.40
	2.40 - 3.20
	3.20 - 4.00
	4.00 - 4.80
	4.80 - 5.60
	5.60 - 6.40
	6.40 - 7.20
	7.20 - 8.00

Contour Data	Intersections
Maximum Density	7.93%
Contour Distribution	Fisher
Counting Circle Size	1.0%

Kinematic Analysis	Wedge Sliding		
Slope Dip	76		
Slope Dip Direction	314		
Friction Angle	30°		
	Critical	Total	%
Wedge Sliding	402780	791674	50.88%

Plot Mode	Pole Vectors
Vector Count	1259 (1259 Entries)
Hemisphere	Lower
Projection	Equal Area

Figure 184 - Kinematic analysis of case study 2 mine wall for wedge failure on geostructural data carried out by DiAna. Orange cyclographic: slope orientation; pink spherical spindle: area of the stereo plot with intersection of planes coupling affected by wedge failure

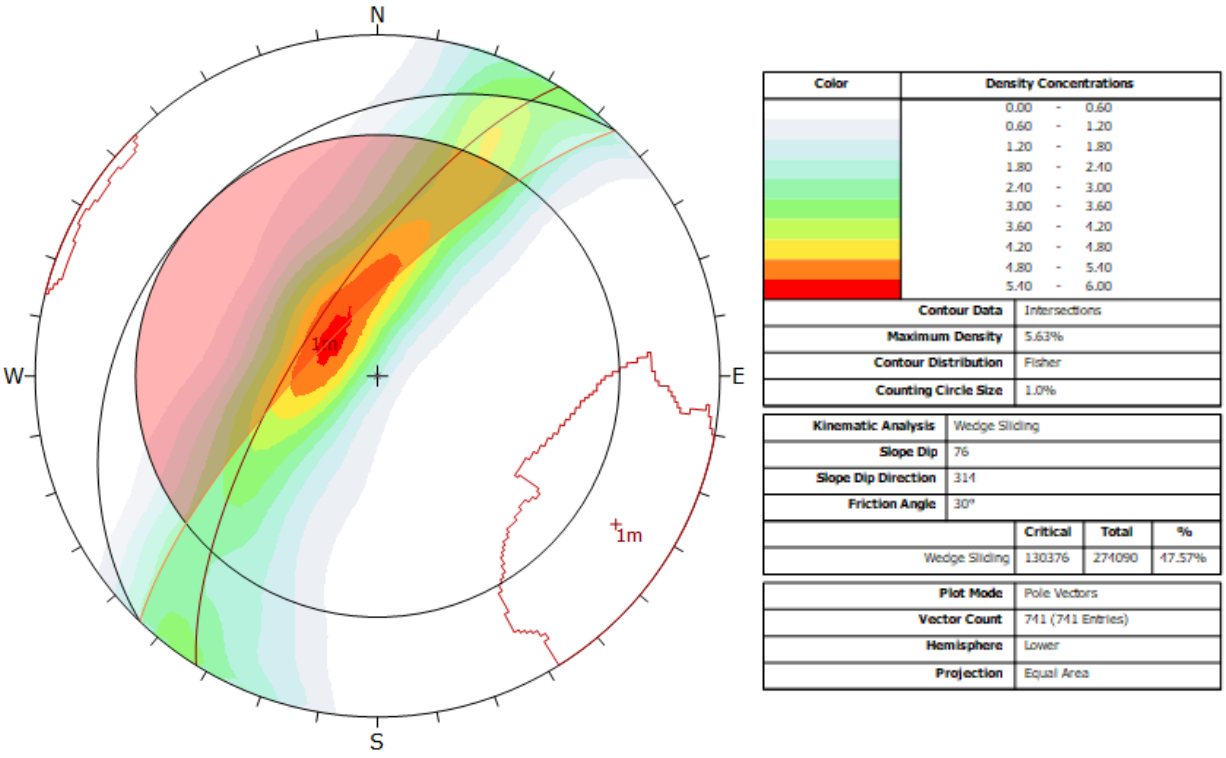

Figure 185 - Kinematic analysis of case study 2 mine wall for wedge failure on geostructural data carried out by Facets plug-in of CloudCompare. Orange cyclographic: slope orientation; pink spherical spindle: area of the stereo plot with intersection of planes coupling affected by wedge failure

7.2.3. Block Toppling

Block toppling conditions, for case study 2, are very rarely satisfied; although, in fact, the basal plane is often present, as suggested for the previous kinematic analysis for the plane failure, the intersections are rarely included in the primary critical zone (Chapter 4.1).

The geostructural survey carried out with SiroJoint has revealed that 3.19% of the intersections only are include within the secondary critical zone (Figure 186) and is moreover related to the - 5m intersection. -4m intersection is instead close to the secondary critical zone. To summarize, most of the intersections critical to block toppling are related to the intersection of anti-dip sets of discontinuities and a set of discontinuities the α of which is normal to the α_{slope} (5m and 4m). If we consider, in fact, only the planes extracted with SiroJoint (Figure 187), the percentage of critical intersections decreases to 0.63% because no set of discontinuities with α is normal to the α_{slope} is constituted by planes.

As regarding block toppling, the kinematic analysis carried out by the discontinuities extracted by I-Site Studio, DiAna and Facets shows results similar to the kinematic analysis on the stereoplot of the planes extracted by SiroJoint: only 0.02%, 0.08%, and 0.14% of the intersections are, in fact, critical (Figure 188, 189, and 190) for block toppling using the stereoplots obtained with the discontinuities extracted by I-Site Studio, DiAna, and Facets respectively. This is due to the absence of discontinuities with α normal to α_{slope}.

We, indeed, remark that most of the basal planes in the stereoplots of the discontinuities extracted with SiroJoint, I-Site Studio, DiAna, and Facets are stepper than the ϕ angle, as for plane failure.

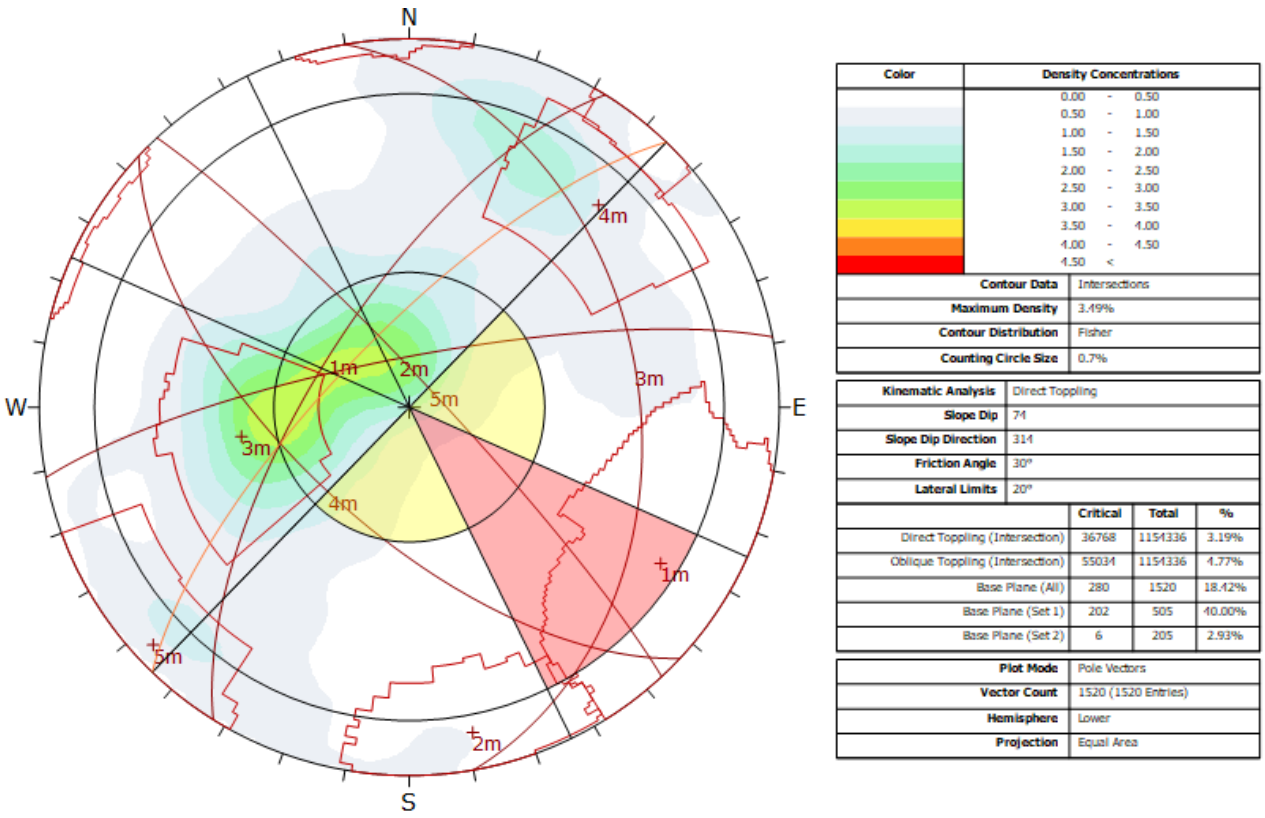

Color	Density Concentrations
	0.00 - 0.50
	0.50 - 1.00
	1.00 - 1.50
	1.50 - 2.00
	2.00 - 2.50
	2.50 - 3.00
	3.00 - 3.50
	3.50 - 4.00
	4.00 - 4.50
	4.50 <

Contour Data	Intersections
Maximum Density	3.49%
Contour Distribution	Fisher
Counting Circle Size	0.7%

Kinematic Analysis	Direct Toppling
Slope Dip	74
Slope Dip Direction	314
Friction Angle	30°
Lateral Limits	20°

	Critical	Total	%
Direct Toppling (Intersection)	36768	1154336	3.19%
Oblique Toppling (Intersection)	55034	1154336	4.77%
Base Plane (All)	280	1520	18.42%
Base Plane (Set 1)	202	505	40.00%
Base Plane (Set 2)	6	205	2.93%

Plot Mode	Pole Vectors
Vector Count	1520 (1520 Entries)
Hemisphere	Lower
Projection	Equal Area

Figure 186 - Kinematic analysis of planes and traces of case study 2 mine wall for block toppling on geostructural data carried out by SiroJoint. Orange cyclographic: slope orientation; pink section of circumference: primary critical area to block toppling; yellow sections of circumference: secondary critical area to block toppling

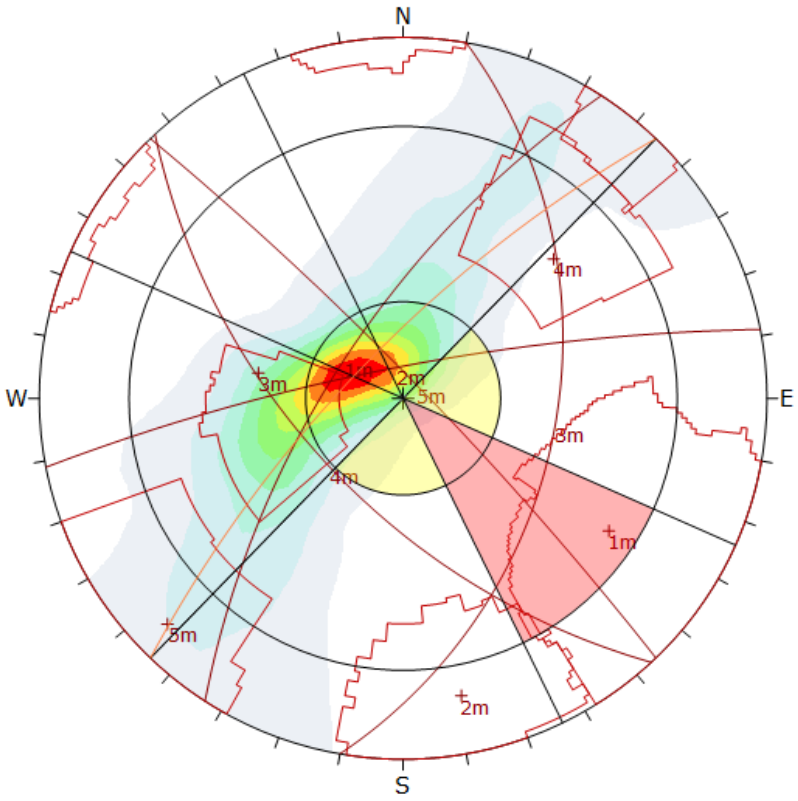

Color	Density Concentrations
	0.00 - 0.70
	0.70 - 1.40
	1.40 - 2.10
	2.10 - 2.80
	2.80 - 3.50
	3.50 - 4.20
	4.20 - 4.90
	4.90 - 5.60
	5.60 - 6.30
	6.30 - 7.00

Contour Data	Intersections
Maximum Density	6.97%
Contour Distribution	Fisher
Counting Circle Size	1.0%

Kinematic Analysis	Direct Toppling
Slope Dip	74
Slope Dip Direction	314
Friction Angle	30°
Lateral Limits	20°

	Critical	Total	%
Direct Toppling (Intersection)	2843	448801	0.63%
Oblique Toppling (Intersection)	20906	448801	4.66%
Base Plane (All)	232	948	24.47%
Base Plane (Set 1)	190	456	41.67%
Base Plane (Set 2)	6	180	3.33%

Plot Mode	Pole Vectors
Vector Count	948 (948 Entries)
Hemisphere	Lower
Projection	Equal Angle

Figure 187 - Kinematic analysis of planes only of case study 2 mine wall for block toppling on geostructural data carried out by SiroJoint. Orange cyclographic: slope orientation; pink section of circumference: primary critical area to block toppling; yellow sections of circumference: secondary critical area to block toppling

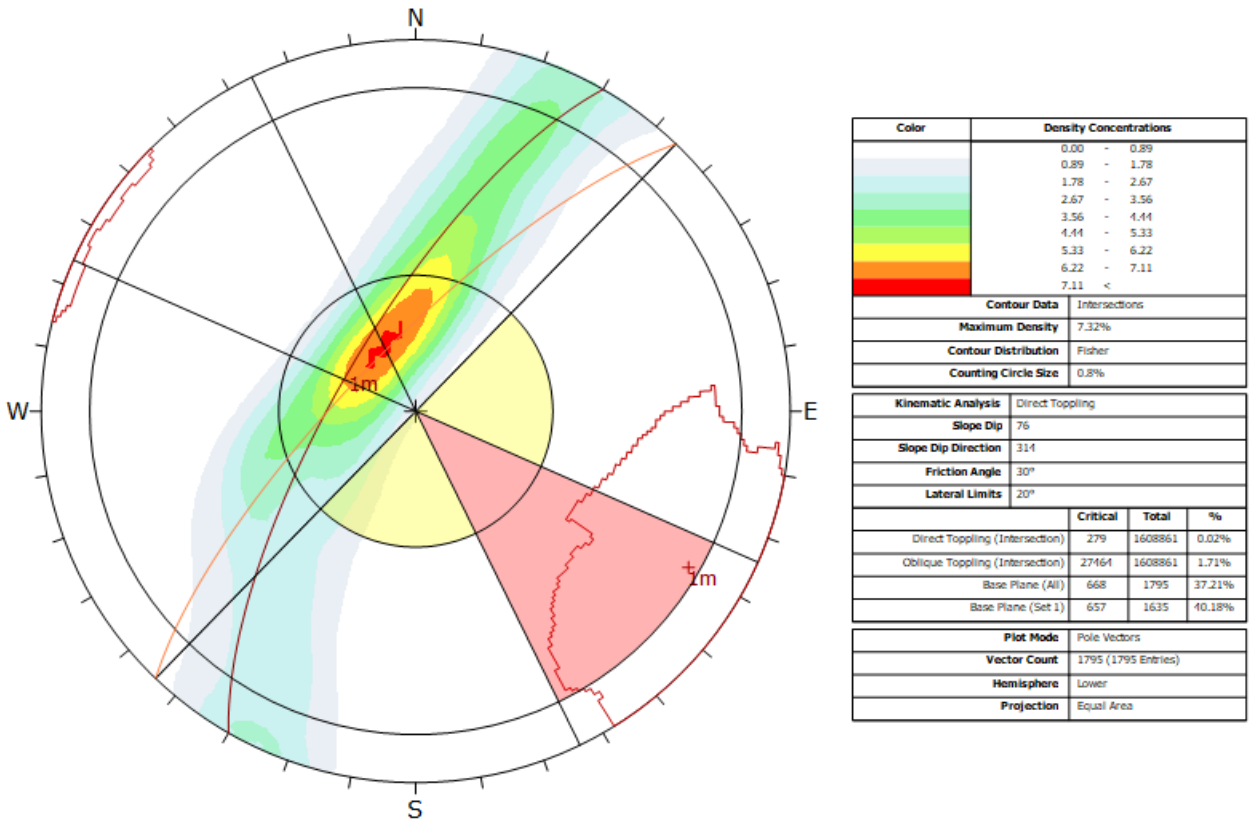

Color	Density Concentrations
	0.00 - 0.89
	0.89 - 1.78
	1.78 - 2.67
	2.67 - 3.56
	3.56 - 4.44
	4.44 - 5.33
	5.33 - 6.22
	6.22 - 7.11
	7.11 <

Contour Data	Intersections
Maximum Density	7.32%
Contour Distribution	Fisher
Counting Circle Size	0.8%

Kinematic Analysis	Direct Toppling		
Slope Dip	76		
Slope Dip Direction	314		
Friction Angle	30°		
Lateral Limits	20°		
	Critical	Total	%
Direct Toppling (Intersection)	279	1608861	0.02%
Oblique Toppling (Intersection)	27464	1608861	1.71%
Base Plane (All)	668	1795	37.21%
Base Plane (Set 1)	657	1635	40.18%

Plot Mode	Pole Vectors
Vector Count	1795 (1795 Entries)
Hemisphere	Lower
Projection	Equal Area

Figure 188 - Kinematic analysis of case study 2 mine wall for block toppling on geostructural data carried out by I-Site Studio. Orange cyclographic: slope orientation; pink section of circumference: primary critical area to block toppling; yellow sections of circumference: secondary critical area to block toppling

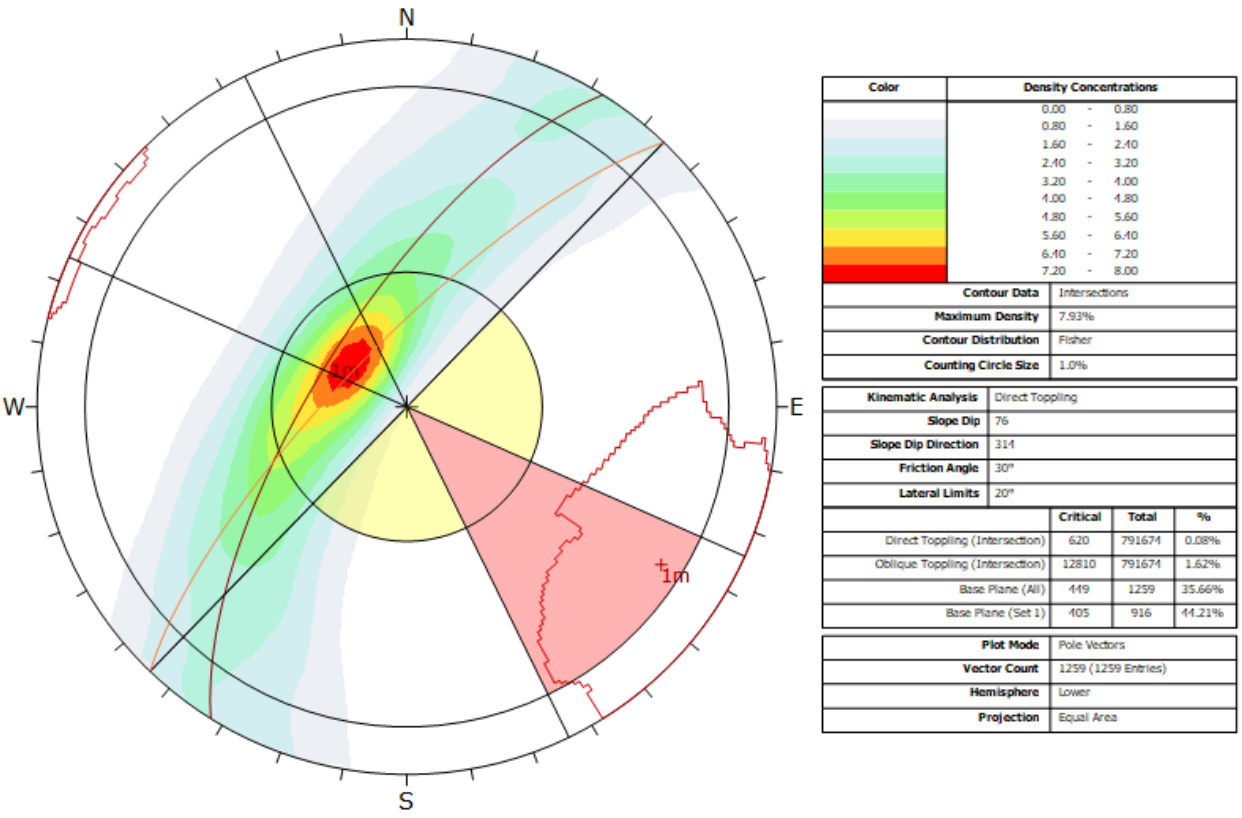

Color	Density Concentrations
	0.00 - 0.80
	0.80 - 1.60
	1.60 - 2.40
	2.40 - 3.20
	3.20 - 4.00
	4.00 - 4.80
	4.80 - 5.60
	5.60 - 6.40
	6.40 - 7.20
	7.20 - 8.00

Contour Data	Intersections
Maximum Density	7.93%
Contour Distribution	Fisher
Counting Circle Size	1.0%

Kinematic Analysis	Direct Toppling		
Slope Dip	76		
Slope Dip Direction	314		
Friction Angle	30°		
Lateral Limits	20°		
	Critical	Total	%
Direct Toppling (Intersection)	620	791674	0.08%
Oblique Toppling (Intersection)	12810	791674	1.62%
Base Plane (All)	449	1259	35.66%
Base Plane (Set 1)	405	916	44.21%

Plot Mode	Pole Vectors
Vector Count	1259 (1259 Entries)
Hemisphere	Lower
Projection	Equal Area

Figure 189 - Kinematic analysis of case study 2 mine wall for block toppling on geostructural data carried out by DiAna. Orange cyclographic: slope orientation; pink section of circumference: primary critical area to block toppling; yellow sections of circumference: secondary critical area to block toppling.

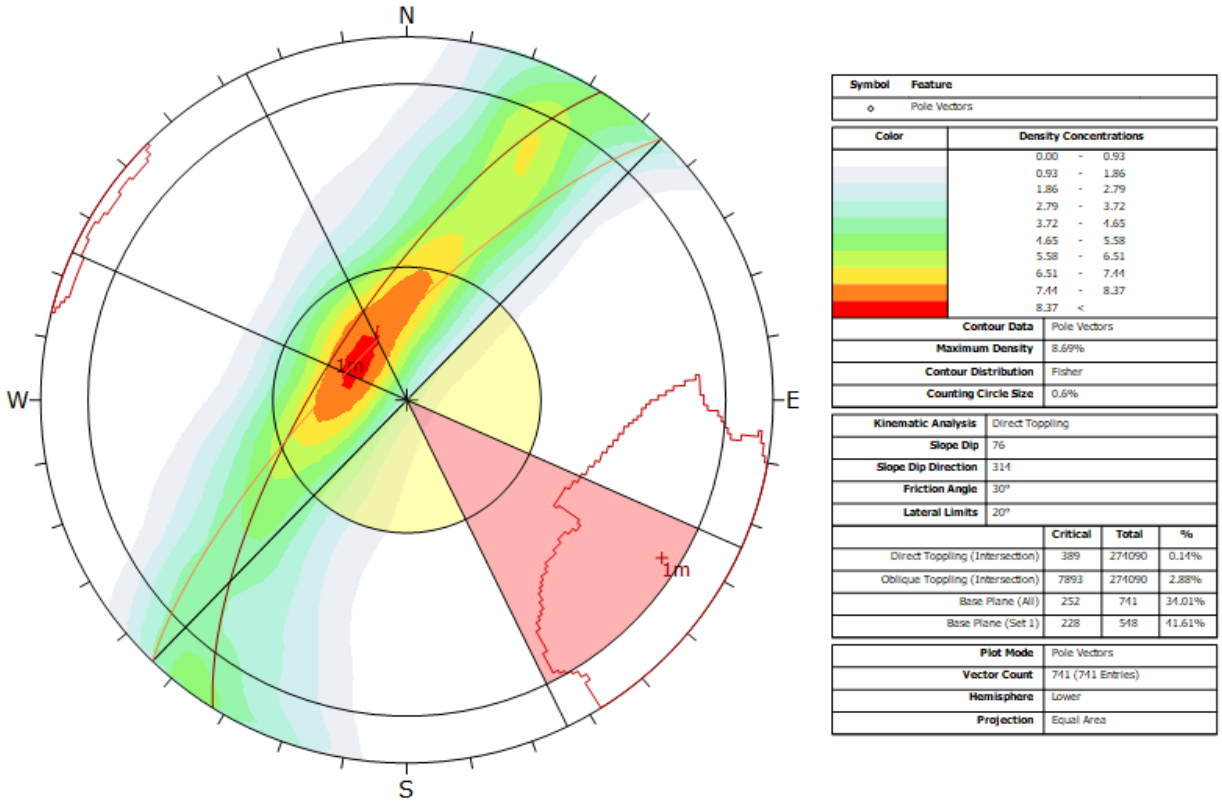

Figure 190 - Kinematic analysis of case study 2 mine wall for block toppling on geostructural data carried out by Facets plug-in of CloudCompare. Orange cyclographic: slope orientation; pink section of circumference: primary critical area to block toppling; yellow sections of circumference: secondary critical area to block toppling

7.2.4. Flexural Toppling

Flexural toppling on the highwall of case study 2 involves a percentage of discontinuities ranging from 1.84% to 6.75%, depending on the code used for the extraction of the discontinuities.

SiroJoint results show that overall 68 discontinuities (overall 4.47% of the discontinuities) are prone to flexural toppling; 15/68 are related to 1m set of discontinuities, 30/68 to set of discontinuities and 23/68 have not been assigned to any set of discontinuities (Figure 191 and 192). The percentage of discontinuities prone to flexural toppling increases considering planes only: in this case, 56 discontinuities on overall 948 planes are prone to failure, corresponding to 5.91%.

I-Site Studio results confirms that 1m set of discontinuities is involved by flexural toppling; on overall 33 discontinuities prone to flexural toppling, 23 are related to 1m set of discontinuities (Figure 193), while the remnant 10 are not related to any set. Finally, the percentage of discontinuities extracted with DiAna (Figure 194) and Facets (Figure 195) and related to flexural toppling is 5.24 % and 6.75 % respectively.

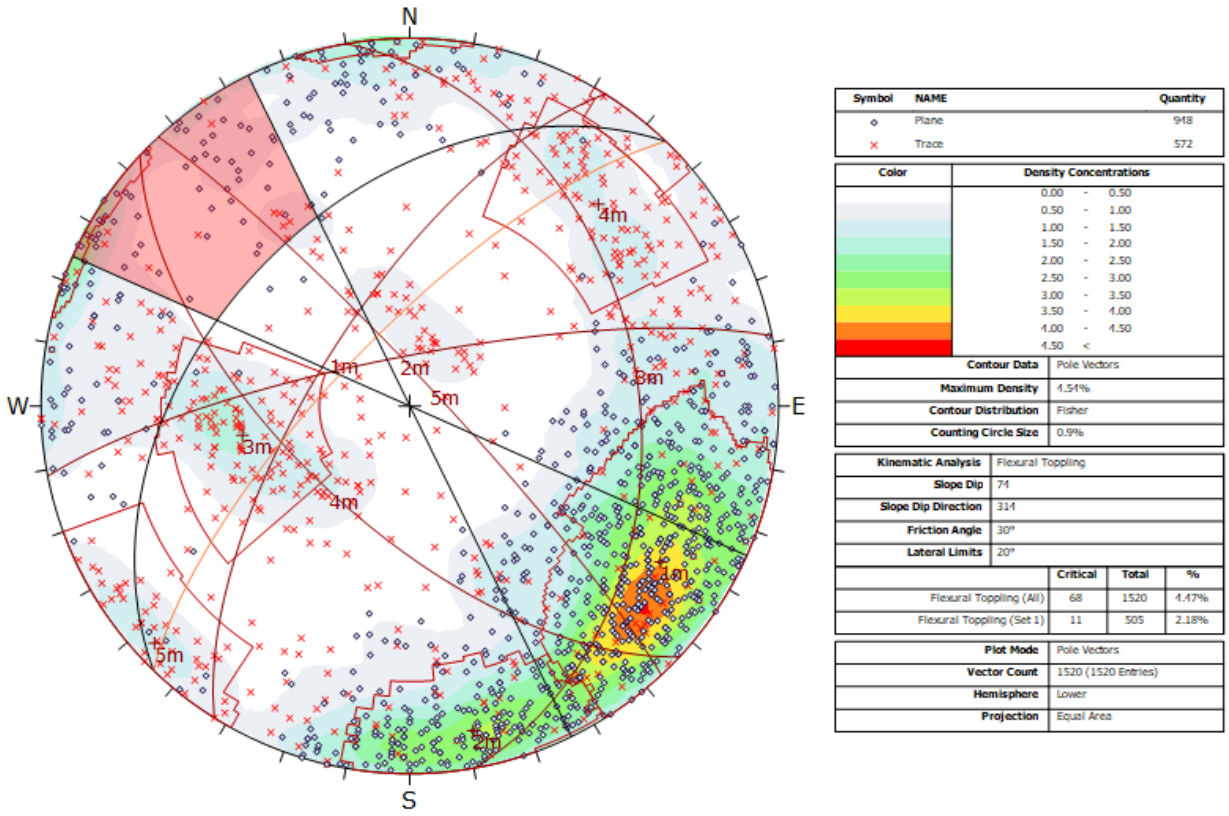

Symbol	NAME	Quantity
◇	Plane	948
×	Trace	572

Color	Density Concentrations
	0.00 - 0.50
	0.50 - 1.00
	1.00 - 1.50
	1.50 - 2.00
	2.00 - 2.50
	2.50 - 3.00
	3.00 - 3.50
	3.50 - 4.00
	4.00 - 4.50
	4.50 <

Contour Data	Pole Vectors
Maximum Density	1.54%
Contour Distribution	Fisher
Counting Circle Size	0.9%

Kinematic Analysis	Flexural Toppling
Slope Dip	74
Slope Dip Direction	314
Friction Angle	30°
Lateral Limits	20°

	Critical	Total	%
Flexural Toppling (All)	68	1520	4.47%
Flexural Toppling (Set 1)	11	505	2.18%

Plot Mode	Pole Vectors
Vector Count	1520 (1520 Entries)
Hemisphere	Lower
Projection	Equal Area

Figure 191 - Kinematic analysis of planes and traces of case study 2 mine wall for flexural toppling on geostructural data carried out by SiroJoint. Orange cyclographic: slope orientation; black cyclographic: instability plane for flexural toppling ($90°-\beta_{slope}+\varphi$; α_{slope}); pink section of spindle of sphere: area of the stereo plot with the poles of the planes affected by flexural toppling

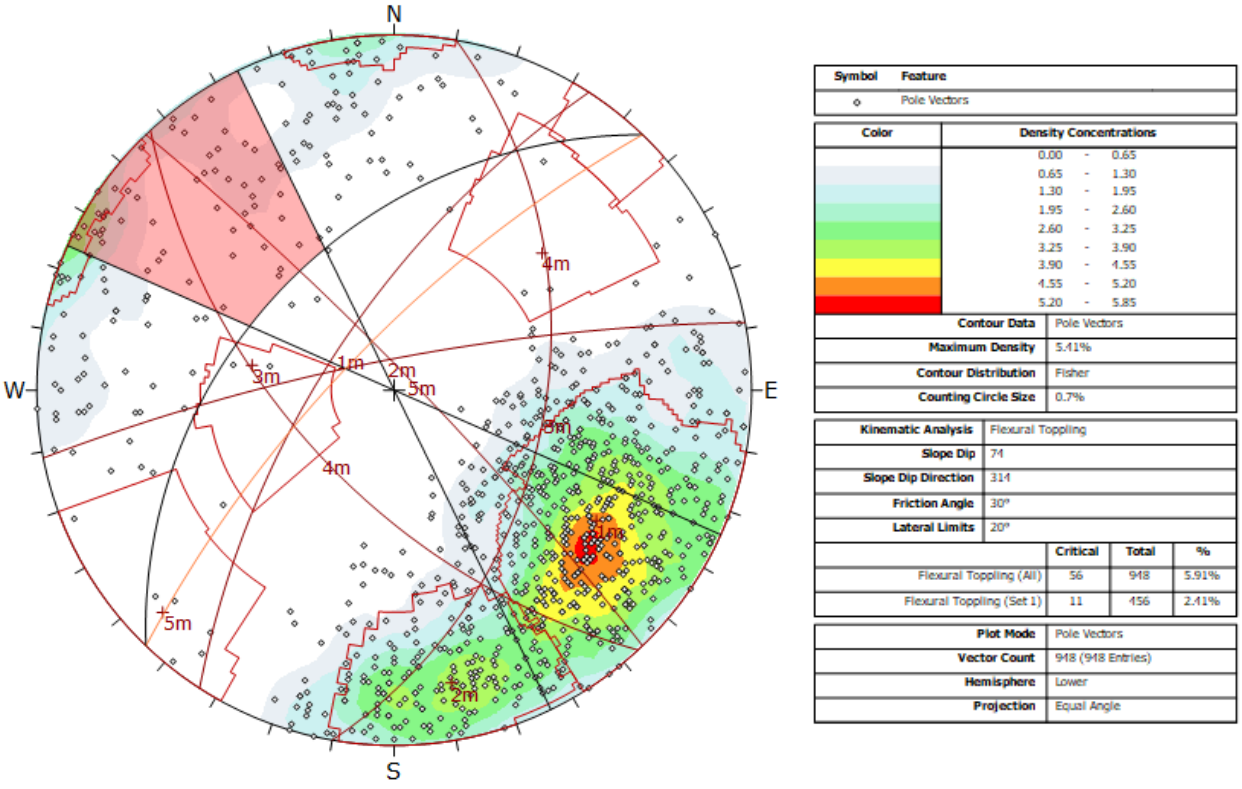

Symbol	Feature
◇	Pole Vectors

Color	Density Concentrations
	0.00 - 0.65
	0.65 - 1.30
	1.30 - 1.95
	1.95 - 2.60
	2.60 - 3.25
	3.25 - 3.90
	3.90 - 4.55
	4.55 - 5.20
	5.20 - 5.85

Contour Data	Pole Vectors
Maximum Density	5.41%
Contour Distribution	Fisher
Counting Circle Size	0.7%

Kinematic Analysis	Flexural Toppling
Slope Dip	74
Slope Dip Direction	314
Friction Angle	30°
Lateral Limits	20°

	Critical	Total	%
Flexural Toppling (All)	56	948	5.91%
Flexural Toppling (Set 1)	11	456	2.41%

Plot Mode	Pole Vectors
Vector Count	948 (948 Entries)
Hemisphere	Lower
Projection	Equal Angle

Figure 192 - Kinematic analysis of planes only of case study 2 mine wall for flexural toppling on geostructural data carried out by SiroJoint. Orange cyclographic: slope orientation; black cyclographic: instability plane for flexural toppling ($90°-\beta_{slope}+\varphi$; α_{slope}); pink section of spindle of sphere: area of the stereo plot with the poles of the planes affected by flexural toppling

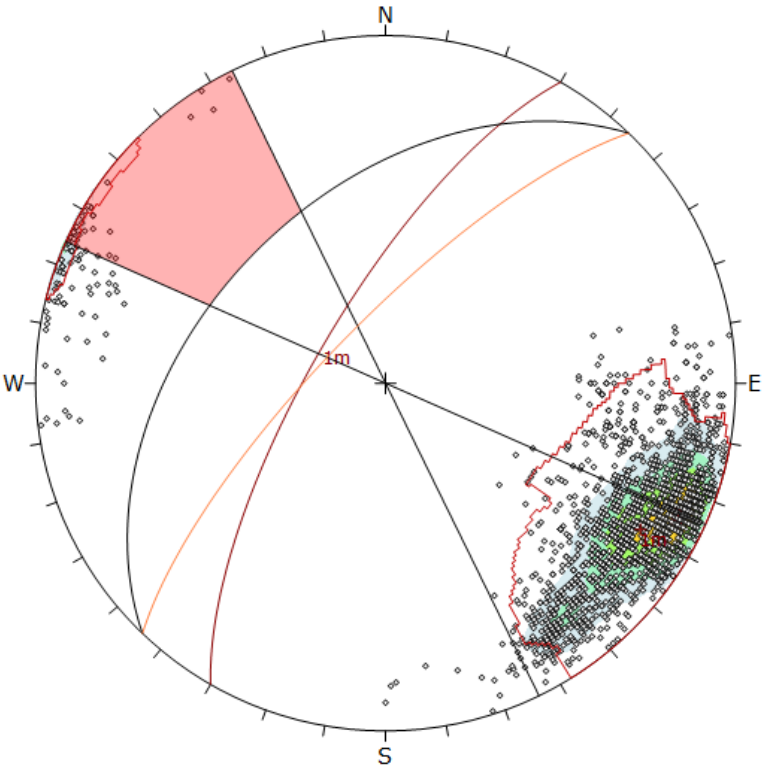

Symbol	Feature
◇	Pole Vectors

Color	Density Concentrations
	< 4.20
	4.20 - 7.50
	7.50 - 10.80
	10.80 - 14.10
	14.10 - 17.40
	17.40 <

Contour Data	Pole Vectors
Maximum Density	18.44%
Contour Distribution	Schmidt
Counting Circle Size	0.7%

Kinematic Analysis	Flexural Toppling
Slope Dip	76
Slope Dip Direction	314
Friction Angle	30°
Lateral Limits	20°

	Critical	Total	%
Flexural Toppling (All)	33	1795	1.84%
Flexural Toppling (Set 1)	20	1635	1.22%

Plot Mode	Pole Vectors
Vector Count	1795 (1795 Entries)
Hemisphere	Lower
Projection	Equal Area

Figure 193 - Kinematic analysis of case study 2 mine wall for flexural toppling on geostructural data carried out by I-Site Studio. Orange cyclographic: slope orientation; black cyclographic: instability plane for flexural toppling ($90°-\beta_{slope}+\varphi$; α_{slope}); pink section of spindle of sphere: area of the stereo plot with the poles of the planes affected by flexural toppling

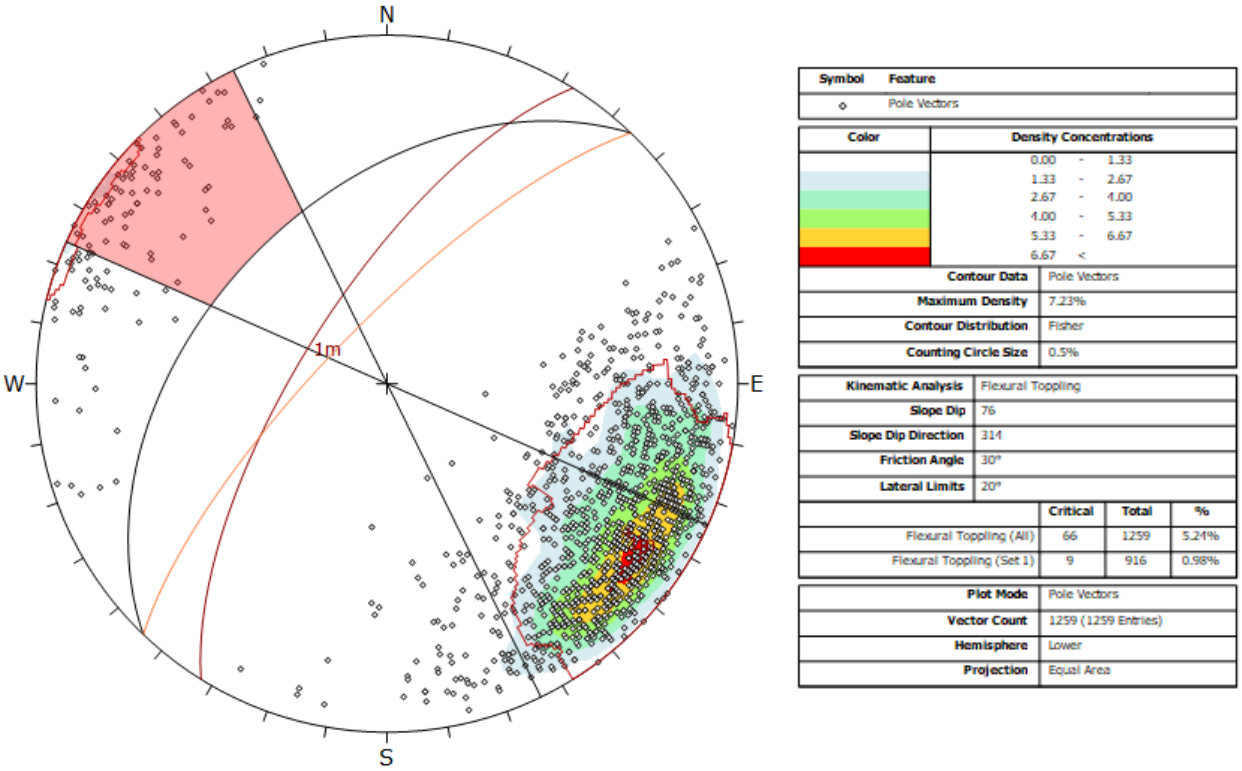

Figure 194 - Kinematic analysis of case study 2 mine wall for flexural toppling on geostructural data carried out by DiAna. Orange cyclographic: slope orientation; black cyclographic: instability plane for flexural toppling ($90°-\beta_{slope}+\varphi$; α_{slope}); pink section of spindle of sphere: area of the stereo plot with the poles of the planes affected by flexural toppling

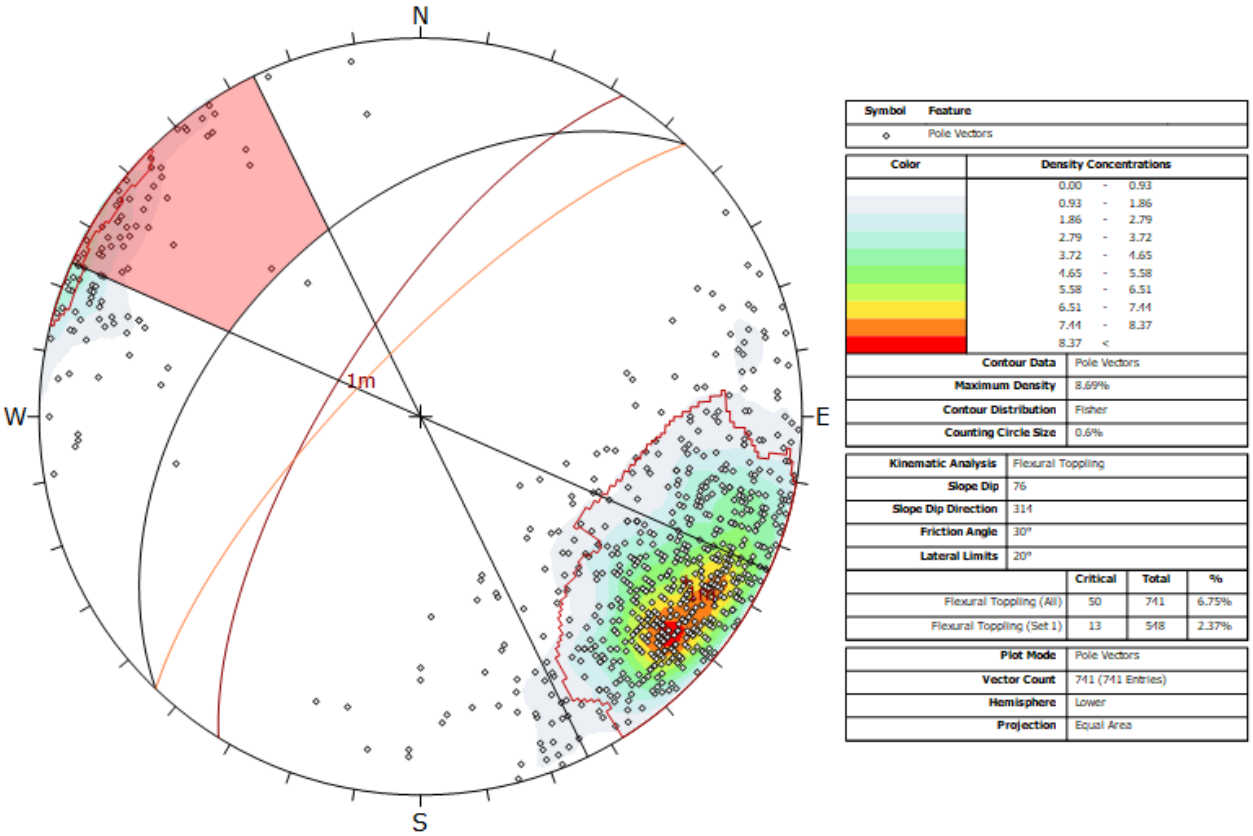

Figure 195 - Kinematic analysis of case study 2 mine wall for flexural toppling on geostructural data carried out by Facets. Orange cyclographic: slope orientation; black cyclographic: instability plane for flexural toppling ($90°-\beta_{slope}+\varphi$; α_{slope}); pink section of spindle of sphere: area of the stereo plot with the poles of the planes affected by flexural toppling

7.2.5. 3D kinematic analysis

Kinematic analysis performed by DiAna code has allowed to give a kinematic index (Casagli & Pini, 1993) for each failure mechanism and to produce one susceptibility map for each kinematic mechanism, illustrated in Figure 127. Plane failure is the most relevant failure mechanism affecting the highwall. Wedge failure too affects many areas of the highwall, while block toppling and flexural toppling are extremely umprobable mechanism. Indeed, free fall sometimes affects overhanging areas.

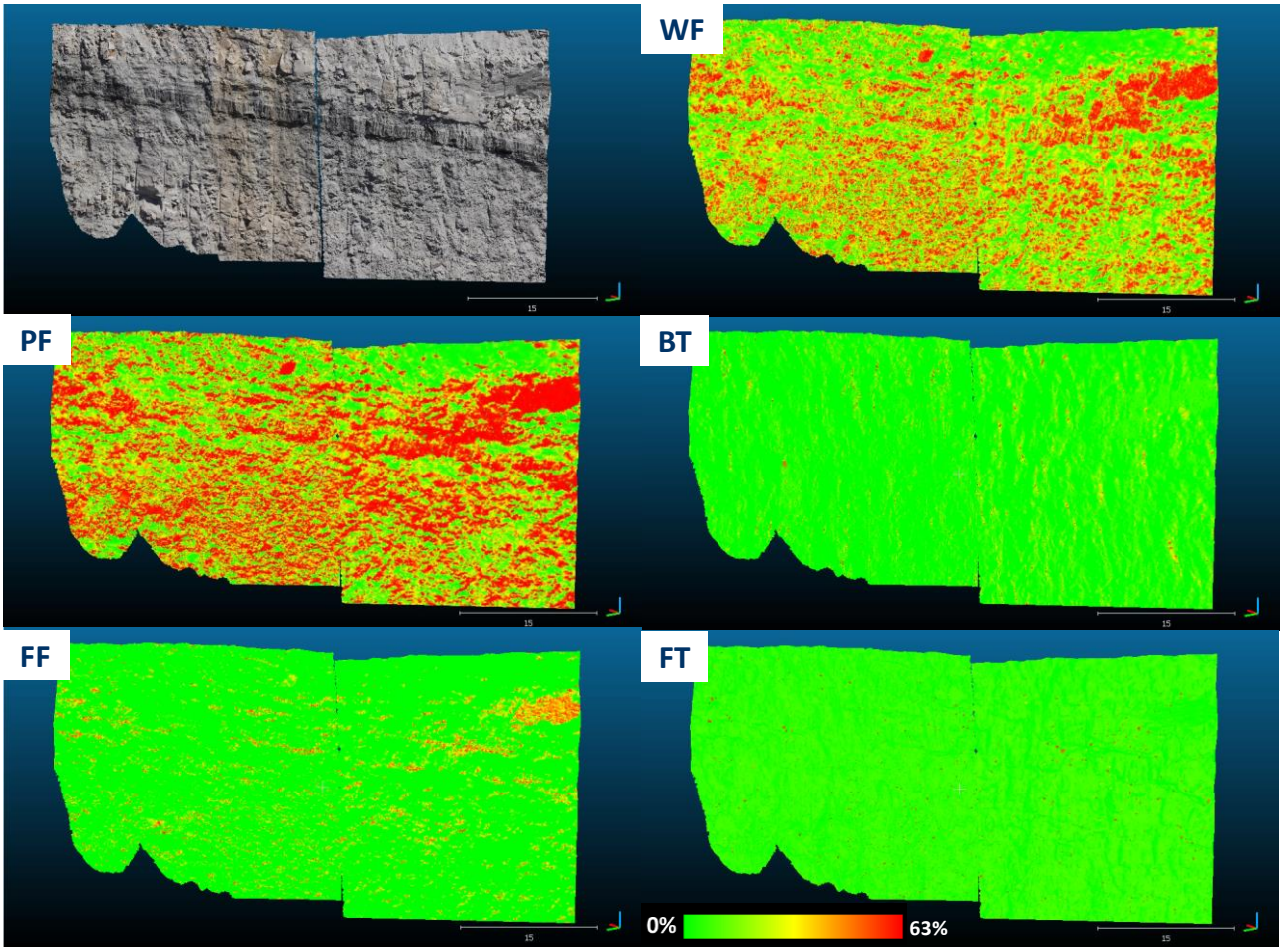

Figure 196 - Susceptibility maps for each failure mechanism, carried out from the kinematic analysis performed by DiAna on case study 2 mine highwall. WF: wedge failure; PF: Plane Failure; BT block toppling; FF: free fall; FT flexural toppling

Figure 197 shows that most of the less step areas of the highwall are not affected from failure mechanisms, while Figure 198 and 199 provide the map of the susceptibility of the local more probable failure mechanism for the left and for the right sector of the slope. Plane failure is the failure mechanism which most of the slope is most prone. The areas prone to plane failure are mostly represented by surfaces the orientation of which is similar to the slope one. Wedge failure is instead the most probable failure mechanism when the local orientation is roughly perpendicular to the slope one; routing of 90° the slope orientation of the stereoplots for kinematic analysis, no one set of discontinuities is prone to plane failure, while 1m and 2m sets of discontinuities intersection in included in the wedge failure prone sector.

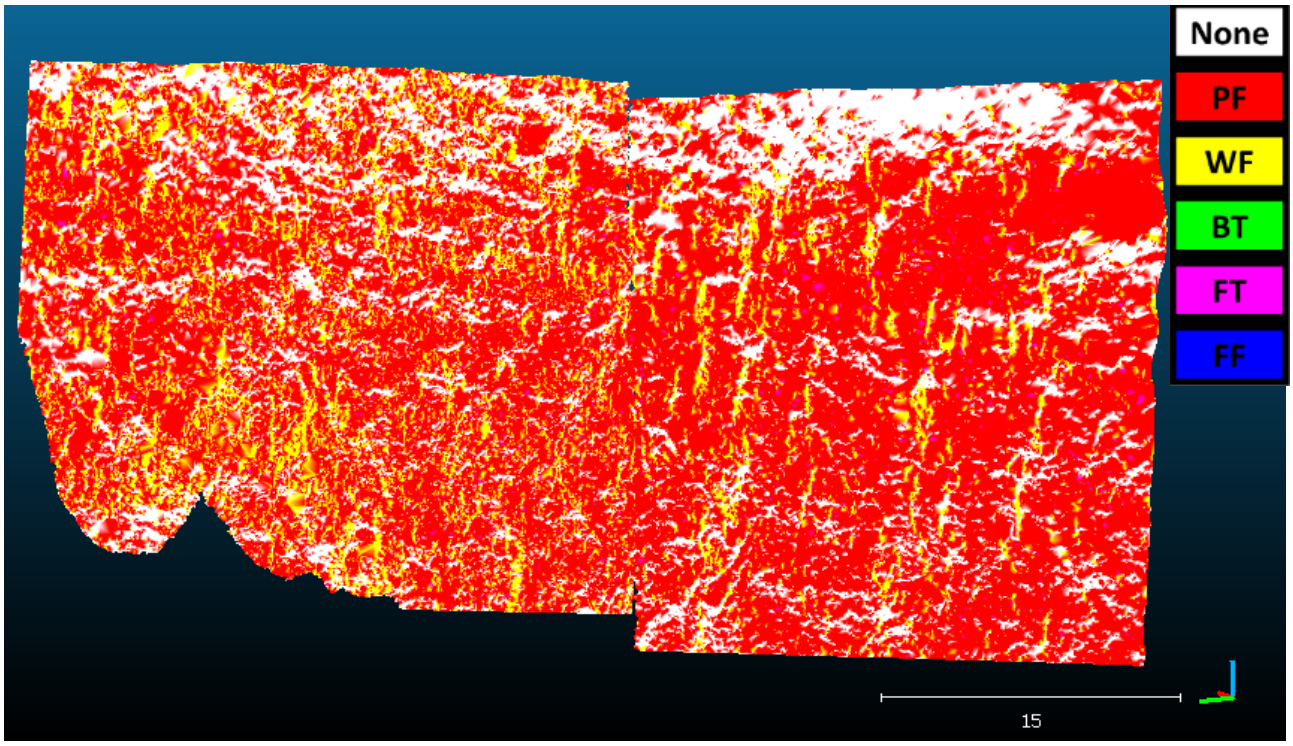

Figure 197 - Most probable failure mechanisms according to DiAna on case study 2 mine highwall. PF: Plane Failure; WF: Wedge Failure; BT: Block Toppling; FT: Flexural Toppling; FF: Free Fall

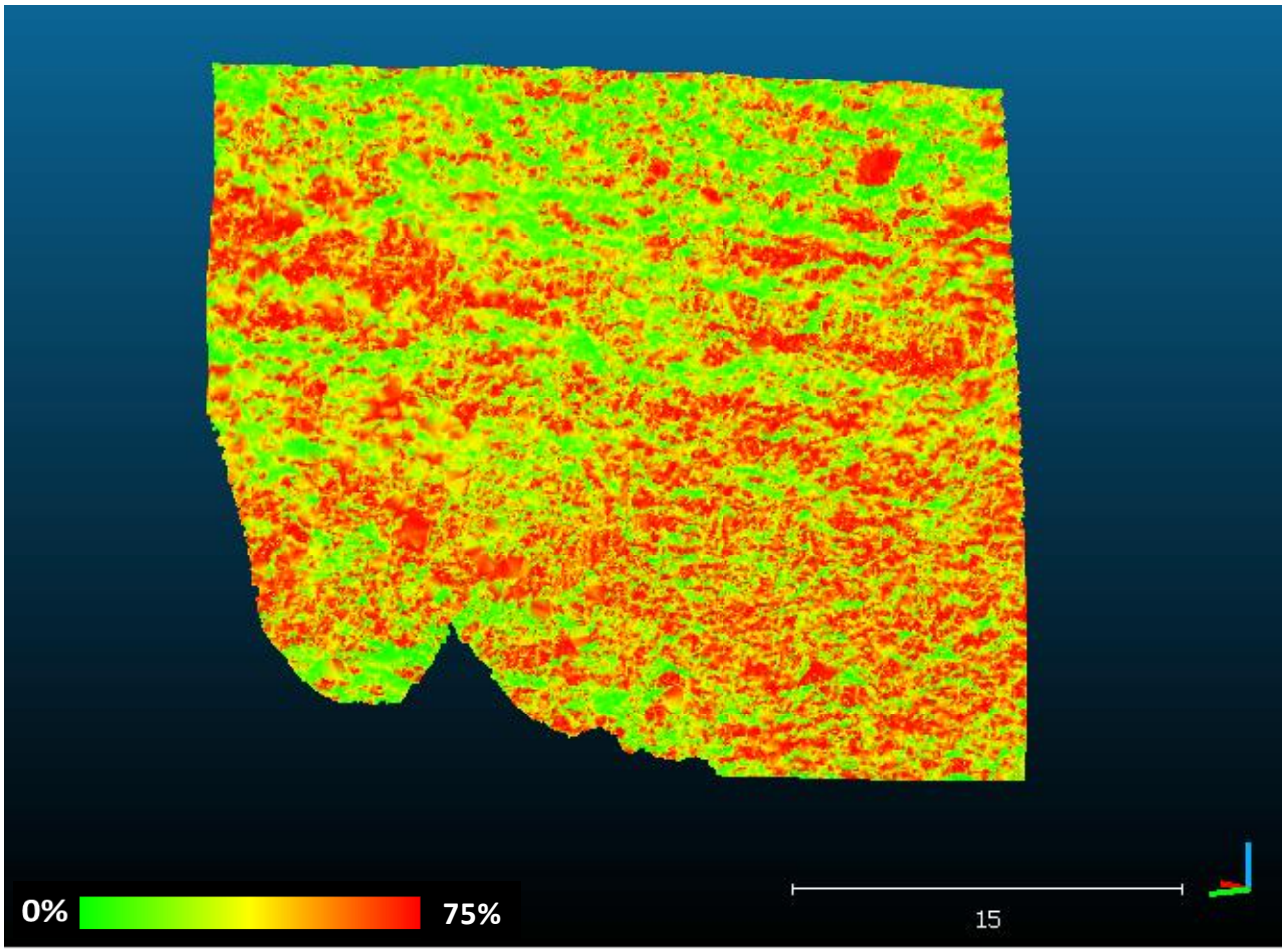

Figure 198 - Susceptibility value map for the left sector of the slope of case study 2

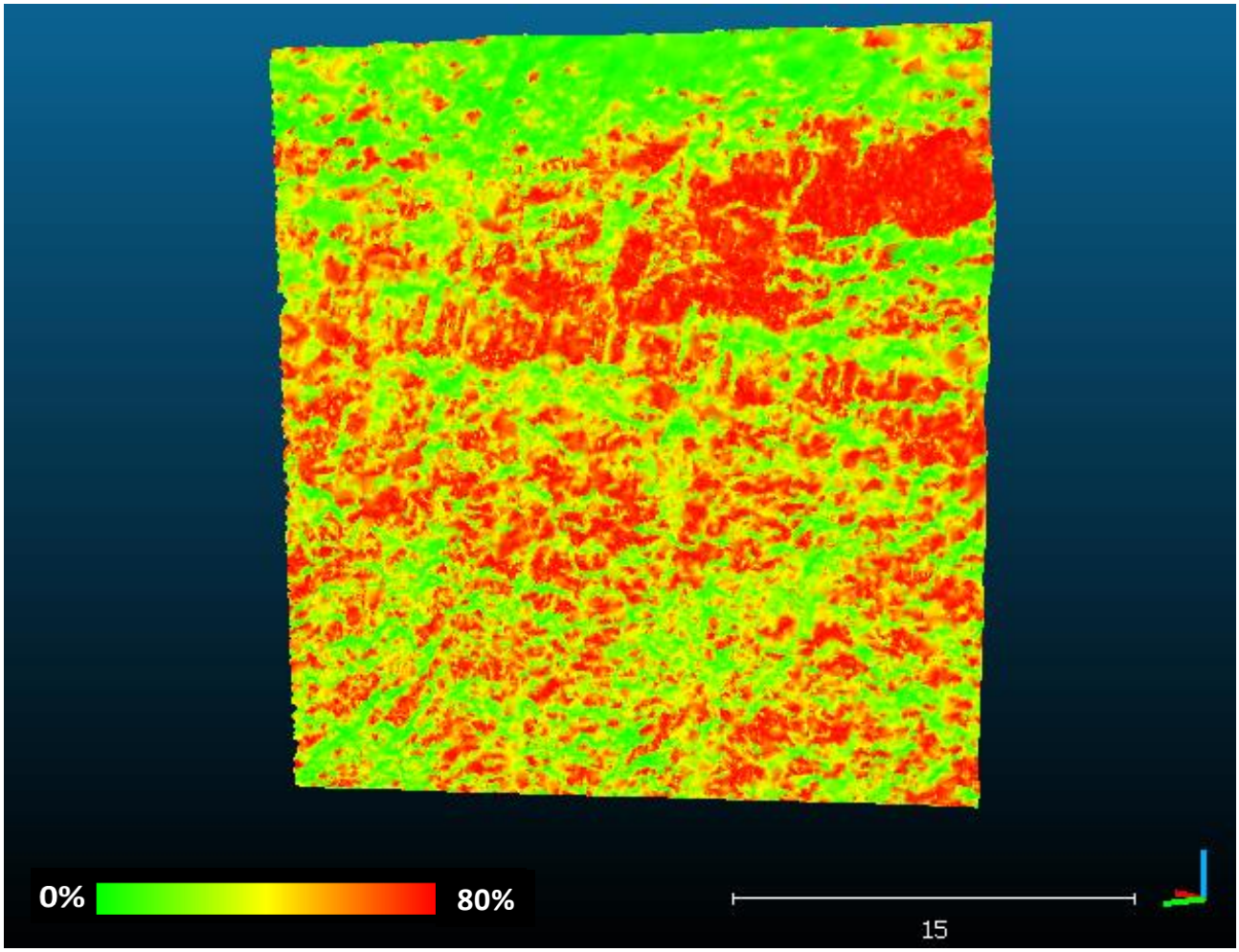

Figure 199 - Susceptibility value map for the right sector of the slope of case study 2

7.3. Stability analysis

As for case study 1 mine, the stability analysis of the slope of case study 2 has been performed with SiroModel (Chapter 4.4.2), that classifies the blocks following the criterion described by Goodman & Shi (1985). 20 simulations have been performed, using as input data a simplified model of the bench (α_{slope} = 134°; β_{slope} = 74°), 8.5 m wide and 26 m height, as the bench. The slope model used for the simulation is drawn in Figure 200. 5 sets of discontinuities extracted by SiroJoint (Figure 168 and Table 15) have been added to the model as stochastic sets of discontinuities. Then, further 10 simulations have performed to compare the results between 20 and 30 simulations and evaluate if the number of simulation is representative, by comparing the blocks diistributions.

The blocks distribution analysis performed on 20 simulations, shows that overall 14487 blocks have been modelled (Figure 201). 1749 have one contact plane and 12738 have two contact planes (letter a in Figure 201). 6727 are removable and stable, 5100 are removable and stable thanks to ϕ, 2660 are removable and unstable. 497/1749 of the blocks with one contact plane only and 2163 of the blocks with two contact planes are unstable (letter b in Figure 201); 62 of the blocks with one contact plane only and 5038 of the blocks with

two contact planes are stable (letter c in Figure 201); 1190 of the blocks with one contact plane only and 5537 of the blocks with two contact planes are stable (letter d in Figure 201).

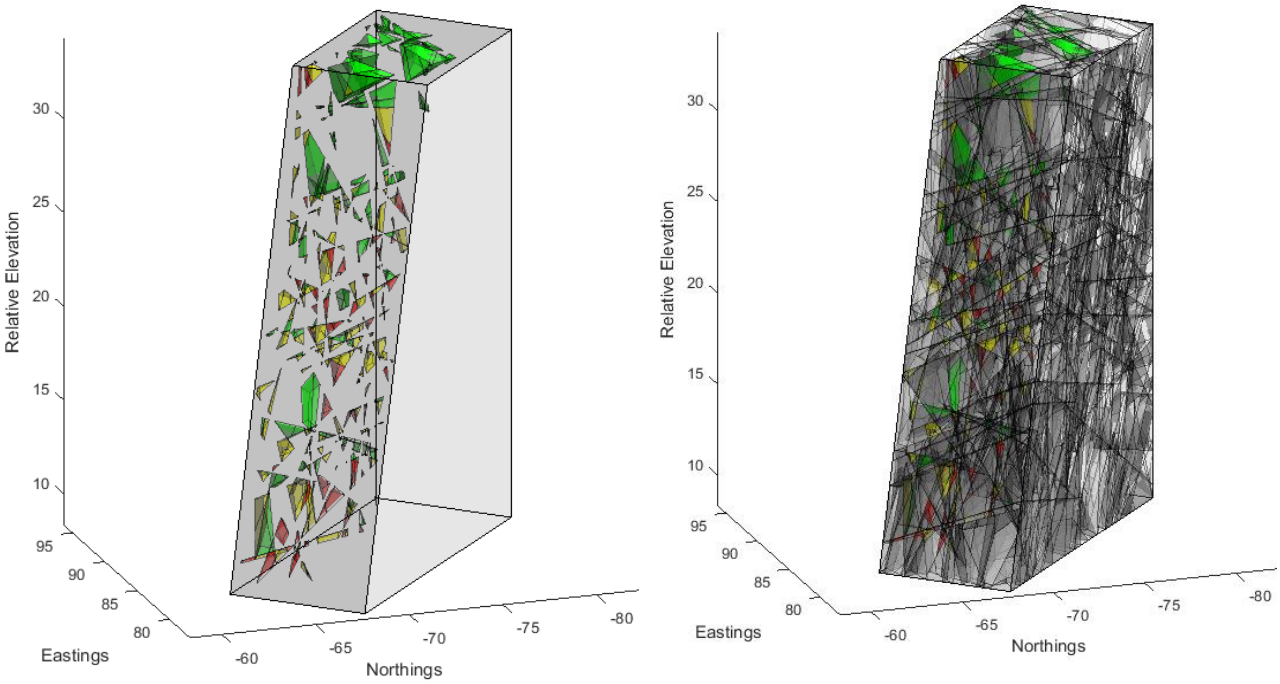

Figure 200 - The model of the slope of SiroModel. Left: the model and the removable blocks; right: the discontinuities generated for the simulation. Red; Type I blocks; yellow: Type II blocks; green: Type III blocks

Because the statistics of Figure 201 take into account also very small blocks, a volume treshold has been set to analyse the distribution of blocks with e significative volume. Among the 6596 blocks with a volume greater than10^{-3} m^3 (Figure 202), 610 have 1 contact plane and 5986 have 2 contact planes (letter a in Figure 202); 888 are related to Type I, 2290 to Type II and 6727 to Type III. Type I blocks have moreover 2 contacts planes instead of 1 (756 vs 132), as among Type II blocks (23 vs 2267). Type III blocks also have mostly 2 contact planes (letter d in Figure 202). The diagrams of the distribution of all blocks by number of conctact planes and FOS does not show relevant differences of blocks distribution with the diagram of the blocks with a minimum threshold of 10^{-3} m^3.

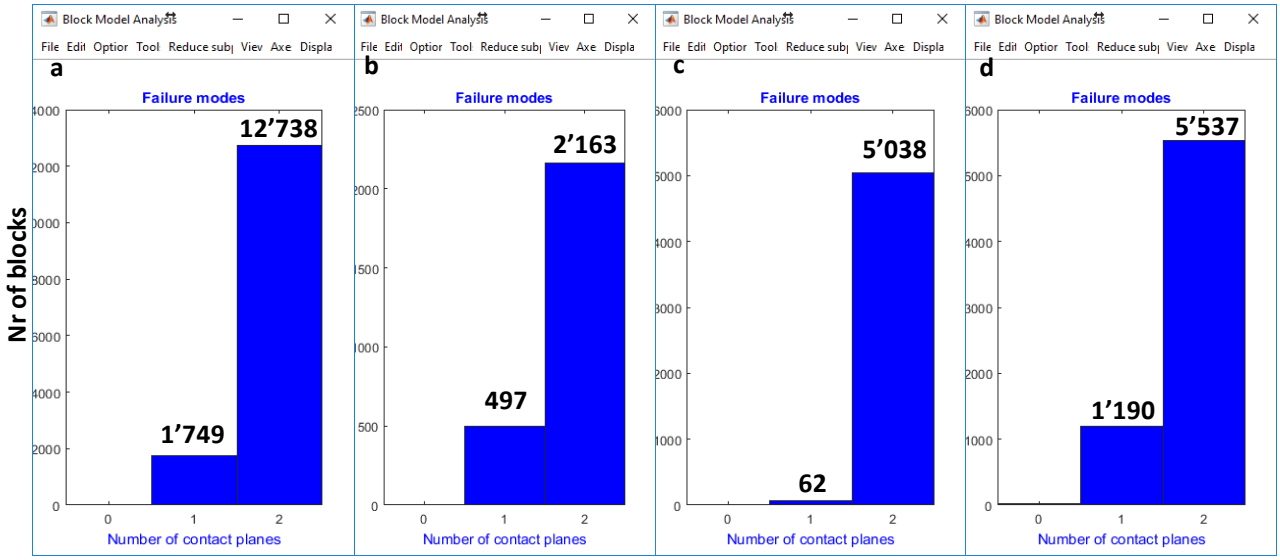

Figure 201 - Failure modes of the highwall of case study 2 mine performed on 20 simulations. a: Type I, Type II and Type III blocks (all removable blocks); b: Type I block (removable unstable blocks); c: Type II blocks (removable and stable with φ); d: Type III blocks (removable and stable)

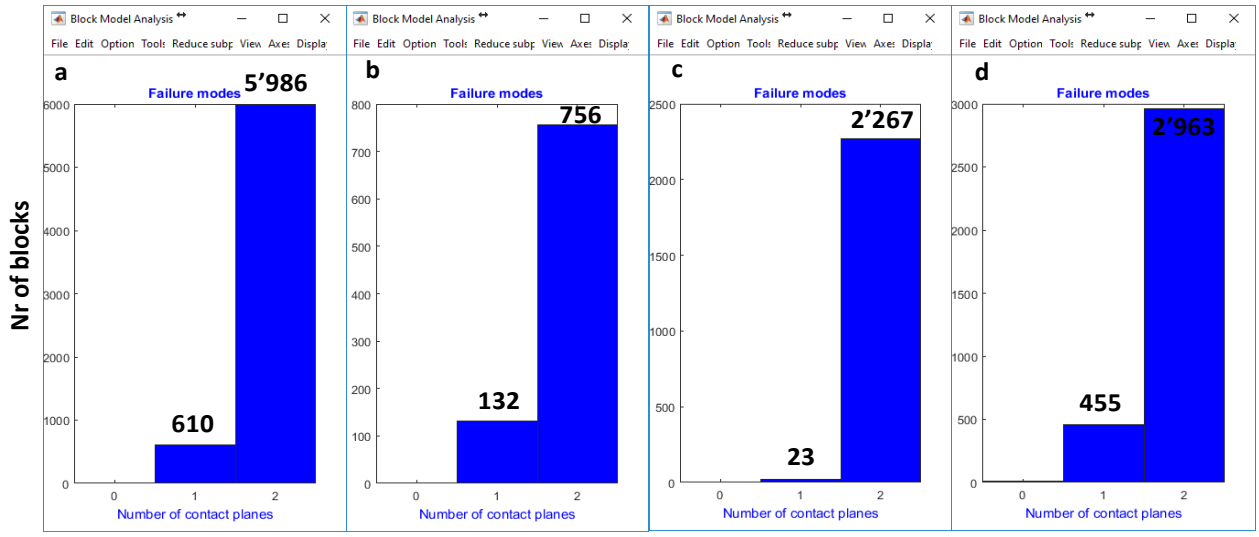

Figure 202 - Failure modes of the highwall of case study 2 mine performed on 20 simulations, considering blocks with a minimum 10^{-3} m^3 volume only. a: Type I, Type II and Type III blocks (all removable blocks); b: Type I block (removable unstable blocks); c: Type II blocks (removable and stable with φ); d: Type III blocks (removable and stable)

10 more simulation have been so performed and the diagrams in Figure 203 have been carried out, extracting overall 20211 removable blocks. Most of the blocks, both for Figure 201 and 202, have two contact planes (17780 towards 2431 with one contact plane). Blocks related to Type I, Type II, and Type III are 3866, 7003, and 9342 respectively. 714 blocks with an only contact plane and 3152 blocks with two contact planes are of Type I (letter b in Figure 203); 78 with an only contact plane and 6925 with two contact planes are of Type II (letter c in Figure 203); 1639 blocks with an only contact plane and 7703 blocks with two contact planes are of Type III stable (letter d in Figure 203).

Also in this case the diagrams of the distribution of the blocks by FOS and by failure mode have been carried out putting a minimum volume treshold of 10^{-3} m^3. 9736 blocks with volume > 10^{-3} m^3 have been extracted with 30 simulations, 887 of them with an only contact plane and 8849 with 2 contact planes (letter a in Figure 204). As regarding the stability of the blocks, 1295 are of Type I, 3340 of Type II, and 5061 are of Type III. As regarding the number of contact planes of the block, 192 of the blocks with an only contact plane and 1103 of the blocks with two contact planes are of Type I (letter b in Figure 204); 35 of the blocks with an only contact plane and 3305 of the blocks with two contact planes are of Type II (letter c in Figure 204); 660 of the blocks with an only contact plane and 4401 of the blocks with two contact planes are of Type III (letter d in Figure 204).

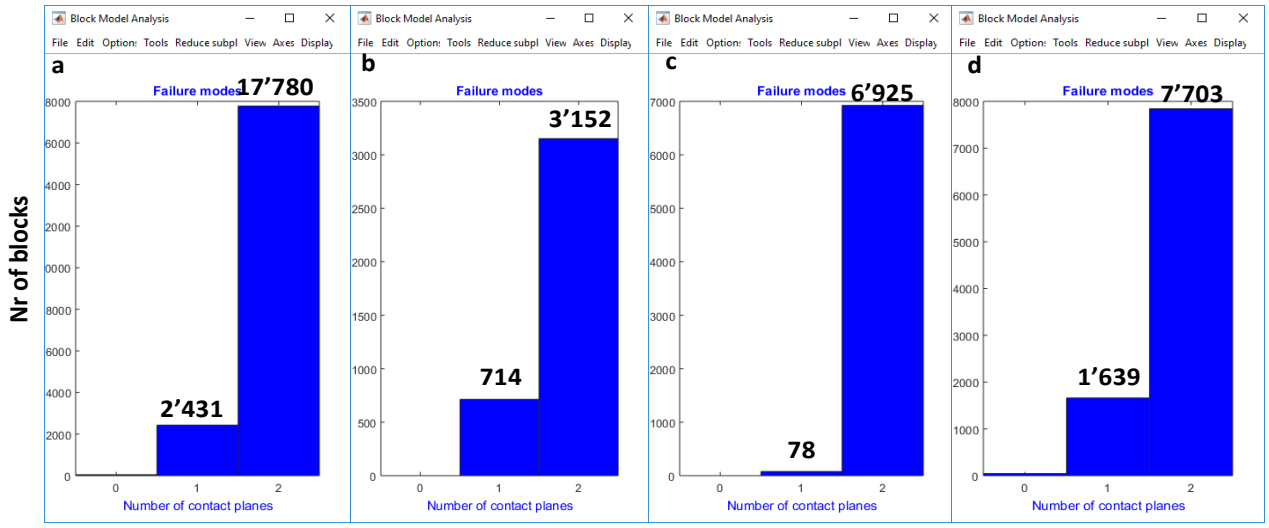

Figure 203 - Failure modes of the highwall of case study 2 mine performed on 30 simulations. a: Type I, Type II and Type III blocks (all removable blocks); b: Type I block (removable unstable blocks); c: Type II blocks (removable and stable with φ); d: Type III blocks (removable and stable)

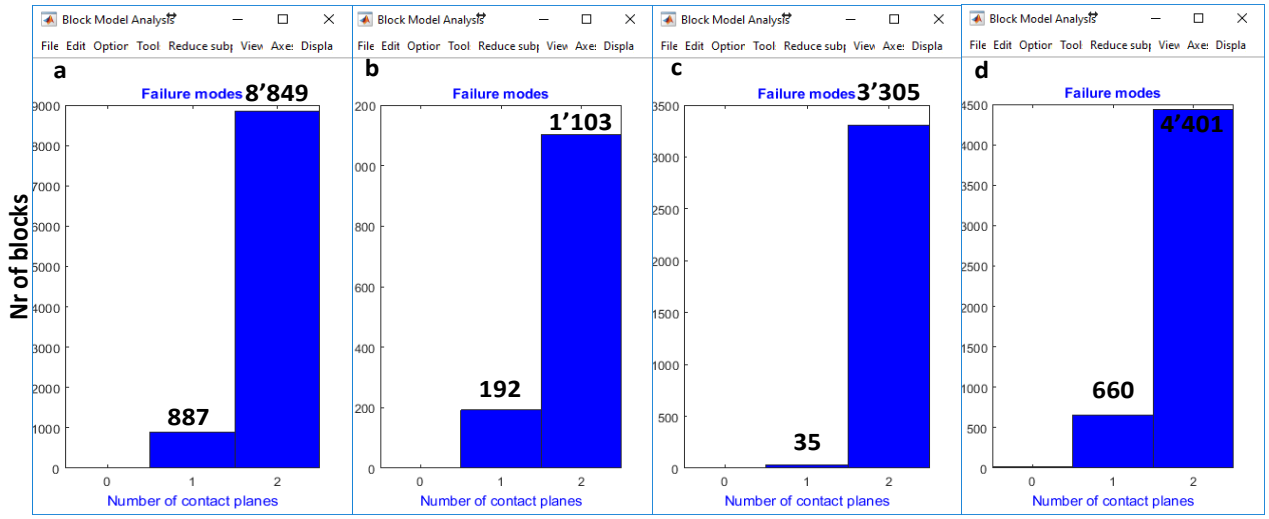

Figure 204 - Failure modes of the highwall of case study 2 mine performed on 30 simulations, considering blocks with a minimum 10^{-3} m^3 volume only. a: Type I, Type II and Type III blocks (all removable blocks); b: Type I block (removable unstable blocks); c: Type II blocks (removable and stable with φ); d: Type III blocks (removable and stable)

Table 20 - nr of blocks sorted by Type of block (Type I: unstable blocks; Type II: blocks stable thanks to φ; Type III: stable blocks) considering 20 and 30 simulations

Nr of simulations	Nr total blocks	All blocks		Type 1 blocks		Type 2 blocks		Type 3 blocks	
		1 contact plane	2 contact planes	1 contact plane	2 contact planes	1 contact plane	2 contact planes	1 contact plane	2 contact planes
20	14487	1749	12738	497	2163	62	5038	1190	5537
30	20211	2431	17780	714	3152	78	6925	1639	7703

Table 21 - average nr of blocks sorted by Type of block (Type I: unstable blocks; Type II: blocks stable thanks to φ; Type III: stable blocks) considering 20 and 30 simulations

Nr of simulations	Nr total blocks	All blocks (average)		Type 1 blocks (average)		Type 2 blocks (average)		Type 3 blocks (average)	
		1 contact plane	2 contact planes	1 contact plane	2 contact planes	1 contact plane	2 contact planes	1 contact plane	2 contact planes
20	724	87	637	25	108	3	252	60	277
30	674	81	593	24	105	3	231	55	257

In Table 20 and 21 are summarized the evaluated number of blocks fr 20 and 30 simulations, divided by block Type and by number of contact planes. Table 20 describes the total number of blocks for 20 and 30 simulations, while Table 21 the average number of blocks. The average number of blocks for 20 simulations does not differ greatly from the average number of blocks for 30 simulations, so the average number of blocks of 30 simulations is statistically representative of the block distribution within the rock mass. On a total number of 674 blocks, 81 have one contact plane and 593 have two contact planes. 129/674 blocks are related to Type I, 234/674 are related to Type II and 312/674 to Type III. Only 3 blocks are stable thanks to ϕ and lie on an only contact plane; this can be explained because 1m and 2m set of discontinuities of Figure 117 are stepper than the ϕ, so blocks with an only sliding plane are unstable (β_{disc} (2m set) > ϕ). This deduction is in agreement with the low probability of block toppling estimated with the kinematic analysis carried out with all the codes used and with the kinematic index of DiAna as well, as described in the following paragraph.

The distribution of the volume on 20 simulations shows that the range of volume of Type III blocks (letter d in Figure 205) is greater than for Type I blocks (letter b in Figure 205) or of Type II blocks (letter c Figure 205). Similar considerations can be conducted performing 30 simulations (Figure 206). Anyway, performing 30 simulations instead of 20 does not increase the value of the maximum volume of Type II (letter c in Figure 205 and 206). As regarding maximum the volumes of the blocks, the greatest volume for Type I blocks is equal to 0.95 m^3 for 20 simulations and 1.08 m^3 for 30 simulations (letter c in Figure 205 and 206), while the greatest volume for blocks removable and stable thanks to ϕ is instead 1.8 m^3 (letter d in Figure 205), both performing 20 simulations and performing 30 simulations.

Indeed, comparing the number of blocks obtained with 20 and 30 simulations, is evident that the number of blocks for each class is proportional to the number of simulational carried out; indeed the maximum volume is equal, as the volume distribution. For these reasons, 30 simulations are sufficient to describe the blocks distribution of this highwall as regarding the volume and the stability condition, and no additional simulation has been carried out.

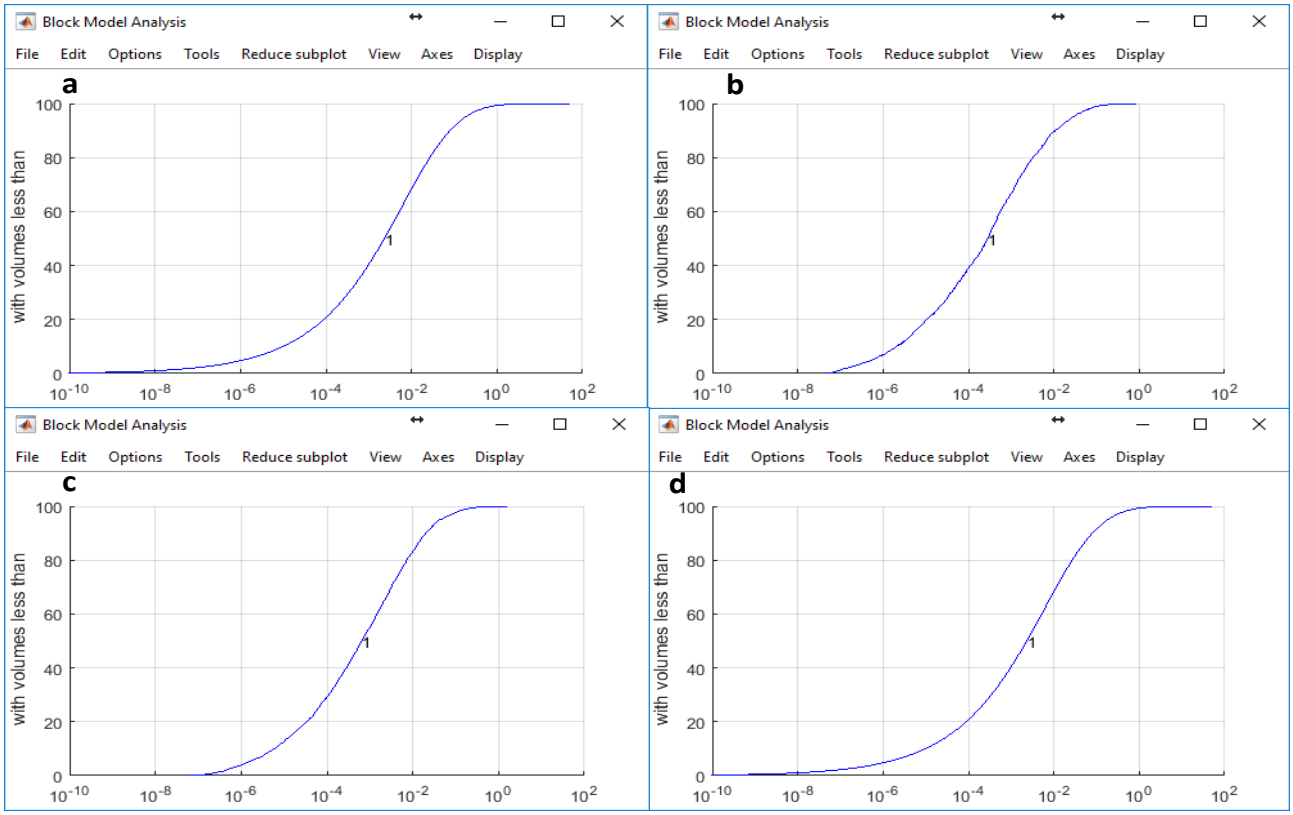

Figure 205 - Volume of removable blocks of the highwall of case study 2 mine performed on 20 simulations. a: Type I, Type II and Type III blocks (all removable blocks); b: Type I block (removable unstable blocks); c: Type II blocks (removable and stable with φ); d: Type III blocks (removable and stable)

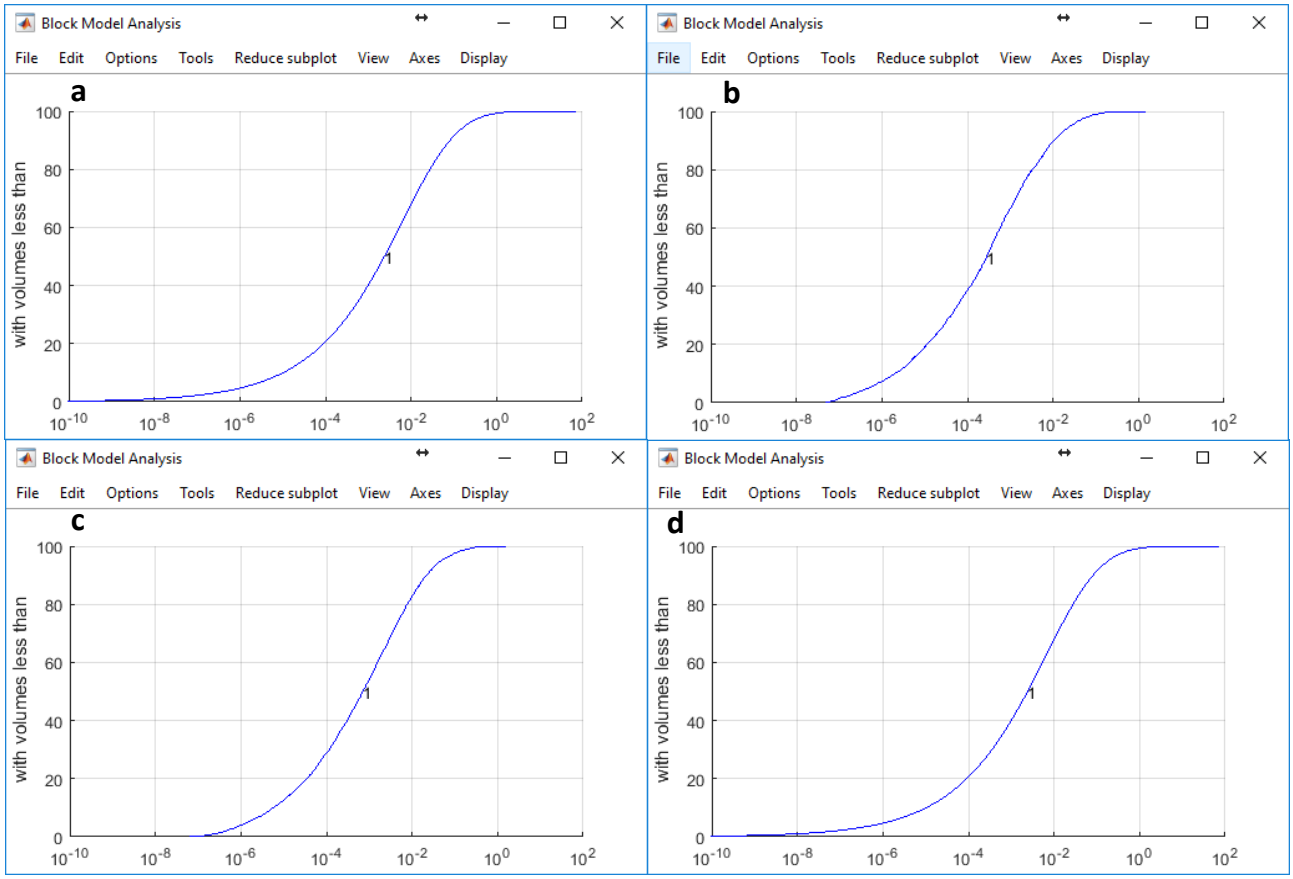

Figure 206 - Volume of removable blocks of the highwall of case study 2 mine performed on 30 simulations. a: Type I, Type II and Type III blocks (all removable blocks); b: Type I blocks (removable unstable blocks); c: Type II blocks (removable and stable with φ); d: Type III blocks (removable and stable)

8. Discussion of the results

Geostructural survey, 2D and 3D kinematic analysis, and stability analysis have been performed on the slopes of two mines in New South Wales, Australia. The geostructural characterisation of the rock mass extracting the discontinuities with manual and semi-automatic codes, 2D and 3D kinematic analysis, and stability analysis have provided a generally coherent overview. Anyway, differences also have been observed among the results of the output data. A critical examination of differences and correlations has been so exposed in this discussion of the results.

The analysis has provided coherent results despite the weathering of the bedrock along the outcrops. The weathering of the rock mass makes the case studies representative of natural weathered slope. Shale and coal beds are, in fact, very alterable to weathering; in particular, the weathering of clay makes a film that often covers the underlying surface of the bedrock, limiting the possibility for discontinuities detection, especially as regarding traces. Anyway, used extraction methods, although remarkable differences have been pointed out, have provided a general accordant overview.

8.1. Comparison of the results of discontinuities extracted by manual and semiautomatic methods

Manual and semiautomatic methods have been used for the extraction of the discontinuities of the rock mass to evaluate the feasibility with different approaches to the geostructural characterisation. The outputs of these two approaches have similarities and differences. A first, important concordance is related to the sets of discontinuities related to the planes. Data shown in Table 22 and 23 provides a general overview of the sets of discontinuities of the two highwalls of case study 1; in Table 24 are, instead reported the data of the sets of discontinuities surveyed on the rock slope of case study 2. Parameters have been reported from the Table 3-10 of Chapter 6.2 and from Table 15, 16, 18, and 19 of Chapter 7.1, that show the sets extracted by a single code and for a single slope, to facilitate the results comparison among the codes for the extraction of the discontinuities. A detailed comparison of the results of the geostructural analysis carried out about the orientation of the sets of the extracted discontinuities (α, σ_α, β, σ_β), L, and σ_L and the number of discontinuities for each set is so given. The comparison between the manual (SiroJoint) and semiautomatic methods (I-Site Studio, DiAna, Facets) is so provided; finally, the output data of the codes for the semiautomatic extraction of the discontinuities have been compared (Figure 207 and 208).

Table 22 - General overview of the sets of discontinuities extracted with the used codes for highwall 1 of case study 1 mine

software	*α (°)*	σ_α	*β (°)*	σ_β	*L (m)*	σ_L	*planes/traces*	*Nr of discontinuities*
	1m set of discontinuities							
SiroJoint	46	11.47	75	10.22	6.60	0.50	Planes	693
I-Site Studio	51	7.91	75	8.53	4.50	0.55	Planes	789
DiAna	49	10.60	69	13.26	6.72	0.52	Planes	1024
Facets	47	7.54	77	8.66	4.26	0.90	Planes	320
	2m set of discontinuities							
SiroJoint	324	23.90	71	11.75	1. 81	2.20	Planes	167
I-Site Studio	-	-	-	-	-	-	-	-
DiAna	-	-	-	-	-	-	-	-
Facets	-	-	-	-	-	-	-	-
	3m set of discontinuities							
SiroJoint	92	15.12	79	8.40	1.98	2.27	Traces	197
I-Site Studio	81	12.52	75	16.23	1.33	0.31	Planes	105
DiAna	89	6.53	77	4.53	1.27	0.21	Planes	27
Facets	71	3.79	75	0.51	1.06	0.13	Planes	25

Table 23 - General overview of the sets of discontinuities extracted with the used codes for highwall 2 of case study 1 mine

software	*α (°)*	σ_α	*β (°)*	σ_β	*L (m)*	σ_L	*planes/traces*	*Nr of discontinuities*
	1m set of discontinuities							
SiroJoint	53	12.52	83	11.46	6.45	0.97	Traces	260
I-Site Studio	-	-	-	-	-	-	-	-
DiAna	-	-	-	-	-	-	-	-
Facets	-	-	-	-	-	-	-	-
	2m set of discontinuities							
SiroJoint	331	20.88	73	12.01	3.91	0.50	Planes	599
I-Site Studio	326	9.63	79	8.09	2.45	0.29	Planes	713
DiAna	323	10.87	80	8.89	1.49	0.12	Planes	638
Facets	325	10.49	79	8.46	4.45	0.63	Planes	565

3m set of discontinuities								
SiroJoint	87	8.26	86	8.32	5.79	0.99	Traces/planes	268
I-Site Studio	-	-	-	-	-	-	-	-
DiAna	-	-	-	-	-	-	-	-
Facets	-	-	-	-	-	-	-	-

Table 24 - General overview of the sets of discontinuities extracted with the used codes for the highwall of case study 2 mine

software	*α (°)*	σ_α	*β (°)*	σ_β	*L (m)*	σ_L	*planes/traces*	*Nr of discontinuities*
1m set of discontinuities								
SiroJoint	289	14.67	72	13.05	11.78	2.20	Planes	626
I-Site Studio	300	13.09	74	9.09	6.39	0.57	Planes	1635
DiAna	302	14.72	74	12.57	5.78	0.78	Planes	384
Facets	303	21.56	74	12.25	0.91	0.09	Planes	489
2m set of discontinuities								
SiroJoint	352	5.82	80	7.47	13.90	1.53	Planes	220
I-Site Studio	-	-	-	-	-	-	-	-
DiAna	-	-	-	-	-	-	-	-
Facets	-	-	-	-	-	-	-	-
3m set of discontinuities								
SiroJoint	147	11.19	59	11.06	8.44	2.27	Traces	35
I-Site Studio	-	-	-	-	-	-	-	-
DiAna	-	-	-	-	-	-	-	-
Facets	-	-	-	-	-	-	-	-
4m set of discontinuities								
SiroJoint	224	14.54	66	7.57	8.18	1.62	Traces	78
I-Site Studio	-	-	-	-	-	-	-	-
DiAna	-	-	-	-	-	-	-	-
Facets	-	-	-	-	-	-	-	-

	5m set of discontinuities							
SiroJoint	49	8.19	84	4.38	8.32	1.57	Traces	53
I-Site Studio	-	-	-	-	-	-	-	-
DiAna	-	-	-	-	-	-	-	-
Facets	-	-	-	-	-	-	-	-

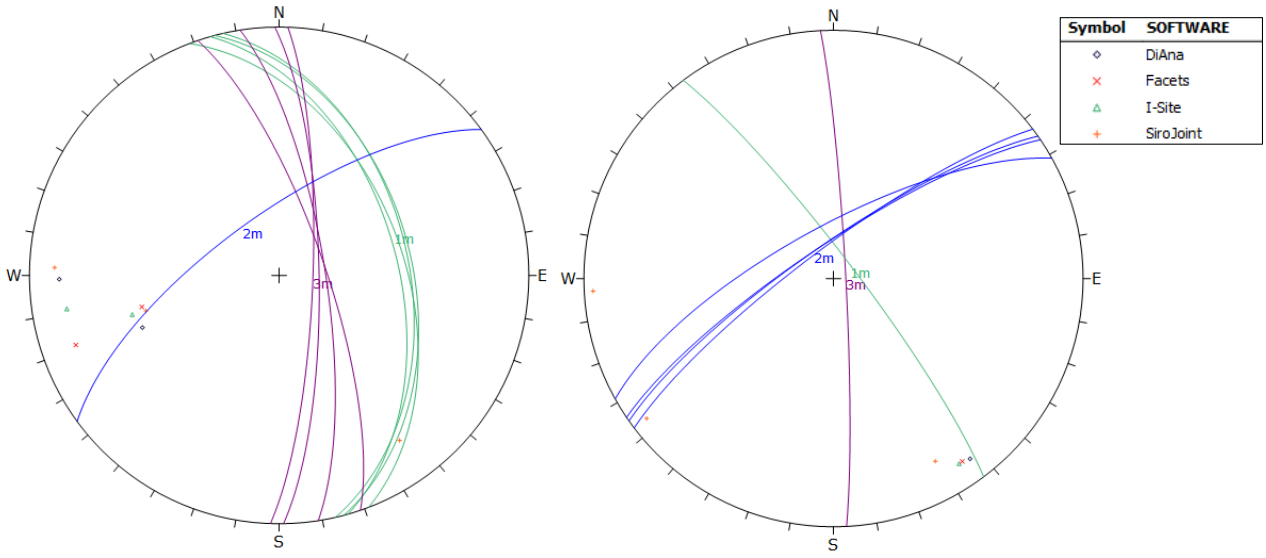

Figure 207 - Stereoplots of the average plane of the sets for the highwall 1 (left) and for the highwall 2 (right) of case study 1 mine. Different symbols indicate the poles of the average planes extracted with different codes

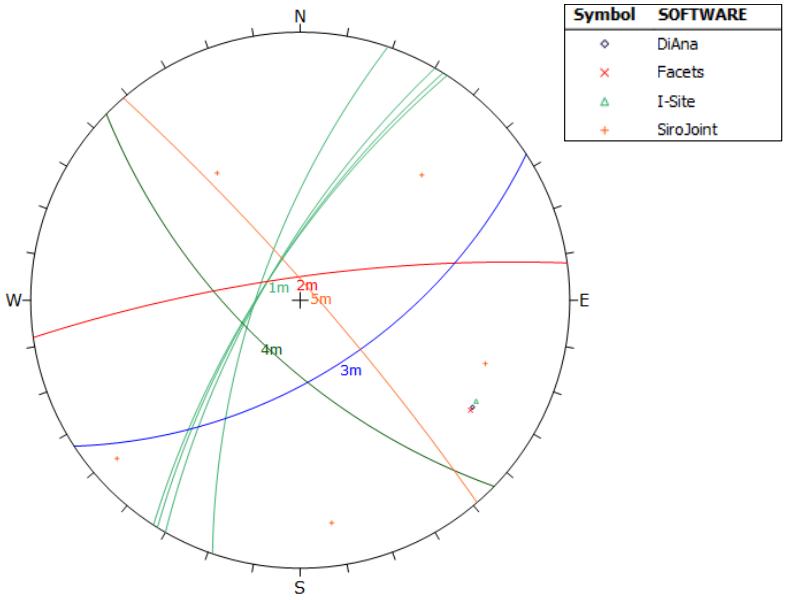

Figure 208 - Stereoplots of the average plane of the sets for case study 2 mine. Different symbols indicate the poles of the average planes extracted with different codes

8.1.1. Discontinuities orientation

α and β of the average planes of the same sets of discontinuities, extracted with manual or semiautomatic methods, have a good agreement and the orientation of the identified sets is similar, also using different codes. On the contrary, discontinuities represented by traces, detected with SiroJoint only and not observed with the codes for the semiautomatic extraction of the discontinuities (i.e.: set 2m for highwall 2 of case study 1 and 3m, 4m, and 5m for case study 2) do not have a correspondence among the discontinuities extracted with semiautomatic methods. Generally speaking, planes and traces have different α: α of the planes is, in fact, generally close to α slope, while α of the traces is about $\alpha_{slope} \pm 90°$. For this reason, sets mainly represented by traces are generally unfavourable for the outcropping of large, easily detectable planes. This observation is corroborated by the analysis of two perpendicular slopes, such as the two highwalls of case study 1 mine. The comparison of 1m and 2m sets for this case study represents a good point for this analysis. While, in fact, 1m outcrops on highwall 1 as planes and on highwall 2 as traces, 2m set outcrops as traces on highwall 1 and mostly as planes on highwall 2. Table 25 and 26 show that 1m and 2m sets are the most populated for highwall 1 and for highwall 2 respectively. Indeed, sets of discontinuities do not have the same relative frequency because the percentage of discontinuities extracted by manual methods shows lower percentage values for discontinuities with α close to α_{slope}, (1m for highwall 1 and 2m for highwall 2); the wider spreading of the poles is related to the extraction with SiroJoint of traces related to 2m set for highwall 1 and to 1m set for highwall 2. The drawing of a line despite the drawing of a plane is much more subjected to a wrong exposition because a little difference of the position along the dimension normal to the slope can greatly affect the orientation.

The main difference of the results is by sure related to the difference of the extraction of the discontinuities with manual despite of semiautomatic methods. A first general overview evidences that semiautomatic methods produce stereoplots of the discontinuities that underrate sets the α_{disc} of which is about $\alpha_{slope} \pm 90°$.

Table 25 - Number of discontinuities extracted by each software for highwall 1 of case study 1 mine

softwares	*sets of discontinuities*						
	1m		*2m*		*3m*		*total*
	nr	%	nr	%	nr	%	
SiroJoint	693	50.1%	197	14.3%	167	12.1%	1382
I-Site Studio	789	85.2%	105	11.3%	-	-	926
DiAna	1024	77.8%	27	2.1%	-	-	1316
Facets	320	67.2%	25	5.3%	-	-	476

Table 26 - Number of discontinuities extracted by each software for highwall 2 of case study 1 mine

softwares	*sets of discontinuities*						
	1m		*2m*		*3m*		*total*
	nr	%	nr	%	nr	%	
SiroJoint	260	16.6%	599	38.2%	268	17.1%	1567
I-Site Studio	-	-	660	92.6%	-	-	713
DiAna	-	-	638	66.5%	-	-	960
Facets	-	-	565	65.3%	-	-	865

So, the orientation of the discontinuities towards the highwall, strongly affects the discontinuity detection of planes and traces. A further consequence is, indeed, related to the kinematic analysis of the highwall. A good

question is so: could the carrying out of the geostructural survey on two normal highwalls related to the same litostructural domain remedy to troubles or impossibility to detect the sets of discontinuities constituted by traces performing it on an only highwall by semiautomatic methods?

Case study 1 has provided an answer to this question. Carrying out the geostructural survey on two perpendicular and contiguous slopes on the same stratigraphic interval without lateral facies eteropy, has enabled the comparison of the stereoplots of the whole rock mass (highwall1+highwall2) obtained with the discontinuities extracted with manual or semiautomatic methods. The usefulness of a comparison of the geostructural surveys on two man-made and straight slopes, each other perpendicular, arises from a reflection about natural slopes. The local orientation on a natural slope is much more scattered than on a man-made one; for this reason most sets of discontinuities outcrop as planes and traces at the same time; a greater number of sets can so be detected also using semiautomatic methods for the extraction of the discontinuities.

The comparison of the stereoplots of the whole rock mass of case study 1, carried out with the codes used in this research, allow to relate the sets extracted analysing the two perpendicular highwalls. Overall 3 sets have been detected with SiroJoint (Figure 210), both on highwall 1 and 2. On both on highwalls (letter a and b in Figure 210) 2 sets are constituted by traces and the remnant one by planes. In both cases, sets constituted by planes have an orientation similar to the slope, while α of the sets constituted by traces is perpendicular to α_{slope}.

A further evidence of the correspondence of the outcropping of planes despite of traces on perpendicular slopes is given by the presence of a cluster of poles of discontinuities represented by traces outside the three recognised sets of highwall 1 (with a mean orientation 120°/60°). In this case too, a cluster of poles of discontinuities represented by planes is evident on the perpendicular slope in the same overlapping area of the stereoplot; indeed, the stereoplot representing the discontinuities detected for both highwalls (letter c in Figure 210) shows a cluster of poles in this area. Of course, this cluster is not very populated because of the low number of discontinuities detected on highwall 2. We hypothesise that the detection difficulties for these planes are related to the very alterable lithologies (mostly pelite and shale) and to high jointing of the rock mass, that makes overhanging surfaces very instable and so affected by rockfall. For this reason, no overhanging surfaces detectable from the distance of the cameras position (about 40 m from the base of the slope) are evident. The comparison so shows that the geostructural characterisation carried out with manual methods on one highwall only allows to describe the whole rock mass, without carrying on the survey on the perpendicular highwall too. Nevertheless, the feasibility of an optical-based data is dependent on the visibility of the targets; for this reason, small surfaces on weathered lithologies could be difficult to detect. Besides the detected sets of discontinuities, the set of discontinuities related to the bedding is present; rock mass bedding is evident especially in correspondence of thick layers of arenite. The extraction of overall 2949 discontinuities (1382 and 1567 for the highwall 1 and for the highwall 2, respectively), on an overall extent of 795 m^2 (482 m^2 for the highwall 1 and 313 m^2 for the highwall 2), has required 60 hours about for the only phase of extraction of the discontinuities with SiroJoint, without keeping in consideration the time necessary for the building of the 3D model from the stereo pairs and for the learning of the software. The surveyed outcrops represent a small part of the sector of the mine: the whole highwall 1 is, in fact, 1.4 km long; an extensive geostructural survey would require so a much longer time.

I-Site Studio has enabled the individuation of 2 sets of discontinuities, constituted by planes and corresponding to the sets of SiroJoint consisting of planes as well. Nor sets corresponding to sets extracted by SiroJoint and consisting of traces, nor sets consisting of planes with orientation perpendicular to the slope have been extracted. Overall, the poles are clustered and so the sets of discontinuities are clearly individuated; as described in Chapter 6, the spreading of the poles on the stereoplot of the discontinuities extracted by I-Site Studio, is related to the sampling mode of the software: it requires, in fact, besides α, β, the minimum number of points, and the maximum standard deviation of the planes, the angular range between the detected plane

and other planes extracted by the point cloud. This sampling mode is responsible for the values of σ_α and $\sigma_{\beta,}$ significantly lower than the values extracted with the other tested codes (Table 22 and 23).

DiAna has shown 2 sets of discontinuities for the two highwalls of case study 1 mine, corresponding to the sets extracted by I-Site Studio and consisting mainly of planes. Besides the sets of discontinuities, the spreading of which has a clustered pattern (1m and 2m in Figure 212) and that are evident, the extraction of the discontinuities on highwall 1 (letter a in Figure 212) allows to hypothesise the presence of a cluster of low dipping discontinuities, maybe related to the bedding (Figure 212). Although β of these discontinuities (

Table 23) is greater than the value of the angle of the bedding described by Lambert et al. (2011) (β = 8.6°), these poles can be nevertheless assigned to the bedding for the following reasons:

- The observation of the images of the bench shows no other set of discontinuities with a low β angle, besides the bedding;
- The angle between the direction of the LOS of the camera and the β_{slope} explains the difference between the value of β of the bedding (Lambert et al., 2011; see Table 2 in Chapter 5.2.1); the presence of shadow areas from the camera position because of the difference in level between the quote of the camera and some part of the slope, especially for the upper part (Figure 209).
- Because the uppermost part of the highwall is 21 m higher in level than the quote of the cameras, that are located about 40 m far from the base of the bench, the β_{slope} of which is 70°, while at the same quote the profile are similar, at the uppermost part the rebuilding of the bedding planes, that are hidden to the camera perspective, can reach the values up to 27°, although the real data is that bedding planes are sub-horizontal. For this reason, planes related to bedding (5m set of discontinuities), are apparently more inclined than the values of β of the bedding reported in Lambert et al. (2011). The different value of α of 5m set of discontinuities in comparison to the values of α of the bedding reported by Lambert et al. (2011) is, instead, related to the scattering of the poles of the discontinuities, that gives rise to α angles related to different quadrants.
-

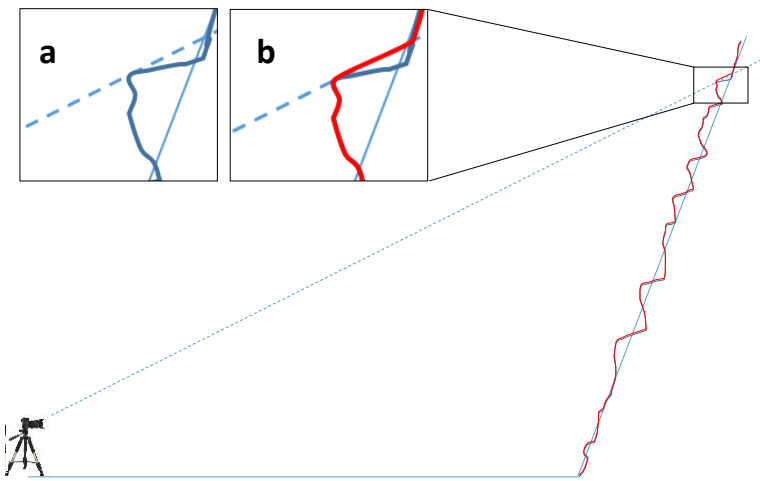

Figure 209 - Schematic representation of the difference between the real slope (a) and the 3d model profile (b). LOS of the camera is partly covered on the top part of the slope. Blue profile represents the real profile and red profile represents the reconstructed profile

DiAna has so allowed to extract 2 sets of discontinuities, besides the set related to the bedding; among these sets, 1m, 2m are clearly singled out both on highwall 1 and on highwall 2.

The stereoplots of the discontinuities extracted with Facets show that the rock mass is affected by 2 sets (Figure 213), that correspond to the sets of the planes 1m and 2m extracted with the other codes. Although no other clusters are clearly detectable, a number of discontinuities have the same orientation of 3m set.

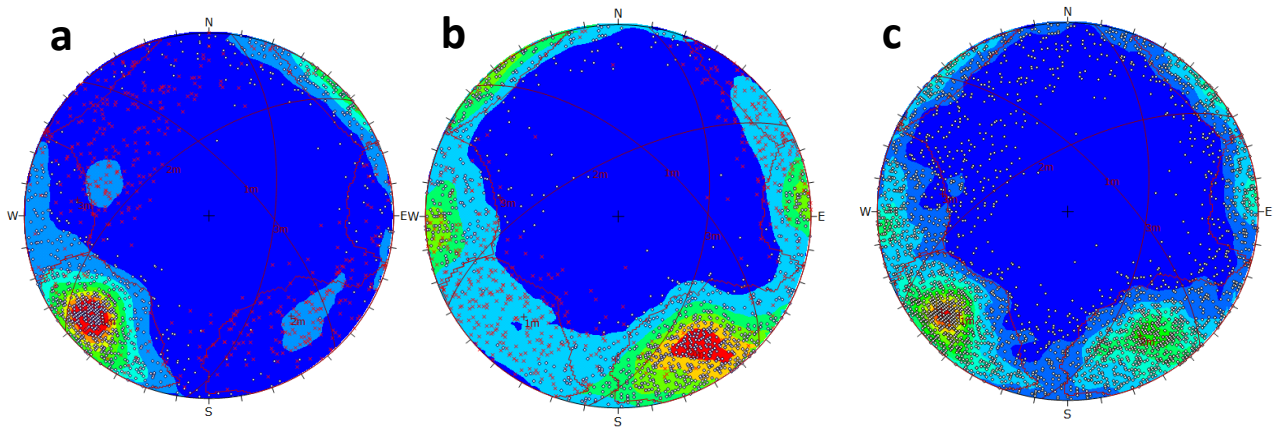

Figure 210 - Stereoplot of the discontinuities extracted by SiroJoint of the case study 1 perpendicular walls: a) poles of planes and traces of wall 1; b) poles of planes and traces of wall 2; c) poles of the discontinuities of wall 1 and wall 2. White rhombus: poles of the planes; red cross: poles of the traces

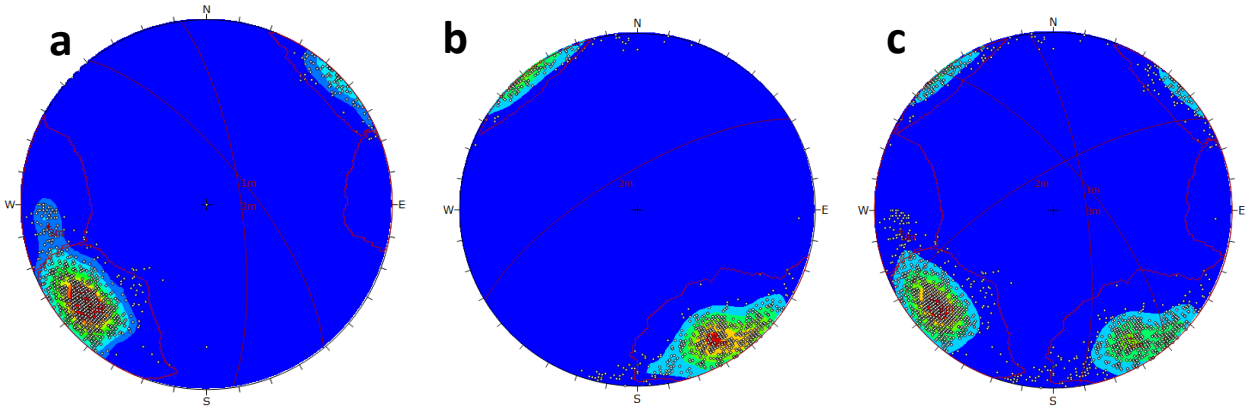

Figure 211 - Stereoplot of the discontinuities extracted by I-Site Studio of the case study 1 perpendicular walls: a) poles of the discontinuities of wall 1; b) poles of the discontinuities of wall 2; c) poles of the discontinuities of wall 1 and wall 2

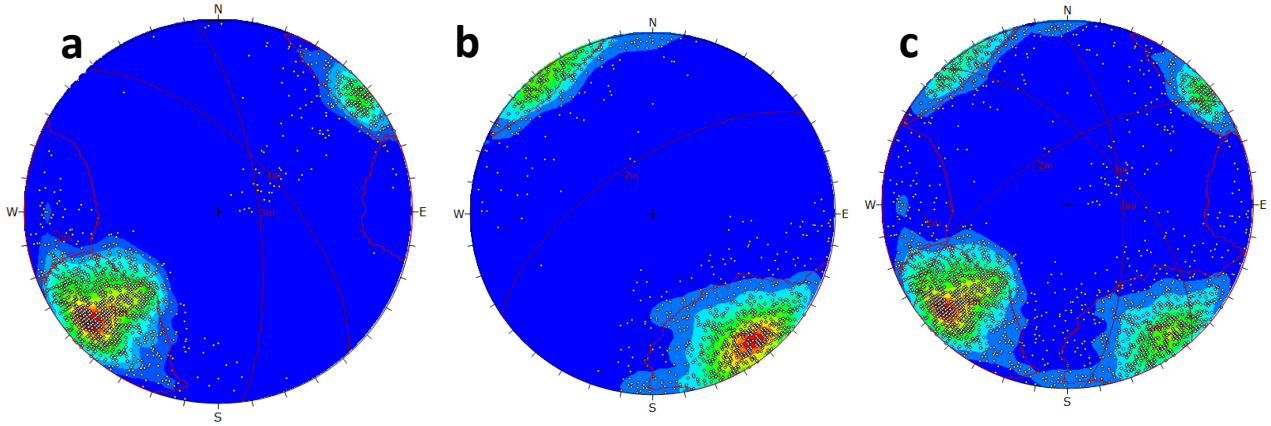

Figure 212 - Stereoplot of the discontinuities extracted by DiAna of the case study 1 perpendicular walls: a) poles of the discontinuities of wall 1; b) poles of the discontinuities of wall 2; c) poles of the discontinuities of wall 1 and wall 2

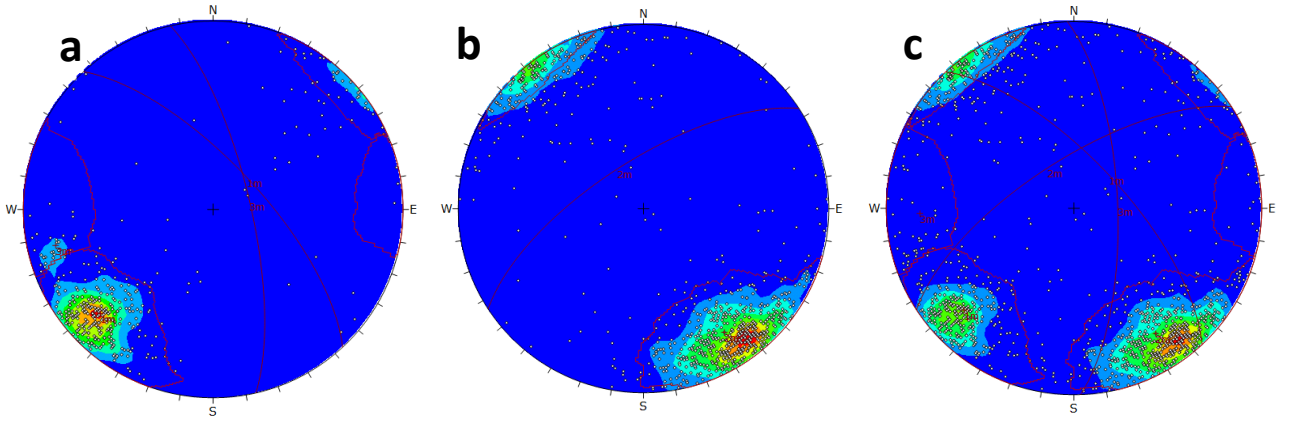

Figure 213 - Stereoplot of the discontinuities extracted by Facets plugin of CloudCompare of the case study 1 perpendicular walls: a) poles of the discontinuities of wall 1; b) poles of the discontinuities of wall 2; c) poles of the discontinuities of wall 1 and wall 2

Lambert et al. (2012) has performed the geostructural characterisation of two highwalls similar to those described for case study 1. The results of the surveys carried out by Lambert et al. (2012) are comparable to the results of the geostructural characterisation of this study. Lambert et al. (2012) have individuated 3 sets of discontinuities, besides the bedding set, not represented in this study to avoid the blurring of other sets. The most populated planes (Figure 214) are represented by the planes with orientation similar to the two slopes and coincide with the most populated sets extracted for each highwall of this study, the 1m set for highwall 1 and with 2m set for highwall 2 (letter a in Figure 214) . Indeed, on highwall 2, two principal sets have been described (letter b in Figure 214); the general stereoplot of the whole rock mass suggests so the occurrence of three main sets, one with the same orientation of 1m set, and two with an orientation similar to 2m set. The two differences between the geostructural characterisation of Lambert et al. (2012) and the geostructural characterisation of this study are related to the joining of these latter two sets into a single set (2m) and to the splitting of the main set described by Lambert et al. (2012) into two sets (1m and 3m). Anyway, this latter the stereoplot of letter a in Figure 214 shows the presence of a second cluster of poles that could be related to 3m set of discontinuities. The stereoplots of the two geostructural surveys are anyway similar and the differences of the two interpretations of the rock mass characterisation are related to the sensitivity and skills of the operator, thus suggesting another key point to be added to this discussion regarding the subjectivity that can affect the manual extraction of discontinuities.

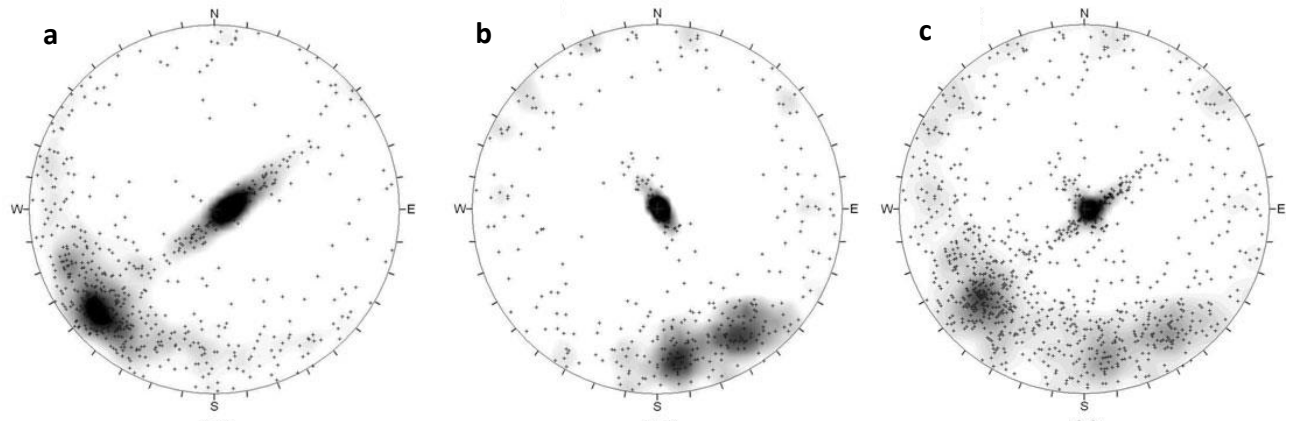

Figure 214 - Stereoplots of the highwalls of case study 1 obtained by the geostructural surveys carried out with SiroJoint by Lambert (2012); a) geostructural characterisation of highwall 1; b) geostructural characterisation of highwall 2; c) geostructural characterisation of highwall 1 and highwall 2. From Lambert et al. (2012)

Geostructural surveys carried out by manual or semiautomatic methods on the studied highwall of site 2 show the presence of a more complex structural setting, characterised by a total of 5 sets of discontinuities (Figure 215).

The traces, extracted by SiroJoint are related to 3m, 4m, and 5m sets; planes are instead related to 1m and 2m sets. The orientation of the traces is generally normal to the slope, while planes have an orientation similar to the slope. The comparison of the stereoplots of the discontinuities extracted shows that sets 1m and 2m, that have a α close to α_{slope}, (sets 1m e 2m) are the most populated (Table 24). The number of discontinuities of each set considerably ranges code by code, although no relevant differences of the geostructural arrangement of the rock mass (Table 27).

Table 27 - Number of discontinuities extracted by each software for case study 2 highwall

softwares	*sets of discontinuities*										
	1m		*2m*		*3m*		*4m*		*5m*		*total*
	nr	%	nr	%	nr	%	nr	%	nr	%	
SiroJoint	626	41.2%	352	23.2%	75	4.9%	224	14.7%	49	3.2%	1520
I-Site Studio	1635	91.1%	-	-	-	-	-	-	-	-	1795
DiAna	916	72.8%	-	-	-	-	-	-	-	-	1259
Facets	548	74.0%	-	-	-	-	-	-	-	-	741

In particular, it is highlighted how the percentage of discontinuities related to the sets with α close to α_{slope} (1m and 2m) and extracted with manual methods is less than the percentage of the discontinuities related to the same sets, but with semiautomatic methods, although representing anyway the majority of the discontinuities. The difference of the values of the concentration of the poles of the discontinuities of these sets and 3m, 4m, and 5m sets influences the contouring of the pole concentration; for this reason, less populated sets are not evident from the analysis of the isodensity lines (Figure 215).

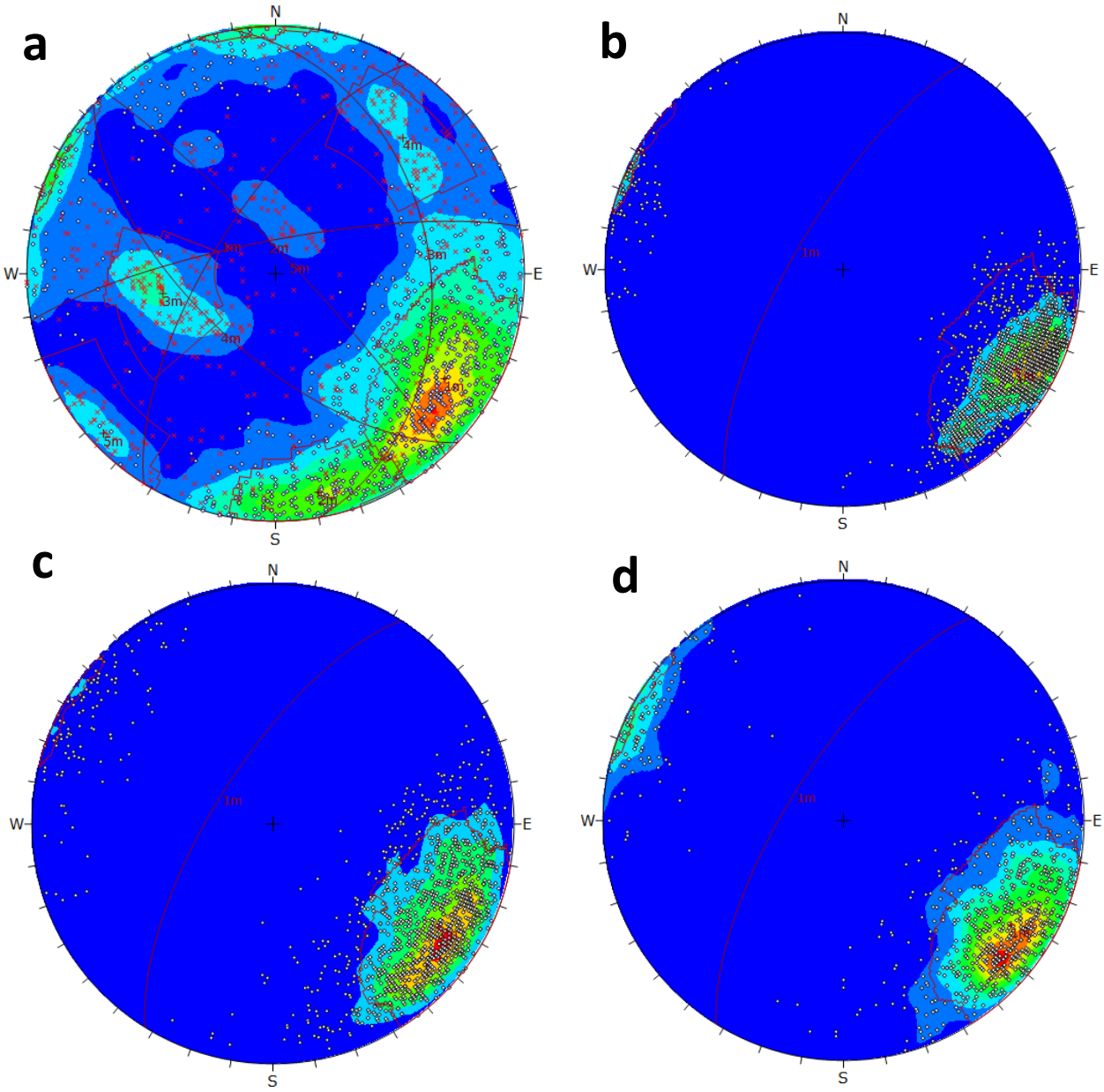

Figure 215 - Stereoplot of case study 2 highwall of the discontinuities extracted by: a) SiroJoint; b) I-Site Studio; c) DiAna; 4) Facets plug in of CloudCompare

5 sets of discontinuities have been detected with SiroJoint (letter a in Figure 215), 2 of which consist of planes and 3 of traces. Among the sets of discontinuities consisting of planes, 1m set is the most populated; 2m set of discontinuities is populated as well. Sets of discontinuities constituted by planes, as for case study 1, are subparallel to the slope orientation.

I-Site Studio (letter b in Figure 215), DiAna (letter c in Figure 215), and Facets (letter d in Figure 215) have shown the presence of one set of discontinuities only, which orientation is subparallel to the slope (1m set).

A relevant capability of discontinuities detection distinguishes so the two case studies. This observation gives some important indications about the best way to employ the discontinuities extraction methods. The complexity of the geostructural framework and the variability of the aspect of the slope, besides the extension of the surveyed surface, should be put on the weighting plate. Manual methods could be, in fact, preferable in case of a complex rock mass surveyed on a slope with a homogeneous aspect (case study 2), while the results of the geostructural survey of a rock mass with a simple framework and/or a slope with local different orientation, such as a natural slope, is not greatly affected by the used discontinuities extraction methods.

8.1.2. Discontinuities persistence

L is one of the 10 parameters defined by ISRM (1978) for the geomechanical characterisation of the rock mass. It has a different geometrical significance since it is related to a geostructural survey performed with manual or semiautomatic methods because the L of the extracted planes does not correspond with the L of the traces associated with the same plane. The L related to a plane is so lower than the L evaluated from the traces. As described in Chapter 2, Riquelme et al. (2018) distinguish 3 types of L when investigating rock masses: visible L, real L, and estimated L. We herein discuss the comparability of discontinuities extracted by manual methods, the L of which corresponds to the visible L, and of discontinuities extracted by semiautomatic methods, to evaluate if the L evaluated with semiautomatic methods can be compared to the visible L of the discontinuities.

The representative value of L for each set has been set at the maximum length of the discontinuities of the set and not at the average L of all the discontinuities. The L of a single discontinuity is the visible persistence of the discontinuity, that is minor or equal to the real persistence of the discontinuity. We could equate the discontinuity to a circle, the real L to its diameter and the visible L to the circumference chord made with the intersection of the circle with the slope. Anyway, real L is the L of the single feature, but not necessarily of the whole set. In case the set is made of traces only on unweathered bedrock, the real L could be associated with the average L of the discontinuities of the set; in case, instead of a set consisting of planes only, the L of the whole set is greater than the average L of each outcropping planes because many planes are often part of an only discontinuity. Assuming that all the discontinuities of a set were, with a reasonable approximation, described with an only value of L, the maximum L of the planes of a set would correspond to the representative value of L of a set of discontinuities entirely represented by planes. For these reasons, the maximum L value of the discontinuities has been proposed to be used as representative value of L of a whole set

In Table 28, 29, and 30 the values of L for the sets of discontinuities extracted with SiroJoint, I-Site Studio, Diana, and Facets are compared. The results of the comparison of the L of the sets consisting of planes with the values of L of the sets consisting of traces, are herein discussed. Hence, the results of the comparison of the values of L evaluated from the sets extracted with manual or semiautomatic methods are exposed.

Table 28 - Comparison of L and σ_L of the discontinuities extracted by SiroJoint, I-Site Studio, DiAna, and Facets for highwall 1 of case study 1 mine

Case study 1 highwall 1

set	*SiroJoint*			*I-Site Studio*			*DiAna*			*Facets*		
	L (m)	σ_L	planes/ traces	L (m)	σ_L	planes/ traces	L (m)	σ_L	planes/ traces	L (m)	σ_L	planes/ traces
1m	6.60	0.50	planes	4.50	0.55	planes	6.72	0.52	planes	4.26	0.90	planes
2m	1.98	2.27	traces	-	-	-	-	-	-	-	-	-
3m	1.81	2.20	planes	1.33	0.31	planes	1.27	0.21	planes	1.06	0.13	planes

Table 29 - Comparison of L and σ_L of the discontinuities extracted by SiroJoint, I-Site Studio, DiAna, and Facets for highwall 2 of case study 1 mine

Case study 1 highwall 2

set	SiroJoint			I-Site Studio			DiAna			Facets		
	L (m)	σ_L	planes/ traces	L (m)	σ_L	planes/ traces	L (m)	σ_L	planes/ traces	L (m)	σ_L	planes/ traces
1m	6.45	0.97	Traces	-	-	-	-	-	-	-	-	-
2m	3.91	0.50	Traces/planes	4.45	0.63	planes	1.49	0.12	planes	4.45	0.63	planes
3m	5.79	0.99	planes	-	-	-	-	-	-	-	-	-

Table 30 - Comparison of L and σ_L of the discontinuities extracted by SiroJoint, I-Site Studio, DiAna, and Facets for case study 2 mine highwall

Case study 2

set	SiroJoint			I-Site Studio			DiAna			Facets		
	L (m)	σ_L	planes/ traces	L (m)	σ_L	planes/ traces	L (m)	σ_L	planes/ traces	L (m)	σ_L	planes/ traces
1m	11.78	2.20	planes	6.39	0.57	planes	5.78	0.78	planes	0.90	0.09	planes
2m	13.90	1.53	planes	-	-	-	-	-	-	-	-	-
3m	13.38	1.99	traces	-	-	-	-	-	-	-	-	-
4m	8.18	1.62	traces	-	-	-	-	-	-	-	-	-
5m	8.32	1.57	traces	-	-	-	-	-	-	-	-	-

The extracted sets of discontinuities have values of L and σ_L differing on base of the outcropping of planes instead of traces and on base of the methods used for the extraction of the discontinuities, manual or semiautomatic.

The comparison of the sets outcropping both planes on one of the highwalls of case study 1 and and traces on the other highwall, shows that the same sets extracted with SiroJoint have similar values of L whether they consist of planes or they consist of traces. This fact is probably due to the weathering of lithologies with a high clay content, the film which produced because of weathering make traces less visible. L of planes extracted by semiautomatic codes is, indeed, minor than the L of discontinuities extracted with manual codes.

The presence of two perpendicular highwalls for case study 1 allows the comparison of the L of planes and traces related to the same set but surveyed on the other highwall as traces despite of planes. The 1m and 2m, sets for the case study 1 outcrop both as traces on a highwall and as planes on the other one. So, it is possible

to compare the L of the planes and of the associated traces on the two orthogonal highwalls and related to the same set of discontinuities extracted by SiroJoint (Table 31).

Table 31 - Comparison of the values of L and $\sigma_{L\ of}$ the sets of discontinuities extracted by SiroJoint for the highwalls of case study 1 mine

highwall	*1m*			*2m*			*3m*		
	L (m)	σ_L	planes/ traces	L (m)	σ_L	planes/ traces	L (m)	σ_L	planes/ traces
Highwall 1	6.60	0.50	planes	1.98	2.27	traces	1.81	2.20	planes
Highwall 2	6.45	0.97	traces	3.91	0.50	planes	5.79	0.99	planes

A comparison between the sets extracted on the same slope with manual and semiautomatic methods has been carried out as regarding the values of the L. The comparison of the values of L of all the extracted sets is reported in Table 22 for the highwall 1 of case study 1, in

Table 23 for the highwall 2 of case study 1, and in Table 24 for the case study 2. The tables indicate that 1m and 3m for the highwall 1 of case study 1, the 2m set for the highwall 2 of case study 1, and the 1m and 2m sets for case study 2 consist of planes extracted with all the codes compared. The L extracted with SiroJoint is the highest for 3 of the 5 sets, while in one case the highest value has been reached with the discontinuities extracted by DiAna and by Facets. The greater value of L detected with SiroJoint is related to the optical support, that makes the merging of close planes easier (Figure 216); anyway, the plane detection capability is user-dependent and the limit of the planes could change operator by operator.

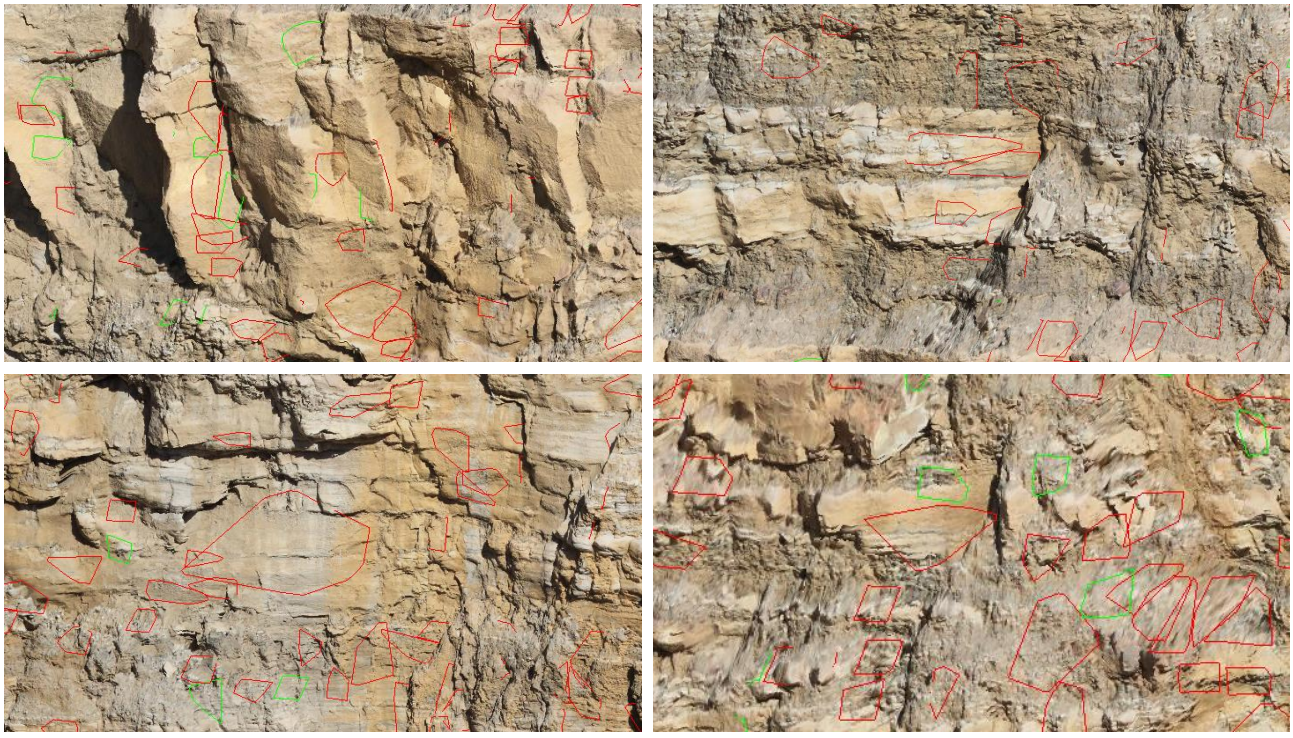

Figure 216 - Example of persistence underestimation due to partial discontinuities reconstruction with semiautomatic methods (Facets)

8.1.3. Traces and planes detection capabilities

The number of discontinuities extracted and so their spatial concentration (linear, areal or volumetric) is a fundamental parameter for the geomechanical description of a rock mass, which concurs to the definition of RMR index (Bieniawski, 1989) and for RQD (Deere, 1966) and Q index (Barton et al., 1974). The number of extracted discontinuities determines the Volumetric joint count J_v (Palmström, 1982) and the Discontinuity intensity I (Dershowitz, 1985; Dershowitz & Einstein, 1988). The Discontinuity Intensity has been defined as the number of discontinuities in a unit area or volume, or as the length of the traces within a surface in case of a 2D analysis (Dershowitz, 1985; Zhang & Einstein, 2000), or the area of the planes within a volume (P_{32}) if the counting has been carried out with a 3D approach (Einstein et al. 1983; Dershowitz, 1985).

The comparison of the geostructural surveys carried out by manual and semiautomathic methods indicate different detection capabilities of planes and traces, although the total number of planes and of traces extracted is comparable (Table 32, 33, and 34). While the discontinuities extracted with semiautomatic methods consist of planes only, about 1/3 of the whole number of discontinuities extracted with manual methods consist of traces (34% for the highwall 1 of case study 1 in Table 32, 33% for the highwall 2 of case study 1 in Table 33, and 38% for the case study 2 in Table 34). Different capabilities detection of traces between manual and semiautomatic methods suggest that guidelines for the use of semiautomatic methods should suggest taking into account benches with different orientation to have a more representative detection of the joints. For this reason, carrying out the survey on more benches with different orientation and similar area, in case of use of semiautomatic methods, allows a better geostructural characterisation, keeping low the time necessary for the extraction of the discontinuities.

As written at the beginning of this Chapter, an only discontinuity within the rock mass can produce, on the slope surface a number of planes, apparently separate; for this reason, Terzaghi weighting (Terzaghi, 1965) has not been applied because underweighting of discontinuities with β_{disc} similar to β_{slope} is compensated by the number of planes extracted, both using manual and semiautomatic methods. Planes are, in fact, more represented than traces with the codes (Table 32, 33, and 34).

Table 32 - Number of discontinuities extracted for highwall 1 of case study 1 mine

software	*planes*	*traces*	*total*
SiroJoint	911	471	1382
I-Site Studio	926	-	926
DiAna	1316	-	1316
Facets	476	-	476

Table 33 - Number of discontinuities extracted for highwall 2 of case study 1 mine

software	*planes*	*traces*	*total*
SiroJoint	1054	513	1567
I-Site Studio	713	-	713
DiAna	960	-	960
Facets	831	-	831

Table 34 - Number of discontinuities extracted for case study 2 mine highwall

software	*planes*	*traces*	*total*
SiroJoint	948	572	1520
I-Site Studio	1795	-	1795
DiAna	1259	-	1259
Facets	741	-	741

8.2. Kinematic analysis results

2D kinematic analysis performed with the stereoplots analysed with Dips software (Rocscience) has allowed the calculation of the kinematic index for plane failure (Hoek & Bray, 1981), for wedge failure (Hoek & Bray, 1981), for Block toppling (Goodman & Bray, 1976; Matheson, 1983), and for flexural toppling (Goodman & Bray, 1976; Hudson & Harrison, 1997).

Table 35, 36, and 37 report the kinematic indices and show that plane failure and wedge failure represent the most probable failure mechanisms for both case studies. The value of the kinematic index for wedge failure on the discontinuities extracted by SiroJoint is similar to the value of the index evaluated from the stereoplots of the discontinuities extracted by semiautomatic methods. Table 35, 36, and 37 show that kinematic indices for plane failure, block toppling, and flexural toppling are, instead, influenced by the extraction method of the discontinuities. In particular, kinematic indices for plane failure and flexural toppling would be lower if the discontinuities were extracted with manual methods, while the kinematic index for block toppling would be greater.

The presence of traces, with α mostly perpendicular to α_{slope}, is the cause of the influences of the methods of extraction on the kinematic indices. Lower values for the kinematic index of plane failure would be related to the lower percentage of critical discontinuities if traces also were plotted into the stereoplot; the poles of the traces for the two case studies are not, in fact, included in the area critical for plane failure. Because the kinematic index for plane failure is the percentage of poles included into the critical area, greater the number of discontinuities outside the critical area, lower the value of kinematic index for plane failure. A confirmation of the deduction that the presence of the traces, and so the adoption of manual or semiautomatic methods for the extraction of the discontinuities, influences the kinematic indices, is given in Table 35, 36, and Table 37, that report also the kinematic indices evaluated considering planes extracted with SiroJoint only, instead of both planes and traces.

The comparison among the kinematic indices of the stereoplots with all the discontinuities extracted and the stereoplots of discontinues related to planes only extracted with SiroJoint, as regarding the kinematic index of plane failure, shows that taking into account planes only, the index is greater (43%, 46%, and 26%), reaching values similar to those calculated from the stereoplots of the discontinuities extracted by semiautomatic methods. For this reason, the exclusion of the poles of the traces from the critical area for plane failure causes a lower value for the kinematic index for plane failure; discontinuities outcropping as planes instead of traces, are so less critical for this failure mechanism. Higher values for the kinematic index of plane failure are so related, also for SiroJoint, to the presence of the poles of the traces outside the area critical for this mechanism.

Table 35, 36, and 37 and Figure 217, 218, and 219 show that the kinematic indices for plane failure and flexural toppling have some analogies. In fact, the highest values of the kinematic index for flexural toppling are reached using semiautomatic methods for the extraction of the discontinuities; indeed, the comparison between the kinematic index for flexural toppling on the stereoplot of the discontinuities extracted using both planes and traces of SiroJoint is less than 45%, 39%, and 32% (Table 35, 36, and 37) compared to the kinematic index for flexural toppling extracted using planes only.

Block toppling is an improbable failure mechanism on all the three examined slopes, whatever is the method used for the extraction of the discontinuities. The values of the kinematic index for block toppling range from 0.09% to 21% for the highwall 1 of case study 1, from 0.34% to 3.40% for the highwall 2 of case study 1, and from 0.02% to 3.31% for the highwall of case study 2. Indeed, a further failure condition, besides the inclusion of the intersection into the secondary critical area, the presence of a basal plane, is necessary for block toppling. A basal plane with a dip-slope α_{disc} and $\beta_{disc} > 90° - \phi$ is then required. If this basal plane had a $\beta_{disc} \geq \phi$, the singled out block would fail sliding on this sliding plane; on the contrary, if this basal plane had a $\beta_{disc} < \phi$, the singled out block would fail toppling on this toppling plane. The sliding plane is anyway a critical discontinuity for plane failure. however, these values are underestimated, especially for highwall 1, due to the removal of the bedding planes that, for this particular geometry can act as low angle basal plane.

Table 35 - Comparison of the values of the kinematic index for plane failure (Hoek & Bray, 1981), Wedge failure (Hoek & Bray, 1981), block toppling (Goodman & Bray, 1976; Matheson, 1983) and flexural toppling (Goodman & Bray, 1976; Hudson & Harrison, 1997) for highwall 1 of case study 1 mine

Kinematic mechanism	*Kinematic index (%)*				
	SiroJoint (planes + traces)	*SiroJoint (planes only)*	*I-Site Studio*	*DiAna*	*Facets*
Plane Failure	14.47	20.75	23. 54	35.11	23.94
Wedge Failure	31.11	30.41	24.21	36.63	26.19
Block Toppling	2.12	0.74	0.09	0.25	0.28
Flexural Toppling	6.80	9.88	8.96	14.29	10.47

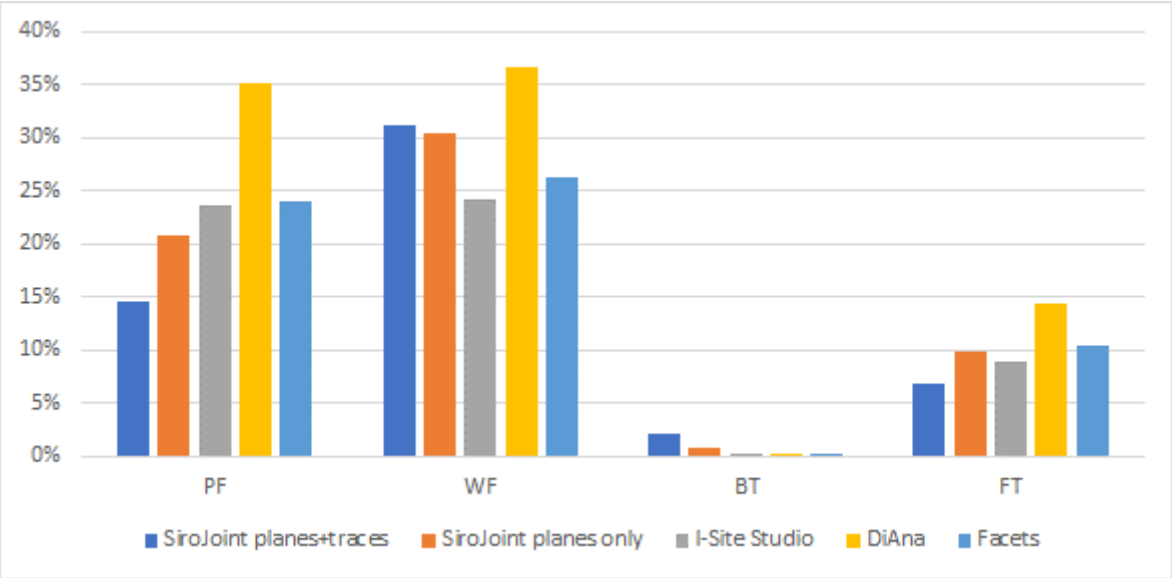

Figure 217 - Diagram of the kinematic indices evaluated since the stereoplots of the discontinuities extracted with each code for highwall 1 of case study 1 mine

Table 36 - Comparison of the values of the kinematic index for plane failure (Hoek & Bray, 1981), Wedge failure (Hoek & Bray, 1981), block toppling (Goodman & Bray, 1976; Matheson, 1983) and flexural toppling (Goodman & Bray, 1976; Hudson & Harrison, 1997) for highwall 2 of case study 1 mine

Kinematic mechanism	*Kinematic index (%)*				
	SiroJoint (planes + traces)	*SiroJoint (planes only)*	*I-Site Studio*	*DiAna*	*Facets*
Plane Failure	12.76	18.69	14.17	16.98	15.40
Wedge Failure	30.98	31.36	17.09	21.70	18.34
Block Toppling	3.40	1.33	0.34	0.73	0.76
Flexural Toppling	6.83	9.49	14.03	18.75	18.53

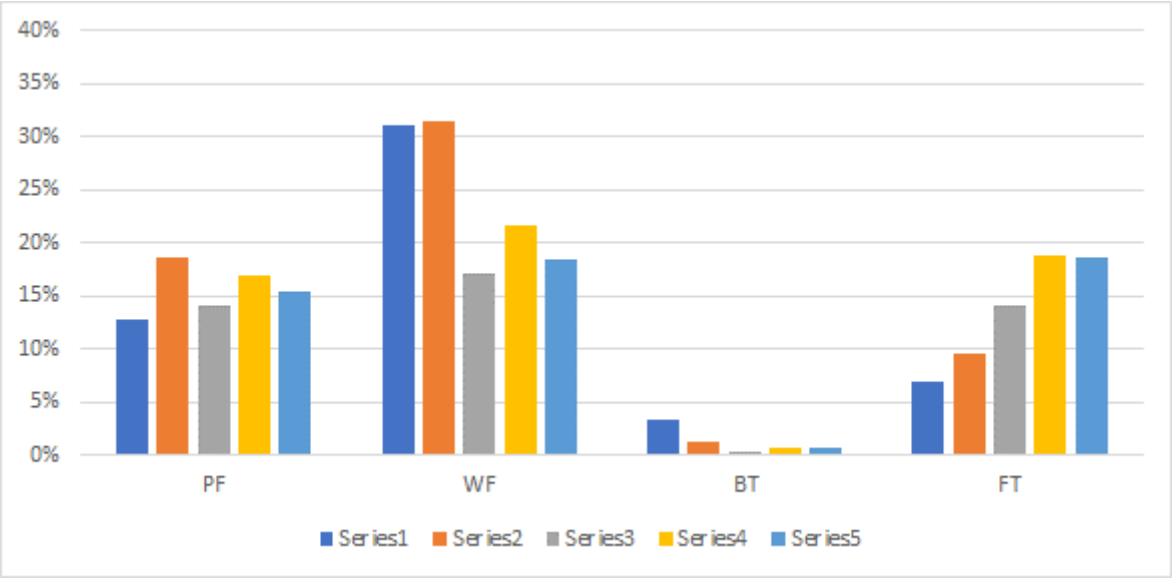

Figure 218 - Diagram of the kinematic indices evaluated since the stereoplots of the discontinuities extracted with each code for highwall 2 of case study 1 mine

Table 37 - Comparison of the values of the kinematic index for plane failure (Hoek & Bray, 1981), Wedge failure (Hoek & Bray, 1981), block toppling (Goodman & Bray, 1976; Matheson, 1983) and flexural toppling (Goodman & Bray, 1976; Hudson & Harrison, 1997) for case study 2 mine highwall

Kinematic mechanism	*Kinematic index (%)*				
	SiroJoint (planes + traces)	*SiroJoint (planes only)*	*I-Site Studio*	*DiAna*	*Facets*
Plane Failure	15.53	23.00	34.09	33.20	31.58
Wedge Failure	37.70	46.53	50.59	50.88	47.57
Block Toppling	3.31	0.63	0.02	0.24	0.14
Flexural Toppling	4.47	5.91	1.84	5.24	6.75

The comparison of the 2D kinematic analysis carried out on stereoplots of the discontinuities extracted by semiautomatic methods evidences similar results and a number of similarities can be listed.

Is noteworthy that the values of the kinematic indices of the stereoplots of the planes extracted by SiroJoint is less similar than the stereoplot of planes and traces to the stereoplots of the discontinuities extracted with semiautomatic methods. Different analysis is needed for the comparison of the kinematic indices for failure mechanism involving mostly planes (plane failure and flexural toppling) than kinematic indices involving both planes and traces (wedge failure and block toppling). The critical intersections related to these latter failure mechanisms often involve, in fact, the average planes both of the sets mostly constituted by traces and of the sets mostly constituted by planes as well.

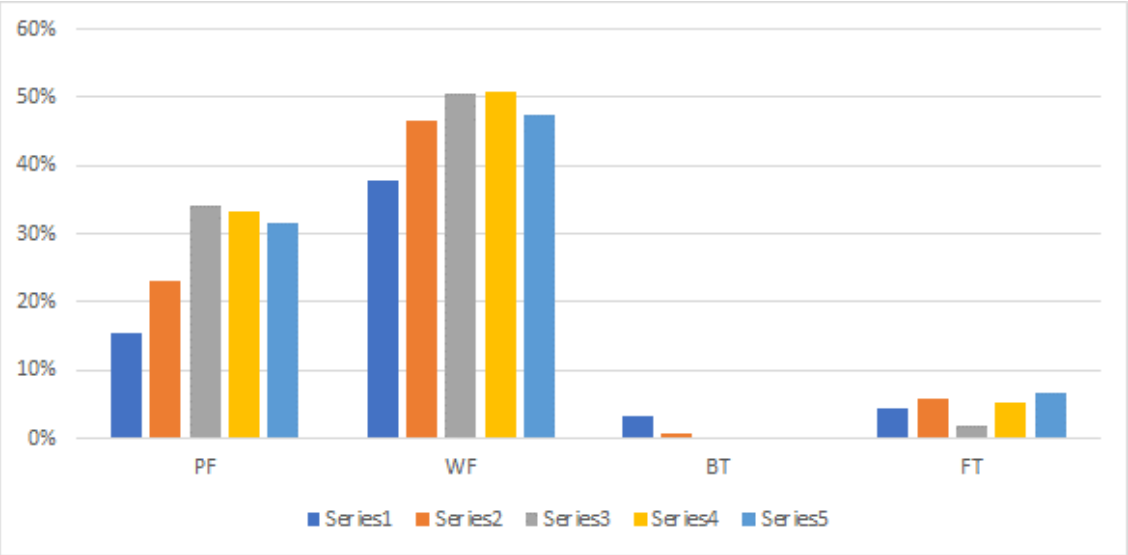

Figure 219 - Diagram of the kinematic indices evaluated since the stereoplots of the discontinuities extracted with each code for case study 2 mine

3D kinematic analysis carried out with DiAna-K has allowed the calculation of the kinematic indices (Casagli & Pini, 1993) for plane failure, wedge failure, block toppling, flexural toppling, and free fall, taking into account as slope, the local orientation of the surface of the mesh made from the stereomodel. As results, kinematic index with DiAna-K gives a value of the susceptibility for each failure mechanism considering the orientation of each triangle of the mesh. The positions of the most critical areas for each failure mechanism have been so detechted; the optical images of these unstable area have provided so an assessment of the volume too of these blocks. These volumes have been then compared with the volume of Type I and Type II blocks (Goodman & Shi, 1985) evaluated with the stability analysis carried out with SiroModel. 3D kinematic analysis carried out with DiAna-K has so underlined that the differences of the local orientation of the slope affects the kinematic indices and that different main kinematics involve areas with different orientation.

Kinematic analysis performed with DiAna-K has, in fact, shown that both on highwall 1 and on highwall 2 of case study 1 the parts with α similar to α_{slope} are mostly involved by plane failure (Figure 220), while the sectors with α perpendicular to α_{slope} are mostly involved by wedge failure. These relevant discrepancies clearly demonstrate the weight of the aspect for the detection of the failure mechanisms that affect the slope and are related to the reduction of the number of poles included into the critical area for plane failure routing the α_{slope} of 90°. On the contrary, the percentage of critical intersection for wedge failure grow up.

The comparison between the highwall 1 and the highwall 2 of case study 1 shows, indeed, that the discontinuities with anti-dip slope orientation affect the susceptibility for flexural toppling mechanism. Although, in fact, areas in which flexural toppling is the most probable failure mechanism are, generally speaking, quite stable and show low susceptibilities values for the other failure mechanisms because just a little steep, highwall 2 (letter b in Figure 220) is a little more exposed to flexural toppling than highwall 1 (letter a in Figure 220). This fact is related to the greater number of discontinuities with anti-dip slope orientation on highwall 2 extracted by DiAna (Figure 148) than the number with anti-dip orientation for highwall 1 (Figure 125). This deduction has been corroborated by the higher value of the kinematic index for block toppling for the stereoplot of highwall 2 (Table 36) than for the stereoplot of highwall 1 (Table 35) of the discontinuities extracted with DiAna.

2D Kinematic analysis carried out on the discontinuities extracted by DiAna (Figure 110, 115, 120, 125, 133, 138, 143, and 148) shows that wedge failure is the most probable kinematic mechanism for case study 1 (Table 35, 36, and 37). This fact is apparently in contrast to the susceptibility maps carried out with DiAna-K. The maps of the most probable failure mechanisms (Figure 128 and 152) show that plane failure is more probable

on the steepest part; maximum poles concentration is located just above the ϕ cone and so small increase of the local β makes plane failure more probable than wedge failure.

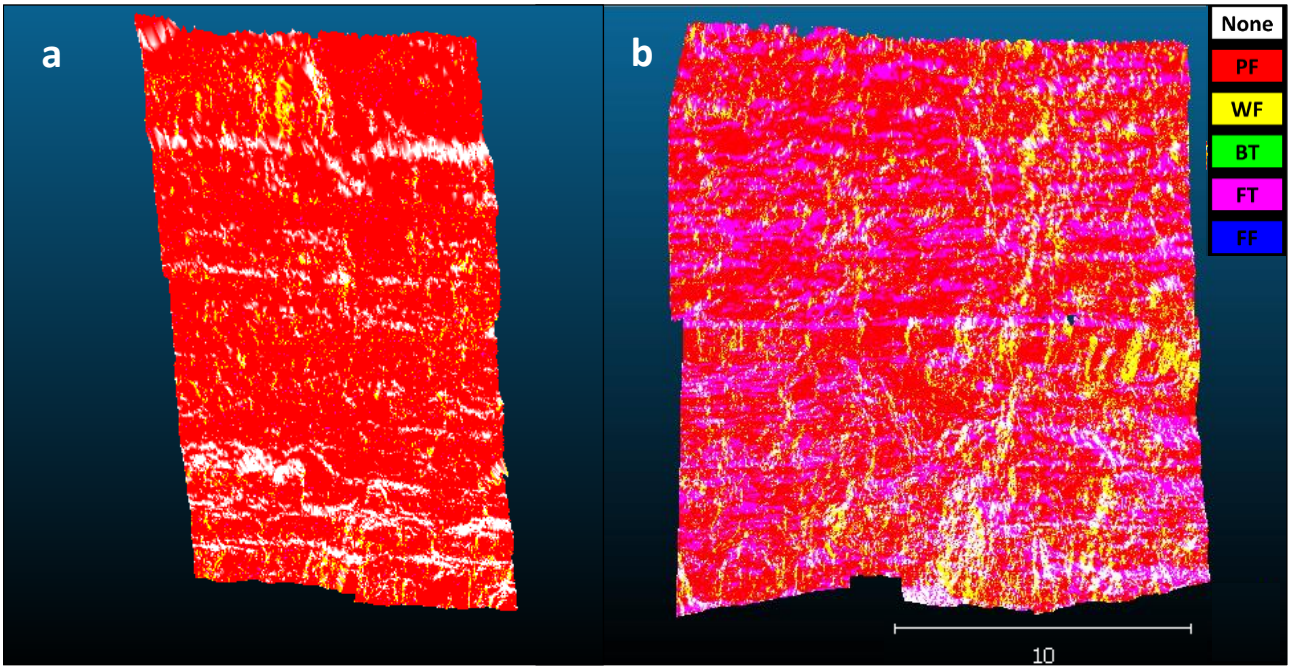

Figure 220 - Most probable failure mechanisms according to DiAna-K on highwall 1 (letter a) and on highwall 2 (letter b) of case study1 mine. PF: Plane Failure; WF: Wedge Failure; BT: Block Toppling; FT: Flexural Toppling; FF: Free Fall

3D kinematic analysis carried out by DiAna-K for case study 2 shows analogies with case study 1. In this case too, in fact, plane failure is the most probable mechanism in many areas, most commonly for areas with α similar to α_{slope}; areas, instead, with α normal to α_{slope} are most prone to wedge failure. The low percentage of discontinuities with anti-dip slope orientation makes flexural toppling a not very suitable mechanism (Figure 179, 184, 189, and 194). Both on case study 1, and on case study 2, indeed, block toppling is very improbable mechanism; free fall is relegated to subvertical or overhanging parts, where is not the most probable mechanism anyway.

In Figure 221 and 222, the positions of the most susceptible areas and their relative detailed views for highwall 1 of case study 1 are reported. Plane failure represents the most probable failure mechanism for these areas (Figure 222); indeed, among 5 reported areas, 4 are related to overhanging blocks (letter a, b, d, and e in Figure 222). In Figure 223 and 224 the positions of the most evident and sharp detachment niches on highwall 1 and their enlargements are reported. Three kinds of detachment niches can be roughly described: roof detachment (letter b in Figure 224) from a thick and resistant uppermost arenitic layer, wedge detachment (letters a, c, and e in Figure 224) and plane detachment (letter b). For these detachment areas, plane failure is the main failure mechanism too; anyway, detachment planes prone to wedge failure (yellow colour of image a, c, and e in Figure 224) are present. The positions of the most critical areas on highwall 2 are reported in Figure 225 and 226; most of them are related to plane failure; locally, (letters b and d) wedge failure is the most important failure mechanism. Wedge failure is probable especially in case the shape of the surface would indicate the possible detachment of the wedges (as images b and d in Figure 226 clearly show).

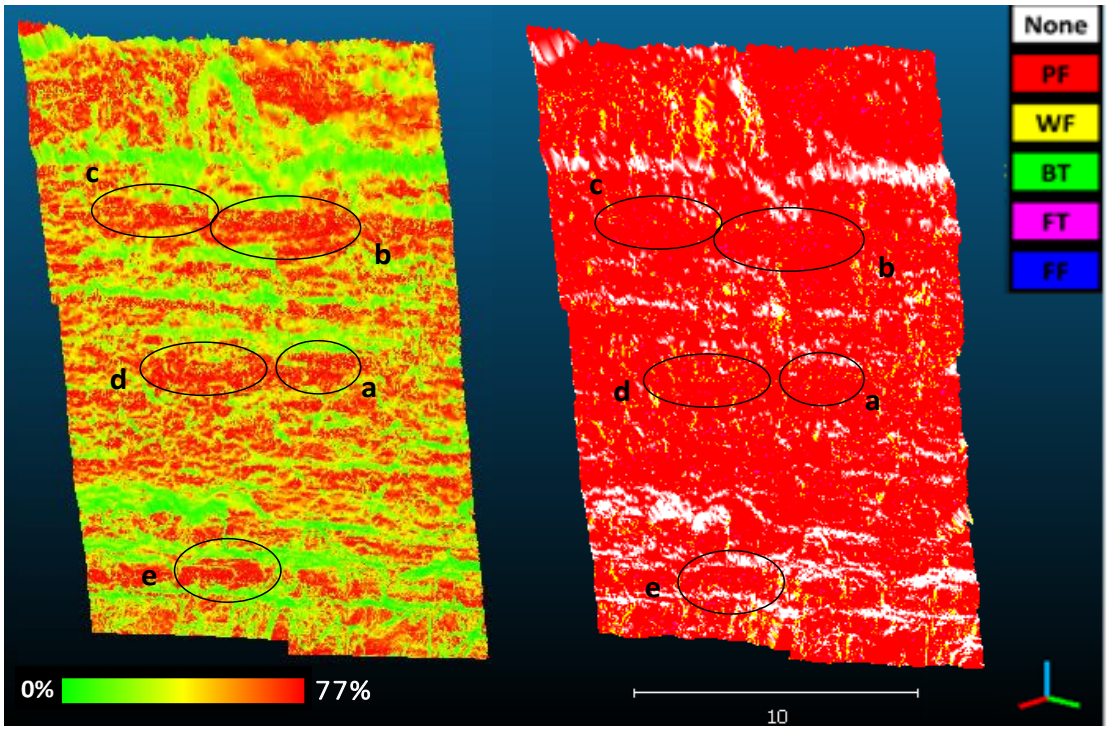

Figure 221 - Location of most critical areas evaluated with DiAna-K on the highwall 1 of case study 1. Left: the colour indicates on a scale from green to red, the local value of the maximum value among all the kinematic indices; Right: most probable failure mechanism: PF: Plane Failure; WF: Wedge Failure; BT: Block Toppling; FT: Flexural Toppling; FF: Free Fall

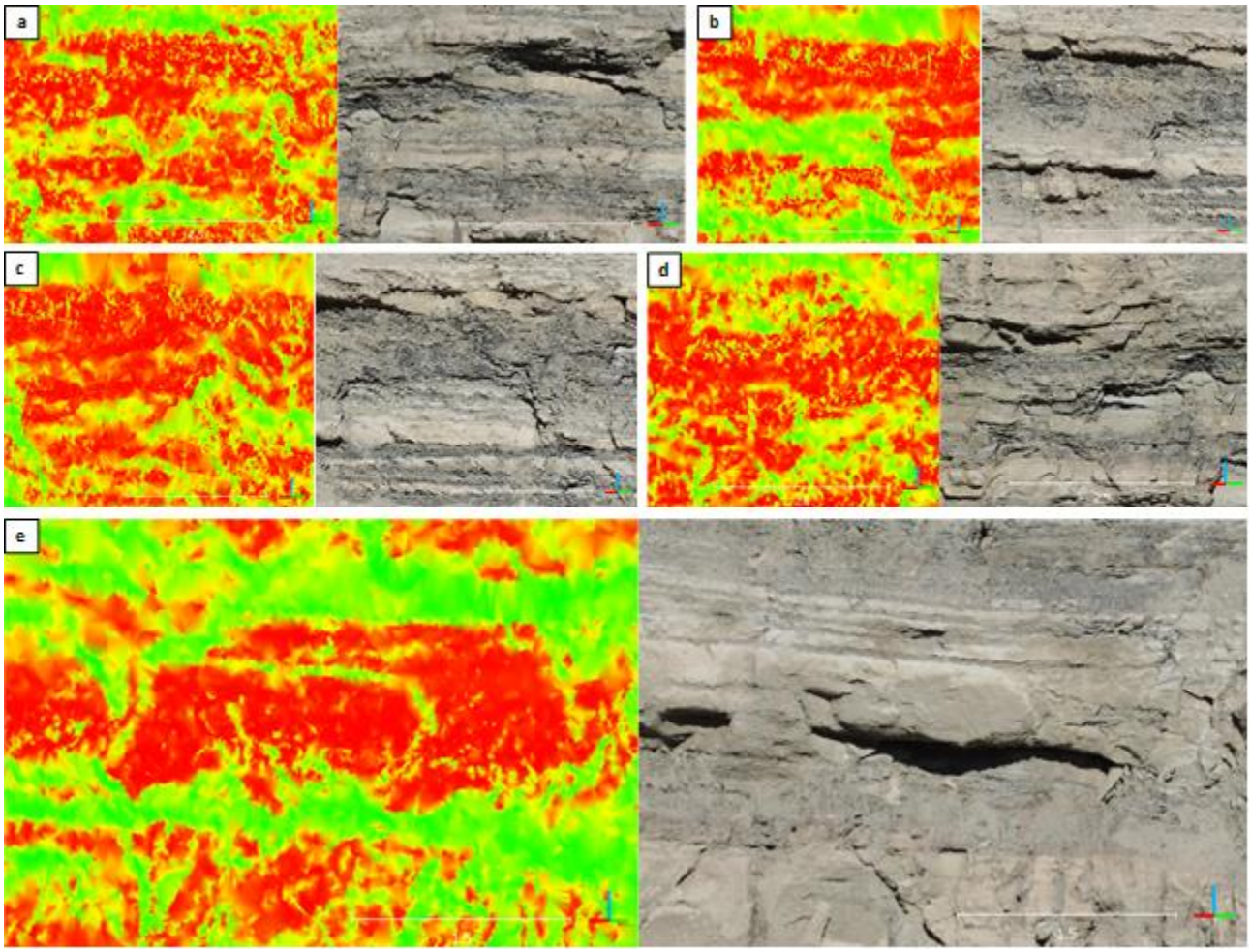

Figure 222 - Enlargements of critical areas for DiAna-K on highwall 1 of case study 1 of Figure 221

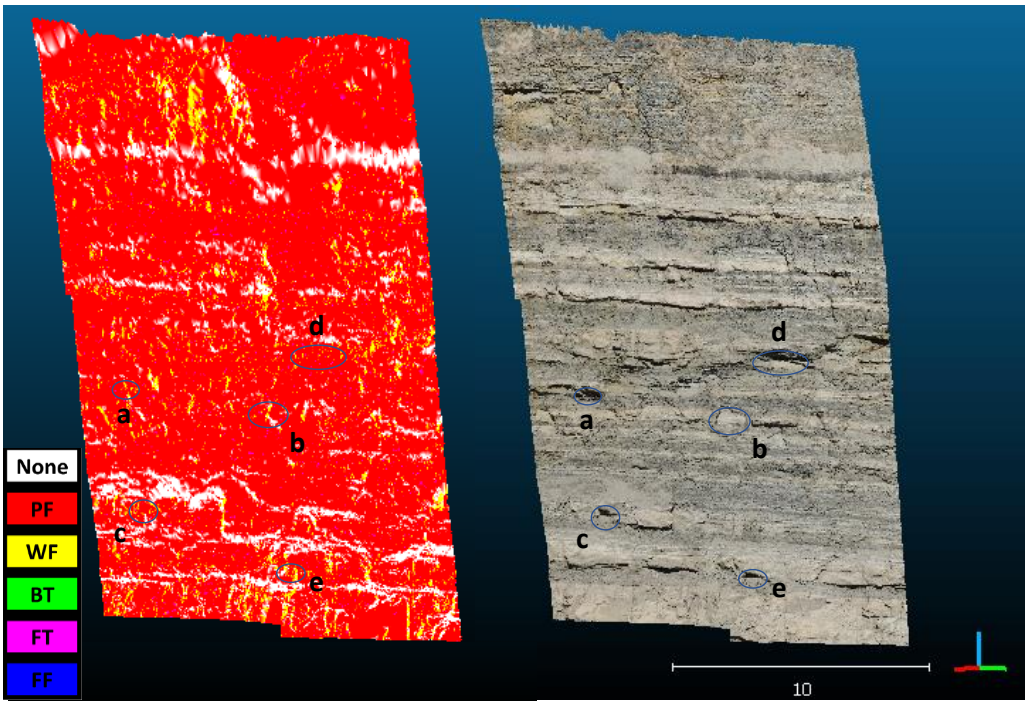

Figure 223 – Position of the detachment niches on highwall 1 of case study 1. Left: most probable failure mechanism: PF: Plane Failure; WF: Wedge Failure; BT: Block Toppling; FT: Flexural Toppling; FF: Free Fall. Right: optical image

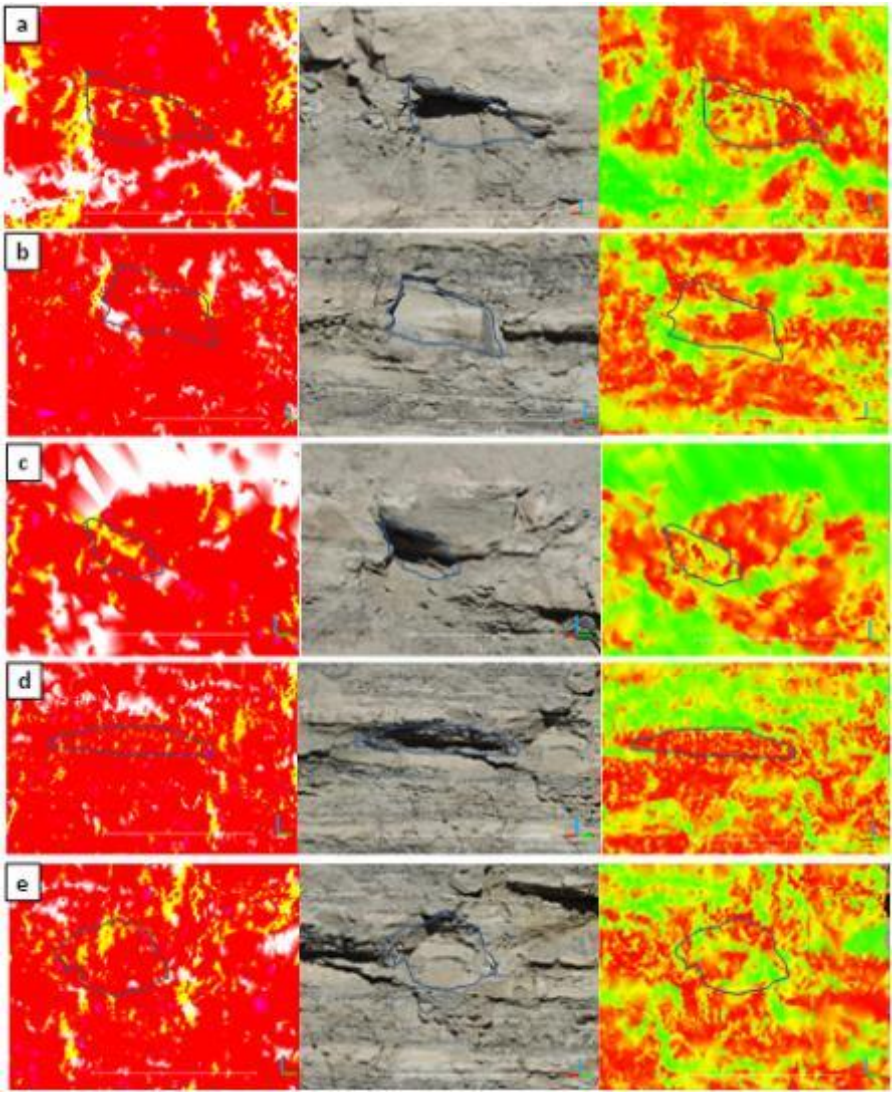

Figure 224 – Enlargements of detachment niches on highwall 1 of case study 1 of Figure 225

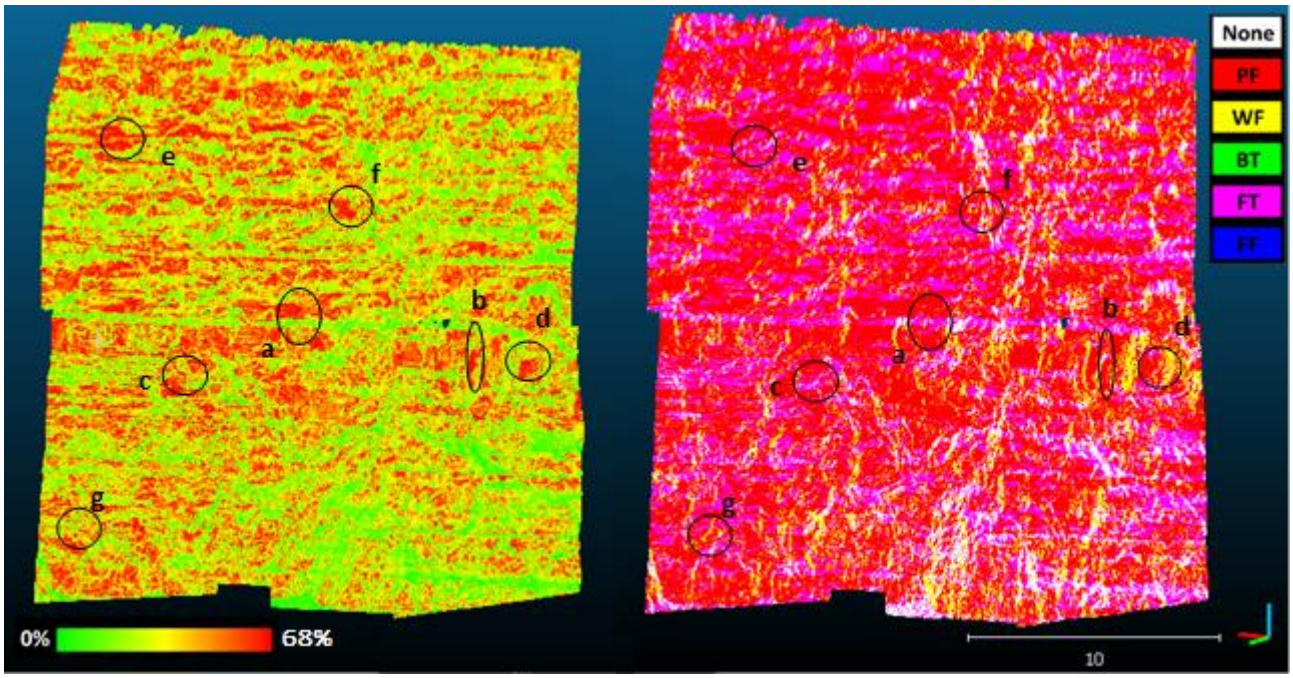

Figure 225 - Location of most critical areas evaluated with DiAna-K on the highwall 2 of case study 1. Left: the colour indicates on a scale from green to red, the local value of the maximum value among all the kinematic indices; Right: most probable failure mechanism: PF: Plane Failure; WF: Wedge Failure; BT: Block Toppling; FT: Flexural Toppling; FF: Free Fall

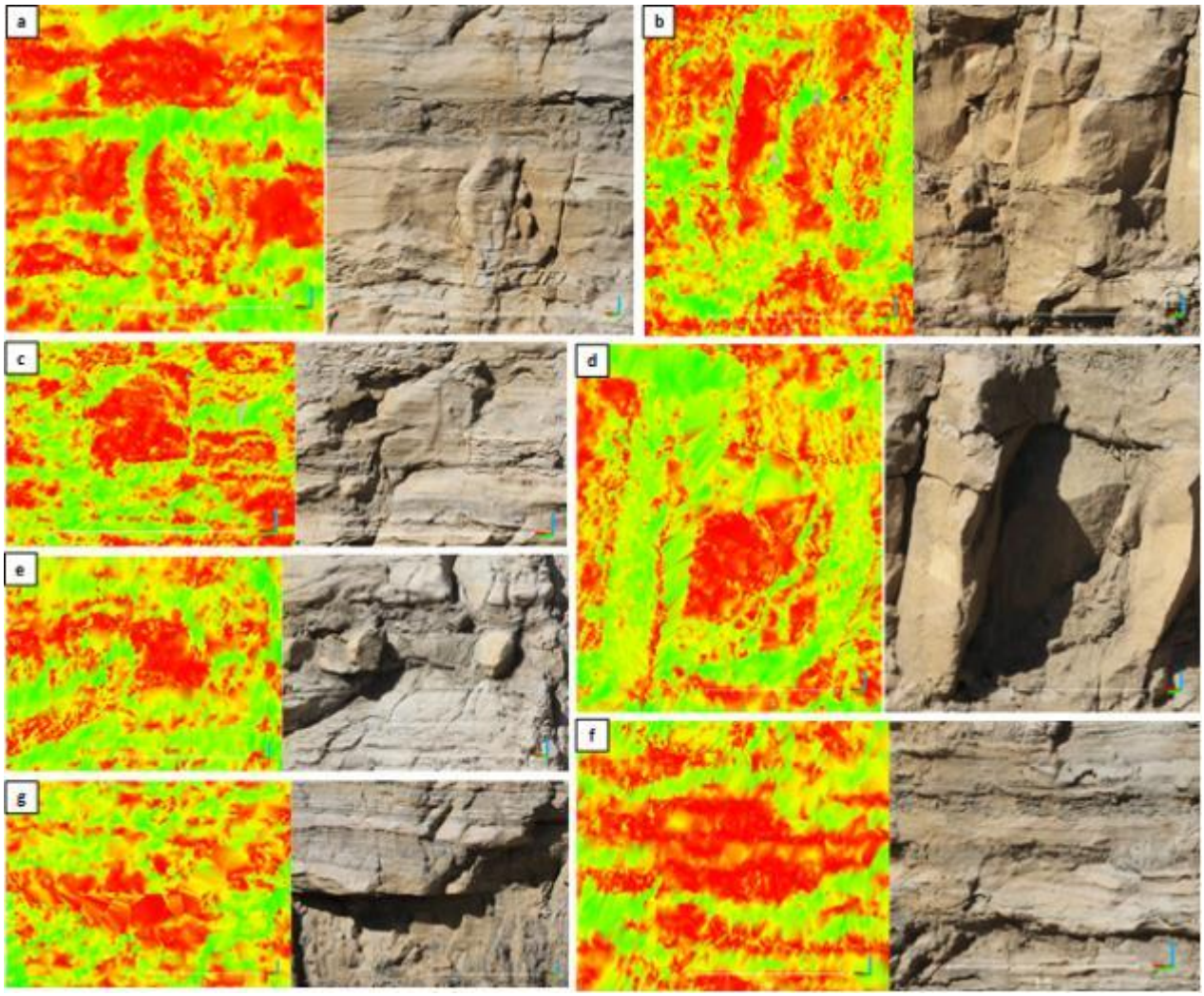

Figure 226 - Enlargements of critical areas for DiAna-K on highwall 1 of case study 1 of Figure 225

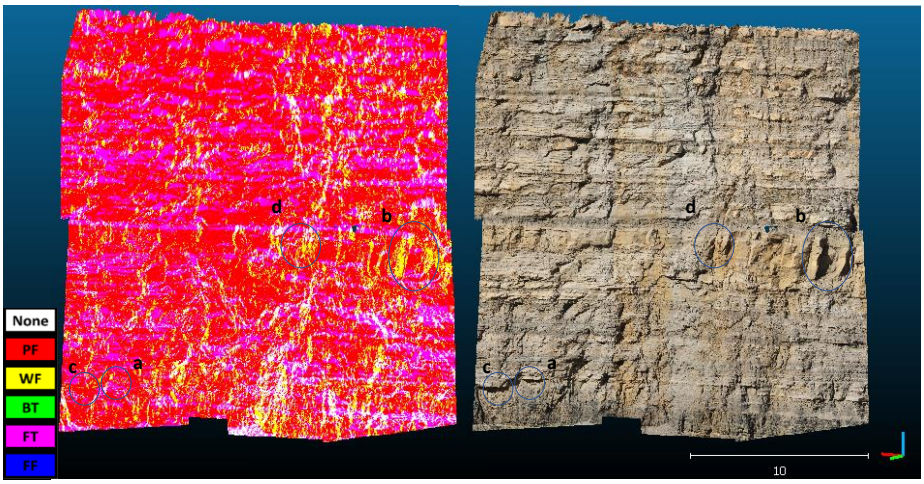

Figure 227 - Position of the detachment niches on highwall 2 of case study 1. Left: most probable failure mechanism: PF: Plane Failure; WF: Wedge Failure; BT: Block Toppling; FT: Flexural Toppling; FF: Free Fall. Right: optical image

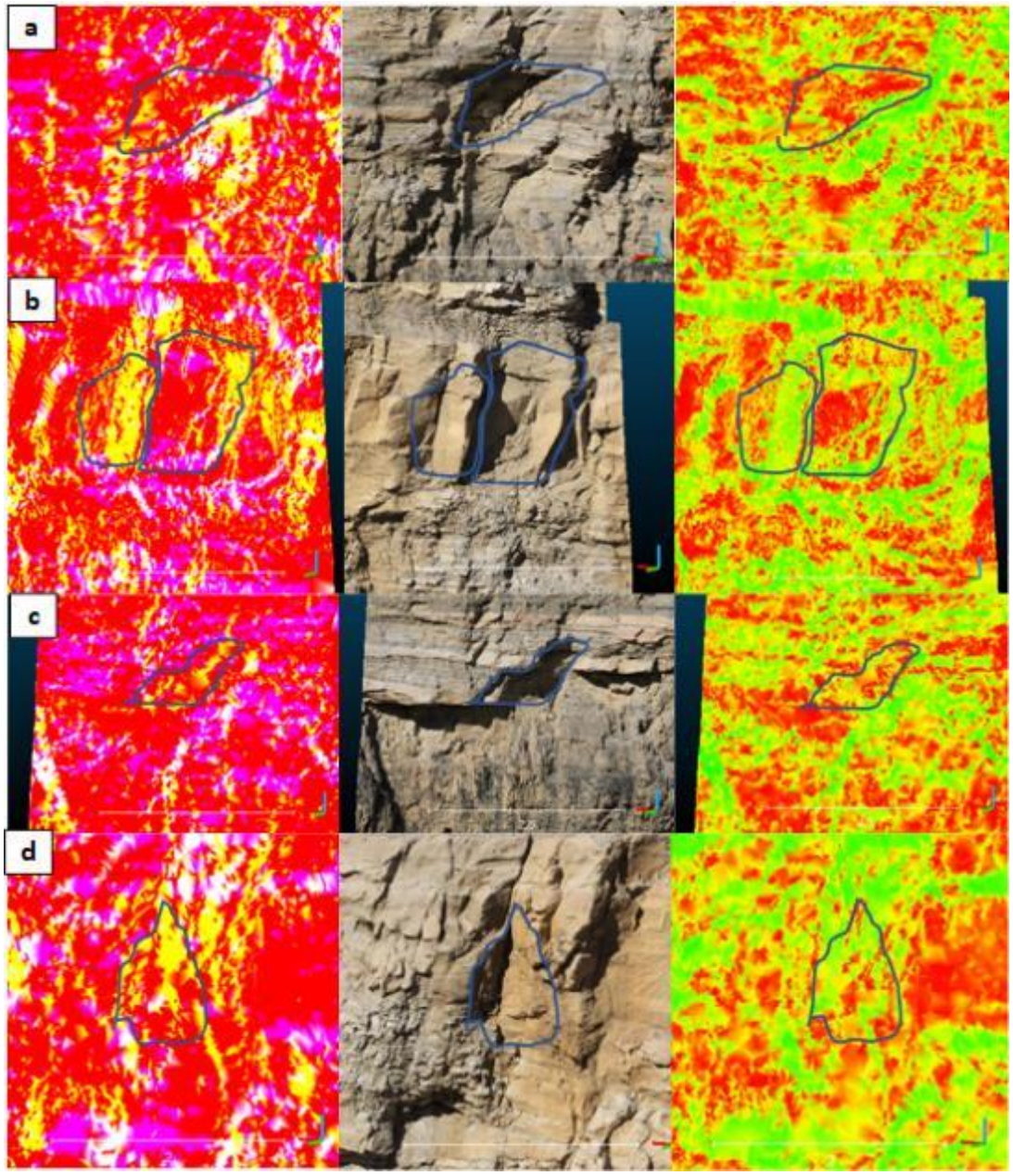

Figure 228 - Enlargements of detachment niches on highwall 1 of case study 1 of Figure 227

Figure 229 and 230 show the location of most critical areas on the slope of case study 2. Plane failure is the main failure mechanism in the most critical areas, although zone more susceptible to wedge failure are present along steep discontinuities, along which the α of the slope varies from the average α_{slope}. The positions of the most relevant detachment niches have been described in Figure 231 and 232 and show that the surfaces of the slope involved for the detachment of the blocks are prone both to plane failure and to wedge failure; indeed, wedge failure is sometimes relevant (letter c in Figure 232).

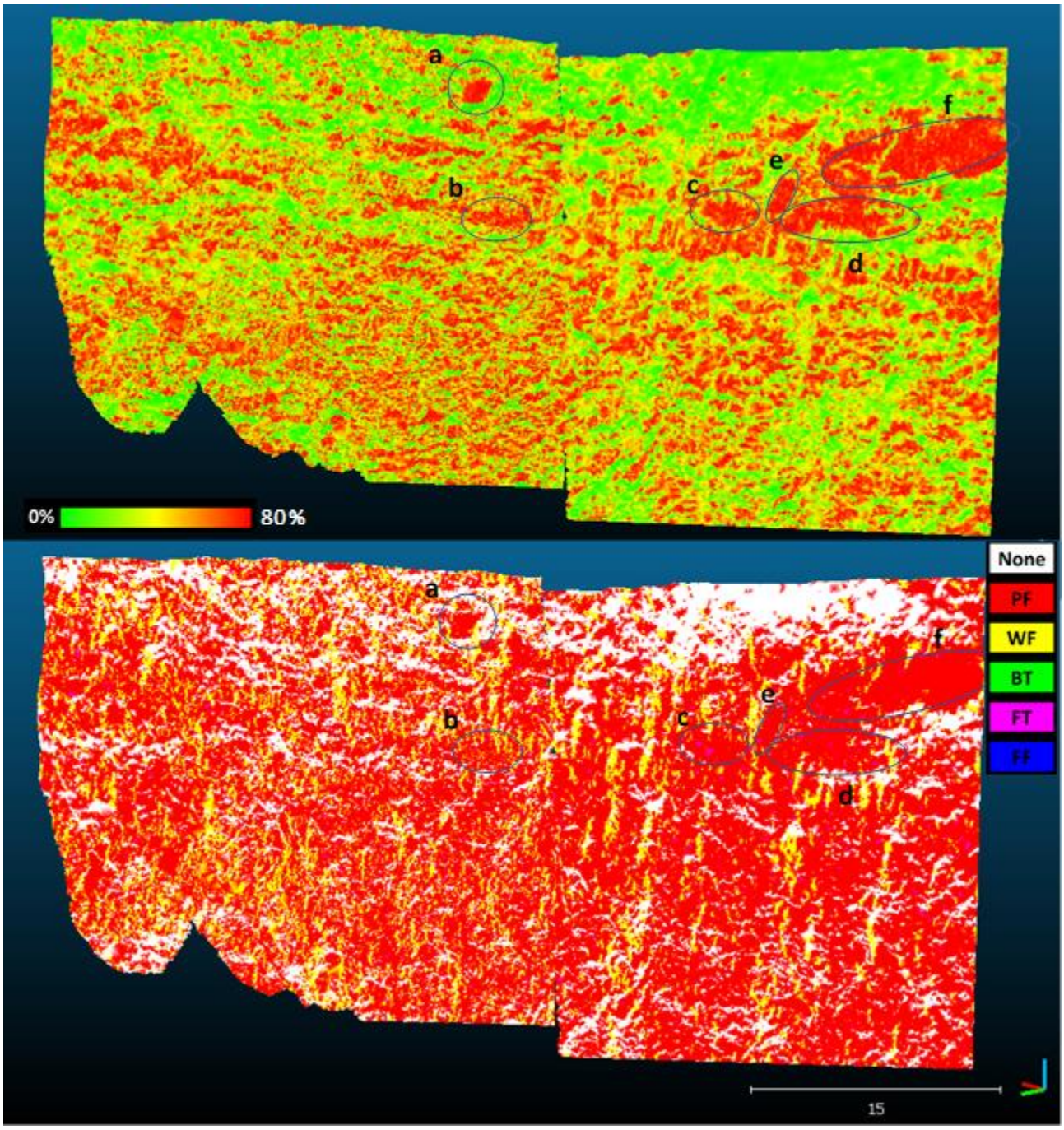

Figure 229 - Location of most critical areas evaluated with DiAna-K on the highwall of case study 2. Above: the colour indicates on a scale from green to red, the local value of the maximum value among all the kinematic indices; below: most probable failure mechanism: PF: Plane Failure; WF: Wedge Failure; BT: Block Toppling; FT: Flexural Toppling; FF: Free Fall

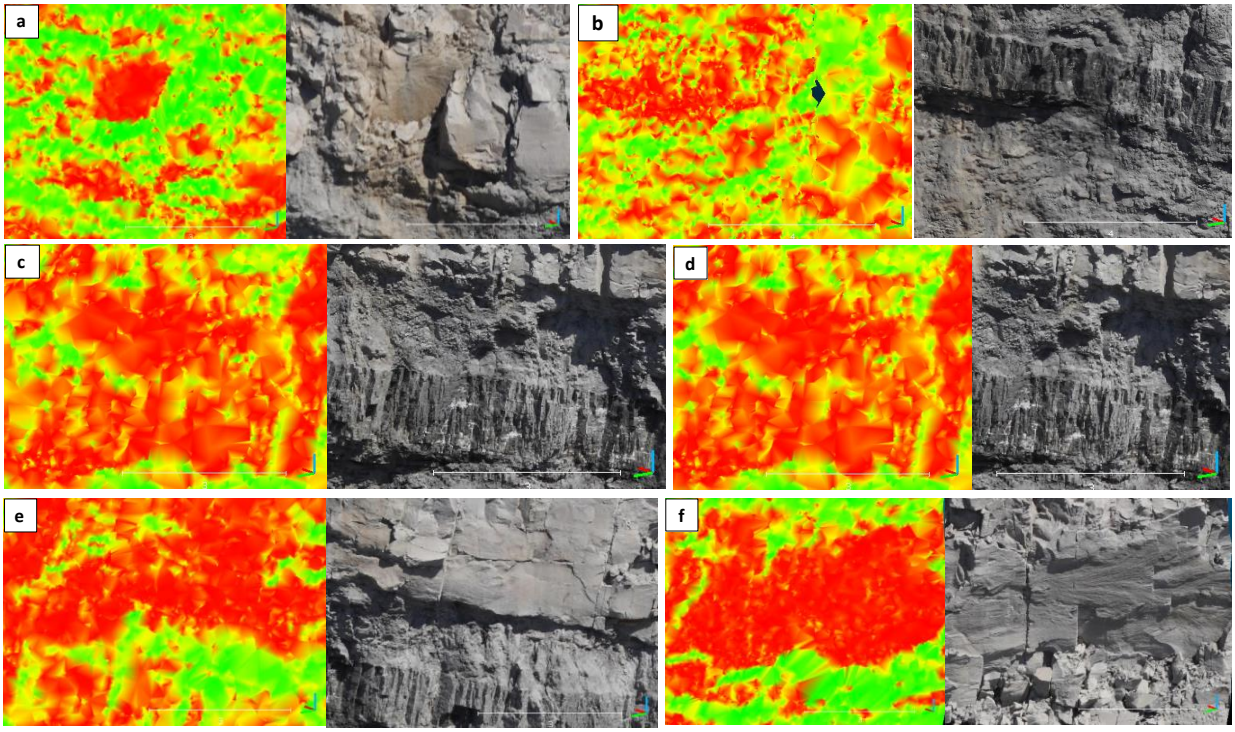

Figure 230 - Enlargements of critical areas for DiAna-K on case study 2 highwall of Figure 229

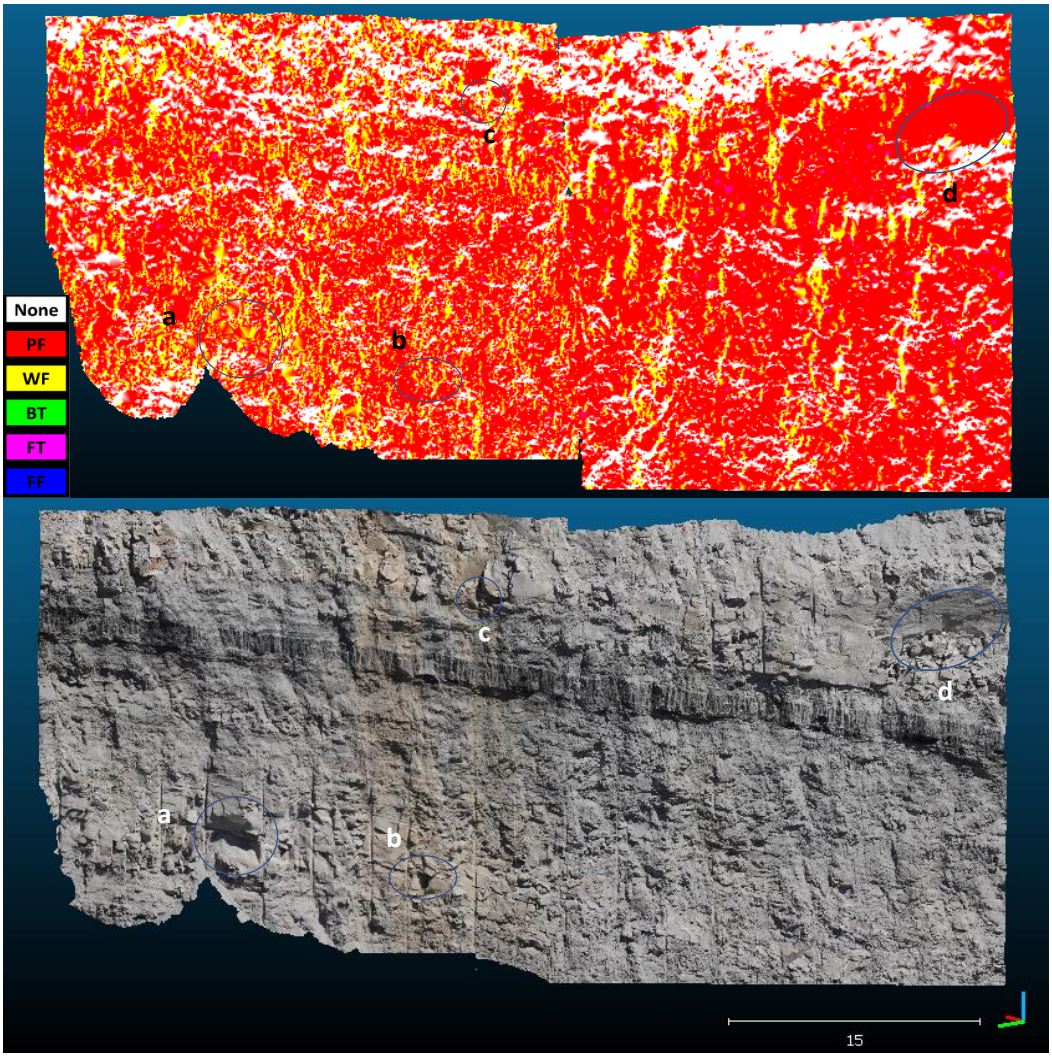

Figure 231 - Position of the detachment niches on highwall 2 of case study 1. Above: most probable failure mechanism: PF: Plane Failure; WF: Wedge Failure; BT: Block Toppling; FT: Flexural Toppling; FF: Free Fall. Below: optical image

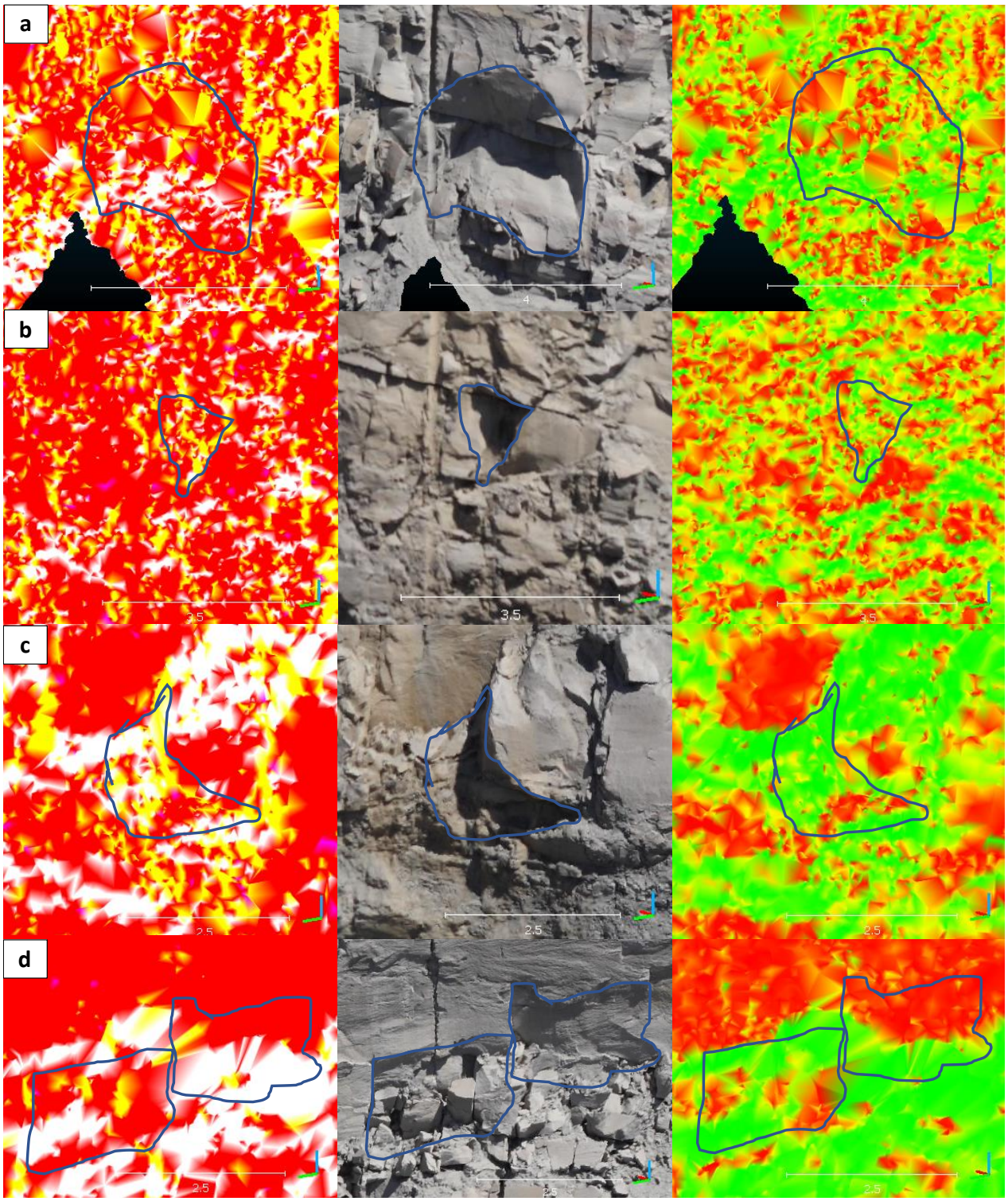

Figure 232 - Enlargements of detachment niches on highwall 1 of case study 1 of Figure 231

8.3. Stability analysis results

The discontinuities extracted with SiroJoint have been used as input data for the stability analysis carried out by SiroModel. The simplified model of each highwall has been built considering the average α, the average β and the height of the bench. 20 simulations plus further 10 simulations have been carried out on each highwall. A 21 m height bench has been associated with the two highwall of case study 1, with [α_{slope}; β_{slope}] = [50°; 70°] and [320°; 70°] for the highwall 1 and 2 respectively. The bench of the case study 2 mine has been sketched with a 26 m height bench, with orientation [α_{slope}; β_{slope}] = [134°; 76°]. Each simulation has been carried out on an 8.5 m wide section to make the time consume reasonable.

Removable blocks have been split by stability conditions following the Block Theory of Goodman & Shi (Type I: unstable blocks; Type II: blocks stable thanks to ϕ; Type III: stable blocks) and by number of contact planes. The comparison of the number of blocks, subdivided as stated above performing 20 and 30 simulations, shows that the number of extracted blocks is coherent and that the number of blocks on 30 simulations is 50% higher than the number of blocks extracted on 20 simulations (Figure 156, 163, and 202); the average number of blocks for single simulation, both in case of overall 20 simulations, and in case of overall 30 simulations, is comparable (Figure 157, 11, 164, 13, 203, and 20). The blocks volume distribution, the maximum volume of Type I and Type II blocks is similar, both performing 20 simulations and performing 30 simulations (Figure 159, 160, 166, 167, 205, and 206); 30 simulations are so sufficient, both for highwall 1 and for highwall 2, and statistically significant to describe the rock mass, both by typology and by volume of removable blocks. The number of blocks split by stability condition and number of contact planes for the three highwalls are described in Table 38. Because blocks with small volumes also, that are not dangerous for the mining operations have been extracted, blocks with volume > 10^{-3} m^3, have been selected and described in Table 39.

Table 38 - Nr of blocks sorted by type of block (Type I: unstable blocks; Type II: blocks stable thanks to φ; Type III: stable blocks) for each case study, considering 30 simulations without minimum block volume selection

Case study	Nr total blocks	All blocks (average)		Type I blocks (average)		Type II blocks (average)		Type III blocks (average)		Max volume (m^3)	
		Nr contact planes		Nr contact planes		Nr contact planes		Nr contact planes		Type I	Type II
		1	2	1	2	1	2	1	2		
Case study 1 highwall 1	10663	3853	6810	1125	410	34	1734	2694	4656	0.88	1.20
Case study 1 highwall 2	10482	3689	7693	1091	304	14	1339	2561	6050	0.72	1.08
Case study 2	20211	2431	17780	714	3152	78	6925	1639	7703	1.08	1.80

Stability analysis carried out with SiroModel shows that the number of removable blocks extracted on 30 simulations using a section 8.5 m width, are similar (10663 and 10482) on the two highwalls of case study 1 mine (Table 38), but the number of blocks with volume > 10^{-3} m^3 is higher on highwall 1 than on highwall 2 (4932 vs 3522) (Table 39). The percentage of blocks with volume > 10^{-3} m^3 is 46% (4932/10663) for highwall 1 and is 33% (3522/10482) for highwall 2.

The maximum volume of the blocks extracted by SiroModel, for highwall 1 and for highwall 2, is equal to 0.88 m^3 and 0.72 m^3 for Type I and to 1.20 m^3 and 1.08 m^3 for Type II. The maximum value of the volume of Type I

and of Type II for the two highwalls confirms that the volume of blocks removable on highwall 1 is greater than the volume of removable blocks on highwall 2.

Table 39 - Nr of blocks sorted by Type of block (Type I: unstable blocks; Type II: blocks stable thanks to φ; Type III: stable blocks) for each case study, considering 30 simulations, considering blocks with a minimum 10^{-3} m^3 volume only

Case study	Nr total blocks	All blocks (average)		Type I blocks (average)		Type II blocks (average)		Type III blocks (average)		Max volume (m^3)	
		Nr contact planes		Nr contact planes		Nr contact planes		Nr contact planes		Type I	Type II
		1	2	1	2	1	2	1	2		
Case study 1 highwall 1	4932	1352	3587	339	108	15	844	1006	2820	0.88	1.20
Case study 1 highwall 2	3522	906	2616	216	67	14	444	676	2105	0.72	1.08
Case study 2	6596	610	5986	132	756	23	2267	455	2963	1.08	1.80

Removable blocks on the highwall of case study 1 with a volume > 10^{-3} m^3 (Table 39) commonly have 2 planes of contacts. Anyway, if blocks were distinguished by type, Type I blocks would be mostly overlying one contact plane, while Type II and Type III blocks would be mostly overlying two contact planes. This observation is not in contrast to the kinematic analysis results because 1m set for highwall 1 and 3m set for the highwall 2, more susceptible to plane failure, have a higher L value than the other set, while kinematic analysis, by definition, assumes that the L of the discontinuities is infinite.

The maximum volume of the blocks extracted by SiroModel has been compared with the block volume evaluated with the block volume evaluated by Palmstrom's equation (Equation 3).

For case study 1, the true spacings for each set can be calculated through DiAna, by merging data from wall 1 and 2. In particular, a specific MATLAB tool was implemented for the geomechanical analysis where spacing is calculated by measuring the normal distance of each discontinuity to the other discontinuities belonging to the same set that overlap along a virtual scanline. In this way, minimum, mean and maximum spacing can be calculated. These values for case study 1 are reported in Table 40, together with the corresponding J_v and V_b considering the abovementioned relation proposed by Palmström (1995, 2001).

The calculated spacings are also in agreement with the values obtained for each set through a specific tool within SiroJoint software (Figure 233, 234, and 235).

The rock mass is thus characterized by few large spacings (> 1 m) and a lot of small spacings (centimetric to decimetric), which imply high probability of small to medium block dimensions (< 0.1 m^3) and lower probability (but possible) of detachment of blocks with volume > 1m^3.

Tha maximum block dimension obtained by considering all the highest spacings for each set (9.85 m^3, see Table 40) is, indeed, quite questionable and, thus overestimated. For these reasons, we believe that the values obtained through the stability analysis are reliable and can be used as reference for rockfall hazard analyses.

Table 40 - Minimum, mean and maximum spacing for each set extracted with the DiAna geomechanical tool and corresponding J_v and block volumes values calculated using the relation proposed by Palmström (1995).

set	Min spacing (m)	Mean spacing (m)	Max spacing (m)
1	0.09	0.29	2.10

3	0.10	0.38	1.90
2	0.08	0.23	1.86
j_v	33.61	10.44	1.54
V_b (m^3)	0.001	0.03	9.85

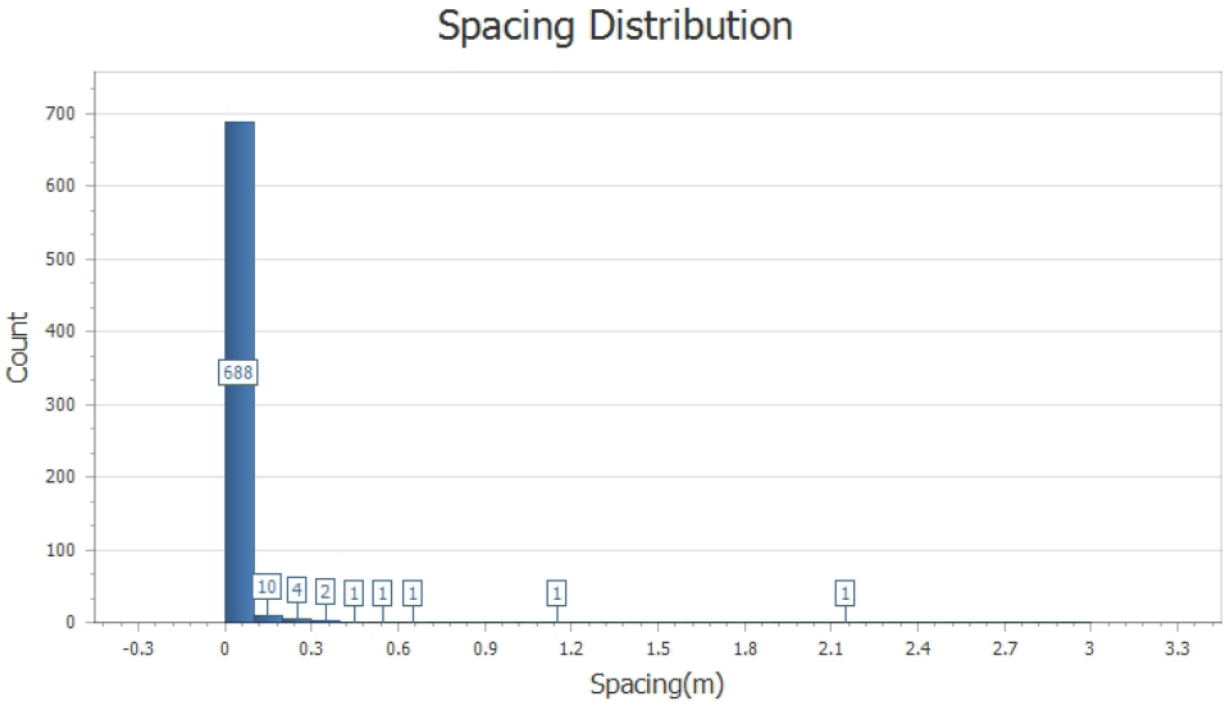

Figure 233 - Case study 1. Set 1 spacing distribution extracted with SiroJoint.

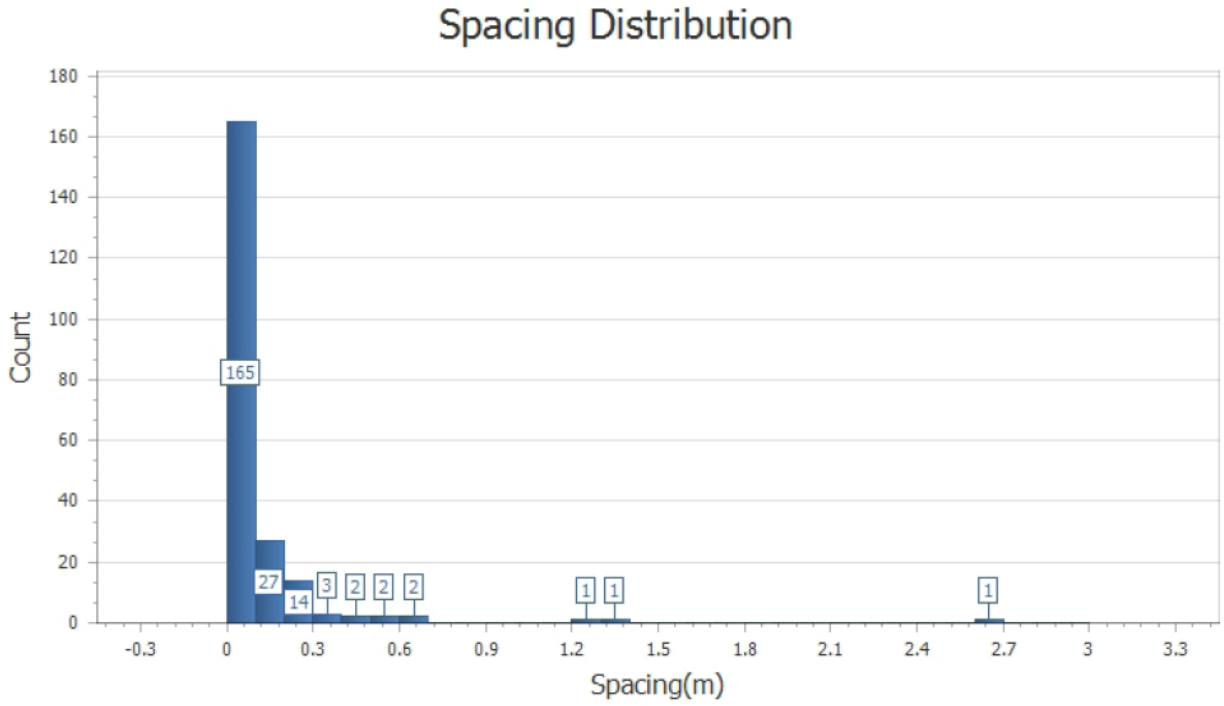

Figure 234 - Case study 1. Set 2 spacing distribution extracted with SiroJoint.

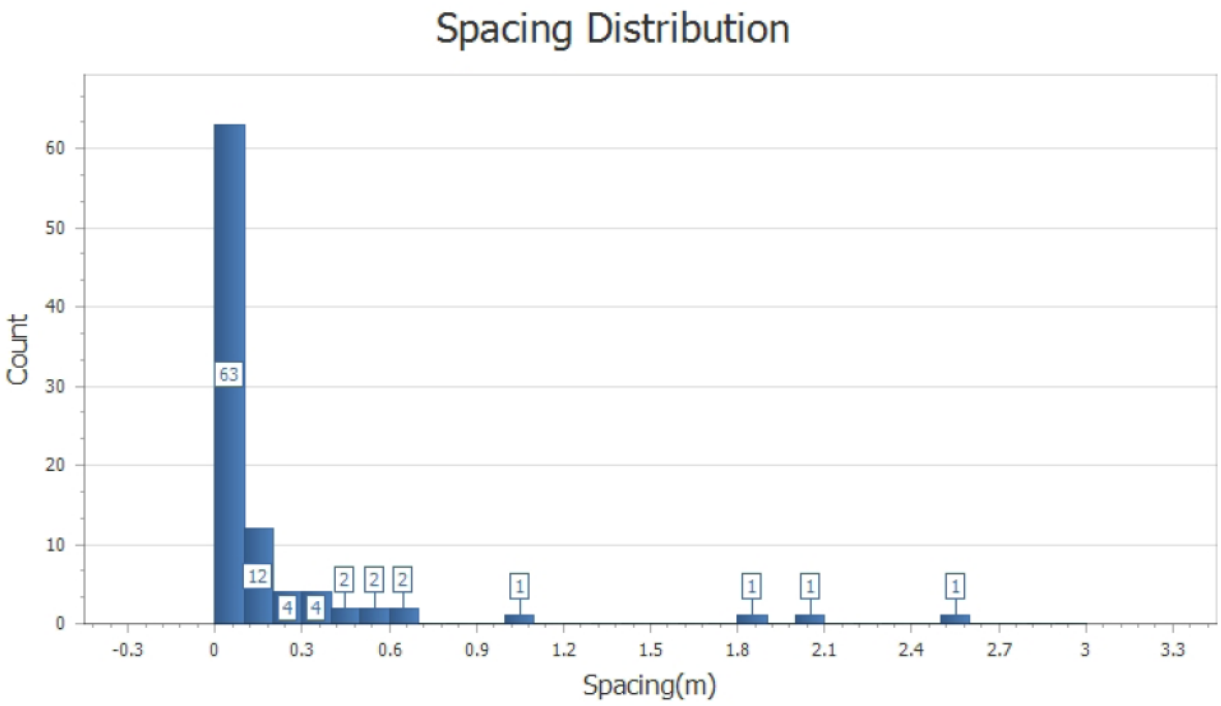

Figure 235 - Case study 1. Set 3 spacing distribution extracted with SiroJoint.

Casagrande (2012) listed the dimensions of 263 of blocks that were observed at the base of the highwall 1 on a section four times longer. Because of stringent safety regulations, the access to the "no go zone" at the base of the bench is limited to the strictly necessary operations. For this reason, only largest blocks were directly measured (Table 41). Smallest blocks were, instead measured by the 3D image obtained since the photographs of the bench (Table 42). Only blocks with dimension > 0.05 m were listed. Because the sampling of the volume of 12 blocks only was passible, a qualitative comparison between the graphs of the volume of the blocks (Figure 160) has been carried out. Maximum volume of the blocks on the scree is 1.5 m^3; other two blocks with a volume of 1 m^3 and 6.5×10^{-1} m^3 had been observed. The maximum volume of the blocks fallen is so comparable to the maximum volume of Type I blocks (8.8×10^{-1} m^3) and to the maximum volume of Type II blocks extracted with SiroModel (1.20 m^3). As regarding the volumes of the Type I and Type II blocks and the volumes of the fallen blocks at the base of highwall 1, the comparison of optical images and susceptible maps carried out by DiAna-K has shown that the dimension of unstable blocks related to areas susceptible to failure, are metric; so, as regarding the highwall 1 of case study 1, both SiroModel and the comparison of DiAna-K susceptibility maps with the optical image, indicate that the dimension of unstable blocks is metric at most (Figure 221 and 222); these hypothesis have been confirmed from the dimensions of the blocks at the base of the slope.

Table 41 - x, y, z dimensions, lithologies and volume of the largest block sampled at the base of the highwall 1 for case study 1 mine. Data collected from Casagrande (2012)

Nr block	*x dimension (m)*	*y dimension (m)*	*z dimension (m)*	*Lithology*	*Volume (m^3)*
1	0.75	0.5	0.3	Arenite	1.125×10^{-1}
2	0.34	0.16	0.07	Arenite	3.8×10^{-3}
3	0.34	0.31	0.2	Arenite	2.108×10^{-2}
4	0.17	0.15	0.15	Arenite	3.825×10^{-3}
5	0.22	0.17	0.12	Arenite	4.488×10^{-3}
6	0.18	0.17	0.15	Arenite within shale beds	4.59×10^{-3}
7	0.3	0.15	0.12	Arenite	5.4×10^{-3}
8	0.45	0.19	0.15	Arenite	1.282×10^{-2}
9	0.28	0.12	0.1	Shale	3.36×10^{-3}
10	1.5	1	1	Arenite	1.5
11	1	1	1	Arenite	1
12	1.3	0.65	0.65	Arenite within shale beds	6.5×10^{-1}

Table 42 - Height and width of small blocks at the base of highwall 1 of case study 1 mine. Data collected from Casagrande (2012)

Nr block	*x dimension (cm)*	*y dimension (cm)*	*Nr block*	*x dimension (cm)*	*y dimension (cm)*	*Nr block*	*x dimension (cm)*	*y dimension (cm)*
1	10	19	92	24	20	184	5	6
2	21	17	93	8	4	185	17	7
3	23	19	94	36	31	186	9	5
4	17	11	95	11	8	187	16	5
5	15	11	96	9	8	188	8	3
6	9	9	97	17	7	189	13	9
7	15	10	98	19	14	190	5	4
8	19	11	99	10	8	191	9	6
9	17	10	100	15	7	192	11	4
10	14	7	101	10	9	193	24	18
11	26	14	102	9	5	194	3	2
12	24	17	103	11	6	195	10	5
13	13	16	104	9	4	196	19	23
14	18	18	105	10	7	197	4	4
15	26	9	106	20	18	198	7	5
16	8	9	107	4	3	199	9	8
17	7	5	108	10	2	200	33	19
18	20	9	109	11	7	201	29	15
19	13	8	110	16	7	202	5	4
20	13	3	111	3	2	203	22	17
21	11	8	112	9	1	204	26	18
21	11	3	113	5	4	205	17	10
22	8	7	114	23	24	206	2	2
23	4	3	115	2	2	207	16	3
24	16	8	116	7	4	208	11	6
25	3	3	117	10	5	209	17	13
26	19	10	118	10	7	210	4	4
27	6	2	119	7	2	211	9	5
28	83	59	120	4	3	212	5	6
29	11	9	121	7	4	213	11	14
30	21	19	122	18	19	214	20	14
31	8	7	123	5	8	215	4	6
32	16	21	124	19	4	216	22	12
33	10	7	125	5	2	217	22	12
34	13	6	126	15	14	218	53	26
35	39	22	127	2	7	219	20	19
36	17	16	128	28	13	220	22	20
37	8	5	129	4	2	221	35	17
38	13	8	130	9	5	222	15	13
39	10	8	131	11	9	223	58	37
40	11	11	132	23	8	224	32	20
41	12	9	133	7	3	225	61	39
42	6	5	134	19	13	226	31	12
43	10	2	135	18	16	227	32	31
44	11	4	136	19	7	228	28	17
45	8	8	137	2	2	229	44	23
46	26	11	138	47	37	230	9	60
47	11	7	139	11	10	231	25	19
48	13	4	140	12	4	232	27	7
49	9	11	141	1	3	233	10	4
50	14	2	142	10	4	234	12	9
51	4	2	143	11	6	235	7	29
52	20	8	144	11	7	236	26	17
53	20	11	145	2	3	237	23	9
54	9	3	146	14	14	238	17	18
55	11	2	147	14	8	239	13	11
56	11	2	148	19	12	240	33	15
57	3	2	149	9	8	241	6	5
58	15	3	150	24	13	242	27	9
59	6	1	151	14	6	243	8	2
60	8	5	152	17	20	244	12	9
61	2	1	153	7	2	245	13	5
62	11	2	154	15	14	246	9	7
63	8	4	155	26	30	247	12	9
64	19	11	156	9	3	248	7	8
65	18	14	157	2	5	249	5	3
66	11	6	158	36	14	250	22	7

67	11	2	159	23	9	251	11	9
68	11	8	160	9	6	252	20	9
69	20	11	161	2	1	253	8	3
70	6	2	162	15	3	254	8	10
71	41	17	163	17	9	255	9	5
72	13	5	164	14	11	256	4	10
73	6	11	165	1	3	257	41	19
74	14	13	166	31	20	258	14	14
75	17	12	167	22	17	259	8	8
76	20	14	168	14	12	260	14	7
77	12	8	169	29	12	261	11	8
78	8	12	170	8	5	262	11	5
79	13	12	171	18	14	263	39	26
80	5	4	172	18	11	264	6	5
81	14	14	173	17	10	265	16	10
82	12	2	174	7	4	266	10	5
83	10	19	175	21	16	267	5	3
84	22	17	176	19	17	268	8	6
85	14	5	177	7	6	269	5	6
86	7	9	178	10	7	270	17	7
87	11	8	179	12	15	271	9	5
88	22	12	180	4	2			
89	22	11	181	8	3			
90	14	14	182	8	8			
91	5	3	183	27	16			

These values are in agreement with those estimated from the geostructural characteristics of the rock mass extracted from remotely acquired data (Table 40 and Figure 233, 234, and 235).

20211 removable blocks have been extracted on the highwall of case study 2, performing 30 simulations (Table 38); 6596 blocks have a volume bigger than 10^{-3} m^3 (Table 39). The number of discontinuities related to the 7 sets individuated (1174) (Table 24) is similar to the number of discontinuities related to the 4 sets identified for the case study 1. Although a greater height of the bench (26 m vs 21 m of case study 1) and so a lower concentration of discontinuities because of the greater height, the bench is more fractured because of the greater value of L of the sets, weighted on the number of discontinuities related to each set, that amounts to 12.07 m. The percentage of blocks with volume > 10^{-3} m^3 amounts to 32% (6596/20211), while the maximum volume to 1.08 m^3 and 1.80 m^3 for Type I and Type II respectively. These volumes are comparable with the metric dimension of the unstable blocks previously evaluated (Figure 225 and 226).

91% of removable blocks (5986/6596) lays on two contact planes. Unlike case study 1, most of the Type I blocks have two contact planes instead of one (756/888, equal to 85%). This divergence is significant for the detection of kinematic mechanisms and confirms the different framework of the discontinuities and of the different complexities of the two rock masses. While, in fact, for case study 1, overall 3 sets of discontinuities, besides the bedding, have been detected, the structural framework of the rock mass of case study 2 is more complex because 5 sets have been recognised. Also for this second case study, the maximum dimension of the Type I and Type II blocks performing 30 simulations (1.08 m^3 and 1.80 m^3 respectively) is comparable to the unstable blocks located in the most susceptible areas of the slope comparing the susceptibility map with the optical images (Figure 229 and 230).

This facilitates a more pervasive fracturing, with all the consequences for the number of removable blocks, sometimes of large dimension, for the water circulation that, weathering the rock, decreases the geomechanical parameters, and that increases the overpressure. Indeed, the probability of wedge failure with critical kinematic conditions is greater because the higher dispersion of the orientation of the discontinuities with a finite value of L makes intersections more frequent than in case of a framework of subparallel discontinuities. For this reason, wedge failure is more feasible on case study 2 slope than on case study 1 slope.

The comparison between the output of the stability analysis carried out with SiroModel on one side, and the 3D kinematic analysis carried out by DiAna, has shown a diversified situation between the two case studies. Stability analysis for case study 1 evidences that most of Type I and Type II blocks lay on an only contact plane (Table 38) and are so more prone to plane failure (Figure 220 and Table 39); 3D kinematic analysis shows, in

fact, that plane failure is the most probable failure mechanism in large part of the slope. Case study 2 shows a more complex geostructural framework and so the geostructural analysis of the rock mass has been more articulated.

The comparison between the stability analysis carried out by SiroModel and 3D kinematic analysis of DiAna-K provides a different pointing for the two case studies. Most of the Type I blocks, in fact, have two contact planes in this second case study and are more prone to wedge failure instead of plane failure; on the other hand, 3D kinematic analysis carried out by DiAna-K demonstrates, both for case study 1, and for case study 2, that surfaces with α similar to α_{slope} are more prone to plane failure and so plane failure is the most probable failure mechanism on most of the surfaces. The comparison of the outputs provided by the two codes provides so different indications for the two case studies. The rock mass of case study 1 is involved, as regarding the geostructural characterisation made with SiroJoint, by 2 sets of traces and 2 sets of planes for the highwall 1 and by 1 set of traces and 2 of planes for highwall 2; although the lithologies of the rock mass (pelite and shale rich of organic matter; arenite) do not have evident jointing, discontinuities extracted thanks to DiAna have allowed the characterisation of the kinematic mechanisms and 3D kinematic analysis performed by DiAna confirms the results of the stability analysis carried out by SiroModel. Case study 2 has, besides, highly weathered lithologies that make planes less evident, a complex discontinuities framework that implies a high level of fracturing. 3 sets of discontinuities on 5 detected by SiroJoint are constituted by traces (Figure 168), while 2 sets of planes have been detected by semiautomatic methods (Figure 170, 173, and 175). Manual methods have been found to be useful tools for the geostructural characterisation in case of weathered lithologies, in which the surface is not related to the inner structure of the rock mass. On the other hand, semiautomatic methods are less time-consuming and so their use is convenient especially in case of survey on large surfaces.

The integration of the results between the stability analysis carried out by SiroModel and the 3D kinematic analysis with DiAna-K has allowed on both cases to get fundamental parameters for the assessment of rockfall risk along the rock slope. In particular, running of a statistical significative number of simulations with SiroJoint has allowed to obtain the distribution of the block volume by Type I, Type II, and Type III (Figure 159, 160, 166, 167, 205, and 206), and by number of contact planes. Indeed, DiAna-K has allowed to obtain 6 susceptibility maps, one for the local most probable failure mechanism and 5 for each failure mechanism (plane failure, wedge failure, block toppling, flexural toppling, free fall) (Figure 128, 152, and 197); the distribution of the probability of failure suggests the most critical areas. The distribution of the volume of the blocks and, assuming a value of rock density, of the mass of the blocks too, with the position of the unstable areas thanks to DiAna-K are two fundamental parameters to perform the rockfall analysis and so to calculate the trajectories and the kinetic energy of the falling blocks, evaluating the run-out area and the parameters for the design of rockfall protection systems (draperies, trench, barriers, embankments, fences).

9. Conclusions

The present research has allowed to point out differences and similarities, pros and cons, strengths and weaknesses of the results of manual (SiroJoint http://www.SiroVision.com/) and semiautomatic methods (I-Site Studio, https://www.maptek.com/products/i-site/i-site_studio.html; DiAna, Gigli & Casagli, 2011; Facets, Dewez et al., 2016) for the extraction of the discontinuities, to assess and confront the 2D kinematic analysis (Goodman & Bray, 1976; Hoek & Bray, 1981; Matheson, 1983; Hudson & Harrison, 1997). Moreover, an integration of the block analysis (Goodman & Shi, 1985) with the 3D kinematic analysis has been proposed to provide fundamental input data for rockfall simulations. The rock masses of two case studies have been analysed, similar in lithology but different in jointing (Chapter 5.2), in order to evaluate the impact of the manual or semiautomatic methods for the discontinuities extraction with different level of fragmentation and with a different pattern of the discontinuities. The comparison of the results of the geostructural analysis carried out with different methods has pointed out operative guidelines and recommendations for the choice of the discontinuities extraction method, the use of the software, and the critical analysis of the results.

Nowadays, the creation of high resolution 3D models of a rock mass lets the extraction of the discontinuities given the quantitative and geometric parameters definition. The parameters of the codes used in this research for the semiautomatic discontinuities extraction (described in Chapter 3.4) vary code by code and include the minimum number of points, the minimum surface of the discontinuity, the σ from the surface, the range of the orientation for each set of discontinuities (α, σ_α, β, σ_β). These codes have import advantages compared to remote manual extraction, such as reducing the user-related bias and expertise and being less time-consuming than traditional geostructural survey, especially facing with large open pit mines or large natural slopes too.

The geostructural surveys carried out in this research have pointed out similarities and differences about the results of manual and semiautomatic discontinuities extraction methods. The geostructural surveys performed by manual or by semiautomatic methods are affected by the different feasibility of the traces detection. Indeed, case study 1 consists in two perpendicular highwalls; the comparison of the geostructural surveys performed on them has shown that the discontinuities that outcrop as planes on a highwall, are represented mainly by traces on the other one. The different methods for the extraction of the discontinuities have provided a coherent general overview for each failure mechanism (plane failure, wedge failure, block toppling, and flexural toppling); nevertheless, sensible differences of the values of the kinematic indices have been reported.

The sets of planes have generally been recognised with each code, both for case study 1 and for case study 2, (Table 22, 23, and 24). In particular, the sets of planes dipping parallel to the slope have been recognised with all methods. Meanwhile the sets constituted by planes dipping perpendicular to the slope have been extracted with manual methods only; they have not been clearly recognised with semiautomatic and only a cluster of poles related to these sets has sometimes been noted. Outcropping lithologies are very alterable (because rich in organic matter) and so overhanging surfaces are unstable. For this reason, no evident planes with anti-dip slope orientation are present and planes related to anti-dip slope set have so a L value lower than planes related to dip slope oriented sets. The research has so shown that the sets constituted by planes have been recognised both with manual and with semiautomatic methods in case of well-exposed and dip-slope oriented planes; in case, instead, of discontinuities the dip direction of which is perpendicular to the slope, semiautomatic methods are less reliable, especially in presence of shale levels, the weathering of which makes the overhanging surface less clearly evident. For this reason, the lithology and the visible L of the planes should influence the choice of a manual or semiautomatic methods; in case, in fact, of weathered lithologies, as for example shale, other sedimentary rocks rich in organic matter, or highly weathered rocks in which the planes of the discontinuities are not sharp anymore, a manual method, if used by an experience operator, could give

more reliable results; in case, instead, of hard rocks with sharp surfaces, the reliability of the detection of planes is similar and so manual and semiautomatic methods have a similar detection reliability.

Thus, the detectability of traces with manual methods make them important predictive features for the geostructural characterisation in case of weathered lithologies, in which the surface is not related to the inner structure of the rock mass, or in case of a survey on a single manmade cut. On the other hand, semiauthomatical methods are less time-consuming and so their use is convenient especially in case of large-scale survey.

The different detectability of traces and planes to semiautomatic methods suggests that the variability of the aspect of the slope influences the reliability; for this reason, the use of semiautomatic methods is recommended especially in case of natural slope or artificial slope with different slope orientation; for example, it is recommended, in case of artificial slope, the carrying out of the survey on two perpendicular slopes to avoid the bias of the detectability of sets of discontinuity outcropping as traces only on a slope.

The recommendation to carry out the geostructural survey of semiautomatic methods on slopes with different orientation, instead on one slope only is, anyway, a good point also for geostructural survey carried out by manual methods. Sets of discontinuities with orientation similar to the slope are, in fact, overrated with remote survey despite of traditional geostructural survey. While with traditional geostructural survey, despite the troubles and dangers to access to the top parts of the slope, the operator can evaluate if different planes are part of a single discontinuities, the remote geostructural survey, both in case of manual methods for the extraction of the discontinuities, and in case of semiautomatic methods, makes it difficult to attribute different planes to a single surface. For this reason, the remote geostructural survey introduces a bias related to the orientation of the slope because the sets of discontinuities with orientation similar to the slope are overrated. The application of Terzaghi weighting to sets represented by planes could increase the bias related to the attribution issues of different planes to an only surface. The aspect variability so affects the feasibility of the discontinuities extraction methods: in case the surveyed slope is constituted by a slope with the same homogeneous orientation, manual methods could be preferable because of the detectability of traces too, besides planes.

The importance of the representation of slopes with different orientation to get the remote geostructural survey suggests that the characterisation of the rock mass is more accurate if slopes with different orientation are surveyed. This observation points the light also on an important aspect of the evaluation of semiautomatic or manual methods for the extraction of the discontinuities, the consume of time. The weight of the consume of time on the balance of the feasibility of the geostructural survey differs from manual to semiautomatic methods, and in case of manual methods, the number of discontinuities present on the studied surface increases it in a linear way. Higher the extension of the surface and the areal concentration of the discontinuities, higher the consume of time with manual methods for the discontinuities extraction. Semiautomatic methods are, instead, less time-consuming, because once set the extraction parameters (operation that requires a careful analysis and validation of the results), the process requires a low data processing time, varying on the base of the dimension of the point cloud and on the computing power. The elaboration of large point clouds, of course, requires high computing power to keep low the amount of time necessary for the data processing. The adoption of a semiautomatic method or of a manual method, depends so on the extent of the studied slope and on its structural complexity: i.e., in our experience, the survey of about 3000 discontinuities on the slopes of case study 1 has required about 60 working hours, while on average the semiautomatic methods used in this research have required one full working day per slope. The necessity of a rapid assessment in emergency condition could suggest the use of a manual or a semiautomatic method in base of the number of discontinuities present on the slope and so on the scale of the stability issue. The suggestion of carrying out the extraction of the discontinuities performed with semiautomatic methods taking into account benches with different orientation (at least 2, if possible perpendicular) so does not greatly

affect the time overall necessary for the geostructural survey, that is anyway less than the time necessary for a structural survey carried out with the manual extraction of the discontinuities.

Manual extraction of discontinuities requires the personal judgement of the operator. For this reason, manual extraction is not an objective procedure, which could lead to neglect smallest surfaces and investigate only those discontinuities, which appear important in the eyes of the operator. The background and the expertise of the operator affects the results. Indeed, the drawing of discontinuities is not systematic and for this reason the same feature could be signed twice, both as planes and as the associated traces; on the other side, the optical support to manual methods for the extraction of the discontinuities is a useful overview to understand that two or more planes, physically divided, are part of the same discontinuity. Although the expert judgement is fundamental as validation of the geostructural survey anyway, manual methods for the extraction of the discontinuities provide less subjective results, although extraction output have to be validated from the observed discontinuities. A detailed geostructural survey of an accessible part of the slope is so highly recommended; in case the direct access to the slope is strictly forbidden, the merging of the manual and semiautomatic methods is useful to reduce the bias related to the operator and to keep into account also small planes, that could be neglected in case of a survey on a large slope with manual methods.

2D and 3D kinematic analysis have been performed on the slopes of the two case studies. 2D kinematic analysis has been performed on the stereoplots of the discontinuities extracted by SiroJoint, I-Site Studio, DiAna, and Facets, given an average slope orientation, described for the two case studies in Chapter 6 and in Chapter 7. The comparison of the values of the kinematic indices for plane failure, wedge failure, block toppling, and flexural toppling has shown that the values for failure mechanisms involving planes only (plane failure and flexural toppling) are higher in case of semiautomatic methods of discontinuities extraction than in case of manual methods. These differences are related to the traces detection, which pole is not included into the critical areas for plane failure or for flexural toppling. Generally traces are more responsible than planes for failure mechanism related to critical intersection, such as wedge failure and block toppling. The values of the kinematic indices for wedge failure and block toppling are, in fact, higher for the dataset of discontinuities extracted using manual methods. The comparison of the values of the kinematic indices for discontinuities extracted with manual and semiautomatic methods has confirmed the adoption of the surveying of slopes with different orientation. Carrying out the geostructural survey on a slope with the same orientation with semiautomatic methods could, in fact, make the kinematic indices for wedge failure and block toppling underrated, and to the kinematic indices for plane failure and flexural toppling overrated.

3D kinematic analysis, performed with DiAna-K, has provided the susceptibility map of rockfall and indicated the most probable failure mechanism calculating the values of the kinematic indices since the local orientation of the mesh of the slope 3D model. Plane failure is the most probable failure mechanism on the triangles of the mesh with an orientation similar to the average slope orientation, while wedge failure is the most probable failure mechanism on the triangles which orientation is normal to the average slope orientation.

Finally, the slope stability has been assessed by comparing and integrating the results of the analysis of the stability of the blocks with SiroModel (CSIRO, 2017), with the 3D kinematic analysis carried out by DiAna- K (Gigli et al., 2012; 2014). The distribution of the volume of the blocks and the maximum volume, obtained with SiroModel, have been then compared and validated with the volumes of the blocks sampled by Casagrande (2012) at the base of highwall 1 of case study 1 mine. The maps of the vulnerability carried out by DiAna-K have been confronted with the optical image in order to detect the detachment niches and validate the failure mode of past rockfall events. The knowledge of the position of the most critical sectors thanks to the 3D kinematic analysis performed by DiAna-K (Chapter 6.3 and 7.3) and to the observation of the detachment niches from the optical images (Chapter 6.4 and 7.4), together with the knowledge of the volume distribution of unstable blocks and to the number of unstable blocks provide fundamental information for further rockfall simulations.

The stochastic distribution of the sets of discontinuities obtained with the geostructural survey carried out with SiroJoint has been used to build the fracture network inside the rock mass with SiroModel. SiroModel has allowed to evaluate the removability of the blocks using the block Theory of Goodman & Shi (1985) and the FOS thanks to the Limit Equilibrium Method described by Hoek & Bray (1981). Indeed, the volumes of the blocks have been validated by comparing the maximum volume of the blocks related to Type I (unstable) and to Type II (stable thanks to friction) of Goodman & Shi classification performed on a significant number of simulations with the maximum volume sampled at the base of the bench by Casagrande (2012) and with the volume of the unstable blocks and of the detachment niches evaluated with the optical images. The comparison has shown that the maximum volume of Type I blocks obtained is lower than the maximum volume of the blocks sampled at the base of one of the highwall. The smaller volume of the maximum volume of Type I blocks compared to the maximum measured volume could be related to the and so an overrating of the number of discontinuities. SiroModel has indeed allowed to split out the blocks of each case study by the number of contacts planes, subdividing the blocks prone to edge failure (with two contact planes) from the blocks prone to plane failure (one contact plane only). The number of contact planes of removable blocks for case study 1 and for case study 2 suggests that the presence of a greater number of sets and so of a more scattered discontinuities framework, makes wedge failure more probable than plane failure because of the higher percentage of critical intersections.

To summarise, the following conclusions have been pointed out:

- The results of the thesis provide useful points to choose semiautomatic or manual methods for discontinuities extraction for the geostructural characterisation of the rock mass. Manual methods for discontinuities extraction allow to individuate both planes and traces thanks to the optical support, while semiautomatic methods allow to extract planes only. The geostructural survey carried out with manual methods for the extraction of discontinuities are so more accurate; nevertheless, the carrying out of the geostructural survey on slopes with different orientation allows, also in case of semiautomatic methods for the discontinuities extraction, a more accurate description of the framework of the discontinuities within the rock mass;
- The results of the discontinuities extraction with semiautomatic methods are more affected than the results carried out with manual methods from the variability of the aspect of the slope. For this reason, the feasibility of semiautomatic methods is related also to the presence of a slope with different orientations of the surface and semiautomatic methods are more recommended in case of a natural slope than in case of manmade cut, in which the aspect is less scattered. The influence of the variability of the aspect with the geostructural characterisation of the rock mass suggest, in case of survey on manmade slope, the execution of the survey on slopes with different orientation;
- Both manual and semiautomatic methods for the extraction of the discontinuities could overrate the number of discontinuities outcropping as planes, with on orientation similar to the orientation of the slope. For this reason, carrying out the geostructural survey on slopes with different orientation is recommended also in case of use of manual methods for the extraction of the discontinuities;
- The use of a manual despite of a semiautomatic method does not affect the consume of time in case of a geostructural survey carried out on a small dataset of discontinuities, while in case of a great number of discontinuities semiautomatic methods are less time-consuming. The benefit to perform the geostructural survey on slopes with different orientation increases this gap;
- Finally, the integration of 3D kinematic analysis with the stability analysis of the removable blocks allows to get fundamental parameter, together with the high-definition 3D model of the slope, for the further rockfall modelling, permitting a more reliable description of the paths, of the height and of the kinetic energy of the blocks, increasing the mine safety conditions.

Acknowledgements

Firstly, I would like to express my sincere gratitude to my advisor Prof. Giovanni Gigli (University of Florence) for the continuous support of my Ph.D study and related research and for the trust he placed in me.

I would like to thank the Faculty of Engineering and Built Environment of the University of Newcastle for the opportunity to bring out the research and to have hosted me, providing the technical and informatic support (licenses for Maptek I-Site Studio and for SiroVision). In particular, I am grateful to Prof. Anna Giacomini (University of Newcastle), coAdvisor of the thesis, for her support, the development proposals of the research and the thought suggestions. Dr Klaus Thoeni (University of Newcastle) and Dr Marina Santise (University of Newcastle) have provided their skilled technical support for the building and the georeferencing of the 3D model of the rockslopes and for the carrying out of the photogrammetric surveys of the rockslopes. Dr Davide Casagrande (University of Newcastle) and Mr Andrea Magnani (University of Newcastle) have provided a useful trainee for the use of SiroVision and a critical comparison of the geostructural results. Dr Mark Elmouttie (CSIRO) has provided a valid support for the elaborations with SiroVision and SiroModel.

Bibliography

Abellán A., Jaboyedoff M., Oppikofer T., & Vilaplana J. M. (2009). Detection of millimetric deformation using a terrestrial laser scanner: experiment and application to a rockfall event. Nat. Hazard. Earth Syst. 9: 365-372.

Abellán, A., Vilaplana, J., Calvet, J., García-Sellés, D., & Asensio, E. (2011). Rockfall monitoring by Terrestrial Laser Scanning-Case study of the basaltic rock face at Castellfollit de la Roca (Catalonia, Spain). Nat. Hazard. Earth Syst. 11: 829-841.

Aitchison, J. C., Flood, P. G., & Spiller, F. C. P. (1992). Tectonic setting and paleoenvironment of terranes in the southern New England orogen, eastern Australia as constrained by radiolarian biostratigraphy. Palaeogeography, Palaeoclimatology, Palaeoecology, 94(1-4): 31-54.

Alzo'ubi, A., Martin, C. D., & Cruden, D. M. (2007). A discrete element damage model for rock slopes. In 1st Canada-US Rock Mechanics Symposium. American Rock Mechanics Association.

Antonello, G., Casagli, N., Farina, P., Leva, D., Nico, G., Sieber, A. J., & Tarchi, D. (2004). Ground-based SAR interferometry for monitoring mass movements. Landslides, 1(1): 21-28.

Baecher, G. B., Lanney, N.A., & Einstein, H.H. (1977). Statistical description of rock properties and sampling. 18th US Symp. On Rock Mech., Colorado School of Mines, Golden CO, 5C1: 1-8.

Baker, B. R., Gessner, K., Holden, E., & Squelch, A. (2008). Automatic detection of anisotropic features on rock surfaces. Geosphere, 4(2): 418-428.

Bandis, S., Lumsden, A.C., & Barton, N.R. (1981). Experimental studies of scale effects on the shear behaviour of rock joints. International journal of rock mechanics and mining sciences & geomechanics abstracts, 18(1): 1-21.

Barker, R., Dixon, L., & Hooke, J., (1997). Use of terrestrial photogrammetry for monitoring and measuring bank erosion. Earth Surface Processes and Landforms, 22: 1217-1227.

Barton, N. R. (1973). Review of a new shear-strength criterion for rock joints. Engineering geology, 7(4): 287-332.

Barton, N. R., Lien, R., & Lunde, J. (1974). Engineering classification of rock masses for the design of tunnel support. Rock mechanics, 6(4): 189-236.

Barton, N.R., & Choubey, V. (1977). The shear strength of rock joints in theory and practice. Rock mechanics, 10(1-2): 1-54.

Barton, N. R., & Bandis, S. (1982). Effects of block size on the shear behavior of jointed rock. In The 23rd US symposium on rock mechanics (USRMS) of the American Rock Mechanics Association, Chapter 76 Issues in Rock Mechanics, 739-760.

Barton, N. R., & Bandis, S. C. (1990). Review of predictive capabilities pf JRC-JCS model in engineering practice. In Rock Joints, Proceedings int symp on rock joints, Loen, Norway, Eds N. *Barton and O. Stephenson,* 603-610.

Barton, N. R. (2013). Shear strength criteria for rock, rock joints, rockfill and rock masses: Problems and some solutions. Journal of Rock Mechanics and Geotechnical Engineering, 5(4): 249-261.

Basden, H. (1969). Sydney Basin - Greta Coal Measures. Journal of the Geological Society of Australia, 16: 323-330.

Beach, A., & McLeod, G. (2007). U.S. Patent No. 7,296,638. Washington, DC: U.S. Patent and Trademark Office.

Beckett, J. (1988). The Hunter Coalfield notes to accompany the 1: 100 000 Hunter Coalfield geological map. Coal Geology Branch - Department of Mineral Resources Report GS1988/051.

Beer A.J., Stead D., & Coggan J. S. (2002). Technical note estimation of the joint roughness coefficient (JRC) by visual comparison. Rock Mech. Rock Eng., 35: 65-74.

Bembrick, C., Herbert, C., Scheibner, E., & Stuntz, J. (1980). Depositional development of the Sydney Basin. In: Herbert, C., & Helby., (1980). A guide to the Sydney Basin. Geological Survey of New South Wales Bulletin, 26: 3-9.

Betts, H. D., DeRose, R. C. (1999). Digital elevation models as a tool for monitoring and measuring gully erosion. International Journal of Applied Earth Observation and Geoinformation, 1(2): 91-101.

Bieniawski, Z. T. (1989). Engineering rock mass classifications: a complete manual for engineers and geologists in mining, civil, and petroleum engineering. John Wiley & Sons, 258 pp.

Bird, S., Hogan, D., Schwab, J. & (2010). Photogrammetric monitoring of small streams under a riparian forest canopy. Earth Surface Processes and Landforms, 35: 952-970.

Bishop, A. W. (1955). The use of the slip circle in the stability analysis of slopes. Geotechnique, 5(1): 7-17.

Blanch, X., Guinau, M., & Royàn, M. J. (2017). Caracterización geomorfológica y estructural de zonas de salida de bloques en una pared rocosa afectada por desprendimientos. IX Simposio Nacional sobre Taludes y Laderas Inestables, Santander.

Booker, F.W. (1957). Studies in Permian sedimentation in the Sydney Basin. Technical Reports of the NSW Department of Mines, 5: 10-62.

Borkowski, A., Perski, Z., Wojciechowski, T., Jóźków G., & Wójcik, A. (2011). Landslides mapping in Roznow Lake vicinity, Poland using airborne laser scanning data. Acta Geodyn. Geomater, 8: 325-333.

Branagan, D. F., McElroy, C. T., & Packham, G. H. (1967). Field geology of New South Wales, Science Press, 191 pp.

Brasington, J., & Smart, R. M. A. (2003). Close range digital photogrammetric analysis of experimental drainage basin evolution. Earth Surface Processes and Landforms, 28(3), 231-247

Brideau, M. A., & Stead, D. (2010). Controls on block toppling using a three-dimensional distinct element approach. Rock Mechanics and Rock Engineering, 43(3): 241-260.

Britten, R. A. (1972). A review of the stratigraphy of the Singleton Coal Measures and its significance to coal geology and mining in the Hunter Valley region of New South Wales. Newcastle Conference AusIMM, 1: 11-22.

Cai, M., & Horii, H. (1992). A constitutive model of highly jointed rock masses. Mech. Mater. 13, 217-246.

Cai, M., Kaiser, P.K., Uno, H., Tasaka, Y., & Minami, M. (2004). Estimation of rock mass deformation modulus and strength of jointed hard rock masses using the GSI system. International Journal of Rock Mechanics and Mining Sciences, 41(1): 3-19.

Chan, L., & Goodman, R. (1983). Prediction of support requirements for hard rock excavations using key-block theory and joint statistics. 24th Symposium on Rock Mechanics, Austin.

Chandler, J. (1999). Effective application of automated digital photogrammetry for geomorphological research. Earth Surface Processes and Landforms, 24(1): 51-63.

Chandler, J. H., Ashmore, P., Paola, C., Gooch, M., & Varkaris, F. (2002). Monitoring river channel change using terrestrial oblique digital imagery and automated digital photogrammetry. Annals of the Associated of American Geographers, 92: 631-644.

Clark, N. R., & Jones, D. C. (1991). Penrith 1:100 000 Geological Sheet 9030, 1st edition. Geological Survey of New South Wales, Sydney.

Colquhoun, G., Cameron, R., Meakin, S., Hendrickx, M., & Vassallo, J. (2004). Stratigraphy and structure of the Cargelligo region, central Lachlan Orogen, NSW. Abstracts of the Geological Society of Australia, 73: 150.

Corsini, A. Borgatti, L., Cervi, F., Dahne, A., Ronchetti, F., Sterzai, P. (2009). Estimating mass-wasting processes in active earth slides - earth flows with time-series of High-Resolution DEMs from photogrammetry and airborne LiDAR. Natural Hazards and Earth System Sciences, 9: 433-439.

Cowan, E. J., Beatson, R. K., Fright, W. R., McLennan, T. J., & Mitchell, T. J. (2002). Rapid geological modeling. In: Applied Structural Geology for Mineral Exploration and Mining, International Symposium, 23-25 September 2002, Kalgoorlie.

Creech, M., & Rigby, R. (2006). Revision of the Wollombi Coal Measures. Minfo, 81: 24-25.

Cruden, D. M., & Hu, X. (1994). Topples on underβ slopes in the Highwood Pass, Alberta, Canada. Quarterly Journal of Engineering Geology, 27: 57-68.

CSIRO (2017) SiroModel User Manual. Document Version of August 2017.

Danis, C., O'Neill, C., Lackie, M., Twigg, L., & Danis, A. (2011). Deep 3D structure of the Sydney Basin using gravity modelling. Australian Journal of Earth Sciences, 58(5): 517-542.

David, T. W. E. (1896). Evidences of glacial action in Australia in Permo-Carboniferous time: Geol. Soc. London Quart. Jour., 85: 289-301.

de Caritat, P., & Braun, J. (1992). Cyclic development of sedimentary basins at convergent plate margins. Structural and tectono-thermal evolution of some Gondwana basins of eastern Australia. Journal of Geodynamics, 16(4): 241-282.

Deere, D. U. (1964). Technical description of rock cores for engineering purpose. Rock Mechanics and Engineering Geology, 1(1): 17-22.

Deere, D. U., & Miller, R. P. (1966). Engineering classification and index properties for intact rock. Illinois Univ., Dept. of Civil Engineering, 327 pp.

Deere, D. U., Hendron, A. J., Patton, F. D., & Cording, E. J. (1966). Design of surface and near-surface construction in rock. In The 8th US symposium on rock mechanics (USRMS) of the American Rock Mechanics Association, Minneapolis.

Dershowitz, W. S. (1985). Rock Joint Systems. Massachusetts Institute of Technology, 918 pp.

Dershowitz, W. S., & Einstein, H. H. (1988). Characterizing rock joint geometry with joint system models. Rock Mech. Rock. Eng., 21: 21-51.

Dewez, T. J., Girardeau-Montaut, D., Allanic, C., & Rohmer, J. (2016). Facets: a CloudCompare plugin to extract geological planes from unstructured 3D point clouds. The International Archives of the Photogrammetry, Remote Sensing and Spatial Information Sciences, Volume XLI-B5, 2016 XXIII ISPRS Congress, 12-19 July 2016, Prague, Czech Republic. International Archives of the Photogrammetry, Remote Sensing & Spatial Information Sciences, 41.

Dewez, T. J., Yart, S., Thuon, Y., Pannet, P., & Plat, E. (2017). Towards cavity-collapse hazard maps with Zeb-Revo handheld laser scanner point clouds. The Photogrammetric Record, 32(160): 354-376.

Dhillon, B. S. (2008). Mining equipment reliability, maintainability, and safety. Springer Science & Business Media, 201 pp.

Đomlija P., Bernat S., Mihalić-Arbanas S., & Benac Č. (2014). Landslide inventory in the area of Dubračina River Basin (Croatia). In Landslide Science for a Safer Geoenvironment; Sassa K., Canuti P., Yin Y., Eds.; Springer: Berlin, Germany, 2: 837-842.

Dotta, G., Gigli, G., Ferrigno, F., Gabbani, G., Nocentini, M., Lombardi, L., Agostini A., Nolesini T., & Casagli, N. (2017). Geomechanical characterization and stability analysis of the bedrock underlying the Costa Concordia cruise ship. Rock Mechanics and Rock Engineering, 50(9): 2397-2412.

Du S., Hu Y., & Hu X. (2009). Measurement of joint roughness coefficient by using profilograph and roughness ruler. J. Earth Sci., 20(5): 890–896.

Dunne, E. F. (1950). Brief history of the coal mining industry in Queensland. Journal of the Royal Historical Society of Queensland, 4(3): 313-339.

Einstein, H. H., Veneziano, D., Baecher, G.B., O'Reilly, K.J. (1983). The effect of discontinuity L on 633 rock slope stability. International Journal of Rock Mechanics and Mining Sciences & Geomechanics Abstr., 20: 227-236.

Elmouttie, M., Poropat, G., & Krähenbühl, G. (2010a) Polyhedral modelling of rock mass structure. Int. J. Rock Mech. Min. Sci., 47: 544-552.

Elmouttie, M., Poropat, G., & Krähenbühl, G. (2010b) Polyhedral modelling of underground excavations. Comput. Geotech., 37: 529-535.

Elmouttie, M., & Poropat, G. (2011) A method to estimate in situ block size distribution. Rock Mech. Rock Eng., 37: 529-535.

El-Soudani, S.M. (1978). Profilometric analysis of fractures. Metallography, 11(3): 247-336.

Engel, B., Roberts, J., Roy, P.S., & Chapman, J. (1991a). Camberwell 1:100 000 Geological Sheet 9333, 1st edition. Geological Survey of New South Wales, Sydney.

Engel, B., Roberts, J., Roy, P. S., & Chapman, J. (1991b). Bulahdelah 1:100 000 Geological Sheet 9333, 1st edition. Geological Survey of New South Wales, Sydney.

Evans, P. R., & Migliucci, A., (1991). Evolution of the Sydney Basin during the Permian as a foreland basin to the Currarong and New England orogens. Advances in the Study of the Sydney Basin, Abstracts of the 25th Newcastle Symposium, 22-29. University of Newcastle, Department of Geology.

Fairbridge, R.W. (1953). Australian Stratigraphy. XII chaps, University of Western Australia. Text Books Board, 2nd edition

Fanti, R., Gigli, G., Lombardi, L., Tapete, D., & Canuti, P. (2013). Terrestrial laser scanning for rockfall stability analysis in the cultural heritage site of Pitigliano (Italy). Landslides, 10(4): 409-420.

Fardin, N., Stephansson, O., & Jing, L. (2001). The scale dependence of rock joint surface roughness. International Journal of Rock Mechanics and Mining Sciences, 38(5): 659-669.

Fardin, N. (2008). Influence of structural non-stationarity of surface roughness on morphological characterization and mechanical deformation of rock joints. Rock Mech. Rock. Eng., 41: 267–297.

Fellenius, W. (1936). Calculations of the Stability of Earth Dams. Proceedings of the Second Congress of Large Dams, Washington DC, 4: 445-463.

Feng, Q.H., & Röshoff, K. (2004). In-situ mapping and documentation of rock faces using a full-coverage 3D laser scanner technique. Int. J. Rock Mech. Min. Sci., 41 (3): 139-144.

Ferrero, A.M., Forlani, G., Roncella, R., & Voyat, H.I. (2009). Advanced geostructural survey methods applied to rock mass characterization. Rock Mechanics and Rock Engineering, 42(4): 631-665.

Fielding, C. R., Frank, T. D., Birgenheier, L. P., Rygel, M. C., Jones, A. T., & Roberts, J. (2008). Stratigraphic imprint of the Late Palaeozoic Ice Age in eastern Australia: a record of alternating glacial and nonglacial climate regime. Journal of the Geological Society, 165(1): 129-140.

Fisher, R. A. (1953). Dispersion on a sphere. Proc. R. Soc. Lond. A., 217(1130): 295-305.

Foden, J., Elburg, M.A., Smith, P.B., Dougherty-Page, J., & Burtt, A. (2006). The timing and duration of the Delamerian orogeny: correlation with the Ross Orogen and implications for Gondwana assembly. The Journal of Geology, 114: 189-210.

Franklin, J.A., Senior, S.A., & Marinos, P. (1997). The Ontario rockfall hazard rating system. In Proceedings of the conference on engineering geology and environment, Athens, 647-658.

Fuenkajorn, K. (2005). Predictability of Barton's Joint Shear Strength Criterion Using Field-Identification Parameters. Suranaree J. Sci. Tech., 12: 296-308.

Geoscience Australia And Australian Stratigraphy Commission, 2014. Australian Stratigraphic Units Database. http://www.ga.gov.au/products-services/data-applications/reference-databases/stratigraphic-units.html

Giacomini, A., Thoeni, K., Kniest, E., & Lambert, C. (2011). In situ experiments of rockfall in an open pit coal mine. Proceeding of slope stability.

Giacomini, A., Lambert, C., & Thoeni, K. (2012). Improved management of the rockfall hazard at the base of the highwalls. ACARP project report C, 19026.

Giani, G. P. (1992). Rock slope stability analysis. CRC Press, 367 pp.

Giani, G. P. (1997). Caduta di massi. Hevelius Edizioni, 218 pp.

Gigli, G., Frodella, W., Mugnai, F., Tapete, D., Cigna, F., Fanti, R., Intrieri, E., & Lombardi, L. (2012a). Instability mechanisms affecting cultural heritage sites in the Maltese Archipelago. Natural hazards and earth system sciences., 12(6): 1883-1903.

Gigli, G., Mugnai, F., Leoni, L., Casagli, N. (2009). Analysis of deformations in historic urban areas using terrestrial laser scanning. Natural Hazards and Earth System Science, 9: 1759-61.

Gigli, G., & Casagli, N. (2011). Semi-automatic extraction of rock mass structural data from high resolution LIDAR point clouds. Int. J. Rock Mech. Min. Sci., 48(2): 187-198.

Gigli, G., Frodella, W., Garfagnoli, F., Morelli, S., Mugnai, F., Menna, F., & Casagli, N. (2014). 3-D geomechanical rock mass characterization for the evaluation of rockslide susceptibility scenarios. Landslides, 11(1): 131-140.

Gigli, G., Morelli, S., Fornera, S., & Casagli, N. (2014). Terrestrial laser scanner and geomechanical surveys for the rapid evaluation of rockfall susceptibility scenarios. Landslides, 11(1): 1-14.

Girard, J. M. (2001). Assessing and monitoring open pit mine highwalls. Proceedings of the 32nd Annual Institute on Mining Health, Safety and Research, Salt Lake City, Utah, 159-171.

Girard, J. M., & McHugh, E. (2000). Detecting problems with mine slope stability. 31st Annual Institute on Mining Health, Safety, and Research, Roanoke, VA, Also NIOSHTIC Report, (10006193).

Glaessner, M., & Daily, B. (1963). The geology of Late Precambrian of the Ediacara fossil reserve. Rec. S. Aus. Mus., 13: 369 - 401.

Glen, R. A. (1992). Thrust, extensional and strike-slip tectonics in an evolving Palaeozoic orogen-a structural synthesis of the Lachlan Orogen of southeastern Australia. Tectonophysics, 214(1-4): 341-380.

Glen, R. A., Belousova, E., & Griffin, W.L. (2016). Different styles of modern and ancient non-collisional orogens and implications for crustal growth: a Gondwanaland perspective. Canadian Journal of Earth Sciences, 53(11): 1372-1415.

Glen, R. A. (2005). The Tasmanides of eastern Australia. In: Vaughan, A.P.M., Leat, P.T., Pankhurst, R.J. (Eds.), Terrane Processes at the Margins of Gondwana. Geological Society, Special Publication, 246: 23-96.

Glencore (2014). Ulan Coal Mines Limited Annual environment review, 1 January 2013 - 31 December 2013, 169 pp.

Goodman, R. E. (1976). Toppling of rock slopes. In: Proc. Speciality Conference on rock engineering for foundation and Slopes. ASCE, Boulder (Colorado), 2: 201-234.

Goodman, R. E., & Shi, G. H. (1985). Block theory and its application to rock engineering Englewood Cliffs, NJ: Prentice-Hall, 26(1): 103-105.

Goodman, R. E. (1995). Block theory and its application. In Proc. of 35th US Symposium on Rock Mechanics (edited by JJK Daemen & RA Schultz). AA Balkema. Rotterdam, 3-15.

Goodman, R. E. (1989). Introduction to Rock Mechanics: John Wiley & Sons, New York, 562 pp.

Gordon, A., Fenton, & Griffiths, V. D. (2008). Risk assessment in geotechnical engineering. John Wiley & Sons, 480 pp.

Grasselli, G., Wirth, J., & Egger, P. (2002). Quantitative three-dimensional description of a rough surface and parameter evolution with shearing, International Journal of Rock Mechanics and Mining Sciences, 39(6): 789-800.

Grasselli G., & Egger P. (2003). Constitutive law for the shear strength of rock joints based on three-dimensional surface parameters. Int. J. Rock Mech. Min. Sci., 40(1): 25-40.

Grevenitz, P., Carr, P., & Hutton, A. (2003). Origin, alteration and geochemical correlation of Late Permian airfall tuffs in coal Measures, Sydney Basin, Australia International Journal of Coal Geology, 55(1): 27-46

Hack, H. R. G. K. (1998). Slope Stability Probability Classification vol. 43. ITC Delft Publication, Enschede, Netherlands, 273 pp.

Hancock, G. R., Willgoose, G. R., (2001). The production of digital elevation models for experimental model landscapes. Earth Surface Processes and Landforms, 26: 475-490.

Haneberg, W. C., Norrish, N. I., & Findley, D. P. (2006). Digital outcrop characterization for 3-D structural mapping and rock slope design along interstate 90 near Snoqualmie Pass, Washington. In Proceedings, 57th annual highway geology symposium, Breckenridge, Colorado, 27-29.

Haneberg, W. C. (2007). Directional roughness profiles from three-dimensional photogrammetric or laser scanner point clouds. In Rock mechanics: meeting society's challenges and demands. Proceedings of the 1st Canada-US rock mechanics symposium, Vancouver, Canada, 101-106.

Haneberg, W. C. (2008). Using close range terrestrial digital photogrammetry for 3-D rock slope modeling and discontinuity mapping in the United States. Bulletin of Engineering Geology and the Environment, 67(4): 457-469.

Haneberg, W.C. (2005). 3-D digital rock mass discontinuity characterization using high-resolution photogrammetric or laser scanner point clouds. Geol. Soc. America Abstr. Prog., 37(7): 245.

Harrison, J. P. (2008). Contributions to Geotechnique 1948–2008: engineering geology rock mechanics and rock engineering. Geotechnique, 58(5): 449-555.

Hatzopoulos, J. N., Stefanakis, D., Georgopoulos, A., Tapinaki, S., Pantelis, V., & Liritzis, I. (2017). Use of various surveying technologies to 3d digital mapping and modelling of cultural heritage structures for maintenance and restoration purposes: The Tholos in Delphi, Greece. Mediterranean Archaeology & Archaeometry, 17(3), 331-366.

Hatzor, Y., & Goodman, R. E. (1992). Application of Block Theory and the critical key block concept in tunnelling; two case histories. In Proc. Int. Soc. Rock Mech. conf. on fractured and jointed rock masses, 632-639.

Hawley, S. P. & Brunton, J. S. (1995). The Newcastle Coalfield. Department of Mineral Resources New South Wales Report GS1995/256.

Heeswijck, A. V. (2001). Sequence stratigraphy of coal-bearing, high-energy clastic units: the Maitland-Cessnock-Greta Coalfield and Cranky Corner Basin. Australian Journal of Earth Sciences, 48(3): 417-426.

Hencher, S. R. (2012). Discussion of Alejano, Gonzalez and Muralha (2012). Rock Mech. Rock. Eng., 45(6): 1137-1139.

Heng, B. C. P., Chandler, J.H., & Armstrong, A. (2010). Applying close-range digital photogrammetry and soil erosion studies. The Photogrammetric Record, 25: 240-265.

Herbert, C., & West, J.L. (1983). Sydney, New South Wales,1:100 000 geological series map sheet 9130. 1st edition. (Map attached to "Geology of the Sydney 1:100 000 sheet 9130" edited by C. Herbert)., Geological Survey of New South Wales, 1v.

Herbert, C., & Helby, R. (1980). A guide to the Sydney Basin. Geological Survey of New South Wales Bulletin 26. Department of Mineral Resources, New South Wales, 603 pp.

Herbert, C. (1972). Palaeodrainage patterns in the southern Sydney Basin. Record of the Geological Survey of New South Wales, 14: 5-18.

Herbert, C. (1970). A synthesis of Narrabeen Group nomenclature, Sydney Basin., Geological Survey of New South Wales. Quarterly Notes, 1: 3-10.

Hoek, E., & Bray, J.W. (1981). Rock Slope Engineering Revised 3rd edition, The Institution of Mining and Metallurgy, London, 358 pp.

Hoek, E. (2000). Practical rock engineering, 341 pp.

Hoek, E., & Brown, E.T. (1980). Underground excavations in rock. CRC Press, 526 pp.

Hoek, E., & Brown, E.T. (1997). Practical estimates of rock mass strength. International journal of rock mechanics and mining sciences, 34(8): 1165-1186.

Hoek, E., Carranza-Torres, C., & Corkum, B. (2002). Hoek-Brown failure criterion-2002 edition. Proceedings of NARMS-Tac, 1: 267-273.

Hocking, G. (1976). A method for distinguishing between single and double plane sliding of tetrahedral wedges International Journal of Rock Mechanics and Mining Sciences & Geomechanics Abstr., 13: 225 - 226.

Hsiung S. M., Ghosh A., Ahola M. P., & Chowdhury A. H. (1993). Assessment of conventional methodologies for joint roughness coefficient determination. Int. J. Rock Mech. Min. Sci., Geomech Abstr, 30(7): 825-829.

Hudson, J. A., Harrison, J. P. (1997). Engineering rock mechanics: an introduction to the principles and Applications. Pergamon ed., Oxford, 456 pp.

Hunt, G. R. (1977). Spectral signatures of particulate minerals in the visible and near infrared. Geophysics, 42(3): 501-513.

Iakovlev, D., Sirkiä, J., Kallio, P. & Uotinen, L. (2016). Determination of joint mechanical parameters for stability analysis in low stress open pit mines. International Society for Rock Mechanics and Rock Engineering, ISRM International Symposium on In-Situ Rock Stress, Tampere 10-12 May 2016, Finland.

Idemitsu Kosan Ltd (2010). Idemitsu Australian resources, Muswellbrook Coal Mine. Viewed 31st October 2018, http://www.idemitsu.com.au/uploads/files/Marketing_MCC_brochure_2.pdf.

Inama, R. (2016). Geological mapping and multiscalar fracture analysis of some Tepuis of the Gran Sabana (Venezuela) by using remote sensing techniques, Master's thesis, University of Padua.

Ives, M., Brunton, J., Edwards, J., Rigby, R., Tobin, C., Weber, C. R. (1999). Revision of the stratigraphy of the Newcastle Coal Measures Coalfield Geology Council of New South Wales. Bulletin, 1: 113-119.

Jaboyedoff, M., Metzger, R., Oppikofer, T., Couture, R., Derron, M.H., Locat, J., & Turmel, D. (2007). New insight techniques to analyze rock-slope relief using DEM and 3D-imaging cloud points: COLTOP-3D software. In: Rock mechanics: meeting society's challenges and demands. Proceedings of the 1st Canada-U.S. rock mechanics symposium, Vancouver, Canada, May 27-31 2007, Eberhardt, E, Stead, D, Morrison, T, editors. London: Taylor & Francis, 61-8.

Jaboyedoff, M., Oppikofer, T., Locat, A., Locat, J., Turmel, D., Robitaille, D., Demers, D., & Locat P. (2009). Use of ground-based LIDAR for the analysis of retrogressive landslides in sensitive clay and of rotational landslides in river banks. Can. Geotech. J., 46: 1379-1390.

Jaboyedoff, M., Oppikofer, T., Minoia, R., Locat, J., Turmel, D. (2008). Terrestrial LIDAR investigation of the 2004 rockslide along Petit Champlain Street, Québec City (Québec, Canada). In: J. Locat, D. Perret, D. Turmel, D. Demers et S. Leroueil, (2008). Comptes rendus de la 4e Conférence canadienne sur les géorisques: des causes à la gestion. Proceedings of the 4th Canadian Conference on Geohazards: From Causes to Management. Presse de l'Université Laval, Québec, 594 pp.

Janbu, N. (1954). Stability analysis of Slopes with Dimensionless Parameters. Thesis for the Doctor of Science in the Field of Civil Engineering, Harvard University Soil Mechanics Series, 46, 81 pp.

Jing, L. (2000). Block system construction for three-dimensional discrete element models of fractured rocks. Int. J. Rock. Mech. Min Sci., 37: 645-659.

Joplin, G. A., Griffin, R. J., Hall, L. R., McElroy, C. T., Rayner, E. O., Stevens, N. C., & Burrows, P. M. (1956). Sydney, New South Wales, 4-mile geological series. Sheets SI/56-05 & SI/56-06, 1st edition., Bureau of Mineral Resources, Australia, 1.

Joplin, G. A., Hanlon, F. N., & Noakes, L. C. (1952). Wollongong N.S.W. 1:250 000 geological series explanatory notes., Bureau of Mineral Resources, Australia.

Kemeny, J., Norton, B., & Turner, K. (2006). Rock slope stability analysis utilizing ground-based LiDAR and digital image processing. Felsbau, 24(3).

Krosley, L. K., Shaffner, P. T., Oerter, E., & Ortiz, T. (2006). Digital ground-based photogrammetry for measuring discontinuity orientations in steep rock exposures. Proceedings of the 41st U.S. Symposium of Rock Mechanics. Golden, Colorado, 1-13.

Lambert, C., Thoeni, K., Giacomini, A., Casagrande, D., & Sloan, S. W. (2012). Rockfall hazard analysis from discrete fracture network modelling with finite persistence discontinuities. Rock mechanics and rock engineering, 45(5): 871-884.

Lane, S. N. (2000). The measurement of river channel morphology using digital photogrammetry. The Photogrammetric Record, 16: 937-961.

Lato, M., Diederichs, M., Hutchinson, D. J., Harrap, R. (2009). Optimization of LiDAR scanning and processing for automated structural evaluation of discontinuities in rock masses. Int. J. Rock Mech. Min., 46: 194-199.

Laubscher, D. H. (1991). A geomechanics classification system for rating of rock mass in mine design. J. S. Afr. Inst. Min. Metall., 90(10): 257-273.

Lee, S., Suh, J., & Choi, Y. (2018). Review of smartphone applications for geoscience: current status, limitations, and future perspectives. Earth Science Informatics, 11: 463-486.

Li, F.K., & Goldstein, R.M. (1990). Studies of multibaseline spaceborne interferometric synthetic aperture radars. IEEE Transactions on Geoscience and Remote Sensing, 28(1): 88-97.

Lichti, D., Stewart, M. P., Tsakiri, M., & Snow, A. J. (2000). Calibration and testing of a terrestrial laser scanner. International archives of Photogrammetry and Remote sensing, 33(B5/2; PART 5): 485-492.

Liu, K., Boult, P., Painter, S., & Paterson, L. (1996). Outcrop analog for sandy braided stream reservoirs: permeability patterns in the Triassic Hawkesbury Sandstone, Sydney Basin, Australia. AAPG bulletin, 80(12): 1850-1865.

Lombardi, L. (2007). Nuove tecnologie di rilevamento e di analisi di dati goemeccanici per la valutazione della sicurezza. Universita degli studi di Firenze, Unedited PhD Thesis.

Lu, J. (2002). Systematic identification of polyhedral rock blocks with arbitrary joints and faults. Computers & Geotechnics, 29: 49-72.

Luyendyk, B. P. (1995). Hypothesis for Cretaceous rifting of East Gondwana caused by subducted slab capture. Geology, 23(4): 373-376.

Lyman, G. (2003). Stereological and Other Methods Applied to Rock Joint Size Estimation - Does Crofton's Theorem Apply?. Mathematical Geology, 35(1): 9-23.

Maerz, N. H., Franklin, J. A., & Bennett, C. P. (1990). Joint roughness measurement using shadow profilometry, International Journal of Rock Mechanics and Mining Sciences and Geomechanics. Abstracts, 27(5): 329-343.

Markland, J. T. (1972). A useful technique for estimating the stability of rock slopes when the rigid wedge slide Type of failure is expected. Interdepartmental Rock Mechanics Project, Imperial College of Science and Technology, 9 pp.

Massiot, C., Nicol, A., Townend, J., McNamara, D. D., Garcia-Sellés, D., Conway, C. E., & Archibald, G. (2017). Quantitative geometric description of fracture systems in an andesite lava flow using terrestrial laser scanner data. Journal of Volcanology And Geothermal Research, 341: 315-331.

Matheson, G. D. (1983). Rock stability assessment in preliminary site investigations-Graphical Methods. Transport and Road Research Laboratory Report 1039. Transport and Road Research Laboratory, Crowthorne, Berkshire, 24 pp.

Mayne, S. J., Nicholas, E., Bigg-Wither, A.L., Rasidi, J.S. & Raine, M. J. (1974). Geology of the Sydney Basin-a review. Bulletin of the Bureau of Mineral Resources, Geology and Geophysics, 229 pp.

McClung, G. R. (1980). Permian marine sedimentation in the northern Sydney Basin. Bulletin of the Geological Survey of New South Wales, 26: 54-72.

McElroy, C. T. (1957). Sydney N.S.W., 4-mile geological series explanatory Notes (first edition), Bureau of Mineral Resources, Australia, 1v.

Meffre, S., Scott, R. J., Glen, R. A., & Squire, R. J. (2007). Re-evaluation of contact relationships between Ordovician volcanic belts and the quartz-rich turbidites of the Lachlan Orogen. Australian Journal of Earth Sciences, 54(2-3): 363-383.

Metcalfe, I., Crowley, J. L., Nicoll, R. S., & Schmitz, M. (2015). High-precision U-Pb CA-TIMS calibration of middle Permian to lower Triassic sequences, mass extinction and extreme climate-change in eastern Australian Gondwana. Gondwana Research, 28(1): 61-81.

Miall, A. D., & Jones, B. G. (2003). Fluvial architecture of the Hawkesbury sandstone (Triassic), near Sydney, Australia. Journal of Sedimentary Research, 73(4): 531-545.

Miller, S. M., Girard, J. M., & McHugh, E. (2000). Computer modeling of catch benches to mitigate rockfall hazards in open pit mines In Pacific Rocks 2000, Proc. of 4th N. Amer. Rock Mech. Symp., eds. J. Girard, M. Liebman, C. Breeds, T. Doe, Rotterdam: Balkema, 539-545.

Mills. K. J. (2002). Relationship between the Delamerian and the Lachlan fold belts in western New South Wales. Abstract of the Geological Society of Australia, 67: 136.

Mills. K. J. (2003). Composition and structure of the Koonenberry region. In: Peljo M. (ed.) Broken Hill Exploration Initiative, Geoscience Australia, Camberra, Record 2003/13, 116-119

Monserrat, O., & Crosetto, M. (2008). Deformation measurement using terrestrial laser scanning data and least squares 3D surface matching. ISPRS Journal of Photogrammetry and Remote Sensing, 63: 142-154.

Monte, J. M. (2004). Rock mass characterization using laser scanning and digital imaging data collection techniques. M.S. thesis of geological engineering. University of Arizona, Tucson, 2004. .

Morgenstern, N. R., & Price, V. E. (1965). The Analysis of the Stability of General Slip Surfaces. Geotechnique, 15(1): 77-93.

Morishima, K., Kuno, M., Nishio, A., Kitagawa, Manabe, Y., Moto, M., Takasaki, F., Fujii, H., Satoh, K., Kodama, H., Hayashi, K., Odaka, S., Procureur, S., Attié, D., Bouteille, S., Calvet, D., Filosa, C., Magnier, P., Mandjavidze, I., Riallot, M., Marini, B., Gable, P., Date, Y., Sugiura, M., Elshayeb, Y., Elnady, T., Ezzy, M., Guerriero, E., Steiger, V., Serikoff, N., Mouret, J-B., Charlès, B., Helal, H., & Tayoubi, M. (2017). Discovery of a big void in Khufu's Pyramid by observation of cosmic-ray muons. Nature, 552(7685): 386.

Myers, N. O. (1962) Characteristics of surface roughness. Wear, 5: 182-189.

Nashar, B. (1964). The geology of the Hunter Valley (Possible coal seams to be indexed at a later date), Jacaranda Press, 49 pp.

Nebel-Jacobsen, Y., Münker, C., Nebel, O., Gerdes, A., Mezger, K., & Nelson, D. R. (2010). Reworking of Earth's first crust: constraints from Hf isotopes in Archean zircons from Mt. Narryer, Australia. Precambrian Research, 182(3): 175-186.

Norvick, M. S., Langford, R. P., Hashimoto, T., Rollet, N., Higgins, K. L., & Morse, M. P. (2008). New insights into the evolution of the Lord Howe Rise (Capel and Faust basins), offshore eastern Australia, from terrane and geophysical data analysis. PESA Eastern Australasian Basins Symposium III, Sydney, 14-17 September 2008, 291-309.

Olsen, M. J., Kuester, F., Chang, B. J., & Hutchinson, T. C. (2009). Terrestrial laser scanning-based structural damage assessment. Journal of Computing in Civil Engineering, 24(3): 264-272.

Oppikofer T., Jaboyedoff M., Blikra L., Derron M. H., & Metzger R. (2009). Characterization and monitoring of the Aknes rockslide using terrestrial laser scanning. Nat. Hazards Earth Syst. Sci., 9: 1003-1009.

Ord, A., & Cheung, C. C. (1991). Image analysis techniques for determining the fractal dimensions of rock joint and fragment size distributions. In Proceedings of the International Conference on Computer Methods and Advances in Geomechanics, Cairns. AA Balkema, Rotterdam, 87-91.

Othman, R., & Ward, C. R. (2002). Thermal maturation pattern in the southern Bowen, northern Gunnedah and Surat basins, northern New South Wales, Australia. International Journal of Coal Geology, 51(3): 145-167.

Packham, G. H. (1969). The geology of New South Wales. Journal of Geological Society of Australia, 16: 654.

Palmström, A. (1982). The volumetric joint count-a useful and simple measure of the degree of rock jointing. Proc. 4th Int. Cong. Int. Assoc. Eng. Geol, 5: 221-228.

Palmström, A. (1995). RMi-a system for characterization of rock masses for rock engineering purposes. Ph.D. thesis, University of Oslo, Norway, 408 pp.

Palmström, A. (1996). The weighted joint density method leads to improved characterization of jointing. In Conference on recent advances in tunnelling technology, New Delhi.

Palmström, A. (2001). Measurement and characterization of rock mass jointing. In Palmstrom, A., Sharma, V.I., & Saxena K. (eds). In situ characterization of rocks. Balkema, 1-40.

Palmström, A. (2005). Measurements of and correlations between block size and rock quality designation (RQD). Tunnelling and Underground Space Technology, 20(4): 362-377.

Percival, I. G., & Glen, R. A. (2007). Ordovician to earliest Silurian history of the Macquarie Arc, Lachlan Orogen, New South Wales. Australian Journal of Earth Sciences, 54(2-3): 143-165.

Percival, I. G., Meakin, S., Sherwin, L., & Flitcroft, P. A. (2012). Permian fossils and palaeoenvironments of the northern Sydney Basin, New South Wales. Geological Survey of New South Wales. , Maitland, 23 pp.

Pierson, L. A., Davis, S. A., & Van Vickle, R. (1990). Rockfall Hazard Rating System Implementation Manual, Oregon, 1990.

Pinetown, K. L. (2012). Geological controls on coal seam gas distribution in the Hunter Coalfield, Sydney Basin, NSW. University of New South Wales, Sydney, Australia.

Poropat, G. V. (2009). Measurement of surface roughness of rock discontinuities. Rock Engineering in Difficult Conditions. In ROCKENG09: Proceedings of the 3rd CANUS Rock Mechanics Symposium, Toronto.

Porter, M., Baumgard, A., & Savigny, K. W. (2002). A hazard and risk management system for large rock slope hazards affecting pipelines in mountainous terrain. In American Society of Mechanical Engineers, 4th International Pipeline Conference, 871-879.

Pratt, H. R., Black, A. D., Brace, W. F. (1974). Friction and deformation of jointed quartz diorite. Advances in Rock Mechanics: 3rd Congress of the International Society for Rock Mechanics. National Academy of Sciences, Denver, 306–310.

Priest, S. D., & Hudson, J. (1976). Discontinuity spacings in rock. International Journal of Rock Mechanics and Mining Sciences & Geomechanics Abstr., 13: 135-148.

Priest, S. D., & Hudson, J. (1981). Estimation of discontinuity spacing and trace length using scanline survey. International Journal of Rock Mechanics and Mining Sciences & Geomechanics Abstr., 18: 183-197.

Priest, S. D. (1993). Discontinuity analysis for rock engineering. Chapman & Hall (eds), London, 472 pp.

Prokop, A., & Panholzer, H. (2009). Assessing the capability of terrestrial laser scanning for monitoring slow-moving landslides. Nat. Hazards Earth Syst. Sci., 9: 1921-1928.

Puppala, A. J., Congress, S. S., Bheemasetti, T. V., & Caballero, S. R. (2018). Visualization of Civil Infrastructure Emphasizing Geomaterial Characterization and Performance. Journal of Materials in Civil Engineering, 30(10), 04018236.

Pyle, C. J., Richards, K. S., & Chandler, J. H. (1997). Digital photogrammetric monitoring of river bank erosion. The Photogrammetric Record, 15: 753-764.

Rahman, Z., Slob, S., & Hack, R. (2006). Deriving roughness characteristics of rock mass discontinuities from terrestrial laser scan data. Proceedings of the 10th IAEG Congress, ''Engineering geology for tomorrow's cities''. Nottingham, United Kingdom: Geological Society of London; 6-10 September, paper 437, 12 pp.

Rasmus, P. L., Rose, D.M., & Rose, G. (1969). Singleton 1:250 000 Geological Sheet SI/56-01, 1st edition, Geological Survey of New South Wales, Sydney.

Redfern, J., Hodgetts, D., & Fabuel-Perez I. (2007). Digital analysis brings renaissance for petroleum geology outcrop studies in North Africa First Break, 25: 81 - 87.

Reinhold, J. (1963). Revised Stratigraphy of the Greta Coal Measures in the South Maitland Coalfield. Joint Coal Board Report CR63/3 (unpubl.).

Renard, F., Coisin, C., Marsan, D., & Schmittbuhl, J. (2006). High resolution 3D laser scanner measurements of a strike-slipe fault quantify its morphlogical anisotropy at all scales. Geoph. Res. Lett., 33: 1-4.

Rieke-Zapp, D.H., Nearing, M.A. (2005). Digital close range photogrammetry for measurement of soil erosion. The Photogrammetric Record, 20: 69-87.

Riquelme, A.J., Tomás, R., & Abellán, A. (2016a). Characterization of rock slopes through slope mass rating using 3D point clouds. International Journal of Rock Mechanics and Mining Sciences, 84: 165-176.

Riquelme, A., Cano, M., Tomás, R., & Abellán, A. (2016b). Using open-source software for extracting geomechanical parameters of a rock mass from 3D point clouds: Discontinuity Set Extractor and SMRTool. Rock Mech. Rock Eng. From Past to Futur, 2: 1091-1096.

Riquelme, A., Cano, M., Tomás, R., & Abellán, A. (2017). Identification of Rock Slope Discontinuity Sets from Laser Scanner and Photogrammetric Point Clouds: A Comparative Analysis. Procedia engineering, 191: 838-845.

Riquelme, A., Tomás, R., Cano, M., Pastor, J.L., & Abellán, A. (2018). Automatic Mapping of Discontinuity L on Rock Masses using 3D Point Clouds. Rock Mechanics and Rock Engineering, 51: 3005-3028.

Roberts, J. (1965). Lower Carboniferous zones and correlation based on faunas from the Gresford-Dungog district, New South Wales., Geological Society of Australia. Journal, 12: 105 - 122.

Roberts, J., Engel, B., Lennox, M., & Chapman, J. (1991a). Dungog 1:100 000 Geological Sheet 9233, 1st edition. Geological Survey of New South Wales, Sydney.

Roberts, J., Engel, B., & Chapman, J. (1991b). Geology of the Camberwell, Dungog, and Bulahdelah 1:100,000 Sheets 9133, 9233, 9333. New South Wales Geological Survey, Sydney, 382 pp.

Roberts, J., & Geeve, R. (1999). Allochthonous forearc blocks and their influence on an orogenic timetable for the Southern New England Orogen. New England Orogen: regional geology, tectonics and metallogenesis, 105-114.

Roberts, J., Offler, R., & Fanning, M. (2006). Carboniferous to Lower Permian stratigraphy of the southern Tamworth Belt, southern New England Orogen, Australia: boundary sequences of the Werrie and Rouchel blocks. Australian Journal of Earth Sciences, 53(2): 249-284.

Romana, M. (1991). SMR classification. In: Wittke, W. Ed. Proceedings 7th Cong. on rock mechanics, ISRM, Aachen, Germany. Balkema, Rotterdam, 955-960.

Rosser, N. J., Petley, D. N., Lim, M., Dunning, S. A., & Allison, R. J. (2005). Terrestrial laser scanning for monitoring the process of hard rock coastal cliff erosion. Quarterly Journal of Engineering Geology and Hydrogeology, 38(4): 363-375.

Rowland, S. M., Duebendorfer, E. M., & Schiefelbein, I. M. (2013). Structural analysis and synthesis: a laboratory course in structural geology. John Wiley & Sons, 320 pp.

Rust, B. R., & Jones, B. G. (1987). The Hawkesbury Sandstone south of Sydney, Australia: Triassic analogue for the deposit of a large, braided river. Journal of Sedimentary Research, 57(2): 222-233.

Sagy, A., Axen, G. J., & Brodsky, E. E. (2005). LIDAR measurements of fault roughness. Eos Trans. AGU 86(52) Fall Meet uppl.: T14B-02.

Salisbury, J. W., & Walter, L. S. (1989). Thermal infrared (2.5-13.5 μm) spectroscopic remote sensing of igneous rock types on particulate planetary surfaces. Journal of Geophysical Research: Solid Earth, 94(B7): 9192-9202.

Sampaleanu, C., Stead, D., Donati, D., Griffiths, C., D'Ambra, S., & LeBreton, R. (2017). Characterizing Brittle Fracture Induced Rockfall in an Open Sub-Level Retreat Excavation. In 51st US Rock Mechanics/Geomechanics Symposium. American Rock Mechanics Association.

Santi, P. M., Russell, C. P., Higgins, J. D., & Spriet, J. I. (2009). Modification and statistical analysis of the Colorado rockfall hazard rating system. Engineering Geology, 104(1-2): 55-65.

Santise, M., Thoeni, K., Roncella, R., Diotri, F., & Giacomini, A. (2018). Analysis of low-light and night-time stereo-pair images for photogrammetric reconstruction. Int. Arch. Photogramm. Remote Sens. Spatial Inf. Sci., 42(2): 1015-1022

Sarma, S. K. (1979). Stability analysis of embankments and slopes. Journal of Geotechnical and Geoenvironmental Engineering, 105(ASCE 15068).

Schenk, T. (2005). Introduction to photogrammetry. The Ohio State University, Columbus, 106 pp.

Slee, K. J. (1968). The geology of the Cranky Corner Basin, NSW. BSc (Hons) thesis, University of Newcastle, Newcastle (unpubl.).

Slob S., & Hack, R. (2004). 3D terrestrial laser scanning as a new field measurement and monitoring technique. In Engineering geology for infrastructure planning in Europe. Springer, Berlin, Heidelberg, 179-189.

Slob, S. (2008). Automated rock mass characterisation using 3D terrestrial laser scanning. PhD thesis, University of Delft, 301 pp.

Smith, H.G. (1891). On the occurrence of Barite (Barytes) in the Hawkesbury Sandstone, near Sydney., Proceedings of the Linnean Society of New South Wales, 6(2), 131-132.

Sniffin, M., & Beckett, J. (1995). Sydney Basin - Hunter Coalfield. In: Ward CR, Harrington HJ, Mallett CW and Beeston JW (eds). Geology of Australian Coal Basins. Geological Society of Australia Incorporated, Coal Group Special Publication No. 1. Geological Society of Australia, Coal Geology Group, Sydney, 177-195.

Spencer, E. (1967). A method of analysis of the stability of embankments assuming parallel interslice forces. Geotechnique. London, 17(1): 11-26.

Standing Committee Coalfield Geol. NSW, 1986, Stratigraphy of the Jerrys Plains Subgroup of the Wittingham Coal Measures in the Singleton-Muswellbrook Coal District of the Hunter Valley., Geological Survey of New South Wales, Records, 22(1): 129-143.

Stead, D., Wolter, A., & Clague, J. J. (2011). A Critical Review of Landslide Failure Mechanisms. In AGU Fall Meeting Abstracts.

Stephenson, A. E., & Burch, G. J. (2004). Preliminary Evaluation of the Petroleum Potential of Australia's Central East Margin Geoscience Australia. Record 2004/06, 69 pp.

Stojic, M., Chandler, J. H., Ashmore, P., & Luce, J. (1998). The assessment of sediment transport rates by automated digital photogrammetry. Photogrammetric Engineering and Remote Sensing, 64(5): 387-395.

Stroud, W.J., Sherwin, L., Roy, H.N., & Baker, C.J. (1985). Wollongong-Port Hacking 1:100 000 Geological Sheet 9029-9129, 1st edition. Geological Survey of New South Wales, Sydney.

Sturzenegger, M., Yan, M., Stead, D., & Elmo, D. (2007). Application and limitations of ground-based laser scanning in rock slope characterization. In: Eberhardt, E., Stead, D., Morrison, T. (Eds.), Proceedings 1st Canada-U.S. Rock Mechanics Symposium, Vancouver, May 27-31 2007, 29-36.

Sturzenegger, M., & Stead, D. (2009a). Close-range terrestrial digital photogrammetry and terrestrial laser scanning for discontinuity characterization on rock cuts. Engineering Geology, 106(3-4): 163-182.

Sturzenegger, M., & Stead, D. (2009b). Quantifying discontinuity orientation and persistence on high mountain rock slopes and large landslides using terrestrial remote sensing techniques. Natural Hazards and Earth System Sciences, 9(2): 267-287.

Sturzenegger, M., Stead, D., Beveridge, A., Lee, S., & van As, A. (2009). Long-range terrestrial digital photogrammetry for discontinuity characterization at Palabora open-pit mine. InThird Canada-US Rock Mechanics Symposium. Paper, 3984.

Suchowerska, A.M. (2014). Geomechanics of single-seam and multi-seam longwall coal mining. University of Newcastle, University of Newcastle, PhD thesis.

Süssmilch, C.A., & David, S.T.W.E. (1919). Sequence, glaciation and correlation of the Carboniferous rocks of the Hunter River district, New South Wales. Journal and Proceedings of the Royal Society of New South Wales, 53: 246-338. Swan, G., Zongqi, S. (1985). Prediction of shear behaviour of joints using profiles. Rock Mech. Rock. Eng., 18: 183–212.

Tadros, N. Z. (1993). The Gunnedah Basin, New South Wales (Vol. 12). Department of Mineral Resources, Coal & Petroleum Geology Branch, 649 pp.

Tadros, N. Z. (1995). Structure and tectonics of the Gunnedah Basin, N. S. W.: implications for stratigraphy, sedimentation and coal resources, with emphasis on the Upper Black Jack group. PhD thesis, University of Wollongong, 162 pp.

Tarchi, D., Casagli, N., Fanti, R., Leva, D.D., Luzi, G., Pasuto, A., Pieraccini, M., & Silvano, S. (2003). Landslide monitoring by using ground-based SAR interferometry: an example of application to the Tessina landslide in Italy. Engineering geology, 68(1-2): 15-30.

Tatone, B.S.A., & Grasselli, G. (2009). A method to evaluate the 3D roughness of fracture surface in brittle geo-materials. Rev. Sci. Instrum., 80(125): 1-10.

Tatone, B.S.A., & Grasselli, G. (2010). A new 2D discontinuity roughness parameter and its correlation with JRC. International Journal of Rock Mechanics and Mining Sciences, 47(8): 1391-1400.

Terzaghi, K. (1951). Theoretical soil mechanics. Chapman and Hall, Limited.; London, 510 pp.

Terzaghi, R.D. (1965). Sources of errors in joint surveys. Geotechnique, 15: 287-304.

Teza, G., Galgaro, A., Zaltron, N., & Genevois, R. (2007). Terrestrial laser scanner to detect landslide displacement fields: a new approach. International Journal of Remote Sensing, 28: 3425-3446.

Thiele, S.T., Grose, L., Samsu, A., Micklethwaite, S., Vollgger, S. A., & Cruden, A. R. (2017). Rapid, semi-automatic fracture and contact mapping for point clouds, images and geophysical data. Solid Earth, 8(6): 1241.

Thoeni, K., Giacomini, A., Sloan, S.W., Lambert, C., & Casagrande, D. (2011a). Numerical analysis of rockfall hazard in open pit coal mines.

Thoeni, K., Lambert, C., Giacomini, A., & Sloan, S.W. (2011b). Discrete modelling of a rockfall protective system. In Particle-Based Methods II: Fundamentals and Applications, IInd International Conference on Particlebased Methods, 24-32.

Thoeni, K., Irschara, A., & Giacomini, A. (2012). Efficient photogrammetric reconstruction of highwalls in open pit coal mines. In 16th Australasian remote sensing and photogrammetry conference, 85-90.

Thoeni, K., Giacomini, A., Murtagh, R., & Kniest, E. (2014). A comparison of multi-view 3D reconstruction of a rock wall using several cameras and a laser scanner. The International Archives of Photogrammetry, Remote Sensing and Spatial Information Sciences, 40(5): 573.

Thoeni, K., Renton, C., & Giacomini, A. (2016). A multirotor platform for mapping and inspecting sub-vertical rock faces. In EGU General Assembly Conference Abstracts, 18: 5264.

Thoma, T., Gupta, S.C., Bauer, M. E., Kirchoff, C.E. (2005). Airborne laser scanning for riverbank erosion assessment. Remote Sens. Environ., 95: 493-501.

Thomas, O.D., Johnston, A. J., Scott, M.M., Pogson, D.J., Sherwin L., & McRae, G.P. (2002). Goulburn 1:100000 Geological Sheet 8828, First Edition. Geological Survey of New South Wales, Orange and Sydney.

Tofani, V., Raspini, F., Catani, F., & Casagli, N. (2013). Persistent Scatterer Interferometry (PSI) technique for landslide characterization and monitoring. Remote Sensing, 5(3): 1045-1065.

Tonon, F., & Kottenstette, J.T. (2007). Laser and photogrammetric methods for rock face characterization. Report on a Workshop Held in Golden, Colorado, June 17-18, 2006. American Rock Mechanics Association (2007).

Trinks, I., Clegg P., McCaffrey K., Jones R., Hobbs R., Holdsworth B., Holliman N., Imber J., Waggott S., & Wilson R. (2006). Mapping and analyzing virtual outcrops. Visual Geosciences, 10: 13-19.

Tse, R., & Cruden, D.M. (1979). Estimating joint roughness coefficients, International Journal of Rock Mechanics and Mining Sciences and Geomechanics Abstracts., 16: 303-307.

Umwelt (2011). Environmental assessment, modification of Ulan Coal - continued operations, North 1 Underground mining area, minor modifications to Ulan No.3 and Ulan West Mine plans and proposed concrete batching plant.

Van Den Eeckhaut M., Poesen J., Verstraeten G., van Acker V., Nyssen J., Moeyersons J., van Beek L.P.H., Vandekerckhove L. (2007). The use of LIDAR-derived images for mapping old landslides under forest. Earth Surf. Process. 32: 754-769.

Van der Meer, F.D., Van der Werff, H.M., Van Ruitenbeek, F.J., Hecker, C.A., Bakker, W.H., Noomen, M.F., Mark van der Meijde, E., Carranza, J.M., Boudewijn de Smeth, J., & Woldai, T. (2012). Multi-and hyperspectral geologic remote sensing: A review. International Journal of Applied Earth Observation and Geoinformation, 14(1): 112-128.

Vasuki, Y., Holden, E.J., Kovesi, P., & Micklethwaite, S. (2014). Semi-automatic mapping of geological Structures using UAV-based photogrammetric data: An image analysis approach. Computers & Geosciences, 69: 22-32.

Vazaios, I., Vlachopoulos, N., & Diederichs, M.S. (2017). Integration of Lidar-based structural input and discrete fracture network generation for underground applications. Geotechnical and Geological Engineering, 35(5): 2227-2251.

Vaziri, A., Moore, L., & Ali, H. (2010). Monitoring systems for warning impending failures in slopes and open pit mines. Natural hazards, 55(2): 501-512.

Voisey, A.H. (1958). Clarke Memorial Lecture. Further remarks on the sedimentary formations of New South Wales, Royal Society of New South Wales. Journal and Proceedings, 91(4): 165-188.

Warburton, P. (1980). A stereological interpretation of joint trace data' Int. J. Rock. Mech. Min. Sci. & Geomech. Abstr., 17: 181-190.

Watts, C.F., Gilliam, D.R., Hrovatic, M.D., & Hongh (2003). User's Manual-ROCKPACK III for Windows: C.F. Watts and Associates, Radford, VA, 33 pp.

Westoby, M.J., Brasington, J., Glasser, N.F., Hambrey, M.J., & Reynolds, J.M. (2012). Structure-from-Motion'photogrammetry: A low-cost, effective tool for geoscience applications. Geomorphology, 179: 300-314.

Whetten, J. T. (1965). Carboniferous glacial rocks from the Werrie Basin, New South Wales, Australia. Geological Society of America Bulletin, 76(1): 43-56.

Whitehouse, F.W. (1926). Notes on Upper Palaeozoic Marine Horizons in Eastern and Western Australia., Australasian Association for the Advancement of Science, 18: 281.

Whyatt, J., Miller, S., & Dwyer, J.G. (2004). NIOSH computer programs for bench crest failure analysis in fractured rock.

Wickens, E.H., & Barton, N.R. (1971). The application of photogrammetry to the stability of excavated rock slopes. The Photogrammetric Record, 7(37): 46-54.

Wilde, S.A., Valley, J.W., Peck, W.H., & Graham, C.M. (2001). Evidence from detrital zircons for the existence of continental crust and oceans on the Earth 4.4 Gyr ago. Nature, 409(6817): 175.

Wolf P.R., & Dewitt B. A. (2000). Elements of Photogrammetry, with Applications in GIS (Third Edition), McGraw-Hill, Boston, 608 pp.

Wolf, P.R., Dewitt, B.A., & Wilkinson, B. E. (2000). Elements of Photogrammetry: with applications in GIS (Vol. 3). New York: McGraw-Hill, 640 pp.

Wu, L., Cui, C., Geng, N., & Wang, J. (2000). Remote sensing rock mechanics (RSRM) and associated experimental studies. International Journal of Rock Mechanics and Mining Sciences, 37(6): 879-888.

Wyllie, D.C., & Mah, C. (2014). Rock slope engineering. CRC Press, 456 pp.

Youssef, A., Maerz, N.H., & Fritz, M.A. (2003). A risk-consequence rockfall hazard rating system for Missouri highways. Highway Geology Symposium (HGS).

Zhang L, & Einstein H.H. (2000). Estimating the intensity of rock discontinuities. International Journal of Rock Mechanics and Mining Sciences, 762(37): 819-837.

Zhang, L., & Einstein, H.H. (1998). Estimating the mean trace length of rock discontinuities. Rock Mechanics and Rock Engineering, 31(4): 217-235.